

WEAR AND CORROSION STUDIES ON PLASMA SPRAYED Al_2O_3 REINFORCED HA COATINGS

A THESIS

*Submitted in partial fulfilment of the
requirements for the award of the degree*

of

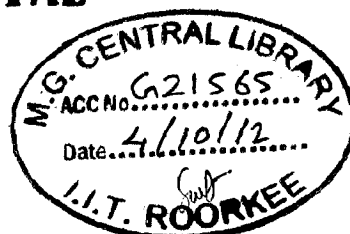
DOCTOR OF PHILOSOPHY

in

METALLURGICAL AND MATERIALS ENGINEERING

by

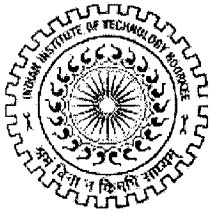
MANOJ MITTAL



DEPARTMENT OF METALLURGICAL AND MATERIALS ENGINEERING
INDIAN INSTITUTE OF TECHNOLOGY ROORKEE
ROORKEE-247 667 (INDIA)

DECEMBER, 2011

© INDIAN INSTITUTE OF TECHNOLOGY ROORKEE, ROORKEE, 2011
ALL RIGHTS RESERVED



INDIAN INSTITUTE OF TECHNOLOGY ROORKEE ROORKEE

CANDIDATE'S DECLARATION

I hereby certify that the work which is being presented in the thesis entitled "WEAR AND CORROSION STUDIES ON PLASMA SPRAYED Al_2O_3 REINFORCED HA COATINGS" in partial fulfilment of the requirements for the award of the Degree of *Doctor of Philosophy* and submitted in the Department of Metallurgical and Materials Engineering of the Indian Institute of Technology Roorkee, Roorkee is an authentic record of my own work carried out during a period from August, 2008 to December, 2011 under supervision of Dr. Sumeer K. Nath Professor and Dr. Satya Prakash, Emeritus Fellow, Department of Metallurgical and Materials Engineering, Indian Institute of Technology Roorkee, Roorkee.

The matter presented in the thesis has not been submitted by me for the award of any other degree of this or any other Institute.

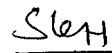

(MANOJ MITTAL)

This is to certify that the above statement made by the candidate is correct to best of our knowledge.

Dated: 28-12-2011



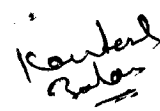
(Satya Prakash)
Supervisor



(Sumeer K. Nath)
Supervisor

The Ph. D. Viva-Voce Examination of **Manoj Mittal**, Research Scholar, has been held on May 31, 2012.


Signature of Supervisors


Signature of External Examiner

The implant and devices used in human body for repair or replacement of damaged organs are based on metals, ceramics and plastics. None of them (except bio-ceramics) make the natural union with bone and tissues in body environment, moreover release of metallic ions and plastic debris and subsequently their accumulation in tissues near implants cause severe pain and inflammation. This leads to requirement of revision surgery to replace the existing implant with new one. The wear rate of ultra high molecular weight polyethylene (UHMWPE) inner socket which articulates against metallic surfaces of cup and femur head in hip joint is as high as 100 $\mu\text{m}/\text{year}$. The poly-methyl-methacrylate (PMMA) bone cement used for joining implant to bone further restricts the service life of these implants in harsh body environment.

The interest of researchers and medical practitioner is changing towards the development of new techniques and materials to overcome the problems associated with conventional metallic-UHMWE articulating surface, which lead to shielding the metallic implant from corrosive body environment by application of coating and use of alumina-on-alumina bearings. Currently plasma spraying process is the only technique approved by Food and Drug Administration (FDA), USA to coat bio-ceramic materials. Since 2002, marketing of alumina-on-alumina articulating hips had been approved in USA.

In this view, after extensively studying the published literature, it is concluded that the possible, practical and reliable way to prevent corrosion of body implants in harsh body environment is the application of hydroxyapatite based composite coating with incorporation of intermediate layer of bond coat which have reliable resistance to wear and corrosion, adequate strength, ability to form natural bond with bone and surrounding tissues and allows no migration of metallic ions from substrate to coating. Very little literature is available regarding utilization of plasma sprayed hydroxyapatite-alumina composite coating and alumina-titania bond coat for biomedical applications is scarce in existing literature.

The current study elucidate effect of Al_2O_3 -13 wt% TiO_2 bond coat in reduction of elemental migration from substrate to coating, enhancement in bonding strength of coating and effect of alumina addition (0-30 wt%) on wear, hardness, bonding strength and corrosion behavior of composite coatings. The effect of post coating heat treatment on

incorporation of reinforcement (alumina) and provision of bond coat. The adhesive wear resistance of coatings (wear between similar articulating coatings) decreased with increase in alumina contents of HA composite coatings. The maximum value of tensile bond strength was recorded for HA-30 wt% Al_2O_3 coating with Al_2O_3 -13 wt% TiO_2 bond coat and minimum for pure HA coating without incorporation of bond coat.

The corrosion and precipitation/dissolution behavior of uncoated and coated specimens was studied in simulated body fluid. All the coatings offered better corrosion resistance as compared to bare substrates; moreover their corrosion current densities were nearly same irrespective of substrate, which suggested that coatings were protective and did not allow interaction of substrate with electrolyte. Most of the amorphous phases got dissolved in simulated body fluid after immersion period of 1 day; dissolution/precipitation occurred up to immersion period of 5 days and thereafter, precipitation of apatite layer was seen on the coating surface.

The coated specimens were subjected to post coating heat treatment at 500, 700 and 900°C in air for 2h in order to regain crystallinity of coatings. The crystallinity of coatings was found to increase with increase in post coating heat treatment temperature from 500°C to 900°C. Development of ultra-fine particles was observed after post coating heat treatment at 900°C for 2h. These ultra-fine particles have great affinity for bone bonding and bone in-growth.

ACKNOWLEDGEMENTS

The author is highly grateful to the Great and Gracious Almighty God who blessed him with spiritual support and fortitude at each and every stage of this work. The author feels a sense of privilege and pleasure to express his gratitude to Dr. Buta Singh, Dean Academics, Punjab Technical University, Jalandhar, Punjab, India for his valuable advice and positive reception to start the present work at Indian Institute of Technology Roorkee, Roorkee, without which author never thought to join such a institute of repute.

The author feels sense of privilege and pleasure to express his sense of gratitude to Dr. Satya Prakash, Emeritus Fellow and Dr. Sumeer K. Nath, Professor, Metallurgical and Materials Engineering Department (MMED), Indian Institute of Technology Roorkee, Roorkee for their valuable guidance and untiring efforts throughout the tenure of this work. They have been a source of inspiration and driving force to overcome to be difficulties faced by author. Their timely help, constructive criticism and painstaking efforts made the author capable of compiling the work in present form.

Nothing can be implemented in seclusion and the author is no exception to this rule. The author feels a sense of arrogance in taking this opportunity to express his sincere thanks to the diverse helping hands during the course of work. Author is highly grateful to Dr. Prakriti K. Ghosh, Head, MMED for his cooperation in extending the required facilities and support during entire span of this work. The author is indebted to Dr. Surendra Singh, Professor, Dr. G.P. Chaudhari, Assistant Professor, Dr. Vinay K. Tewari, Professor, MMED and Dr. Bhanu K. Mishra, Professor, Mechanical and Industrial Engineering Department, IIT Roorkee for their valuable suggestions and timely help during the course of this work. The author wishes to record his deep sense of gratitude to technical and administrative staff of Metallurgical and Materials Engineering Department, Institute Instrumentation Center and Department of Chemistry, IIT Roorkee, for assisting in performing necessary experimentation and analysis work.

The author is grateful to Dr. T.S. Sidhu, Director, Shaheed Bhagat Singh College of Engineering and Technology, Ferozpur, Punjab, India, Dr. Harpreet Singh, Assistant Professor, School of Mechanical, Materials and Energy Engineering, Indian Institute of Technology Ropar, Roopnagar, Punjab, India, Dr. Kantesh Balani, Assistant Professor, Department of Materials Science, Indian Institute of Technology Kanpur, Kanpur, India and Dr. Hiroaki Takadama, Associate Professor, Department of Biomedical Sciences, College of Life and Health Sciences, Chubu University, Japan for their timely help during the course of

PREFACE

The entire work carried out for this investigation has been presented in nine chapters.

Chapter-1 contains the introductory remarks about the materials used for repair/replace the damaged tissues in human body, their bone bonding ability and their limitations. The requirement of bioceramic coatings and methods adopted for improvement in their mechanical properties is briefly discussed.

Chapter-2 presents the extensive literature review on orthopedic and dental implant materials, their failure mechanism, various joint simulator and wear testing equipments, role of coatings, coating deposition techniques. The need of coating on metallic body implants, the coating techniques adopted to coat body implants, advantages and limitations of these techniques and post coating treatments are discussed.

Chapter-3 deals with the experimental part and presents the experimental techniques and details of the equipments used in current study. The procedures and equipment/machines employed for depositing the coatings, their characterization, evaluation of mechanical properties, corrosion and immersion behavior in SBF and post coating heat treatment have been discussed.

Chapter-4 presents the characterization studies which include the study related to morphology, roughness and porosity of coatings.

Chapter-5 includes the results of mechanical properties of coatings, which includes wear resistance of coating against 400 grit abrasive, between similar coatings, hardness of coating across substrate-coating interface and bonding strength evaluation.

Chapter-6 contains the results related to open circuit potential (OCP), linear polarization, potentiodynamic polarization and Tafel polarization tests on bare and coated specimens in simulated body fluid. The biocompatibility of coated specimens was studied by in vitro examination in SBF for immersion period of 5, 10, 15 and 20 days at a controlled temperature of $37\pm 1^\circ\text{C}$.

Chapter-7 deals with the characterization of post coating heat treated specimens. The coated specimens were heat treated at 500°C , 700°C and 900°C for 2h in air.

Chapter-8 includes the comprehensive discussions of the results obtained in present study.

Chapter-9 summarizes the conclusions from the results obtained within the present research and scope for future work.

CONTENTS

	Page No.
Candidates declaration	i
Acknowledgements	ii
Abstract	iv
Contents	vii
List of Figures	xiii
List of Tables	xxxii
List of publications	xxxiv
Abbreviations	xxxvi
Chapter 1 Introduction	1
Chapter 2 Literature Review	5
2.1 Orthopedic and dental implant materials	5
2.1.1 Metallic implant materials	5
2.1.2 Biomaterials based on Ca and P	9
2.1.2.1 Tri-calcium phosphate (TCP)	11
2.1.2.2 Tetra-calcium phosphate (TTCP)	12
2.1.2.3 Amorphous calcium phosphate (ACP)	13
2.1.2.4 Apatite	13
2.1.2.5 Porous and dense HA materials	14
2.1.2.6 HA based composites	16
2.1.2.7 HA based composite coatings	17
2.1.2.8 Bond coat	22
2.1.2.9 Significance of bone implant interface	25
2.1.2.10 Comparison of biological and synthetic HA	27
2.2 Failure mechanism of HA coatings	29
2.2.1 Failure mechanism of HA coatings	30
2.2.2 Unresolved issues of hydroxyapatite	34
2.2.3 Wear of body implants	35
2.2.4 Joint simulators	40
2.2.4.1 Six station rolling sliding tribotester	41
2.2.4.2 Howmedica biaxial line contact wear	42

3.4.1	Surface morphology and EDAX analysis	86
3.4.2	Cross-sectional analysis	86
3.4.3	X-ray mapping analysis	87
3.5	Thermo-gravimetric analysis/differential thermal analysis	87
3.6	Fourier transform infrared spectroscopy	87
3.7	X-ray diffraction (XRD) analysis	88
3.8	Mechanical properties of coatings	89
3.8.1	Measurement of microhardness	89
3.8.2	Measurement of bond strength	89
3.8.3	Tensile bond strength fixture	90
3.8.4	Wear resistance analysis of coatings	90
3.9	In-vitro study of coatings	93
3.9.1	Preparation of simulated body fluid	93
3.9.2	Electrochemical studies in simulated body fluid (SBF)	94
3.9.3	Experimental setup for in-vitro studies	97
3.10	Post coating heat treatment	98
Chapter 4	Characterization of coatings	101
4.1	Introduction	101
4.2	Results	101
4.2.1	Coating feedstock	101
4.2.2	Surface morphology of coatings	102
4.2.3	FE-SEM/EDAX analysis of coatings	109
4.2.3.1	Coating thickness	109
4.2.3.2	Porosity analysis of coatings	109
4.2.4	Surface roughness of coatings	110
4.2.5	X-ray mapping of coatings	116
4.2.5.1	Surface analysis	116
4.2.5.2	Cross-sectional analysis	116
4.2.6	X-ray diffraction (XRD) analysis of coatings	150
4.2.7	Fourier transform infrared (FTIR) spectroscopy of coatings	154
4.2.8	Thermo-gravimetric analysis/differential thermal	159

7.2	Results	261
7.2.1	Surface morphology and EDAX analysis of post coating heat treated specimens	261
7.2.2	X-ray diffraction analysis of post coating heat treated specimens	276
7.2.3	Surface morphology of post coating heat treated specimens	289
7.2.4	FTIR analysis of post coating heat treated specimens	301
7.3	Discussion	305
7.4	Conclusions	309
Chapter 8	Comprehensive discussion	311
8.1	Mechanical characterization	311
8.2	Studies in simulated body fluid	313
8.3	Post coating heat treatment	314
Chapter 9	Conclusions	323
9.1	Characterization of coatings	323
9.2	Mechanical properties of coatings	324
9.3	Corrosion and in-vitro studies in simulated body fluid	325
9.4	Recrystallization and grain refinement of coatings	327
	Scope for future work	329
	References	330

LIST OF FIGURES

Fig. No.	Caption of Figure	Page No.
Fig. 2.1	Model of an implanted total hip prosthesis, (Johnson, 2005)	8
Fig. 2.2	Flow chart showing the material related causes and the intermediate events leading up to implant loosening, (Bell Jr., 2004)	10
Fig. 2.3	Structure of hydroxyapatite projected down the c-axis onto basal plane, (Zhang, 2000)	15
Fig. 2.4	Interface of bone and HA coated implant	27
Fig. 2.5	Schematic representation of the events occurring at the bone implant interface: (a) Protein adsorption from tissue fluid and blood cell; (b) Inflammatory and connective tissue cells approach the implant; (c) Formation of a febrillar mineralized layer and adhesion of osteogenic cells; (d) Bone deposition on implant and bone surface; (e) Remodeling of newly formed bone by osteoclasts, (Moses et al., 2003)	28
Fig. 2.6	Micrographs showing osseointegration into HA coated implant, (Soballe, 1996)	28
Fig. 2.7	Micrographs showing the formation of a fibrous membrane on titanium implant and no membrane on HA coated titanium implant, (Soballe, 1996)	29
Fig. 2.8	Solubility isotherms for various phases in the system $\text{CaO-P}_2\text{O}_5\text{-H}_2\text{O}$ at 25°C, (Ray, 2004 and Raemdonck et al., 1984)	33
Fig. 2.9	Equilibrium diagram for hydroxyapatite, solid lines are pH invariant lines on the solubility surface and broken line separates the stability domain of various solution species, (Chander et al., 1979)	36
Fig. 2.10	Multi-station rolling sliding tribotester: (a) Macrograph of tribotester, (b) Contact conditions in one of the stations (Kennedy et al., 2007), (c) CAD model of one of the six stations, (Van Citters, 2004)	43
Fig. 2.11	Three stations of AMTI-Boston six station knee simulator, Model KS2-6-1000, (Advanced Mechanical Technology Inc., USA)	43

Fig. 2.26	Phase equilibrium diagram of calcium phosphates ($\text{CaO-P}_2\text{O}_5$) at high temperature in water atmosphere, (Klein et al., 1993)	65
Fig. 3.1	FESEM morphology and EDAX analysis of hydroxyapatite: (a) at lower magnification (100x) with EDAX analysis; (b) at higher magnification (400x)	81
Fig. 3.2	FESEM morphology and EDAX analysis of alumina-titania (Al_2O_3 -13 wt% TiO_2): (a) at lower magnification (100X) and (b) at higher magnification (1000X)	82
Fig. 3.3	FESEM morphology and EDAX analysis of aluminum oxide (Al_2O_3): (a) lower magnification (100X) and (b) higher magnification (1500X)	83
Fig. 3.4	Photograph of tensile bond strength fixture	91
Fig. 3.5	Schematic diagram specimen assembly and loading fixture used for tensile bond strength testing	92
Fig. 3.6	Schematic representation of penetration of adhesive (Glue) in the coating and mechanism of failure (Yang and Chang, 2003)	92
Fig. 3.7	Schematic illustration of 'Flat on disc' type wear testing equipment (not to the scale)	96
Fig. 3.8	Experimental setup for post coating heat treatment: (a) silicon tube furnace; (b) control unit and (c) specimen in alumina boat placed in silicon tube furnace	99
Fig. 3.9	Surface macrographs of coated specimens: (a) as-coated specimen and (b) post coating heat treated specimen at 900°C in air for 2h	100
Fig. 3.10	Cross-sectional macrograph of post coating heat treated specimen at 900°C in air for 2h	100
Fig. 4.1	FE-SEM image (400X) showing morphology of HA – 10 wt% Al_2O_3 : (a) particle morphology and EDAX analysis (wt% of elements) and (b) X-ray mapping	103
Fig. 4.2	FE-SEM image (400X) showing morphology of HA – 20 wt% Al_2O_3 : (a) particle morphology and EDAX analysis (wt% of elements) and (b) X-ray mapping	104
Fig. 4.3	FE-SEM image (400X) showing morphology of HA – 20 wt% Al_2O_3 : (a) particle morphology and EDAX analysis (wt% of elements) and (b) X-ray mapping	105

Fig. 4.17	FE-SEM image and X-ray mapping of surface of HA-10 wt% Al ₂ O ₃ coated titanium	122
Fig. 4.18	FE-SEM image and X-ray mapping of surface of HA-20 wt% Al ₂ O ₃ coated titanium	123
Fig. 4.19	FE-SEM image and X-ray mapping of surface of HA-30 wt% Al ₂ O ₃ coated titanium	124
Fig. 4.20	FE-SEM image and X-ray mapping of surface of HA coated AISI 316L SS with bond coat of Al ₂ O ₃ -13 wt% TiO ₂	125
Fig. 4.21	FE-SEM image and X-ray mapping of surface of HA-10 wt% Al ₂ O ₃ coated AISI 316L SS with bond coat of Al ₂ O ₃ -13 wt% TiO ₂	126
Fig. 4.22	FE-SEM image and X-ray mapping of surface of HA-20 wt% Al ₂ O ₃ coated AISI 316L SS with bond coat of Al ₂ O ₃ -13 wt% TiO ₂	127
Fig. 4.23	FE-SEM image and X-ray mapping of surface of HA-30 wt% Al ₂ O ₃ coated AISI 316L SS with bond coat of Al ₂ O ₃ -13 wt% TiO ₂	128
Fig. 4.24	FE-SEM image and X-ray mapping of surface of HA coated titanium with bond coat of Al ₂ O ₃ -13 wt% TiO ₂	129
Fig. 4.25	FE-SEM image and X-ray mapping of surface of HA-10 wt% Al ₂ O ₃ coated titanium with bond coat of Al ₂ O ₃ -13 wt% TiO ₂	130
Fig. 4.26	FE-SEM image and X-ray mapping of surface of HA-10 wt% Al ₂ O ₃ coated titanium with bond coat of Al ₂ O ₃ -13 wt% TiO ₂	131
Fig. 4.27	FE-SEM image and X-ray mapping of surface of HA-30 wt% Al ₂ O ₃ coated titanium with bond coat of Al ₂ O ₃ -13 wt% TiO ₂	132
Fig. 4.28	FE-SEM image and X-ray mapping of cross-section of HA coated AISI 316L SS	134
Fig. 4.29	FE-SEM image and X-ray mapping of cross-section of HA-10 wt% Al ₂ O ₃ coated AISI 316L SS	135
Fig. 4.30	FE-SEM image and X-ray mapping of cross-section of HA-20 wt% Al ₂ O ₃ coated AISI316L SS	136
Fig. 4.31	FE-SEM image and X-ray mapping of cross-section of HA-30 wt% Al ₂ O ₃ coated AISI 316L SS	137
Fig. 4.32	FE-SEM image and X-ray mapping of cross-section of HA coated titanium	138
Fig. 4.33	FE-SEM image and X-ray mapping of cross-section of HA-10 wt%	139

	wt% TiO ₂ bond coat: (a) HA coating; (b) HA-10 wt% Al ₂ O ₃ coating; (c) HA-20 wt% Al ₂ O ₃ coating and (d) HA-30 wt% Al ₂ O ₃ coating	
Fig. 4.49	X-ray diffraction pattern of as coated titanium with Al ₂ O ₃ -13 wt% TiO ₂ bond coat: (a) HA coating; (b) HA-10 wt% Al ₂ O ₃ coating; (c) HA-20 wt% Al ₂ O ₃ coating and (d) HA-30 wt% Al ₂ O ₃ coating	155
Fig. 4.50	FTIR spectra of feedstock for plasma spray coatings: (a) HA; (b) HA-10 wt% Al ₂ O ₃ ; (c) HA-20 wt% Al ₂ O ₃ ; (d) HA-30 wt% Al ₂ O ₃	156
Fig. 4.51	FTIR spectra of plasma spray coatings: (a) HA; (b) HA-10 wt% Al ₂ O ₃ ; (c) HA-20 wt% Al ₂ O ₃ ; (d) HA-30 wt% Al ₂ O ₃	157
Fig. 4.52	FTIR spectra of plasma spray coatings with Al ₂ O ₃ -13 wt% TiO ₂ bond coat: (a) HA; (b) HA-10 wt% Al ₂ O ₃ ; (c) HA-20 wt% Al ₂ O ₃ ; (d) HA-30 wt% Al ₂ O ₃	158
Fig. 4.53	DTA/TGA plot for hydroxyapatite powder	159
Fig. 4.54	DTA/TGA plot for HA-10 wt% Al ₂ O ₃ powder	160
Fig. 4.55	DTA/TGA plot for HA-20 wt% Al ₂ O ₃ powder	161
Fig. 4.56	DTA/TGA plot for HA-30 wt% Al ₂ O ₃ powder	162
Fig. 4.57	DTA/TGA plot for Al ₂ O ₃ powder	162
Fig. 5.1	Wear behavior of coatings against 400 grit abrasive	168
Fig. 5.2	Wear behavior of coatings against similar coatings	169
Fig. 5.3	FE-SEM image of surface of pure HA coatings after wear test against 400 grit abrasive at different magnifications: (a) at 100X; (b) at 300X; (c) at 500X; (d) at 1000X and (e) at 2500X	172
Fig. 5.4	FE-SEM image of surface of HA-10 wt% Al ₂ O ₃ coating after wear test against 400 grit abrasive at different magnifications: (a) at 300X; (b) at 800X; (c) at 1600X; (d) at 3000X; (e) at 5000X and (f) at 8000X	173
Fig. 5.5	FE-SEM image of surface of HA-20 wt% Al ₂ O ₃ coating after wear test against 400 grit abrasive at different magnifications: (a) at 100X; (b) at 300X; (c) at 500X; (d) at 1000X and (e) at 2500X	174
Fig. 5.6	FE-SEM image of surface of HA-30 wt% Al ₂ O ₃ coating after wear test against 400 grit abrasive at different magnifications: (a) at 100X; (b) at 300X; (c) at 500X; (d) at 1000X and (e) at 2000X	175
Fig. 5.7	FE-SEM image of surface of pure HA coating after wear test against pure HA coating at different magnifications: (a) at 500X; (b) at	176

	13 wt% TiO ₂ bond coat	
Fig. 5.17	Surface macrographs of coatings after ASTM C633 79 tensile test: (a) HA coating; (b) HA-10 wt% Al ₂ O ₃ coating; (c) HA-20 wt% Al ₂ O ₃ coating; (d) HA-30 wt% Al ₂ O ₃ coating; with Al ₂ O ₃ -13 wt% TiO ₂ bond coat (e) HA coating; (f) HA-10 wt% Al ₂ O ₃ coating; (g) HA-20 wt% Al ₂ O ₃ coating and (h) HA-30 wt% Al ₂ O ₃ coating	189
Fig. 5.18	FE-SEM image and X-ray mapping of fractured surface of pure HA coating	190
Fig. 5.19	FE-SEM image and X-ray mapping of fractured surface of pure HA coating with Al ₂ O ₃ -13 wt% TiO ₂ bond coat	191
Fig. 5.20	FE-SEM image and X-ray mapping of fractured surface of HA-10 wt% Al ₂ O ₃ coating	192
Fig. 5.21	FE-SEM image and X-ray mapping of fractured surface of HA-10 wt% Al ₂ O ₃ coating with Al ₂ O ₃ -13 wt% TiO ₂ bond coat	194
Fig. 5.22	FE-SEM image and X-ray mapping of fractured surface of HA-20 wt% Al ₂ O ₃ coating	195
Fig. 5.23	FE-SEM image and X-ray mapping of fractured surface of HA-20 wt% Al ₂ O ₃ coating with Al ₂ O ₃ -13 wt% TiO ₂ bond coat	196
Fig. 5.24	FE-SEM image and X-ray mapping of fractured surface of HA-30 wt% Al ₂ O ₃ coating	197
Fig. 5.25	FE-SEM image and X-ray mapping of fractured surface of HA-30 wt% Al ₂ O ₃ coating with Al ₂ O ₃ -13 wt% TiO ₂ bond coat	198
Fig. 6.1	Open circuit potential curves for uncoated and coated AISI 316L SS	206
Fig. 6.2	Open circuit potential curves for uncoated and coated titanium	207
Fig. 6.3	Potentiodynamic polarization curves for uncoated and coated AISI 316 L SS	210
Fig. 6.4	Potentiodynamic polarization curves for uncoated and coated titanium	211
Fig. 6.5	Tafel plot for uncoated and coated AISI 316L SS	213
Fig. 6.6	Tafel plot for uncoated and coated titanium	214
Fig. 6.7	Weight change (mg/cm ²) and Ca ²⁺ ion concentration (ppm) plots versus immersion period for pure HA coatings	215
Fig. 6.8	Weight change (mg/cm ²) and Ca ²⁺ ion concentration (ppm) plots versus immersion period for HA-10 wt% Al ₂ O ₃ coatings	216

- coating after immersion in SBF for 10 days: (a) at 250X; (b) at 500X; (c) at 1000X; (d) at 2000X and (e) EDAX surface analysis of (c)
- Fig. 6.21** FE-SEM micrographs and EDAX surface analysis of pure HA coating 231
after immersion in SBF for 15 days: (a) at 1000X; (b) at 2210X; (c) at 4000X (d); at 8000X; (e) at 2000X from different location and (f) EDAX surface analysis of (d)
- Fig. 6.22** FE-SEM micrographs and EDAX surface analysis of HA-10 wt% Al₂O₃ 232
coating after immersion in SBF for 15 days: (a) at 400X; (b) at 800X; (c) at 1600X; (d) at 3000X; (e) at 4000X and (f) EDAX surface analysis of (e)
- Fig. 6.23** FE-SEM micrographs and EDAX surface analysis of HA-20 wt% Al₂O₃ 233
coating after immersion in SBF for 15 days: (a) at 400X; (b) at 800X; (c) at 1500X; (d) at 3000X; (e) at 4000X and (f) EDAX surface analysis of (e)
- Fig. 6.24** FE-SEM micrographs and EDAX surface analysis of HA-30 wt% Al₂O₃ 234
coating after immersion in SBF for 15 days: (a) at 400X; (b) at 800X; (c) at 1600X; (d) at 3000X from different location and (e) EDAX surface analysis of (d)
- Fig. 6.25** FE-SEM micrographs and EDAX surface analysis of pure HA coating 237
after immersion in SBF for 20 days: (a) at 500X; (b) at 2500X; (c) at 2500X from different location; (d) at 5000X and (e) EDAX surface analysis of (d)
- Fig. 6.26** FE-SEM micrographs and EDAX surface analysis of HA-10 wt% Al₂O₃ 238
coating after immersion in SBF for 20 days: (a) at 500X; (b) at 4000X; (c) at 10000X and (d) EDAX surface analysis of (c)
- Fig. 6.27** FE-SEM micrographs and EDAX surface analysis of HA-20 wt% Al₂O₃ 239
coating after immersion in SBF for 20 days: (a) at 1000X; (b) at 4000X and (c) EDAX surface analysis of (b)
- Fig. 6.28** FE-SEM micrographs and EDAX surface analysis of HA-30 wt% Al₂O₃ 240
coating after immersion in SBF for 20 days: (a) at 200X; (b) at 400X; (c) at 6000X and (d) EDAX surface analysis of (c)
- Fig. 6.29** FESEM showing cross-sectional morphology of HA-30 wt% Al₂O₃ 241
coating after immersion in SBF for 1 day at different magnifications:

- Fig. 7.3** Surface morphology and EDAX point analysis from different spots on 266
 pure HA coated titanium: (a) as coated; (b) heat treated at 500° C
 for 2 h in air; (c) heat treated at 700° C for 2 h in air and (d) heat
 treated at 900° C for 2 h in air
- Fig. 7.4** Surface morphology and EDAX point analysis from different spots on 267
 pure HA coated titanium with bond coat of Al₂O₃ – 13 wt% TiO₂: (a)
 as coated; (b) heat treated at 500° C for 2 h in air; (c) heat treated at
 700° C for 2 h in air and (d) heat treated at 900° C for 2 h in air
- Fig. 7.5** Surface morphology and EDAX point analysis from different spots on 268
 HA – 10 wt% Al₂O₃ coated AISI 316L SS: (a) as coated; (b) heat
 treated at 500° C for 2 h in air; (c) heat treated at 700° C for 2 h in air
 and (d) heat treated at 900° C for 2 h in air
- Fig. 7.6** Surface morphology and EDAX point analysis from different spots on 269
 HA – 10 wt% Al₂O₃ coated AISI 316L SS with bond coat of Al₂O₃ – 13
 wt% TiO₂: (a) as coated; (b) heat treated at 500° C for 2 h in air; (c)
 heat treated at 700° C for 2 h in air and (d) heat treated at 900° C for
 2 h in air
- Fig. 7.7** Surface morphology and EDAX point analysis from different spots on 270
 HA – 10 wt% Al₂O₃ coated titanium: (a) as coated; (b) heat treated at
 500° C for 2 h in air; (c) heat treated at 700° C for 2 h in air and (d)
 heat treated at 900° C for 2 h in air
- Fig. 7.8** Surface morphology and EDAX point analysis from different spots on 271
 HA – 10 wt% Al₂O₃ coated titanium with bond coat of Al₂O₃ – 13 wt%
 TiO₂: (a) as coated; (b) heat treated at 500° C for 2 h in air; (c) heat
 treated at 700° C for 2 h in air and (d) heat treated at 900° C for 2 h
 in air
- Fig. 7.9** Surface morphology and EDAX point analysis from different spots on 272
 HA – 20 wt% Al₂O₃ coated AISI 316L SS with bond coat of Al₂O₃ – 13
 wt% TiO₂: (a) as coated; (b) heat treated at 500° C for 2 h in air; (c)
 heat treated at 700° C for 2 h in air and (d) heat treated at 900° C for
 2 h in air
- Fig. 7.10** Surface morphology and EDAX point analysis from different spots on 273
 HA – 20 wt% Al₂O₃ coated titanium with bond coat of Al₂O₃ – 13 wt%

heat treated at 500° C for 2h in air; (c) post coating heat treated at 700° C for 2h in air and (d) post coating heat treated at 900° C for 2h in air

Fig. 7.19 X-ray diffraction pattern of HA – 10 wt% Al₂O₃ coated titanium: (a) as coated; (b) post coating heat treated at 500° C for 2h in air; (c) post coating heat treated at 700° C for 2h in air and (d) post coating heat treated at 900° C for 2h in air 283

Fig. 7.20 X-ray diffraction pattern of HA – 10 wt% Al₂O₃ coated titanium with Al₂O₃ – 13 wt% TiO₂ bond coat: (a) as coated; (b) post coating heat treated at 500° C for 2h in air; (c) post coating heat treated at 700° C for 2h in air and (d) post coating heat treated at 900° C for 2h in air 284

Fig. 7.21 X-ray diffraction pattern of HA – 20 wt% Al₂O₃ coated AISI 316L SS with Al₂O₃ – 13 wt% TiO₂ bond coat: (a) as coated; (b) post coating heat treated at 500° C for 2h in air; (c) post coating heat treated at 700° C for 2h in air and (d) post coating heat treated at 900° C for 2h in air 285

Fig. 7.22 X-ray diffraction pattern of HA – 20 wt% Al₂O₃ coated titanium with Al₂O₃ – 13 wt% TiO₂ bond coat: (a) as coated; (b) post coating heat treated at 500° C for 2h in air; (c) post coating heat treated at 700° C for 2h in air and (d) post coating heat treated at 900° C for 2h in air 286

Fig. 7.23 X-ray diffraction pattern of HA – 30 wt% Al₂O₃ coated AISI 316L SS (a) as coated; (b) post coating heat treated at 500° C for 2h in air; (c) post coating heat treated at 700° C for 2h in air and (d) post coating heat treated at 900° C for 2h in air 287

Fig. 7.24 X-ray diffraction pattern of HA – 30 wt% Al₂O₃ coated titanium: (a) as coated; (b) post coating heat treated at 500° C for 2h in air; (c) post coating heat treated at 700° C for 2h in air and (d) post coating heat treated at 900° C for 2h in air 288

Fig. 7.25 FE-SEM micrograph showing surface morphology of pure HA coating on AISI 316L SS after post coating heat treatment at 900°C for 2h in air at different magnifications: (a) 500X; (b) 800X; (c) 1500X and (d) 3000X 289

Fig. 7.26 FE-SEM micrograph showing surface morphology of pure HA coating 290

Al₂O₃ coating on titanium with bond coat of Al₂O₃-13 wt% TiO₂ after post coating heat treatment at 900°C for 2h in air at different magnifications: (a) 800X; (b) 1600X; (c) 3000X and (d) 6000X

- Fig. 7.35** FE-SEM micrograph showing surface morphology of HA-30 wt % Al₂O₃ coating on AISI 316L SS after post coating heat treatment at 900°C for 2h in air at different magnifications: (a) 800X; (b) 1600X; (c) 3000X and (d) 6000X (filling of crack by nano-scale HA particles is shown by arrow) 299
- Fig. 7.36** FE-SEM micrograph showing surface morphology of HA-30 wt % Al₂O₃ coating on titanium after post coating heat treatment at 900°C for 2h in air at different magnifications: (a) 800X; (b) 1500X; (c) 3000X and (d) 3000X from different location 300
- Fig. 7.37** FTIR spectra of pure HA coating: (a) as sprayed coating; (b) post coating heat treated at 500°C; (c) post coating heat treated at 700°C and (d) post coating heat treated at 900°C 302
- Fig. 7.38** FTIR spectra of HA-10 wt% Al₂O₃ coating: (a) as sprayed coating; (b) post coating heat treated at 500°C; (c) post coating heat treated at 700°C and (d) post coating heat treated at 900°C 303
- Fig. 7.39** FTIR spectra of HA-20 wt% Al₂O₃ coating: (a) as sprayed coating; (b) post coating heat treated at 500°C; (c) post coating heat treated at 700°C and (d) post coating heat treated at 900°C 304
- Fig. 7.40** FTIR spectra of HA-30 wt% Al₂O₃ coating: (a) as sprayed coating; (b) post coating heat treated at 500°C; (c) post coating heat treated at 700°C and (d) post coating heat treated at 900°C 306
- Fig. 8.1** Microhardness profile of different coatings on AISI 316 L stainless steel and titanium substrate without incorporation of bond coat: HSS: HA coated AISI 316L SS; H10AS: HA-10 wt% Al₂O₃ coated AISI 316L SS; H20AS: HA-20 wt% Al₂O₃ coated AISI 316L SS; H30AS: HA-30 wt% Al₂O₃ coated AISI 316L SS; HT: HA coated Ti; H10AT: HA-10 wt% Al₂O₃ coated Ti; H20AT: HA-20 wt% Al₂O₃ coated Ti; H30AS: HA-30 wt% Al₂O₃ coated Ti 315
- Fig. 8.2** Microhardness profile of different coatings on AISI 316 L stainless steel and titanium substrate with incorporation of bond coat: HSS: 316

LIST OF TABLES

Table No.	Caption of Table	Page No.
Table 2.1	Biomaterials used in body system, (Zhang, 2000)	6
Table 2.2	Relevant properties of materials used in orthopedic and dental implants, (Long and Rack, 1998)	7
Table 2.3	Abbreviations, formula and Ca/P ratio of calcium phosphorus ceramics, (Liven, 2007, Shi, 2004 and Levingstone, 2008)	11
Table 2.4	Phosphate minerals and their occurrence in human body, (Le Geros and Le Geros, 1984)	12
Table 2.5	Comparison of bone and synthetic HA ceramic, (Nicholson, 2002)	30
Table 2.6	Chemical reactions in Ca-P-H ₂ O solution system, each of reaction is plotted in Fig. 2.9 and marked by respective alphabet, (Chander et al., 1979)	37
Table 2.7	Limits to concentration of heavy metals	37
Table 2.8	Hydroxyapatite coating techniques, (Azom.com)	51
Table 2.9	Effect of heating temperature on Hydroxyapatite	66
Table 3.1	Chemical composition (wt %) of substrate materials	79
Table 3.2	Parameters of the argon shrouded plasma spray process	80
Table 3.3	Comparison of ion concentration of simulated body fluid and human blood plasma	95
Table 3.4	Chemical regents for preparation of simulated body fluid	97
Table 4.1	Microstructural properties of plasma sprayed hydroxyapatite and aluminum oxide composite coatings on AISI SS316L	110
Table 4.2	Microstructural properties of plasma sprayed hydroxyapatite and aluminum oxide composite coatings on titanium	111
Table 4.3	Microstructural properties of plasma sprayed hydroxyapatite and aluminum oxide composite coatings on AISI SS316L with bond coat of Al ₂ O ₃ -13wt% TiO ₂	111
Table 4.4	Microstructural properties of plasma sprayed hydroxyapatite and aluminum oxide composite coatings on titanium with bond coat of Al ₂ O ₃ -13wt% TiO ₂	111

heat treatment

Table 7.10	Crystallinity of HA-20 wt% Al ₂ O ₃ coatings on titanium with Al ₂ O ₃ -13 wt% TiO ₂ bond coat: as sprayed and after post coating heat treatment	286
Table 7.11	Crystallinity of HA-30 wt% Al ₂ O ₃ coatings on AISI 316L SS: as sprayed and after post coating heat treatment	287
Table 7.12	Crystallinity of HA -30 wt% Al ₂ O ₃ coatings on titanium: as sprayed and after post coating heat treatment	288
Table 8.1	Results of electrochemical tests in simulated body fluid of bare and coated specimens	319
Table 8.2	Crystallinity of as-sprayed and post coating heat treated specimens	322

RESEARCH PAPERS PUBLISHED / PRESENTED

International Journals:

1. **Manoj Mittal, S.K.Nath, Satya Prakash, "Splat Formation and Degradation of Hydroxyapatite During Plasma Spray Process", Advances in Materials Science, Vol. 11 (2), pp. 26-36.**
2. **Manoj Mittal, S.K.Nath, Satya Prakash, "Recrystallization of Amorphous Phases via Post Coating Heat Treatment of Plasma Sprayed HA Coatings", Materials and Manufacturing Processes. ACCEPTED.**
3. **Manoj Mittal, S.K.Nath, Satya Prakash, "Characterization of Plasma Sprayed HA Coatings on AISI 316L SS and Ti Substrate and their Corrosion Behavior in SBF, Journal of Materials, Manufacturing and Composite Engineering. ACCEPTED.**
4. **Manoj Mittal, S.K.Nath, Satya Prakash, "Improvement in Mechanical Properties of Plasma Sprayed HA Coatings by Alumina Reinforcement, Materials Science and Engineering C, UNDER REVIEW.**
5. **Manoj Mittal, S.K.Nath, Satya Prakash, "Effect of Al₂O₃ Reinforced and Al₂O₃-13% TiO₂ Bond Coat on Plasma Sprayed HA Coatings", Journal of Defense Science, UNDER REVIEW.**
6. **Manoj Mittal, S.K.Nath, Satya Prakash, "Post Coating Heat Treatment: Recrystallization of Amorphous Phases and Grain Refinement of Plasma Sprayed Hydroxyapatite", Journal of Composite Materials, UNDER REVIEW.**
7. **Manoj Mittal, S.K.Nath, Satya Prakash, "Shrouded Plasma Sprayed and Flame Sprayed HA Coatings: Morphology and Mechanical Characterization", Current Science, UNDER REVIEW.**
8. **Manoj Mittal, S.K.Nath, Satya Prakash, "Wear Behaviour of Plasma Sprayed Hydroxyapatite and Aluminum Oxide Reinforced Hydroxyapatite Coatings, Wear, UNDER REVIEW.**
9. **Manoj Mittal, S.K. Nath, Satya Prakash, "Wear Testing Equipments for Measuring Wear Resistance of Body Implants-A Review", Journal of Materials, Manufacturing and Composite Engineering, COMMUNICATED.**

ABBREVIATIONS

BSE	Back Scattered Electrons
CaO	Calcium Oxide
CLA	Center Line Average
EDAX	Energy Dispersive X-ray Analysis
FE-SEM	Field Emission Scanning Electron Microscopy
h	Hour
HA	Hydroxyapatite
Hv	Vickers Hardness
i_{corr}	Corrosion Current Density
LPR	Linear Polarization Resistance
min	Minute
mM	mili mole
mp	melting point
SEM	Scanning Electron Microscopy
SBF	Simulated Body Fluid
SOD	Stand off Distance (Spraying Distance)
TCP	Tri Calcium Phosphate
TTCP	Tetra Calcium Phosphate
Wt%	Weight Percentage
XRD	X-ray Diffraction
ϕ	Diameter (mm)

CHAPTER 1

INTRODUCTION

Human's intrinsic desire to remain active and to challenge his limitation to movement due to orthopedic degradation propel research into the improvement of orthopedic intervention. The incidence of orthopedic interventions has increased enormously since the human being entered the era of industrialization, largely due to accidents caused by the use of machines and automobiles for his convenience. The knee is one of the most important and most studied joints in the human body. Unfortunately, it is highly susceptible to osteoarthritis which causes pain and loss of function and in some cases leads to total knee replacement.

According to Arthritis Foundation, arthritis related problems are second to heart disease and the leading cause of work disability. Mechanical loading and especially dynamic loading is believed to play a major role in the degenerative process (Setton et al., 1998 and Tetsworth and Paley, 1994). Over 500000 total joint replacements primarily hip and knees and 100000-300000 dental implants were used in USA alone annually (Shin et al., 2003). According to American Academy of Orthopedic Surgeons, approximately 120000 hip replacement operations (hip prostheses) are performed each year in USA (Neville-Smith et al., 2000).

Since the late 1970's, there has been a growing awareness of the complications related to long-term use of cemented body implants. The loss of implant may be caused by one or more of the reasons which includes wear, loosening, fracture and infection at later stage. The probability of implant failure is directly related to the time, which increases with time and in many cases the complications are synergistic. The analysis of failure of body implants have made the practitioner reconsider the use of acrylic bone cement for fixation at bone/implant interface since it is the progressive deterioration at this interface that results in the failure of either the bone or the implant (Hench, 1987). Load bearing implants in orthopedics have to sustain complex mechanical loads without failure under corrosive environmental conditions. Further, permanent implants e.g. joint prostheses or dental implants, which are designed for service throughout the life span of the patient and have to bond tightly to surrounding bone need more attention (Bearinger et al., 1997).

properties along with biological benefits of coatings (Thomas, 1994). Considerable efforts are being made to produce biocompatible, bioactive, corrosion resistant coatings with well defined structure, morphology and phase composition. The various coating processes currently used for hydroxyapatite based coatings are plasma spraying, high velocity oxyfuel (HVOF), high velocity suspension flame spraying (HVSFS) (Gadow et al., 2010), flame spraying, sol gel, flame assisted chemical vapor deposition, chemical vapor deposition (Trommer et al., 2007), electrochemical, electrophoresis with and without sintering, pulsed laser deposition, isostatic compression and frit slurry enameling (Zhang, 2000). The most commonly used technique is plasma spraying, introduced in the early 1980's (Gottlander, 1994). The plasma spray technique for coating of hydroxyapatite powder is approved by US Food and Drug Administration (FDA).

Hydroxyapatite is slightly resolvable in water or acidic solution and this accelerate dramatically at lower pH (< 4) value. The dissolution of hydroxyapatite is a complex process: at constant pH, rate of dissolution is initially fast; the dissolution is strongly affected by the H^+ ion concentration, but H^+ diffusion from bulk to the solid interface is not a controlling step. Some researchers propose that during initial reaction calcium ions are adsorbed on the surface and the adsorbed calcium ions cover a part of the surface area and limit the accessibility to the surface. The available area for hydrogen attack is much less than the total material surface area, which leads to a much lower dissolution rate in this calcium rich layer. The other causes of dissolution of hydroxyapatite are etches and pits formation due to structural defects, dislocations and inclusions, high coating porosity and Ca/P ratio other than 1.67 (Wang, 2004). The failure of body implant may be due to wear of one of the joining parts in the body environment. The wear in the implant and surrounding bone may be abrasive, adhesive or fatigue. Some wear testing devices are used to simulate the wear in body environment. The knee simulator; one of the most complex wear testing device which tests actual knee prostheses is very expensive with some commercial models costing in excess of \$ 200000. Wang et al. (1999) and Blun et al. (1991) have reported an inexpensive alternative to knee simulators to test knee replacement materials. The other simpler and inexpensive models for wear testing are: pin-on-flat, pin-on-disc, flat-on-disc and cyclic sliding wear testing machine. Morks et al. (2007), carried out wear tests using SUGA abrasion tester, which follows NUS-ISO-3 standards (Japan), a similar wear testing machine is built to calculate the wear resistance of coated specimens in this study.

Literature review relevant to the research has been divided into four phases. First phase contains a comprehensive review of existing literature on materials used for orthopedic and dental implants, their properties, bone-implant interface and hip prosthesis. The second phase contains the critical review of wear mechanism and failure mechanism of coatings. In third phase, critical review of coatings, their deposition processes with detailed description of plasma spray process, post coating treatment and in vitro studies have been described. The last phase of this chapter is related to the problem formulation, scope and objective of present research work.

2.1 ORTHOPEDIC AND DENTAL IMPLANT MATERIALS

Biomaterials refer to synthetic materials used to replace a part of a living system or to function in the intimate contact with living tissue. From the nature of materials point of view, biomaterials can be classified as polymers, ceramics, metals and composites. This classification may be overlaid on each other due to the fact that composites are made from two or more type of materials. Various kinds of biomaterials that have been used in human body are reported in Table 2.1.

2.1.1 Metallic Implant Materials

In biomedical applications 70% of implants consist of metals (Sarao et al., 2009). The majority of metallic implants used in the skeletal system are based on three types of alloys: austenitic stainless steels, cobalt-chromium alloys and titanium based alloys (Bonfield, 1987). The fixation of these metallic implants to bone has been one of the most difficult problems and the fixation is obtained through the acrylic bone cement. Cobalt-chromium (Co-Cr) alloys show excellent wear resistance, corrosion resistance and fatigue resistance, although they have higher elastic modulus and are less biocompatible than titanium as reported in Table 2.2. A process where the stiff implant carries much higher load than the surrounding bone, called stress shielding is found to be increased due to high modulus of elasticity of Co-Cr alloys. In addition, over 10% of the population that goes for body implant is hypersensitive to at least one of the elements in Co-Cr alloys (9.6% Ni, 9.3% Cr and 6.0%

such as infection and stem breakage are largely avoided now a days but the long term failure of an implant is most often attributed to implant loosening, which can cause severe pain, loss of joint function that necessitate revision surgery (Netter et al., 1989, Spector, 1990, Spector et al., 1991 and Long and Rack, 1998).

Table: 2.2 Relevant properties of materials used in orthopedic and dental implants, (Long and Rack, 1998)

Materials	Elastic Modulus (GPa)	Tensile Strength (MPa)	Advantages	Disadvantages
cp Ti	110	400	Biocompatible, corrosion resistance	Poor fatigue resistance, wear resistance
Ti-6Al-4V	124	940	Biocompatible, corrosion resistance, fatigue strength	Poor wear resistance (fretting)
SS 316 L	193	540	Low cost, easy availability and processing	Poor biocompatibility, corrosion, high modulus
Co-Cr	214	480	Wear and corrosion resistance, fatigue strength	High modulus, poor biocompatibility
UHMWPE	0.4	3	Low friction and wear	Susceptible to three body wear, particle creation
PMMA	3	35 – 50	Rapid fixation, strong fixation for short time	Low impact and fatigue resistance, poor biocompatibility
Bone	10 – 30	70 – 150	---	---

cp: commercially pure

Hench, (1998) reported that the failure analysis have made practitioners to reconsider the use of acrylic bone cement at bone/implant interface since progressive deterioration of bone cement at this interface results in the failure of either the bone or the implant. Consequently, there is a growing interest in alternative, cement-less methods for

Ideally, orthopedic and dental implants should not only be biocompatible, but also bioactive, which means that the implants can be osteoconductive or osteoinductive, i.e. they promote new bone growth around the implants. Bioactive fixation requires implant materials to be bioactive, which can establish bone bonding with living tissue by physiochemical or cell-mediated biological process. There are two types of bioactive materials currently in use for orthopedic and dental applications: bioglass and calcium phosphates. Bioglass was invented by Hench in late 1960's. He developed a surface reactive bioglass, containing SiO_2 , Na_2O , CaO and P_2O_5 , which could be chemically bonded to bone. Nowadays, this type of bioglass is widely used in clinical applications. Further, these materials have very good bioactive properties but their mechanical properties are very poor.

In a study of radiographic examination of hip arthroplasty of patients after ten years, 30 – 40% of the patients showed femoral loosening and 10 – 30 % showed acetabular loosening. After 15 years of implantation the rates of failure were much higher (Netter et al., 1989). Implant loosening by mechanical failure of supporting cancellous bone due to bone resorption (osteolysis) and break down of material tissue interface has been reported, but the cascade of events leading to failure are complex and can take many years to develop (Spector, 1990, and Spector et al., 1991). Flowchart of many events leading to implant failure is reported in Fig. 2.2.

At the root of these problems there are two major causes: osteolytic response to wear particles generated from the articulating surface and osteolytic response due to poor long term biocompatibility and/or loss of fixation at bone-biomaterial interface. Many of these problems depend fundamentally on material selection and implant design.

2.1.2 Biomaterials Based on Ca and P

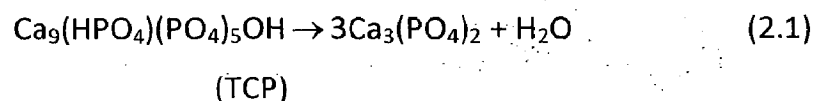
Calcium phosphates are an integral component of geological and biological systems. They are found in virtually all the rocks and are major structural component of vertebrates. Calcium and phosphate are widely distributed elements on earth. The surface layer of earth contains about 3.4% calcium and 0.10% phosphorus (Weast, 1985-1986). Table 2.3 presents most of the Ca-P ceramics with their calcium to phosphorus molar ratio. The most widely used Ca-P ceramic for biomedical purpose are hydroxyapatite (HA), tri-calcium phosphate and their biphasic combinations (Le Geros, 1991, Chow, 2000, Suchanek and Yoshimura, 1998 and Vallet-Regi and Gozalez-Calbet, 2004). Combinations of oxides of Ca and P with or without incorporation of water give different calcium phosphates. All calcium phosphates

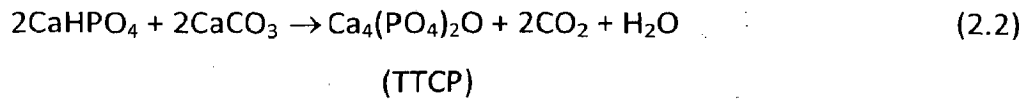
Table 2.3 Abbreviations, formula and Ca/P ratio of calcium phosphorus ceramics, (Liven, 2007, Shi, 2004 and Levingstone, 2008)

Compound name	Abbreviation	Formula	Ca/P ratio
Mono-calcium phosphate monohydrate	MCPM	$\text{Ca}(\text{H}_2\text{PO}_4)_2 \cdot \text{H}_2\text{O}$	0.5
Mono-calcium phosphate anhydrous	MCPA	$\text{Ca}(\text{H}_2\text{PO}_4)_2$	0.5
Di-calcium phosphate dehydrate	DCPD	$\text{CaHPO}_4 \cdot 2\text{H}_2\text{O}$	1.0
Di-calcium phosphate anhydrate	DCPA	CaHPO_4	1.0
Octacalcium phosphate	OGP	$\text{Ca}_8\text{H}_2(\text{PO}_4)_6 \cdot 5\text{H}_2\text{O}$	1.33
α -tricalcium phosphate	α -TCP	$\alpha\text{-Ca}_3(\text{PO}_4)_2$	1.5
β -tricalcium phosphate	β -TCP	$\beta\text{-Ca}_3(\text{PO}_4)_2$	1.5
Amorphous calcium phosphate	ACP	$\text{Ca}_x(\text{PO}_4)_y \cdot n\text{H}_2\text{O}$	1.2 – 1.5
Calcium deficient hydroxyapatite	CDHA	$\text{Ca}_{10-x}(\text{HPO}_4)_x(\text{PO}_4)_{6-x}(\text{OH})_{2-x}$	1.5 – 1.67
Hydroxyapatite	HA	$\text{Ca}_{10}(\text{PO}_4)_6(\text{OH})_2$	1.67
Tetracalcium phosphate	TTCP	$\text{Ca}_4(\text{PO}_4)_2\text{O}$	2.0

2.1.2.1 Tri-calcium phosphate (TCP)

β -tri-calcium phosphate ($\text{Ca}_3(\text{PO}_4)_2$) is a calcium phosphate of the stoichiometric composition, having rhombohedral structure which can not be precipitated from solution. It may only be prepared by calcification of calcium deficient HA at a temperature above 800° C by following chemical reaction:





2.1.2.3 Amorphous calcium phosphate (ACP)

Crystalline hydroxyapatite is generally considered to be the final stable product in the precipitation of calcium and phosphate ions from neutral to basic solutions. However, there is a broad range of solution conditions in which precipitation occurs spontaneously, that may lead to precipitation of unstable amorphous calcium phosphates. Amorphous calcium phosphates are unique among the calcium phosphate salts as they do not have long range periodic arrangement of crystalline materials. The morphology of ACP consists of roughly spherical $\text{Ca}_9(\text{PO}_4)_6$ clusters randomly distributed with their inter-cluster spaces filled with water. Sedlak and Beebe (1974) reported that temperature programmed dehydroxylation of ACP indicates that about 75% of this water is tightly bound inside the ACP particles. The rest is more loosely held surface water. The transition of ACP to crystalline materials is not gradual but occurs rather rapidly, which is further sensitive to temperature and pH (Boskey and Posner, 1973). The transformation process occurs via multiplicative proliferation of small crystals possibly through a dendrite-like growth mechanism. The concentration level falls off sharply at $\text{pH} < 9.25$.

2.1.2.4 Apatite

The term apatite defines three unique minerals, hydroxyapatite ($\text{Ca}_{10}(\text{PO}_4)_6(\text{OH})_2$), fluorapatite ($\text{Ca}_{10}(\text{PO}_4)_6\text{F}_2$) and chlorapatite ($\text{Ca}_{10}(\text{PO}_4)_6\text{Cl}_2$). The atomic arrangement of the three apatite phases differ principally in the positions of the occupants of anion position i.e. hydroxyl, fluorine and chlorine groups, for three end members respectively (Hughes and Rakovan, 2002). These materials demonstrate similar structure and possess the structural formula, $\text{X}_3\text{Y}_2(\text{TO}_4)_6\text{Z}$. In nature apatite compositions include $\text{X} = \text{Y} = \text{Ca}$, Sr, Ba, Re, Pb, U or Mn (rarely Na, K, Y, Cu); $\text{T} = \text{P}$, As, V, Si, S or C (as CO_3) and $\text{Z} = \text{F}$, Cl, OH or O. In medicine, apatite of interest possess $\text{X} = \text{Y} = \text{Ca}$; $\text{T} = \text{P}$; $\text{Z} = \text{F}$ or OH. Out of these three apatites hydroxyapatite is most studied and used biomaterial for orthopedic and dental implants. Hydroxyapatite has a crystalline structure of hexagonal rhombic prism as shown in Fig. 2.3

revealed that hydrothermal processing of potassium di-hydrogen phosphate can cause a complete transformation to apatite.

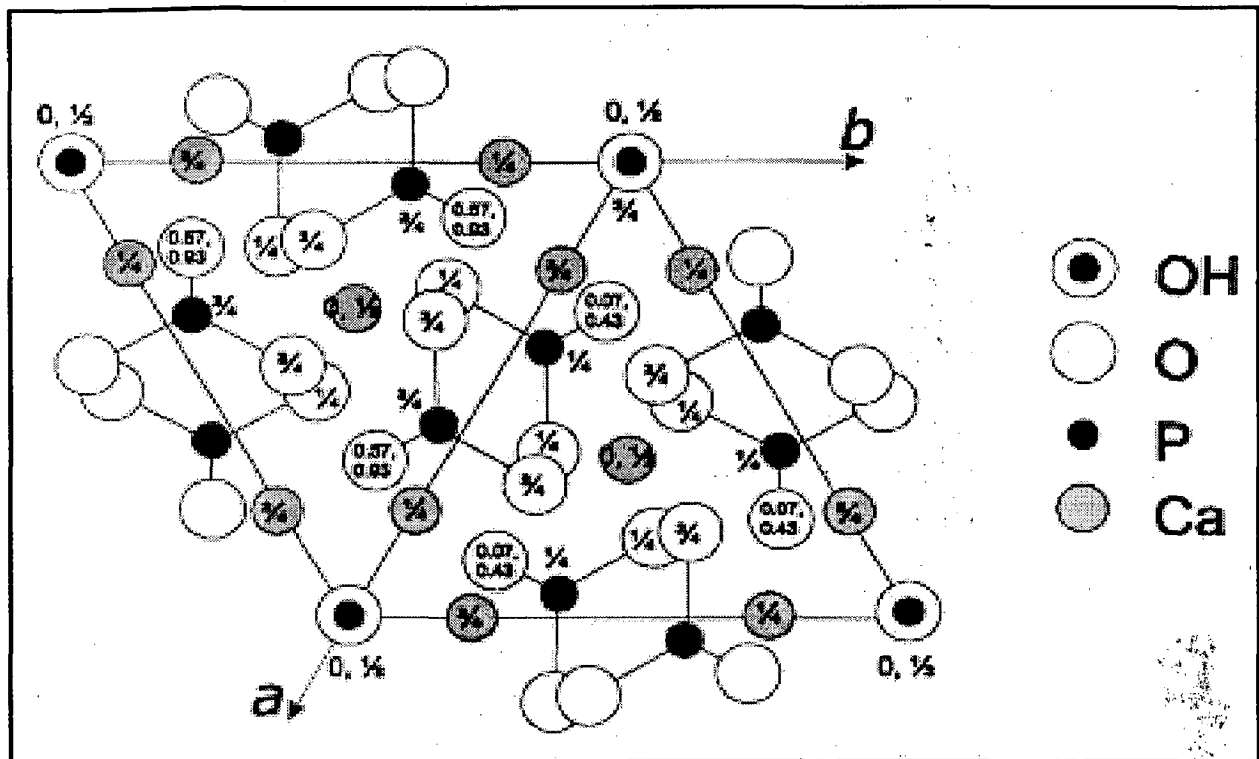


Fig. 2.3 Structure of hydroxyapatite projected down the c-axis onto basal plane, (Zhang, 2000)

Pure and dense ceramics can be obtained through sintering process, which involves calcification and compaction at room temperature followed by heating at high temperature. The calcification is performed at 600-900°C and adsorbed moisture, carbonates and chemicals like ammonia and nitrates which remained from synthesis stage are removed as gaseous products, leading to production of dense HA material during sintering. The increase in crystal size and decrease in specific surface area are the result of processing. The product with a Ca/P molar ratio more than 1.67 and formation of CaO is the result of sintering. The presence of CaO is reported to decrease the strength (especially cohesion) due to stresses arising from formation of $\text{Ca}(\text{OH})_2$, which subsequently transforms to CaCO_3 (Slosarczyk et al., 1996). The presence of CaO may alter the rate and extent of biodegradation. A Ca/P molar ratio less than 1.67 favors the presence of α -TCP or β -TCP in HA ceramics (Raynaud et al., 2002). The Ca/P ratio does not influence significantly the grain growth of HA ceramics. Moreover, due to formation of a new phase and evaporation of water, the decomposition process may have negative affect on densification of the HA ceramics.

bioactive glass are reviewed and classified with focus of attachment to the bone (Hench, 1991). It is reported that in spite of significantly improved strength and toughness, HA based composites do not find wide applications due to decrease in their bioactivity and biocompatibility as well as difficulties in processing.

2.1.2.7 HA based composite coatings

The metallic materials used for the body implants have very good mechanical properties but they are not bioactive and biocompatible, so their service life is restricted to 10 to 15 years and the failure is associated with the bone implant-interface. Bioceramics have very good bioactivity and biocompatibility but they do not have even fair mechanical properties, where tensile strength, brittleness, fracture toughness and wear resistance are concerned. Thus, one of the most important clinical applications of HA is the coating of HA on metal implants to form a macro-composite material. This macro-composite material combines mechanical advantages of metallic substrate with excellent biocompatibility and bioactivity of HA. Such composite provide natural fixation of implant to bone and minimize an adverse reaction caused by release of metal ions from the metallic substrate. Furthermore, HA coatings have been reported to promote early bone formation around implants and promote the deposition and differentiation of mesenchymal cells in osteoblasts on HA coated implant surface (Cleries et al., 2000). Ability of osteoblast adhesion onto the surface is due to the increased adsorption and production of proteins. In addition, a study by Gottlander et al., (1992) has indicated HA coated implants have a higher percentage of bony contact after six weeks implantation as compared to commercially pure Ti screws. Histologically comparison of osseous apposition to HA coated implants and Ti Implants has demonstrated mineralization of bone directly on HA surface with no fibrous tissue layer formation. However, a predominately fibrous tissue interface was observed on Ti implants with only minimal areas of direct bone contact (Thomas et al., 1987). Many investigators reported that histometric studies in animal models have demonstrated that bone adapts in much less time to HA coated implants than to uncoated Ti Implants (Gottlander and Albrektsson, 1991 and Weimlaender et al., 1992).

The HA coatings were tested based on their initial fixation, stable bone in-growth and remodeling around the stem in total hip prosthesis. The studies have revealed that the micro-motions of HA coated stems were comparable to that of cemented stems. Comparative studies have shown HA coated stems had higher survival rate and less bone

HA-15 wt% SiO₂-10 wt% Ti was plasma sprayed on SUS 304 stainless steel substrate. The adhesive strength of coating layer adhered to substrate was expected to be higher than cohesive tensile strength of the coatings (Morks et al., 2008). Results of investigation by Morks, (2008) confirmed the improvement of the adhesive strength of HA coatings by reinforcing with SiO₂ and Ti particles when compared with pure HA coatings. An impact theory was utilized to logically explain the HA-TiO₂ composite coating formation and mutual chemical reaction between HA and titania during HVOF spraying by Li et al., (2003). It was found that the crater caused by impingement of completely un-melted titania particle upon HA matrix was far smaller than the titania feedstock. A chemical bond between HA and titania within the composite coatings was suggested, which may be responsible for the entrapment of titania particles during impingement process.

Gu et al. (2003) reported in an investigation that plasma sprayed HA composite coatings with 50 wt% Ti-6Al-4V showed superior mechanical stability than the pure HA coatings in physiological environment, indicating much better long term stability of composite coatings in physiological environment. Zheng et al. (2000) reported that mean bonding strength increased from 12.9 MPa to 14.5 MPa and 17.3 MPa by reinforcing the plasma sprayed HA coating with 20 wt% Ti and 60 wt% Ti respectively. The enhancement of adhesion of the coating to substrate was reported by increasing the contents of Ti to HA.

The effect of plasma gas composition on the bond strength of HA-Ti composite coatings was investigated by Inagaki et al., (2006). The plasma spray process was controlled to get titanium rich coating near substrate surface and HA rich coating at the top (graded coating). The bond strength of coating prepared by plasma gas containing Ar-N₂ increased by 1.5-2 times than the bond strength of coating prepared by Ar-O₂ as plasma gas. In another study, Inagaki et al., (2003) investigated the effect of partially nitriding HA composite coating during plasma spraying and reported substantial increase in bonding strength by adding 0.8% N₂ to argon during spraying as compared to coatings sprayed by pure argon, further the bonding strength obtained was almost doubled by adding 1.8% N₂ to argon during plasma spraying as compared to pure argon as plasma gas.

Young's modulus and fracture toughness of HVOF sprayed HA, HA-10 wt% titania and HA-20 wt% titania were investigated by Li et al., (2002C). The results showed significant increase in Young's modulus by addition of 10 wt% titania to HA as compared to pure HA coating, while by addition of 20 wt% titania, the value of modulus decreased but it was still higher than pure HA coating. The decrease in value of modulus by addition of 20 wt% titania

(1995) also agreed to the fact that Al_2O_3 addition helps increasing the bending strength of HA composite.

Alumina, which is classified as one of the chemically and biologically inert material, has been investigated as reinforcement material for hydroxyapatite (Champion et al., 1996). Alumina particles retained their bio-inertness without affecting the biocompatibility of HA. Alumina with high density and high purity (>99.5) was the first bioceramic widely used clinically. It is used in load bearing hip prostheses and dental implant because of its combination of excellent corrosion resistance, high wear resistance, high strength, bio-inertness and stability in physiological environment (Hulbert et al., 1987, Hench and Ethridge, 1982, Plenk, 1982 and Griss and Heimke, 1981). Most of implant devices are made of very fine grained polycrystalline $\alpha\text{-Al}_2\text{O}_3$; a very small amount of magnesia (MgO) is used to limit grain growth during sintering. Due to lack of chemical bonding between alumina and tissue, its applications as potential bone substitute are limited. In 2002, the United States Food and Drug Administration (FDA) have approved marketing of alumina ceramic-on-ceramic articulated hips in USA. Addition of nano-size alumina into HA resulted in smaller thermal expansion coefficient nearer to Ti-6Al-4V. Fu et al. (2002) also reported similar trend and in addition they reported a significant reduction in decomposition of HA during high temperature thermal spray process.

The interaction between HA powder and human monocytes results in liberation of inflammatory cytokines. The addition of 0.5-2% Zn was proposed to retard the inflammatory processes (Grandjean-Laquerriere et al., 2006).

Eduardo et al., (2008) prospectively followed 288 patients (319 hips) (age in a range of 14-70 years) in which alumina-on-alumina cup was used with hydroxyapatite stem for a minimum period of three years. The cumulative probability of not having a revision surgery of one or both components for any cause was reported to be 97%. They observed that alumina-on-alumina prostheses had reasonable outcomes after five years and suggested that continued follow up will be required to determine the wear between alumina-on-alumina bearings resulting in osteolysis and loosening.

Four hundred seventy five hips with alumina-on-alumina bearing surface with hydroxyapatite coated titanium stem were implanted for comparing alumina-on-alumina ceramic bearing with chrome cobalt-on-polyethylene bearing by D'Antonio et al., (2006) for a follow up period of 4 to 9 years. They reported significantly higher survivorship of alumina

bond coating has been proposed by Çelik et al., (1997). The fine bond coating layer fits in the grooves of metallic substrate and improves the surface roughness/finish of metallic surface. Beyond matching the thermal expansion coefficients of substrate and coating, several other reasons have been proposed for using bond coats. For instance, direct contact of Ti with HA is not advisable because it is supposed that it catalyzes thermal transformation of HA to tri-calcium phosphate, tetra-calcium phosphate and CaO. Bond coat can act as barrier to reduce release of metal ions from substrate to living tissues (Kurzweg et al., 1998A).

Bond coat or intermediate coat is an additional coating layer that is applied between the substrate and top coat. The addition of intermediate layer to substrate coating system offers a number of advantages, mainly improvement in adhesion strength of coating to substrate. The bond coat reduces the release of metal ions from metallic substrate, which improves the biocompatibility in case of body implants. This layer of coating can also reduce the thermal gradient mismatch between substrate and coating at substrate/coating interface and hence reduces the forces that give rise to cracking and delamination. The interface of HA coating and titanium alloy substrate is a site of critical weakness when compared with the strength of inter-lamellar and intra-lamellar structure of HA coating. Investigators used different materials as bond coat including zirconia (ZrO_2), titania (TiO_2), alumina (Al_2O_3) and the combination of these oxides and di-calcium silicate.

The adhesive strength between bioactive coatings and medical metal substrate can be improved by mechanically interlocking the interface (Tucker, 1982). Mechanical interlocking was established via introduction of porous anodic Al_2O_3 intermediate layer on physically vapor deposited (PVD) aluminum film on titanium by Wu et al., (2006).

The bond strength of HA- ZrO_2 coating on Ti substrate was found to increase substantially by incorporation of ZrO_2 bond coat. Chou and Chang, (2002A and 2002B) suggested possible strengthening mechanism of two layer coating is the rougher surface provided by ZrO_2 intermediate layer, which promotes better mechanical interlocking between HA top coat and ZrO_2 bond coat. The surface morphology of ZrO_2 bond coat promotes the bonding strength by increase in surface area. In addition, the toughness of ZrO_2 could play a role in strengthening. The inter-diffusion of elements between HA and ZrO_2 also promotes a better interface bonding. Kurzweg et al., (1998A) investigated CaO stabilized ZrO_2 ($CaOZrO_2$) and 73 mol% titania-27 mol% non-stabilized ZrO_2 (TiO_2+ZrO_2) bond layers. Results of adhesion tests showed that the CaO stabilized ZrO_2 lowered adhesion

induced micro-cracking and coefficient of thermal expansion mismatch substantially decreased (Lu et al., 2004).

Bioglass was plasma sprayed onto a titanium substrate with and without Al₂O₃-40 wt% TiO₂ as bond layer. The bond strength of specimens with bond coat was increased by three times as compared with the specimens without bond coat and the adhesive bonding at metal bioglass interface turned into cohesive bonding by application of bond coating layer (Goller, 2004).

2.1.2.9 Significance of bone implant interface

When attempt is made to regenerate bone via the conduction of bone into biomaterials, the conduit is implanted adjacent to bone tissue. Implant when prosthesis into bone, it is primarily held in place by press-fit mechanical fixation. Cells from the tissue begin to invade and populate the material, lay down new matrix and eventually form new bone. Following implantation of biomaterial in bone, events analogous to those that occur during fracture healing may occur. It may include formation of a hematoma between bone and scaffold for infiltration of cells.

The mechanism of tissue attachment is directly related to type of tissue response at implant interface (Hench and Ethridge, 1982). No implanted material in living tissue system is inert; all materials elicit a response from living tissues. The four types of response allow different means of achieving attachment of prostheses to musculoskeletal system.

- If the implant material is toxic, the tissues surrounding the implant will die.
- If the implant material is non-toxic and biologically inactive, a fibrous tissue of variable thickness will form.
- If the material is nontoxic and biologically active, an interfacial bond will form.
- If the material is nontoxic and dissolve, the surrounding tissue will replace the material.

The bone and coated implant interface is shown in Fig. 2.4. A schematic illustration is presented in Fig. 2.5 (Kunz-Schughart et al., 2000 and Moses et al., 2003). Two crucial steps have been identified for intimate contact to occur and to minimize conditions that would lead to the formation of fibrous capsule: first, adhesion of the desired type of cells,

secondary fixation provided by the chemical bond prevents loosening of implant. The mechanism is similar to the healing of fractured bone. Micro-motion at the bone implant interface must be less than 50 μm in order for successful osseointegration and adequate fixation to occur (Scheller and Jani, 2003).

2.1.2.10 Comparison of biological and synthetic HA

Biological HA that is present in mineral contents of bone, teeth and teeth enamel contains many impurities, because the apatite structure is very hospitable and allows substitution of many other ions. Biological HA is typically calcium deficient and carbonate substituted. The minor elements/ions associated with biological apatite are magnesium (Mg^{2+}), carbonate (CO_3^{2-}), sodium (Na^+), chloride (Cl^-), potassium (K^+), fluoride (F^-) and acid phosphate (HPO_4). Trace elements include strontium (Sr^{2+}), barium (Ba^{2+}) and lead (Pb^{2+}). The bioactivity and biocompatibility of synthetic HA is not only suggested by its similar composition to that of biological HA but also by the results of in vivo implantation, which has produced no inflammation, no foreign body response and no local or systemic toxicity (Klein et al., 1993). The confirmation of biocompatibility of HA is reported by Ducheyne et al., (1990A), Buma et al., (1997) and Ducheyne and Qiu, (1999). The composition of bone and synthetic HA are reported in Table. 2.5.

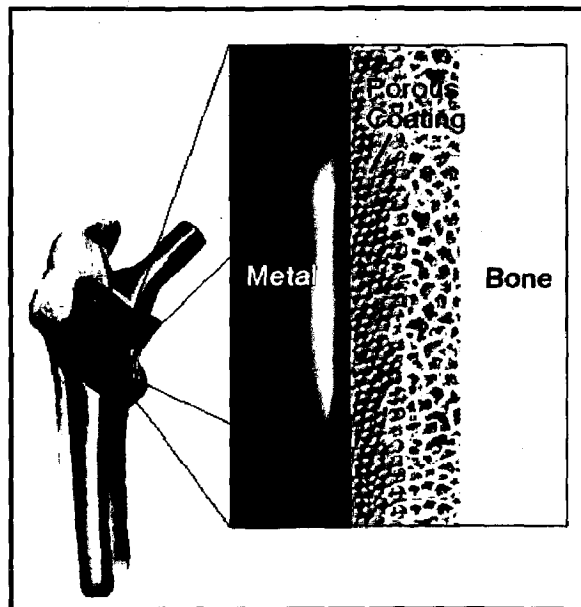


Fig. 2.4 Interface of bone and HA coated implant (Kunz-Schughart et al. 20)

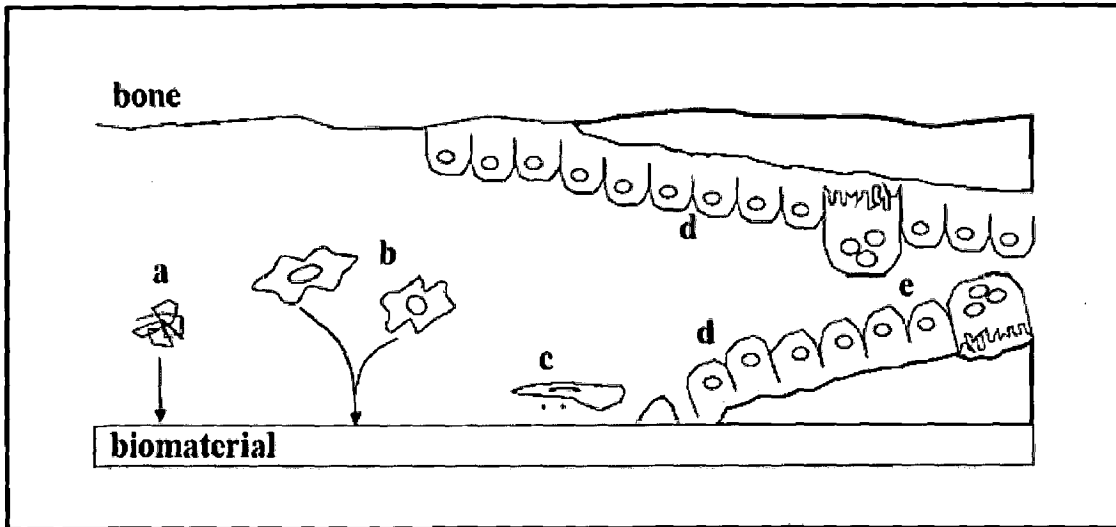


Fig. 2.5 Schematic representation of the events occurring at the bone implant interface: (a) Protein adsorption from tissue fluid and blood cell; (b) Inflammatory and connective tissue cells approach the implant; (c) Formation of a fibrillar mineralized layer and adhesion of osteogenic cells; (d) Bone deposition on implant and bone surface; (e) Remodeling of newly formed bone by osteoclasts, (Moses et al., 2003)

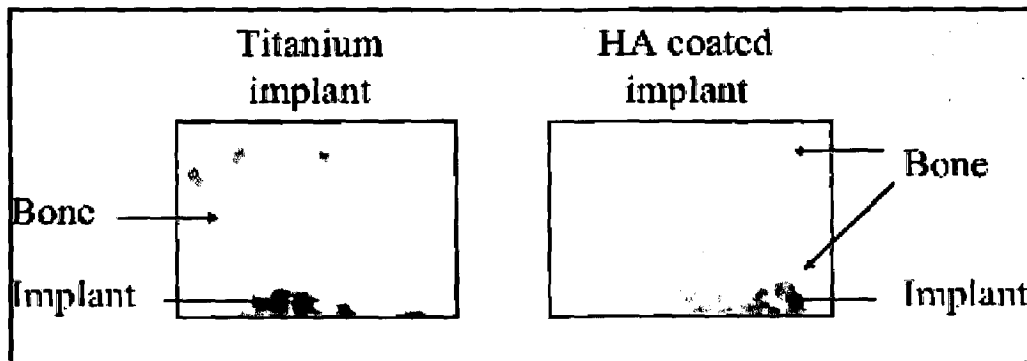


Fig. 2.6 Micrographs showing osseointegration into HA coated implant, (Soballe, 1996)

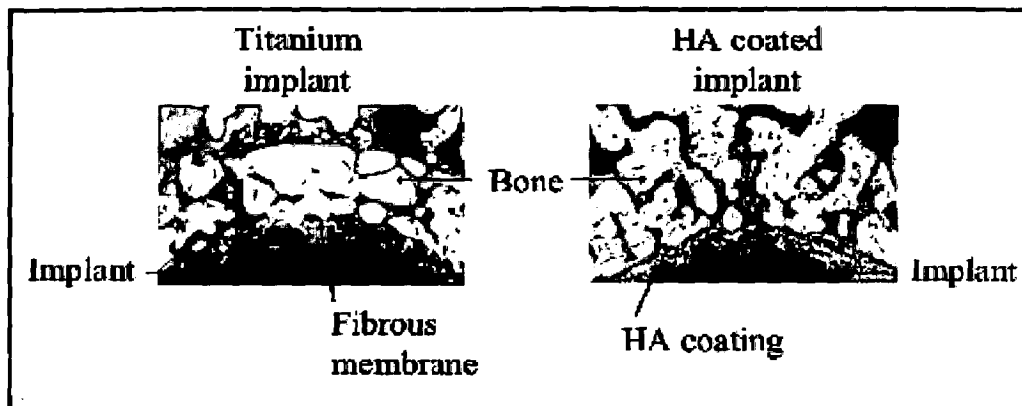


Fig. 2.7 Micrographs showing the formation of a fibrous membrane on titanium implant and no membrane on HA coated titanium implant, (Soballe, 1996)

2.2 FAILURE MECHANISM OF HA COATINGS

The main failure mechanism of HA coatings are dissolution and wear. HA is slightly resolvable in water or acidic solution (Ryu et al., 2002). Several mechanisms are proposed by investigators to explain the dissolution behavior of HA (Raemdonck et al., 1984 and Le Geros, 1988). The pH value of less than 4 dramatically accelerate this process and CaHPO_4 (monetite) or $\text{CaHPO}_4 \cdot 2\text{H}_2\text{O}$ (DCPD, brushite) is more stable than HA at this pH value. There are three primary wear mechanisms namely, abrasive or third body wear, adhesive wear and fatigue or delamination wear in bone and implant system.

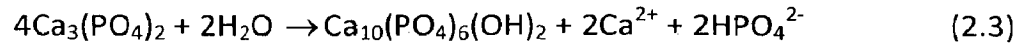
Abrasive wear is removal of material from one surface by other. Since no surface is perfectly smooth, local asperities on harder surface will plough through the softer material and gouge out wear particles. Presence of localized chemical bonding between two surfaces due to high pressure is the cause of adhesive wear. This wear is more common in hip joint replacement than in knee joint replacement. Fatigue or delamination wear cause formation of sub-surface cracks and propagates due to cyclic loading. The tip of crack experience high stresses, which propagate the crack until one crack joins the other and surface flakes off, which creates large wear particles. The third body wear is most common in the bone implant system and is studied in detail in Section 2.2.3 of present study.

Table 2.5 Comparison of bone and synthetic HA ceramic, (Nicholson, 2002)

Composition (wt%)	Bone	HA
Ca	24.5	39.4
P	11.5	18.5
Ca/P ratio	1.65	1.67
Na	0.7	Traces
K	0.03	Traces
Mg	0.55	Traces
CO ₃ ²⁻	5.8	---

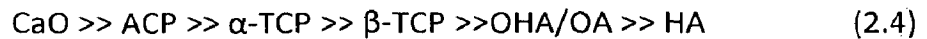
2.2.1 Dissolution Behavior of Hydroxyapatite

The crystallinity and composition of calcium and phosphate phases and pH are the main factors which controls the rate of in-vitro/in-vivo dissolution of HA. The rate of dissolution also depend on the type and concentration of the surrounding solution, the pH of solution, the degree of saturation of the solution, the solid/solution ratio and length of suspension in the solution. Factors such as the Ca/P ratio, impurities like F⁻ or Mg²⁺, the degree of micro and macro porosities, defective structure and amount and type of other phases have significant effects on biodegradation. Only two calcium phosphates materials are stable at room temperature when in contact with aqueous solution and pH of the solution determines the stability of one of two materials (Klein et al., 1993). The solubility of various calcium phosphates in an aqueous solution at room temperature (25°C) is represented in Fig. 2.8. The equilibrium diagram of predominant calcium and phosphorous is shown in Fig. 2.9, while Table 2.6 gives all the equilibrium chemical reactions which could take place in Fig. 2.9. At a pH lower than 4.2, di-calcium phosphate (DCP) is more stable while at higher pH, (more than 4.2), HA is a stable phase (Schneider Jr., 1991 and Klein et al., 1993). The un-hydrated high temperature calcium phosphates when interacts with water or body fluid, at 37°C, forms HA.



The pH of physiological environment is 7.4. As presented in Fig. 2.8 the crystalline HA is stable at this condition, whereas β - tri-calcium phosphate, octo-calcium phosphate, di-calcium phosphate anhydrous and di-calcium phosphate dihydrate are less stable than crystalline HA at physiological conditions (Le Geros and Le Geros, 1993).

When HA is placed in an aqueous solution in the absence of any soluble salt of calcium or phosphorous, the system will equilibrate along dotted line Z-Z' as presented in Fig. 2.9. Decomposition phases, such as calcium oxide (CaO), α -tri-calcium phosphate (α -TCP), β -tri-calcium phosphate (β -TCP), oxy-hydroxyapatite (OHA) and oxy-apatite (OA) are less stable than HA in vivo. The dissolution order that follows in the physiological solution is given hereunder (Heimann, 2006):



Chow, (1991) showed that the amount dissolved at equilibrium depends upon the thermodynamic solubility product of the compound and the pH of solution. Further, it was suggested that at pH of 7.0, the solubility decreases in an order as shown below:



Klein, (1990) suggested that in particular, decomposition products which are formed even during the extremely short residence time of HA particles in hot plasma jet, dissolves more rapidly as compared to well crystallized HA particles in following order:



The mechanism of degradation of calcium phosphate in the human body is not very clear. Some investigators, such as Nagano et al., (1996), De Groot, (1984) and Yamada et al., (2001) believe that the process is a physio-chemical one, in which particles are ingested by osteoclast cells attached to the surface and intracellular dissolution of these particles occurs.

investigation, the implantation of nitrogen and helium ions was done on AISI 316L SS by Muthukumar et al., (2010). A significant improvement in corrosion resistance and pitting corrosion was observed with both nitrogen and helium ion implantation as compared to virgin AISI 316L SS in NaCl solution (9 g/l of H₂O) at pH value of 6.3 and temperature of 37°C. Resistance to pit initiation, lesser susceptibility to localized attack and no change in HA phase during sintering are the findings of Kannan et al., (2003) on H₂SO₄ treated, HA coated SS 316L in Ringer's solution (NaCl: 8.6g/l, CaCl₂·2H₂O: 0.66 g/l and KCl: 0.6 g/l of H₂O). The presence of HA coating over passive layer was suggested as the primary cause, which played a dual role in preventing metal ion release and making the surface more bioactive.

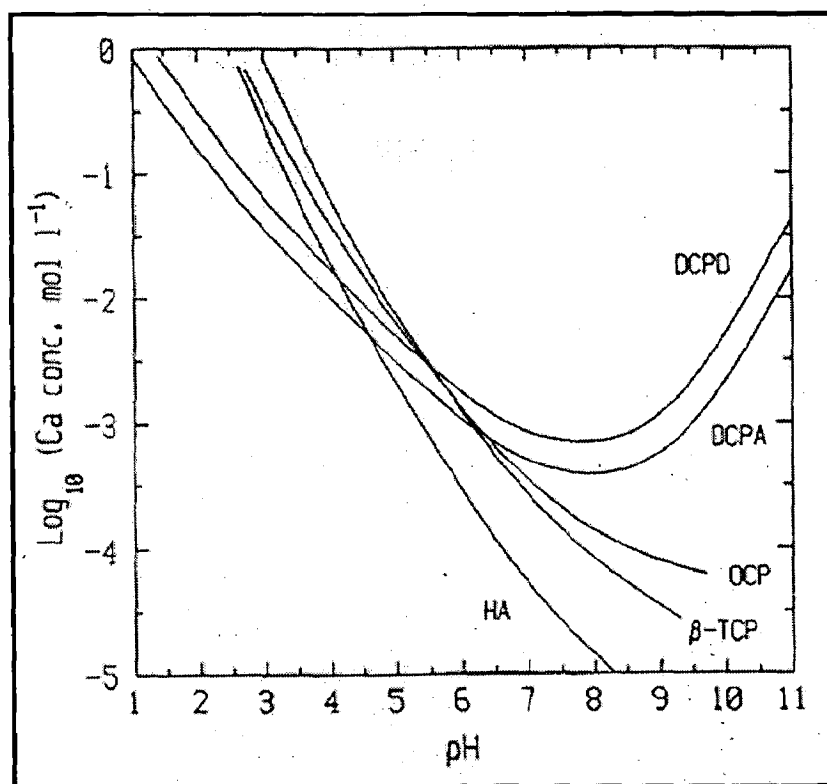


Fig. 2.8 Solubility isotherms for various phases in the system CaO-P₂O₅-H₂O at 25°C, (Ray, 2004 and Raemdonck et al., 1984)

Porter et al., (2002) compared the in-vivo behavior of the HA coating with a crystallinity of 70±5% with an annealed coating with a crystallinity of 92±1%. The non-annealed coatings demonstrated the precipitation of plate-like biological apatite crystallites

could cause mechanical failure of implant after long term use (Bauer et al., 1993, Hemmerle et al., 1997 and Gledhill et al., 2001B).

The inconsistent osseointegration of HA caused by HA dissolution is accompanied not only by biological conditions, a diversity of HA material fabrication and use conditions also play an important role. For HA composite processing, it is more complicated according to the shape or form and performance which will be accomplished.

The ASTM standard specification (ASTM F1185-88), (2003) states that ceramic HA for surgical implants has to have a minimum HA contents of 95% by quantitative X-ray diffraction analysis. The concentration of heavy elements should be limited to the values shown in Table 2.7. The properties of HA required by the International Standards Institute (ISO 13778-1: 2000, Implants for surgery, Hydroxyapatite-Part I: Ceramic hydroxyapatite), (2000) should have a crystallinity of at least 45%, the maximum allowable limit of heavy metals up to 50 ppm and the Ca/P ratio for HA used for surgical implants between 1.65 and 1.82. The shape and microstructure of HA particles also affect the quality of coating.

2.2.3 Wear of Body Implants

The production of wear debris and subsequent tissue inflammatory response has emerged as a central problem limiting the long term clinical outcome of total hip replacements (Harris, 1995, MaGee et al., 1997 and Wroblewski, 1997). The main types of wear seen on retrieved knee prosthesis include delamination caused by surface failure of polyethylene, pitting of surface, third body wear and adhesive wear (Hood et al., 1983, Landy and Walker, 1988 and Collier et al., 1991). Low conformity designs were found to be associated with delamination (Engh et al., 1992), while in a relative conforming design, surface damage was found to be associated with entrapped acrylic particles (Hood et al., 1983).

Table 2.6 Chemical reactions in Ca-P-H₂O solution system, each of reaction is plotted in Fig. 2.9 and marked by respective alphabet, (Chander et al., 1979)

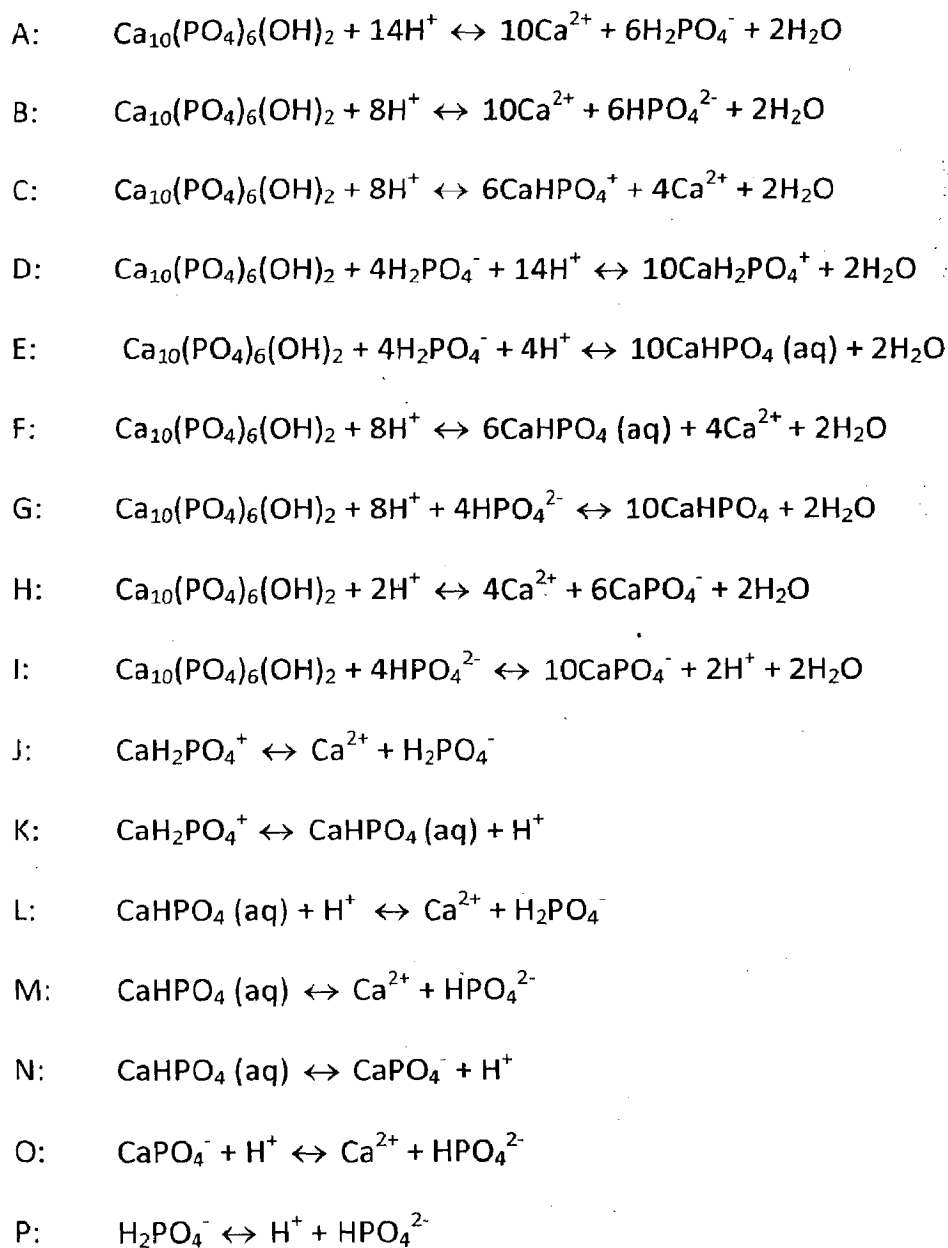


Table 2.7 Limits to concentration of heavy metals

Elements	ppm (maximum limit)
Arsenic (As)	3
Cadmium (Cd)	5
Mercury (Hg)	5
Lead (Pb)	30

that wear of hydroxyapatite pin against glass-infiltrated alumina occurred primarily by fracture and deformation. The hydroxyapatite wear particulates mixed with wear products from glass infiltrate in alumina and water to form an intermediate surface layer. Because of this adhered debris layer, steady state wear is more appropriately described as three body wear as compared to two body wear. Pin-on-disc experiments with HA pin and glass-infiltrated alumina (in-ceram alumina) conducted by Kalin et al., (2002) showed that the wear volume of HA increased as surface roughness of glass-infiltrated alumina and load was increased, while for a given surface roughness value, the wear factor remained independent of load. Further, polished glass-infiltrated surface showed no evidence for material transfer at low load, while mechanical wear with removal of glass infiltrate was observed at higher loads.

Morks et al., (2007) investigated the role of arc current in plasma spray technique on abrasion behavior of coatings and reported that with increase in arc current the abrasion resistance of HA coating increases mainly due to increase in hardness of coating. The resistant to abrasion wear was found to be dependent on coating thickness also as the abrasion wear resistance increased as thickness of HA coating become less than 30 μm due to the increase in hardness of thin HA coatings. The dependence of gas flow rate in plasma sprayed HA coatings was studied by Morks and Kobayashi, (2006), they reported that HA coatings sprayed at high gas flow rates exhibit higher abrasive wear resistance as compared to those sprayed at low gas flow rate due to higher cohesion bonding among the splats and lower porosity.

The wear resistant properties of HA can be improved by reinforcing the secondary phase to HA to produce composite coatings. Several researchers have used various reinforcement materials such as silica (SiO_2), titania (TiO_2), alumina (Al_2O_3), zirconia (ZrO_2), carbon nano-tubes (CNT), diamond like carbon, P_2O_5 -CaO glass, yttria stabilized zirconia (YSZ), Ni_3Al and titanium and its alloys. A composite powder of HA with 4 wt% multi-walled CNT was deposited on Ti-6Al-4V. Both HA and HA-CNT composite coatings showed better wear resistance than Ti-6Al-4V substrate while, HA-CNT composite coatings result in reduced weight and volume loss in comparison to HA coatings and Ti-6Al-4V substrate. Low weight loss of HA-CNT coating during wear was due to under-propping and self-lubricating nature of CNT and the pinning of wear debris assisted by CNT bridging and stretching (Balani et al., 2007A).

azide limits bacterial growth in the fluid and has a role in inhibiting protein adsorption on the surface of implant, while EDTA discourages calcium phosphate precipitation. Overall, a joint simulator provides a reasonable good idea regarding wear performance for artificial joints. The time taken for analysis, variability of lubricants and foremost the cost inputs are major limitations for their use. Unfortunately, the cost of commercial models of knee simulator is in excess of \$200,000 (Rs. 1 crore).

The most complex wear testing devices are knee simulators, which test actual knee prosthesis. Most knee simulators provide physiologic loading and can reproduce at least four degrees of freedom: Flexion/Extension (F/E), Anterior/Posterior (A/P), tibial rotation and abduction/adduction. Some of the joint simulators are discussed in details hereunder.

2.2.4.1 Six station rolling sliding tribotester

The six station rolling sliding tribotester is quite effective machine for testing the contact fatigue behavior of different orthopedic polymers (Van Citters et al., 2004) and is equally useful in testing their wear behavior due to clinically relevant stress and motion environment. The tribotester articulates cobalt-chromium cylinders against UHMWPE pucks. The contact stresses resulting from this specimen geometry can be determined through Hertzian line contact theory. Moreover the non-confirming contact creates surface-subsurface stresses that are similar to those found in contemporary total knee replacement bearings (Kennedy et al., 2000 and Van Citters et al., 2004). Alignment of the articulating cylinders is performed through placing pressure sensitive films at contact between a Co-Cr cylinder and an UHMWPE puck. The image of rolling sliding tribotester is presented in Fig. 2.10.

The intensity of color on otherwise translucent film is related to contact pressure at that particular location. Shims are generally inserted in the bearing mounts until the two i.e. Co-Cr cylinder and UHMWPE puck become parallel and uniform contact pressure profile appears. After the insertion of shims all the six stations should show similar pressure distribution across the contact width. Each station incorporates a fluid bath to provide lubrication and cooling at contact points. The contact can be viewed through the acrylic windows incorporated with the system. The design of the testing machine ensures that all the contact axes are perpendicular to direction of sliding. Each pair can be loaded independently as per the requirement of test, as constant load pneumatic system is incorporated with each pair of cylinder and puck. A crank and rocker arm powered by a fixed speed motor is used for articulation. Backlash is prevented by adjustable gears as well

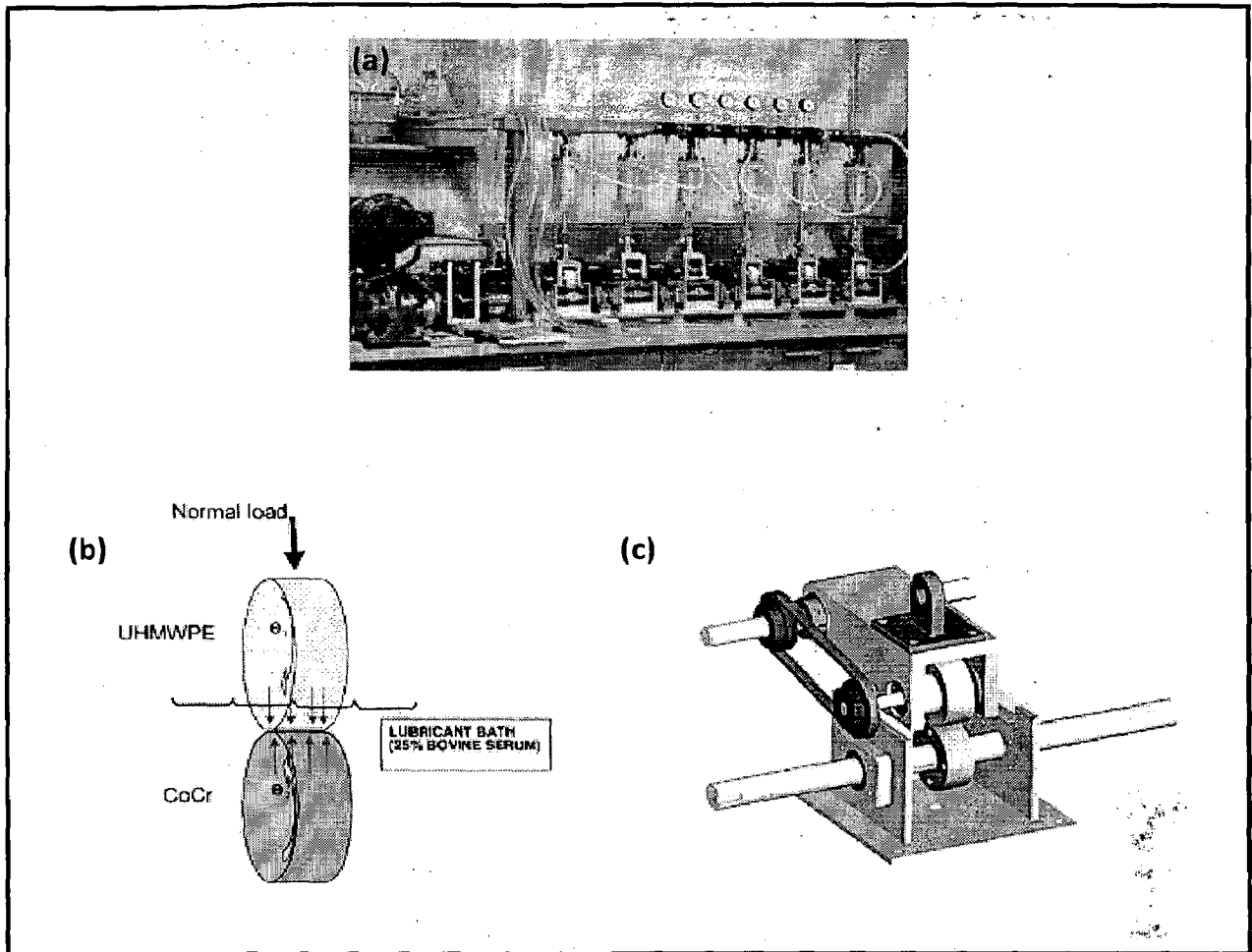


Fig. 2.10 Multistation rolling sliding tribotester: (a) Macrograph of tribotester, (b) contact conditions in one of the stations (Kennedy et al., 2007), (c) CAD model of one of the six stations, (Van Citters, 2004)

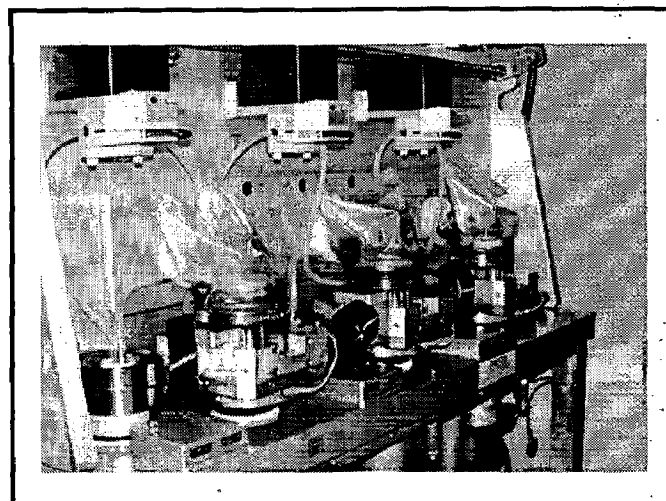


Fig. 2.11 Three stations of AMTI-Boston six station knee simulator, Model KS2-6-1000, (Advanced Mechanical Technology Inc., USA)

The frame, motor and loading system of an old five station, uniaxial hip joint simulator were utilized to complete one station of three axis knee wear simulator. The Co-Cr ball 54 mm in diameter with 42.4° F/E motion revolve on the disc and a vertical upward static load of 2kN is applied on the lower side of the disc as shown in Fig 2.13. The detailed design of machine is reported by Saikko et al., (2001).

2.2.4.4 Fein focus X-ray microscope and fretting wear apparatus

The equipment consists of a Fein Focus X-ray image processing system (Fein Focus Roentgen-system, Germany) with a beam spot size 4-20 μm in diameter. Micro-focused X-rays directly penetrate the contact surfaces and forms a visible image on a fluorescent screen placed below specimen. A high speed digital camera captures the images developed on fluorescent screen and convert to visual images which can be displayed on a monitor. A definite time interval is selected to capture the images and image processing functions are used to treat and enhance the images to reveal the detailed phenomenon of fretting wear. The line diagram of the equipment is represented in Fig. 2.14.

This equipment is improved version of simple ball-on-flat fretting wear testing machine. The upper specimen is a ball made from hardened stainless steel AISI 410 with a diameter of 25 mm as shown in Fig. 2.14. The material to be investigated for wear studies is made in form of a flat and mounted on table which reciprocates at a specified frequency. Electromagnetic exciters are used to oscillate the table at a given frequency. A function generator controls the displacement via a power amplifier. A piezoelectric force transducer is used to measure tangential frictional force and amplitude of oscillatory movement is measured by laser sensor with a minimum resolution of 2 μm (Fu et al., 1998).

2.2.4.5 Wear testing equipments

All of the joint simulators which simulates motions and loading of the actual human knee joint are very expensive for procurement and very difficult to handle and manage. Many investigators have used some simple machines to estimate the wear lose of the coated as well as bare metallic specimens used for body implants. Khan et al., (1996), Balani et al., (2007B), Kalin, (2003), Kalin et al., (2002), investigated wear resistance of specimens on pin-on-disc wear testing equipment using phosphate buffered saline; simulated body fluid, carboxymethyl cellulose in distilled water, distilled water to lubricate the contact respectively, while Gross and Babovic, (2002), Sidhu et al. (2007), Bolelli et al., (2006)

Inspired by the above design which offers better wear measurement due to line contact, combination of sliding and rotational motion, which reproduces two degrees of motion i.e. anterior-posterior and flexion-extension (flat sliding specimen and rotating disc) out of six degrees of motion of knee joint, similar equipment was built for present study. Flannery et al., (2008) simulated the same two degrees of motion in three station wear simulator to measure wear of tibial inserts.

2.3 ROLE OF COATINGS

Early failure of body implants frequently occurs due to complex reactions between metallic materials and harsh body environment. It is important to clarify the degradation mechanism of materials used for implants by typical salts present in body fluid so as to increase the service life of implants. Materials for body implants need excellent mechanical properties, including resistance to corrosion, stability of microstructure, good strength and natural union with bone and ability to grow new bone at interface. These requirements especially which are related to osseointegration can not be achieved by presents alloys alone.

Bioactivity is widely accepted as the essential requirement for an artificial biomaterial to exhibit chemical bonding to living tissues upon the formation of a bone like apatite layer on its surface in any simulated or actual body environment (Kokubo et al., 1990). The human body is a harsh environment for metals and alloys which consists of an oxygenated saline solution with salt content of about 0.9 % at pH of 7.4 and temperature of $37 \pm 2^\circ\text{C}$. The body fluid constitutes water, complex compounds, dissolved oxygen and large amounts of sodium and chloride ions and other electrolytes like bicarbonates and small amount of potassium, calcium, magnesium, phosphate and amino acid, proteins, plasma, lymph etc (Morks and Kobayashi, 2007B and Mudali et. al., 2003). The following are the needs and some major requirements for coating and substrate for body implants.

2.3.1 Need of Coating

- Major drawback of using uncoated metals and alloys for body implants is biological incompatibility and degradation in harsh body environment.

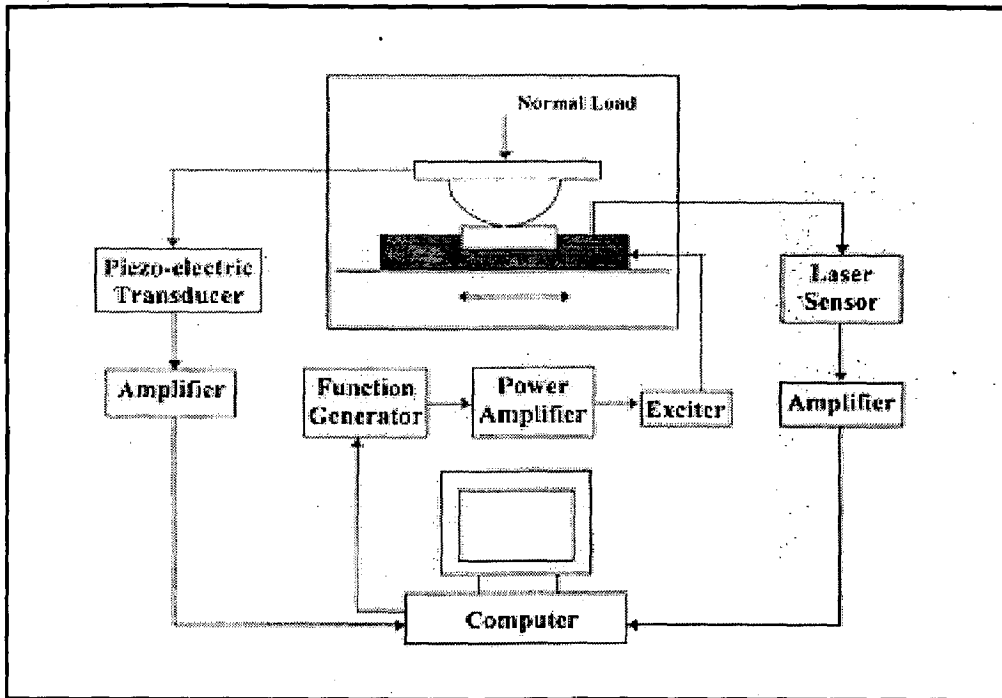


Fig. 2.14 Schematic illustration of fretting wear tribometer, (Fu et al., 1998)

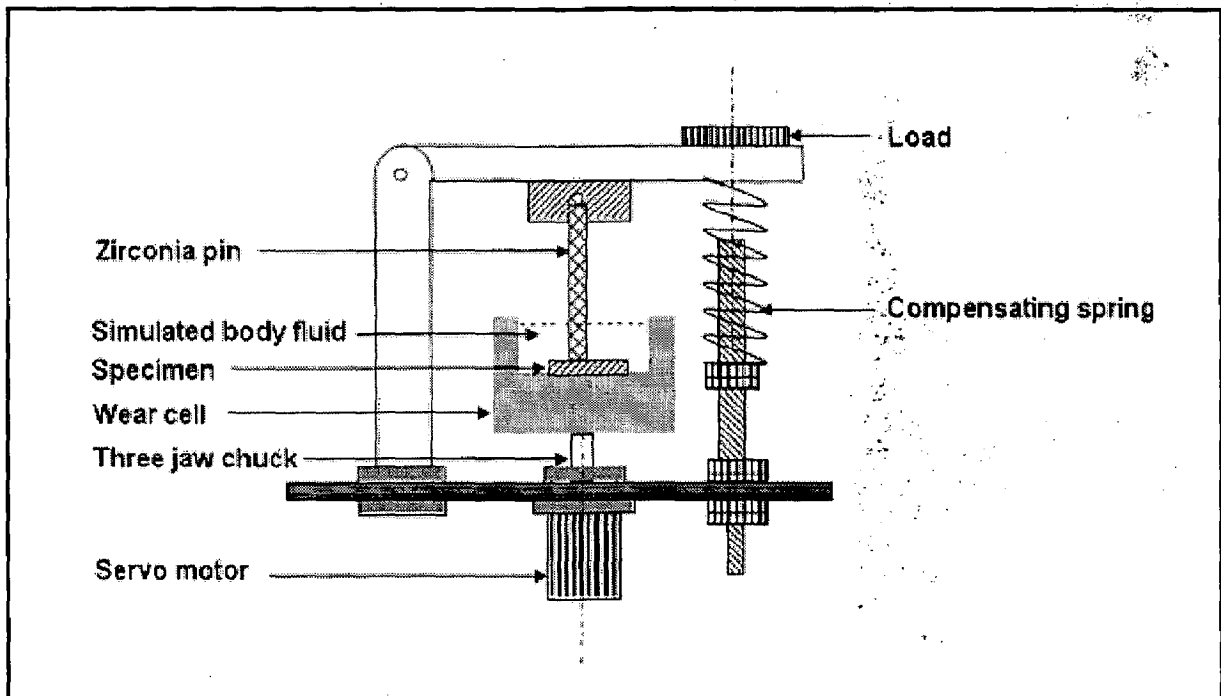


Fig. 2.15 Schematic illustration of pin on disc wear machine with lubrication facility, (Balani et al., 2007A)

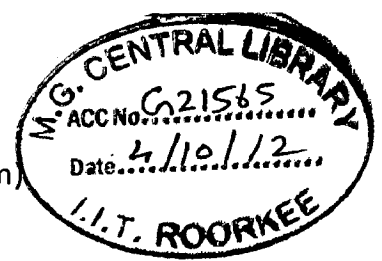


Table 2.8 Hydroxyapatite coating techniques, (Azom.com)

Coating process	Coating thickness	Advantager/limitations
Dip coating	0.05 – 0.5 mm	Complex substrate can be coated Requires high sintering temperature Thermal expansion mismatch is common
Electrophoretic deposition	0.1 – 2.0 mm	Can coat complex substrates Cannot produce crack-free coatings without difficulty Requires high sintering temperatures
Hot Isostatic Pressing	0.2 – 2.0 mm	HIP cannot coat complex substrates High temperature is required, producing thermal expansion mismatch Produces dense coatings
Sol – Gel	<1µm	Complex shapes at low processing temperatures Expensive raw materials
Sputter Coating	0.02 – 1 µm	Line of sight technique Produces amorphous coatings Uniform coating thickness on flat substrates
Thermal Spraying	30 – 200 µm	High processing temperature and rapid cooling leads to amorphous coatings Line of sight technique

Vacuum plasma spray and high pressure plasma spray have also been introduced. The introduction of robots in the spraying was another important technological advancement. The thermal energy in the plasma spray process is provided by high energy plasma that is formed within the plasma gun. The spray gun consists of a tungsten cathode (electrode) and a high purity copper anode (nozzle) separated by a small gap. DC current is supplied to the cathode, which than arcs across to the anode creating an electric arc. An ionizing gas, such as argon, helium, hydrogen or nitrogen is fed into the arc where it becomes ionized and forms a plasma flame. In some cases a mixture of gases is used. The gas get excited to high energy level and plasma so formed is unstable and it recombines to form a gas again, releasing a large amount of thermal energy. Schematic representation of plasma spray gun and shrouded plasma spray gun are shown in Fig. 2.18 and Fig. 2.19 respectively

Vacuum plasma spraying (VPS), also known as low pressure plasma spraying (LPPS) is recently being used for production of HA coatings (Gledhill et al., 1999 and Gledhill et al., 2001A). The VPS process consists of a conventional plasma spraying system enclosed in an evacuated chamber which provides an inert atmosphere for the gun and the work piece.

The pressure in the chamber is generally in the range of 50-100 mBar. In a vacuum the velocity of plasma jet can be much higher, reaching the speed of up to three times the speed of sound (Nicholson, 2002). The plasma spraying is most flexible and versatile thermal spraying process with respect to the sprayed materials. The high temperature plasma spray process permit the deposition of coatings of metals, composite, cermets and ceramics and it has special applications for thermal, electrical and biomedical purposes (Bunshah, 2001). Plasma techniques are capable of producing thick coating of more than 100 μm at high production rates with no degradation of mechanical properties of substrate (Yoshida, 1993). Among other key features of plasma spraying are formation of microstructures with fine, non-columnar and equiaxed grains, ability to produce homogeneous coatings that do not change in composition with thickness, ability to process materials in virtually any environment e.g. air, reduced pressure inert gas, high pressure and underwater (National Materials Advisory Board, 1996).

2.5 THE PLASMA SPRAY PROCESS

2.5.1 Arc Formation

Plasma is a complicated phenomenon. It is often referred to as the 'Fourth State of Matter' (Rossmagel et al., 1990), as it differs from solid, liquid and gaseous state and does not obey the classical physical and thermodynamic laws. Plasma are used in many different techniques e.g. for modification and activation of surfaces. There is currently much research being carried out into understanding them and controlling them. The actual processes involved in plasma formation are complicated. All gases at a nonzero absolute temperature contain some charged particles, electrons and ions, along with some neutral gas atoms. The charged particles only substantially affect the properties of the gas at concentrations where the space charge found by the particles is large enough to restrict their motion. Dissociation and ionization of the gas leads to free electric charge carriers. As the charge concentration increases, the restriction on particle motion becomes more and more stringent and at sufficiently high concentrations, the interaction of positively and negatively charged particles results in persistent neutrality within the whole gas. Any disturbance of neutrality

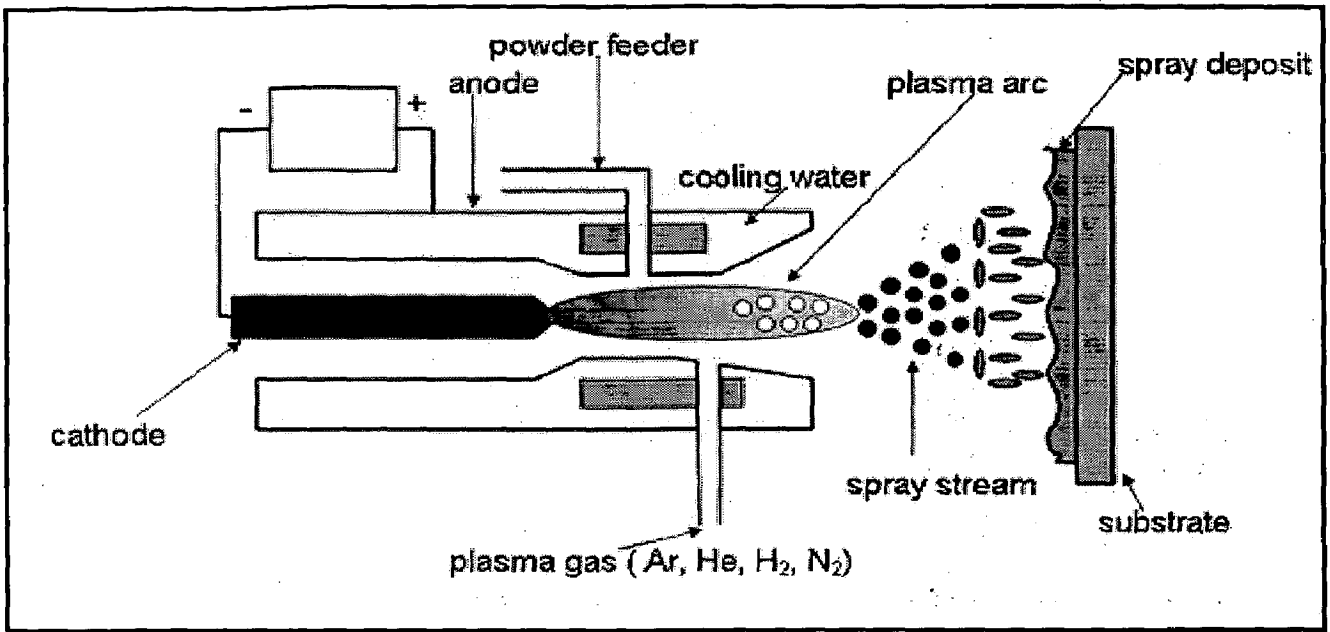


Fig. 2.18 Schematic illustration of plasma spraying process, (Paital and Dahotre, 2009)

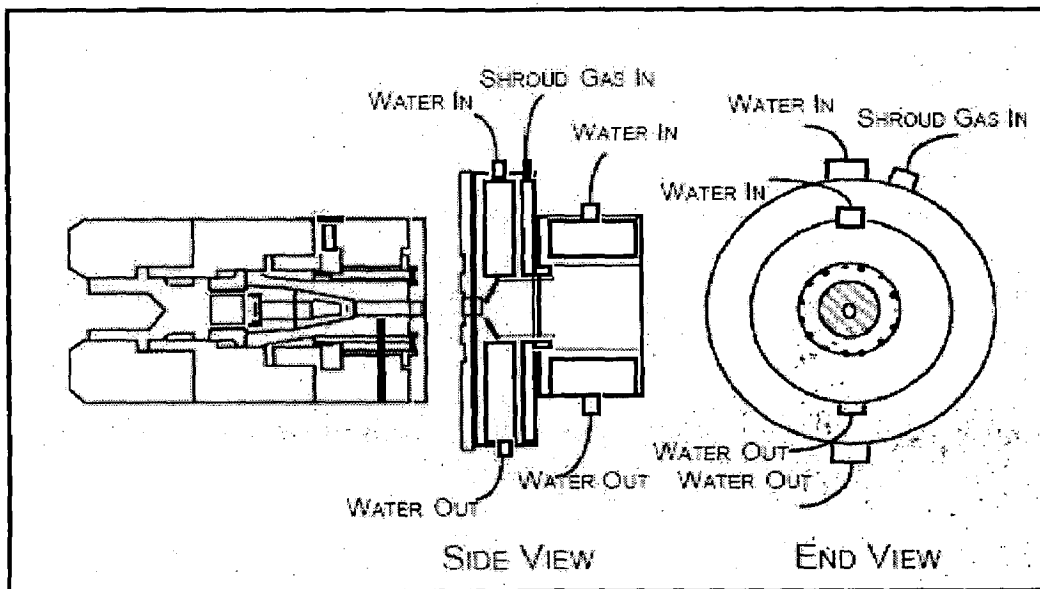


Fig. 2.19 Schematic illustration of shrouded plasma spraying process, (in.materials.drexel.edu)

Solidification begins after deformation is completed at the particle substrate interface (or previously deposited layer), as this interface acts as heat sink.

The solidified particle on substrate is called lamella or splat. The solidification time for HA particles has been suggested to be as short as 10^{-7} - 10^{-6} s (Tong et al., 1998), which further depends on the thermal conductivity of substrate material and the thickness of any previously deposited lamella on which they impact. The temperature of substrate is affected by heat transfer from both the plasma flame and droplets impacting on it, which can be in excess of 1000°C depending on the spray parameters used (Oosterbos et al., 2004). The particles flatten, cool down and solidify so rapidly that the next impinging particulate hit already solidified lamella (Fantassi et al., 1992). Successive impacting particles cause lamella to built-up to form the coating. One pass of plasma gun generally produces a coating layer of about 10 – 15 lamellae thick. Between the depositions, reaction between the surface of deposited lamella and surrounding environment may occur, such as absorption of water or oxidation. The number of lamellae deposited depends on the requirements of the thickness of coating.

Particle size, velocity and temperature have been recognized as plasma spray conditions that have a greatest influence on lamella formation (Yankee and Pletka, 1991). The properties of substrate or previously deposited layer also effect the lamella formation. The lamella may exhibit one of the two principle morphologies: pancake or flower as represented in Fig. 2.22.

The effect of plasma gas flow rate, percentage of secondary gas, velocity and temperature of plasma and particle on splat characteristics was investigated by Yankee and Pletka (1991). The results showed that the splat size was inversely proportional to the plasma velocity, with smaller droplets being formed at high plasma velocity. This was thought to be due to shorter residence time of the HA particles in the flame leading to less superheating of droplets. Relatively low plasma velocity was observed to produce large lamellae.

Hotter plasma conditions produced lamellae of 'pancake' while less hot plasma conditions produced 'flower' morphology. The formation of arms of the 'flower' lamellae depend on the viscosity of molten particles. The appearance of the 'flower' splat shows that solidification occurred after the effect of surface tension became dominant over viscous flow forces.

The size and the mass of the particles were also seen to influence the splat characteristics, larger particles being more likely to create 'flower' morphology. A variety of lamellae can be obtained in one spraying operation, because the particles due to their different size and injection velocity distribution, experience different trajectories and thus different thermal and momentum histories (Fantassi et al., 1992).

The structure of the coating at grain level is termed as ultra-structure. Examination of the ultra-structure of a coating looks at the crystals that are formed during recrystallization. The size and structure of crystals formed depend on the phenomenon that occurs inside each newly generated coating layer. The micro-structural features such as pores, cracks and splat boundaries influence the coating quality. During the solidification, crystals generally grow in on preferential direction within the splat. Two types of lamellae generally forms during recrystallization, either columnar or fine grained equiaxed also referred as brick wall (Pawlawski, 1995). Fine grained equiaxed crystals grow parallel to the surface. Both types of ultra-structures are represented in Fig. 2.23. The dimensions of crystal in thermal spray coating are of nanometer range.

The rapid cooling and solidification generally results in columnar ultra-structure, while the slow heat removal rate at interface results in fine-grained equiaxed microstructure (Pawlawski, 1995). If the cooling rate is very high, the coating may solidify before any crystals can be formed which leads to higher contents of amorphous phases in the coating (Tong et al., 1998). The variation of grain size and phase stability of HA coating as a function of coating thickness is reported by Yankee and Pletka, (1992). Crystal size of the initial layers is very small as rapid cooling and rapid solidification at substrate restrict crystal growth. The size of the crystal increases from interface towards coating surface due to smaller cooling rates (LeGeros and LeGeros, 1991 and Ji et al., 1992)

Sun et al., (2003) deposited HA coating on by plasma spraying process and developed a model (Fig. 2.24) based on previous researches showing formation of various phases upon deposition of droplet on substrate. They suggested that formation of various phases in plasma sprayed droplets depend upon hydroxyl state and cooling rate of droplet during solidification and accumulation of heat and hydroxyl group during coating buildup. A droplet consists of three layers as discussed earlier. A critical cooling rate may lead to recrystallization of stoicheometric melt (Fig. 2.24a) and transformation of de-hydroxylated melt to amorphous phases. Decreased cooling rate may lead to recrystallization of de-hydroxylated melt as shown in Fig. 2.24b whereas, accumulation of hydroxyl group and heat transferred by incoming molten particles or by plasma to previously deposited splat may

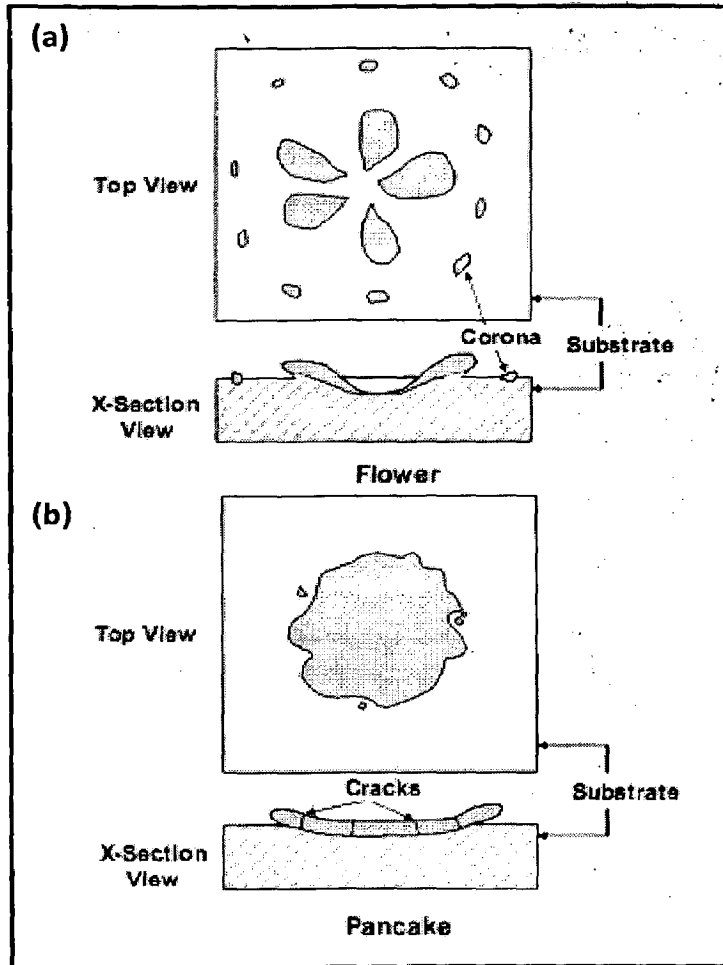


Fig. 2.22 Splat morphologies of particle by plasma spray process (a) flower morphology and (b) pancake morphology, (Pawlowski, 1995)

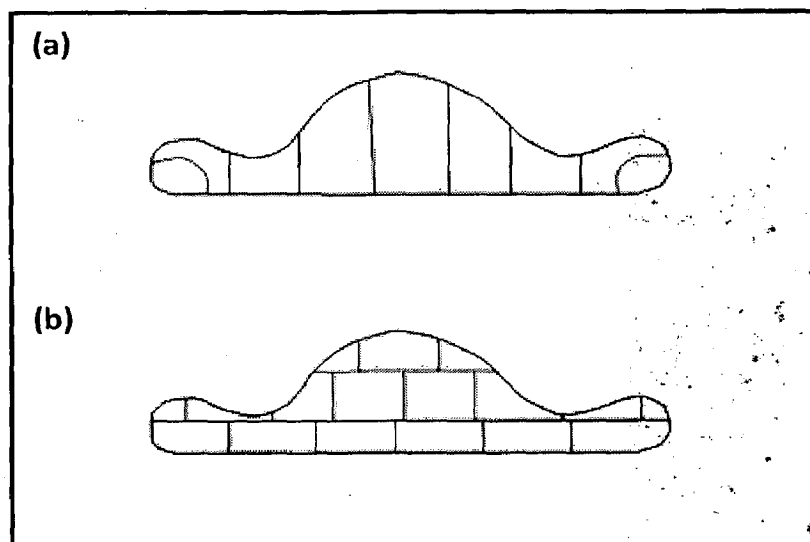


Fig. 2.23 Ultra-structure of lamellae resulting after recrystallization (a) columnar ultra-structure and (b) fine-grained equiaxed ultra-structure, (Pawlowski, 1995)

The stoichiometry of HA powder and partial pressure of water in surrounding atmosphere have the greatest effect on the formation of various phases when HA is heated. The consequences of changing stoichiometry of HA and partial pressure of water have been investigated by many researchers (Sridhar et al., 2003, Fang et al., 1994 and Park et al., 2002). Fang et al., (1994) showed the effect of stoichiometry on the thermal stability of HA from his experiments in which HA powders with Ca/P ratio of 1.52-1.68 were heated to 1100°C. The results showed that the powder with Ca/P ratio of 1.57 fully decomposed to TCP, the powder with Ca/P ratio of 1.67 partially decomposed to TCP, while no change was observed to the powder with Ca/P ratio of 1.68. Tampieri et al., (2000) also reported that stoichiometric HA endures thermal treatment at significant higher temperature in respect to non-stoichiometric HA.

The thermal behavior of CaO-P₂O₅ system at high temperature without presence of water vapor is shown in Fig. 2.25, while Fig. 2.26 presents the thermal behavior of CaO-P₂O₅ system at high temperature in presence of water vapors. It can be seen from Fig. 2.25 that HA is not stable under these conditions and various calcium phosphates including TTCP (Ca₄P), TCP (Ca₃P), monetite (Ca₂P) and mixture of calcium oxide (CaO) and Ca₄P are formed.

Figure 2.26 shows the CaO-P₂O₅ system at a partial water pressure of 500 mm of Hg. Under these conditions HA is found to be stable up to a maximum temperature of 1550°C. The Ca/P ratio is generally not exactly equal to 10/6; hence other calcium phosphates such as CaO or TTCP are also stable at this temperature. It can be concluded that in order to avoid de-hydroxylation and decomposition of HA during thermal spraying a highly crystalline, stoichiometric HA powder should be used.

Although, there is agreement between researchers about the processes that occurs during thermal decomposition of HA, it is difficult to predict the exact temperature at which these reactions take place. This is because of the reason that reaction does not occur instantly but take place over a wide range of temperature. Researchers have used several techniques to determine the effect of temperature on HA, such as Thermo-gravimetric Analysis (TGA) (Lazic et al., 2001 and Tampieri et al., 2000), Differential Thermal Analysis (DTA) (Park et al., 2002 and Deram et al., 2003), heat treatment in-situ using high temperature X-ray Diffraction (XRD) (Liao et al., 1999), and heat treatment in-situ using Fourier Infrared Spectroscopy (FTIR) (Liao et al., 1999) to find out the temperature at which decomposition of HA take place. The evaporation of water from hydroxyapatite has been reported to occur in a wide range of temperature (25°C – 600°C) (Sridhar et al., 2003, Lazic

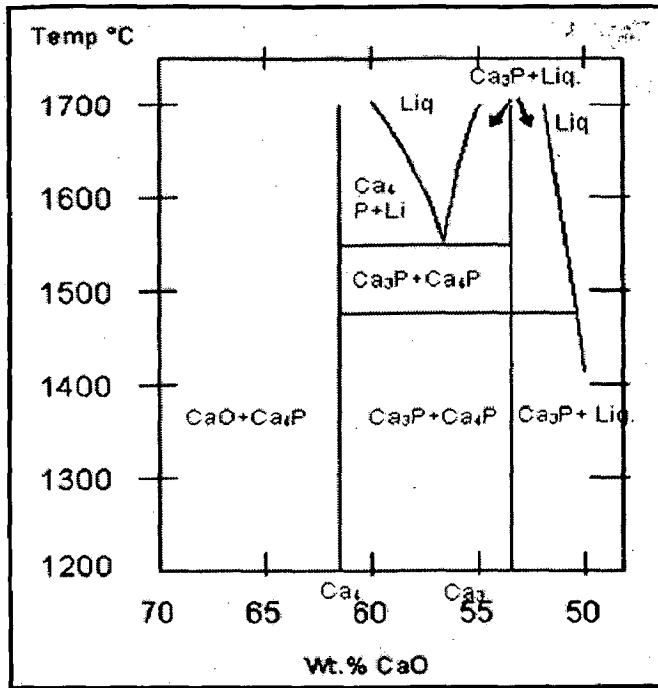


Fig. 2.25 Phase equilibrium diagram of calcium phosphates ($\text{CaO-P}_2\text{O}_5$) at high temperature without water vapors, (Klein et al., 1993)

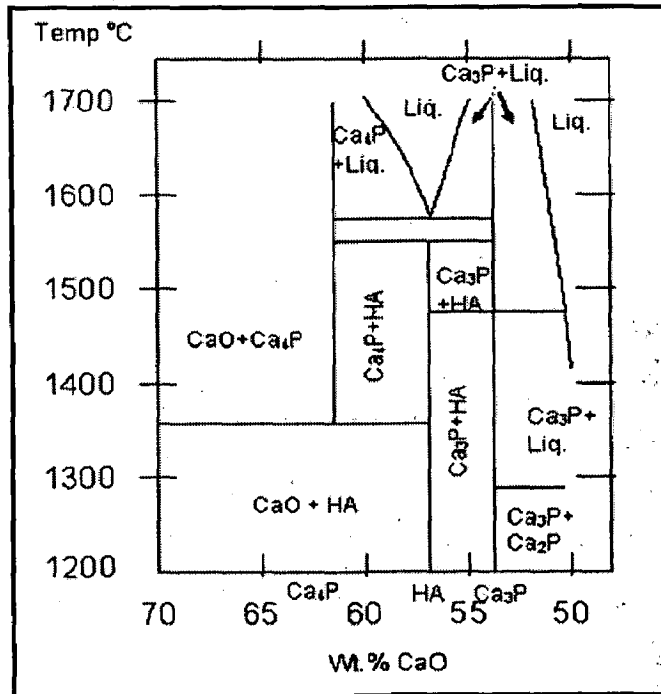


Fig. 2.26 Phase equilibrium diagram of calcium phosphates ($\text{CaO-P}_2\text{O}_5$) at high temperature in water atmosphere, (Klein et al., 1993)

interface and increase in adhesive strength, shear strength and Young's modulus of HV₀₁ sprayed HA coatings by heat treating them in air at 750°C for 30 min was reported by Li et al., (2002B).

Post spray treatment at 800°C on plasma sprayed HA reinforced α -TCP coating eliminated the TCP phase from either decomposition of HA or TCP feed stock and TTCP and CaO phases produced by decomposition of HA retained (Wang et al. 1998).

Laser treatments were performed to increment the degree of crystallinity of plasma sprayed titania-HA functionally graded coatings by Cannillo et al., (2009) and concluded that laser power of 80 or 100W increased the degree of crystallinity and reduced the contents of by-products present in as-sprayed plasma sprayed HA coatings. It was further concluded by them that the increment in crystallinity was not as high as could be achieved by thermal treatment but the very short time requirement and the selectivity of treatment were found as the benefits of laser treatment over thermal treatment.

To enhance crystallinity and purity of sol-gel derived HA coatings, the coatings were annealed in vacuum at a sintering temperature of 300°C, 600°C and 900°C and IR spectra showed considerable improvement of molecular arrangement manifested through clearly distinguishable absorption peaks (Balamurugan et al., 2006). Sol-gel derived hydroxyapatite coatings were heat treated at a temperature ranging between 500-900°C and analyzed by XRD. The results of XRD suggest that crystallization starts at a temperature between 500-600°C, but a temperature of 800°C is required to remove most of the organic material and produce thin homogeneous coating (Gross et al., 1998).

Post coating heat treatment at 600°C for 2h on specimen produced by deposition of HA-2% CNT by electrophoresis technique resulted in adequate bonding strength between coating and implant surface against peeling (Kaya, 2008).

Water vapor (hydrothermal) treatment has been employed to promote the transformation of amorphous phases to crystalline phase in the as-sprayed HA coating. Weng et al., (1995), treated the as-sprayed coatings in an environment containing water vapor with a vapor pressure of 0.15 MPa for different periods of time. They observed that water reacted with amorphous oxy-apatite, which lead to reoccupation of lattice vacancies on the missing hydroxyl positions by hydroxyl groups and transformation of the amorphous oxy-apatite to crystalline oxy-hydroxyapatite. The enhancement of growth of crystallites and reconversion of decomposition resultants, such as TCP, TTCP and CaO into crystalline phase was reported by water vapor treatment.

Zyman et al., (1993B) investigated structural changes in the surface layers of as-sprayed HA coatings during immersion in water. They reported that the disappearance of

remarkable activity in simulated body fluid, with the formation of a silica-rich layer and hydroxyapatite crystals. However, hydroxyapatite did not appear as a thin film on top of the silica-rich layer, but rather as regions dispersed inside each layer (Bolelli et al., 2009).

Hamdi and Ide-Ekessabi (2007) studied dissolution behavior of simultaneous vapor deposited calcium phosphate coatings on silicon substrate in calcium free Hank's balanced salt solution for testing the corrosion behavior of implant materials. The results showed that amorphous coatings dissolved almost immediately with no coating left after 1.5 days of immersion, α -TCP dissolved steadily with time, while HA phase was stable with no sign of dissolution even after 14 days of immersion period in calcium free Hank's solution.

Balamurugan et al., (2007C) studied the in-vitro behavior of sol-gel derived CaO-P₂O₅-SiO₂-ZnO bioglass in simulated body fluid and reported that incorporation of Zn into bioglass does not reduce bioactivity of bioglass, however Zn addition was found to be beneficial for cell attachment and for maintaining pH of SBF within physiological limit by forming zinc hydroxide in SBF solution. Stimulation of early cell proliferation in bioglass was also reported by addition of limited amount of Zn.

Khor et al., (2004) reported that the extent of HA thermal decomposition in HVC sprayed coating is significantly reflected through the melt state of powders. HA splat markedly dissolve more readily than un-melted part. Two types of coatings were developed on Ti-6Al-4V substrate using two different processes namely vacuum plasma spraying (VPS) and detonation gun (D-Gun) spraying by Gledhill et al., (1999). The results showed that the D-Gun process produce a denser coating with higher proportion of amorphous phase such as β -TCP than VPS. The higher crystallinity and lower residual stress found in the VPS coatings result in a slow rate of dissolution in-vitro and in-vivo relative to D-Gun coatings. In a study conducted by Zhang et al., (2010), Al₂O₃/diopside (diopside: MgCa(SiO₃)₂) ceramic composite were prepared by uniaxial hot-pressing and their biological activity in SBF was determined. They detected Ca and P on the surface of Al₂O₃/diopside ceramic composites after soaking in SBF for 9 days with formation of an apatite like layer. They reported that addition of excess diopside to alumina resulted in poor mechanical properties of composite and suggested appropriate amount of diopside in alumina would provide both good mechanical properties and biological activity.

Muthukumaran et al., (2010) studied the nitrogen and helium ion implanted AISI 316L SS against corrosion resistance in sodium chloride (NaCl) (9g/l of H₂O) solution at pH 6.3 and temperature of 37°C. The general corrosion and pitting corrosion behavior of both helium and nitrogen implanted steel showed a significant improvement as compared to virgin steel, further helium implanted steel showed better corrosion resistance as compared to virgin steel.

FHA coatings. The apatite layer took 28 days to smoothen in SBF with bovine serum albumin, while took only 7 days in standard SBF and glucose-containing SBF.

Balamurugan et al., (2007B) investigated TiO₂ reinforced HA coatings on SS 316L developed by sol-gel process for resistance against electrochemical corrosion in Hank's solution. The physical degradation of thick coatings (> 24 μm) was observed on immersion. The mechanism of degradation suggested was de-agglomeration of HA and TiO₂ particles accompanied by subsequent inter-particle fissure formation and eventual particle detachment from substrate. The results suggested that coating thickness of 20-24 μm was effective range for titania reinforced HA coating on 316L SS.

In 1990 Kokubo et al. used simulated body fluid to perform in vitro simulation of in vivo conditions. Oyane et al., (2003) proposed a revised SBF to take into account the fact that a large proportion of calcium and magnesium species present in serum were bound to proteins and unavailable for apatite formation. The revised SBF had a 40% lower concentration of calcium and 33% lower concentration of magnesium.

After a long span of time of research in this field, the opinion of large part of biomaterials community is that the formation of apatite on a material immersed in SBF is a proof of bioactivity and can be used to anticipate its bone bonding ability in-vivo.

Cell culture involves growing osteoblasts on the coating and evaluating their response to coating over a period of time. Changes that can be monitored include cell morphology (changes in shape of cells), cell proliferation (quantity of cells present) and cell viability (number of cells that are living or dead). Biochemical changes, such as expression of different genes, within the cell can also be measured. These changes indicate the level of cell differentiation occurring i.e. how quickly the cells are becoming bone tissue. Measuring the proliferation of cells gives important information about how well these cells can grow on the coatings. Cellular behavior can be influenced by characteristics of the material, including chemistry, composition and topography and the absorption and release of compounds into the cell culture media (Rouahi et al., 2006). Calcium phosphate particles on the anodic oxidation surface affect cellular attachment and spreading. Pre-incubation in medium prior to cell seeding and cell culture medium may affect the calcium phosphate coatings: Long-term in-vitro cellular assays and in-vivo experiments are necessary to find out the effect of calcium phosphate deposition to biological responses (Lee et al., 2010). Phases such as CaO dissolve in SBF in initial soaking period i.e. within seven days of immersion and as consequence the Ca ion concentration in the solution increases. Mechanical properties of HA/Ti-6Al-4V composite coatings were found to be superior than pure HA coatings, which indicated the better long-term stability of composite coatings in physiological environment (Gu et al., 2003).

Lim et al., (1999) deposited HA-ZrO₂ composite coating by plasma spray process onto Ti-6Al-4V substrate and reported that phase transformation of ZrO₂ from tetragonal to monoclinic during plasma spraying played a significant role in strengthening of HA-ZrO₂ coating. They further suggested that phase transformation of ZrO₂ led to volumetric increase of ZrO₂, which strengthen the coating and retarded crack growth due to generation of compressive stresses. Khor et al., (2000) studied the effect of phase compositions of plasma sprayed HA-ZrO₂ composite coating. They observed that HA, ZrO₂, CaO, TCP, TTCP and CaZrO₃ as the main phases of coatings were related to different contents of ZrO₂. They further reported that content of these amorphous phases decreased with increase in amount of zirconia from 10 wt% to 50 wt%. The presence of CaZrO₃ was observed in composite coatings with zirconia contents less than 30 wt% and reaction of CaO with zirconia was suggested as the possible reason. During plasma spraying the tetragonal zirconia transformed to cubic zirconia and the cause suggested for improvement in phase composition of composite coating was same as suggested by Lim et al., (1999). In a study Morks (2008) deposited HA-SiO₂ (SiO₂ 10-20 wt%) composite coating onto SUS 304 stainless steel substrate and reported increase in hardness, wear resistance and adhesive bond strength of composite coating as compared to HA coating. The causes suggested for improvement in mechanical properties of composite coating as compared to HA coatings were: slight increase in hardness of composite coating was due to decrease in coating porosity by SiO₂ reinforcement, improvement in abrasive wear resistance was due the fact that SiO₂ act as solid self-lubricant and the increase in bond strength was due to the reason that semi-molten SiO₂ particles strongly adhered with HA particles and metallic substrate.

Bond coats are already widely used between substrate and top coat in industrial applications mainly to compensate thermal expansion coefficient mismatch between substrate and topcoat, to reduce diffusion of substrate elements into coating and to enhance the mechanical properties of coating especially bond strength of coating. The application of bond coat to enhance mechanical propertied of thermal sprayed HA coatings are also available in literature. Chou and Chang (2002B) studied the strengthening of bonding at HA coating and Ti-6Al-4V interface by addition of intermediate layer of ZrO₂ as bond coat and reported an increase in bond strength by application of bond coat to 36.2±3.02 MPa as compared to 28.6± 3.22 without bond coat. The suggested cause for improvement in bond strength by incorporation of bond coat was diffusion of Ca ions from HA to ZrO₂ and rougher surface morphology provided by ZrO₂ bond coat. In a study by

hydrothermal heat treated specimens showed better erosion resistance as compared to as-sprayed coatings on all impact angles and significant improvement in bonding strength. The increase in erosion resistance of hydrothermal heat treated specimens was due to impeded cracks propagation, which was related to increase in fracture toughness of the hydrothermal heat treated coatings. Further, it was reported that wear fractures depend on the fracture toughness of materials.

Lahiri et al., (2010) demonstrated wear behavior of plasma sprayed HA-CNT coatings against alumina ball of 3 mm diameter for a total travel distance of 100 m using ball-on-disc wear tester. A normal load of 5 N was applied and wear test were conducted in dry conditions as dry conditions are more aggressive as compared to lubricated by physiological solutions. Addition of CNT resulted in about 80% decrease in wear volume and increase in wear resistance of composite coating as compared to HA coating. Two major factors were found to be responsible for increase in wear resistance of composite coating: decrease in coefficient of friction by addition of CNT and toughening of HA coating by CNT reinforcement, which reduced material removal. In a study conducted by Coathup et al., (2005), plasma sprayed porous HA surface were more effective than other un-cemented interfaces and cemented implants in resisting progressive osteolysis along the acetabular cup-bone interface. Further, results showed the significant effect of HA coated porous implant in term of bone contact and in-growth in the presence of wear debris and in prevention of interfacial wear particle migration.

Little work has been published on composite coatings developed by hydroxyapatite and aluminum oxide and application of Al_2O_3 -13 wt% TiO_2 bond coat as intermediate layer between HA and substrate to the best of knowledge of the author. Two different substrate materials namely AISI 316L stainless steel and pure titanium have been selected as substrate materials for present study. These materials are widely used for orthopedic and dental repair/replacement. The present study has been performed to evaluate mechanical properties and corrosion behavior of plasma sprayed pure and reinforced (0-30 wt% Al_2O_3) HA coatings. The corrosion and dissolution/precipitation behavior of coatings was conducted in simulated body fluid. In aim to re-crystallize the amorphous calcium phosphate phases developed during plasma spraying and to refine the grain size of HA coating, post coating heat treatment at 500°C, 700°C and 900°C was carried out for 2h in air. Behavior of these coatings regarding mechanical properties such as hardness, bonding strength and wear resistance; corrosion resistance and development of amorphous phases

EXPERIMENTAL TECHNIQUES AND PROCEDURES

This chapter presents the experimental techniques and procedures employed for deposition and characterization of coatings. Techniques to analyze properties like surface roughness (Ra), porosity, microhardness, bond strength are described in this chapter. A detailed description of processes used for corrosion and immersion behavior of coatings in simulated body fluid (SBF) has been furnished in this chapter. The details of procedure for wear testing and post coating treatment has been described. The procedures for analyzing the specimens after corrosion and immersion in SBF, post coating treatment and wear testing have been described. The specifications of the equipments utilized are furnished.

3.1 SUBSTRATE MATERIALS

Low carbon surgical grade stainless steel AISI 316L SS and titanium have been selected as the substrate materials for the present study. The substrate materials were procured commercially from Guru Steel and Engineering Limited, Mumbai (India) in the rolled bar form. The nominal chemical compositions of these materials, as provided by supplier are presented in Table 3.1. The actual chemical composition of AISI SS316L has been determined with help of Optical Emission Spectrometer (Thermo Jarrel Ash, TJA 181/81, USA) and that of titanium has been determined using EDAX analysis; which are reported in Table 3.1. These metallic materials find wide applications in bone and dental implants and repair.

3.2 DEVELOPMENT OF COATINGS BY PLASMA SPRAY PROCESS**3.2.1 Preparation of Substrate Materials**

Surface conditions of substrate significantly affect the bond strength of thermal spray coatings. The surface finish, texture and topography of the substrate are of particular importance. Impurities or any oily product such as grease on the surface of the substrate will greatly reduce the coating adhesion and may cause cracking or delamination. The specimens should not be held in bare hands after it is prepared for coating and also after the coating has been developed. In most of the cases an oxide free substrate is required for

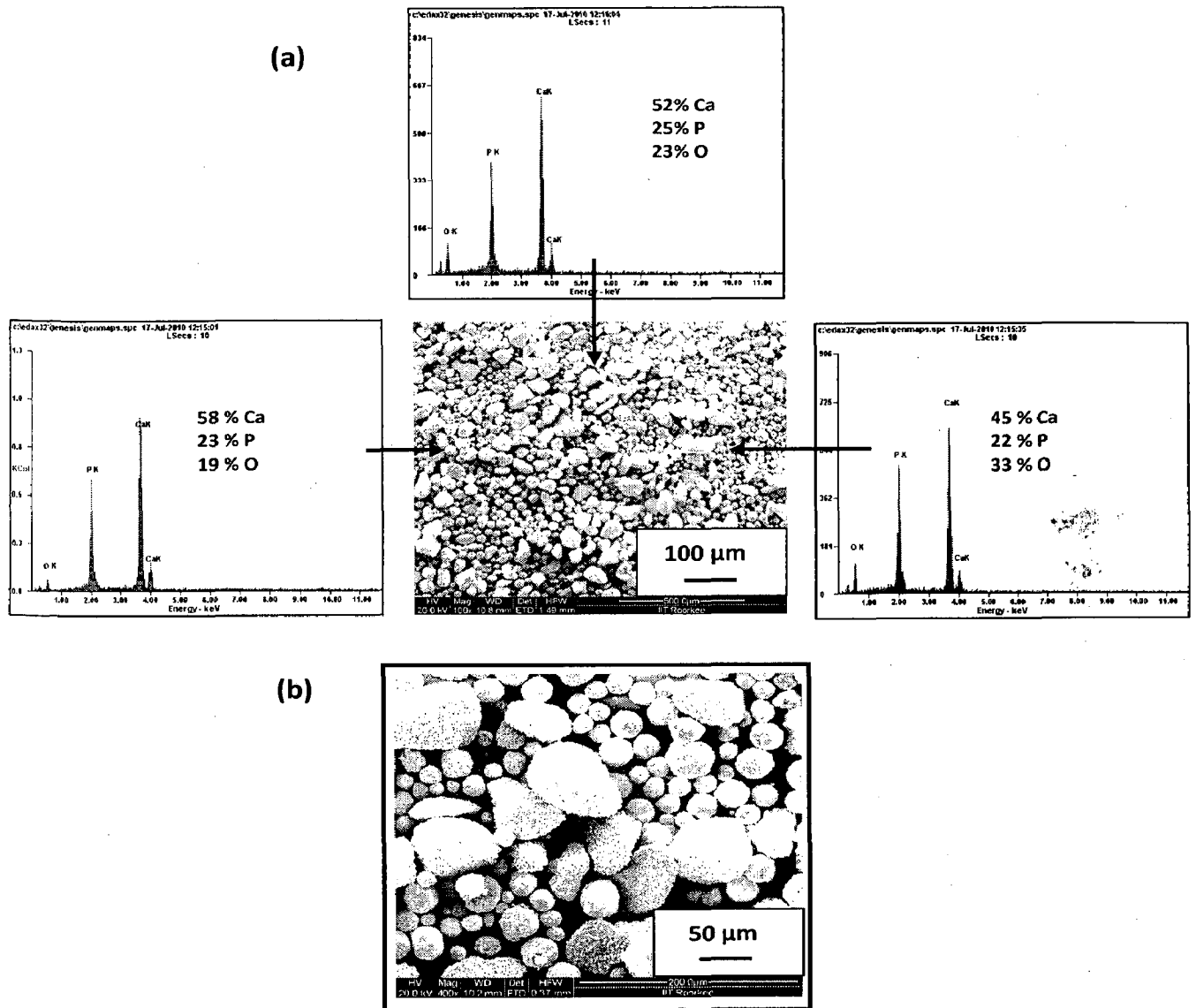
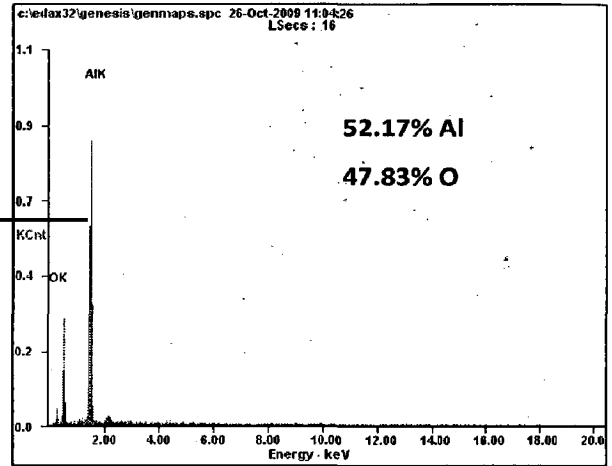
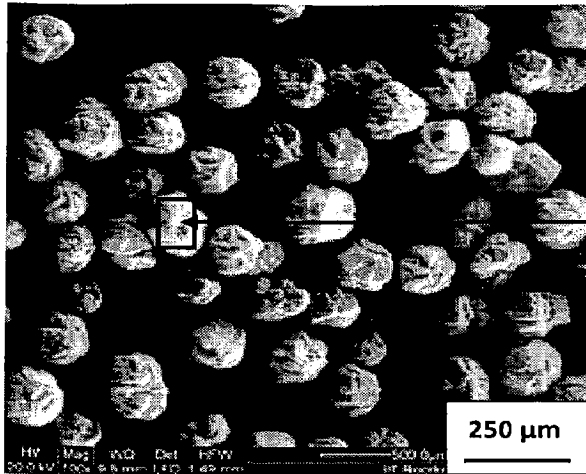


Fig. 3.1 FESEM morphology and EDAX analysis of hydroxyapatite: (a) at lower magnification (100X) with EDAX analysis and (b) at higher magnification (400X)

(a)



(b)

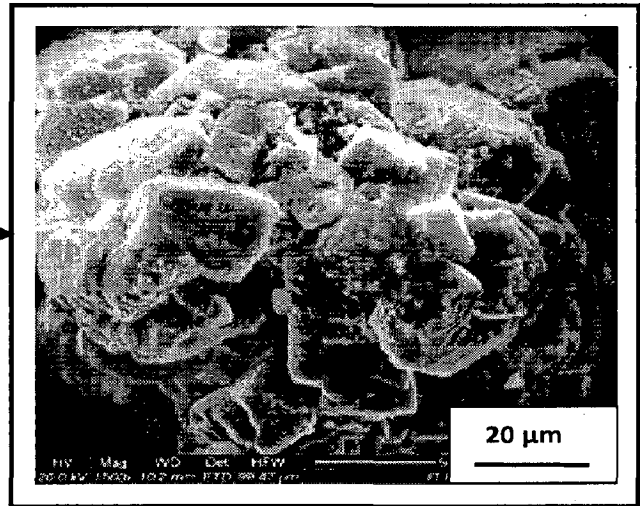
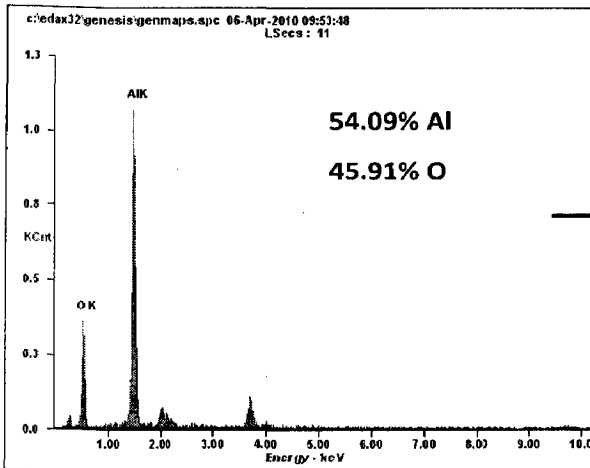


Fig 3.3

FESEM morphology and EDAX analysis of aluminum oxide (Al_2O_3): (a) lower magnification (100X) and (b) higher magnification (1500X)

the porosity by color difference technique. The software determines the pore area size in view field by converting the pore areas (grey-level areas) into a background color such as red in this case, while the rest of microstructure remains in its original color. The area of one feature is numerically related to the total area of the picture and the software counts the number of one color pixels and sets that as ratio of total number of pixels in the picture (total area of micrograph). Twenty different points, five in each orthogonal direction were chosen to determine porosity on the coated surface. Porosity measurement of plasma sprayed coatings has also been made from polished cross-sections of the specimens. Ten different points were selected along the cross-section to determine porosity along the cross-section. An average of twenty readings on coated surface and an average of ten readings along cross-section were taken as the value of porosity and are reported in Chapter 4 of present study.

3.3.4 Measurement of Surface Roughness

The surface roughness can be described using a number of different measures, such as Ra, Rq, and Rmax. In engineering applications, roughness is most often described as Ra, which is defined by equation 3.1.

$$Ra = \frac{\int_0^l |y| dx}{l} \quad (3.1)$$

Where y is the height or depth of the peak with reference to mean line (central line), while l is the length of the mean line. Ra is the average height (height above line or depth below line) between the surface of coating and mean line.

The Ra values of coated specimens were measured using non-contact optical profilometer (Model: Wyco NT1100, Veeco Instrumentation Inc., USA) with software vision – 32. The scanning mode used was vertical scanning interferometry. The center line average (CLA) method was used to obtain Ra values. Twenty points were selected for observation (five in each orthogonal direction). The surface roughness of coatings has been reported in Chapter 4.

3.4.3 X-ray Mapping Analysis

To obtain surface and cross-sectional analysis for presence of different elements in the coatings, the specimens were cut along cross-section, mounted in transoptic powder and polished in accordance with the procedure already discussed in Section 3.3.1 and made conductive as discussed in Section 3.4.2. X-ray mapping analysis of specimens (surface as well as cross-section) was performed on FE-SEM, for image acquisition, back scattered electron (BSE) and/or secondary electron (SE) image mode was entailed. An accelerating voltage of 20 kV, a working distance of 9-10 mm and an image size of 1024 x 884 pixels were used to get quality images. Energy dispersive X-ray (EDAX) analysis and X-ray mapping was employed to obtain elemental composition at different points on coating and surface of coatings. The selected area for cross-sectional analysis has three regions i.e. substrate, coating (top coat and/or bond coat) and epoxy region. The analyses were done for the substrate and the coatings elements and are presented in Chapter 4, 5, 6 and 7 of this report.

3.5 THERMOGRAVIMETRIC ANALYSIS/DIFFERENTIAL THERMAL ANALYSIS

To study the effect of temperature on feedstock during plasma spraying, thermogravimetric and differential thermal analysis were used. Starting powders and feedstock were analyzed using TGA/DTA technique in a temperature range of 30°C – 1500°C in nitrogen environment with nitrogen flow rate of 200 ml/min. The temperature was increased at a rate of 10°C/min. Aluminum oxide powder (10.5 mg) was used as reference. TGA/DTA plots were obtained using TG/DTA (Model: EXSTAR A6300, SII Nano Technology Inc., Japan) equipment. The results obtained are presented in Chapter 4 of the present study.

3.6 FOURIER TRANSFORM INFRARED SPECTROSCOPY

To analyze the presence of different groups (hydroxyl, phosphate, carbonate etc.) in feedstock and coated specimens FTIR spectroscopy was conducted on feedstock, as-coated specimens, specimens after immersion in SBF and post coating heat treated specimens. The transmittance or reflectance mode was adopted for FTIR analysis. For transmittance mode

scanned with scanning speed of 1°/min in 2θ range of 10° to 60° and intensity of peaks were recorded. The diffractometer interfaced with Bruker DIFFRAC^{plus}, X-ray diffraction software provides 'd' values directly on diffraction pattern. These 'd' values were then used for identification of various phases with help of JCPDS data cards. The software X'pert high score version 1.0a was also used to confirm the presence of respective phases. The results obtained from X-ray diffraction patterns are presented in Chapter 4, 6 and 7 of this study.

3.8 MECHANICAL PROPERTIES OF COATINGS

The mechanical properties of coatings such as microhardness, bond strength and wear were evaluated and compared for various types of coatings.

3.8.1 Measurement of Microhardness

To obtain microhardness of plasma sprayed coatings, the specimens were cut, mounted and polished as explained in Section 3.3.1. The microhardness of coatings along cross-section was measured by using SHV 1000 Digital Micro Vickers Hardness Tester fitted with Vickers pyramid diamond indenter (Chennai Metco, India). A load of 2.942 N was applied for penetration for a dwell time of 10 s and hardness was measured in Hv. Hardness values obtained were calculated by the software installed with Micro Vickers hardness tester by following relationship:

$$H_v = \frac{1885.4 \times F}{d^2}$$

Where F is the applied load, g
d is the mean of two diagonals of indent, μm.

Each reported value of the hardness is the average value of three measurements. These microhardness values are plotted as a function of distance from coating-substrate interface and incorporated in Chapter 5 of present study.

3.8.2 Measurement of Bond Strength

The tensile bond strength of the plasma sprayed coatings was measured using the ASTM C633 79 standard with help of universal mechanical testing system (H25 K-S Material Testing Machine, Hounsfield, England) with a capacity of 20 kN fitted with the Hounsfield S – Series testing software for Windows. This method covers the determination of adhesion

horizontally at 10.6 strokes/min against coated disc rotating at 10.6 rpm. The combination of sliding motion of flat and rolling motion of disc produces a sliding/rolling motion which is not present in conventional pin on disc wear tester. The width of the disc and flat was 1 cm and a line contact of 1 cm was established for experimentation. The tests were conducted in dry environment i.e. the contact of flat and disc was not lubricated with any fluid. A weight of 120 g (1.1772 N) was applied for evaluation of wear resistance of plasma sprayed coatings. Weight loss was measured after every 40 cycles using electronic weighing scale with an accuracy of 0.1 mg. Two types of wear tests were conducted: first, the coated disc with coating on its periphery was rotated against horizontally reciprocating flat specimen covered with 400 grit silicon carbide (SiC) abrasive; second, the coated disc was rotated against flat specimen coated with same type of coating.

After each run of 40 cycles the specimens were visually examined. If coating on the specimen were found to worn out completely, the weight loss readings were discarded and the specimens were replaced with fresh specimens and run of 200 cycles started with fresh set of specimens.

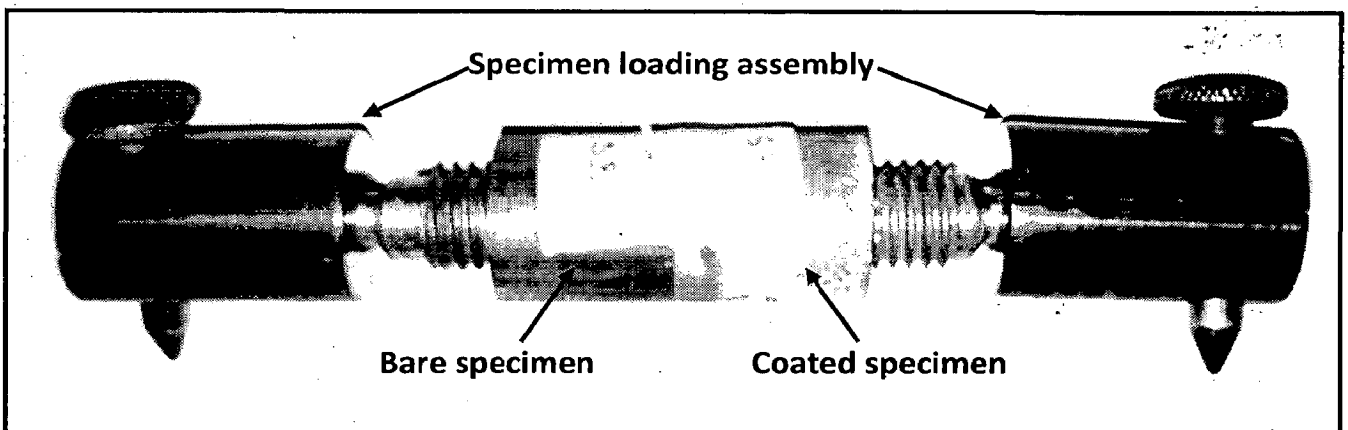


Fig. 3.4 Photograph of tensile bond strength fixture

For abrasive wear test (coating against abrasive), abrasive was changed after each run of 200 cycles. Two types of wear conditions i.e. abrasive and coating; coating and coating were used to find wear behavior of coatings. To characterize the type of wear, surface obtained after wear experiments were analyzed with FE-SEM. The as coated surface of the specimen was very rough however, due to wear the surface asperities were worn out and a smooth surface was observed by visual examination. To find the surface morphology and roughness of worn out specimens, the specimens were analyzed by atomic force microscopy using scanning probe microscope (Model: NTEGRA; Make: NT-MDT, Moscow, Russia).

Atomic force microscopy (AFM) in semi contact mode with silicon nitrate probe was utilized to analyze the surface profile (2-D and 3-D) of specimens after wear test. The resolution of microscope in this mode was 1 Å. The results obtained from wear tests: weight loss measurement versus no. of cycles; FE-SEM images of worn out surfaces showing surface morphology and AFM images showing surface profile and roughness are presented in Chapter 5 of present study.

3.9 IN-VITRO STUDY OF COATINGS

3.9.1 Preparation of Simulated Body Fluid

The simulated body fluid (SBF) which has ion concentration nearly equal to human blood plasma was used for in-vitro study. SBF was prepared as per the method suggested by Kokubo and his colleagues (Kokubo and Takadama, 2006). The comparison of ion concentration of SBF and human blood plasma is presented in Table 3.3. The chemical reagents with the amount required to prepare one liter of SBF are reported in Table 3.4. The minimum purity of all the reagents was 99%. Glass containers were not used for preparation of SBF. Smooth and scratch free good quality plastic/polyethylene wares were used for preparation of SBF because apatite nucleation can be induced on surface of glass or edge of a scratch. Prior to preparing SBF all wares were washed with 1 N HCl solution and placed in same for 10-12 h. After removing from the solution wares were washed with distilled water and dried by blowing hot air. In order to prepare 1000 ml of SBF, 700 ml of

Table 3.3 Comparison of ion concentration of simulated body fluid and human blood plasma

Ion	Simulated Body Fluid (mM)	Human Blood Plasma (mM)
Na ⁺	142.0	142.0
K ⁺	5.0	5.0
Mg ²⁺	1.5	1.5
Ca ²⁺	2.5	2.5
Cl ⁻	147.8	103.0
HCO ³⁻	4.2	27.0
HPO ₄ ²⁻	1.0	1.0
SO ₄ ²⁻	0.5	0.5
pH	7.40	7.20-7.40

The working electrode was test specimen of 1 cm² area, counter electrodes were two highly pure graphite rods and reference electrode was saturated calomel electrode (SCE) housed in Luggin capillary. Test sample was prepared in such a way that total exposed area of sample to electrolyte was 1 cm². The rest of the surface of sample was covered with non-toxic and non-conductive enamel. Each sample was allowed to stabilize at its open circuit potential (OCP) for 30 min in 'Cell off' mode before starting electrochemical tests.

The electrochemical tests were conducted for LPR, potentiodynamic polarization and Tafel polarization studies. The primary reason for LPR test was that the surface of test sample does not damage as test is carried out in very small potential range (-20 mV to +20 mV with respect to OCP) and a good idea of initial corrosion current density and polarization resistance can be obtained. Potentiodynamic polarization tests were carried out in range -250 mV versus OCP to 1600 mV versus SCE. All the tests were conducted with a scan rate of 0.1 mV/s. The plots so obtained were interpreted with help of Electrochemistry PowerSuite software provided by the manufacturer. The results obtained from electrochemical experiments are presented in Chapter 6 of present study.

Table 3.4 Chemical reagents for preparation of simulated body fluid

Order of Addition	Reagent	Amount	Measuring container
1	NaCl	8.035 g	Weighing glass
2	NaHCO ₃	0.355 g	Weighing glass
3	KCl	0.225 g	Weighing glass
4	K ₂ HPO ₄ .2H ₂ O	0.231 g	Weighing glass
5	MgCl ₂ .6H ₂ O	0.311 g	Weighing glass
6	1M – HCl	39 ml	Graduated cylinder
7	CaCl ₂	0.292 g	Weighing glass
8	Na ₂ SO ₄	0.072g	Weighing glass
9	(CH ₂ OH) ₃ CNH ₂	6.118 g	Weighing glass
10	1.0 mM HCl	0-5 ml	Syringe/dropper

3.9.3 Experimental Setup for In-vitro Studies

In order to evaluate activity of coatings in simulated body fluid, precipitation/dissolution behavior of coatings was investigated. Plastic beakers measuring 50 ml were utilized for soaking the specimens in SBF. The beakers were soaked in 1N HCl solution for 10-12 h to sterilize them, removed, washed with distilled water and dried at room temperature.

The as coated specimens were washed ultrasonically in distilled water and dried at room temperature. The coated specimens after cleaning in ultrasonic bath were never touched by bare hands. Each sample to be used for immersion test was weighed with accuracy of 0.1 mg prior to soaking in SBF. The volume of SBF for soaking was calculated by following equation suggested by Kokubo and Takadama, (2006),:

$$V_s = \frac{S_a}{10} \quad (3.1)$$

Where, V_s is volume of SBF in ml and S_a is the apparent surface area of the specimen in mm².

for 2 h, the specimen was allowed to cool in the furnace for 12h or until the room temperature had been attained. Then the boat carrying the specimen was removed from the furnace and subjected to visual observation carefully with respect to color change and other physical aspects of cracking or peeling of the coatings.

The post coating heat treated specimens were then subjected to FE-SEM/EDAX analysis to evaluate surface morphology of coatings, XRD analysis to find out various phases present and FTIR analysis to evaluate existence of various groups.

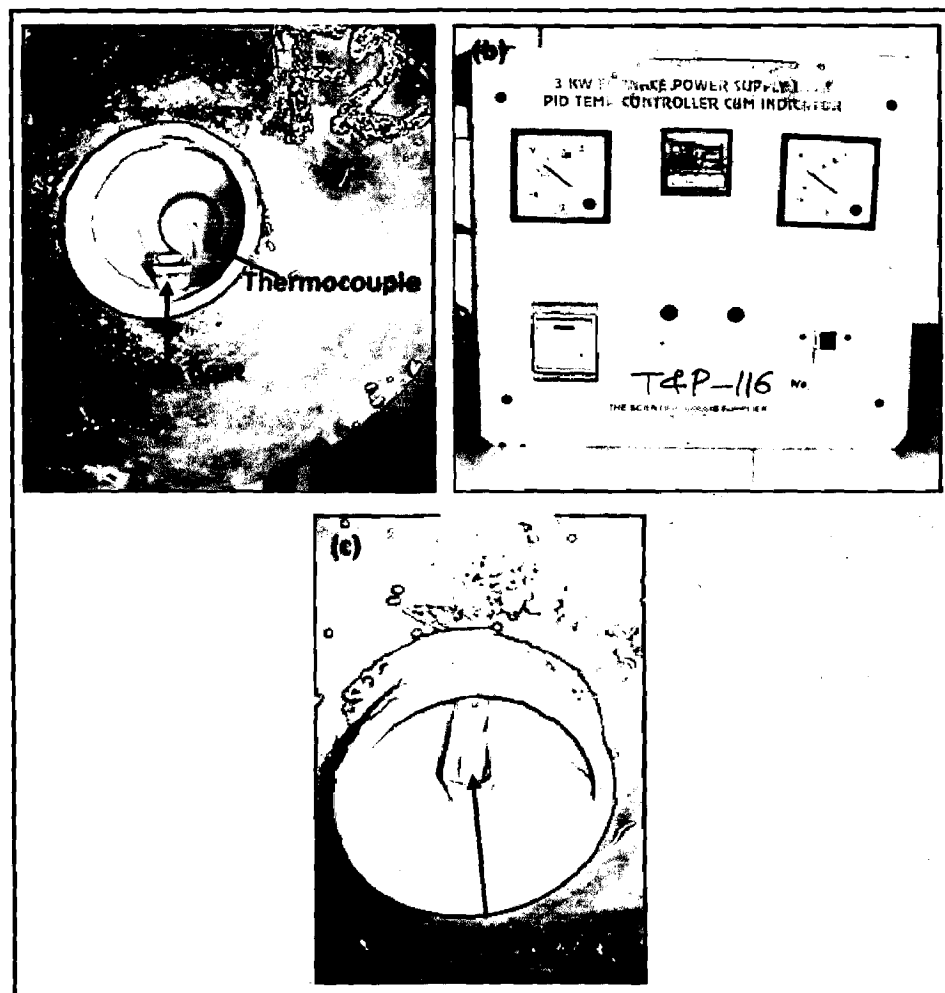


Fig. 3.8 Experimental setup for post coating heat treatment: (a) silicon tube furnace; (b) control unit and (c) specimen in alumina boat placed in silicon tube furnace

The surface morphology of as-sprayed and post coating heat treated specimen are shown in Fig. 3.9. The cross-sectional macrograph of post coating heat treated specimen is shown in Fig. 3.10. It can be seen from macrographs that color of as-sprayed coating is light gray, whereas the color of post coating heat treated specimen is sea green, which is similar to the color of starting HA powder used to prepare feedstock for plasma spraying. Delamination of coating was not observed by visually examining the coated specimens after post coating heat treatment. The results obtained from analysis of post coating heat treatment of specimens are presented in Chapter 7 of present study.

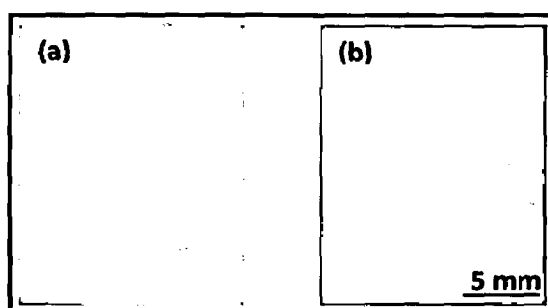


Fig. 3.9 Surface macrographs of coated specimens: (a) as-coated specimen and (b) post coating heat treated specimen at 900°C in air for 2h

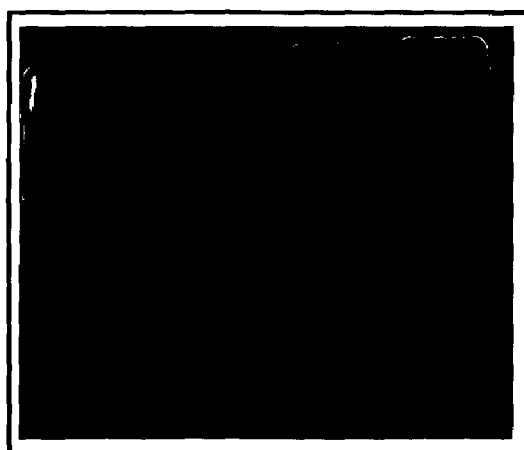


Fig. 3.10 Cross-sectional macrograph of post coating heat treated specimen at 900°C in air for 2h

CHARACTERIZATION OF COATINGS

This chapter deals with the characterization of plasma sprayed pure hydroxyapatite (HA: $\text{Ca}_{10}(\text{PO}_4)_6(\text{OH})_2$), HA-10 wt% aluminum oxide (alumina: Al_2O_3), HA-20 wt% aluminum oxide and HA-30 wt% aluminum oxide coatings on AISI 316L stainless steel and titanium with and without incorporation of a bond coat of aluminum oxide-13 wt% titanium oxide (Al_2O_3 -13 wt% TiO_2).

4.1 INTRODUCTION

In the present chapter the coating characterization has been described. It includes the results related to surface and cross-sectional morphology, porosity, coating thickness, surface roughness, elemental analysis, X-ray mapping and phase analysis of coatings using field emission scanning electron microscopy/energy dispersive X-ray (FE-SEM/EDAX), X-ray mapping, X-ray diffraction (XRD), TGA/DTA and FTIR techniques.

4.2 RESULTS

4.2.1 Coating Feedstock

The feedstock for the coating was prepared by mechanically mixing hydroxyapatite with different weight composition (0-30 wt%) of aluminum oxide in a blender for 30 min. at 3000 rpm without any medium. The microstructure, EDAX point analysis and X-ray mapping of HA-10 wt% Al_2O_3 , HA-20 wt% Al_2O_3 and HA-30 wt% Al_2O_3 powders are presented in Fig. 4.1 to Fig. 4.3 respectively. The microstructure, EDAX point analysis and elemental X-ray mapping of pure HA, Al_2O_3 (reinforcement) and Al_2O_3 -13 wt% TiO_2 (bond coat) powders are already presented in Chapter 3 of present study. It is evident from the micrographs and elemental mapping of powders that aluminum oxide is evenly distributed in matrix of hydroxyapatite powder. The hydroxyapatite powder particles shows a combination of spherical and angular morphology with varying particle size in a wide range of 20-75 μm while, aluminum oxide powder particles are spherical agglomerates of irregular shaped particles (8-24 μm). The size of aluminum oxide agglomerates vary in a narrow range of 85-100 μm .

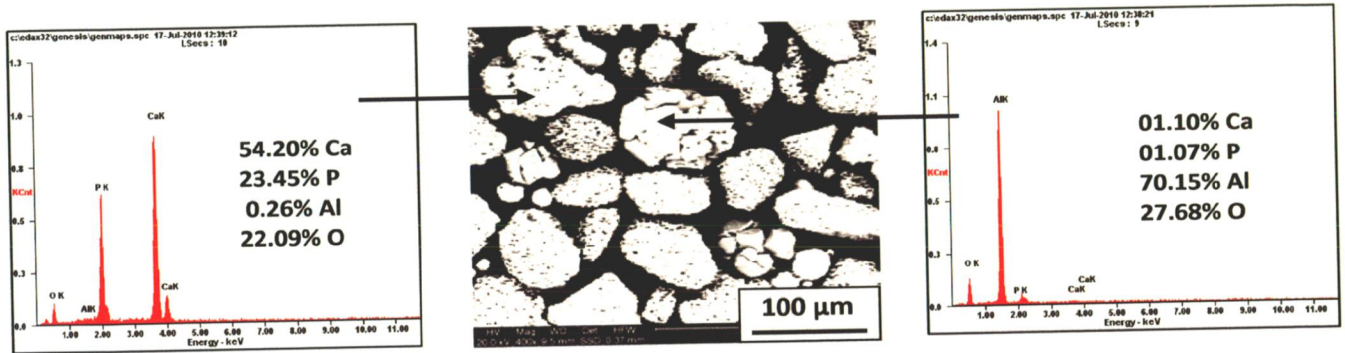
4.2.2 Surface Morphology of Coatings

The surface morphology of as-sprayed and along cross-section is shown in Fig. 4.4 and 4.5 respectively. The plasma sprayed HA composite coatings with varying amount of alumina (0-30 wt %) shows typical splat surface morphology with distinct splat boundaries. The surface morphology of coatings clearly shows the splat boundaries, un-melted/partially molten splats and voids. Some cracks can be seen in morphology of HA-20 wt% Al₂O₃ coatings (Fig. 4.4). The cross-section of coatings show that bond coat and top coat are intact with each other and to the substrate except for pure HA coating in which the interface of bond coat and top coat is partially damaged due to grinding and polishing during sample preparation. The micro-cracks can be seen in the cross-section of coating, however a network of cracks as characterized by plasma sprayed HA coatings is absent. A little amount of pores can also be seen in the microstructure of coating along its cross-section. FE-SEM micrographs of coating surface along with EDAX point analysis of plasma sprayed HA, HA-10 wt% Al₂O₃, HA-20 wt% Al₂O₃ and HA-30 wt% Al₂O₃ on AISI 316L SS are shown in Fig. 4.6. Characteristic plasma sprayed coating microstructure is observed on coated surfaces. Overall coatings are dense with some un-melted/partially melted HA particles present on completely molten HA splats (Fig. 4.6a – d). Cracks are not visible on the coating surface at lower magnification however; their presence can be seen at higher magnification. Micro-cracks are clearly visible within the molten splats (Fig. 4.6d). Micro-cracks may have formed due to reduction in volume of molten splats during cooling/solidification and difference in cooling rates of coating splats and substrate. EDAX analysis at different points indicates mainly the presence of coating elements i.e. Ca, P, O and Al with negligible amount of substrate elements. The element analysis of HA coating (Fig. 4.6a) indicates constituents of HA. However, weight % of Ca at point 1 is much higher than at point 2. EDAX point analysis of HA-10 wt% Al₂O₃ (point 3 and 4 in Fig. 4.6b) shows presence of Ca, P, O and Al. At both the points the composition of aluminum oxide is nearly same and no substrate elements have been detected. Figure 4.6c and d illustrate the micrographs and element analysis of HA coatings with 20 wt% Al₂O₃ and 30 wt% Al₂O₃ respectively. The EDAX analysis at different spots in these micrographs show uneven distribution of aluminum oxide with negligible amount (less than 1 wt%) of substrate elements such as Fe, Cr and Ni.

Figure 4.7 illustrates the plasma sprayed HA, HA-10 wt% Al₂O₃, HA-20 wt% Al₂O₃ and HA-30 wt% Al₂O₃ coatings on titanium substrate. Micro-cracks and some un-melted/partially

melted HA particles embedded in fully molten splats could be observed. EDAX analysis indicates a similar trend as for coating on AISI 316L SS for distribution of elements with negligible presence of titanium (substrate). The as sprayed coatings were light in color as shown in Fig. 3.12a in Chapter 3 of present study. The EDAX point analysis on the surface of as sprayed coatings does not show the actual distribution of reinforcement material (Al_2O_3).

(a)



(b)

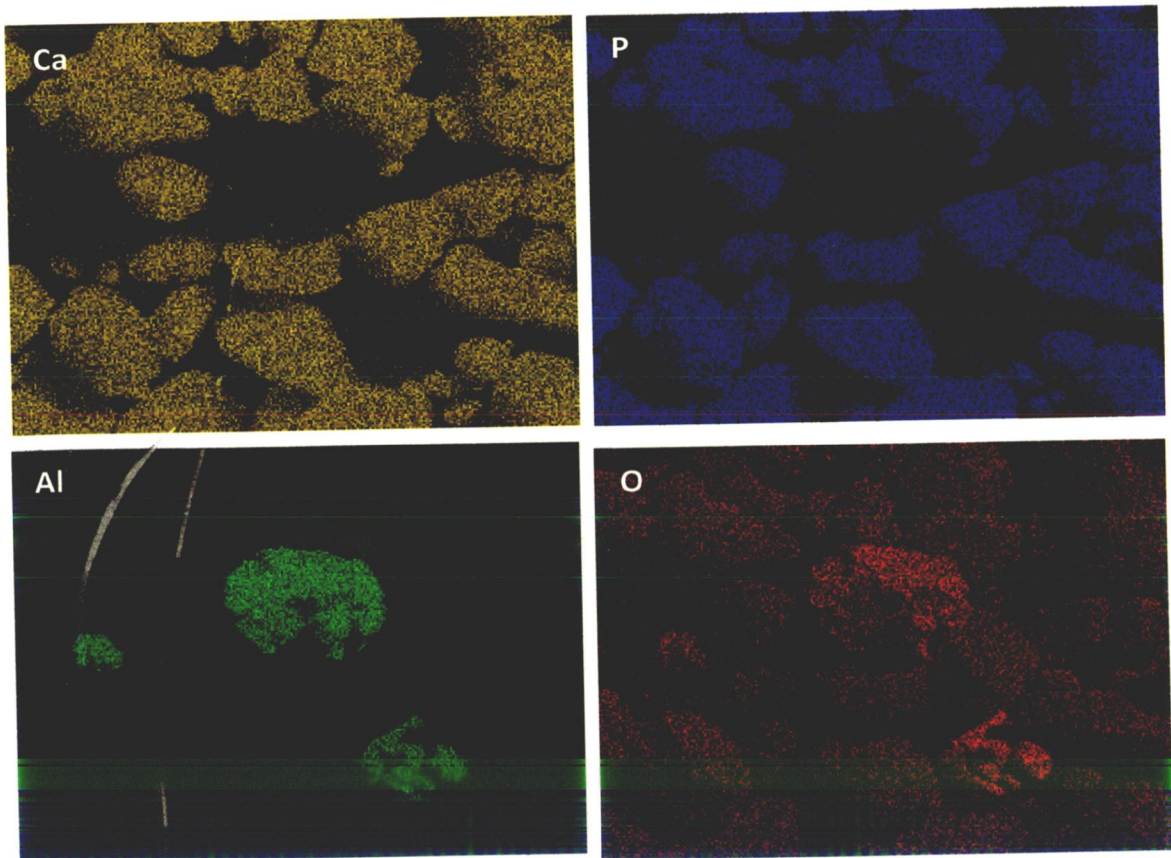
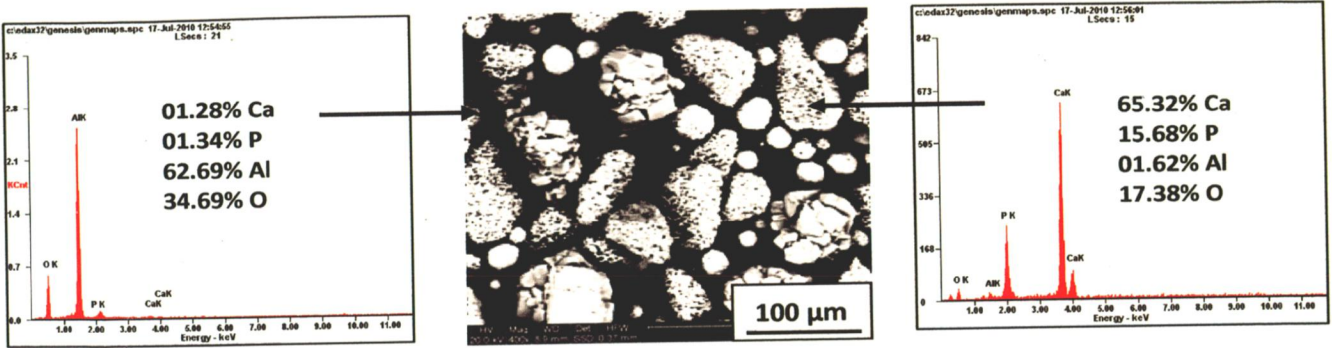


Fig. 4.1 FE-SEM image (400X) showing morphology of HA-10 wt% Al_2O_3 feedstock: (a) particle morphology and EDAX point analysis (wt% of elements) and (b) X-ray mapping

(a)



(b)

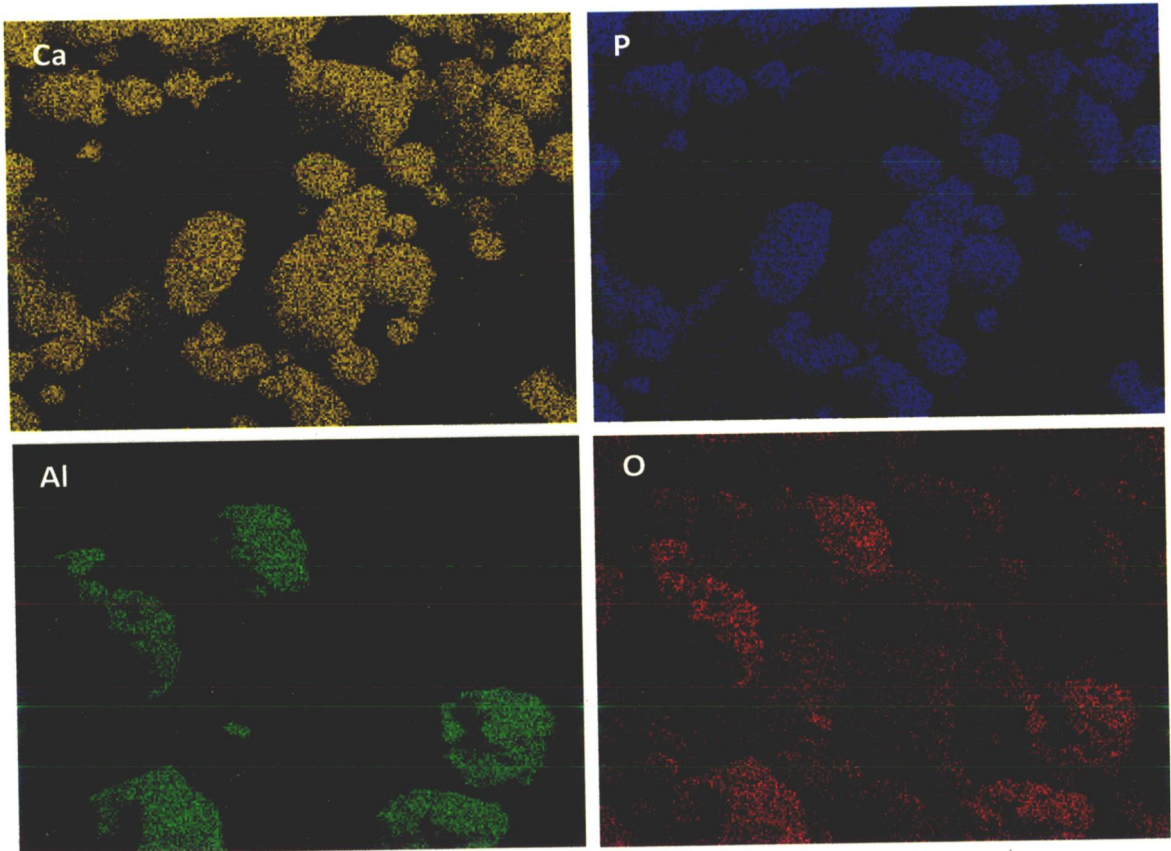
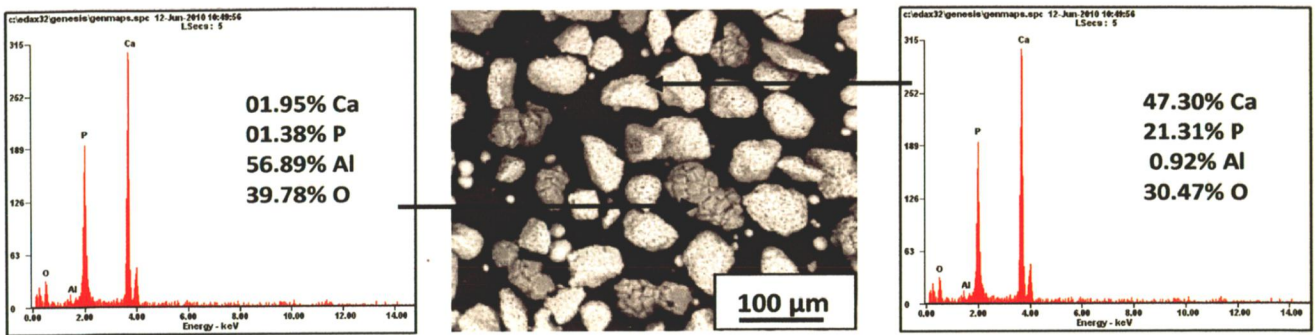


Fig. 4.2 FE-SEM image (400X) showing morphology of HA-20 wt% Al₂O₃ feedstock: (a) particle morphology and EDAX point analysis (wt% of elements) and (b) X-ray mapping

(a)



(b)

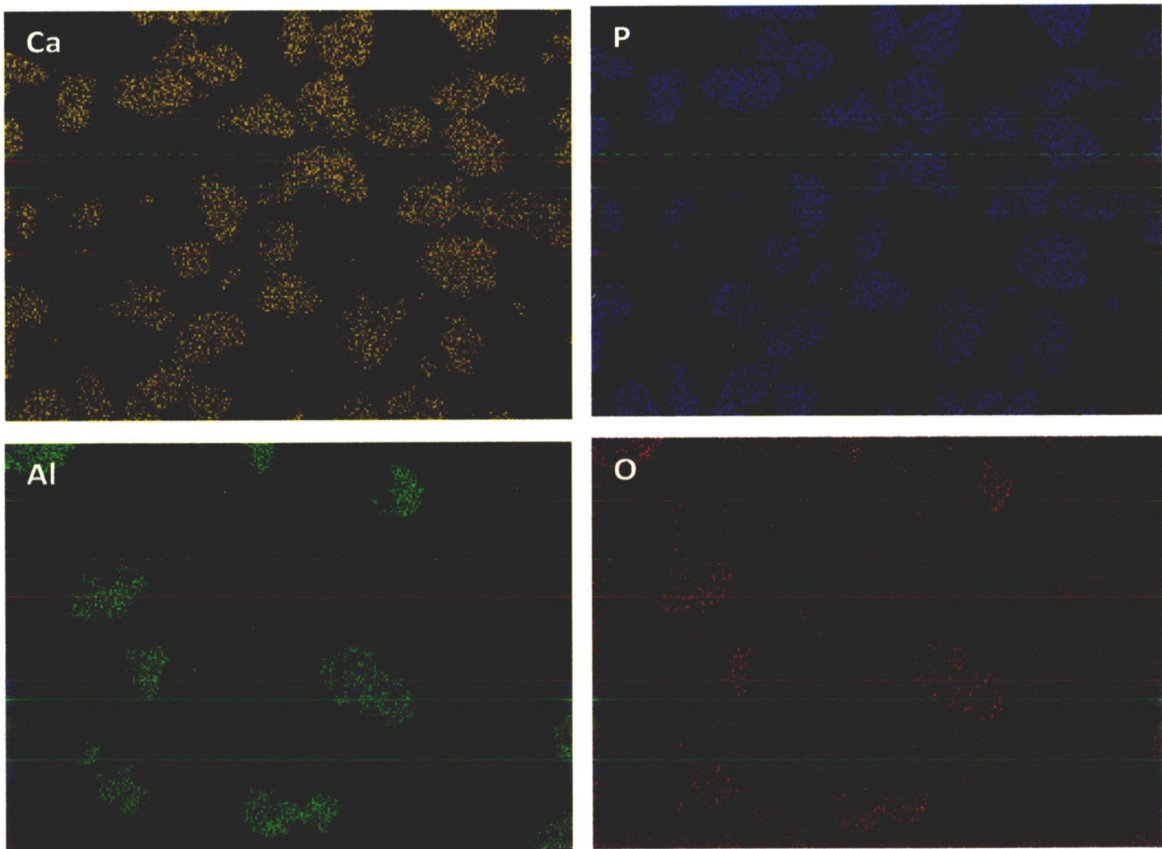


Fig. 4.3 FE-SEM image (400X) showing morphology of HA-30 wt% Al₂O₃ feedstock: (a) particle morphology and EDAX point analysis (wt% of elements) and (b) X-ray mapping

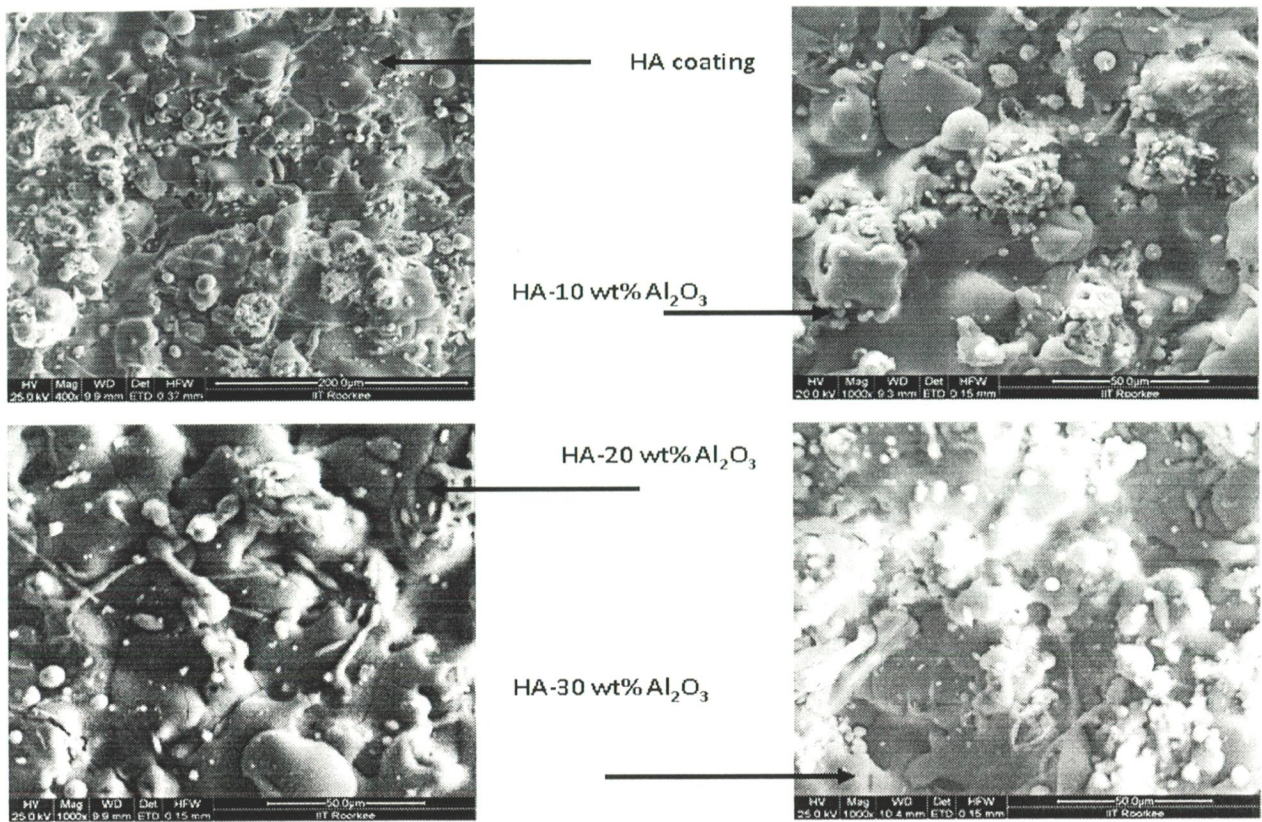


Fig. 4.4 Surface morphology of as-sprayed coatings

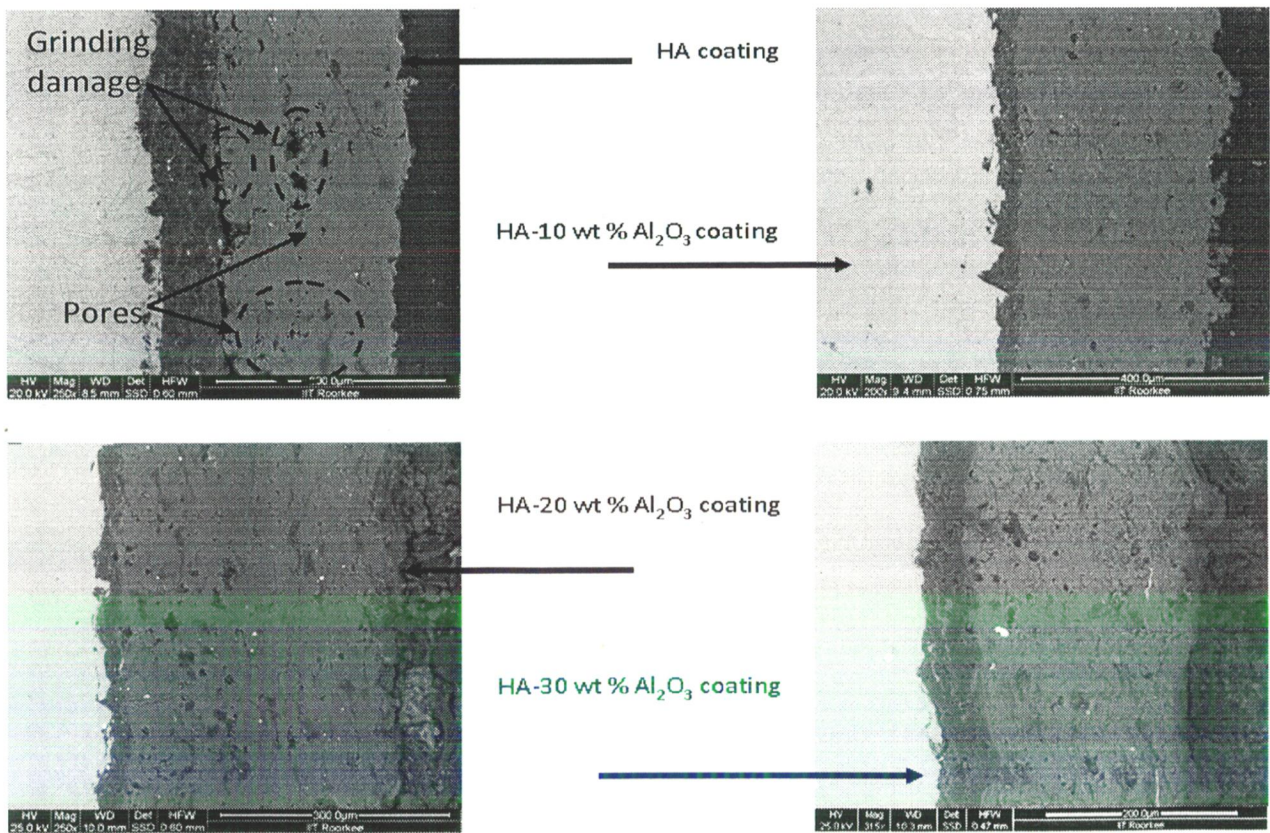


Fig. 4.5 Cross-sectional morphology of coatings with bond coat of Al₂O₃-13 wt% TiO₂

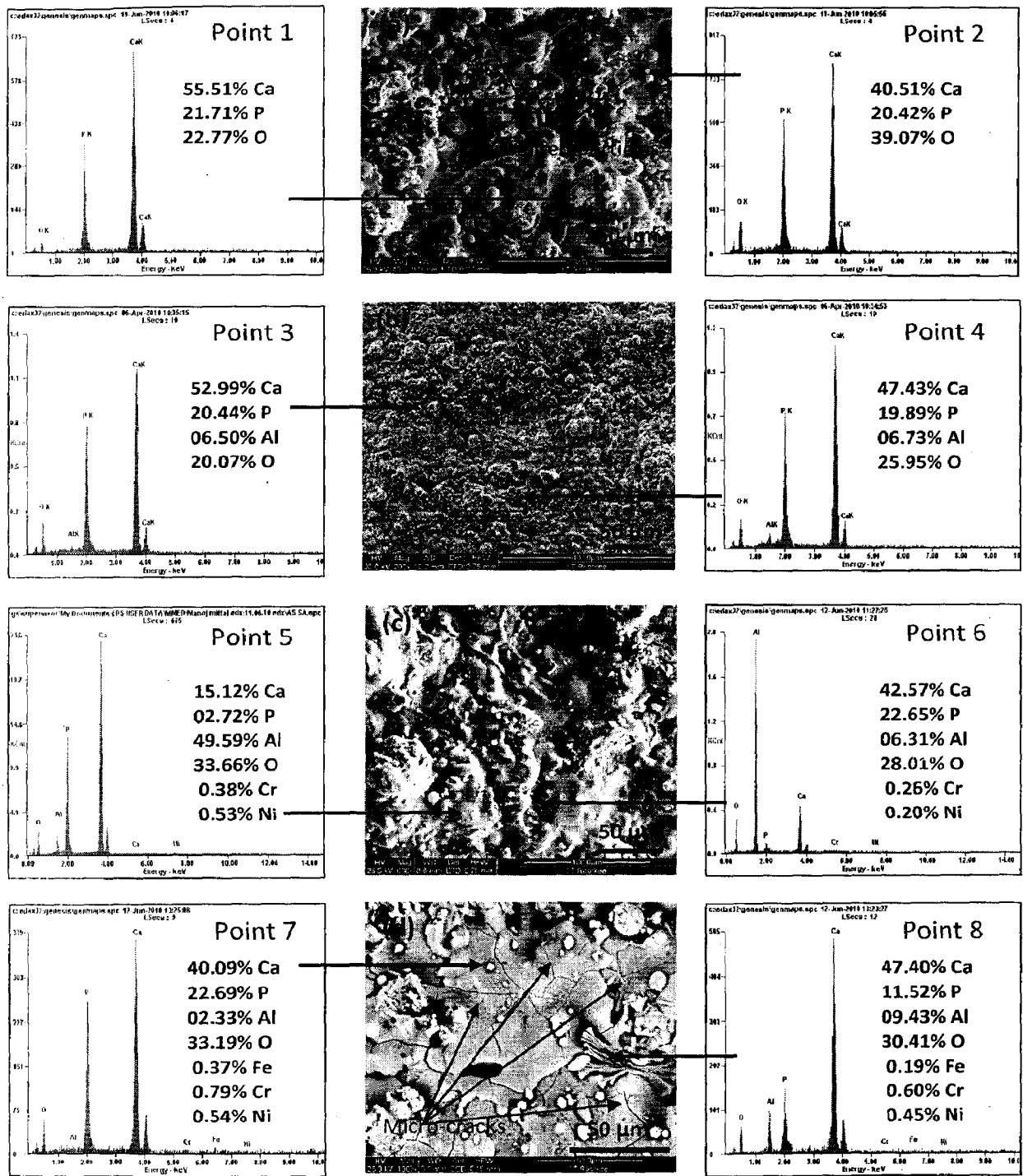


Fig. 4.6 Surface morphology and EDAX point analysis from different spots on plasma sprayed AISI 316L SS: (a) HA coating; (b) HA-10 wt % Al_2O_3 ; (c) HA-20 wt% Al_2O_3 and (d) HA-30 wt% Al_2O_3

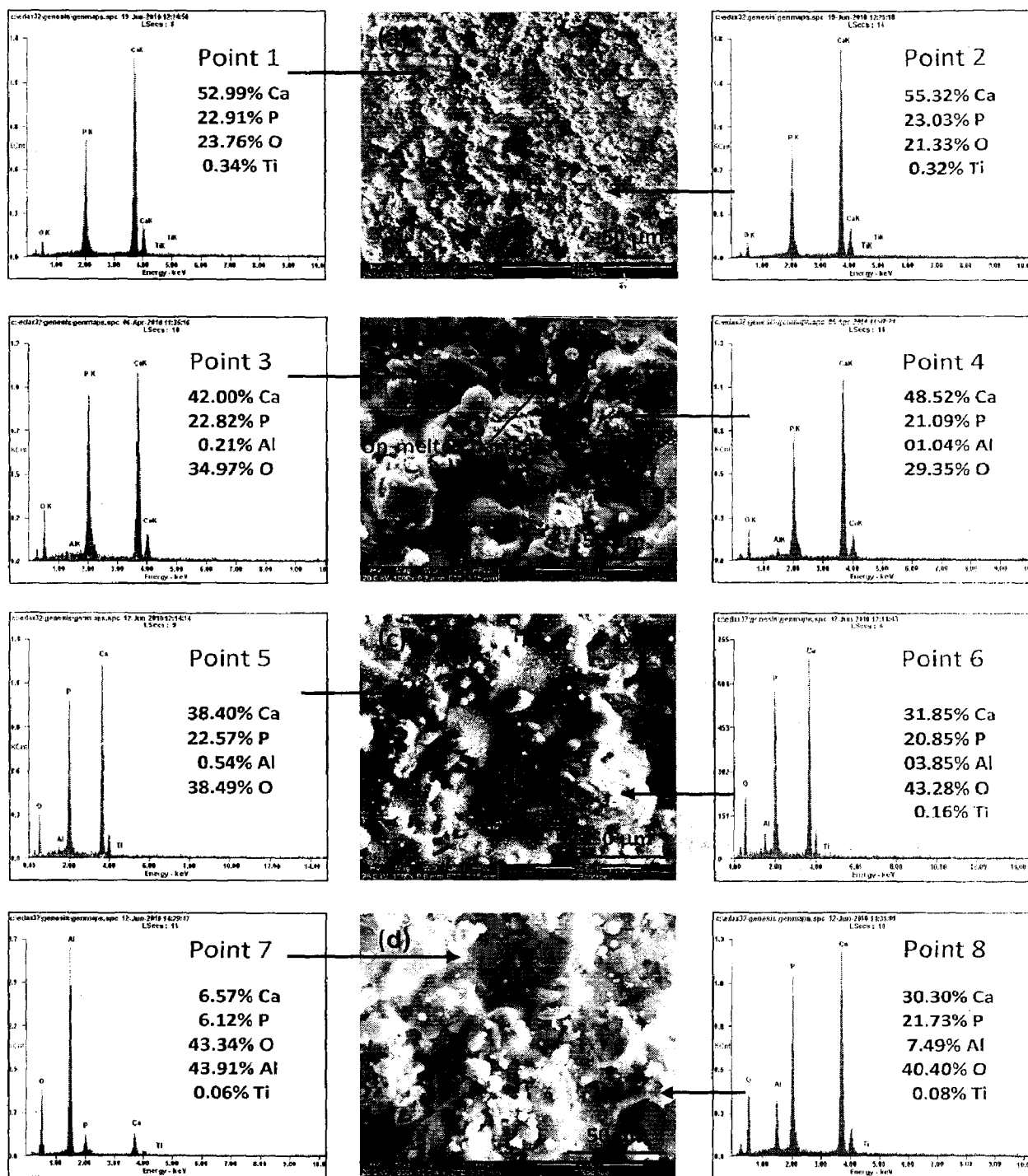


Fig. 4.7 Surface morphology and EDAX point analysis from different spots on plasma sprayed titanium: (a) HA coating; (b) HA-10 wt % Al_2O_3 ; (c) HA-20 wt% Al_2O_3 and (d) HA-30 wt% Al_2O_3

4.2.3 FE-SEM/EDAX Analysis of Coatings

The FE-SEM micrographs and EDAX point analysis along the cross-section are presented in Fig. 4.8 – Fig. 4.11. The FE-SEM micrographs show that coating is continuous and intact with the substrate in all the substrate-coating combinations. The coating is damaged at the interface during sample preparation (grinding and polishing) as presented in Fig. 4.8d (at bond coat/top coat interface), in Fig. 4.9c (at substrate/coating interface) and in Fig. 4.9d (at bond coat/top coat interface). The black colored spots in coatings are the pits generated due to removal of un-melted or partially melted powder particles during sample preparation. Some micro-cracks are present in the coating but the network of cracks which starts at interface and expand through out the coating is absent. Micro-cracks arise from shrinkage of splats during cooling/solidification and differential thermal contraction between substrate and coating. Dark colored streaks and spots in light grey HA matrix represent aluminum oxide particles, which are distributed along a direction parallel to substrate coating interface. White colored streaks in bond coat correspond to TiO_2 particles.

EDAX point analysis of coatings was carried out at different points along the cross-section of plasma sprayed coatings and results are shown in Fig. 4.8 to 4.11. The results depict that no substrate element has migrated to the coating. EDAX analysis at dark colored streaks and spots confirm the presence of aluminum oxide as shown at point 4 in Fig. 4.9b, point 6 in Fig. 4.9d, point 4 in Fig. 4.10a, point 4 in Fig. 4.10c and point 5,9,6,6 in Fig. 4.11a, b, c, d respectively.

4.2.3.1 Coating thickness

The as coated specimens were cut along the cross-section, mounted in transoptic mounting resin and subsequently mirror polished to obtain FE-SEM images. The coating thickness values were measured at some randomly selected locations on back scattered electron (BSE) or secondary electron (SE) images and average coating thickness for various coatings is reported in Table 4.1-4.4.

4.2.3.2 Porosity analysis of coatings

The porosity of bioceramic coatings is of prime importance. Porosity influences physical and mechanical characteristics of hydroxyapatite coatings. It effects the body's

reaction with this mineral component of bone as porous structure allows fibro-vascular in-growth thereby helping implant to resist migration. Micro-pores are generally produced during plasma spraying due to solidification contraction and splat filling effects. Porosity of coatings was measured on as-coated surface and on the polished cross-section at ten different points and results are reported in Table 4.1-4.4. Lower porosity values were found in case of as-coated surface as compared to that for polished cross-section. The higher value of porosity on polished cross-section may be attributed to pullout of un-melted particle cores during grinding and polishing process.

4.2.4 Surface Roughness of Coatings

As coated surface was very rough due to presence of un-melted/partially melted HA and alumina particles in completely molten splats. A non contact profilometer was used to determine the surface roughness of as sprayed coatings. The centre line average (CLA) method was used to obtain the surface roughness of as sprayed coatings with vertical scanning interferometry mode. Surface roughness (Ra) was measured at twenty different points (five in each orthogonal direction) and average surface roughness has been reported in Table 4.1-4.4.

Table 4.1 Microstructural properties of plasma sprayed hydroxyapatite and aluminum oxide composite coatings on AISI SS316L

Coating		HA	HA-10 wt% Al ₂ O ₃	HA-20 wt% Al ₂ O ₃	HA-30 wt% Al ₂ O ₃
Coating thickness (μm)		176	190	220	223
Porosity (%)	As coated surface	3.26	3.34	3.42	3.61
	Polished cross-section	7.15	7.21	7.35	7.46
Surface roughness (μm)		3.1-7.31	4.12-7.56	4.96-7.98	4.84-8.37

Table 4.2 Microstructural properties of plasma sprayed hydroxyapatite and aluminum oxide composite coatings on titanium

Coating		HA	HA-10 wt% Al ₂ O ₃	HA-20 wt% Al ₂ O ₃	HA-30 wt% Al ₂ O ₃
Coating thickness (μm)		180	180	207	180
Porosity (%)	As coated surface	3.2	3.25	3.3	3.32
	Polished cross-section	7.07	7.12	7.15	7.17
Surface roughness (μm)		5.01-7.26	6.05-7.41	7.1-7.94	7.39-8.56

Table 4.3 Microstructural properties of plasma sprayed hydroxyapatite and aluminum oxide composite coatings on AISI SS316L with bond coat of Al₂O₂ – 13wt% TiO₂

Coating		HA	HA-10 wt% Al ₂ O ₃	HA-20 wt% Al ₂ O ₃	HA-30 wt% Al ₂ O ₃
Coating thickness (μm)		209	198	205	236
Bond coat thickness (μm)		50	48	34	53
Porosity (%)	As coated surface	3.32	3.42	3.49	3.71
	Polished cross-section	7.22	7.31	7.42	7.48
Surface roughness (μm)		4.61-7.82	4.53-7.98	4.67-8.21	4.26-8.62

Table 4.4 Microstructural properties of plasma sprayed hydroxyapatite and aluminum oxide composite coatings on titanium with bond coat of Al₂O₂ – 13wt% TiO₂

Coating		HA	HA-10 wt% Al ₂ O ₃	HA-20 wt% Al ₂ O ₃	HA-30 wt% Al ₂ O ₃
Coating thickness (μm)		238	226	206	148
Bond coat thickness (μm)		75	79	40	63
Porosity (%)	As coated surface	3.26	3.31	3.41	3.47
	Polished cross-section	7.18	7.23	7.29	7.34
Surface roughness (μm)		5.2-7.45	5.36-7.62	6.65-8.19	6.98-8.84

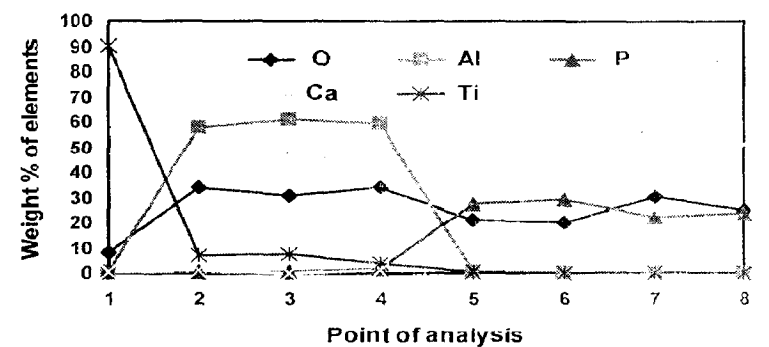
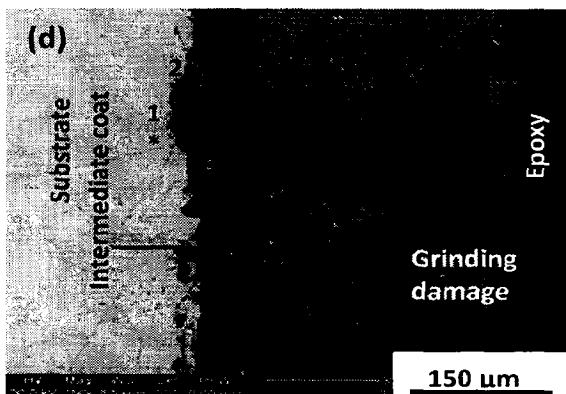
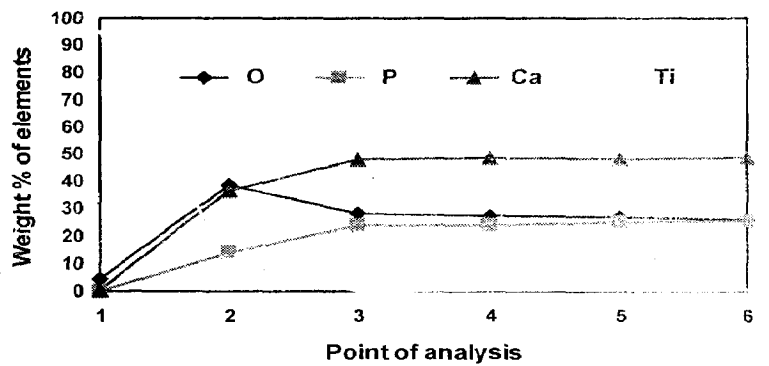
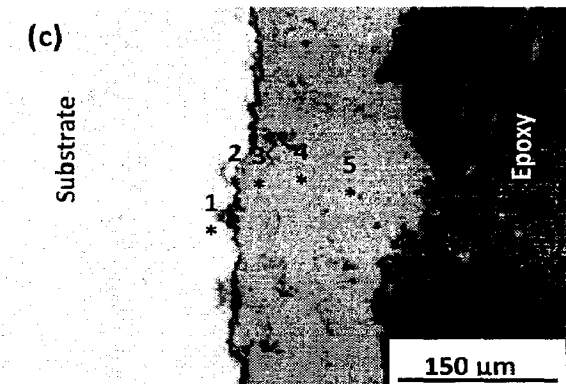
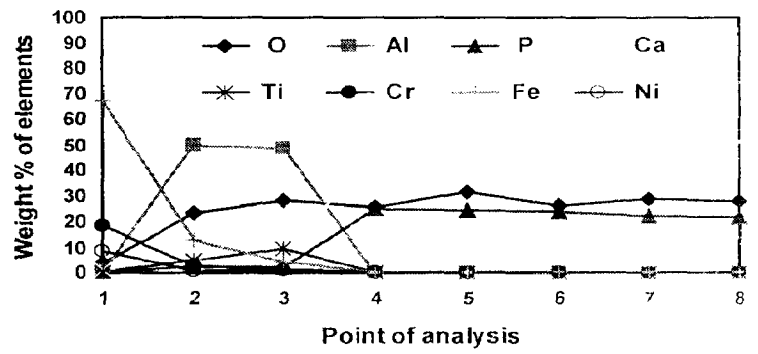
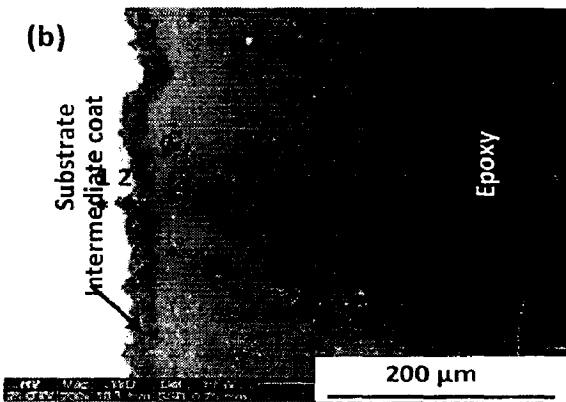
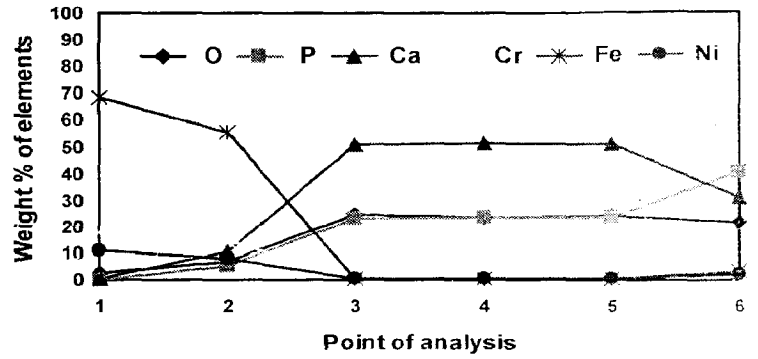
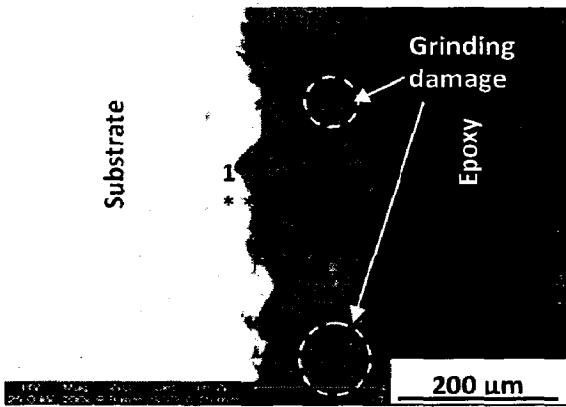


Fig. 4.8 FE-SEM/EDAX point analysis along the cross-section: (a) HA coated AISI 316L SS; (b) HA coated AISI 316L SS with bond coat of Al₂O₃-13 wt% TiO₂; (c) HA coated Ti; (d) HA coated Ti with bond coat of Al₂O₃-13 wt% TiO₂

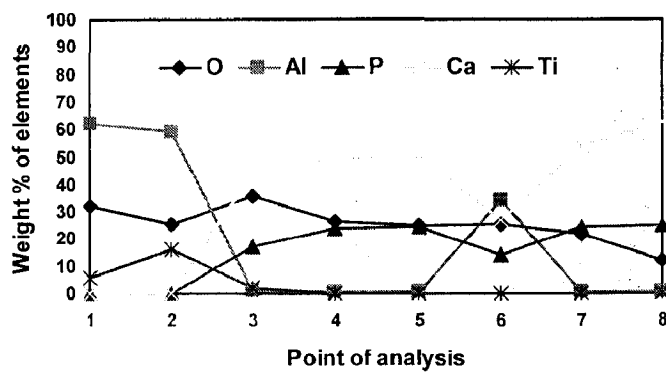
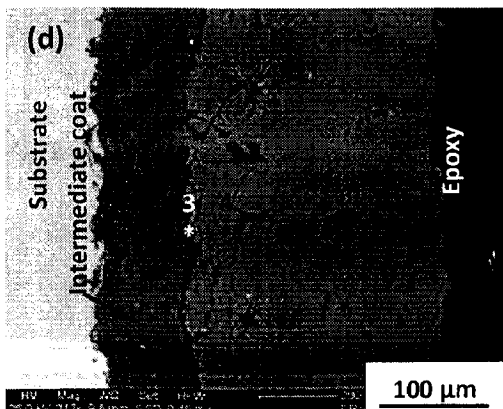
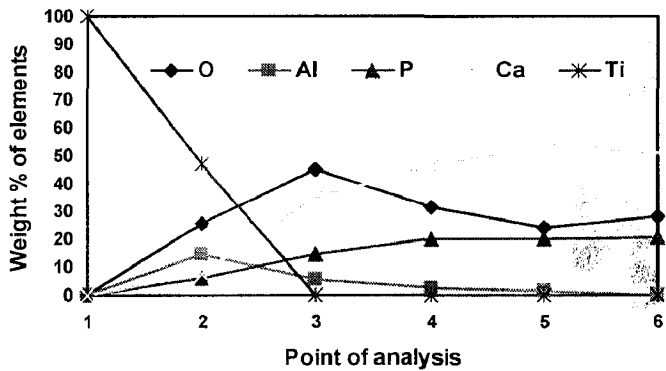
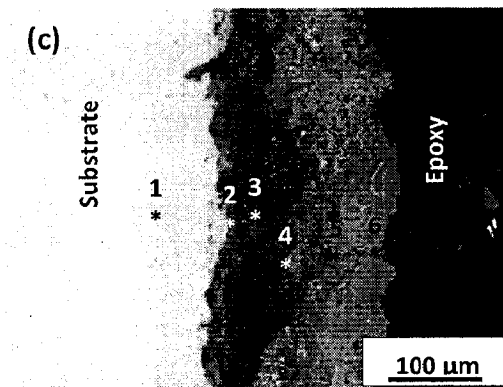
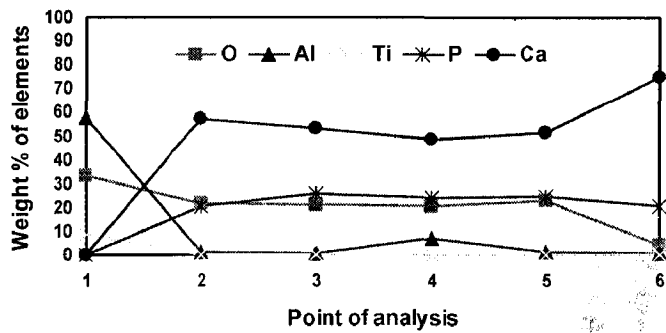
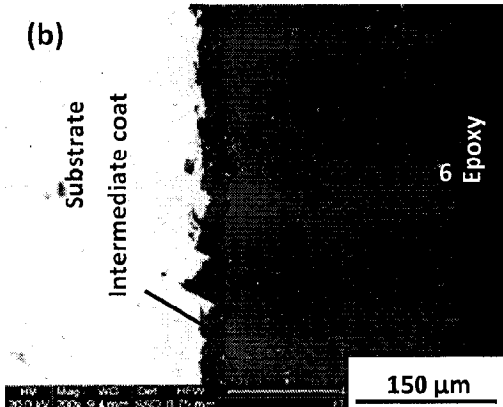
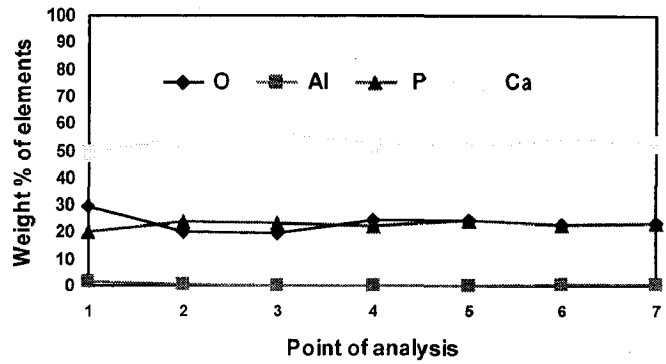
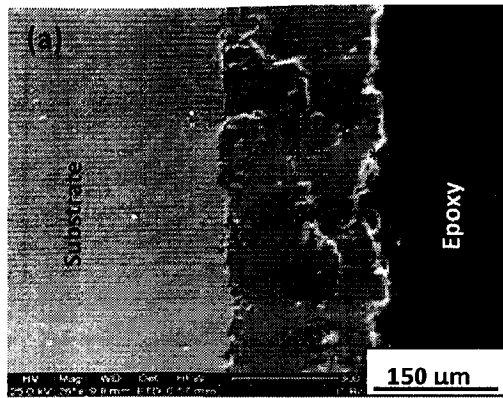


Fig. 4.9 FE-SEM/EDAX point analysis along the cross-section: (a) HA-10 wt% Al₂O₃ coated AISI 316L SS; (b) HA-10 wt% Al₂O₃ coated AISI 316L SS with bond coat of Al₂O₃-13 wt% TiO₂; (c) HA-10 wt% Al₂O₃ coated Ti; (d) HA-10 wt% Al₂O₃ coated Ti with bond coat of Al₂O₃-13 wt% TiO₂

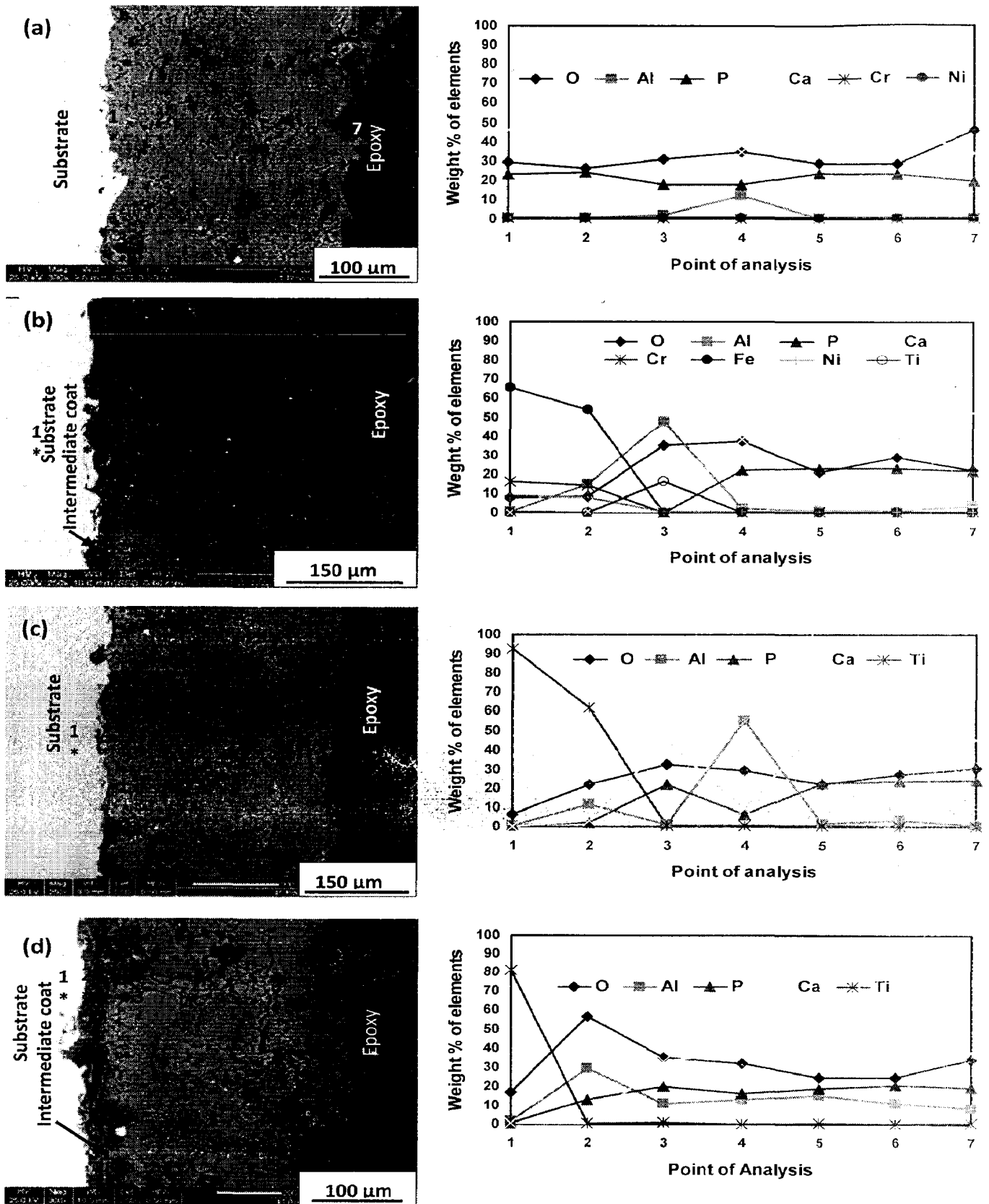


Fig. 4.10 FE-SEM/EDAX point analysis along the cross-section: (a) HA-20 wt% Al₂O₃ coated AISI 316L SS; (b) HA-20 wt% Al₂O₃ coated AISI 316L SS with bond coat of Al₂O₃-13 wt% TiO₂; (c) HA-20 wt% Al₂O₃ coated Ti; (d) HA-20 wt% Al₂O₃ coated Ti with bond coat of Al₂O₃-13 wt% TiO₂

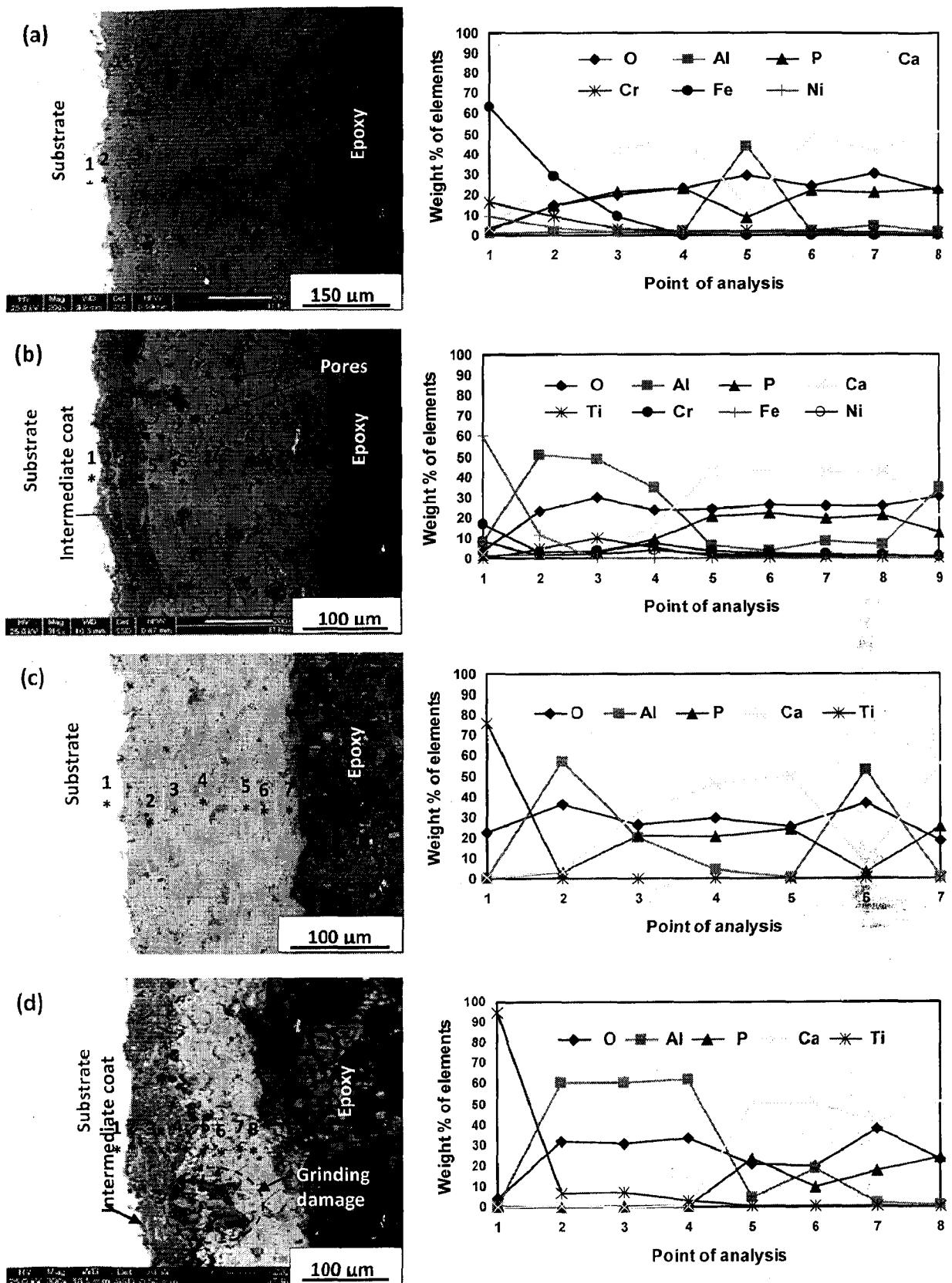


Fig. 4.11 FE-SEM/EDAX point analysis along the cross-section: (a) HA-30 wt% Al₂O₃ coated AISI 316L SS; (b) HA-30 wt% Al₂O₃ coated AISI 316L SS with bond coat of Al₂O₃-13 wt% TiO₂; (c) HA-30 wt% Al₂O₃ coated Ti; (d) HA-30 wt% Al₂O₃ coated Ti with bond coat of Al₂O₃-13 wt% TiO₂

4.2.5 X-Ray Mapping of Coatings

Plasma sprayed hydroxyapatite and aluminum oxide composite coatings on AISI 316L SS and titanium with and without incorporation of Al₂O₃-13 wt% TiO₂ bond coat were analyzed by X-ray mapping. The surface of as-sprayed specimens and polished cross-sections were analyzed to find the distribution of coating elements. The effect of bond coat on diffusion/migration of substrate elements to the coatings was also studied.

4.2.5.1 Surface analysis

FE-SEM micrographs and X-ray mapping for HA, HA-10 wt% Al₂O₃, HA-10 wt% Al₂O₃ and HA-10 wt% Al₂O₃ on AISI 316L SS and titanium substrates without and with incorporation of bond coat are shown in Fig. 4.12 to Fig. 4.27. The surface analysis of coatings shows that the coatings are rich with elements of hydroxyapatite i.e. calcium and phosphorus. A negligible amount of substrate elements are visible in the images of X-ray mapping as shown in Fig. 4.12-4.19. X-ray mapping of HA-20 wt% Al₂O₃ and HA-30 wt% Al₂O₃ coating on AISI 316L SS and HA-10 wt% Al₂O₃ and HA-20 wt% Al₂O₃ coating on titanium show that aluminum oxide is present in a scattered form (Fig. 4.14-4.15 and Fig. 4.17-4.18). However, Fig. 4.13 and 4.19 show the uniform distribution of aluminum oxide.

Figure 4.20-4.27 show the FE-SEM micrographs and X-ray mapping of coatings with incorporation of Al₂O₃-13 wt% TiO₂ bond coat. The elemental distribution is in similar manner as that for the coatings without bond coat. However, substantial reduction in diffusion of substrate elements has been observed. X-ray mapping images (Fig. 4.21, 4.22 and 4.25) indicate even distribution of aluminum oxide. X-ray mapping along cross-section of coated specimens was conducted to investigate in detail distribution of aluminum oxide in hydroxyapatite matrix, which is discussed in subsequent section.

4.2.5.2 Cross-sectional analysis

X-ray mapping was carried out on mounted and wheel polished specimens to analyze the distribution of elements across the coating thickness of bond coat and top coat. Figure 4.28-4.43 shows the FE-SEM images and X-ray mapping of coated specimens along their cross-sections.

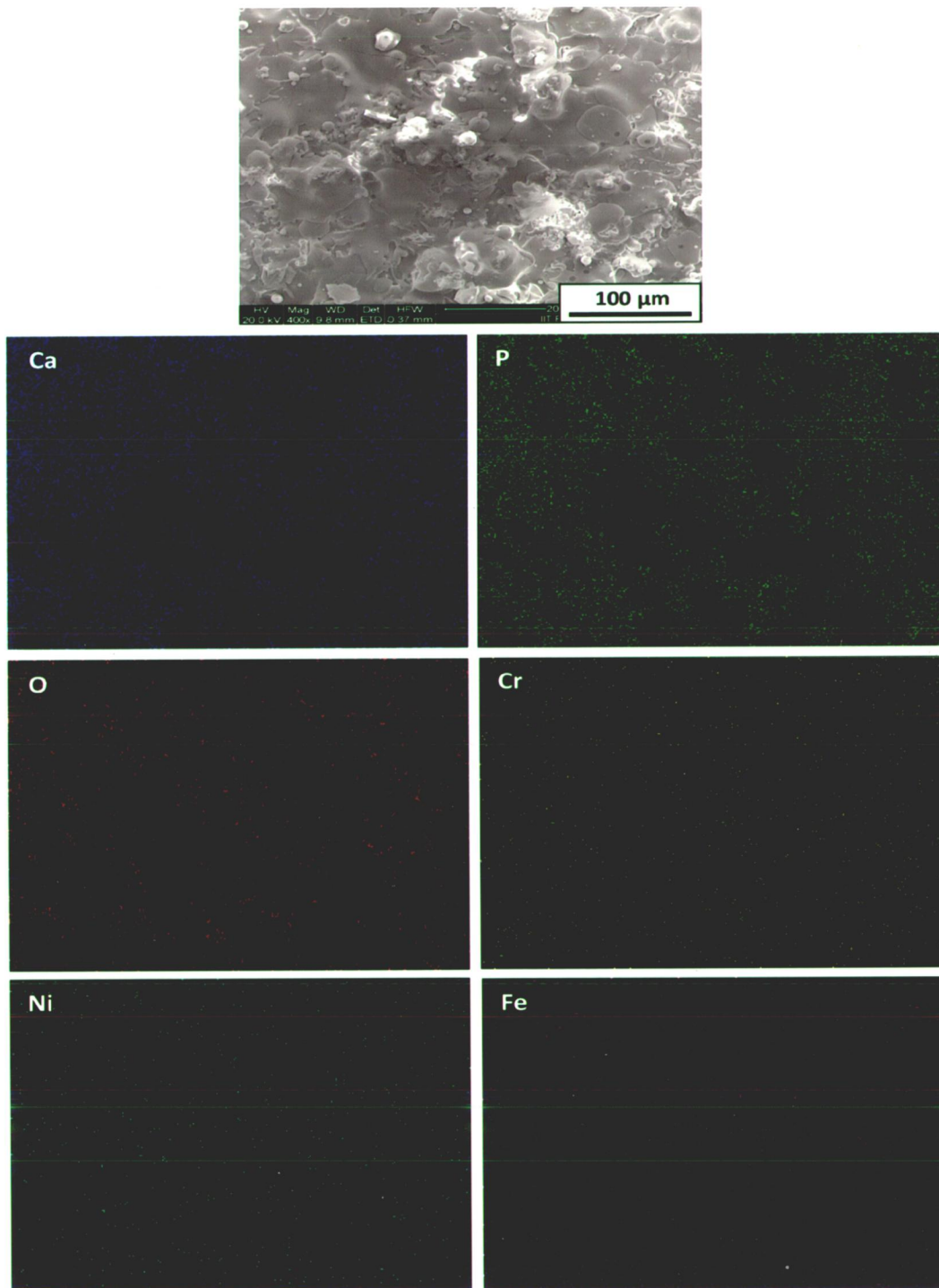


Fig. 4.12 FE-SEM image and X-ray mapping of surface of HA coated AISI 316L SS

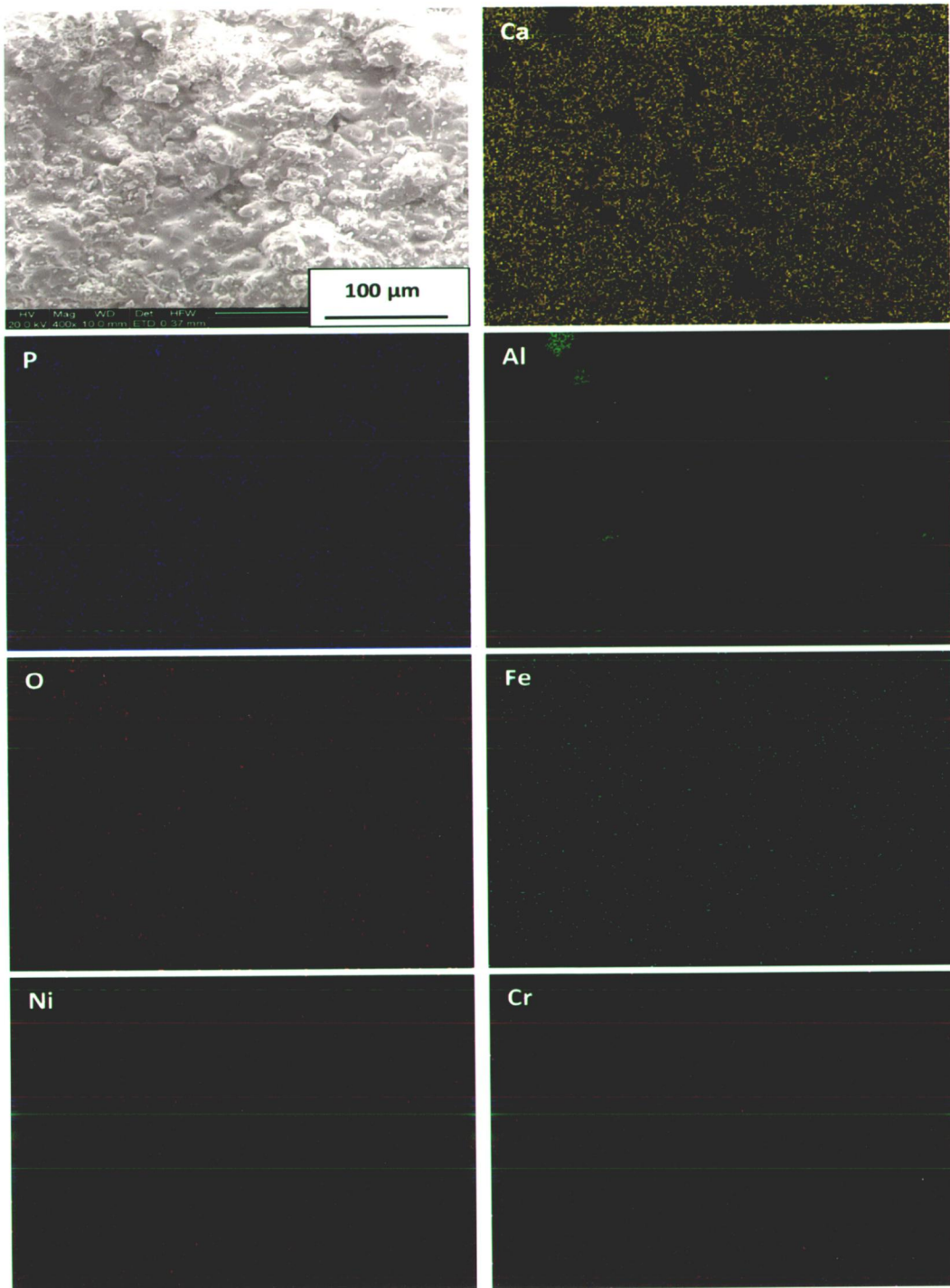


Fig. 4.13 FE-SEM image and X-ray mapping of surface of HA-10 wt% Al₂O₃ coated AISI 316L SS

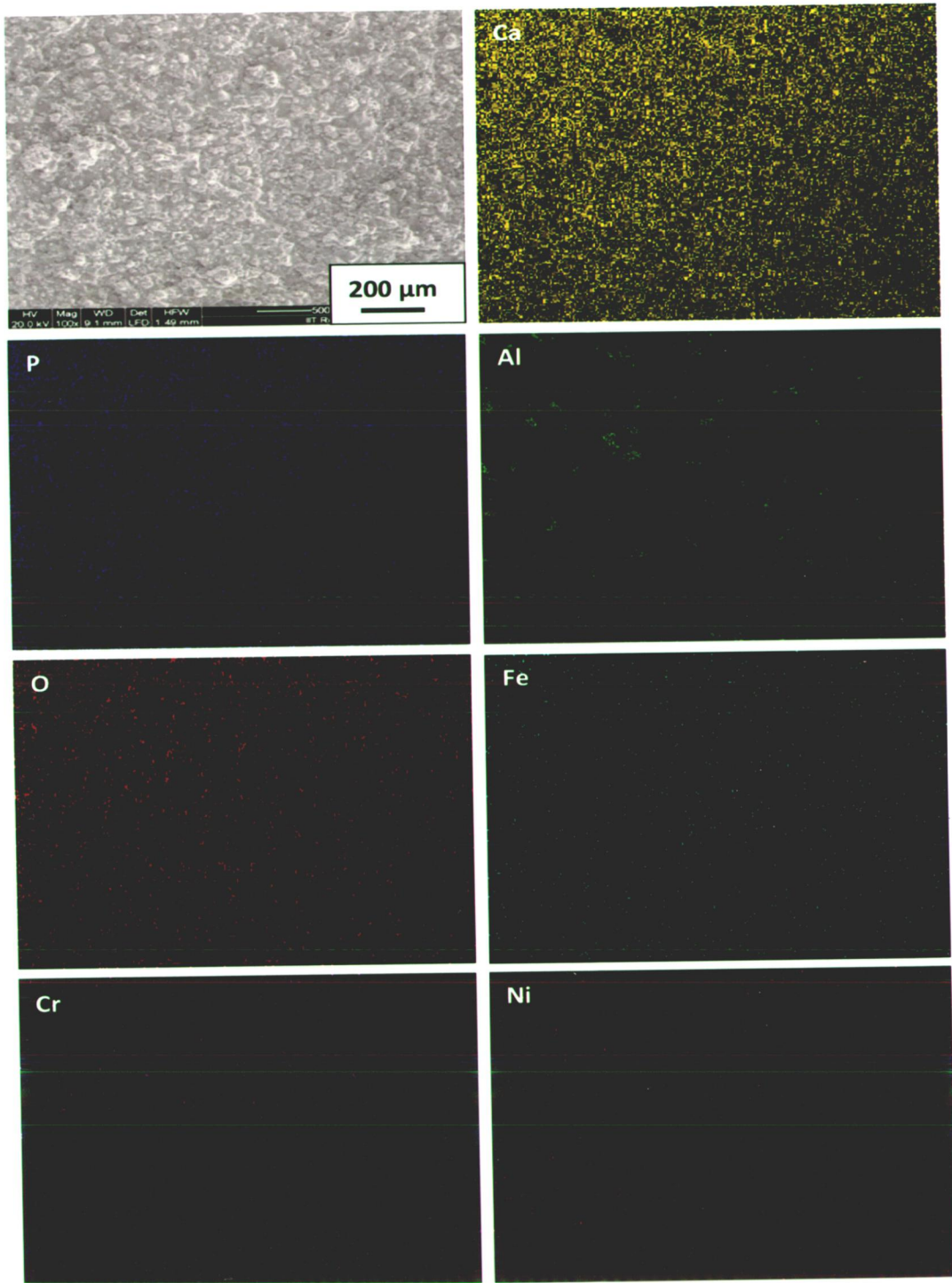


Fig. 4.14 FE-SEM image and X-ray mapping of surface of HA-20 wt% Al₂O₃ coated AISI 316L SS

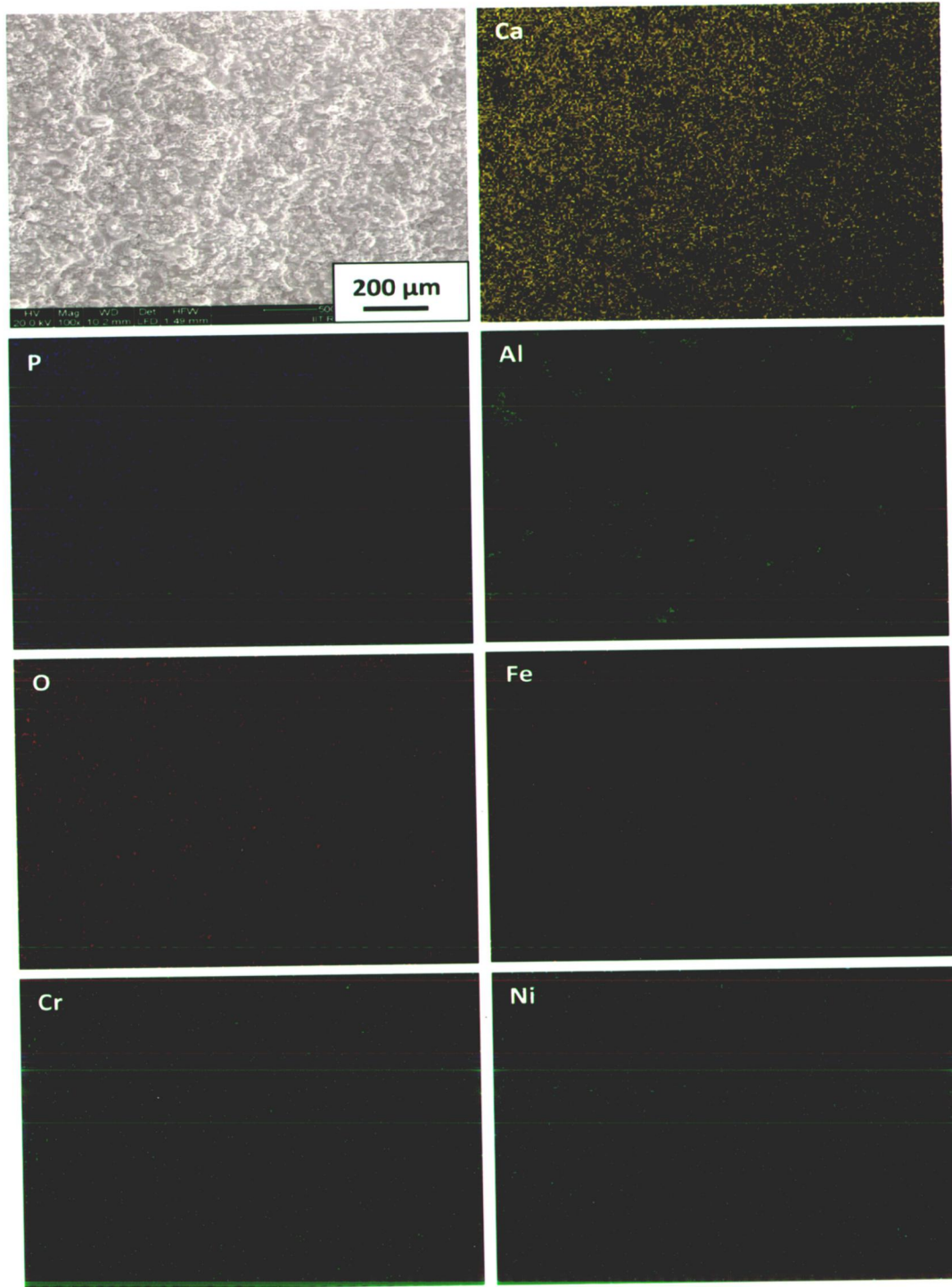


Fig. 4.15 FE-SEM image and X-ray mapping of surface of HA-30 wt% Al₂O₃ coated AISI 316L SS

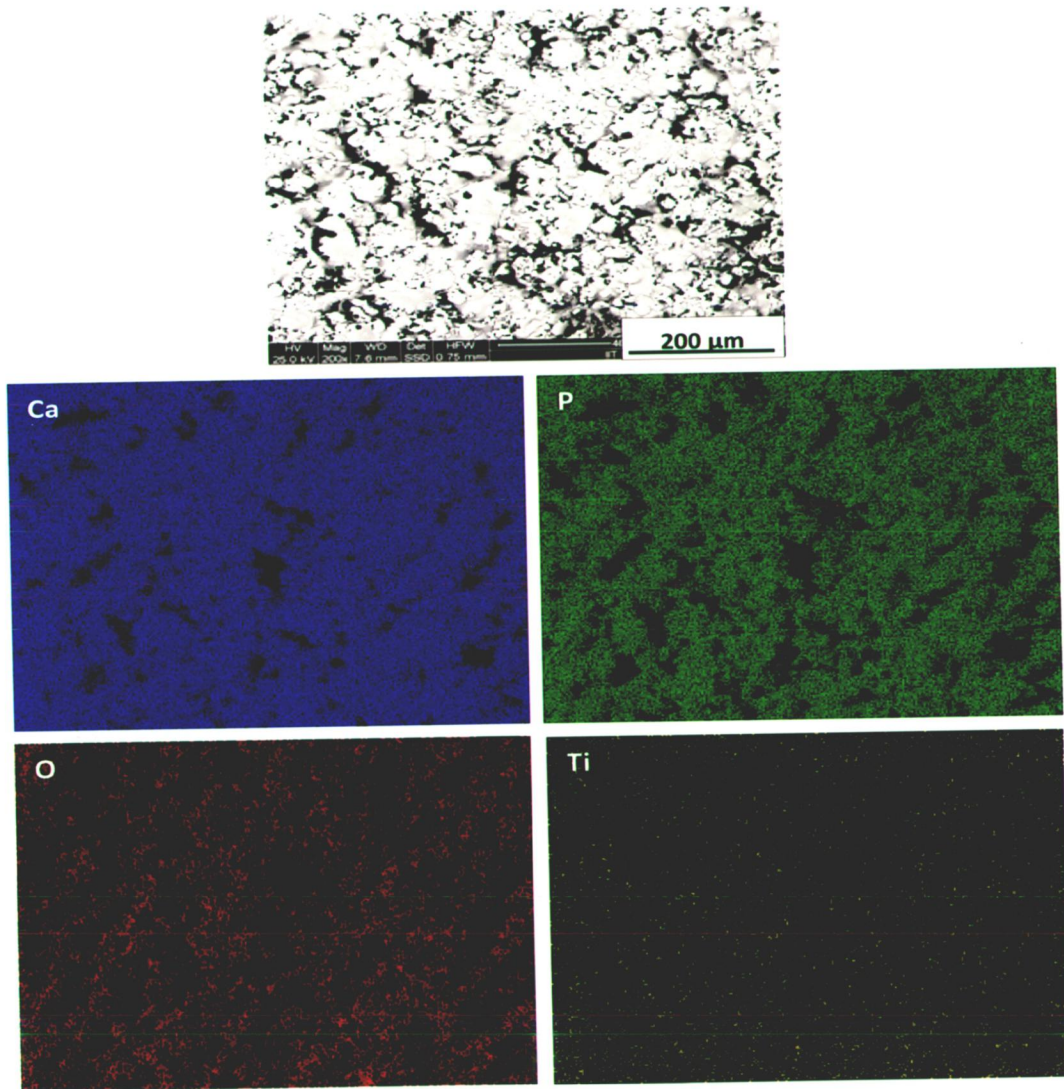


Fig. 4.16 FE-SEM image and X-ray mapping of surface of HA coated titanium

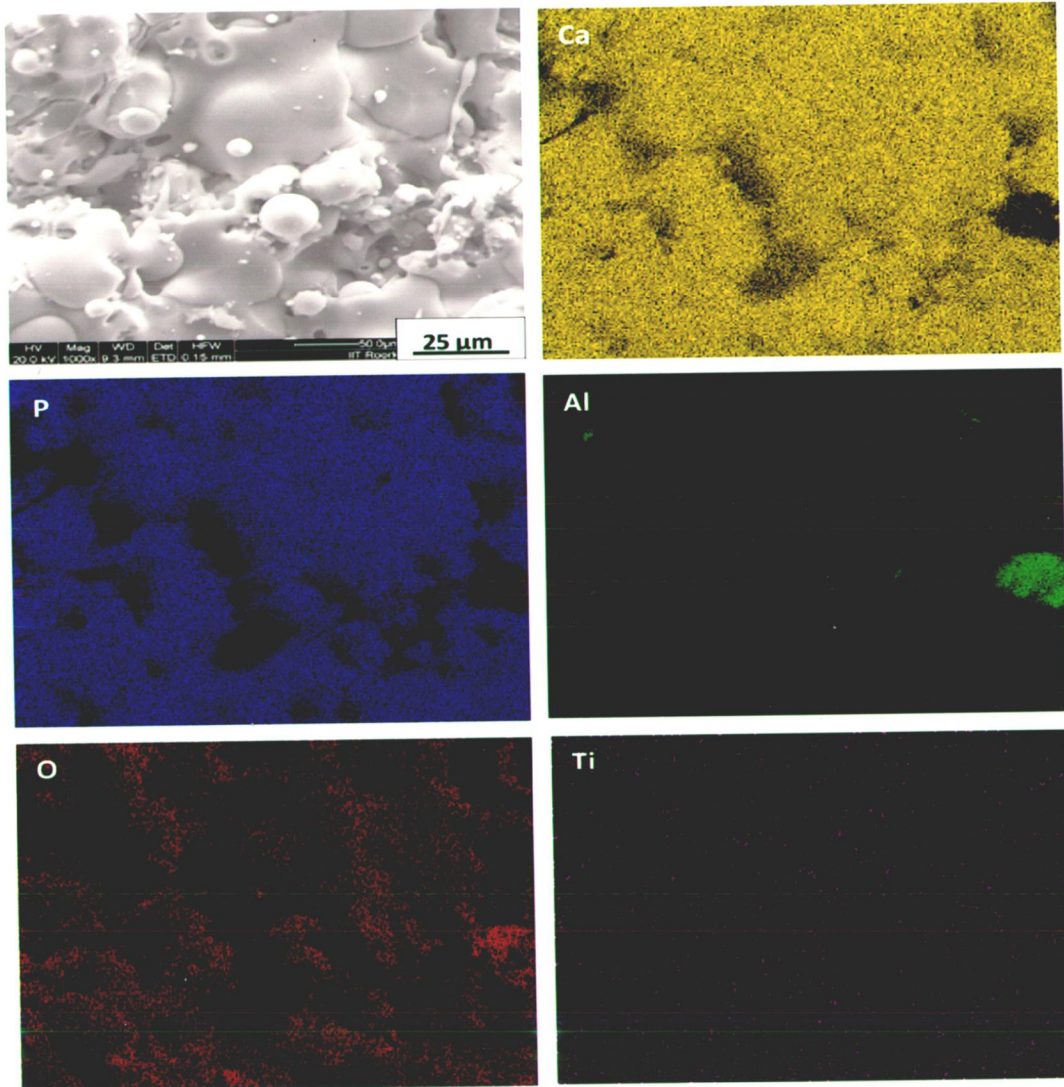


Fig. 4.17 FE-SEM image and X-ray mapping of surface of HA-10 wt% Al₂O₃ coated titanium

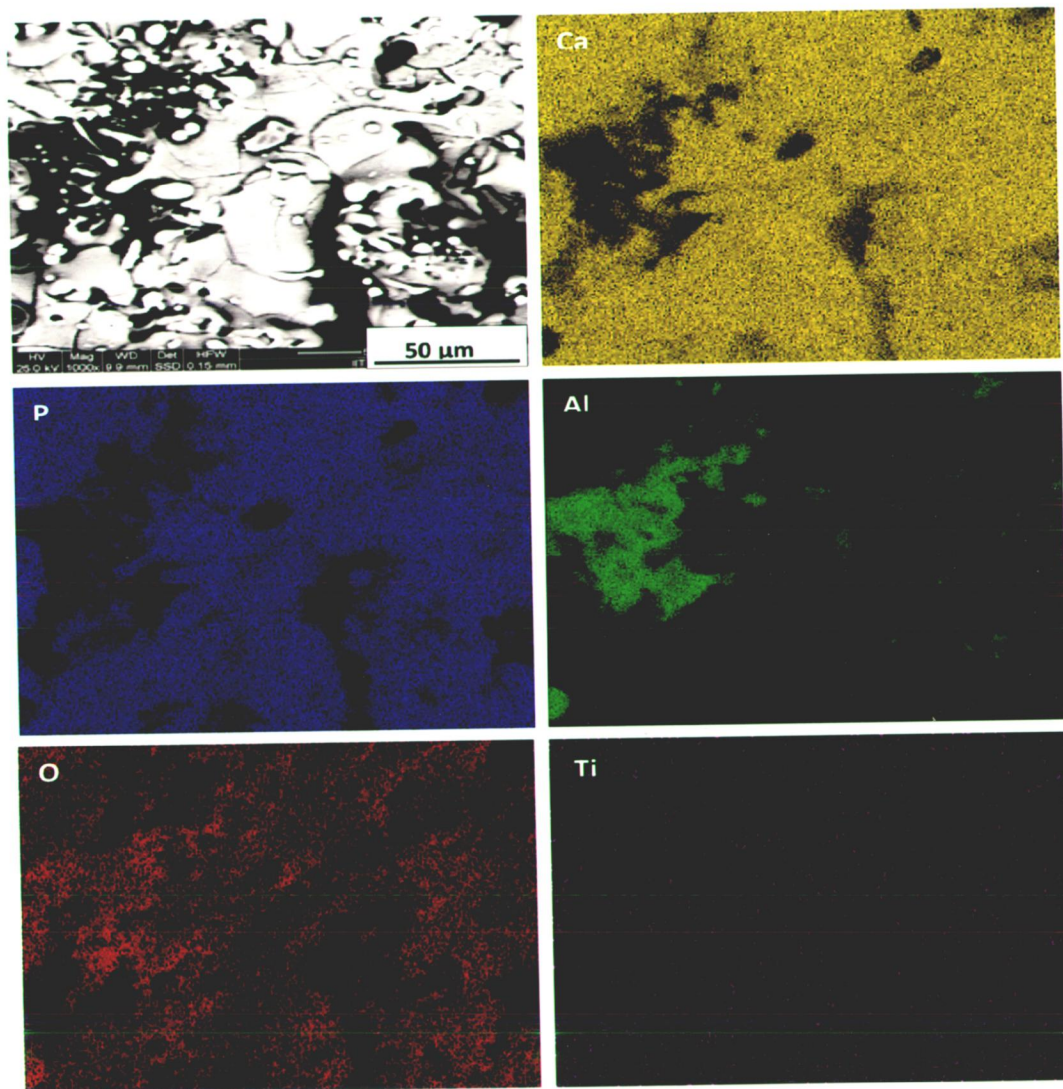


Fig. 4.18 FE-SEM image and X-ray mapping of surface of HA-20 wt% Al₂O₃ coated titanium

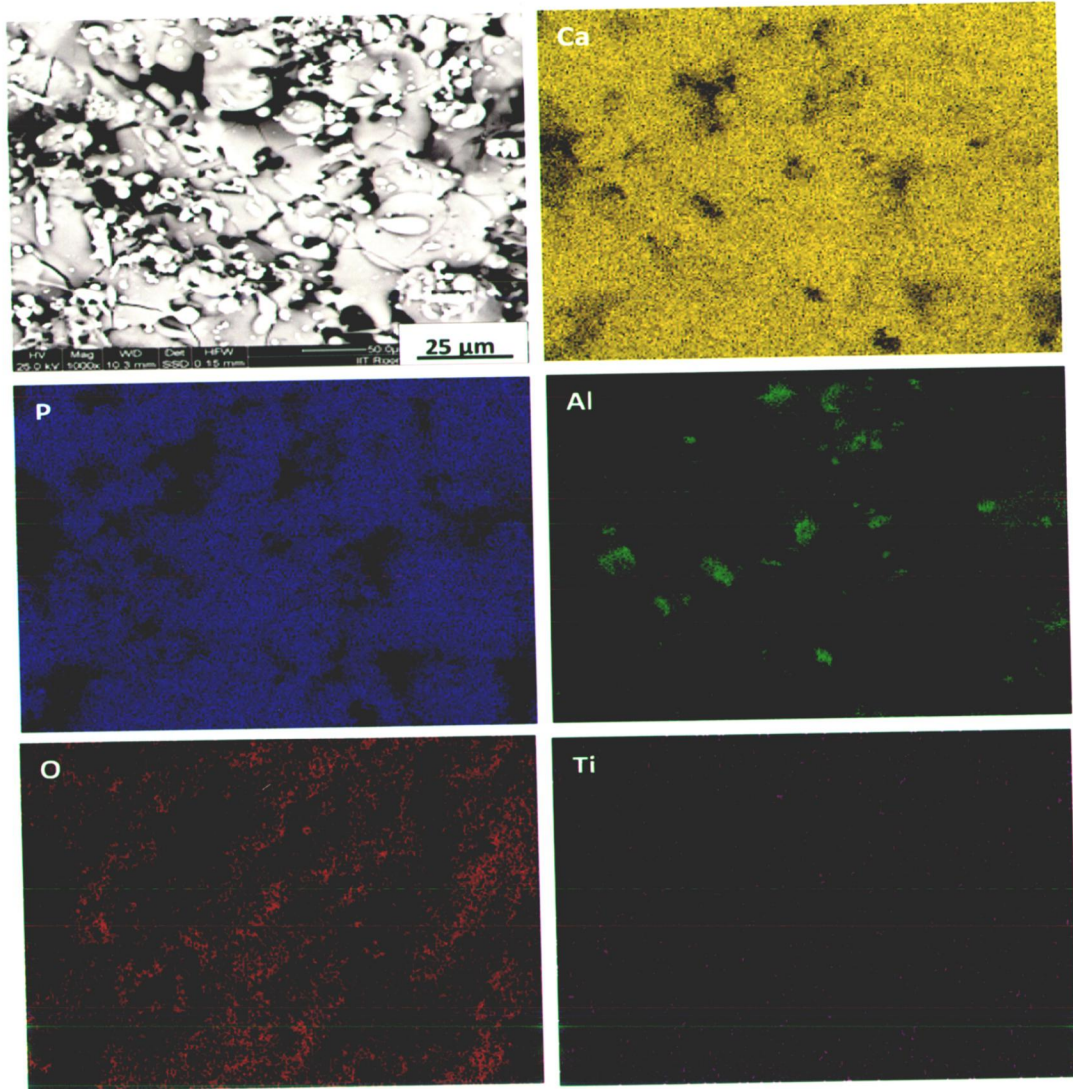


Fig. 4.19 FE-SEM image and X-ray mapping of surface of HA-30 wt% Al₂O₃ coated titanium

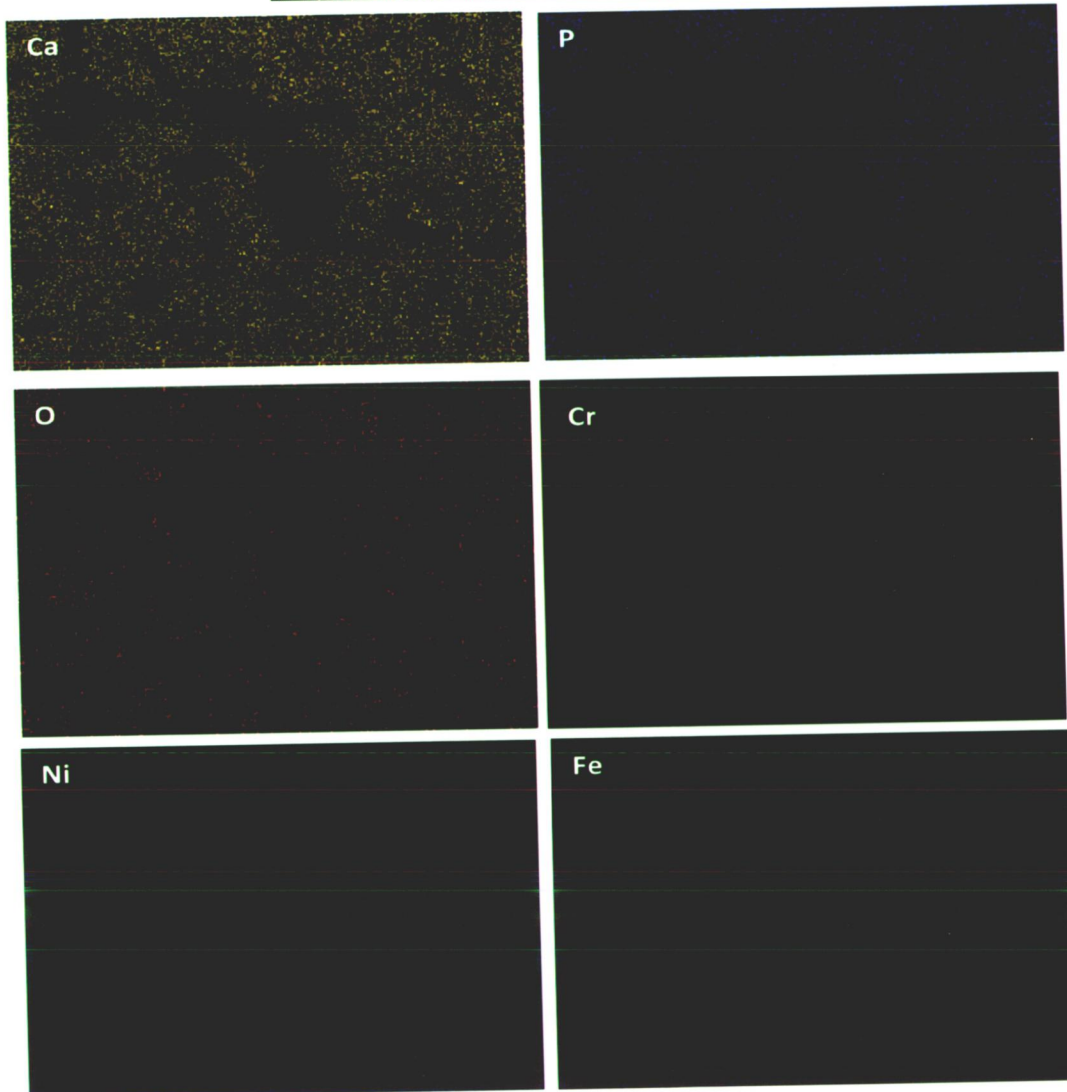
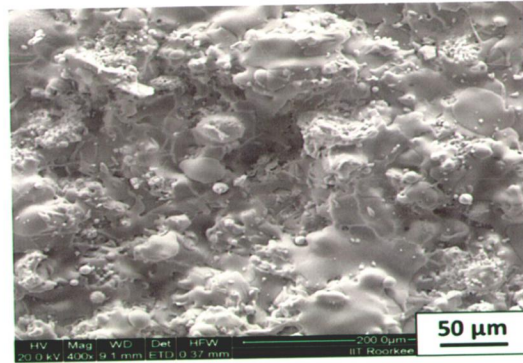


Fig. 4.20 FE-SEM image and X-ray mapping of surface of HA coated AISI 316L SS with bond coat of Al_2O_3 -13 wt% TiO_2

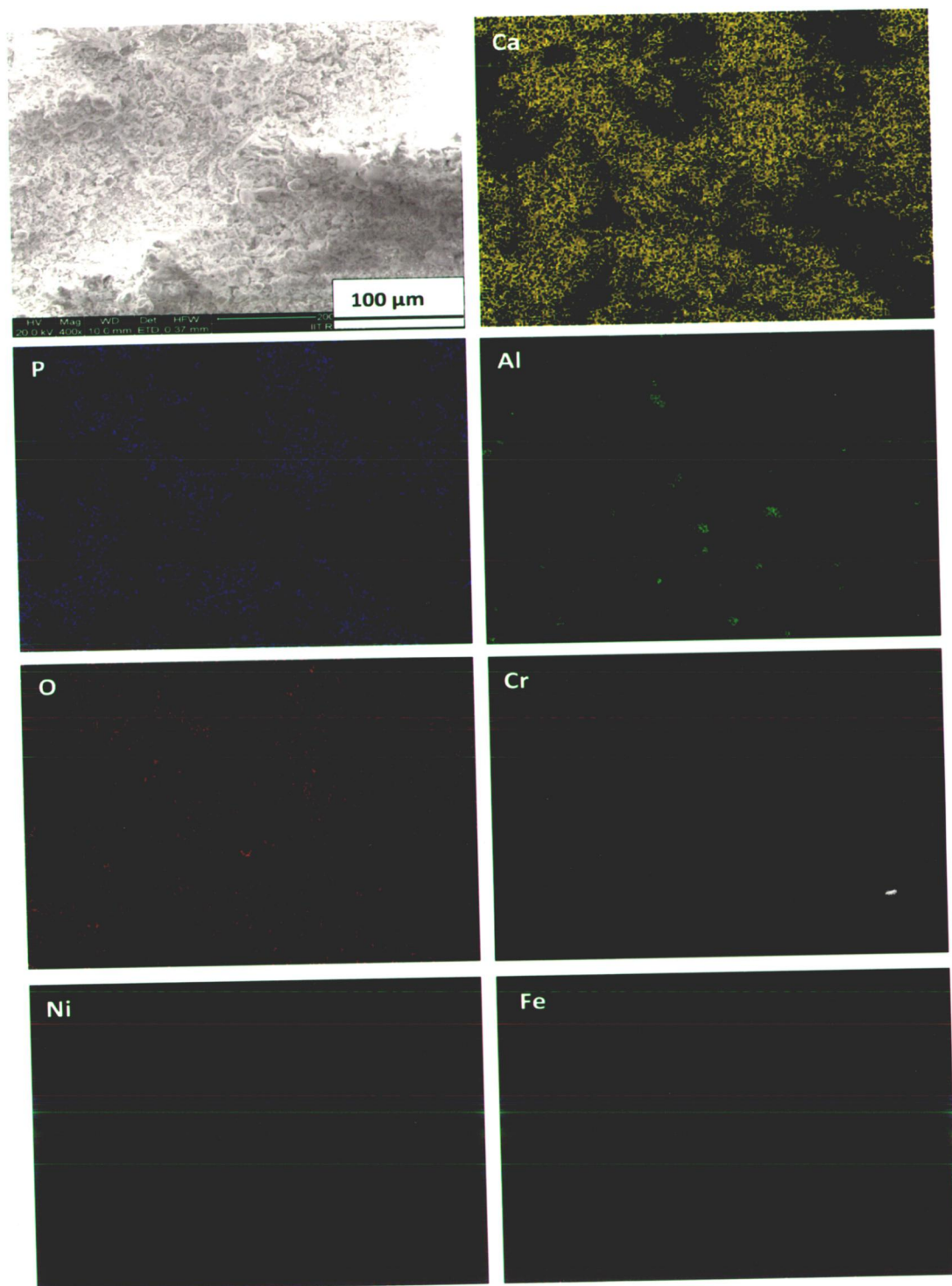


Fig. 4.21 FE-SEM image and X-ray mapping of surface of HA – 10 wt% Al₂O₃ coated AISI 316L SS with bond coat of Al₂O₃-13 wt% TiO₂

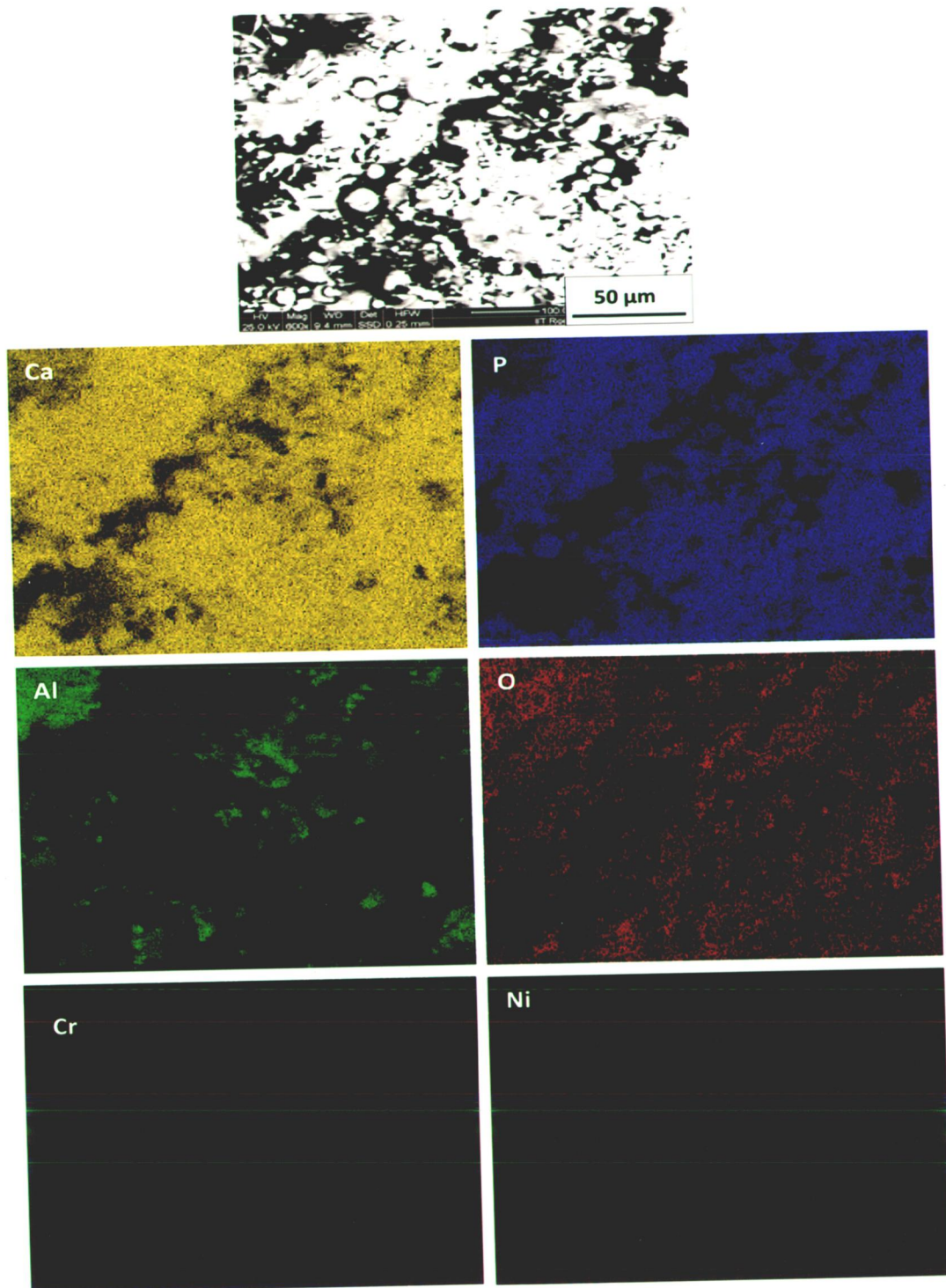


Fig. 4.22 FE-SEM image and X-ray mapping of surface of HA – 20 wt% Al₂O₃ coated AISI 316L SS with bond coat of Al₂O₃-13 wt% TiO₂

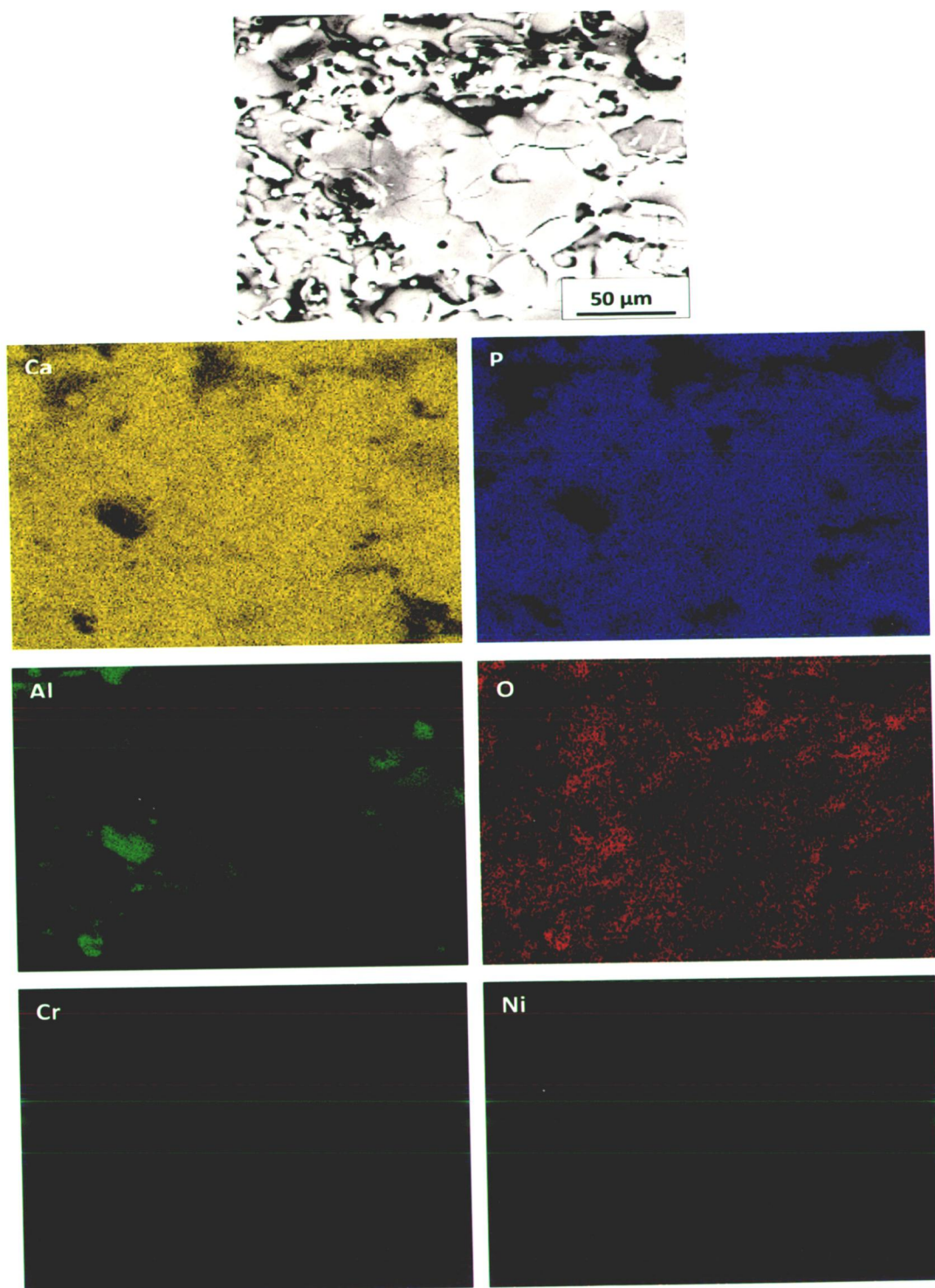


Fig. 4.23 FE-SEM image and X-ray mapping of surface of HA-30 wt% Al_2O_3 coated AISI 316L SS with bond coat of Al_2O_3 -13 wt% TiO_2

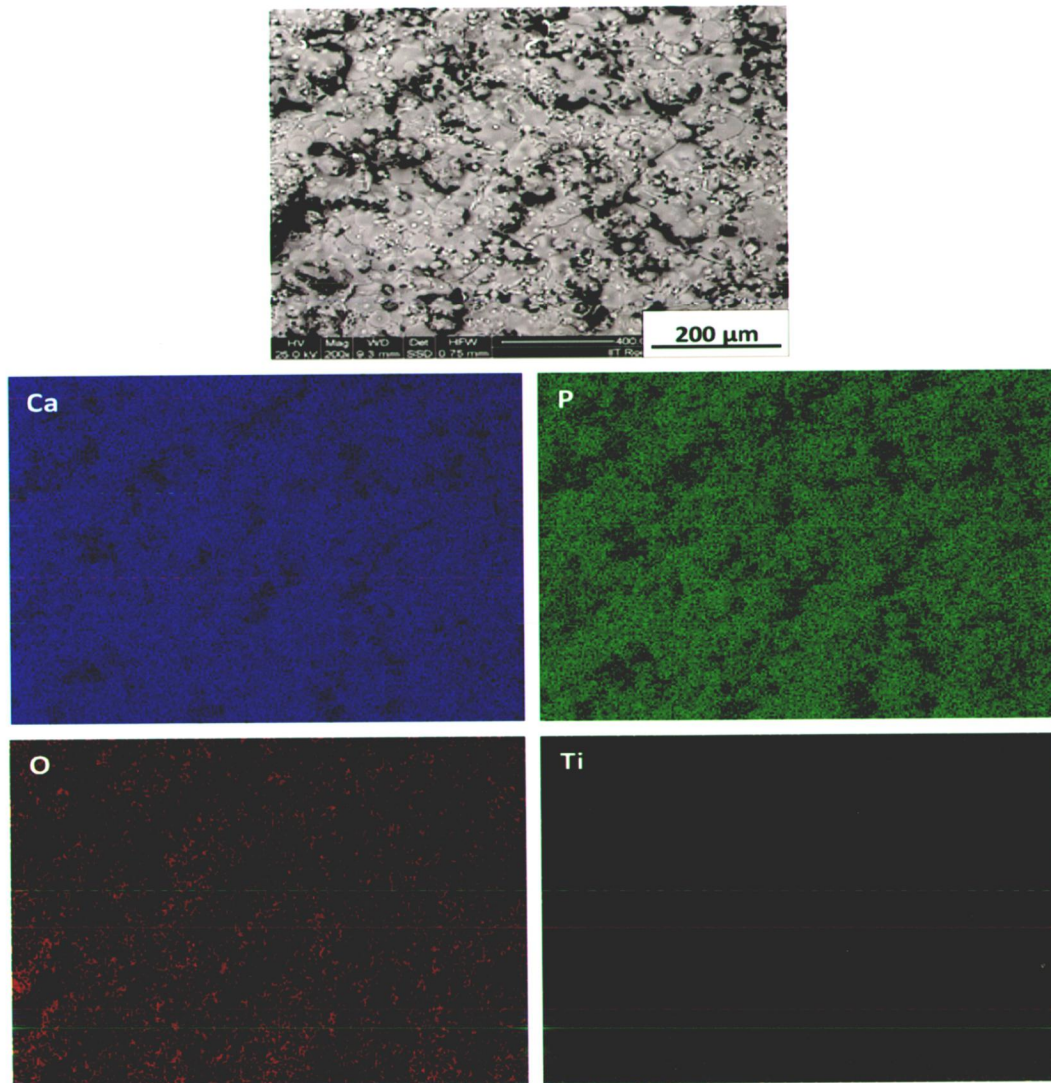


Fig. 4.24 FE-SEM image and X-ray mapping of surface of HA coated titanium with bond coat of Al_2O_3 -13 wt% TiO_2

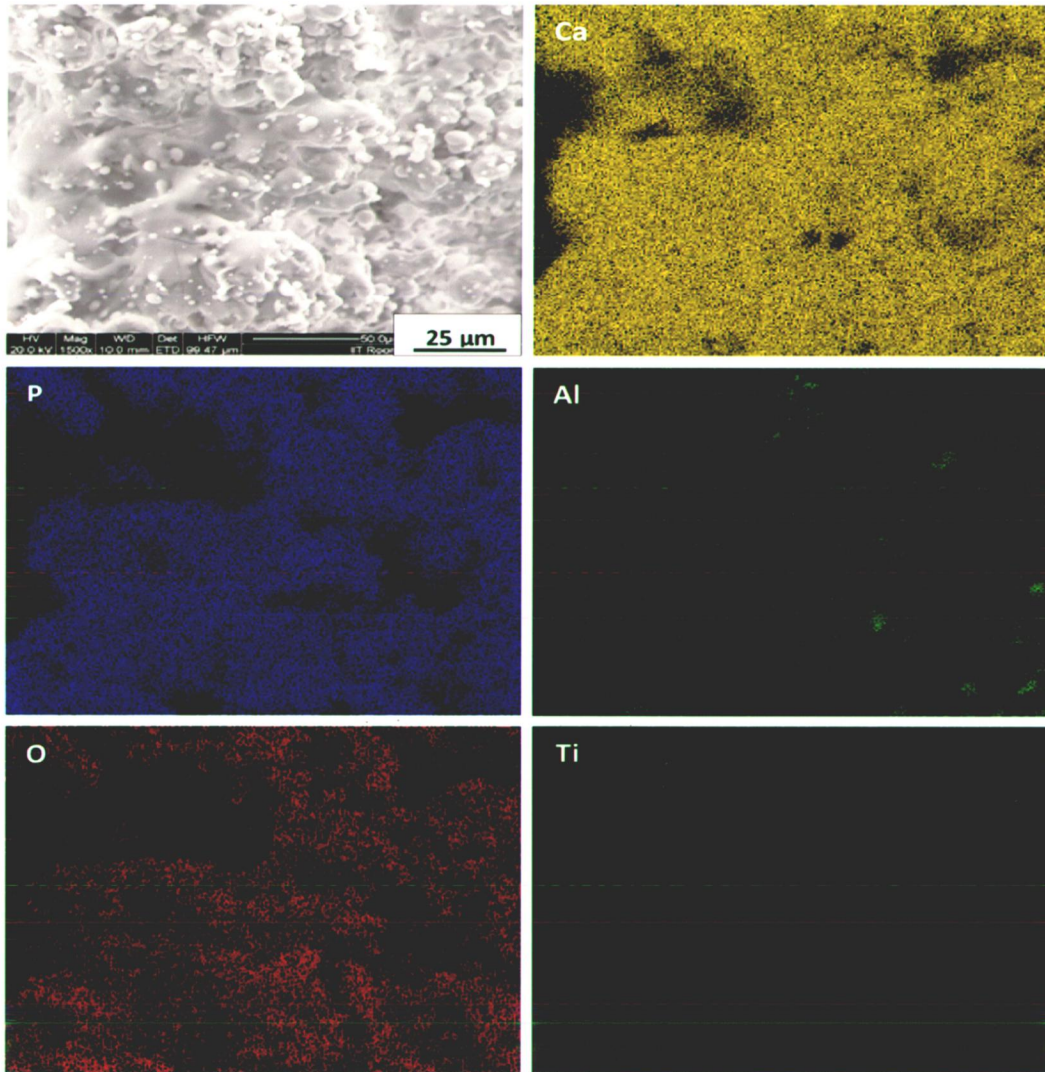


Fig. 4.25 FE-SEM image and X-ray mapping of surface of HA – 10 wt% Al₂O₃ coated titanium with bond coat of Al₂O₃-13 wt% TiO₂

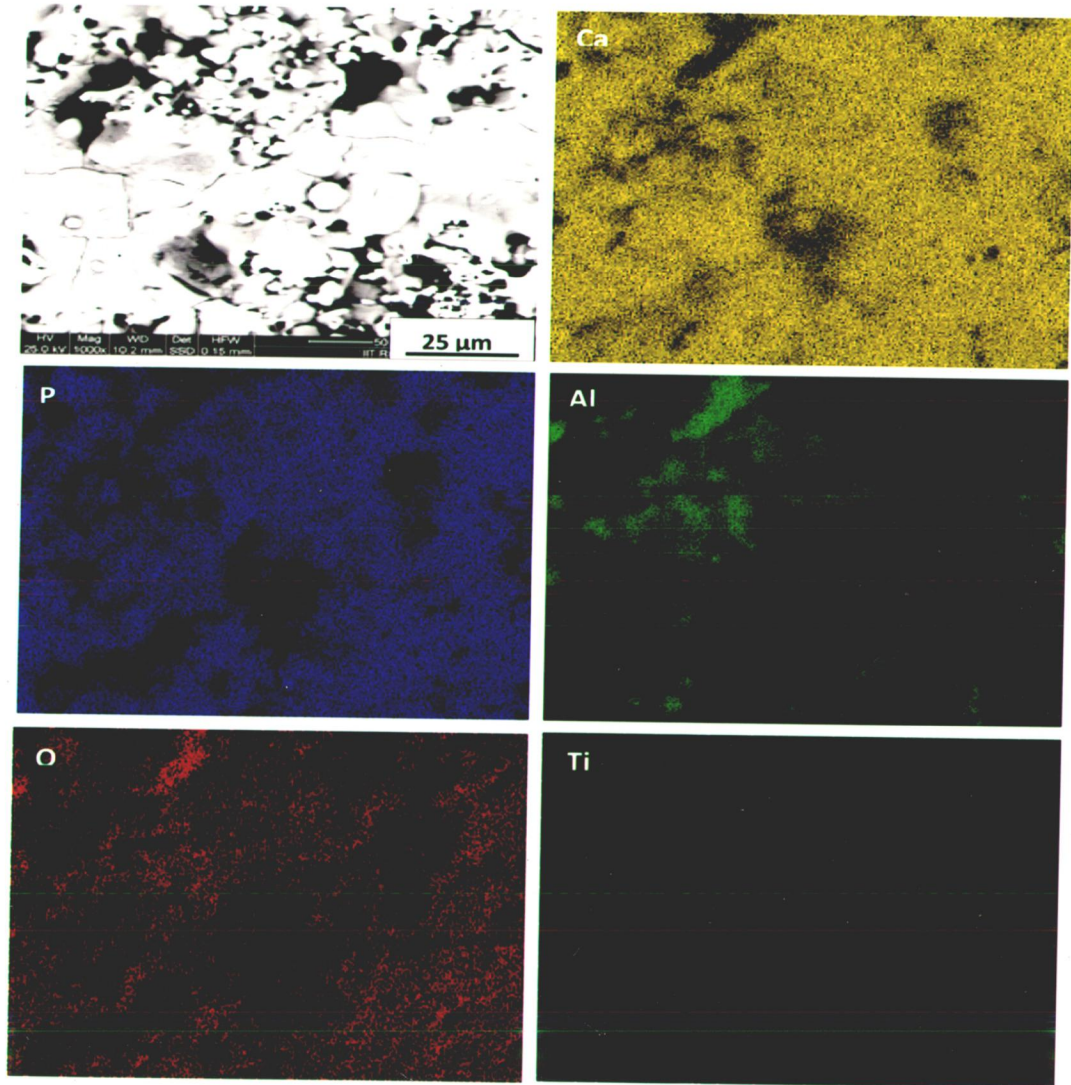


Fig. 4.26 FE-SEM image and X-ray mapping of surface of HA-20 wt% Al_2O_3 coated titanium with bond coat of $\text{Al}_2\text{O}_3 - 13 \text{ wt}\% \text{TiO}_2$

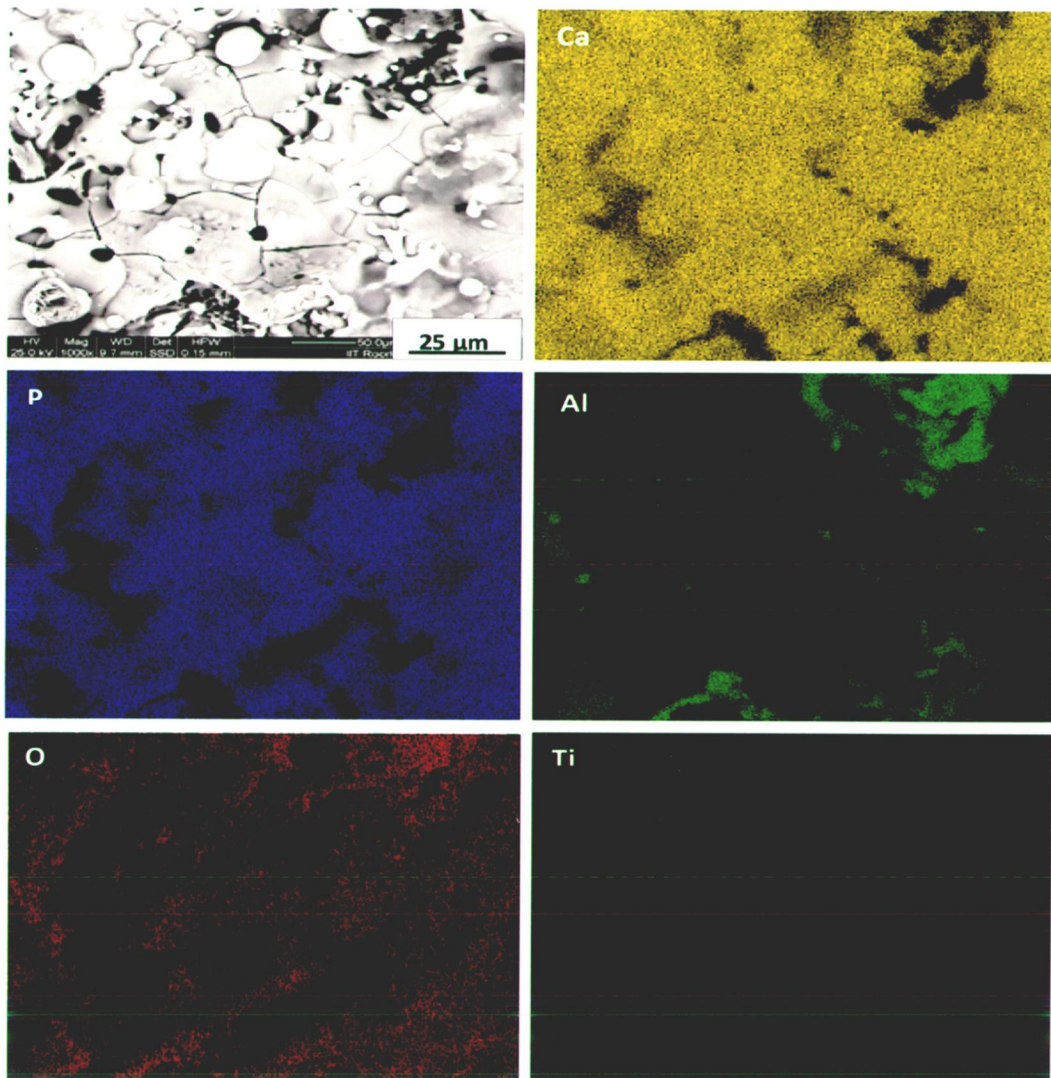


Fig. 4.27 FE-SEM image and X-ray mapping of surface of HA-30 wt% Al_2O_3 coated titanium with bond coat of $\text{Al}_2\text{O}_3 - 13 \text{ wt}\% \text{TiO}_2$

The dark streaks in the light background in FE-SEM images are aluminum oxide particles (reinforcement), which was confirmed by comparing micrograph with corresponding X-ray mapping image for Al.

X-ray mappings of plasma sprayed HA, HA-10 wt% Al₂O₃, HA-20 wt% Al₂O₃ and HA-30 wt% Al₂O₃ coatings on AISI 316L substrate are presented in Fig. 4.28-4.31 respectively, whereas Fig. 4.32-4.35 represents X-ray mapping of these coatings on titanium substrate. X-ray mapping of HA indicates the presence of Ca and P (Fig. 4.28 and 4.32). X-ray mapping of composite coatings show the presence of Al in Ca and P rich matrix (Fig. 4.29-4.31 and Fig. 4.33-4.35). In all the coating-substrate combinations the aluminum oxide is evenly distributed in the matrix of hydroxyapatite, which was not visible in X-ray mapping of surface of as sprayed coatings (Fig. 4.12-4.27). Moreover, it can be inferred from the cross-sectional X-ray mappings that alumina is present at the splat boundaries of hydroxyapatite. The presence of alumina at splat boundaries is supposed to increase the strength of composite coatings. Negligible diffusion/migration of substrate elements to the coatings had been indicated by X-ray mappings.

Figure 4.36-4.39 show the X-ray mappings of plasma sprayed HA, HA-10 wt% Al₂O₃, HA-20 wt% Al₂O₃ and HA-30 wt% Al₂O₃ coatings on AISI 316L substrate with bond coat of Al₂O₃-13 wt% TiO₂ respectively, whereas X-ray mapping of coatings on titanium substrate with bond are presented in Fig. 4.40-4.43. The distribution of coating elements show a similar trend as that for coatings without bond coat and the diffusion of substrate elements in coatings seems to be restricted by incorporation of intermediate layer of bond coat. From X-ray elemental distribution of coatings with and without incorporation of bond coat of Al₂O₃-13 wt% TiO₂, it can be inferred that with application of bond coat the diffusion/migration of substrate elements is restricted.

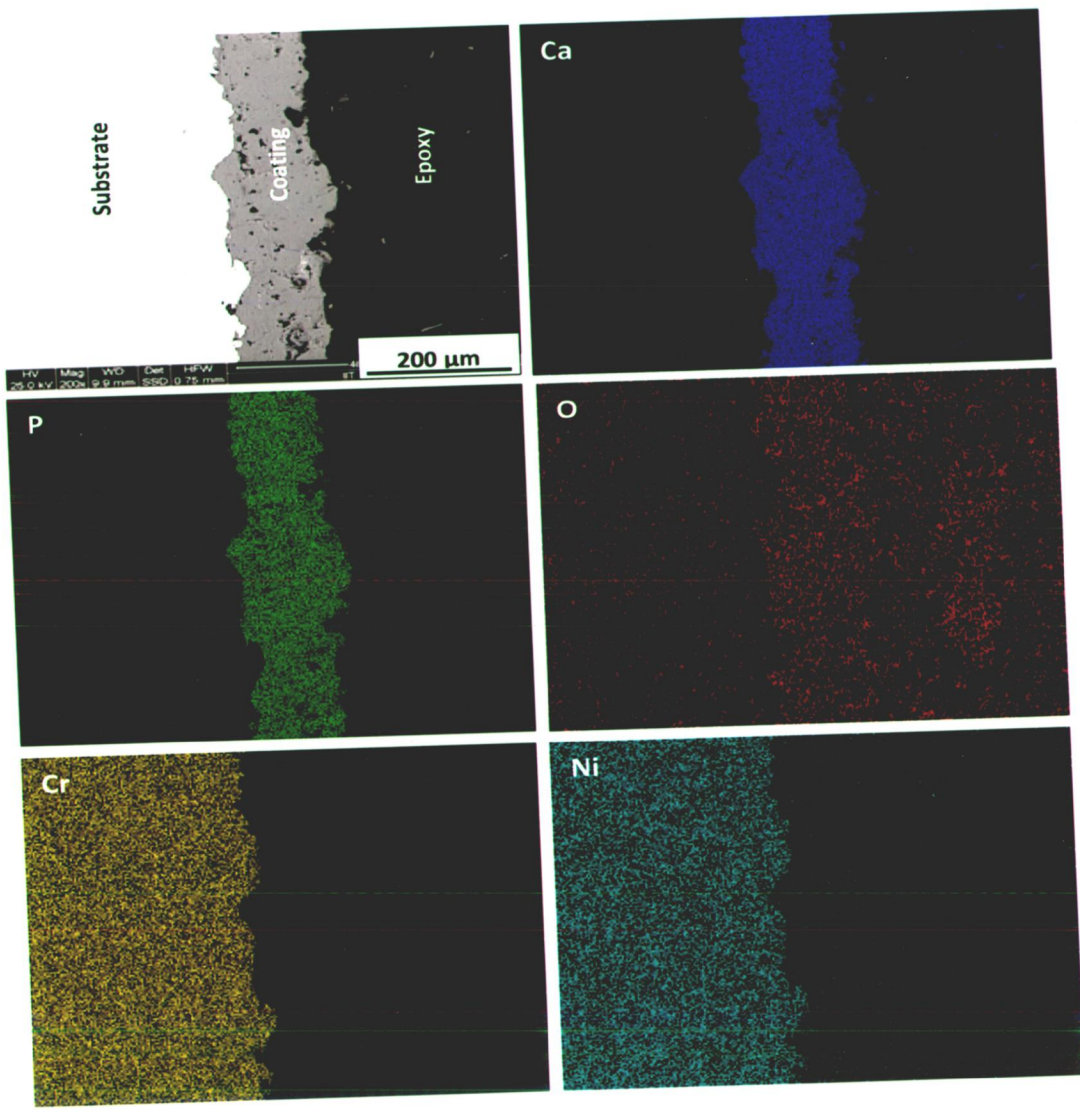


Fig. 4.28 FE-SEM image and X-ray mapping of cross-section of HA coated AISI 316L SS

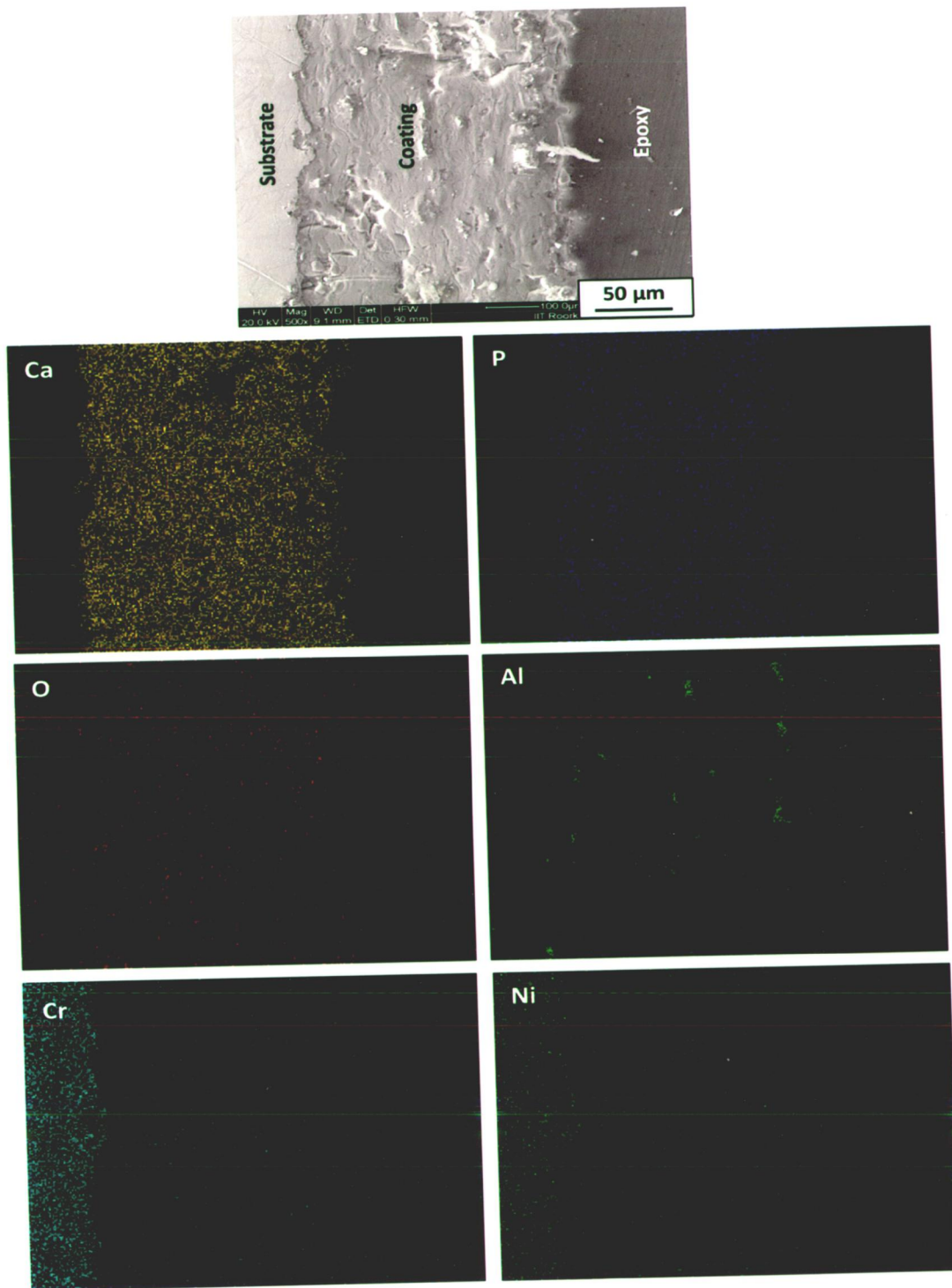


Fig. 4.29 FE-SEM image and X-ray mapping of cross-section of HA-10 wt% Al₂O₃ coated AISI 316L SS

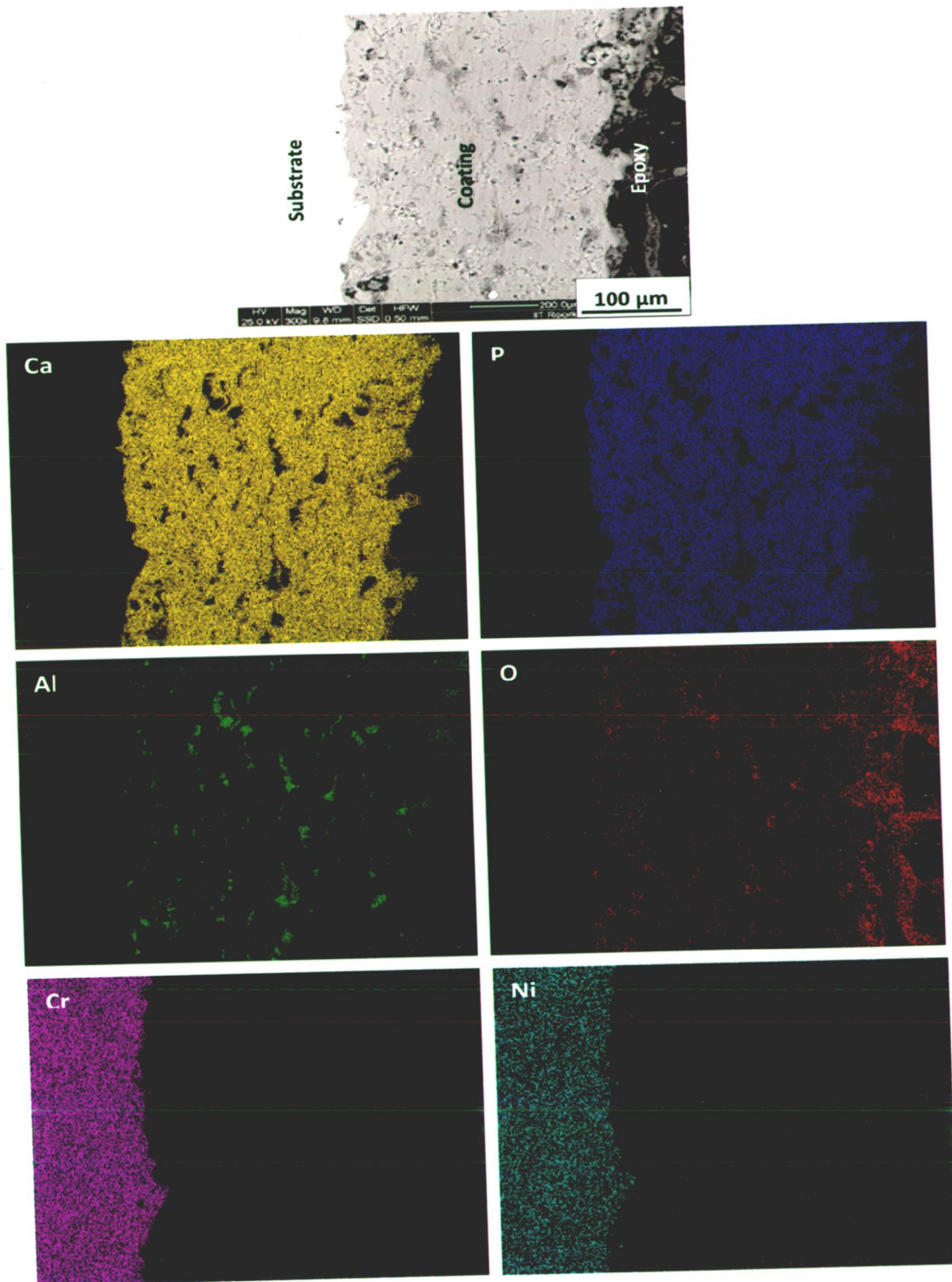


Fig. 4.30 FE-SEM image and X-ray mapping of cross-section of HA-20 wt% Al_2O_3 coated AISI316L SS

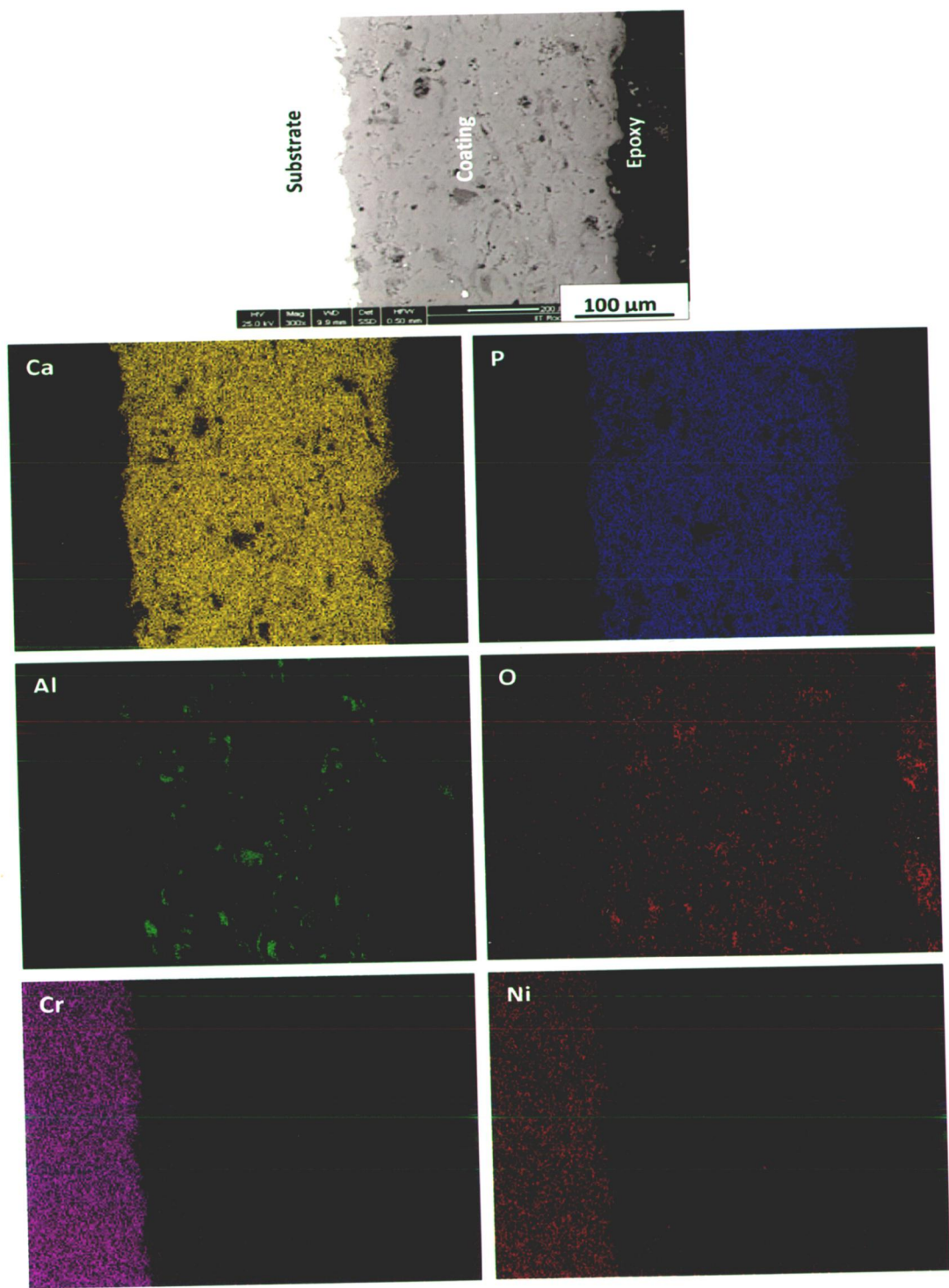


Fig. 4.31 FE-SEM image and X-ray mapping of cross-section of HA-30 wt% Al₂O₃ coated AISI 316L SS

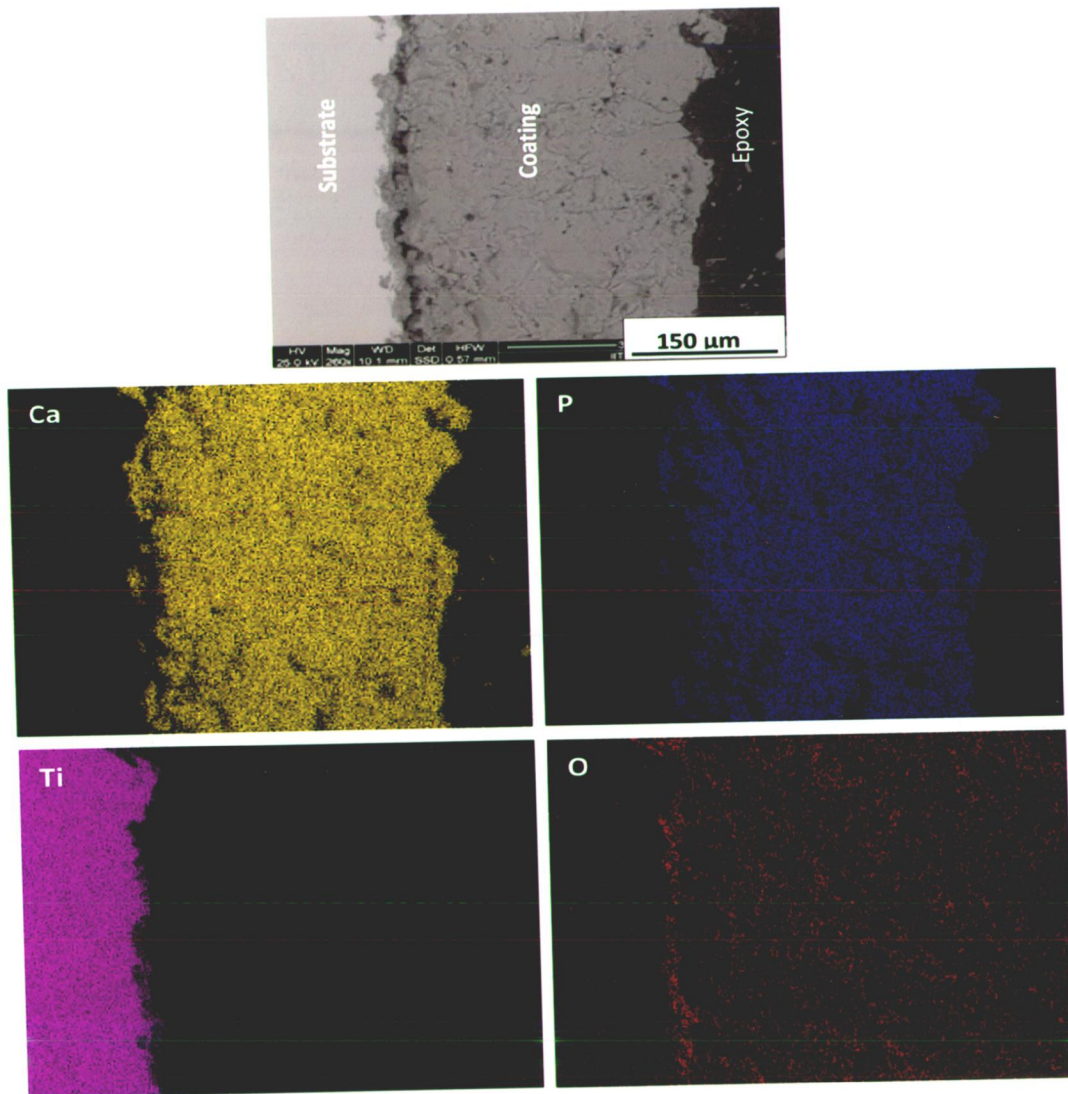


Fig. 4.32 FE-SEM image and X-ray mapping of cross-section of HA coated titanium

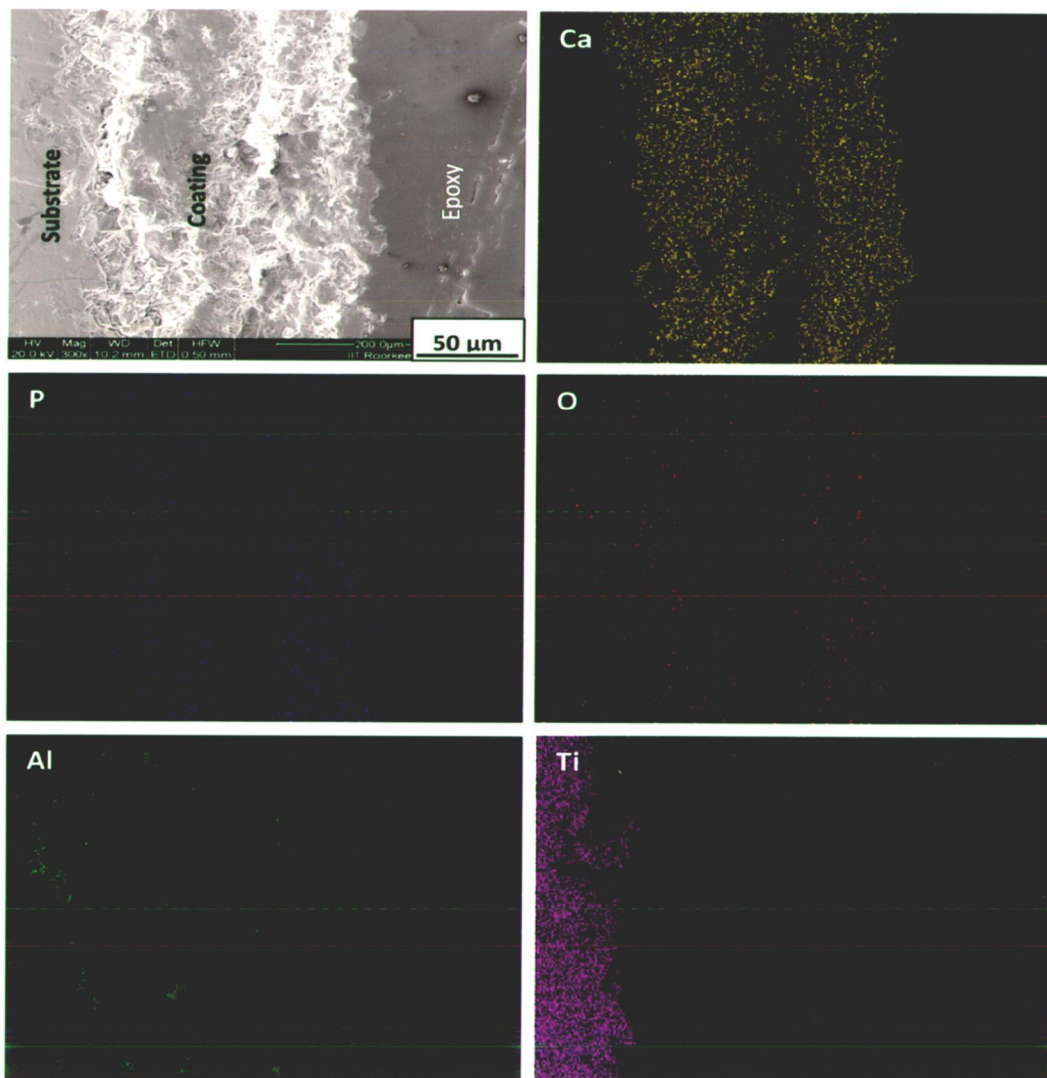


Fig. 4.33 FE-SEM image and X-ray mapping of cross-section of HA-10 wt% Al₂O₃ coated titanium

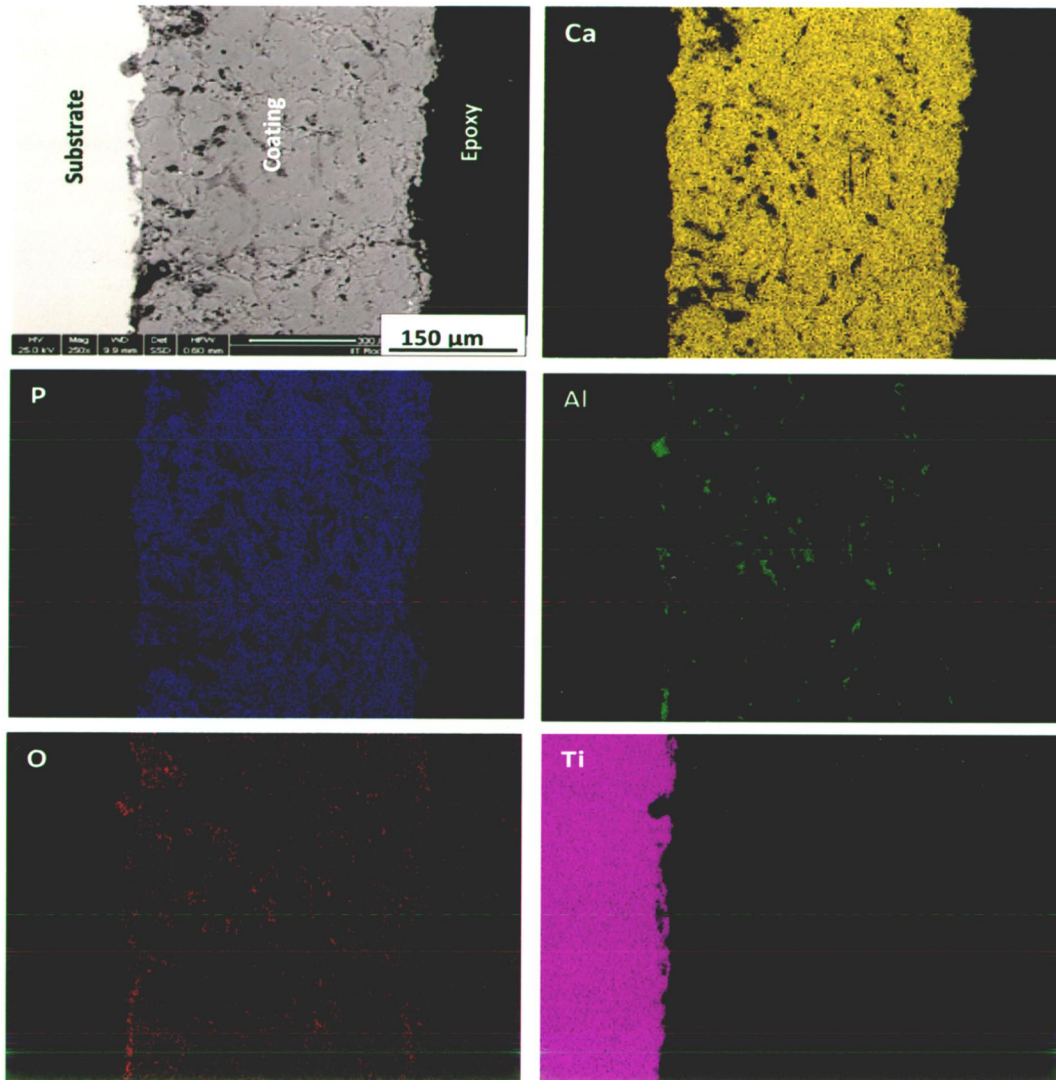


Fig. 4.34 FE-SEM image and X-ray mapping of cross-section of HA-20 wt% Al₂O₃ coated titanium

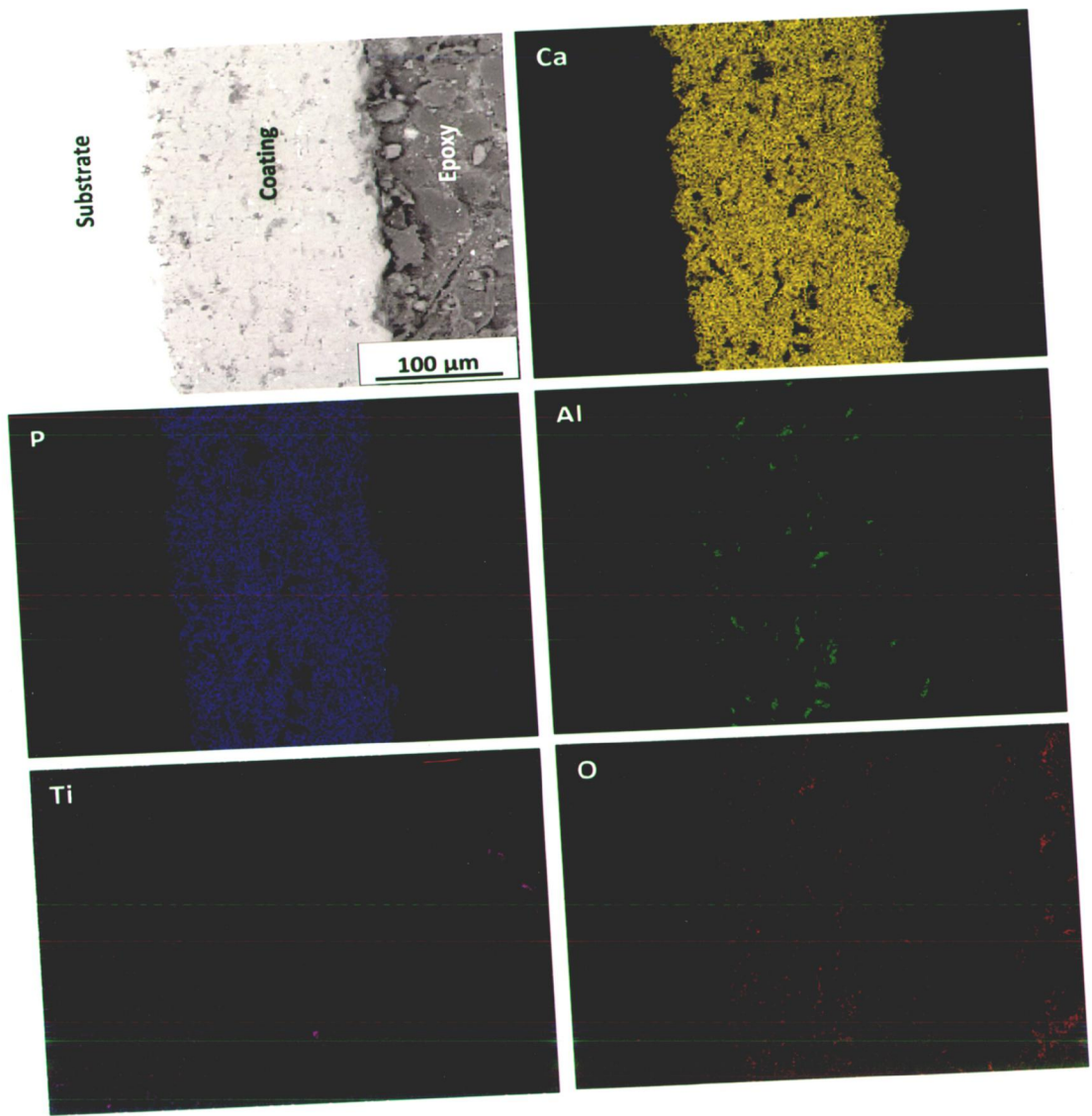


Fig. 4.35 FE-SEM image and X-ray mapping of cross-section of HA-30 wt% Al₂O₃ coated titanium

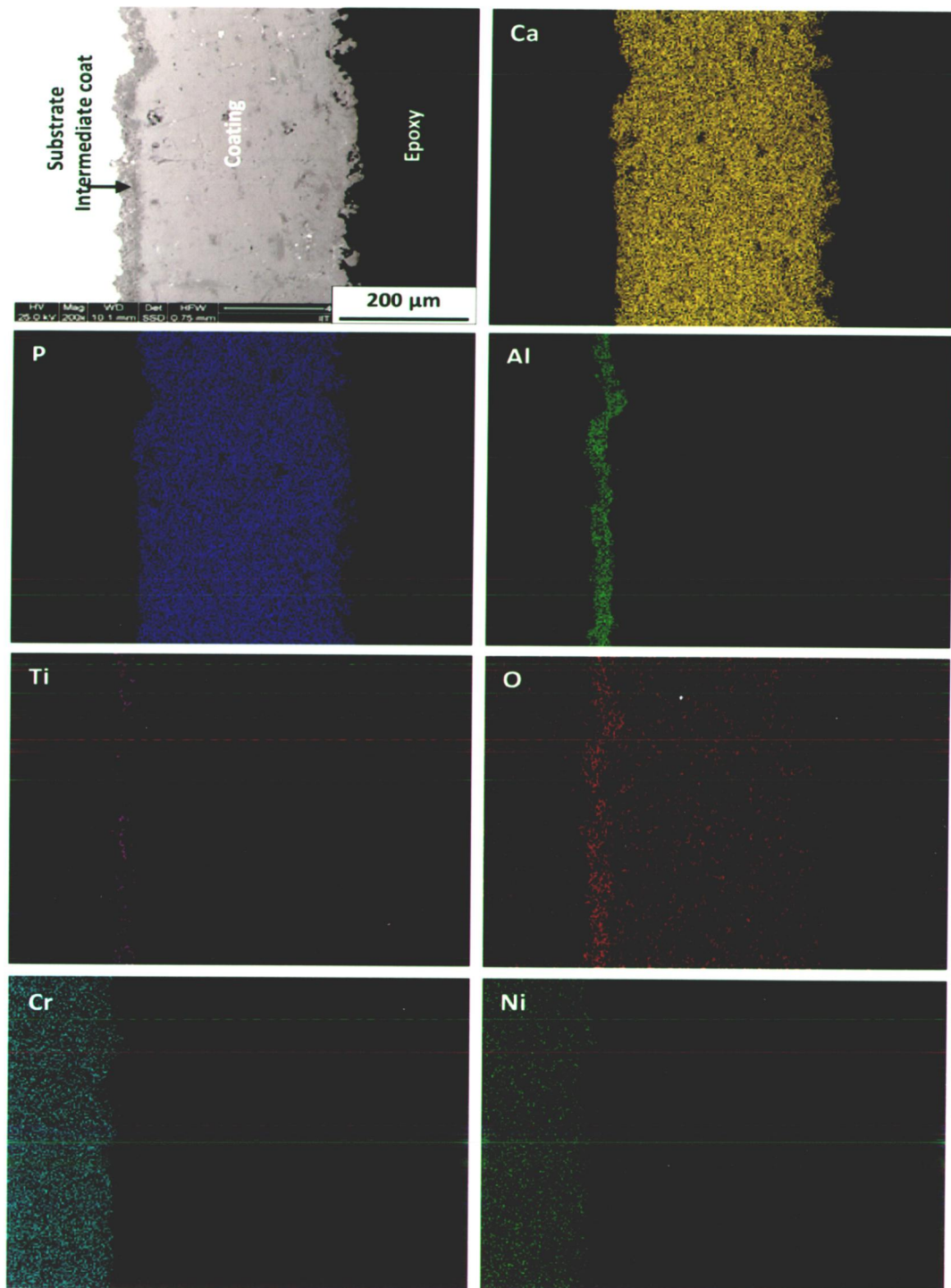


Fig. 4.36 FE-SEM image and X-ray mapping of cross-section of HA coated AISI 316L SS with bond coat of Al_2O_3 -13 wt% TiO_2

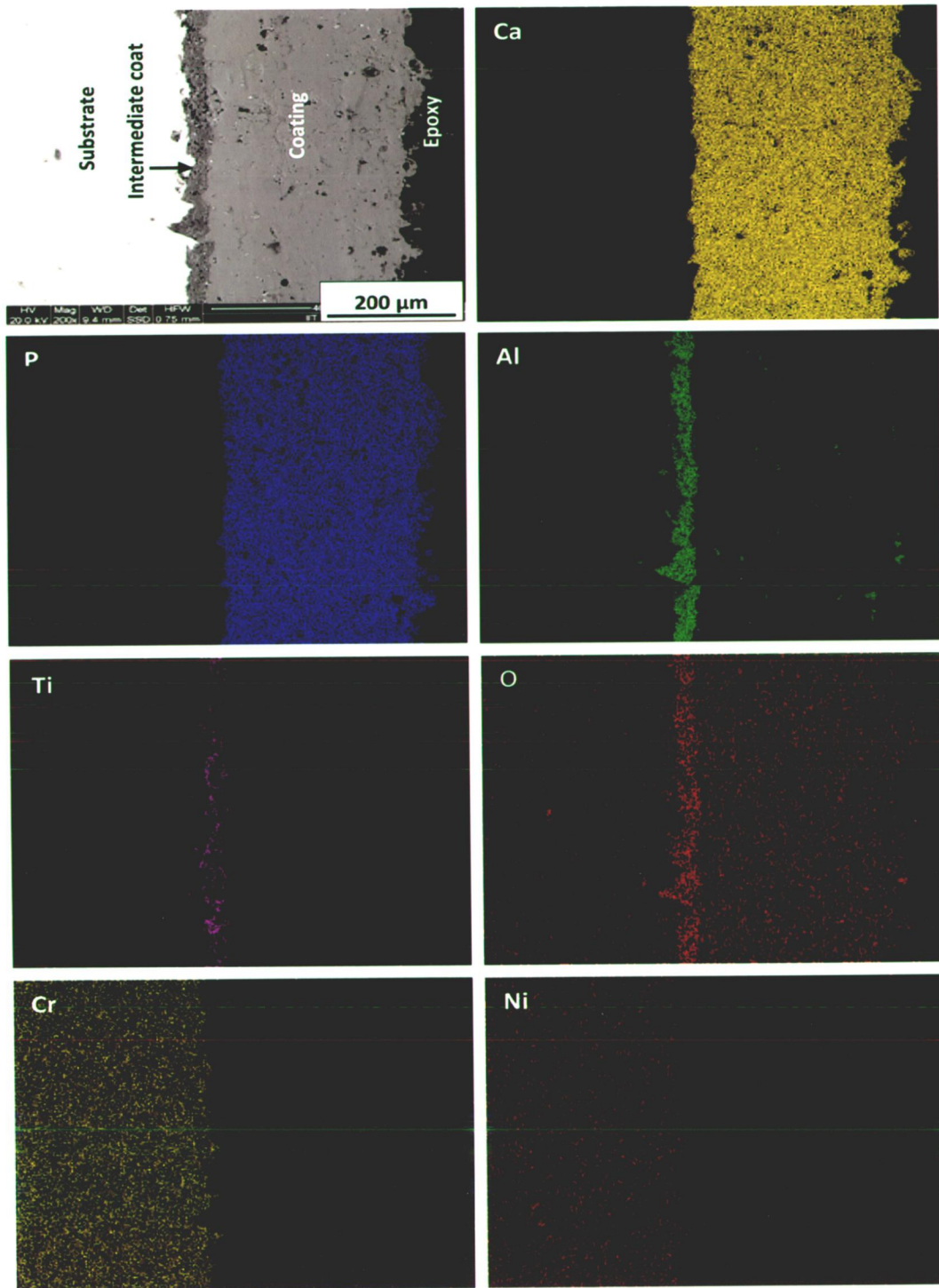


Fig. 4.37 FE-SEM image and X-ray mapping of cross-section of HA-10 wt% Al_2O_3 coated AISI 316L SS with bond coat of Al_2O_3 -13 wt% TiO_2

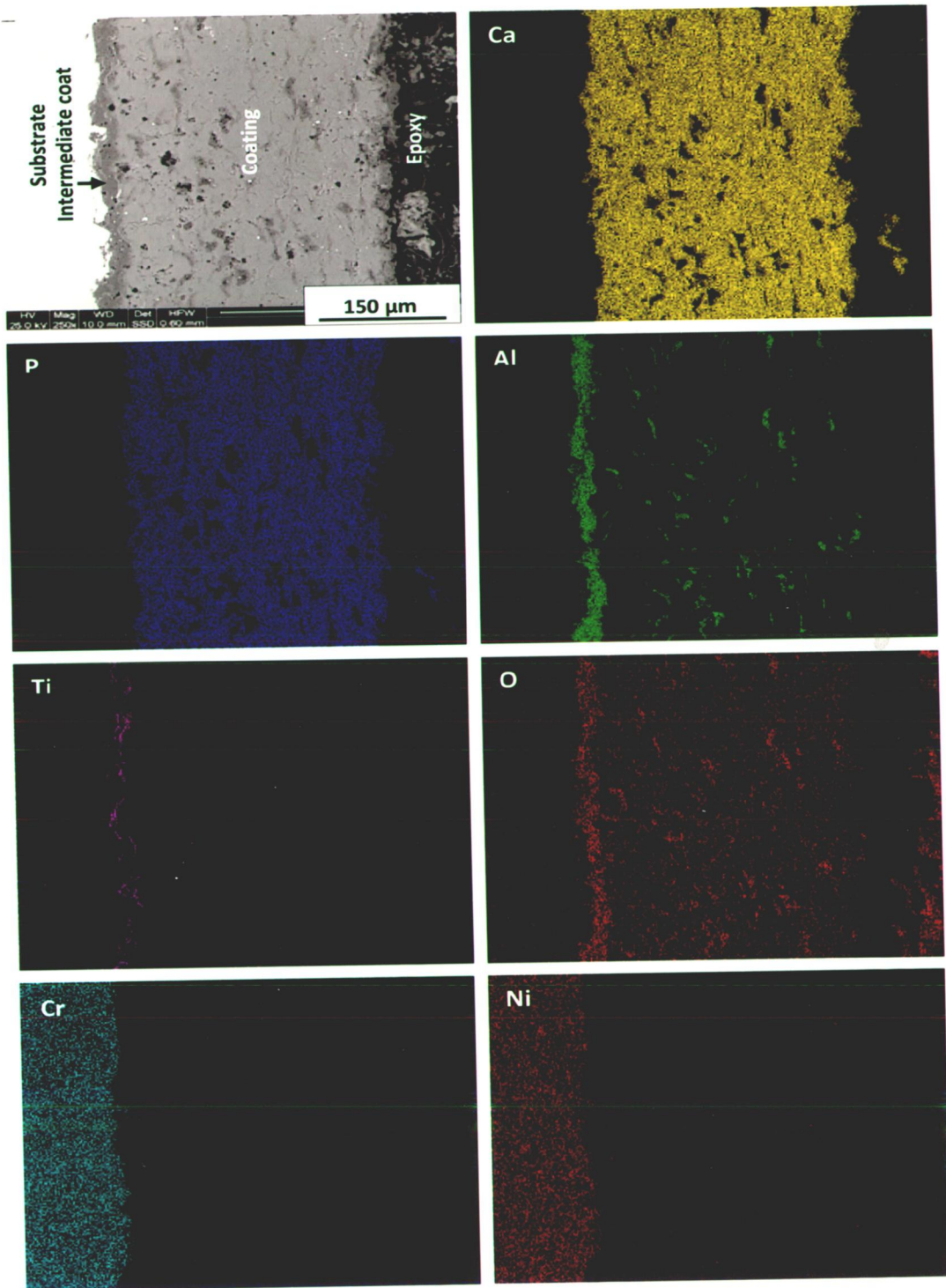


Fig. 4.38 FE-SEM image and X-ray mapping of cross-section of HA-20 wt% Al_2O_3 coated AISI 316L SS with bond coat of Al_2O_3 -13 wt% TiO_2

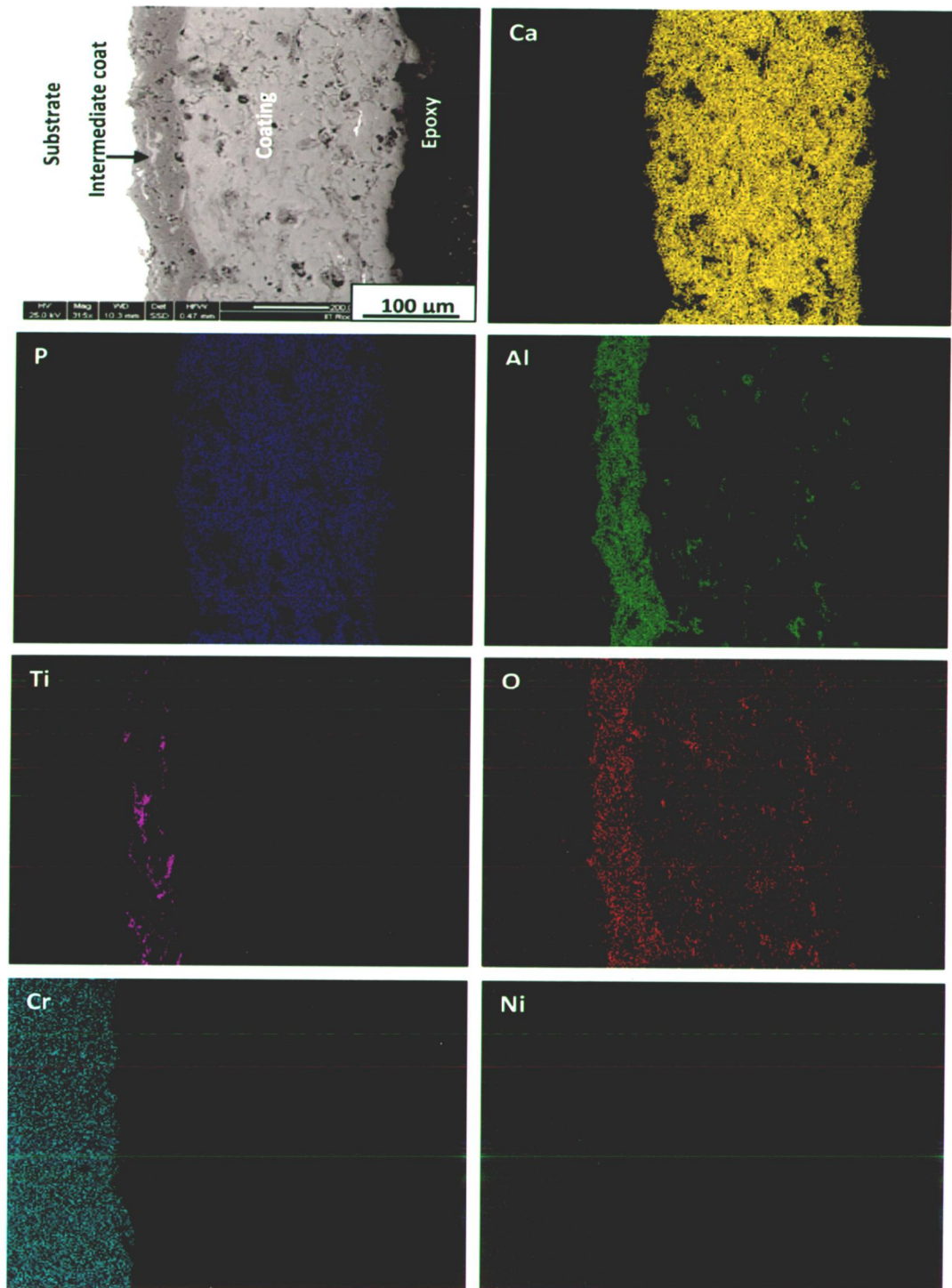


Fig. 4.39 FE-SEM image and X-ray mapping of cross-section of HA-30 wt% Al₂O₃ coated AISI 316L SS with bond coat of Al₂O₃-13 wt% TiO₂

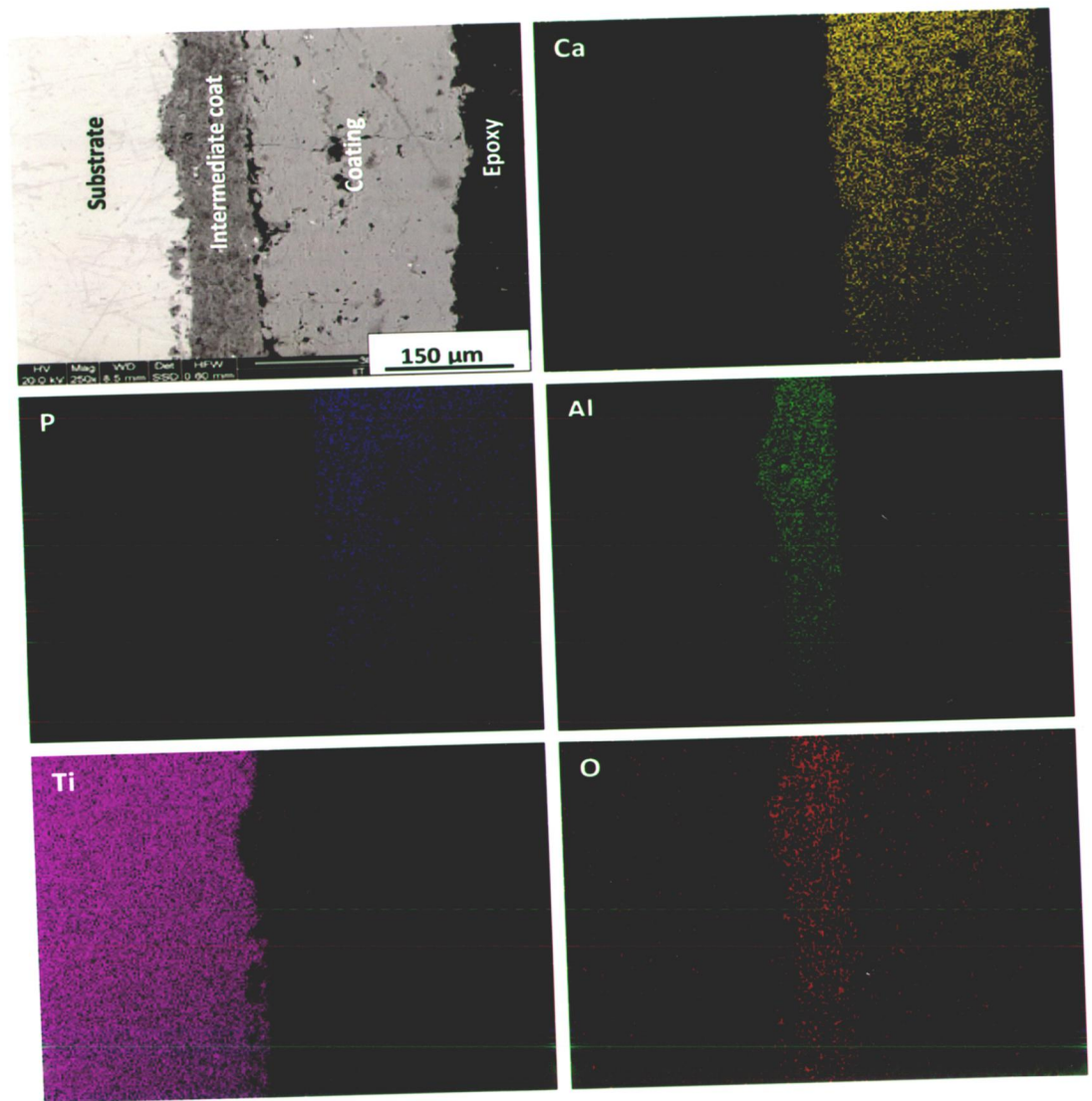


Fig. 4.40 FE-SEM image and X-ray mapping of cross-section of HA coated titanium with bond coat of Al_2O_3 -13 wt% TiO_2

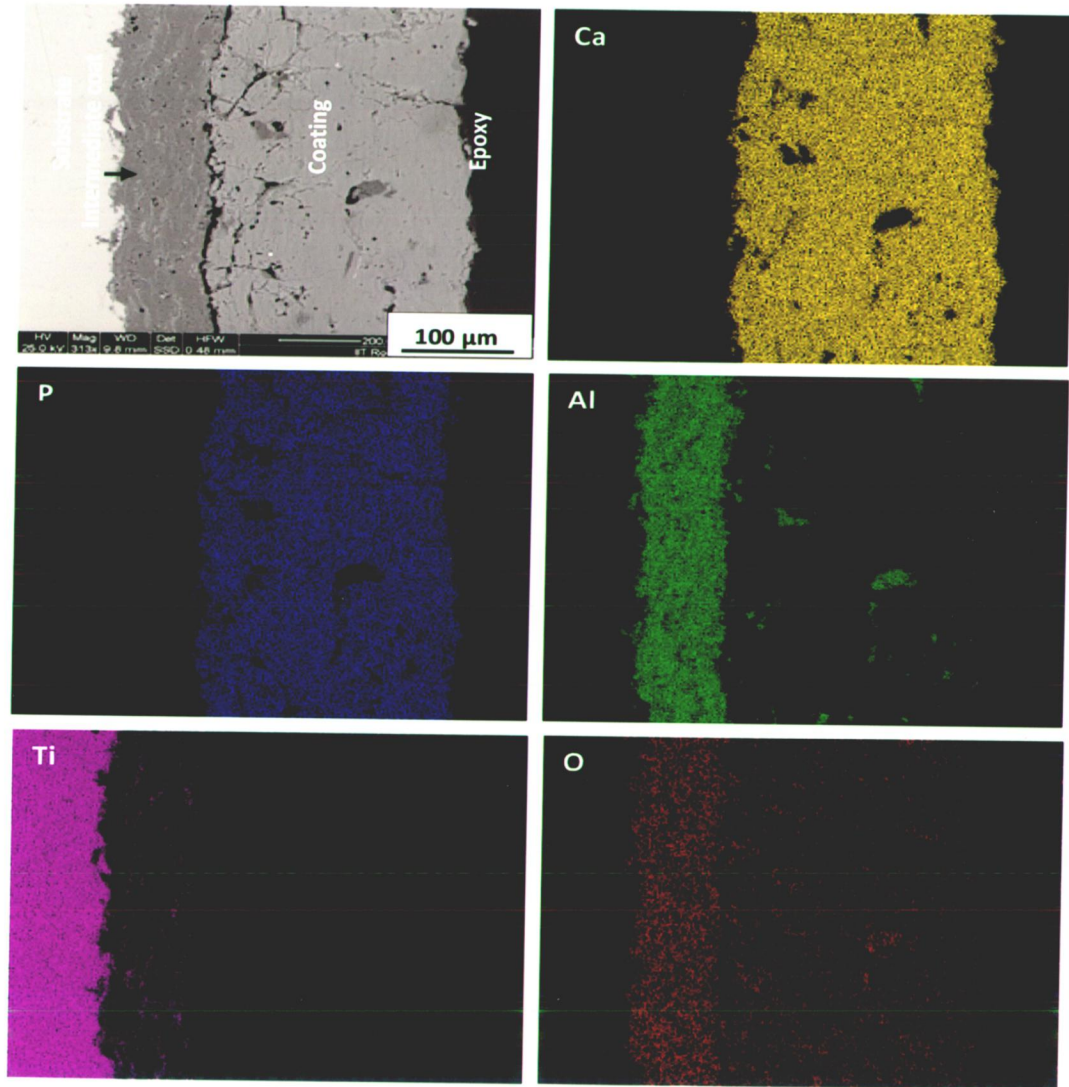


Fig. 4.41 FE-SEM image and X-ray mapping of cross-section of HA-10 wt% Al_2O_3 coated titanium with bond coat of Al_2O_3 -13 wt% TiO_2

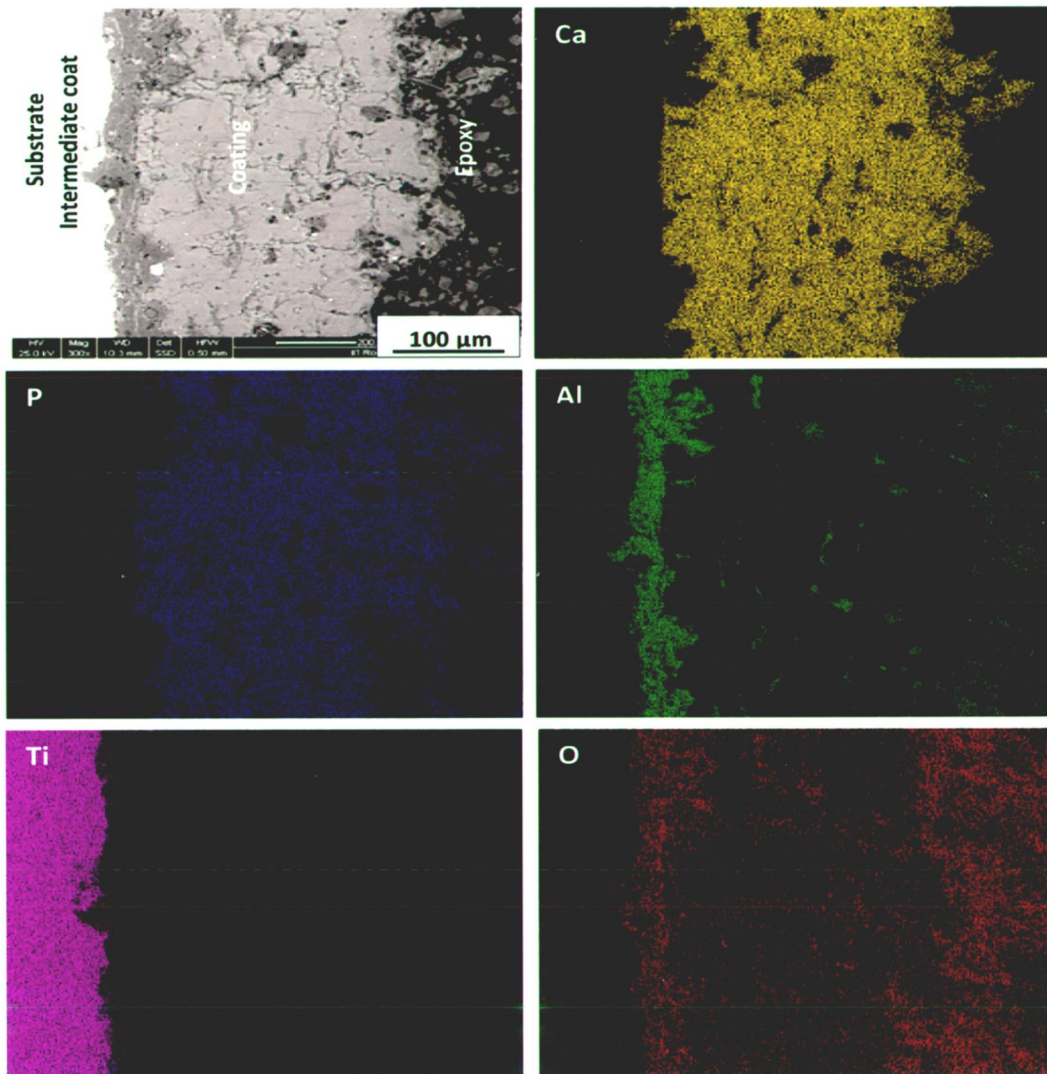


Fig. 4.42 FE-SEM image and X-ray mapping of cross-section of HA-20 wt% Al_2O_3 coated titanium with bond coat of Al_2O_3 -13 wt% TiO_2

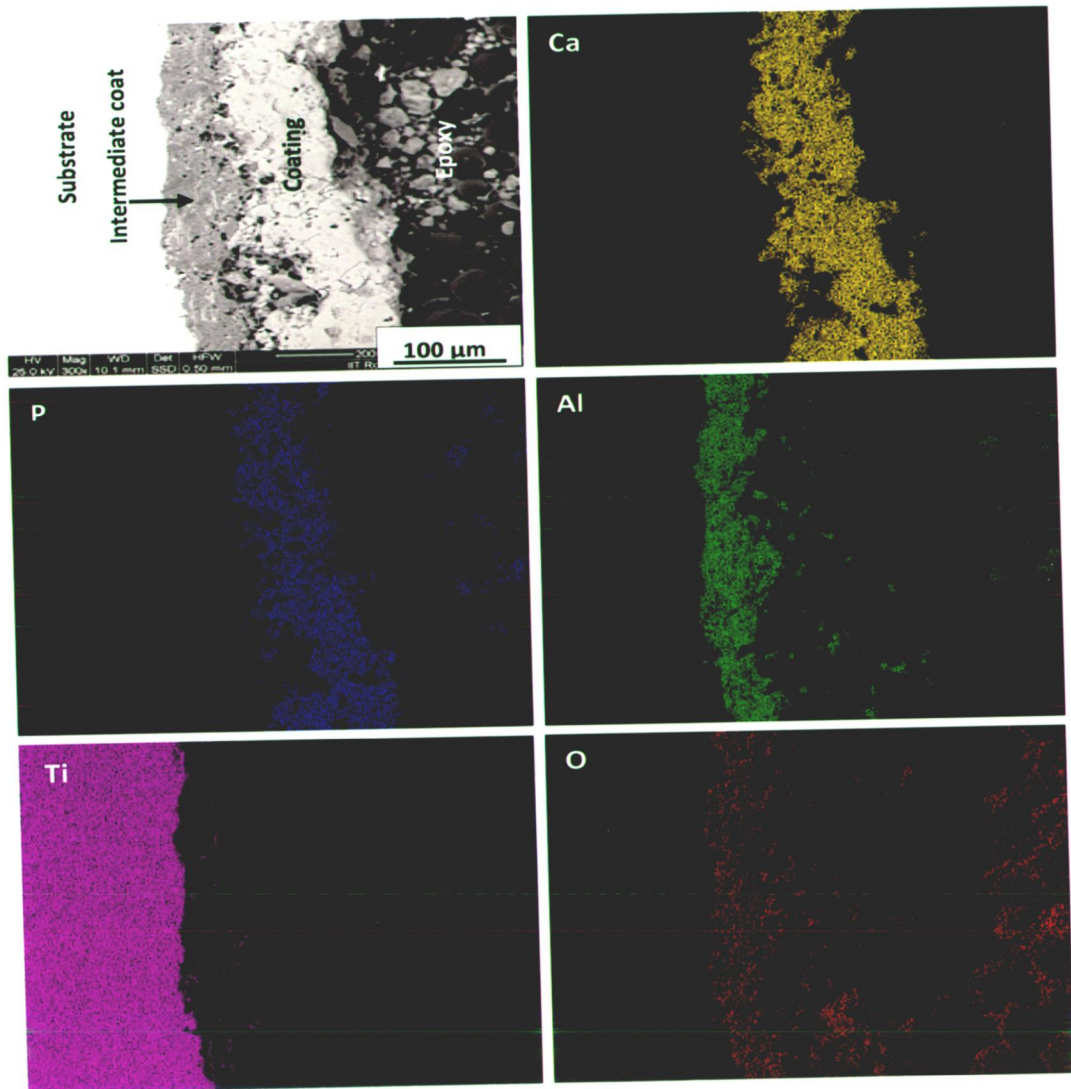


Fig. 4.43 FE-SEM image and X-ray mapping of cross-section of HA-30 wt% Al_2O_3 coated titanium with bond coat of Al_2O_3 -13 wt% TiO_2

4.2.6 X-Ray Diffraction (XRD) Analysis of Coatings

XRD diffractograms for feed stock and as-sprayed coatings on AISI 316L SS and titanium substrate with and without incorporation of bond coat are depicted in Fig. 4.44 to 4.49 on relative scale. Figure 4.44 shows the XRD patterns of different feedstock used for main coating. Diffractograms for pure HA, HA-10 wt% Al_2O_3 , HA-20 wt% Al_2O_3 and HA-30 wt% Al_2O_3 are shown in Fig. 4.44a-d respectively. Hydroxyapatite is the main phase present in the feedstock as depicted by Fig. 4.44 a-c, whereas with increasing the amount of aluminum oxide in hydroxyapatite the intensity of HA peaks decreased substantially and more intense peaks of aluminum oxide could be seen in Fig. 4.44 d.

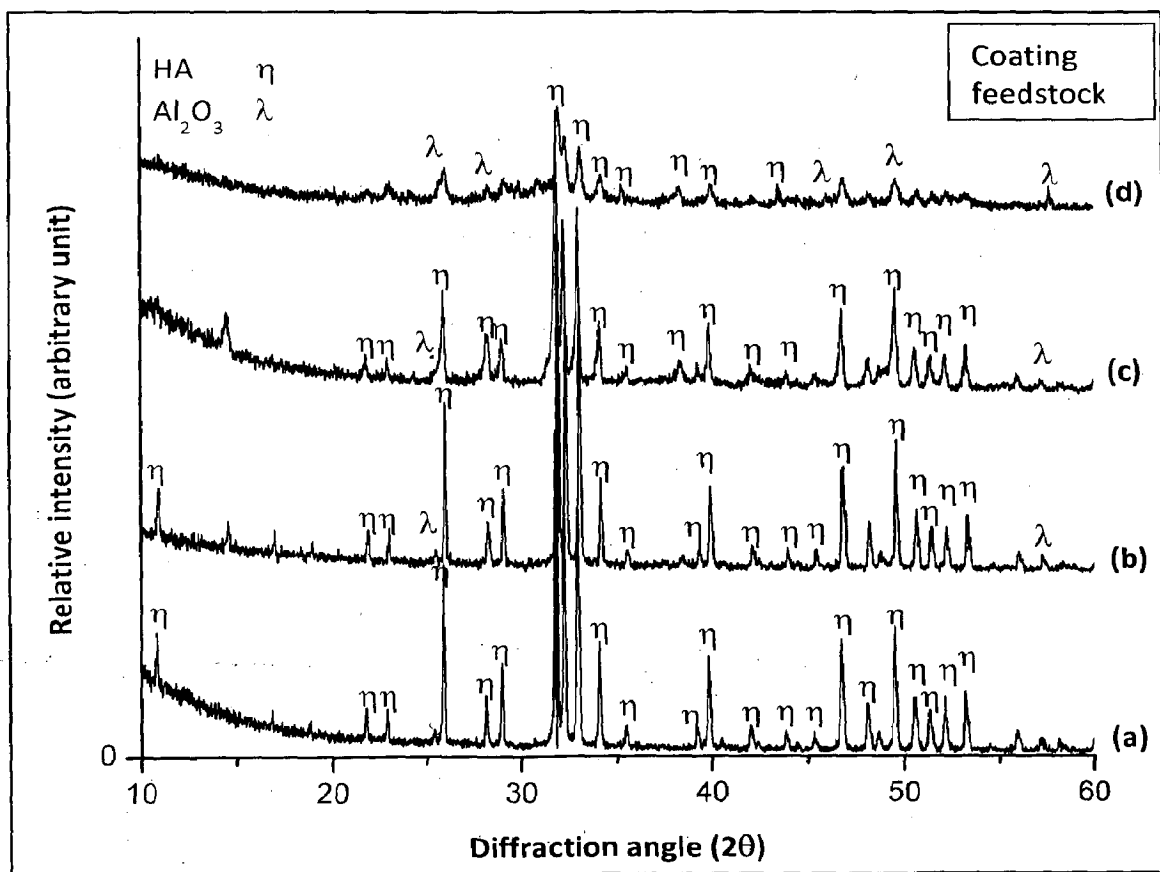


Fig. 4.44 X-ray diffraction pattern of feedstock for plasma spray coating: (a) HA; (b) HA-10 wt% Al_2O_3 ; (c) HA-20 wt% Al_2O_3 and (d) HA-30 wt% Al_2O_3

Figure 4.45 present the XRD diffractogram for powders used as reinforcement and for application of bond coat. XRD pattern for aluminum oxide is shown in Fig. 4.45a and for Al_2O_3 -13 wt% TiO_2 is presented in Fig. 4.45b.

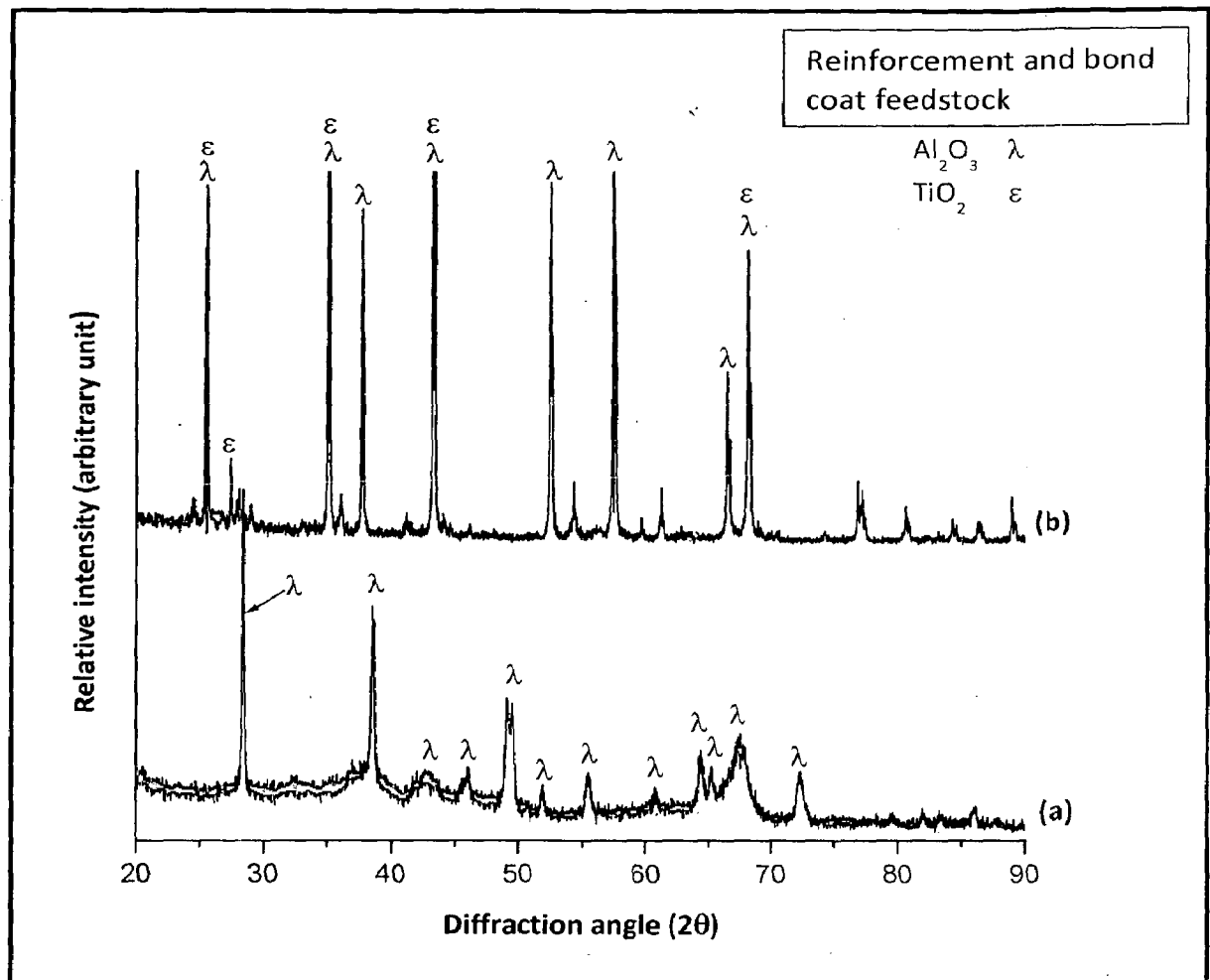


Fig. 4.45 X-ray diffraction pattern of powders for plasma spray coating: (a) Al_2O_3 (reinforcement) and (b) Al_2O_3 -13 wt% TiO_2 (bond coat)

The X-ray diffractograms for as-sprayed coatings are presented in Fig. 4.46 to 4.49. The X-ray patterns of plasma sprayed HA coatings with different composition (0-30 wt%) of aluminum oxide on AISI 316L SS and titanium are shown in Fig. 4.46 and Fig. 4.47 respectively. Hydroxyapatite is the main phase present in coatings with varying alumina contents on both the substrates. The main (most intense) hydroxyapatite peak is present between $31\text{-}32^\circ$ (2θ) in the XRD diffractograms. Intensity of all the peaks belonging to hydroxyapatite (2θ : $25^\circ\text{-}35^\circ$) initially decreases with addition of 10 wt% aluminum oxide (Fig. 4.46b and 4.47b) however, intensity of these peaks increase with further increase in reinforcing phase (Fig. 4.46 c, d and 4.47c, d). The intensity of these (HA) peaks as seen from XRD patterns is relatively more than intensity of peaks that belong to pure hydroxyapatite coatings on both substrates i.e. AISI 316L SS and titanium. Peaks of substrate elements are not present in XRD patterns.

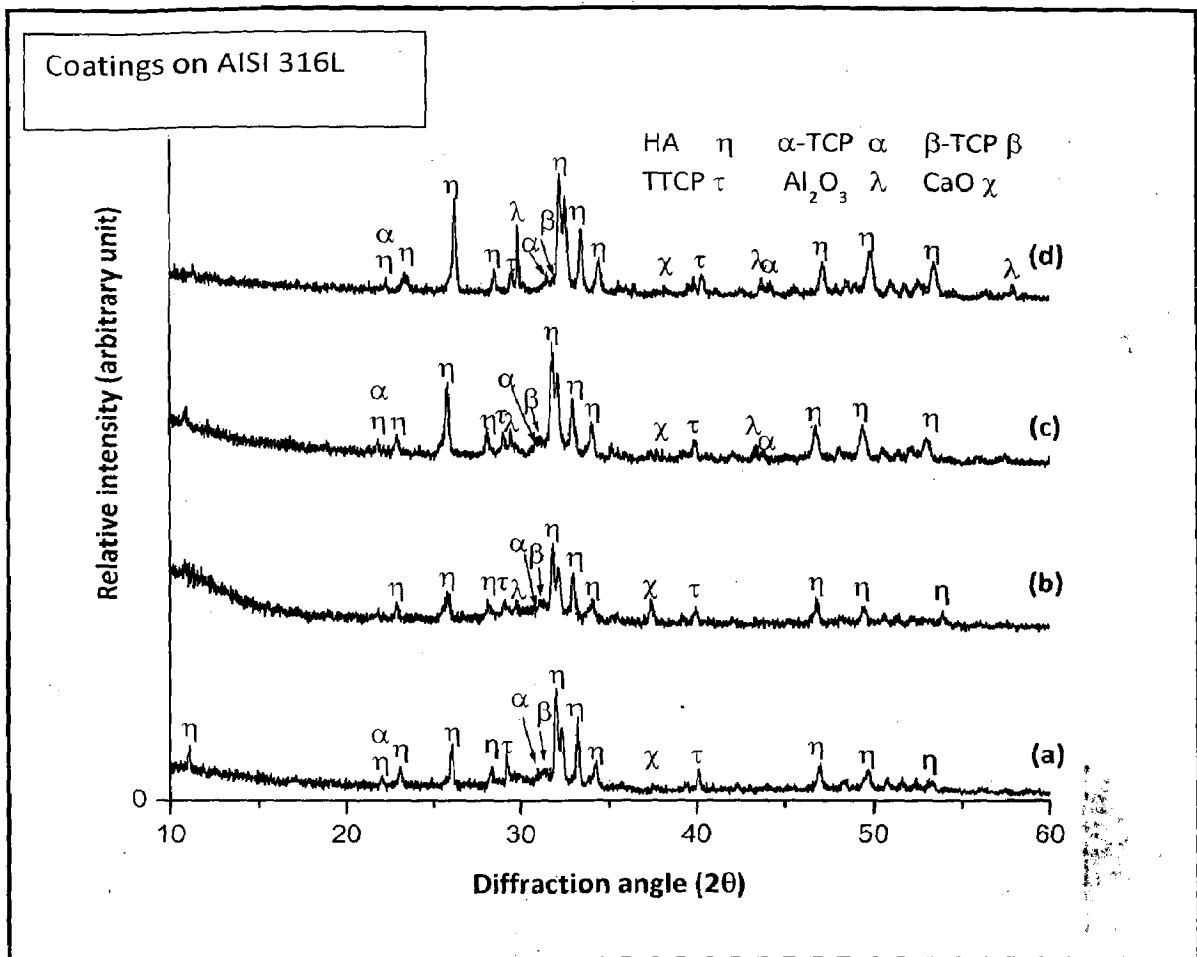


Fig. 4.46 X-ray diffraction pattern of as coated AISI 316L SS: (a) HA coating; (b) HA-10 wt% Al_2O_3 coating; (c) HA-20 wt% Al_2O_3 coating and (d) HA-30 wt% Al_2O_3 coating

Along with hydroxyapatite other phases of calcium and phosphorous are present in the X-ray pattern. These undesirable phases are generally present in plasma sprayed hydroxyapatite coatings. These phases include α -tri-calcium phosphate (α -TCP), β -tri-calcium phosphate (β -TCP), tetra-calcium phosphate (TTCP) and calcium oxide (CaO). α -TCP and β -TCP are present in the pattern at 30.8° and 31.1° (2θ) respectively. Very low intensity peaks that belong to tri-calcium phosphates can be seen in the pattern of all coating substrate combinations (Fig. 4.46 and 4.47). The most intense peak of tetra calcium phosphate is visible between 29° - 30° and 40° - 41° (2θ) in Fig. 4.46 and Fig. 4.47 which shows variation in intensity with aluminum oxide addition. The peak belonging to calcium oxide is visible at 37.3° (2θ) in all coatings. Aluminum oxide peaks are visible between 43° - 44° and 57° - 58° (2θ) in the XRD pattern of coatings (Fig. 4.46 b-d and Fig. 4.47 b-d).

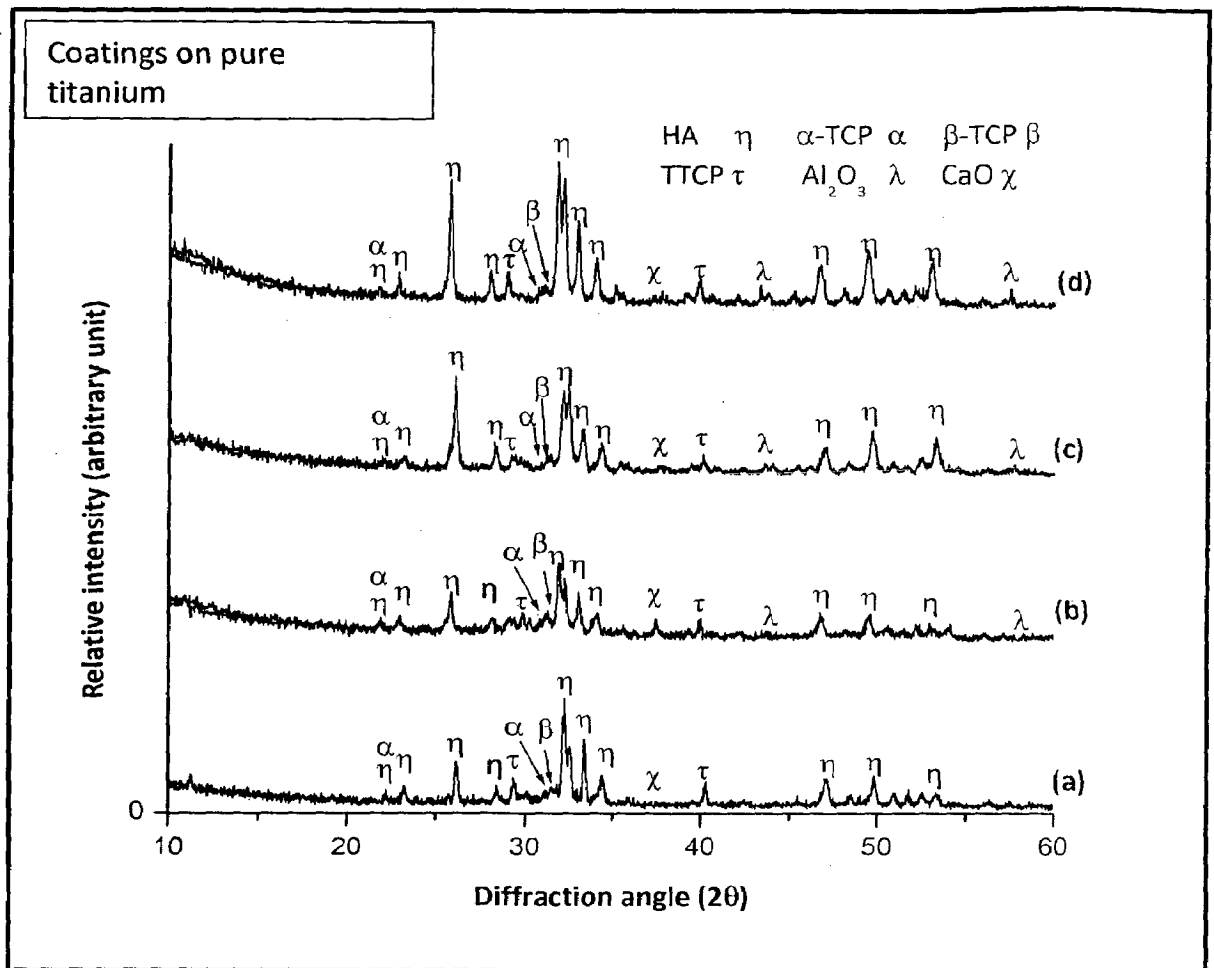


Fig. 4.47 X-ray diffraction pattern of as coated titanium: (a) HA coating; (b) HA-10 wt% Al_2O_3 coating; (c) HA-20 wt% Al_2O_3 coating and (d) HA-30 wt% Al_2O_3 coating

High intensity peaks of aluminum oxide only appear in the XRD pattern of coatings with its higher concentration (20 wt% and 30 wt%). The most intense peak of aluminum oxide is visible at 29.8° (2θ) in Fig. 4.46d.

The X-ray diffractograms of plasma sprayed HA coatings with different composition (0-30 wt%) of aluminum oxide on AISI 316L SS with titanium substrates with Al_2O_3 -13 wt% TiO_2 bond are shown in Fig. 4.48 and Fig. 4.49 respectively. The XRD pattern contains main peaks corresponding to hydroxyapatite with some peaks of other calcium phosphates. The intensity of main HA peak (31.8° 2θ) (Fig. 4.48a-c and Fig. 4.49 a-c) initially increases with addition of aluminum oxide from 0 to 20 wt% and show the similar behavior as that for the coatings without bond coat (Fig. 4.46 and Fig. 4.47) .

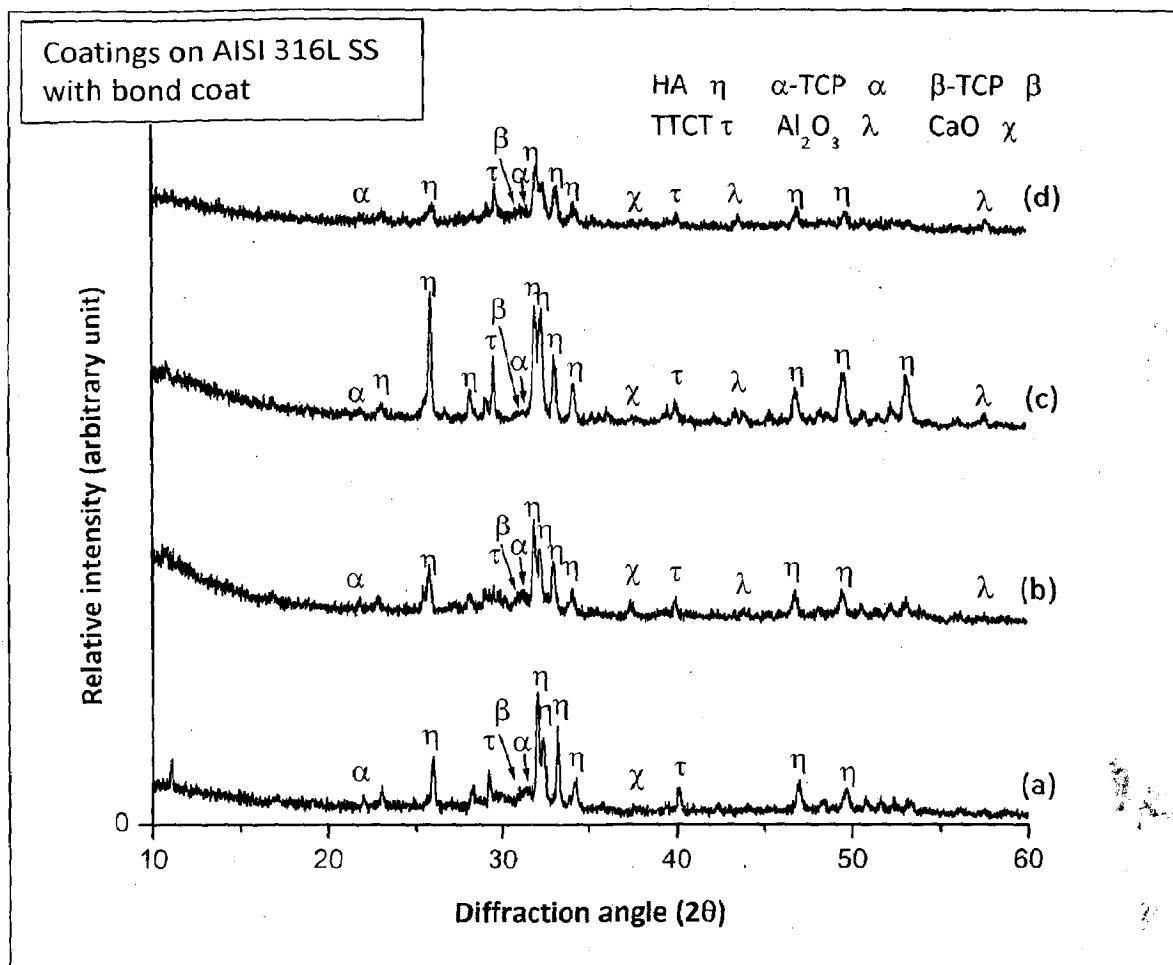


Fig. 4.48 X-ray diffraction pattern of as coated AISI 316L SS with Al_2O_3 -13 wt% TiO_2 bond coat: (a) HA coating; (b) HA-10 wt% Al_2O_3 coating; (c) HA-20 wt% Al_2O_3 coating and (d) HA-30 wt% Al_2O_3 coating

However, the intensity of this (HA) peak decreases for the coatings with 30 wt% aluminum oxide addition as shown in Fig. 4.48d and Fig. 4.49d. A similar trend is observed for the HA peak at 26° (2θ). Aluminum oxide peaks in XRD pattern are visible at 28.4° and 55.5° (2θ) in Fig. 4.48b-d and 4.49b-d. However, intensity of main aluminum oxide peak (2θ : 28.4°) decreases with increase in contents of reinforcement material to HA as shown in Fig. 4.48c, d and Fig. 4.49b-d.

4.2.7 Fourier Transform Infrared (FTIR) Spectroscopy of Coatings

FTIR is another characterization technique for analysis of feedstock and coatings since it can provide information concerning structural distortion and de-hydroxylation,

which can not be obtained readily from XRD method. The FTIR plots for feedstock and plasma sprayed coatings are presented in Fig. 4.50 to Fig. 4.52.

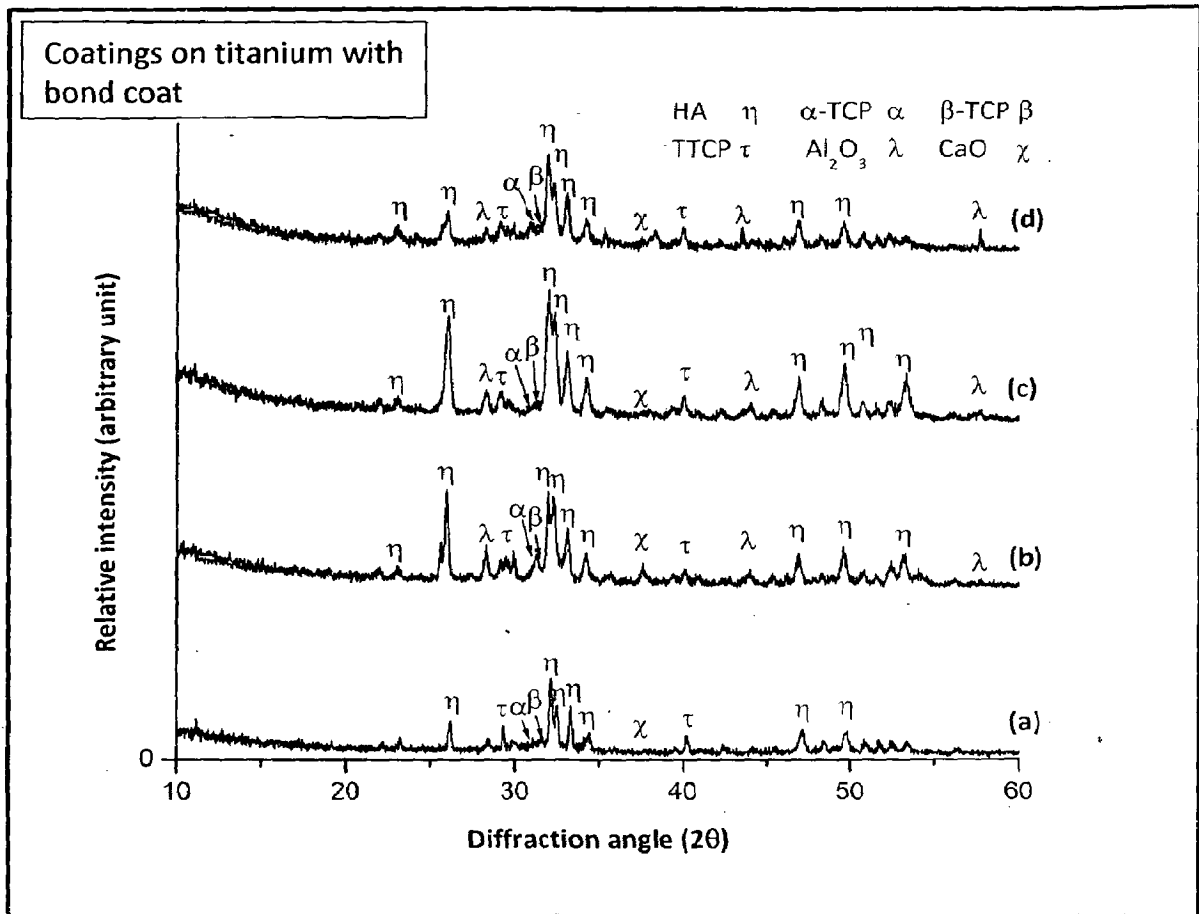


Fig. 4.49 X-ray diffraction pattern of as coated titanium with Al_2O_3 -13 wt% TiO_2 bond coat: (a) HA coating; (b) HA-10 wt% Al_2O_3 coating; (c) HA-20 wt% Al_2O_3 coating and (d) HA-30 wt% Al_2O_3 coating

The FTIR plot for feedstock of plasma spray coatings is shown in Fig. 4.50. The sharp peaks corresponding to hydroxyl group (OH^-) are present around 3564.5 cm^{-1} and 635.7 cm^{-1} in spectra of pure HA powder (Fig. 4.50a) whereas for reinforced powder it is observed around 3578.8 cm^{-1} and 635.7 cm^{-1} as shown in Fig. 4.50b-d. Moreover, it can be seen from the FTIR spectra that intensity of hydroxyl peaks decrease with increase in alumina content to HA. Phosphate group (PO_4^{3-}) can be seen around 1095.7 cm^{-1} , 1056.7 cm^{-1} , 953.2 cm^{-1} , 603.5 cm^{-1} and 571.3 cm^{-1} in FTIR spectrum of pure HA powder whereas, it is present around 1095.7 cm^{-1} , 1051 cm^{-1} , 953.2 cm^{-1} , 603.2 cm^{-1} and 569.7 cm^{-1} for HA-10 wt% Al_2O_3 powder (Fig 4.50b). In FTIR spectrum of HA-20 wt% Al_2O_3 feed stock (Fig. 4.50c), PO_4^{3-} is present

around 1100 cm^{-1} , 1051.7 cm^{-1} , 953.2 cm^{-1} , 603 cm^{-1} , and 559.2 cm^{-1} while in spectrum of HA-30 wt% Al_2O_3 , PO_4^{3-} is observed at 1095.7 cm^{-1} , 1051.7 cm^{-1} , 953.2 cm^{-1} , 603.2 cm^{-1} and 559.2 cm^{-1} . The absorbed CO_2 or CO_3^{2-} group can be seen around 2350 cm^{-1} in HA and HA-10 wt% Al_2O_3 feedstock in Fig. 4.50a and b.

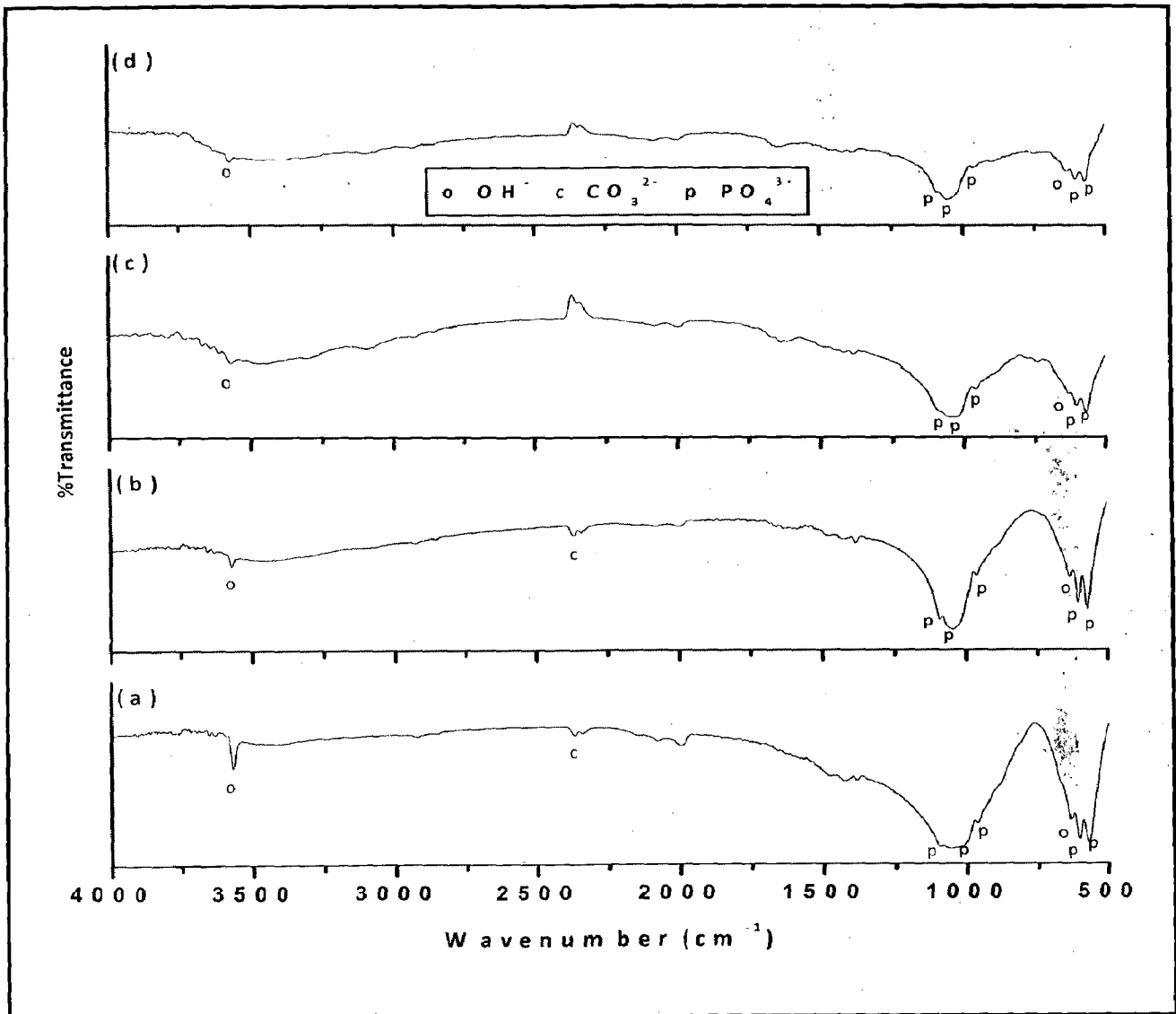


Fig. 4.50 FTIR spectra of feedstock for plasma spray coatings: (a) HA; (b) HA-10 wt% Al_2O_3 ; (c) HA-20 wt% Al_2O_3 ; (d) HA-30 wt% Al_2O_3

The FTIR spectra for plasma sprayed coatings are shown in Fig 4.51. Hydroxyapatite has a tendency to absorb CO_2 from atmosphere during plasma spraying. FTIR spectrum of all coatings show the presence of carbonate (CO_3^{2-}) group. CO_3^{2-} is present in a range of 2350 cm^{-1} to 2500 cm^{-1} in pure HA, HA-10 wt% Al_2O_3 , HA-20 wt% Al_2O_3 and HA-30 wt% Al_2O_3 coating. Moreover pure HA coating has lesser affinity for carbon di-oxide absorption as low

intensity broad peak can be seen in FTIR spectra of pure HA coatings (Fig. 4.51a). The higher intensity of carbonate group in composite coating might be due to higher affinity of alumina to absorb CO_2 on its surface. Hydroxyl (OH) group can be seen in a range of 3550 cm^{-1} to 3750 cm^{-1} and 635 cm^{-1} to 660 cm^{-1} in spectrum of pure HA; HA-10 wt% Al_2O_3 ; HA-20 wt% Al_2O_3 ; HA-30 wt% Al_2O_3 coatings as shown in Fig 4.51a-d. FTIR spectra of coatings show the presence of phosphate group (PO_4^{3-}) at 567 cm^{-1} , 607 cm^{-1} in all type of coatings (Fig 4.51).

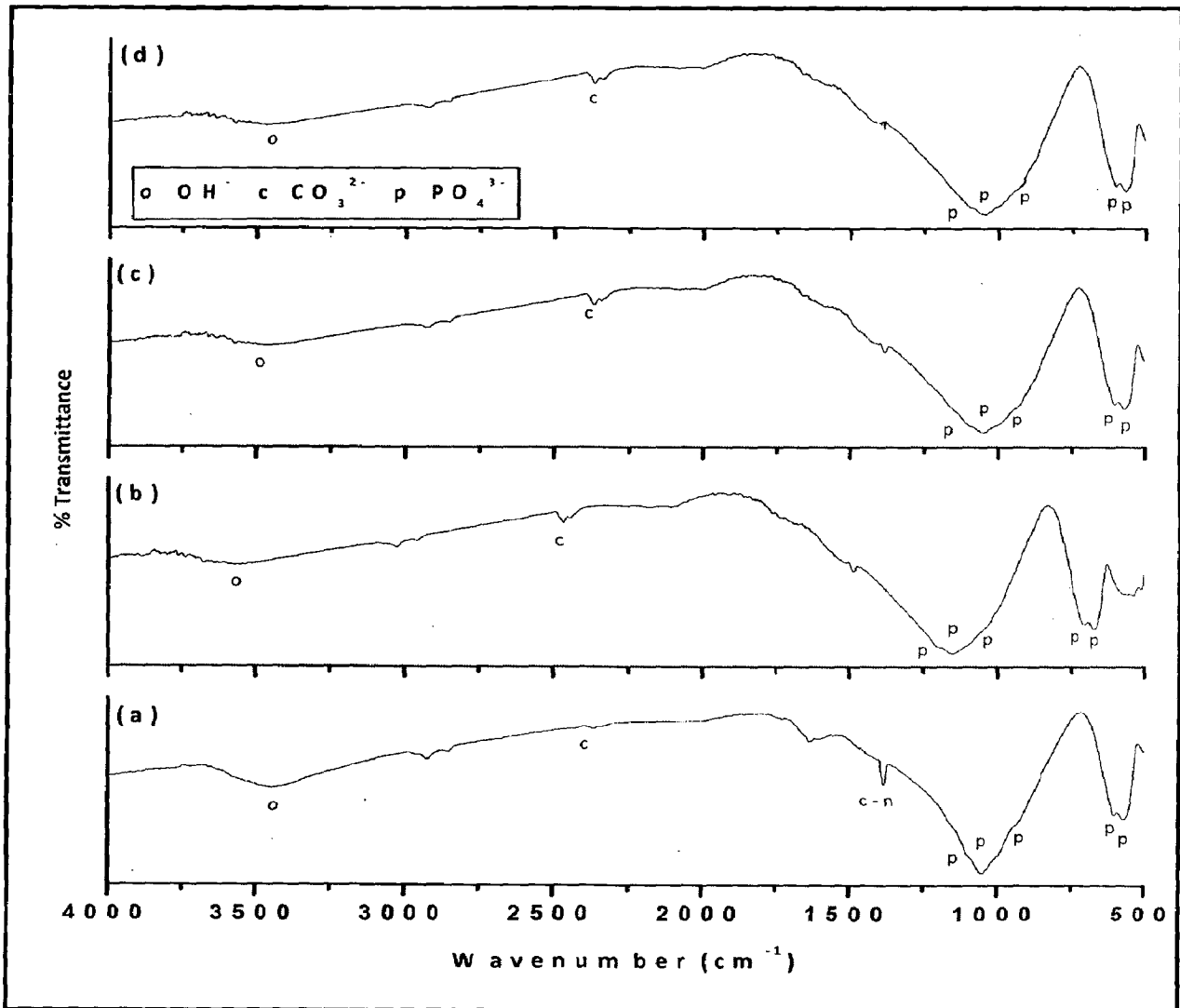


Fig. 4.51 FTIR spectra of plasma spray coatings: (a) HA; (b) HA-10 wt% Al_2O_3 ; (c) HA-20 wt% Al_2O_3 ; (c) HA-30 wt% Al_2O_3

PO_4^{3-} is also present in a range of 1095 cm^{-1} to 920 cm^{-1} for pure HA, HA-10 wt% Al_2O_3 , HA-20 wt% Al_2O_3 and HA-30 wt% Al_2O_3 coatings. The intensity of phosphate group peaks in coatings is comparatively lower than their intensity in feedstock.

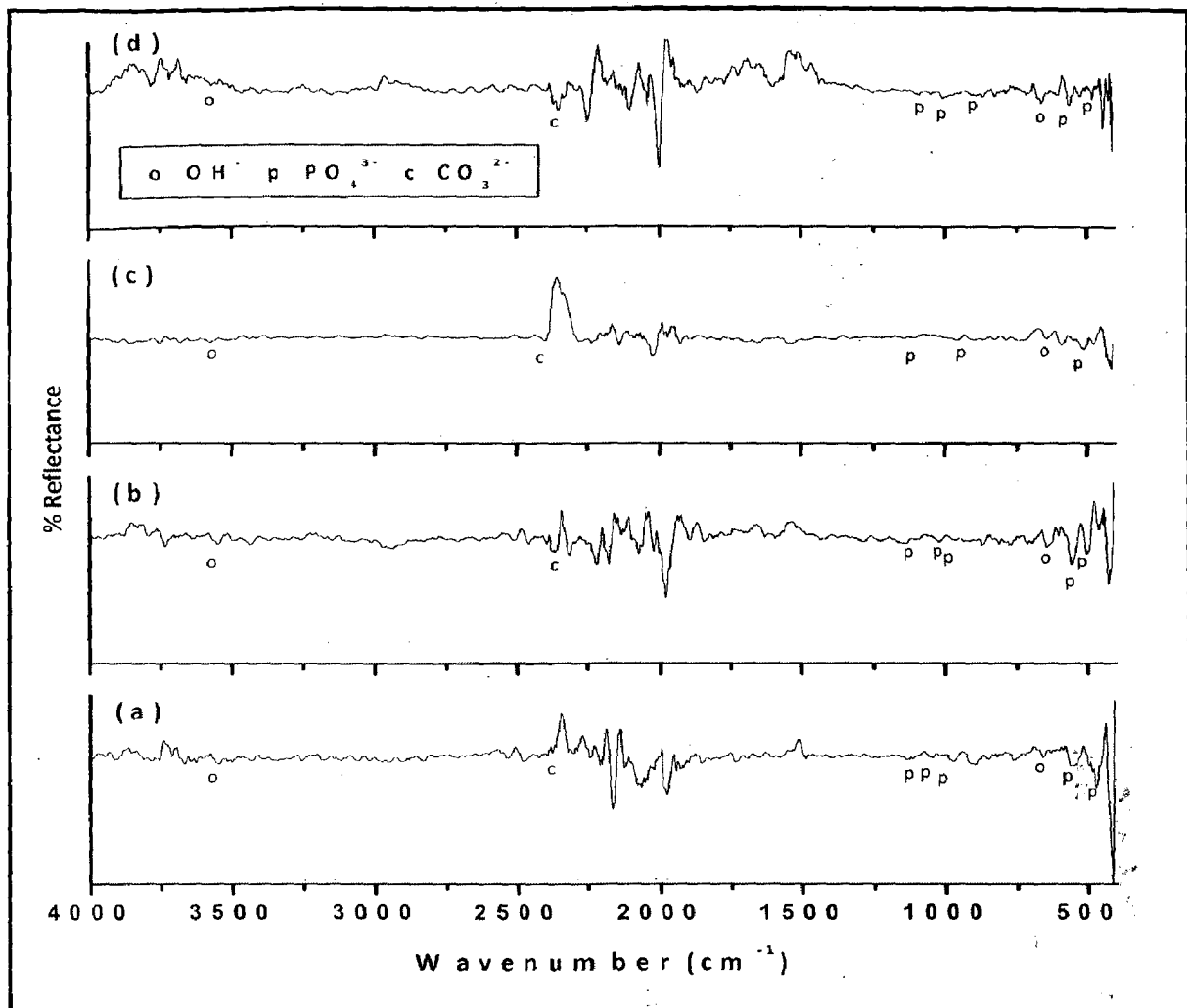


Fig. 4.52 FTIR spectra of plasma spray coatings with Al_2O_3 -13 wt% TiO_2 bond coat: (a) HA; (b) HA-10 wt% Al_2O_3 ; (c) HA-20 wt% Al_2O_3 ; (d) HA-30 wt% Al_2O_3

Figure 4.52 presents FTIR spectra of plasma sprayed coatings with incorporation of Al_2O_3 -13 wt% TiO_2 bond coat. Spectra of these coatings show similar pattern as that of coatings without bond coat (Fig. 4.51). Hydroxyl group can be seen at 3356 cm^{-1} and 655 cm^{-1} ; 3556 cm^{-1} and 642 cm^{-1} ; 3568 cm^{-1} and 635 cm^{-1} ; 3568 cm^{-1} and 660 cm^{-1} in spectrum of pure HA; HA-10 wt% Al_2O_3 ; HA-20 wt% Al_2O_3 ; HA-30 wt% Al_2O_3 coatings with bond coat respectively as shown in Fig 4.52a-d. The presence of CO_3^{2-} group can be observed at 2394 cm^{-1} and 2396 cm^{-1} for HA-20 wt% Al_2O_3 and pure HA coatings with bond coat respectively while, in spectra of HA-10 wt% Al_2O_3 and HA-30 wt% Al_2O_3 with bond coat it is seen at 2364 cm^{-1} . In FTIR spectra other peaks represent phosphate group. The intensity of all the peaks is considerably lower in this case. This might be due to the fact that the FTIR for coatings with bond coat was conducted in reflectance mode.

4.2.8 Thermo-gravimetric Analysis/Differential Thermal Analysis (TGA/DTA)

TGA/DTA analysis of pure HA, HA-10 wt% Al₂O₃, HA-20 wt% Al₂O₃, HA-30 wt% Al₂O₃, pure Al₂O₃ are shown in Fig. 4.53 to Fig. 4.57. Total weight loss for pure HA powder is 2.6% as shown by TG curve in Fig. 4.53. The first stage weight loss (0.9%) in pure HA powder between 29°C-600°C correspond to evaporation of absorbed water and de-hydroxylation. A second stage weight loss (0.1%) accompanied by broad endothermic peak of DTA appeared from 800°C to 1000°C correspond to de-hydroxylation and decomposition of HA. In temperature range of 800°C-1000°C HA de-hydroxylate to partially de-hydroxylated (oxy-hydroxyapatite: OHA) or completely de-hydroxylated (oxy-apatite: OA).

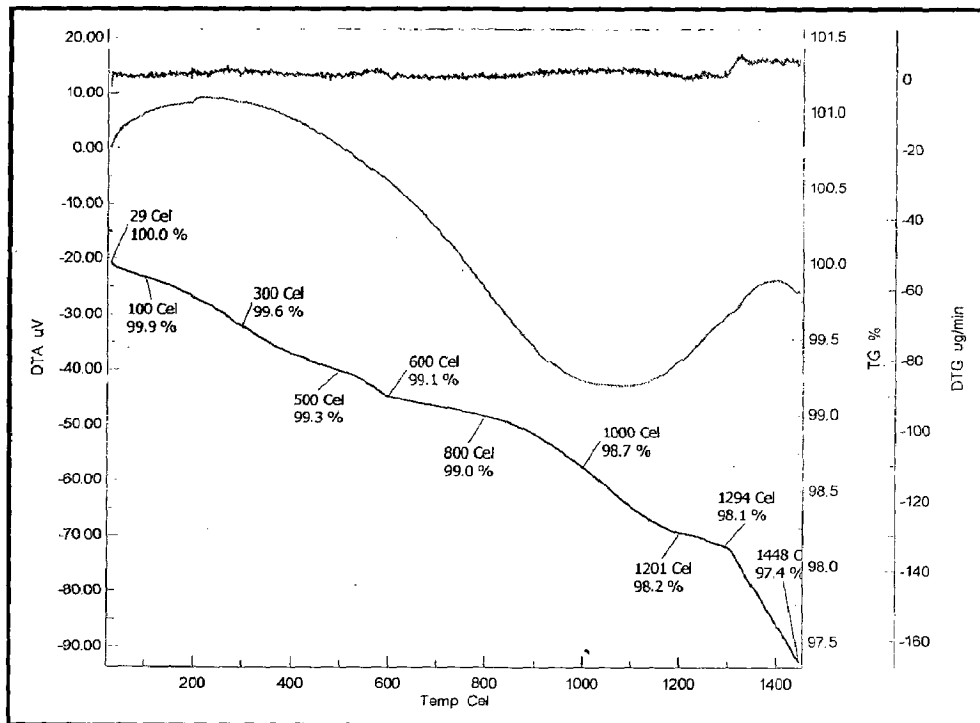


Fig. 4.53 DTA/TGA plot for hydroxyapatite powder

Decomposition of HA to β -tri-calcium phosphate (β -TCP) and tetra-calcium phosphate starts at 1050°C. β -tri-calcium phosphate is stable up to 1120°C and convert to α -tri-calcium phosphate (α -TCP) between 1120°C-1490°C. Third stage weight loss (1.3%) as shown by TGA curve belongs to formation of α -TCP.

In TGA curves of reinforced powders total weight loss increases with increase in Al₂O₃ content. This might be due the higher affinity of Al₂O₃ to absorb water on its surface.

Total weight loss of 3.8%, 5.3% and 7.1% is measured from TGA curves of HA-10 wt% Al₂O₃, HA-20 wt% Al₂O₃ and HA-30 wt% Al₂O₃ respectively as shown in Fig. 4.54 to Fig. 4.56. Initial weight loss of 1.9%, 4.2% and 5.6% between 30°C-600°C, 30°C-625°C and 30°C-600°C correspond to evaporation of absorbed water and de-hydroxylation of hydroxyapatite as shown TGA curve of HA-10 wt% Al₂O₃, HA-20 wt% Al₂O₃ and HA-30 wt% Al₂O₃ respectively (Fig. 4.54-4.56).

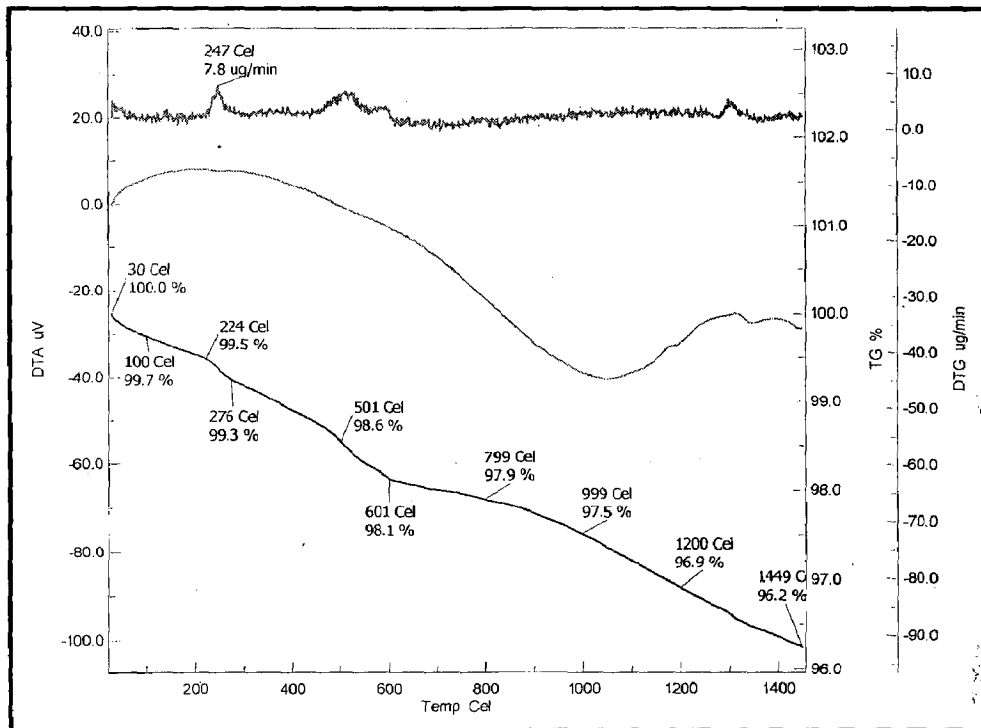


Fig. 4.54 DTA/TGA plot for HA-10 wt% Al₂O₃ powder

Second stage weight loss in case of HA-10 wt% Al₂O₃ (Fig. 4.54) accompanied by broad DTA peak between 601°C-1450°C correspond to de-hydroxylation and decomposition of HA. Weight loss of 0.6% is due to de-hydroxylation of HA in temperature range of 601°C-999°C whereas, 1.3% due to decomposition of HA into other calcium phosphates. Endothermic peaks corresponding to 1350°C show conversion of β-TCP to α-TCP as β-TCP is stable up to 1120°C only. In DTA analysis of HA-20 wt% Al₂O₃ powder (Fig. 4.55) 1.1% weight loss between 625°C-1450°C has been recorded. Two endothermic peaks at 1200°C and 1350°C correspond to conversion of β-TCP to α-TCP.

Figure 4.56 show DTA/TGA analysis of HA-30 wt% Al₂O₃ powder. TGA curve show weight loss of 1.5% between 600°C-1450°C and DTA curve show endothermic peaks at 1220°C and 1350°C for conversion of β-TCP to α-TCP.

DTA/TGA analysis of Al₂O₃ is shown in Fig. 4.57. TGA curve (Fig. 4.57) show 5.4% weight loss between 29°C-236°C which is due to removal of absorbed water. In temperature range of 236°C-273°C and 451°C-579°C weight loss of 0.9% and 4.1% is accompanied by endothermic peak at 263°C and 529°C. Weight loss of 1.4% between 799°C-1100°C is accompanied by broad endothermic peak. The maximum weight loss in temperature range of 30°C to 1500°C is recorded for alumina, which might be due to greater affinity of alumina to absorb water.

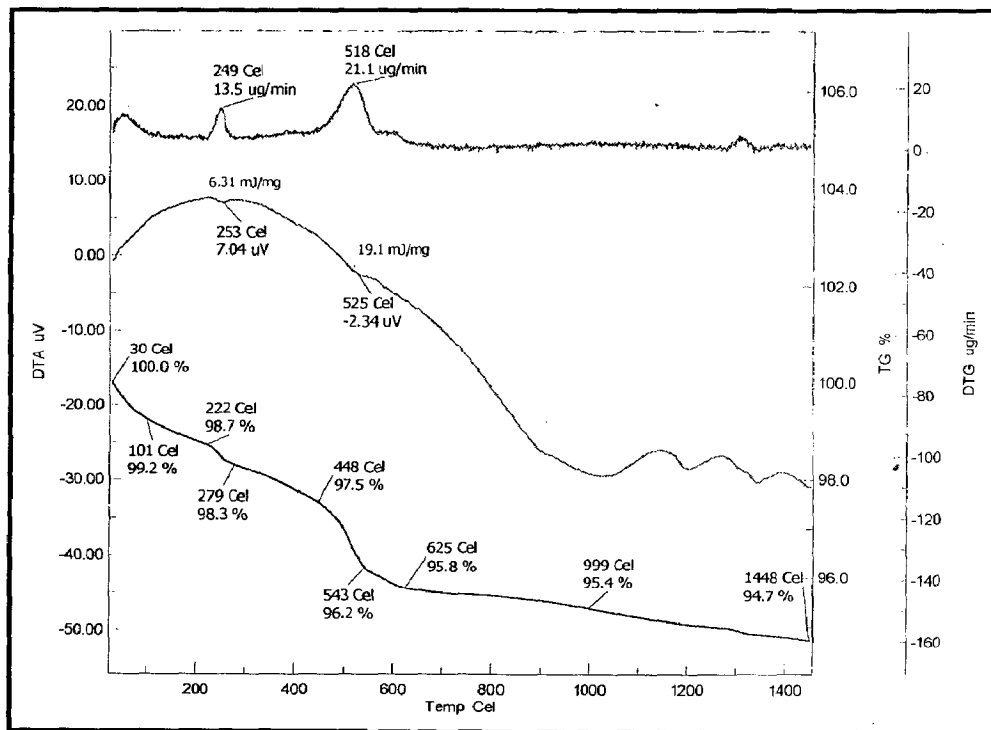


Fig. 4.55 DTA/TGA plot for HA-20 wt% Al₂O₃ powder

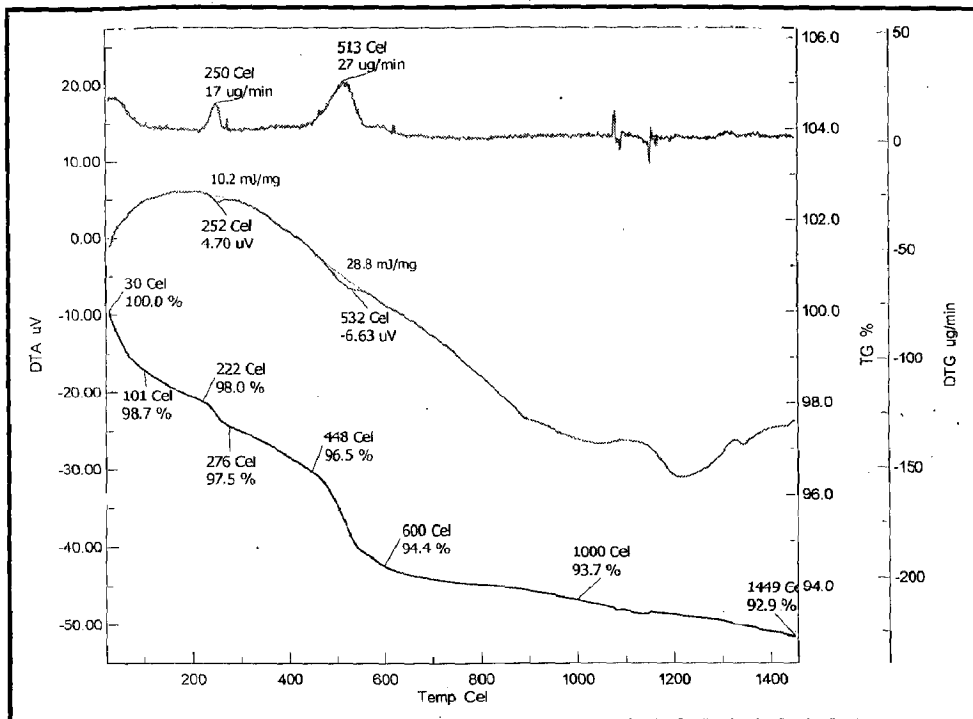


Fig. 4.56 DTA/TGA plot for HA-30 wt% Al₂O₃ powder

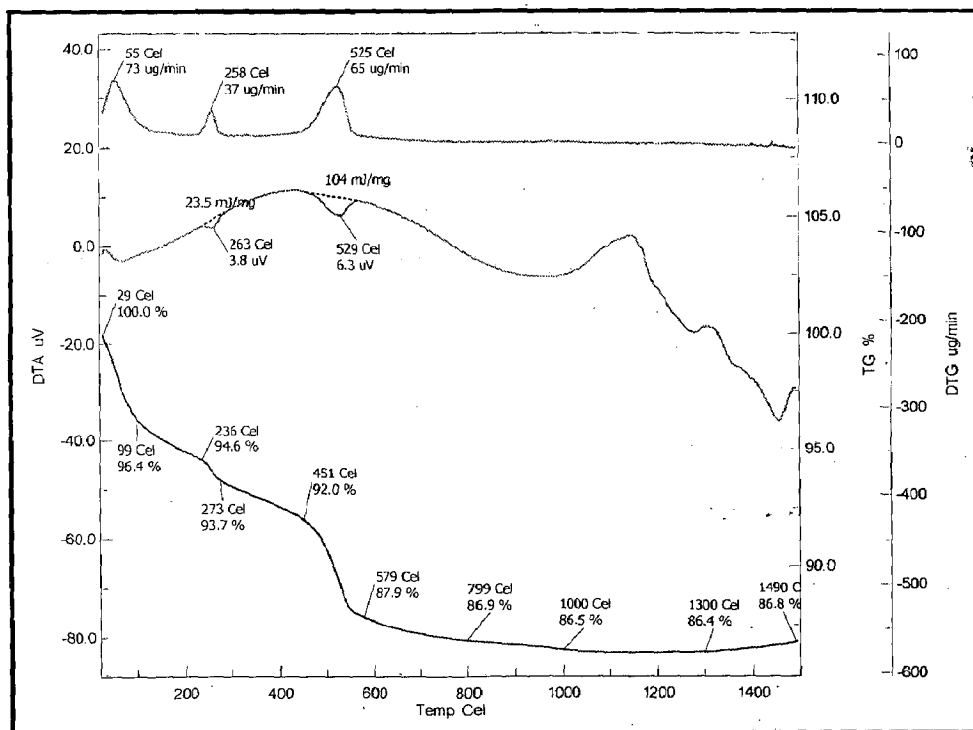


Fig. 4.57 DTA/TGA plot for Al₂O₃ powder

4.3 DISCUSSION

Pure HA and reinforced HA coatings show characteristic plasma spray splat surface morphology with clearly distinct splats and some un-melted, partially melted, re-solidified particles on the completely molten splats. The characteristic plasma splat surface morphology has been reported by Singh et al., (2007) for plasma sprayed metallic coatings. Molten splats have pancake structure with some cracks visible at higher magnification (1000X). Large variation in size of splat is visible from FE-SEM images of coatings. Porosity of as-sprayed coatings and polished cross-sections is less than 4% and 7.5% respectively, however surface roughness increased slightly with increase in reinforcement content. Porosity influences the physical and mechanical characteristics of hydroxyapatite coatings and also affects body's reaction with mineral component of bone (Gauthier et al., 1998). Gledhill et al., (1999) reported that porous structure allows vascular in-growth, which help in restricting migration of ions from implant; they further reported that a high porosity will affect mechanical properties of the coating. They suggested that a balance in porosity should be established where strength of the material is not compromised.

All type of coatings were found to be rough and surface roughness (Ra) slightly increased with increase in Al₂O₃ content. This may be due to slightly larger particle size and higher melting temperature of Al₂O₃ as compared to HA. Surface roughness plays an important role for cell in-growth. It has been reported that morphological roughness is beneficial for biocompatibility as it promotes the protein on the surface favoring cell attachment (Li et al., 2002B and Balani et al., 2007B).

SEM micrographs with EDAX point analysis reveal surface morphology of plasma sprayed coatings on AISI 316L and titanium as shown in Fig. 4.4 and Fig. 4.5 respectively. The presence of Ca and P in pure HA coatings (Fig. 4.4a and 4.5a) and Ca, P and Al in reinforced HA coatings (Fig. 4.4 b-d and Fig. 4.5 b-d) is revealed by surface EDAX analysis. Negligible amount of substrate elements are revealed from EDAX surface analysis for all coating-substrate combinations. Weight % of substrate elements is less than 1% (Fig. 4.4 – 4.5). Cross-sectional morphology with EDAX point analysis of coatings is shown in Fig. 4.6 to Fig. 4.9. Micrographs reveal grinding damage, pores and cracks, but a network of cracks which start at substrate-coating interface and develop in coating as characterized by plasma sprayed HA coatings is absent. No substrate elements are present in EDAX point analysis of

cross-section. X-ray mapping of surfaces of plasma sprayed coatings without bond coat on AISI 316L (Fig. 4.10 – 4.13) and on titanium (Fig. 4.14 – 4.17) show diminutive presence of substrate elements for both substrates whereas, X-ray mapping of coating surfaces with bond coat on AISI 316L (Fig. 4.18 – 4.21) and on titanium (Fig. 4.22 – 4.25) show traces of substrate elements which suggest that bond coat helps in restricting the substrate elements migration to coating. Reduction in migration/diffusion of substrate elements to coating by incorporation of bond coat has been reported by Üstel, (1995), Çelik et al., (1997) and Oktar, (1999).

In X-ray mapping of plasma sprayed pure HA and reinforced HA coatings on AISI 316L along polished cross-section (Fig. 4.26 – 4.29), diffusion of substrate elements in coatings is seen whereas, in case of coatings on titanium substrate (Fig. 4.30 – 4.33) diffusion of substrate elements is not seen with exception of HA – 30 wt% Al_2O_3 coating (Fig. 4.33). The diffusion of substrate elements in coatings decreased substantially with incorporation of Al_2O_3 – 13 wt% TiO_2 bond coat for coatings on AISI 316L substrates (Fig. 4.34 – 4.37). X-ray mapping of coatings with bond coat on titanium (Fig. 4.38 – 4.41) substrate do not show any substrate element in the coating.

It can be seen from XRD pattern that HA feedstock is 100% crystalline and no amorphous phase is present (Fig. 4.42). XRD analysis of Al_2O_3 and Al_2O_3 -13 wt% TiO_2 is shown in Fig 4.43a and Fig. 4.43b. Amorphous calcium phosphate and CaO are present in plasma sprayed coatings as shown in Fig. 4.44 to Fig. 4.47. According to phase diagram of CaO- P_2O_5 - H_2O system, decomposition of HA starts at 1050°C and between 1050°C and 1400°C HA decomposes to β -TCP and TTCP. β -TCP is stable up to 1120°C and convert to α -TCP between 1120°C and 1490°C. (CaO- P_2O_5 - H_2O phase diagram and reactions leading to formation of these phases are presented in Chapter 2). Sun et al. (2006) reported that at 1550°C HA decompose to TCP, TTCP and water. Presence of similar amorphous phases has been reported by many researchers (Morks and Kobayashi, 2007A; Morks et al. 2008; Que et al., 2008; Sun et al., 2006; Lu et al., 2003A and Mondragon-Cortez and Varagas-Gutiérrez, 2004). These amorphous phases are undesirable as they readily dissolve in body fluids. The intensity of HA peaks in XRD spectra of composite coatings without bond coat is found to decrease with 10 wt% Al_2O_3 , whereas it increase with 20 wt% and 30 wt% alumina addition to composite coating. A different XRD pattern has been seen for composite coatings with

bond coat in which high intensity HA peaks were seen for HA-20 wt% Al₂O₃ composite coatings.

FTIR spectra for powder and coatings (Fig. 4.48 – Fig.450) show that the feedstock does contain carbonate group whereas, plasma sprayed coatings with and without incorporation of bond coat show the presence of carbonate group in range of 2296 cm⁻¹ to 2396 cm⁻¹ respectively (Fig. 4.49 and Fig. 4.50). The presence of carbonate group might be due to absorption of CO₂ from environment during spraying. The presence of carbonate group in plasma sprayed HA coatings have been reported by many investigators (Li et al., (2002B), Dey et al., (2009A and 2009B), Mahabole et al., (2005) and Morales et al., (2001)).

4.4 CONCLUSIONS

The plasma sprayed pure HA and HA-Al₂O₃ composite coatings on AISI 316L SS and pure titanium have been characterized for surface and cross-sectional morphology, elemental distribution, effect of incorporation of bond coat, porosity and surface roughness. The following conclusions have been drawn:

1. The surface morphology of coatings showed characteristic plasma sprayed coating morphology which includes: clear splat boundaries, un-melted powder particles and cores, micro-cracks and voids.
2. The cross-sectional morphology of coatings suggest that coatings are continuous, have pores and micro-cracks, however typical crack network as characterized by plasma sprayed HA coatings is absent.
3. The porosity of coatings slightly increased with increase in alumina content of composite coating. Porosity allows vascular in-growth, which reduce migration of metallic ions from substrate. Moreover, porosity measured on polished cross-sections was almost double than that measured on as-sprayed coating surfaces, which can be attributed to damage of surface caused during cutting, grinding and polishing for cross-section preparation. The surface roughness of coating also increased with increase in alumina content to HA, which is helpful for biocompatibility of implants.

4. It was found that diffusion or migration of substrate elements to the coatings was substantially reduced by incorporation of bond coat layer between substrate and top coat. Therefore, bond coat are found to restrict the diffusion of substrate elements to coating.
5. The as-procured powder was 100% pure and crystalline, however plasma sprayed coatings contained a considerable amount of amorphous phases of calcium and phosphorous and CaO. De-hydroxylation (removal of hydroxyl group) and carbonation (absorption of carbon di-oxide) of hydroxyapatite took place during plasma spraying. To regain the crystallinity and hydroxyl ion post coating heat treatments are required on plasma sprayed HA-Al₂O₃ composite coatings.

MECHANICAL PROPERTIES OF COATINGS

This chapter deals with the results and discussion of mechanical properties of plasma sprayed pure HA, HA-10 wt% Al₂O₃, HA-20 wt% Al₂O₃ and HA-30 wt% Al₂O₃ coatings. These include determination of wear resistance, tensile bond strength and microhardness of coatings.

5.1 INTRODUCTION

In the present chapter mechanical properties of coatings have been described. It includes the results related to resistance to wear, microhardness and tensile bond strength of coatings. The wear resistance of coatings was evaluated using 'flat-on-disc' wear tester, microhardness by nano-indentation technique and bonding strength using ASTM C 633-79 pull off test. The wear tests of coatings were conducted against 400 grit SiC abrasive and between similar coatings. The details of 'flat-on-disc' wear tester are already furnished in Chapter 3 of present study. The worn out surfaces after wear tests and bond strength tests were characterized using field emission scanning electron microscopy (FE-SEM). The worn out surfaces after wear tests were also analyzed using atomic force microscopy (AFM).

5.2 RESULTS

5.2.1 Wear Resistance of Coatings

Wear resistance of coatings against 400 grit SiC abrasive in form of cumulative weight loss versus number of cycles is shown in Fig. 5.1. It can be seen from the plot that wear resistance of coatings against 400 grit SiC abrasive increase with increase in Al₂O₃ (reinforcement) content of HA composite coatings i.e. weight loss of coating per cycle decrease with increase in Al₂O₃ content to HA. Further, it can be seen from plot that weight loss up to 80 cycles is comparatively less than the weight loss in next 120 cycles in all type of coatings. The maximum cumulative weight loss of 47.9 mg/cm² was recorded for pure HA coating, whereas the

minimum cumulative weight loss of 15.8 mg/cm² was measured for HA-30 wt% Al₂O₃ coating after a run of 200 cycles. Wear resistance of coatings against similar coatings in form of cumulative weight loss versus number of cycles is shown in Fig. 5.2. In this case the wear resistance of coatings is found to decrease with increase in Al₂O₃ content of HA composite coatings. In this case also, higher weight loss has been recorded for first 80 cycles as compared to last 120 cycles. The minimum cumulative weight loss of 44.5 mg/cm² was recorded for pure HA coating, whereas the maximum cumulative weight loss of 68.5 mg/cm² was measured for HA-30 wt% Al₂O₃ coating after a run of 200 cycles.

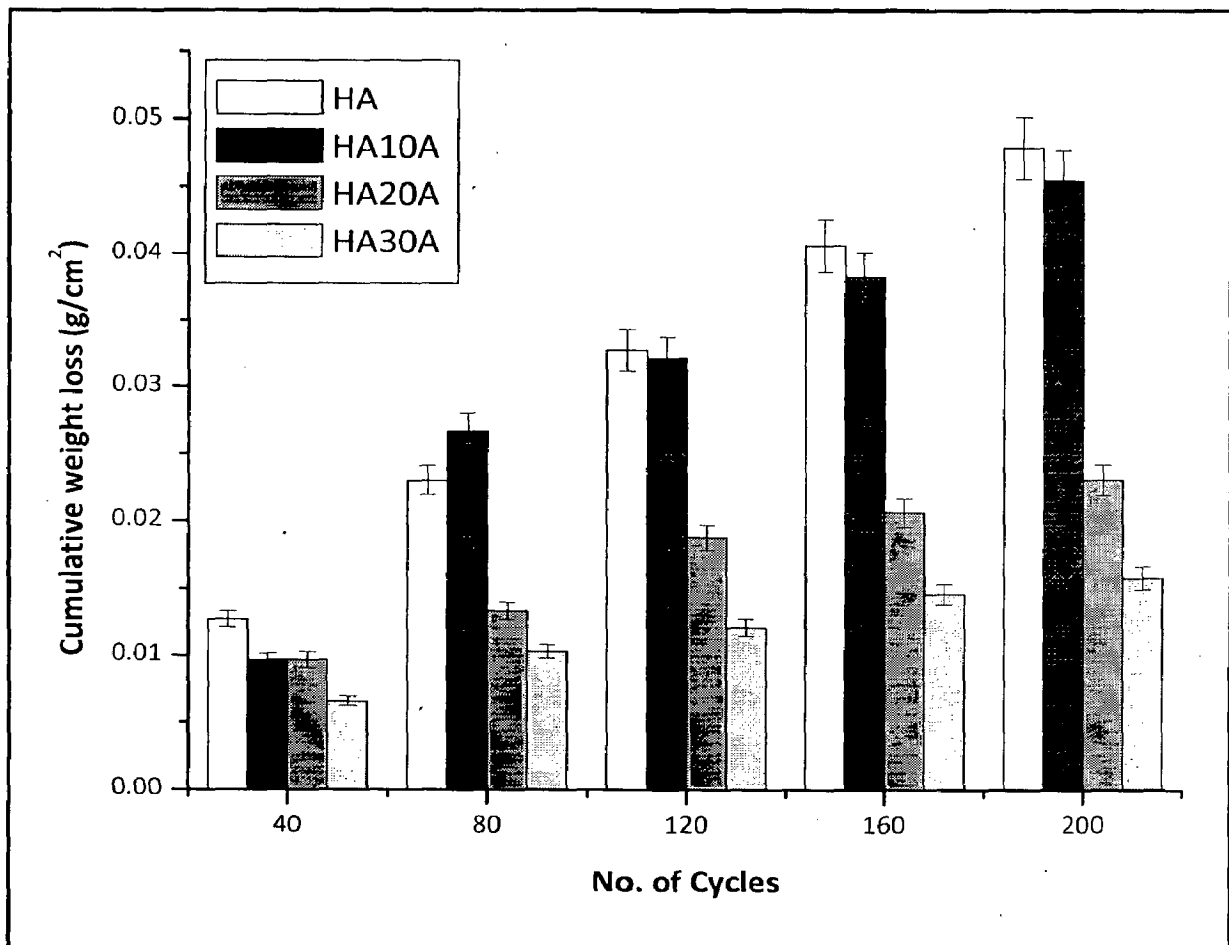


Fig. 5.1 Wear behavior of coatings against 400 grit abrasive

5.2.1.1 FE-SEM analysis of coatings after wear test

Surface micrographs of plasma spray coated specimens after conducting wear test for 200 cycles against 400 grit abrasive are shown in Fig. 5.3 to Fig. 5.6. Surface smoothing, wear marks, coating fragmentation and wear debris are present in FE-SEM micrographs of surface after conducting wear test. Surface micrograph of pure HA coating after wear test show surface smoothing, wear marks, wear debris and coating fragmentation (Fig. 5.3b-d). The wear debris can be seen in magnified view (2500X) of the worn out surface as shown in Fig. 5.3e. FE-SEM micrograph of HA-10 wt% Al_2O_3 coating surface after conducting wear test against SiC abrasive is shown in Fig. 5.4. At lower magnification of 300X, ploughing and surface smoothing can be seen in Fig. 5.4a, however wear debris and wear marks can be seen at higher magnifications (Fig. 5.4b-d).

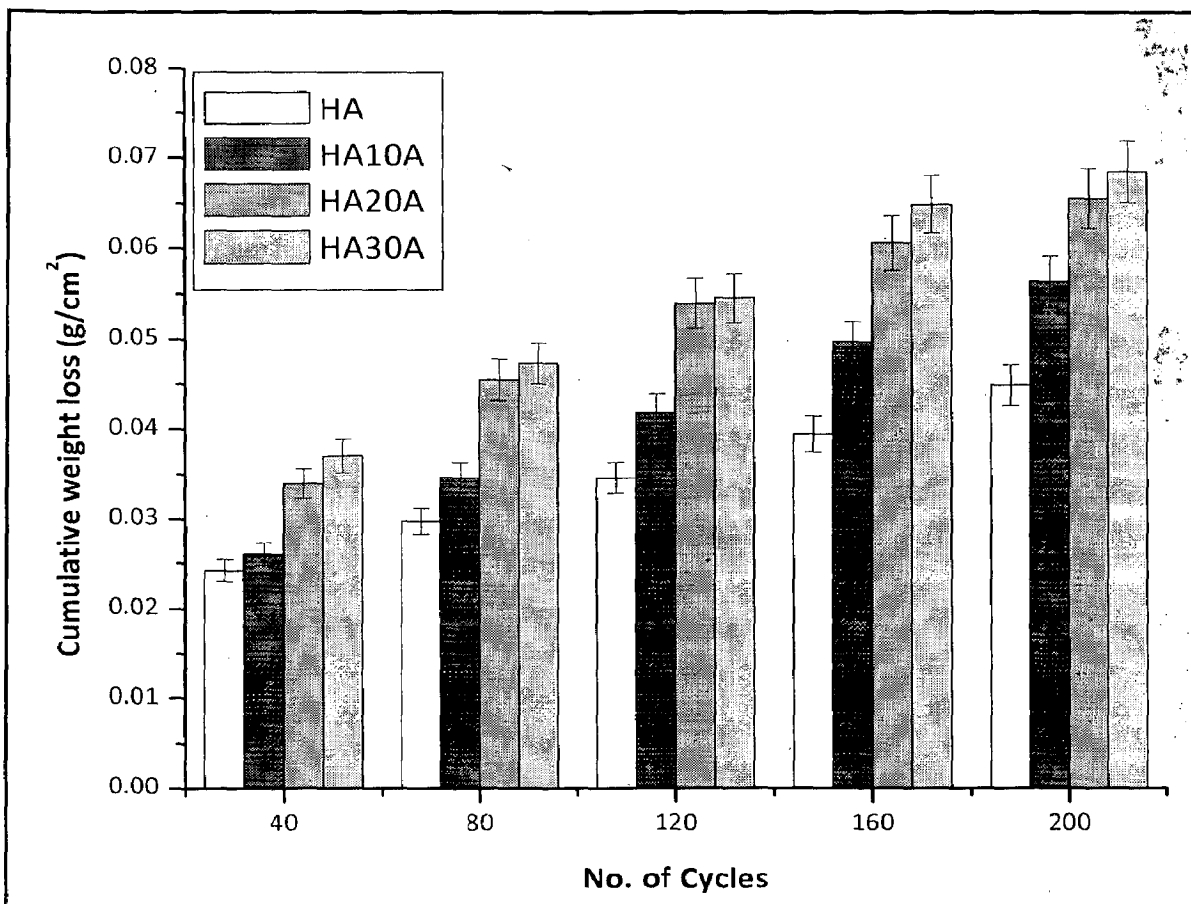


Fig. 5.2 Wear behavior of coatings against similar coatings

Some craters filled with wear debris can be seen in between worn out splats at further higher magnification as shown in Fig. 5.4 e-f. The micrographs of HA-20 wt% Al₂O₃ coating after conducting wear test against abrasive are shown in Fig. 5.5. Micrograph at lower magnification of 100X reveal ploughing of the coating as can be seen in Fig. 5.5a, which can be also seen in Fig. 5.5c. However, coating fragments along with ploughing are visible in Fig. 5.5b and d. Wear debris are visible in Fig. 5.5e taken at 1000X, further the varying shape and size of these wear debris can be seen in Fig. 5.5f taken at 2500X magnification. Surface micrographs of HA-30 wt% Al₂O₃ coating after conducting wear test against abrasive are shown in Fig. 5.6. Wear mark, surface smoothing and wear debris can be seen in micrograph at lower magnification of 100X (Fig. 5.6a). Figure 5.6b (300X magnification) show coating surface covered with wear debris, the wear marks can also be seen in the background. Magnified image of Fig. 5.6b show coating surface completely covered with wear debris (Fig. 5.6c). Wear marks on comparatively smooth surface and wear debris around the smoothed splat can be seen in Fig. 5.6d, however wear marks and wear debris are visible on smoothed surface as can be seen in Fig. 5.6e.

FE-SEM images of worn out surfaces after conducting wear test against similar coatings for 200 cycles are shown in Fig. 5.7 to Fig. 5.10. The surface morphology of coatings, in general, shows plastic flow of coatings along with wear debris. FE-SEM micrograph of pure HA coating after conducting wear test against pure HA coating is shown in Fig. 5.7. Wear debris can be seen on the coating splat in Fig. 5.7a, whereas plastic flow of coating and wear debris are visible in Fig. 5.7b. Figure 5.7c to 5.7f show the surface morphology of coating at 1500X, 3000X, 5000X and 8000X respectively. Wear debris are visible around the splat in top right corner as shown in Fig. 5.7c, whereas wear debris can also be seen on the splats in Fig. 5.7d-f. Surface micrographs of HA-10 wt% Al₂O₃ coating after conducting wear test against similar coating are shown in Fig. 5.8. Plastic flow of coating along with wear debris is visible in micrographs as can be seen in Fig. 5.8a and b. Wear debris are present on the surface and in the valleys (lower area between two coating splats) as can be seen in the images taken at higher magnification (Fig. 5.8c-f). Surface micrographs of HA-20 wt% Al₂O₃ coating after conducting wear test against similar coating are shown in Fig. 5.9. Plastic flow of coating splats with wear debris is visible in micrographs as shown in Fig. 5.9a-f. Wear debris are also visible on the surface of coating (Fig. 5.9f). Figure 5.10

shows the surface morphology of HA-30 wt% Al₂O₃ coating after conducting wear test against similar coating for a run of 200 cycles. Plastic flow of coating along with accumulation of wear debris around splat can be seen in Fig 5.10a and b. The worn out surface covered with wear debris can be seen at higher magnification (Fig. 5.10c-f).

5.2.1.2 AFM analysis of coatings after wear test

The surface topography of coatings after conducting wear test against 400 grit SiC abrasive and against similar coatings was studied using Atomic Force Microscopy (AFM) in semi-contact mode. AFM surface morphology of coatings after conducting wear test against 400 grit SiC abrasive and against similar coatings are shown in Fig. 5.11 and Fig. 5.12 respectively. 2-D and 3-D images of HA; HA-10 wt% Al₂O₃; HA-20 wt% Al₂O₃; HA-30 wt% Al₂O₃ coatings after conducting wear test against 400 grit abrasive are shown in Fig. 5.11a and b; c and d; e and f; g and h respectively, whereas 2-D and 3-D images of HA; HA-10 wt% Al₂O₃; HA-20 wt% Al₂O₃; HA-30 wt% Al₂O₃ coatings after conducting wear test against similar coatings are shown in Fig. 5.12a and b; c and d; e and f; g and h respectively. The difference in morphology of coating surfaces after conducting wear test by two different techniques can be inferred by comparing the 3-D images of coatings as shown in Fig. 5.11 and Fig. 5.12. The overall surface roughness of coatings after conducting wear test against abrasive is less than that of coatings after conducting wear test against similar coatings.

The surface roughness of as-coated and worn out specimens after conducting wear tests is shown in Table 5.1. The surface roughness of as sprayed coatings was in the range of 5.01 μm to 8.56 μm as reported in Section 4.2.4 of Chapter 4 of present study, whereas surface roughness of coatings after conducting wear test against abrasive and against similar coatings is in the range of 67.86 nm to 81.87 nm and 69.81 nm to 284.62 nm respectively. In general, the surface of coatings after conducting wear test has been substantially reduced as compared to that of as-sprayed coatings. However, comparatively smooth surface is obtained after conducting wear test against abrasive than that obtained after conducting wear test against similar coatings. The crystallite size after wear test has been also reported in Table 5.1.

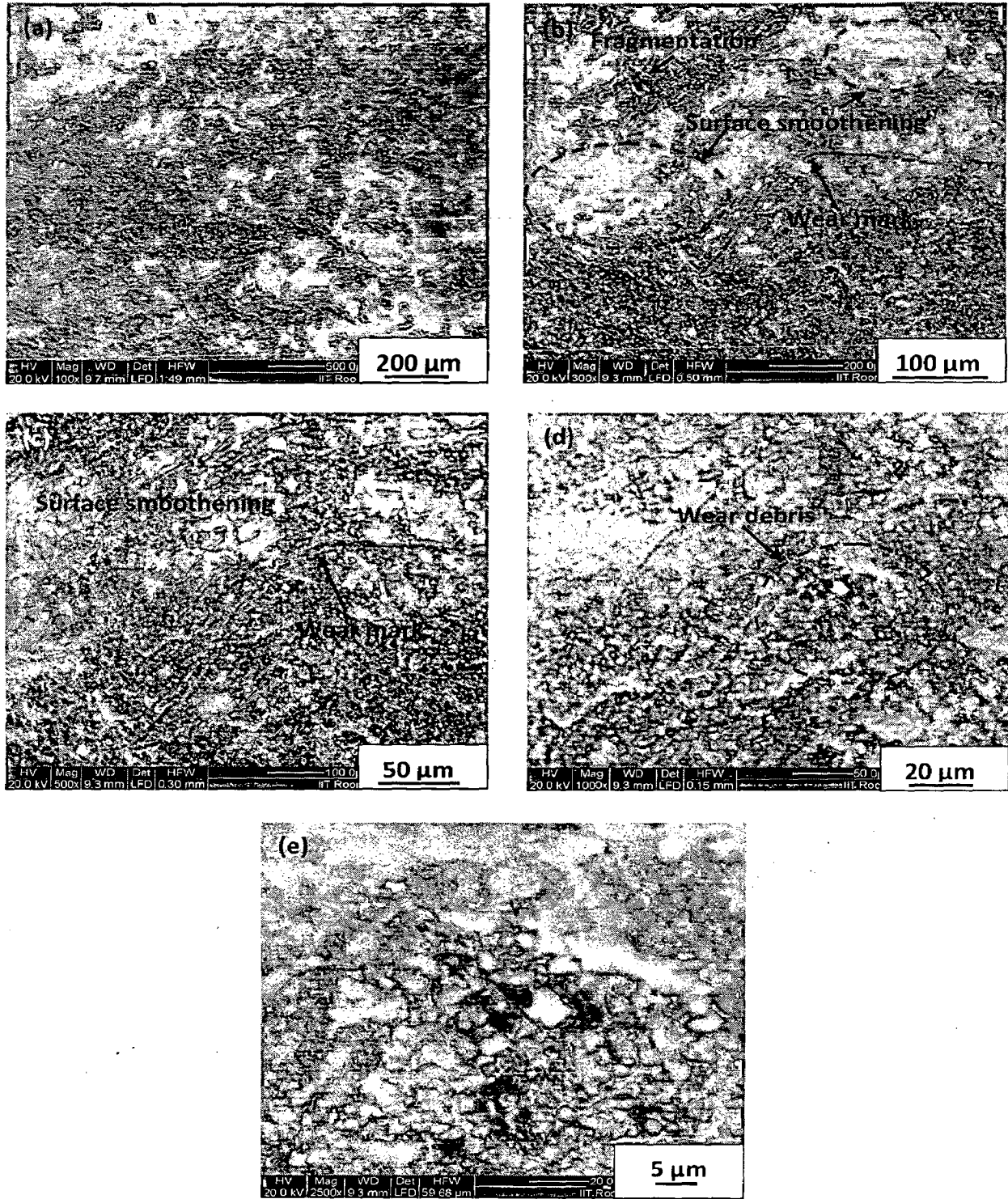


Fig. 5.3 FE-SEM image of surface of pure HA coatings after wear test against 400 grit abrasive at different magnifications: (a) at 100X; (b) at 300X; (c) at 500X; (d) at 1000X and (e) at 2500X

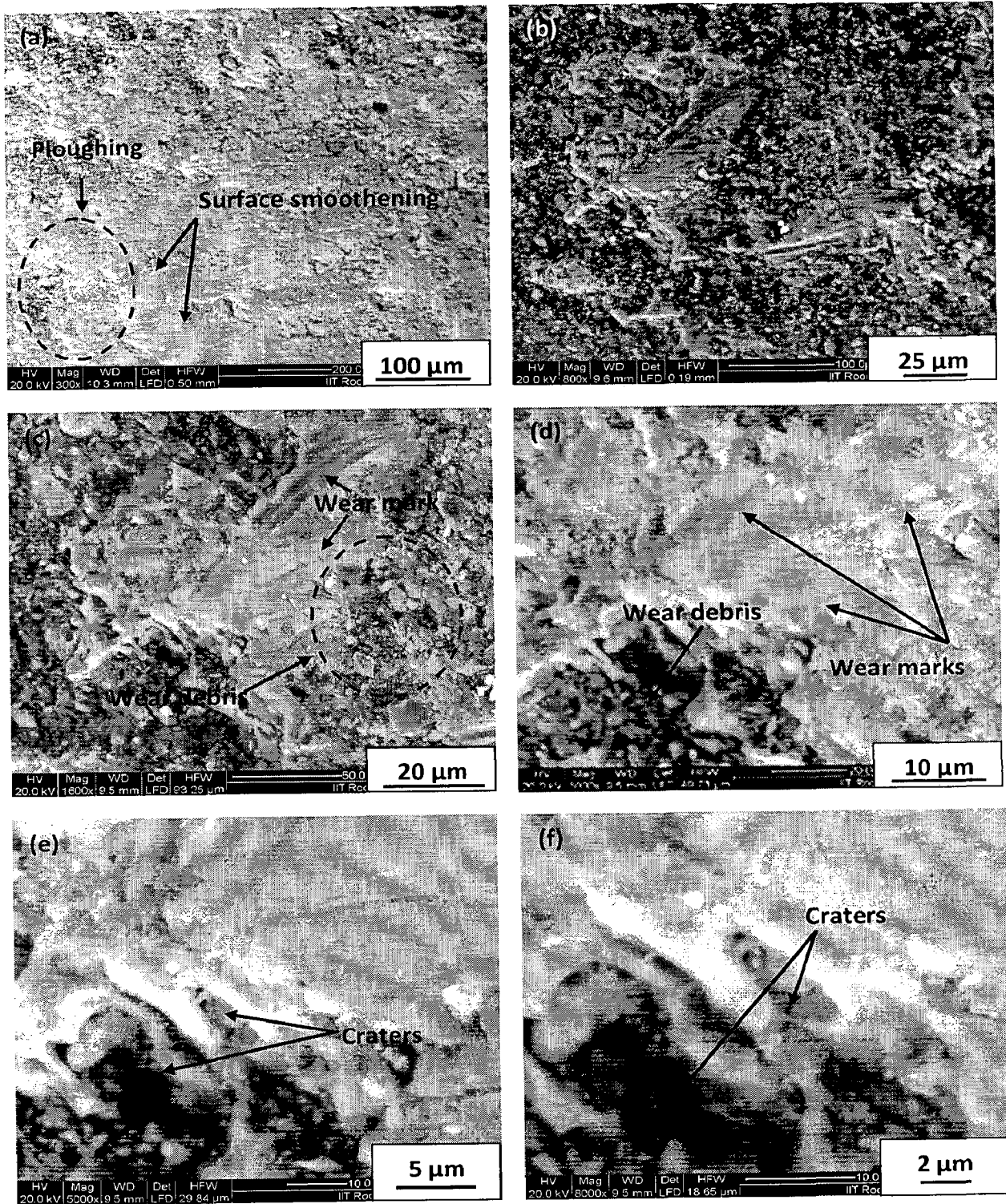


Fig. 5.4 FE-SEM image of surface of HA-10 wt% Al₂O₃ coating after wear test against 400 grit abrasive at different magnifications: (a) at 300X; (b) at 800X; (c) at 1600X; (d) at 3000X; (e) at 5000X and (f) at 8000X

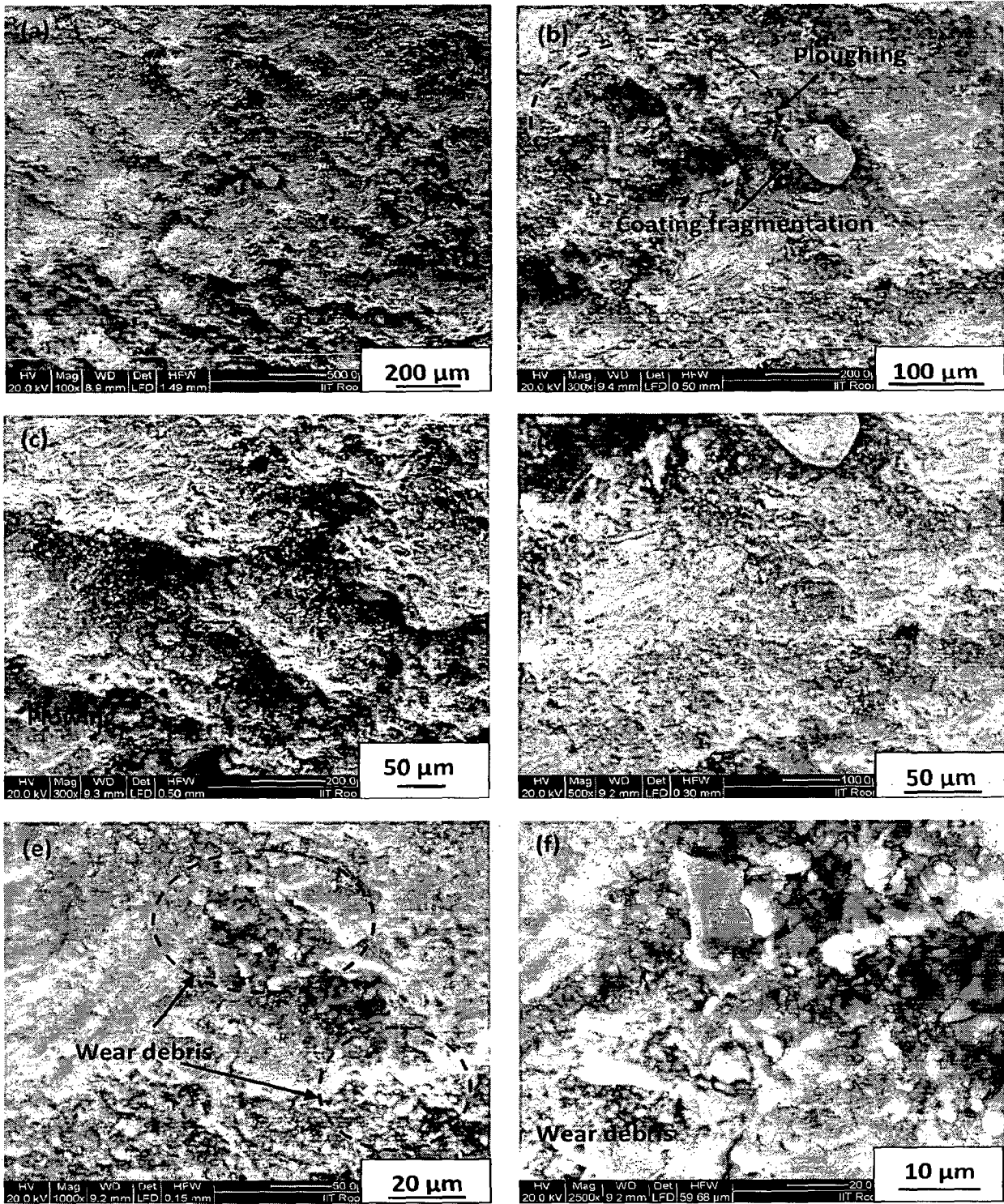


Fig. 5.5 FE-SEM image of surface of HA-20 wt% Al₂O₃ coating after wear test against 400 grit abrasive at different magnifications: (a) at 100X; (b) at 300X; (c) at 300X ; (d) at 500X; (e) at 1000X and (f) at 2500X

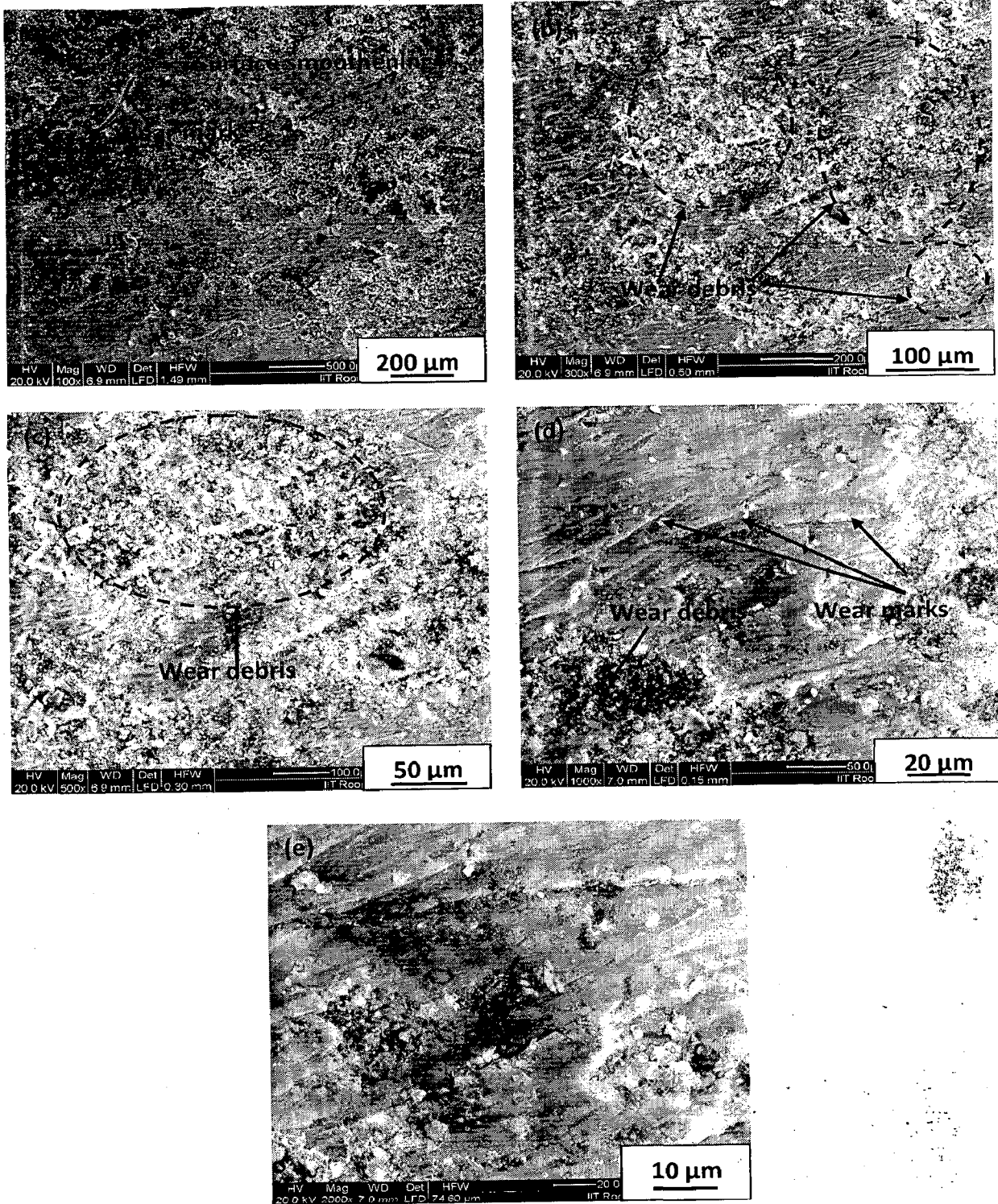


Fig. 5.6 FE-SEM image of surface of HA-30 wt% Al₂O₃ coating after wear test against 400 grit abrasive at different magnifications: (a) at 100X; (b) at 300X; (c) at 500X; (d) at 1000X and (e) at 2000X

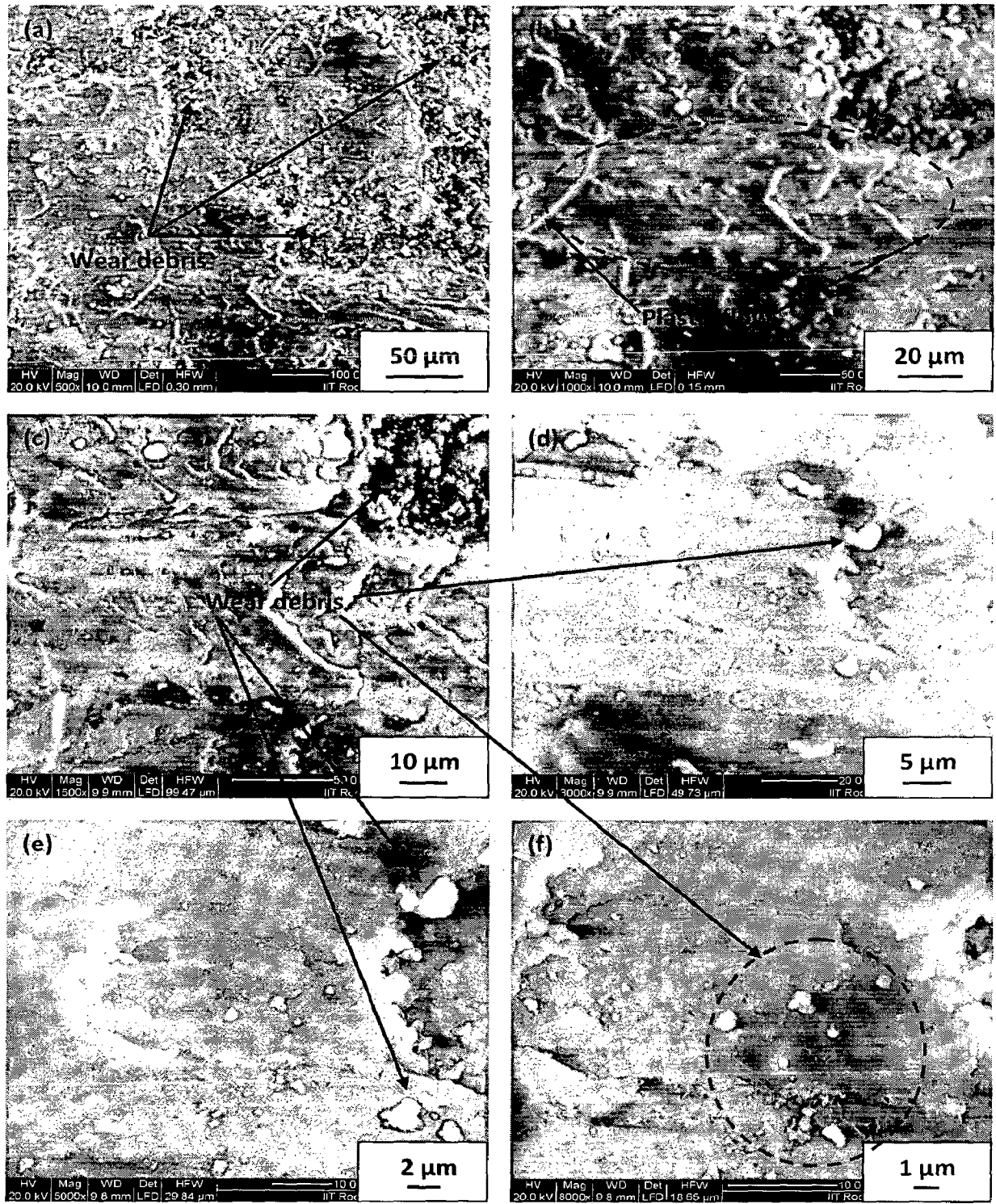


Fig. 5.7 FE-SEM image of surface of pure HA coating after wear test against pure HA coating at different magnifications: (a) at 500X; (b) at 1000X; (c) at 1500X; (d) at 3000X; (e) at 5000X and (f) at 8000X

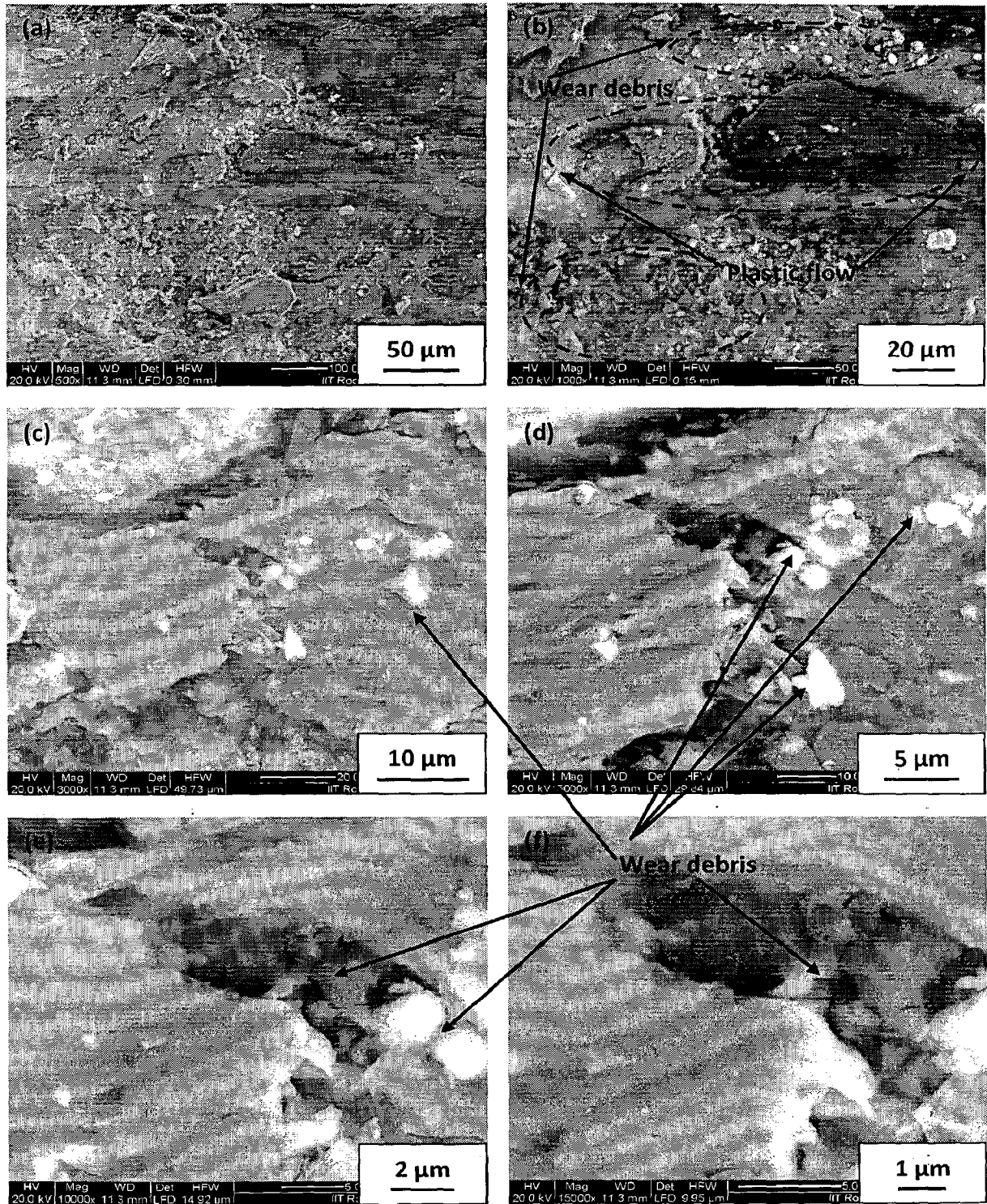


Fig. 5.8 FE-SEM image of surface of HA-10 wt% Al₂O₃ coating after wear test against HA-10 wt% Al₂O₃ coating at different magnifications: (a) at 500X; (b) at 1000X; (c) at 3000X; (d) at 5000X; (e) at 10000X and (f) at 15000X

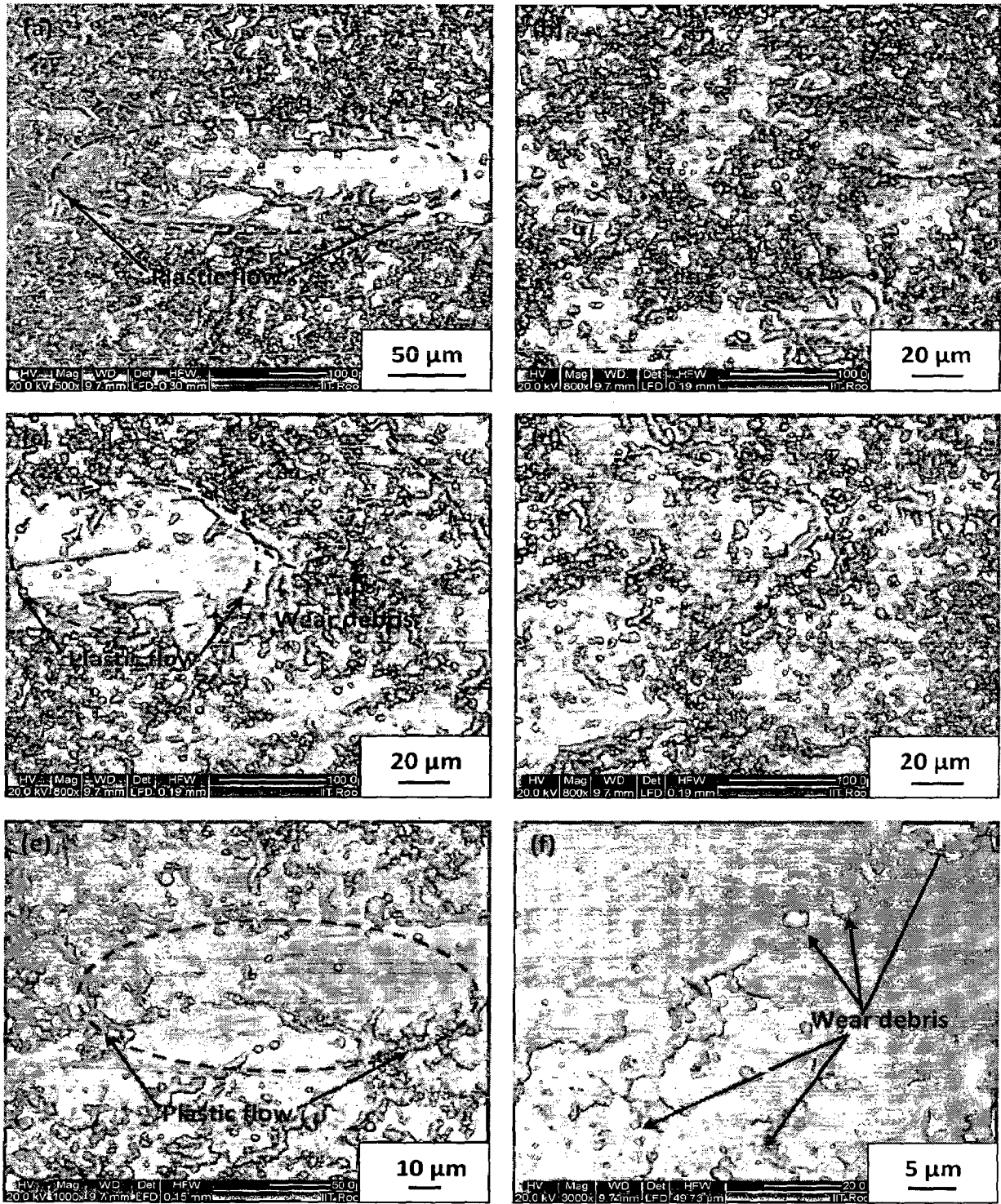


Fig. 5.9 FE-SEM image of surface of HA-20 wt% Al₂O₃ coating after wear test against HA-20 wt% Al₂O₃ coating at different magnifications: (a) at 500X; (b) at 800X; (c) at 800X; (d) at 800X; (e) at 1000X and (f) at 3000X

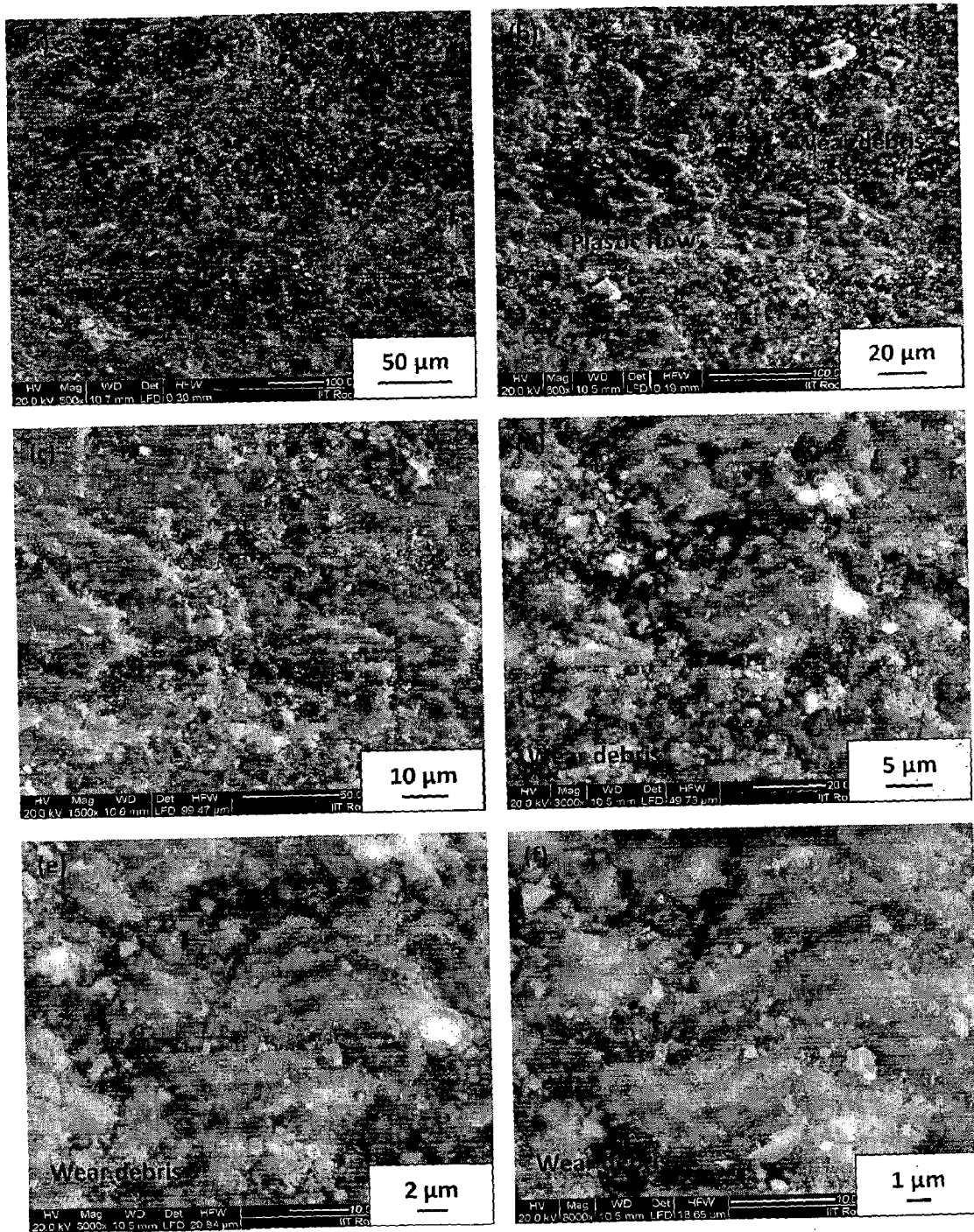
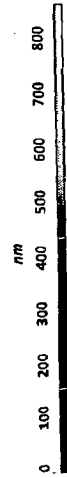
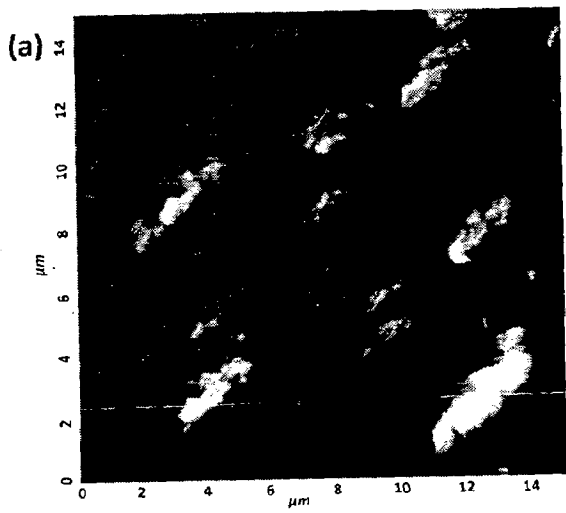
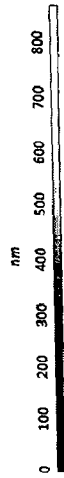
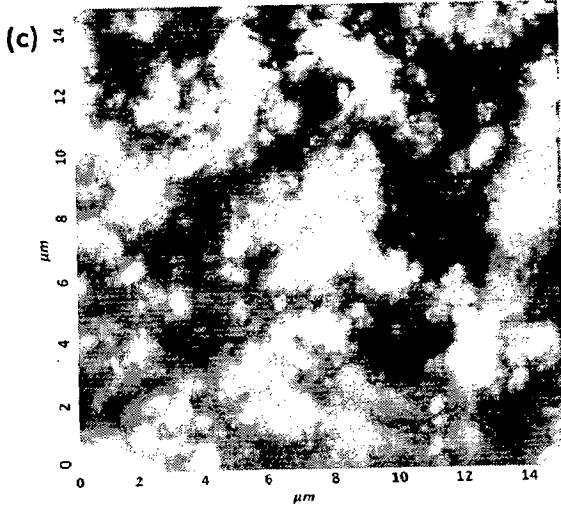
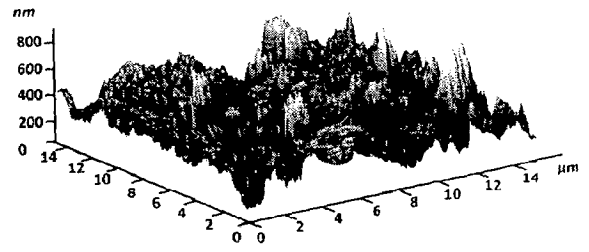


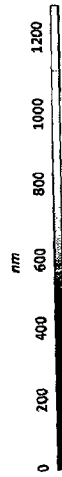
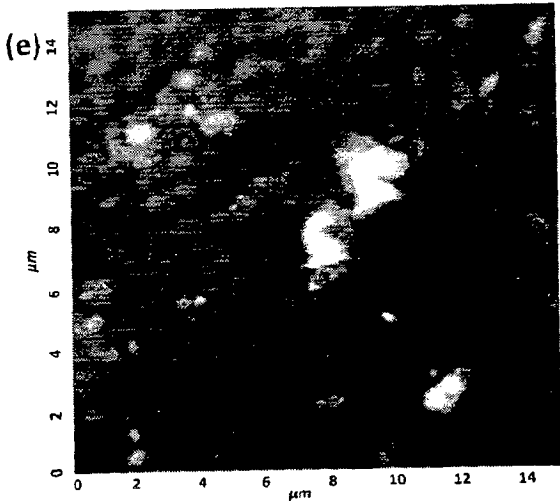
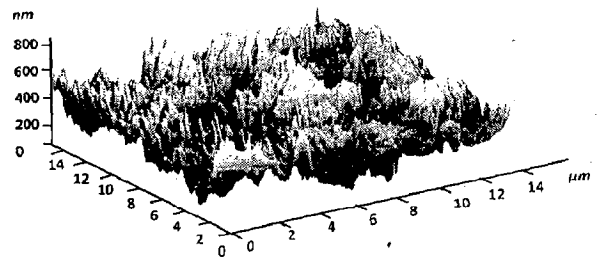
Fig. 5.10 FE-SEM image of surface of HA-30 wt% Al₂O₃ coating after wear test against HA-30 wt% Al₂O₃ coating at different magnifications: (a) at 500X; (b) at 800X; (c) at 1500X; (d) at 3000X; (e) at 5000X and (f) at 8000X



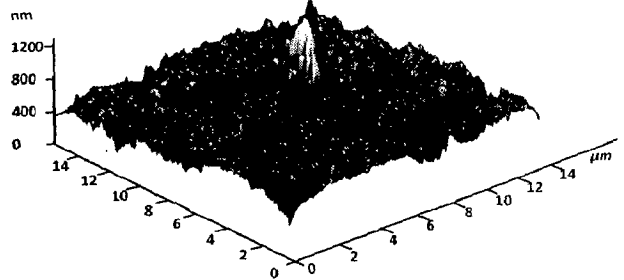
(b)



(d)



(f)



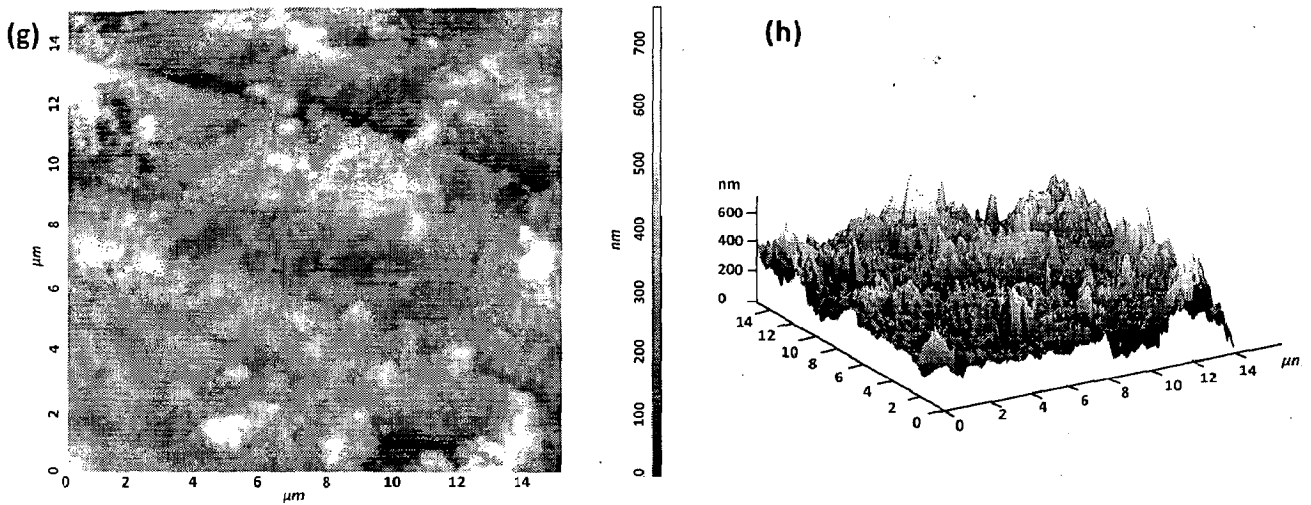
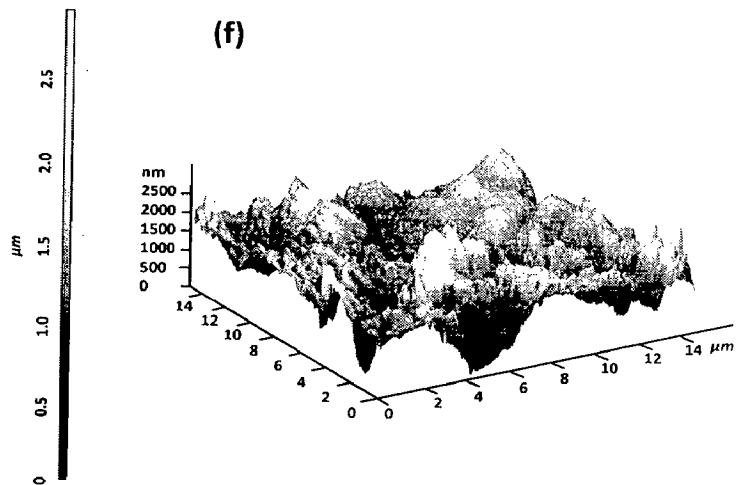
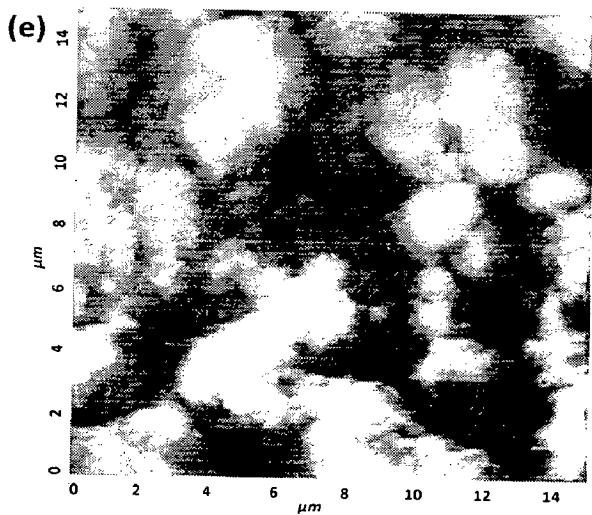
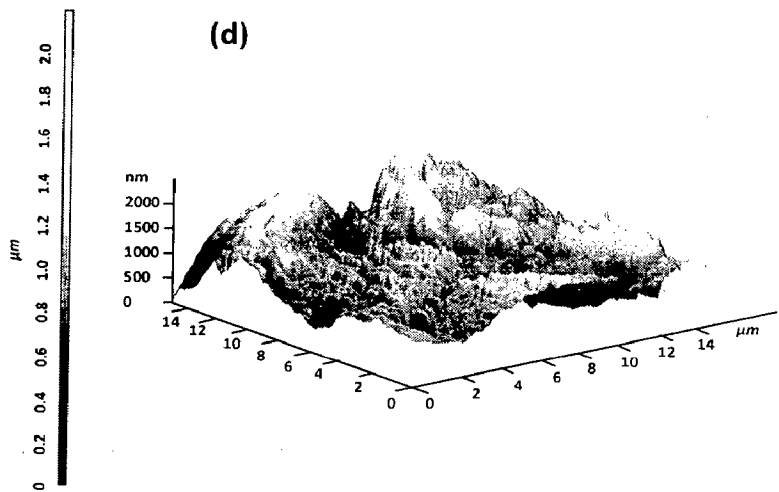
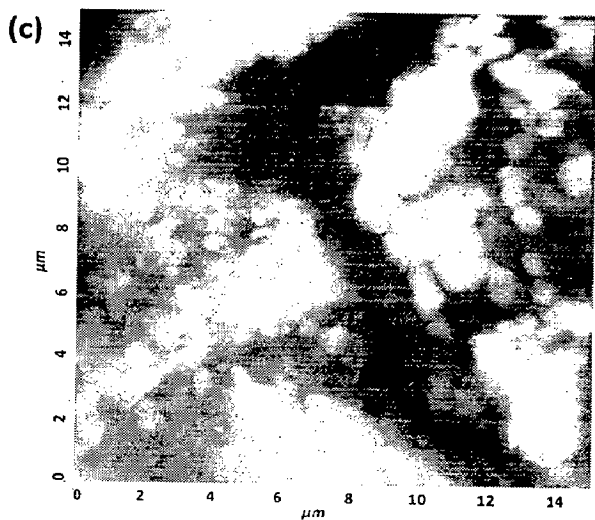
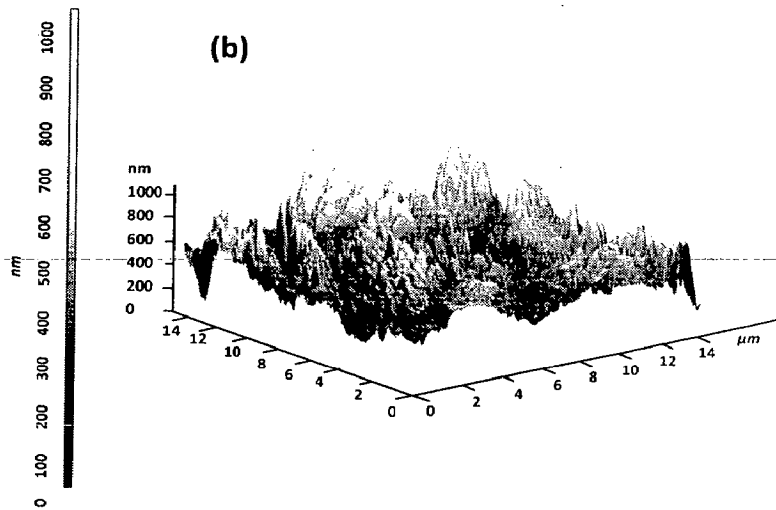
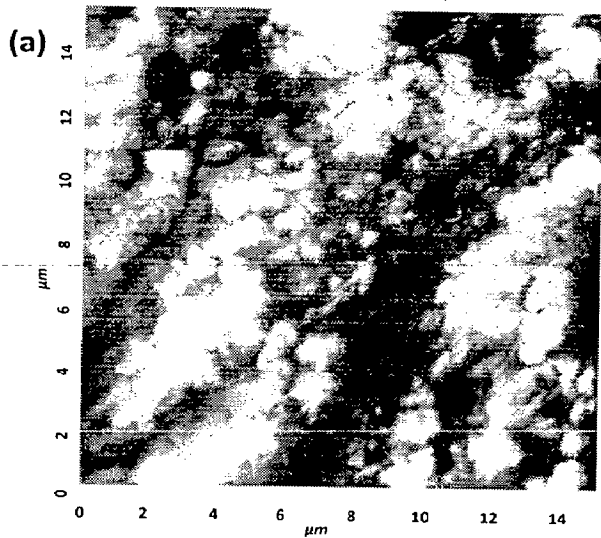


Fig. 5.11 Atomic force microscopy (AFM) images showing surface morphology of coatings after wear test against 400 grit abrasive: (a) 2-D image of pure HA coating; (b) 3-D image of pure HA coating; (c) 2-D image of HA-10 wt% Al₂O₃ coating; (d) 3-D image of HA-10 wt% Al₂O₃ coating; (e) 2-D image of HA-20 wt% Al₂O₃ coating; (f) 3-D image of HA-20 wt% Al₂O₃ coating; (g) 2-D image of HA-30 wt% Al₂O₃ coating and (h) 3-D image of HA-30 wt% Al₂O₃ coating

Table 5.1 Surface roughness of as coated and worn out coatings

Coating	Surface roughness (Ra) (μm) of as coated specimens measured using non contact profilometer	Surface roughness (Ra) (μm) and size of wear debris (nm) of worn out specimens after wear test measured using AFM			
		Abrasive		Similar coatings	
Pure HA coating	5.01-7.26	0.0818	84	0.105	153
HA-10 wt% Al ₂ O ₃ coating	6.05-7.41	0.0817	86	0.197	148
HA-20 wt% Al ₂ O ₃ coating	7.1-7.94	0.0685	79	0.284	217
HA-30 wt% Al ₂ O ₃ coating	7.39-8.56	0.0678	78	0.0698	83



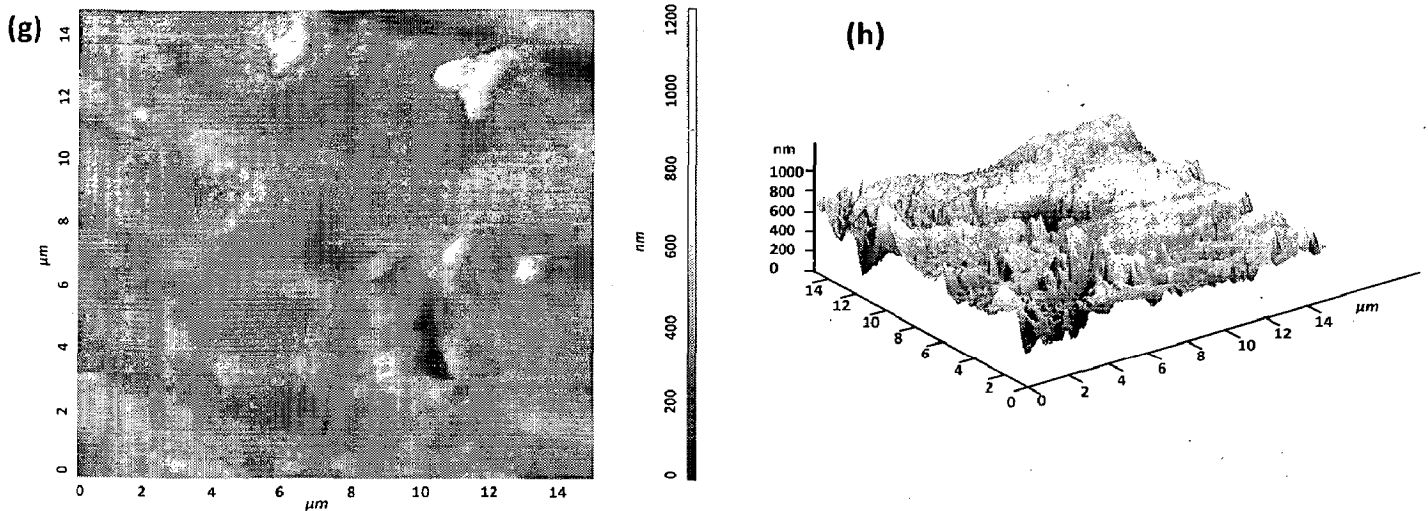


Fig. 5.12 Atomic force microscopy (AFM) images showing surface morphology of coatings after wear test against similar coatings: (a) 2-D image of pure HA coating; (b) 3-D image of pure HA coating; (c) 2-D image of HA-10 wt% Al_2O_3 coating; (d) 3-D image of HA-10 wt% Al_2O_3 coating; (e) 2-D image of HA-20 wt% Al_2O_3 coating (f) 3-D image of HA-20 wt% Al_2O_3 coating; (g) 2-D image of HA-30 wt% Al_2O_3 coating and (h) 3-D image of HA-30 wt% Al_2O_3 coating

5.2.2 Microhardness of Coatings

Microhardness was measured on polished cross-sectioned specimens on either side of coating substrate interface. The microhardness values (Hv) plotted against distance (μm) from interface is shown in Fig. 5.13 to 5.16. The microhardness profile of HA, HA-10 wt% Al_2O_3 , HA-20 wt% Al_2O_3 and HA-30 wt% Al_2O_3 on AISI 316L SS without incorporation of Al_2O_3 -13 wt% TiO_2 bond coat is shown in Fig. 5.13. It can be seen from microhardness profile, that microhardness of coatings increase with increase in Al_2O_3 (reinforcement) contents to HA. Further, the value of microhardness is highest near substrate coating interface for all type of coatings. The highest and least value of microhardness for HA; HA-10 wt% Al_2O_3 ; HA-20 wt% Al_2O_3 ; HA-30 wt% Al_2O_3 coatings are 312 and 210 Hv; 399 and 317 Hv; 414 and 336 Hv; 419 and 346 Hv respectively. It can be observed from the plot that substrate also has highest microhardness value (230 to 240 Hv for AISI 316L SS substrate) near interface as compared to average microhardness value of 200 Hv. The microhardness profile of HA, HA-10 wt% Al_2O_3 , HA-20 wt% Al_2O_3 and HA-30 wt% Al_2O_3 on AISI 316L SS with incorporation of Al_2O_3 -13 wt% TiO_2 bond coat is shown in Fig. 5.14. It

can be seen from microhardness profile, that microhardness of coatings increase with increase in Al_2O_3 (reinforcement) contents to HA. Further, the value of microhardness is highest near substrate coating interface for all type of coatings. The highest and least value of microhardness for HA; HA-10 wt% Al_2O_3 ; HA-20 wt% Al_2O_3 ; HA-30 wt% Al_2O_3 coatings are 320 and 210 Hv; 401 and 317 Hv; 427 and 386 Hv; 426 and 325 Hv respectively. It can be observed from the plot that substrate also has highest microhardness value (≈ 240 Hv) near interface as compared to average microhardness value of 200 Hv. The microhardness value of bond coat is found to vary between 580 to 610 Hv with average of 592.5 Hv.

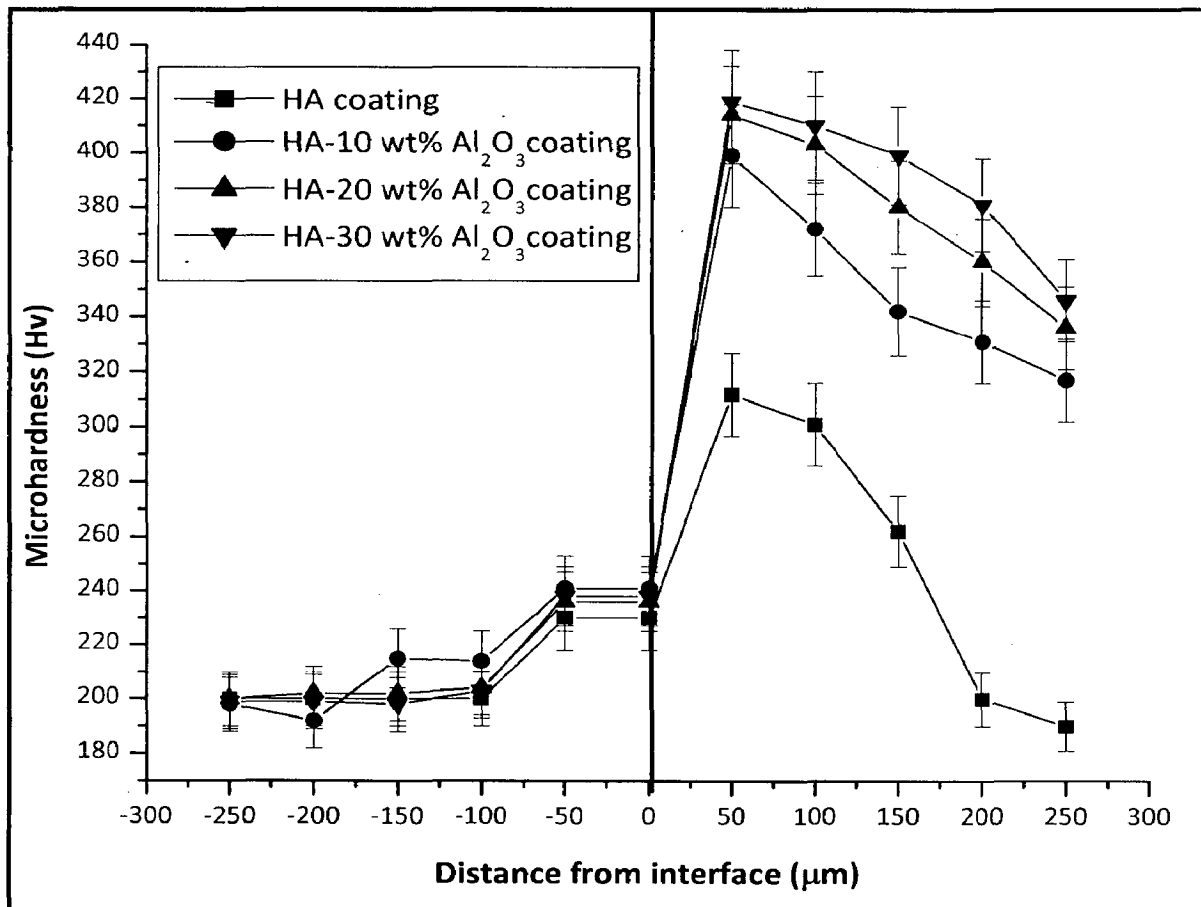


Fig. 5.13 Microhardness profile of different coatings on AISI 316 L stainless steel substrate

The microhardness profile of HA, HA-10 wt% Al₂O₃, HA-20 wt% Al₂O₃ and HA-30 wt% Al₂O₃ coated titanium without incorporation of Al₂O₃-13 wt% TiO₂ bond coat is shown in Fig. 5.15. It can be observed from the microhardness plot that substrate and all type of coatings have highest value of microhardness near the substrate coating interface, while least value of microhardness is found at farthest point from the substrate coating interface. The highest and least value of microhardness for HA; HA-10 wt% Al₂O₃; HA-20 wt% Al₂O₃; HA-30 wt% Al₂O₃ coatings were found to be 360 and 231 Hv; 380 and 300 Hv; 396 and 369 Hv; 423 and 391 Hv respectively. The highest value of microhardness for titanium (substrate) is 187 Hv against average value of 172 Hv.

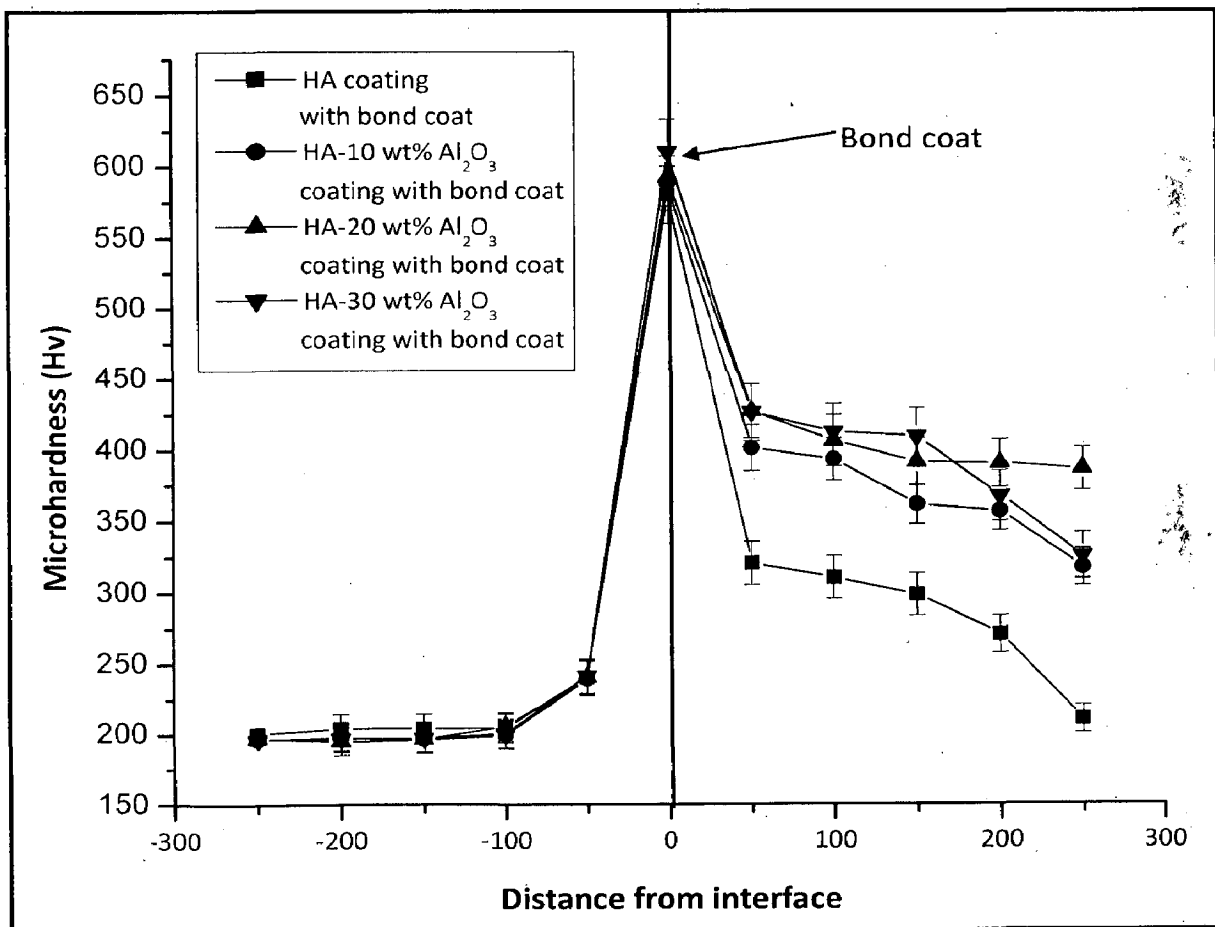


Fig. 5.14 Microhardness profile of different coatings on AISI 316 L stainless steel with Al₂O₃-13 wt% TiO₂ bond coat

The microhardness profile of HA, HA-10 wt% Al₂O₃, HA-20 wt% Al₂O₃ and HA-30 wt% Al₂O₃ coated titanium with incorporation of Al₂O₃-13 wt% TiO₂ bond coat is shown in Fig. 5.16. It can be seen from the microhardness plot that substrate and all type of coatings have highest value of microhardness near the substrate coating interface, while least value of microhardness is found at farthest point from the substrate coating interface. The highest and least value of microhardness for HA; HA-10 wt% Al₂O₃; HA-20 wt% Al₂O₃; HA-30 wt% Al₂O₃ coatings were found to be 365 and 260 Hv; 394 and 310 Hv; 414 and 356 Hv; 452 and 372 Hv respectively. The highest value of microhardness for titanium (substrate) is 191 Hv against average value of 172 Hv. The highest value of microhardness for bond coat is 616 Hv for HA-30 wt% Al₂O₃ coating.

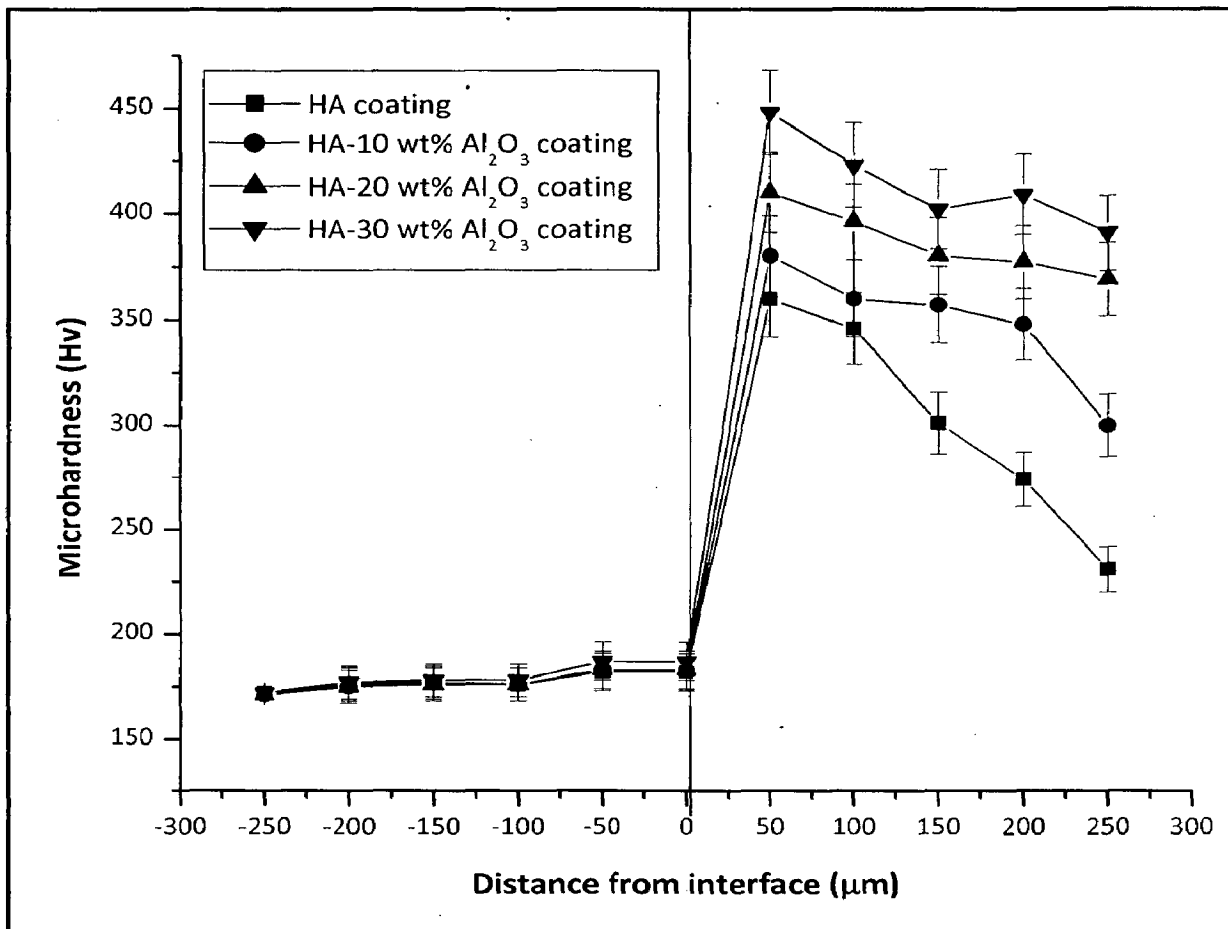


Fig. 5.15 Microhardness profile of different coatings on titanium substrate

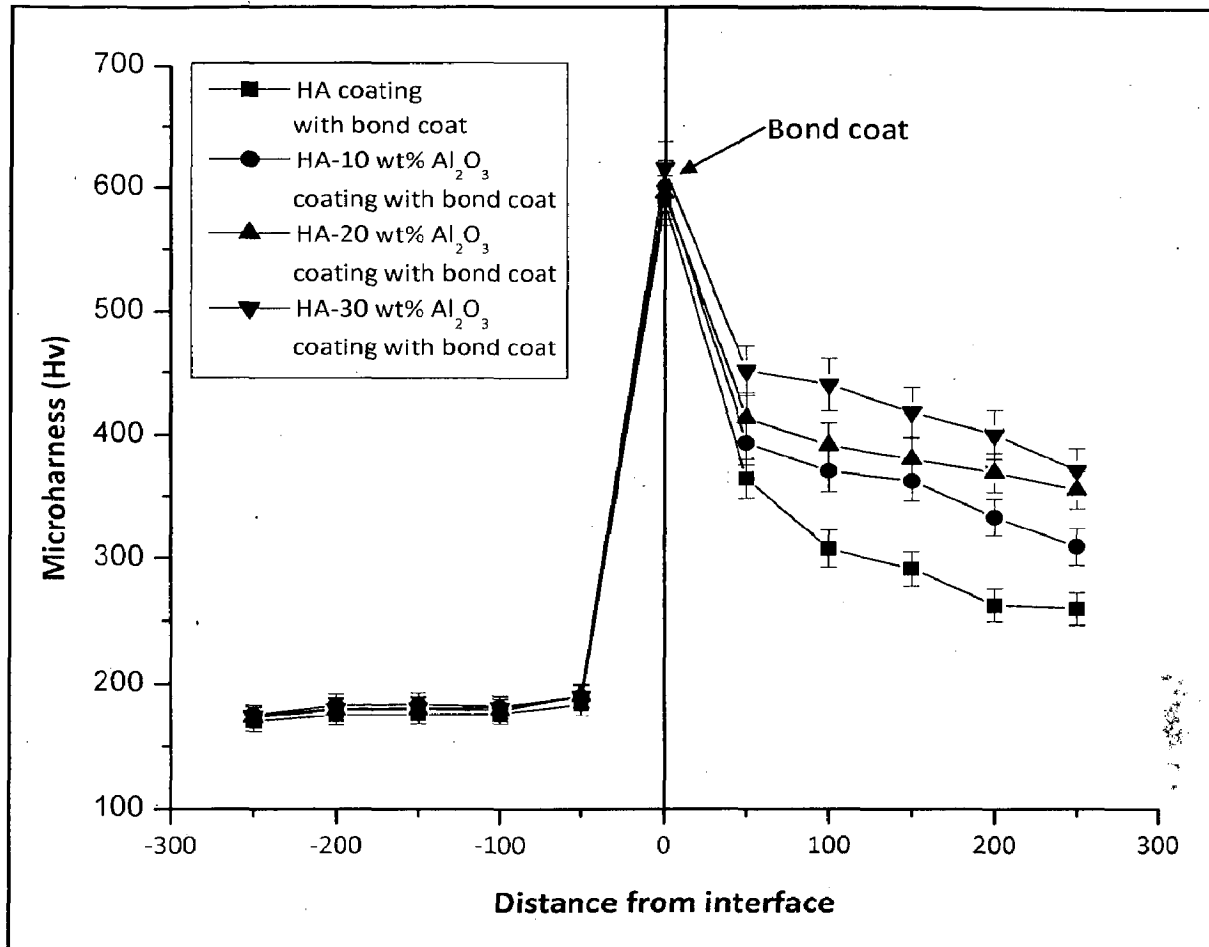


Fig. 5.16 Microhardness profile of different coatings on titanium with Al₂O₃-13 wt% TiO₂ bond coat

5.2.3 Tensile Bond Strength of Coatings

The macrographs of fractured surface of coatings after ASTM C633 79 tensile test are shown in Fig. 5.17. Macrographs of fractured surface of HA, HA-10 wt% Al₂O₃, HA-20 wt% Al₂O₃ and HA-30 wt% Al₂O₃ coatings after ASTM C633 79 test are shown in Fig 5.17a-d respectively. It can be seen from these macrographs that failure of coatings took place partially within the coating and partially at substrate coating interface. Moreover, the area of adhesive failure (at substrate coating interface) decreased with increase in Al₂O₃ (reinforcement) content of HA composite coatings. Macrographs of fractured surface of HA, HA-10 wt% Al₂O₃, HA-20 wt% Al₂O₃ and HA-30 wt% Al₂O₃ coatings with Al₂O₃-13 wt% TiO₂ bond coat after ASTM C633 79 test are shown in Fig 5.17e-h respectively.

Failure of coatings took place within the coating, at substrate coating interface and at bond coat topcoat interface. In case of HA and HA-10 wt% Al₂O₃ coatings, the bond coat was intact with the substrate as shown in Fig. 5.17e and f, whereas for HA-20 wt% Al₂O₃ and HA-30 wt% Al₂O₃ coatings, part of substrate can also be seen in Fig. 5.17g and h. The tensile bond strength values are presented in Table 5.2. The results show that the tensile of coatings increased with increase in Al₂O₃ contents of HA coatings as well as with incorporation of bond coat to the coatings. The minimum value of tensile bond strength was observed for HA coating without bond coat, while the maximum value of tensile bond strength was observed for HA-30 wt% Al₂O₃ coating with bond coat.

The area near the junction of cohesive (within the coating) and adhesive (coating/substrate or coating/bond coat) failure was analyzed using scanning electron microscopy and X-ray mapping. The FE-SEM micrographs with X-ray mapping of coatings without and with incorporation of bond coat after conducting tensile bond strength test using ASTM C633 79 standard are shown in Fig. 5.18 to Fig. 5.25. In all the coatings with or without bond coat mixed cohesive and adhesive failure took place.

FE-SEM micrograph along with X-ray mapping of HA coating after ASTM C633 79 tensile test is shown in Fig. 5.18. The failed area shown in micrograph suggests that the failure of the coating took place within the coating. Further, coexistence of elements of HA (Ca and P) and substrate elements (Fe) suggest that a thin layer of HA remained on the substrate after tensile testing. The presence of carbon (C) might be due to seepage of epoxy adhesive through coating during joining process.

FE-SEM image along with X-ray mapping of HA coating with incorporation of bond coat after performing tensile test is shown in Fig. 5.19. The micrograph and corresponding X-ray mapping suggest that the failure is mainly within the coating. The low intensity of Ca and P elements and high intensity of Al element corresponding to lower right portion of micrograph (dark grey) suggest that bond coat is intact and is covered with a very thin layer of HA coating. The white region in the micrograph may correspond to epoxy adhesive, which is present due to seepage through coating.

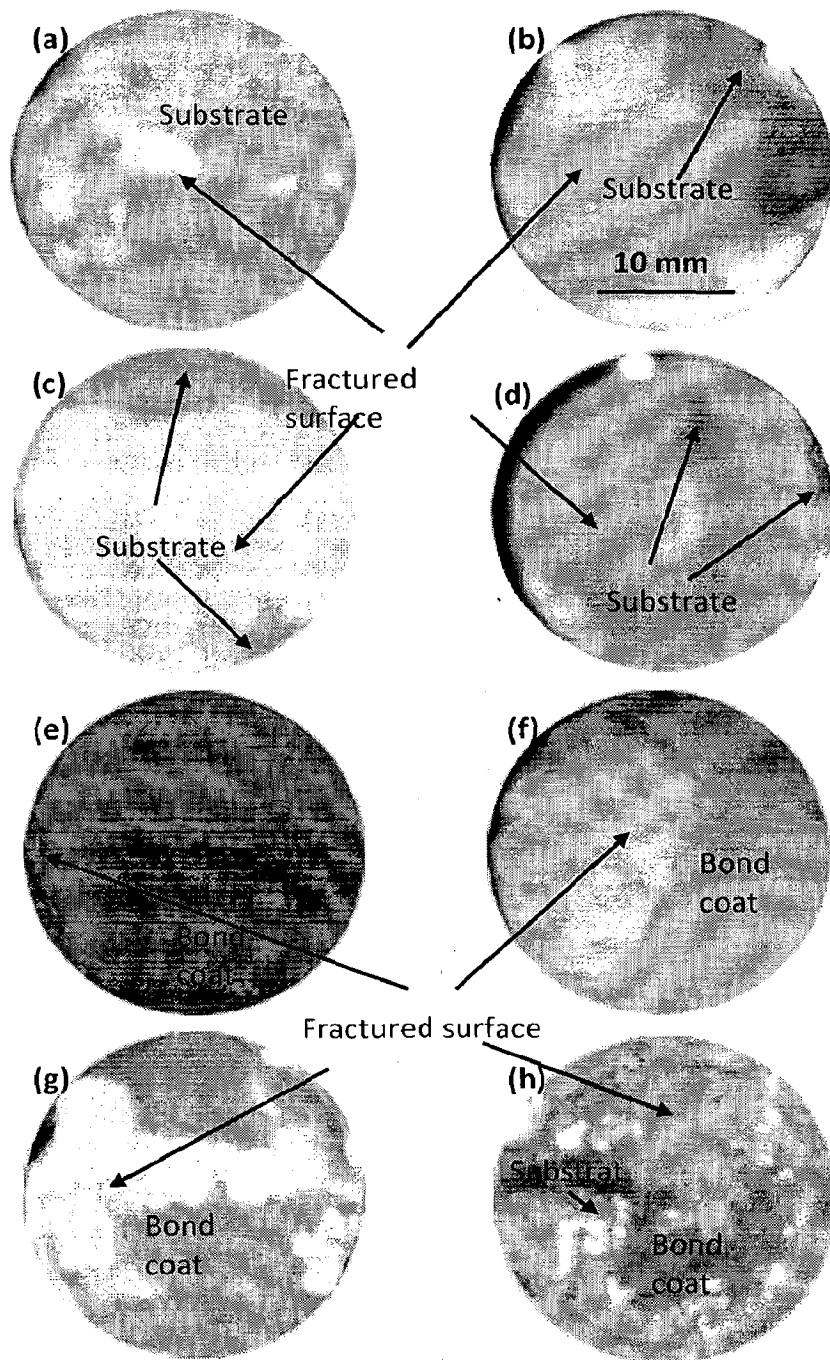


Fig. 5.17

Surface macrographs of coatings after ASTM C633 79 tensile test: (a) HA coating; (b) HA-10 wt% Al_2O_3 coating; (c) HA-20 wt% Al_2O_3 coating; (d) HA-30 wt% Al_2O_3 coating; with Al_2O_3 -13 wt% TiO_2 bond coat (e) HA coating; (f) HA-10 wt% Al_2O_3 coating; (g) HA-20 wt% Al_2O_3 coating and (h) HA-30 wt% Al_2O_3 coating

Note: the color change or shine in macrographs is due to gold sputter coating used for conducting FE-SEM/EDAX analysis prior to taking photographs.

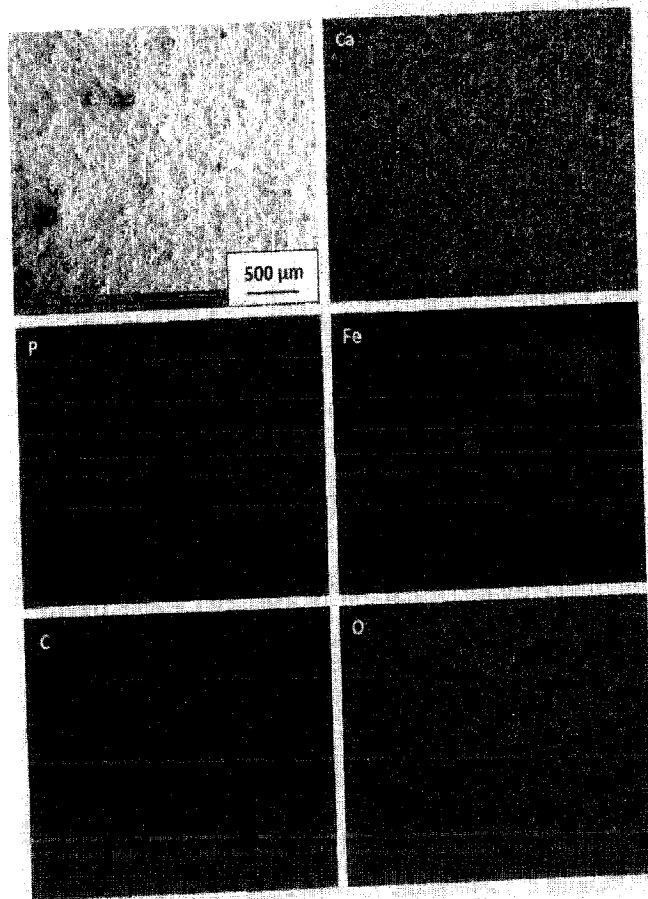


Fig. 5.18 FE-SEM image and X-ray mapping of fractured surface of pure HA coating

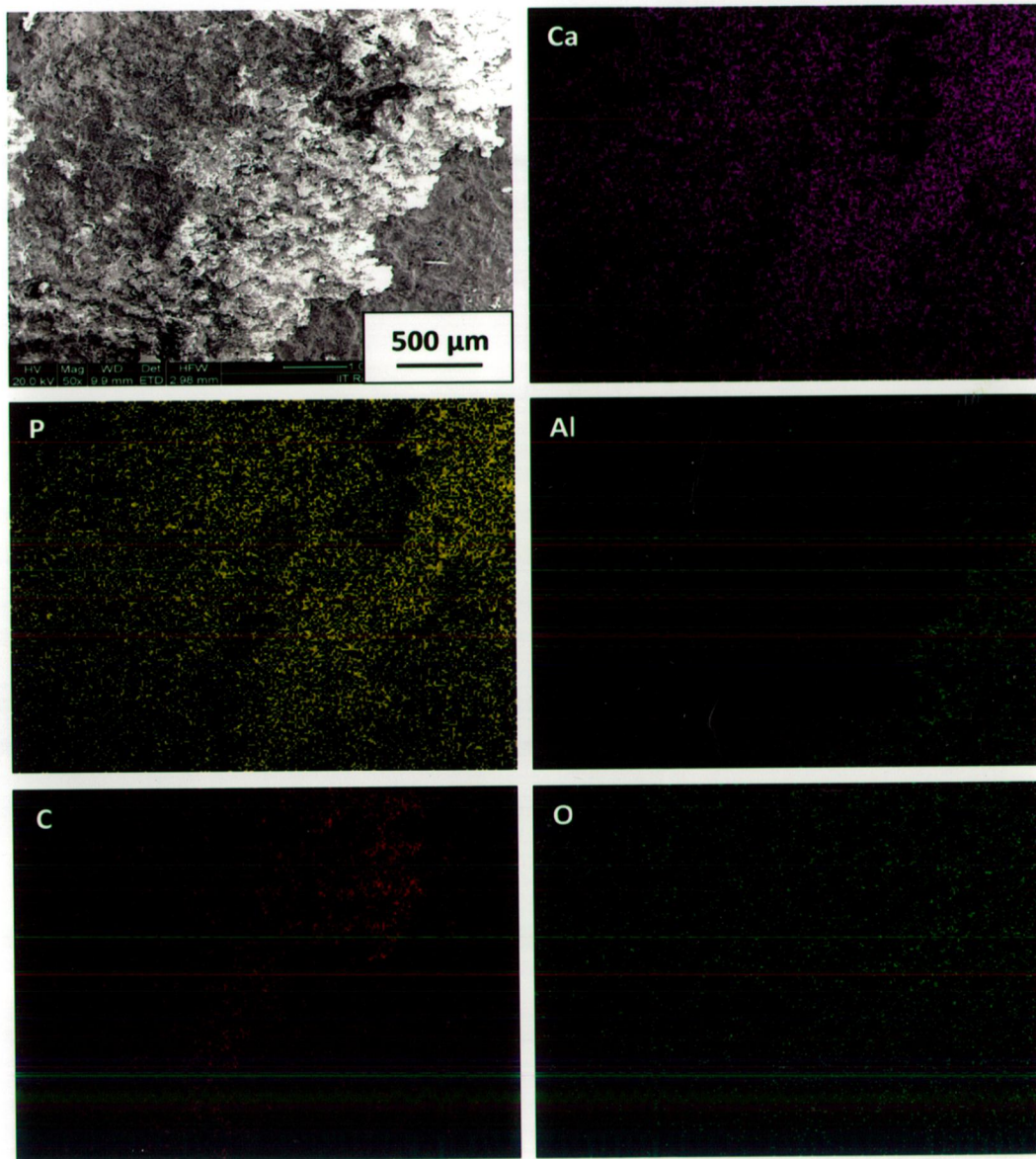


Fig. 5.19 FE-SEM image and X-ray mapping of fractured surface of pure HA coating with Al_2O_3 -13 wt% TiO_2 bond coat

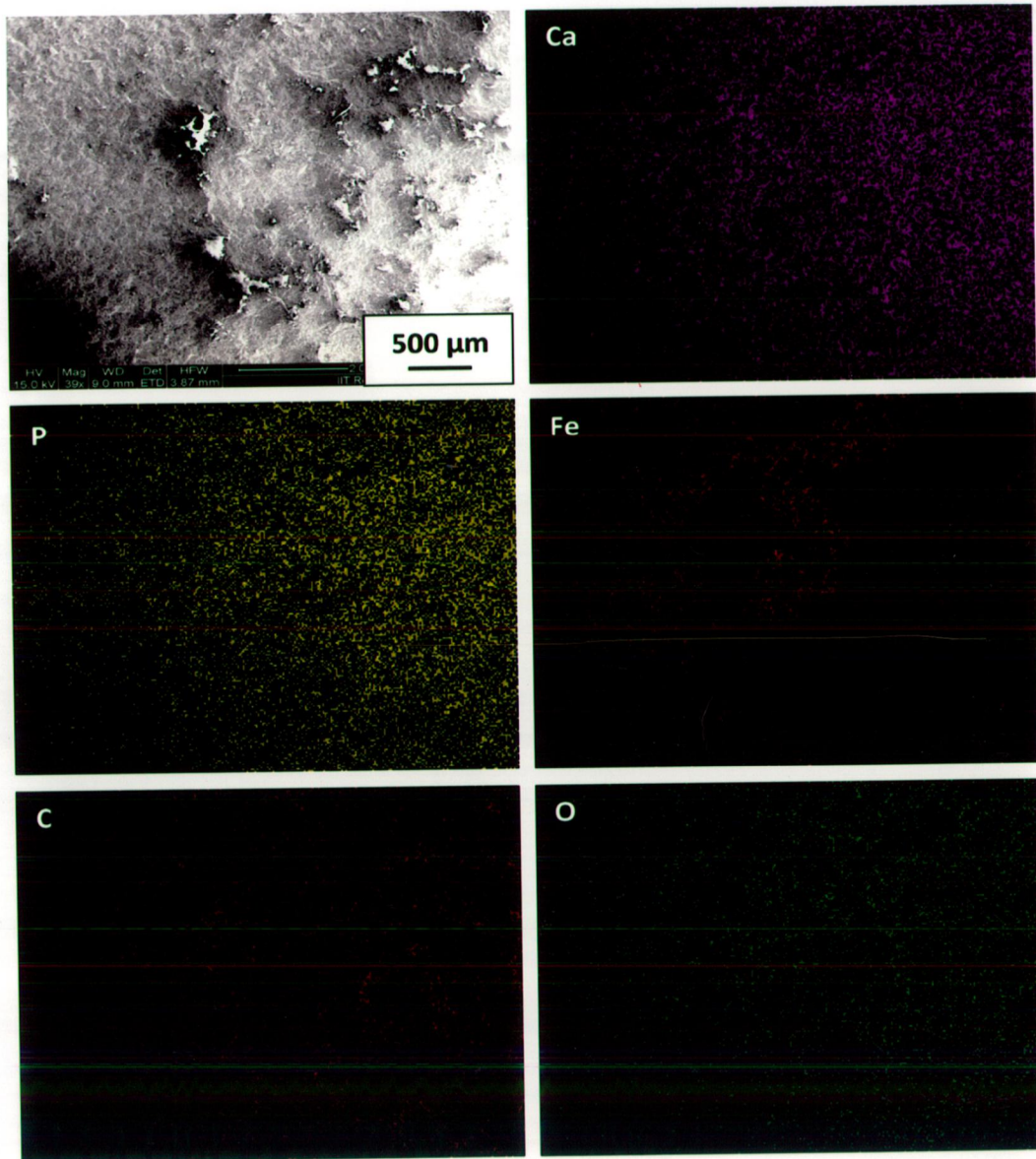


Fig. 5.20 FE-SEM image and X-ray mapping of fractured surface of HA-10 wt% Al₂O₃ coating

Figure 5.20 shows FE-SEM micrograph along with X-ray mapping of HA-10 wt% Al₂O₃ coating without incorporation of bond coat. The failure of coating took place in similar fashion as that of HA coating. The coexistence of HA components and substrate element suggest that at this portion substrate is covered with a very thin layer of HA. The failure took place within the coating as suggested by X-ray mapping of remaining area. The presence of carbon may be due to seepage of adhesive through top coat.

FE-SEM micrograph along with X-ray mapping of HA-10 wt% Al₂O₃ with incorporation of bond coat after performing tensile bond strength test is shown in Fig. 5.21. It can be clearly seen that micrograph is divided into two portions by a diagonal (showing coating thickness); the upper left portion correspond to bond coat, whereas lower right area correspond to top coat. The coexistence of components of HA (Ca and P) and bond coat (Al) in upper left portion of the images suggest that bond coat is intact to substrate and is covered with a very thin layer of top coat, whereas in lower portion, thick layer of top coat can be seen. The intensity of C is higher in lower region as compared to upper region as can be seen in X-ray mapping of carbon. This may be due to layer of epoxy adhesive on the coating surface.

FE-SEM micrograph along with X-ray mapping of HA-20 wt% Al₂O₃ without incorporation of bond coat after performing tensile bond strength test is shown in Fig. 5.22. The white patches in the micrograph represent substrate, black region represents adhesive and grey region corresponds to coating. It can be seen from X-ray mapping of Ca and P that coating is completely peeled off from the substrate as shown by black patches in X-ray mapping. These black patches correspond to substrate as can be seen in X-ray mapping of Fe. The black region in micrograph corresponds to adhesive as can be seen as high intensity region in X-ray mapping of C in Fig. 5.22.

FE-SEM micrograph along with X-ray mapping of HA-20 wt% Al₂O₃ coating with incorporation of Al₂O₃-13 wt% TiO₂ bond coat is shown in Fig. 5.23. The failure of coating took place in similar fashion as that of HA-20 wt% Al₂O₃ coating without bond coat. The grey region in lower left corner of the micrograph represents bond coat, white region corresponds to top coat and black spots represent adhesive. The absence of Ca and P elements in their X-ray mapping in lower left region and presence of Al element in this region in X-ray mapping of Al confirm that this region belong to bond coat. The black spots in micrograph correspond to high intensity of Carbon as can be seen in X-ray mapping of C.

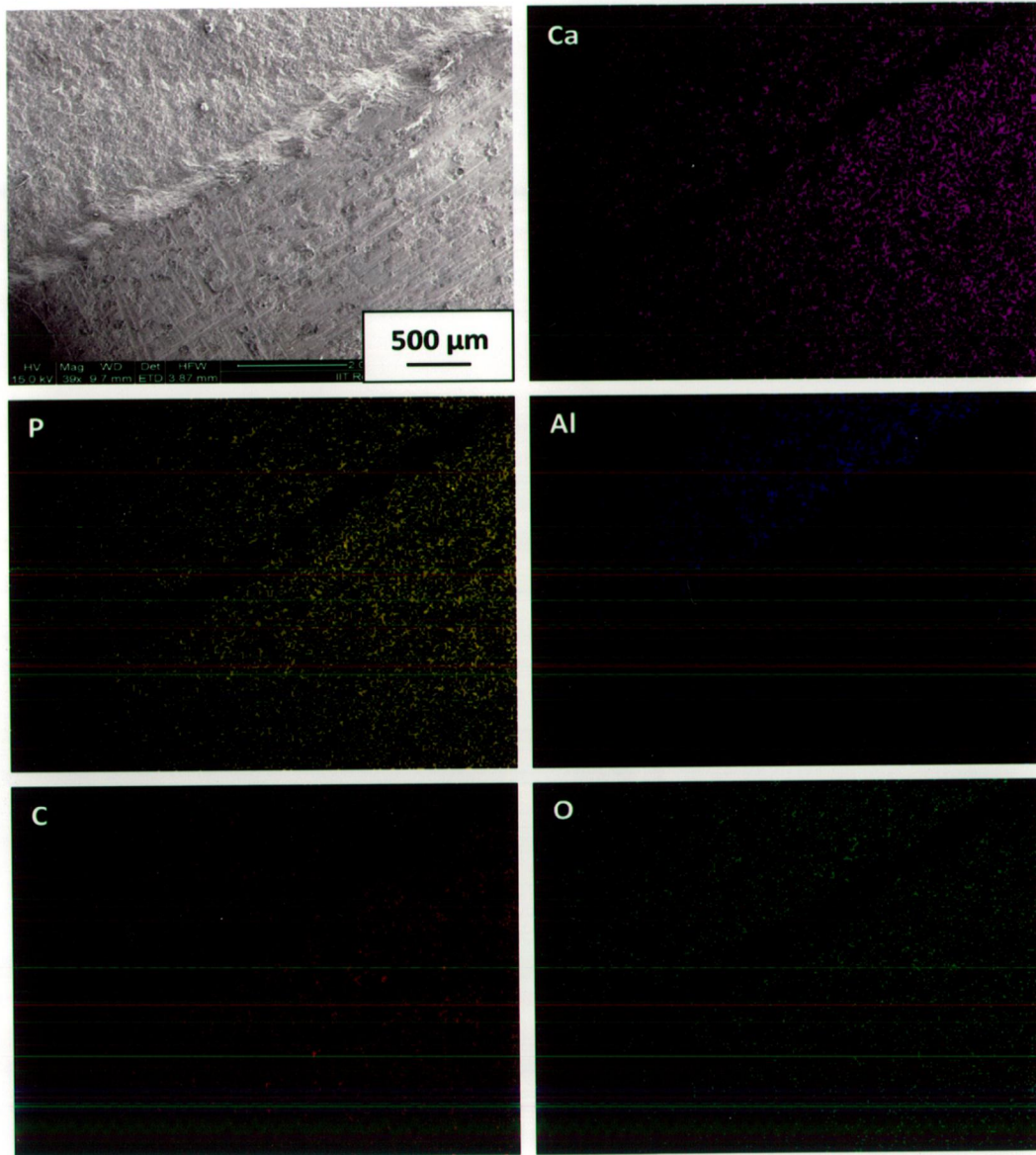


Fig. 5.21 FE-SEM image and X-ray mapping of fractured surface of HA-10 wt% Al_2O_3 coating with Al_2O_3 -13 wt% TiO_2 bond coat

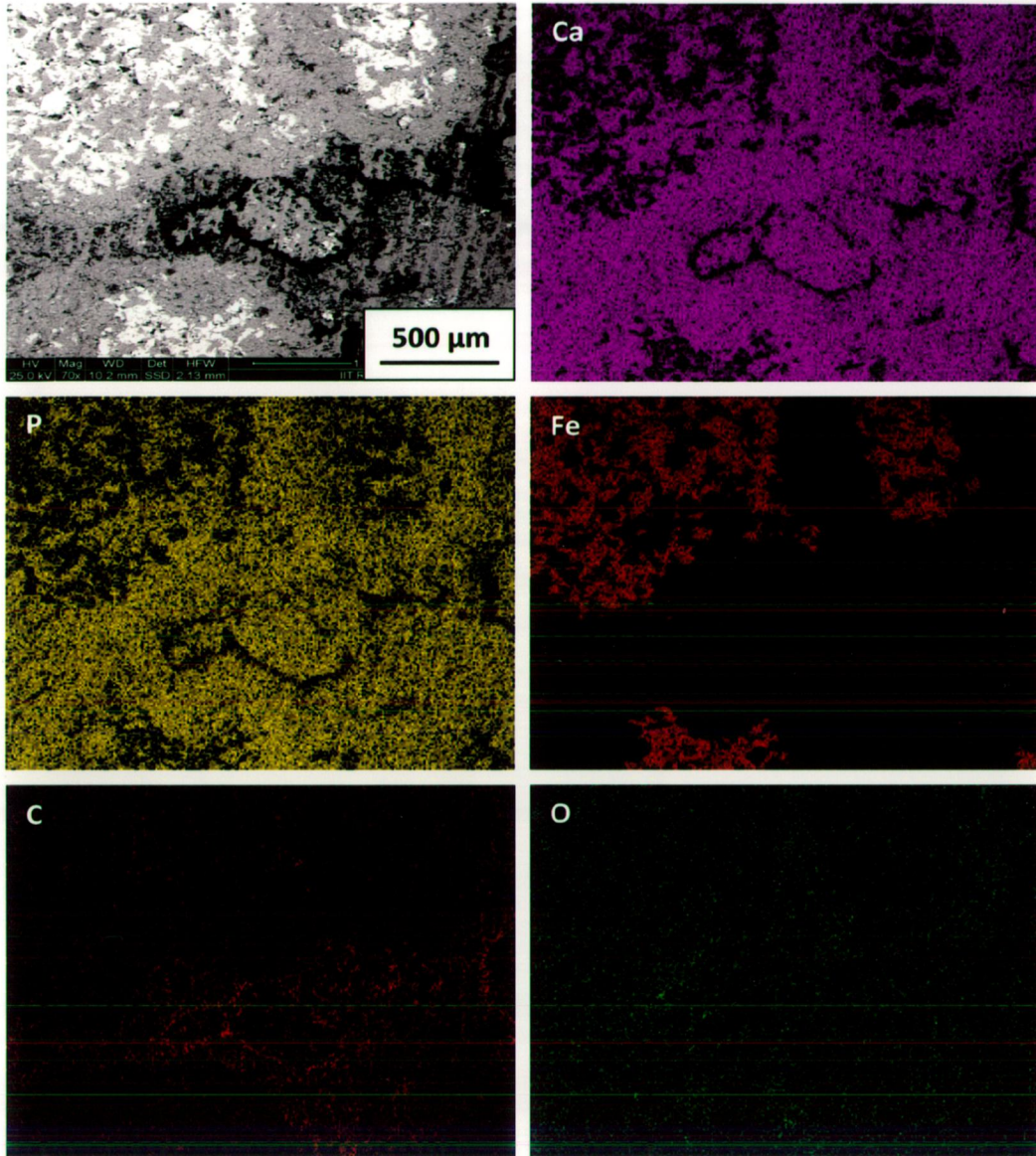


Fig. 5.22 FE-SEM image and X-ray mapping of fractured surface of HA-20 wt% Al₂O₃ coating

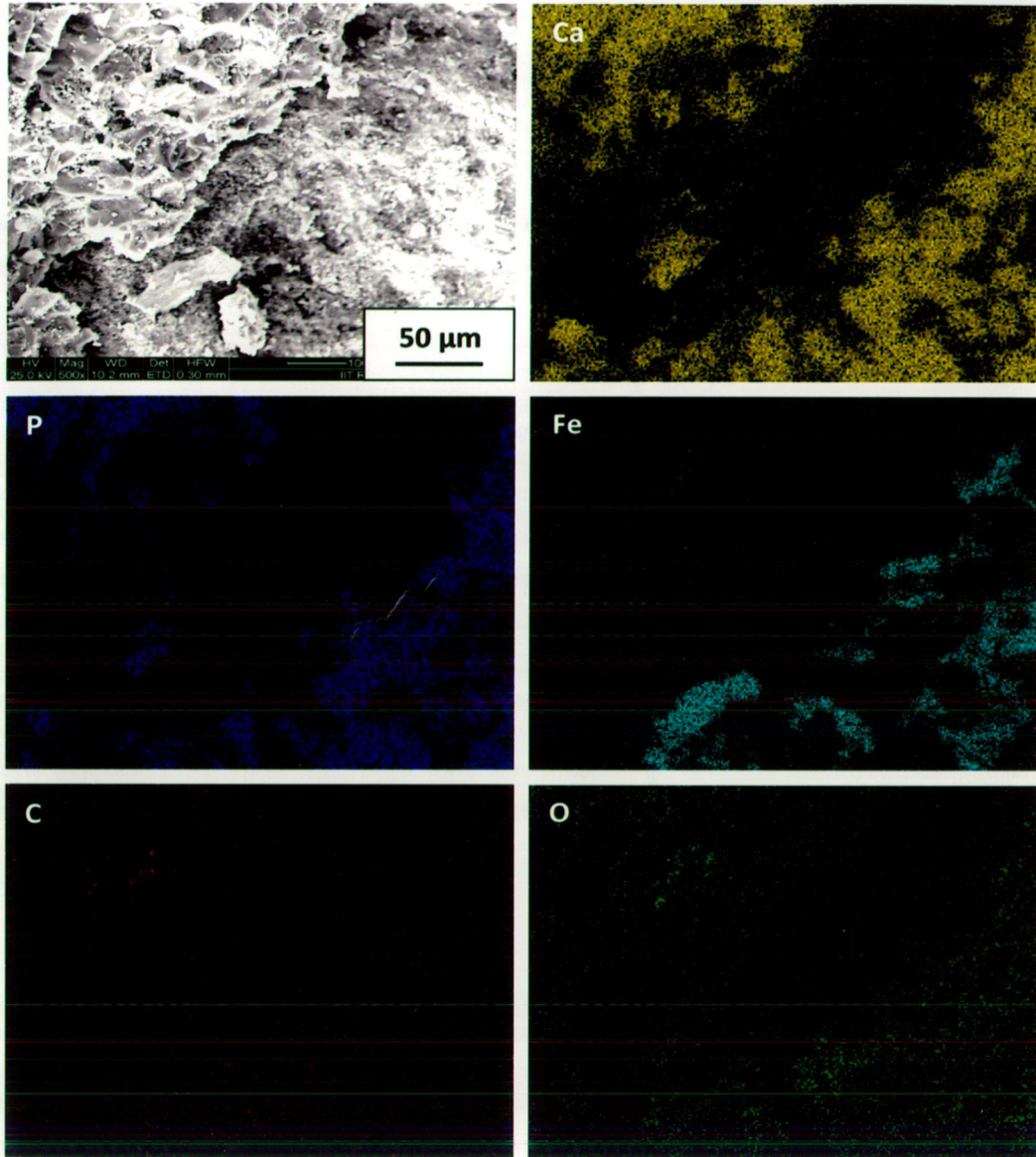


Fig. 5.24 FE-SEM image and X-ray mapping of fractured surface of HA-30 wt% Al₂O₃ coating

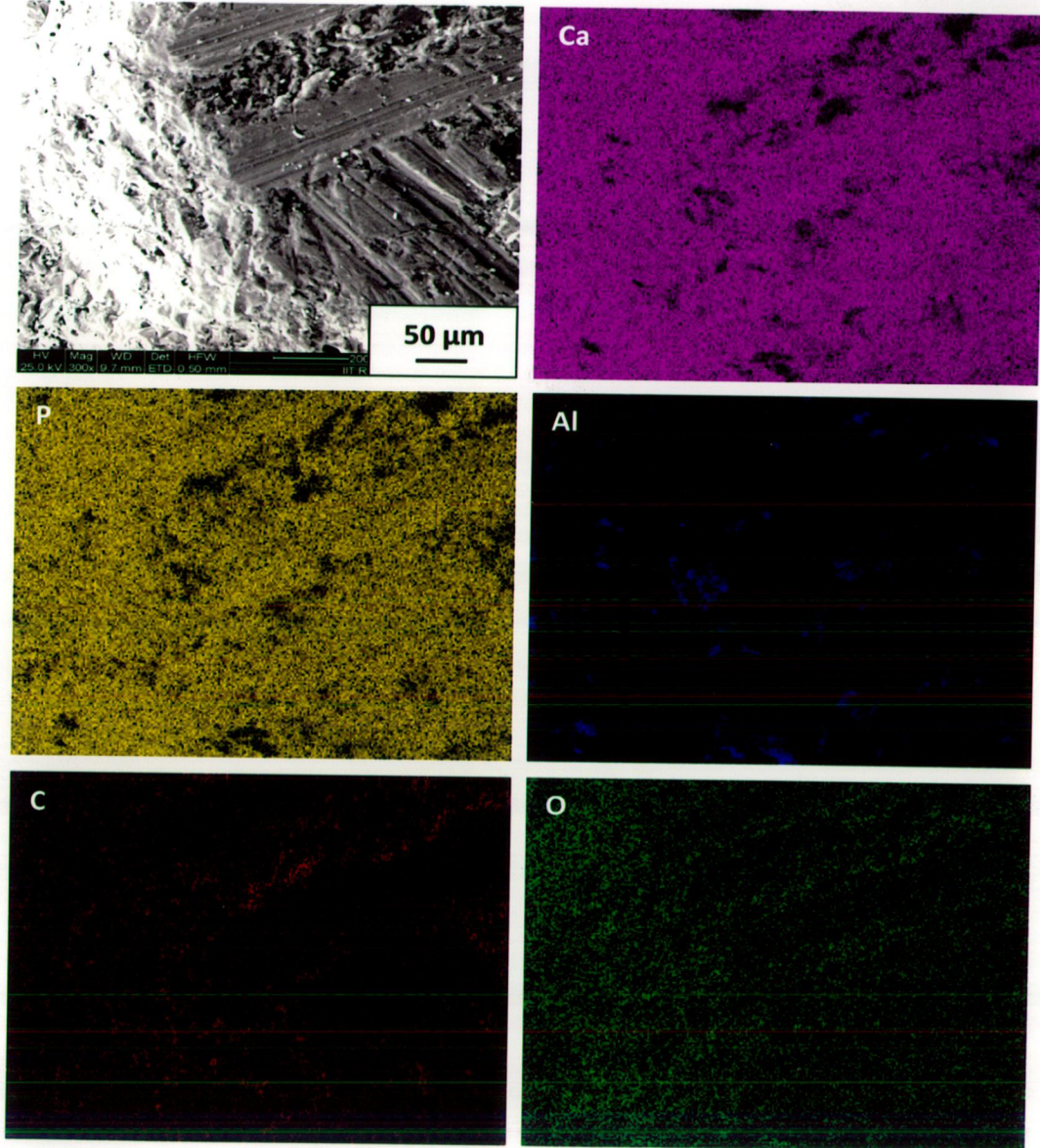


Fig. 5.25 FE-SEM image and X-ray mapping of fractured surface of HA-30 wt% Al₂O₃ coating with Al₂O₃-13 wt% TiO₂ bond coat

Table 5.2 Tensile bond strength of coatings

Coating	Without incorporation of bond coat (MPa)	With incorporation of Al ₂ O ₃ -13 wt% TiO ₂ bond coat (MPa)
Pure HA coating	28.4±2.7	42.1±3.7
HA-10 wt% Al ₂ O ₃ coating	32.7±2.3	49.3±3.9
HA-20 wt% Al ₂ O ₃ coating	38.1±2.6	56.7±4.2
HA-30 wt% Al ₂ O ₃ coating	43.6±2.2	65.4±4.5

Figure 5.24 shows the FE-SEM micrograph along with X-ray mapping of HA-30 wt% Al₂O₃ coating without incorporation of bond coat. The morphology of fractured coating and corresponding X-ray mapping suggests that the failure took place mainly within the coating. The coexistence of constituent of coating (Ca and P) and substrate element (Fe) in lower right region of images suggest that substrate is covered with a very thin layer of coating in this region. The upper right region of micrograph and X-ray mapping suggests that relative thick coating is present in this area.

FE-SEM image along with X-ray mapping of HA-30 wt% Al₂O₃ coating with incorporation of bond coat is shown in Fig. 5.25. It can be seen from the micrograph and corresponding X-ray mapping that the failure took place mainly within the coating. Some patches of Al can be seen in X-ray mapping of Al, whereas black patches between two coating strips (ribbons) and at central right area in micrograph correspond to adhesive as shown in X-ray mapping of carbon.

5.3 DISCUSSION

The weight change plot of coatings against abrasive shows increase in wear resistance of coatings from pure HA to composite coatings, further increase in wear resistance of coating is marked with increase in amount of Al₂O₃ added to hydroxyapatite. The increase in wear resistance of coatings with Al₂O₃ reinforcement might be due to two major factors involved by reinforcing Al₂O₃ to HA. The first factor might be high hardness of aluminum oxide, which resulted in lower wear and second and more predominant might be strengthening and toughening of HA coating with Al₂O₃ reinforcement, which might have made mass removal

more difficult. The wear in plasma sprayed coatings may be caused by different mechanisms, such as abrasion, fracture due to which coating fragments are removed, chipping resulting in wear debris and ploughing, as shown in Fig. 5.3 to Fig. 5.6. The particle removal is found to be mainly due to abrasive wear. The increase in wear resistance of coatings with increase in alumina reinforcement might also be contributed by the increase in hardness of coatings by increase in reinforcement content. The increase of microhardness by increase in Al_2O_3 content of HA coating is shown in plots of microhardness versus distance from interface (Fig. 5.13 to Fig. 5.16). Moreover, it can be seen from these plots that microhardness of substrate near interface is slightly higher (20-25 Hv) as compared to microhardness of substrate away from interface. The increase in hardness of substrate near interface might be due to impact of high speed coating particles during plasma spraying process as suggested by Singh (2003) and Sidhu et al., (2004 and 2005). The hardness of coating near interface is also found to be higher than that at a distance away from the interface. The higher coating hardness near interface might be due to rapid solidification of incoming particles which formed first few lamellae, because metallic substrate acts as heat sink. The findings are similar to the findings of study conducted by Morks et al., (2007) in which they developed HA coatings by gas tunnel plasma spraying process.

Morks, (2008) investigated the abrasive wear behavior of plasma sprayed HA coatings reinforced with 10 and 20 wt% SiO_2 and reported that wear resistance of the coatings increased significantly with increase in SiO_2 content to HA, the results of present investigation in regard to increase in wear resistance of coating by addition of secondary phase are similar to findings of Morks (2008).

In present study, the increase in wear resistance can also be related to increase in hardness of coatings. Morks and Akimoto, (2008) also related the wear behavior of plasma sprayed Al_2O_3 - TiO_2 coatings with hardness of coating. They suggested that increase in hardness resulted in decrease in weight loss of coatings during abrasive wear using SUGA abrasion tester.

The surface roughness of composite coatings is found to increase with addition of Al_2O_3 to HA as shown in Table 5.1. The higher surface roughness of composite coatings is expected to provide relatively small contact area for loading and when combined with counter motion of abrasive against coating, it results in coating fragmentation and deep wear marks. Moreover,

when these fragments come in contact with abrasive, due to three body wear, they get crushed between coating and abrasive resulting in wear debris.

As discussed earlier in Section 5.2.1, the weight loss of coatings is comparatively higher in initial cycles than that for later cycles. This may be attributed to their higher initial surface roughness, since a higher surface roughness brings surface asperities in direct contact with abrasive, which lead to chipping of splats due to direct impact. These asperities separate from coating by fracture when sliding force exceed their fracture strength. The weight loss decreases in later cycles and reaches to almost constant value. Higher weight loss due to higher surface roughness of coating at initial stage and fracture of elevated areas are supported by the findings of Gross and Babovic (2002), when they studied wear behavior of flame sprayed HA coatings with different surface roughness against 6.3 mm diameter bone analogue made from wood. Fu et al., (1998) suggested wear behavior of HA coatings in un-lubricated conditions may be attributed to micro-cracks, pores present in lamellar structure of coating, which facilitates propagation of cracks and generation of wear debris due to fretting wear. Higher wear rate of plasma sprayed fly ash coatings for initial periods as compared to later stage is also reported by Sidhu et al., (2007).

The weight change plot (Fig. 5.2) showing wear resistance between similar coatings show decrease in wear resistance of coatings with increase in content of Al_2O_3 of hydroxyapatite coatings. Wear debris and plastic flow of surface can be seen in Fig. 5.7 to Fig. 5.10. The particle removal in this case is mainly due to adhesive wear. The decrease in wear resistance of coatings with reinforcement might be due to the fact that alumina acts as a weak interface and might be pulled out from HA matrix when it comes in contact with alumina particles present in HA matrix of counter surface. To simulate the actual wear behavior of composite coatings against bone in the body environment, the wear resistance of composite coatings should be evaluated against pure HA pallets, which are very similar to natural bone.

The increase in tensile bond strength of coatings (without bond coat) with increase in Al_2O_3 content to HA might be due to increase in area of cohesive failure with increase in Al_2O_3 content to HA as shown in Fig. 5.17a-d and presented in Table 5.2. It can be seen from Fig. 5.17e-h (macrographs of failed specimens with bond coat) that area of cohesive failure

decreased for HA-10 wt% Al₂O₃ (Fig. 5.17e) coating as compared to HA coating (Fig. 5.17f), whereas it slightly increased for HA-20 wt% Al₂O₃ coatings (Fig. 5.17g). The area of cohesive failure is more in case of HA-30 wt% Al₂O₃ coatings (Fig. 5.17h); moreover part of substrate can also be seen in this case.

In present study the increase in tensile bond strength of coatings with increase in Al₂O₃ content might be due to strengthening of the HA-Al₂O₃ matrix and reduction in coefficient of thermal expansion of HA by alumina reinforcement. Increase in bonding strength of HA-Al₂O₃-CaF₂ composite coating as compared to HA coating developed on Ti-6Al-4V by cold pressing and sintering had been reported by Evis and Doremus, (2005), they suggested matching of thermal expansion coefficient of ceramic coating and metallic substrate improved the bonding and minimized crack formation, further reduction in coefficient of thermal expansion of HA by addition of alumina particulates and bringing it near to that of Ti-6Al-4V have been reported.

In present investigation bond coat is found to be more favorable factor in increasing the tensile bond strength of coatings. In a study carried out by Yilmaz, (2009) on plasma sprayed Al₂O₃ and Al₂O₃-13 wt% TiO₂ with and without bond coat of Ni-5 wt% Al₂O₃ on titanium, significant increase in bonding strength was reported in coatings with bond coat. The reason attributed to increase in bonding strength of coatings with bond coat was attributed to compensation of thermal expansion mismatch between coating and substrate and coarser surface of bond coat, which might provided better interlocking to the top coat. The similar findings are reported by Zheng et al., (2000) for HA-Ti composite coatings and by Li et al., (2009) for HA-YSZ composite coatings with ZrO₂ bond coat. Li et al., (2009) reported that coating was more prone to fail at coating bond coat interface due to partial compensating coefficient of thermal expansion of HA and metallic substrate by incorporation of ZrO₂ bond coat. The increase in tensile bond strength of coating by incorporation of bond coat and addition of alumina to HA in present investigation matches the findings of Yilmaz, (2009), Zheng et al., (2000) and Li et al., (2009).

Goller, (2004) deposited bioglass onto titanium substrate with bond coat of Al₂O₃-40 wt% TiO₂ by plasma spraying and reported increase in bonding strength of coating with bond coat as compared to coating without bond coat. Oktar et al., (2006) deposited HA with Al₂O₃-40

wt% TiO₂ bond coat by plasma spraying process and suggested that by using bond coat the difference in thermal properties of substrate and top coat substantially reduced, which led to increase in bonding strength of coating with bond coat. Chou and Chang (2002A) found increase in bond strength of plasma sprayed pure HA coating with ZrO₂ bond coat as compared to pure HA and HA-10 wt% ZrO₂ coatings without bond coat. The results obtained in present investigation are quite similar to findings of Oktar et al., (2006) and Chou and Chang, (2002A).

5.4 CONCLUSIONS

The mechanical properties such as wear resistance, hardness and tensile bond strength of plasma sprayed HA coatings with varying aluminum oxide content (0-30 wt% with increment of 10 wt%) were studied and detailed results are presented in current Chapter of this study. The conclusions drawn are presented hereunder:

1. Wear resistance of plasma sprayed coatings against abrasive (SiC) increased with increase in Al₂O₃ content of HA composite coating (maximum cumulative weight loss of 47.9 mg/cm² for pure HA coatings and minimum of 15.8 mg/cm² for HA-30 wt% Al₂O₃ coatings), which might be due to increase in hardness by increase in alumina content to HA. Hence alumina can be used as reinforcing agent to HA to increase wear resistance of coatings.
2. Wear resistance between the similar coatings was found to decrease with increase in Al₂O₃ content of HA composite coating. The minimum cumulative weight loss of 44.5 mg/cm² was measured for pure HA coatings and maximum of 68.5 mg/cm² was measured for HA-30 wt% Al₂O₃ coatings.
3. Coating fragments, surface ploughing and surface smoothening was observed in surface morphology of coatings obtained after abrasive wear. Plastic flow was recorded in surface morphology of coatings obtained after wear between the similar coatings.
4. Hardness of coatings as measured by nano-indentation was observed to increase with increase in Al₂O₃ content to HA with highest hardness near substrate coating interface. The hardness of bond coat (580 to 610 Hv) was found to be higher than all the coatings.

- Alumina can be reinforced to HA to increase hardness of plasma sprayed HA-Al₂O₃ composite coatings.
5. The hardness of coatings as well as substrate was found to be highest near substrate-coating interface for all substrate-coating combination. This might be due to fast cooling rate of incoming splats at substrate.
 6. The tensile bonding strength of coatings was found to increase (28.4 MPa to 43.6 MPa) with increase in alumina content (0-30 wt%) of HA composite coating, whereas bond coat showed significant effect in increasing the tensile bonding strength of coatings with 42.1 MPa for pure HA coating and 65.4 MPa for HA-30 wt% Al₂O₃ coatings . Therefore, to increase the tensile bond strength of coatings bond coats are more appropriate than reinforcement of secondary phase.

ANALYSIS OF COATINGS IN SIMULATED BODY FLUID

This chapter deals with the results and discussion of electrochemical behavior and in-vitro studies of plasma sprayed pure hydroxyapatite (HA: $\text{Ca}_{10}(\text{PO}_4)_6(\text{OH})_2$), HA-10 wt% aluminum oxide (alumina: Al_2O_3), HA-20 wt% aluminum oxide and HA-30 wt% aluminum oxide coatings in simulated body fluid (SBF).

6.1 INTRODUCTION

In the present chapter electrochemical behavior and in-vitro studies of plasma sprayed coatings has been described. It includes the results related to open circuit potential (OCP), linear polarization, potentiodynamic polarization and Tafel polarization of coated and bare specimens in simulated body fluid (SBF). The detailed technique and composition of reagents for preparation of SBF is given in Chapter 3 of present study. The biocompatibility of coated specimens was studied by in-vitro examination in SBF for immersion period of 5, 10, 15 and 20 days at a controlled temperature of $37\pm 1^\circ\text{C}$. The SBF was examined using inductively coupled plasma mass spectroscopy (IC-PMS) for Ca^{2+} ion concentration before and after immersion of coated specimens for designated period. The specimens after immersion were gently rinsed with double distilled water and dried at room temperature. Specimens were weighted before and after immersion using electronic weighing scale with an accuracy of 0.1 mg. The weight change (weight gain or weight loss) is plotted against immersion period. SEM/EDAX, XRD and FTIR were utilized for examining the specimens after immersion.

6.2 RESULTS

6.2.1 Open Circuit Potential (OCP) Measurement

Open circuit potential of uncoated and plasma sprayed specimens was measured in simulated body fluid. The specimens were immersed in electrochemical cell filled with SBF and OCP was measured for 30 min in 'cell off' mode. The measurement was started as soon as specimens were immersed to avoid localized corrosion. The plot of OCP versus time for

coatings on AISI 316L SS and titanium are shown in Fig. 6.1 and Fig. 6.2 respectively. The average values of open circuit potentials obtained from this curves are presented in Table 6.1. The maximum value of OCP of -153 mV (for AISI 316L SS substrate) was obtained for HA-30 wt% Al₂O₃ coating, whereas maximum value of OCP of -128 mV (for titanium substrate) was obtained for HA-10 wt% Al₂O₃ coating.

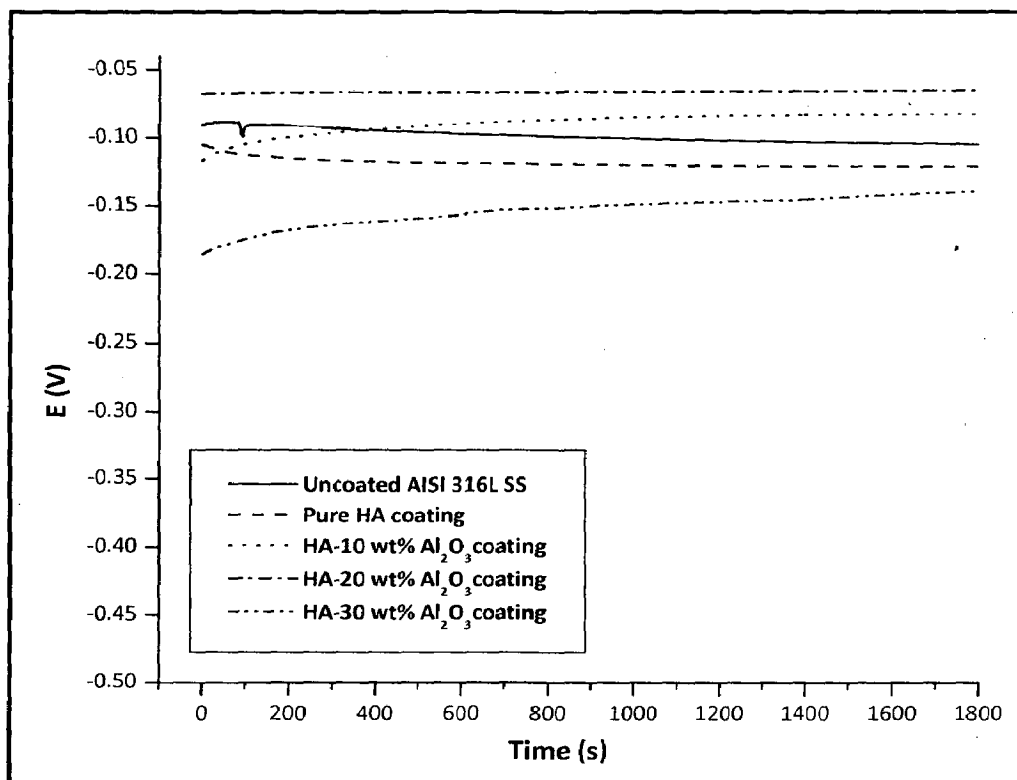


Fig. 6.1 Open circuit potential curves for uncoated and coated AISI 316L SS

Table 6.1 Open circuit potential (mV) of uncoated and coated specimens

Coatings Substrate	Uncoated	Pure HA coating	HA-10 wt% Al ₂ O ₃ coating	HA-20 wt% Al ₂ O ₃ coating	HA-30 wt% Al ₂ O ₃ coating
AISI 316L SS	-98 mV	-118 mV	-88 mV	-66 mV	-153 mV
Titanium	-72 mV	-62 mV	-128 mV	-111 mV	-94 mV

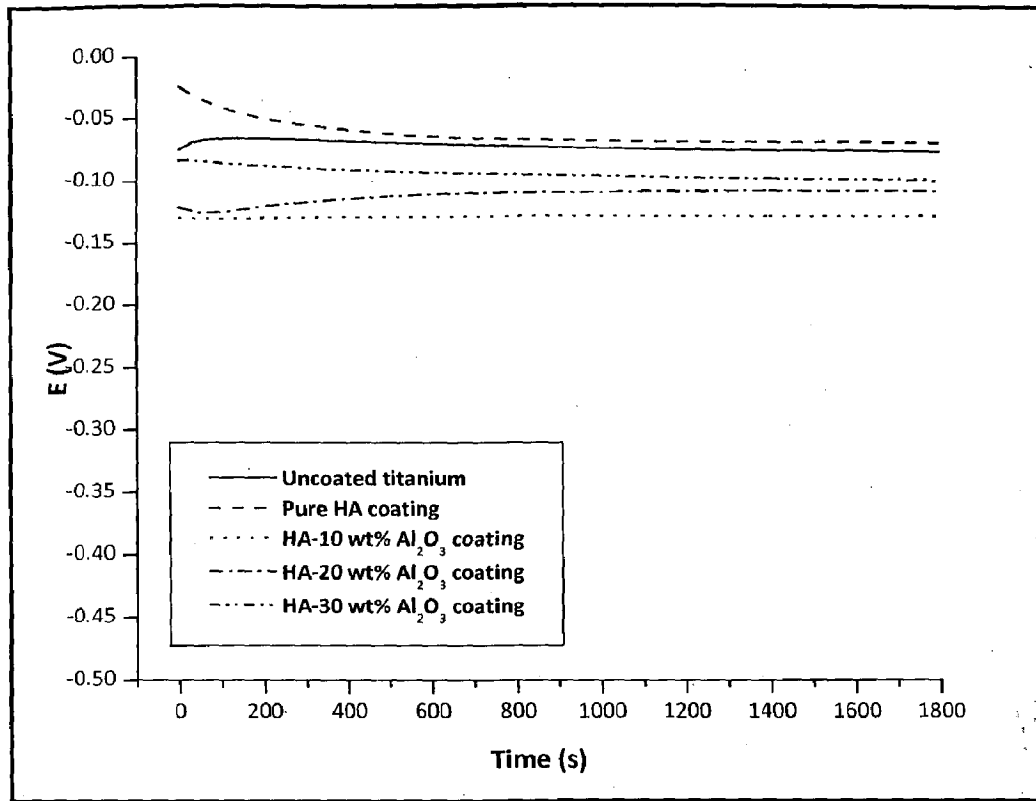


Fig. 6.2 Open circuit potential curves for uncoated and coated titanium

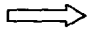

6.2.2 Linear Polarization Experiments

Linear polarization tests were conducted in SBF at room temperature in order to evaluate corrosion behavior of uncoated and coated specimens. The linear polarization resistance (LPR) and corrosion current density was measured using linear polarization tests in SBF. In linear polarization tests, a small range of potential (-20 mV to +20 mV versus OCP) is applied, which does not damage the exposed surface of specimen. The corrosion data obtained from linear polarization test conducted on uncoated and coated AISI 316L SS is presented in Table 6.2. The rate of corrosion of uncoated and coated specimens is obtained using Stern-Geary equation (Eq. 6.1).

$$i_{corr} = \frac{1}{2.303} \times \frac{\beta_a \beta_c}{R_p \times (\beta_c + \beta_a)} = \frac{Z}{R_p} \quad (6.1)$$

Where, β_a and β_c are anodic and cathodic slopes, R_p is polarization resistance and i_{corr} is corrosion current density.

Table 6.2 Results of linear polarization test of uncoated and coated AISI 316L SS

Parameters 	E_{corr} (mV)	i_{corr} ($\mu\text{A}/\text{cm}^2$)	β_a (V/decade)	β_c (V/decade)	R_p ($\text{k}\Omega\text{-cm}^2$)
Substrate/coating 					
AISI 316L SS	-126	0.245	0.12	0.12	106
Pure HA coating	-142	0.00542	0.12	0.12	4797
HA-10 wt% Al_2O_3 coating	-103	0.00735	0.12	0.12	3538
HA-20 wt% Al_2O_3 coating	-152	0.0234	0.12	0.12	1112
HA-30 wt% Al_2O_3 coating	-85	0.076	0.12	0.12	342

The corrosion current density i_{corr} of all coatings is found to be lesser than uncoated AISI 316L SS and titanium as indicated by linear polarization test results in terms of current density and polarization resistance (Table 6.2 and 6.3). However, the corrosion current densities of reinforced HA coatings are slightly higher than pure HA coating.

The corrosion data obtained from linear polarization test conducted on uncoated and coated titanium is presented in Table 6.3. The corrosion current density of uncoated titanium is substantially lower than uncoated AISI 316L SS. However, coatings on titanium substrate show a similar trend (Table 6.3) as shown by coatings on AISI 316L SS. This suggests that the coatings did not allow the penetration of electrolyte through them. The lower corrosion rate of the coated specimens means less severe invasion to human body due to reduced metallic ions released from the metallic implant. Therefore, the smaller corrosion current densities (i_{corr}) of coatings indicate that the coatings would have a better biocompatibility than the uncoated AISI 316L SS and titanium.

Table 6.3 Results of linear polarization test of uncoated and coated titanium

Parameters \rightarrow	E_{corr} (mV)	i_{corr} ($\mu\text{A}/\text{cm}^2$)	β_a (V/decade)	β_c (V/decade)	R_p ($\text{k}\Omega\text{-cm}^2$)
Substrate/coating \downarrow					
Titanium	-88	0.083	0.12	0.12	314
Pure HA coating	-131	0.00534	0.12	0.12	4864
HA-10 wt% Al_2O_3 coating	-148	0.00695	0.12	0.12	3740
HA-20 wt% Al_2O_3 coating	-130	0.00629	0.12	0.12	4129
HA-30 wt% Al_2O_3 coating	-119	0.0254	0.12	0.12	1024

6.2.3 Potentiodynamic Polarization Experiments

Potentiodynamic polarization curves of uncoated and coated AISI 316L SS and titanium specimens are shown in Fig. 6.3 and Fig. 6.4 respectively. The data obtained from potentiodynamic tests for plasma sprayed AISI 316L SS and titanium is presented in Table 6.4 and Table 6.5 respectively. From polarization tests the percentage protection offered by coatings, (Protective efficiency (P_i)) has been calculated using Eq. 6.2. as proposed by Yoo et al., (2008).

$$P_i(\%) = \left[1 - \left(\frac{i_{corr}}{i_{corr}^o} \right) \right] \times 100 \quad (6.2)$$

Where, i_{corr} and i_{corr}^o are corrosion current density of coating and substrate respectively.

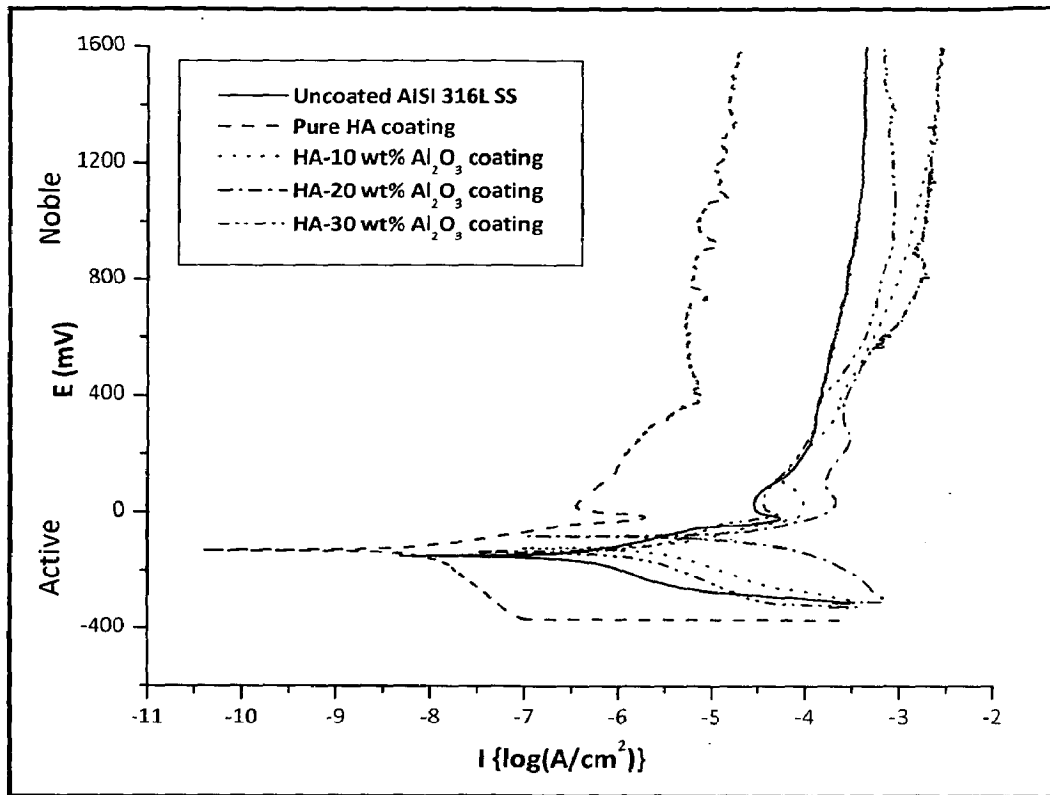


Fig. 6.3 Potentiodynamic polarization curves for uncoated and coated AISI 316 L SS

It can be seen from the results that pure HA coatings are most protective with corrosion current density of $0.0085 \mu\text{A}/\text{cm}^2$ and $0.0091 \mu\text{A}/\text{cm}^2$ for HA coatings on AISI 316L SS and titanium substrate respectively. Moreover, all the coatings have lesser corrosion current density as compared to uncoated substrates. The results obtained from potentiodynamic polarization tests are comparable with results obtained from linear polarization tests. Protective efficiency is a relative measurement of corrosion current density of coatings to that of substrate. The protective efficiency of coatings is presented in Table 6.3 and 6.4 for coatings on AISI 316L SS and titanium respectively. It can be seen from the results that protective efficiency is maximum for pure HA coatings on both the substrates.

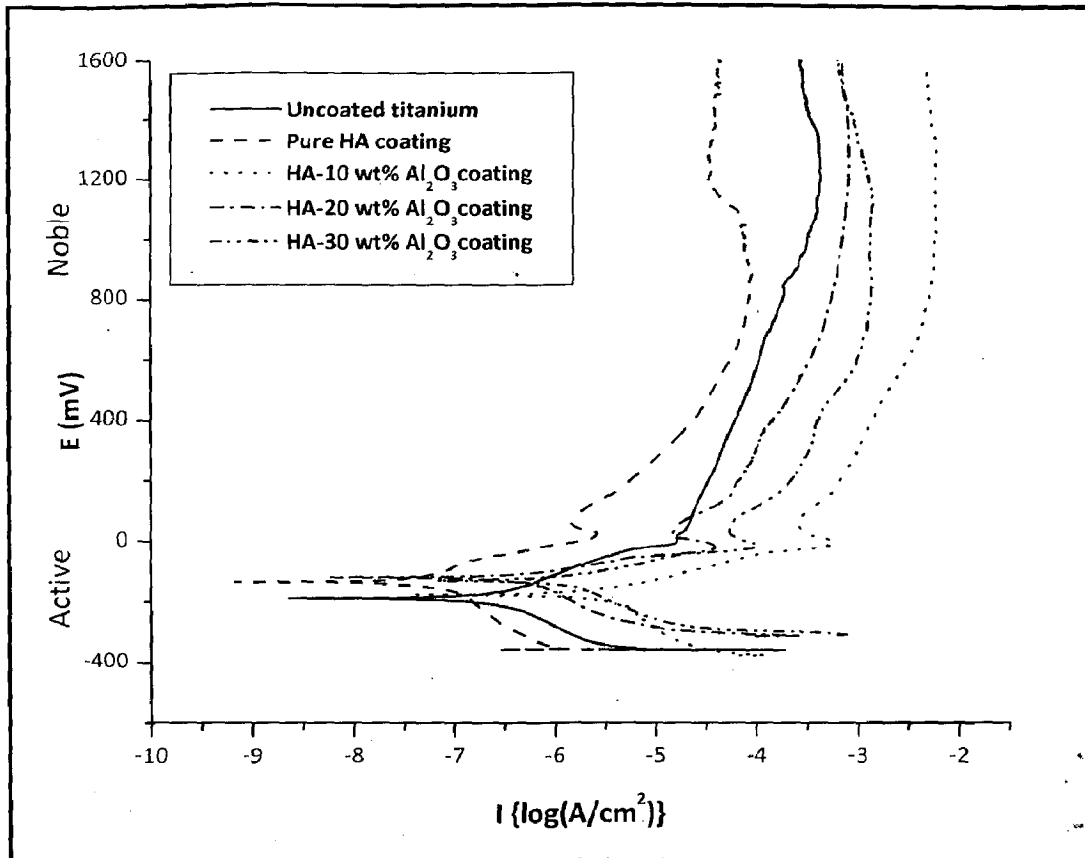


Fig. 6.4 Potentiodynamic polarization curves for uncoated and coated titanium

Table 6.4 Results of potentiodynamic polarization test of uncoated and coated AISI 316L SS

Substrate/coating	E_{corr} (mV)	i_{corr} ($\mu\text{A}/\text{cm}^2$)	β_a (V/decade)	β_c (V/decade)	R_p ($\text{k}\Omega\text{-cm}^2$)	P_i
AISI 316L SS	-148	0.233	0.0523	0.0773	5.81	---
Pure HA coating	-132	0.0085	0.0611	0.2422	249.55	96.35
HA-10 wt% Al_2O_3 coating	-125	0.0306	0.8424	0.1302	61.26	73.39
HA-20 wt% Al_2O_3 coating	-80	0.0285	0.1095	0.1014	80.16	87.76
HA-30 wt% Al_2O_3 coating	-137	0.0259	0.1324	0.1752	125.97	89.70

Table 6.5 Results of potentiodynamic polarization test of uncoated and coated titanium

Substrate/coating	E_{corr} (mV)	i_{corr} ($\mu\text{A}/\text{cm}^2$)	β_a (V/decade)	β_c (V/decade)	R_p ($\text{k}\Omega\text{-cm}^2$)	P_i
Titanium	-188	0.0693	0.0972	0.2329	42.96	---
Pure HA coating	-131	0.0091	0.06	0.2403	228.34	86.82
HA-10 wt% Al_2O_3 coating	-177	0.0304	0.0896	0.1942	87.61	56.13
HA-20 wt% Al_2O_3 coating	-120	0.0373	0.0539	0.1257 ^a	43.93	46.19
HA-30 wt% Al_2O_3 coating	-131	0.0539	0.0741	0.093	33.3	22.38

6.2.4 Tafel Polarization Experiments

Tafel polarization plots for uncoated and coated AISI 316L SS and titanium specimens are shown in Fig. 6.5 and Fig. 6.6 respectively. The corrosion data obtained from Tafel polarization tests for plasma sprayed AISI 316L SS and titanium is presented in Table 6.6 and Table 6.7 respectively. It can be seen from the results that pure HA coatings are most protective with corrosion current density of $0.0067 \mu\text{A}/\text{cm}^2$ and $0.0112 \mu\text{A}/\text{cm}^2$ for HA coatings on AISI 316L SS and titanium substrate respectively.

Moreover, all the coatings have lesser corrosion current density as compared to uncoated substrates. The results obtained from Tafel polarization tests are comparable with results obtained from linear polarization and potentiodynamic polarization tests. The protective efficiency of coatings is presented in Table 6.5 and 6.6 for coatings on AISI 316L SS and titanium respectively. As the corrosion current density of pure HA coatings is least out of all coatings on both the substrates, it can be seen from the results that protective efficiency is maximum for pure HA coatings on both the substrates.

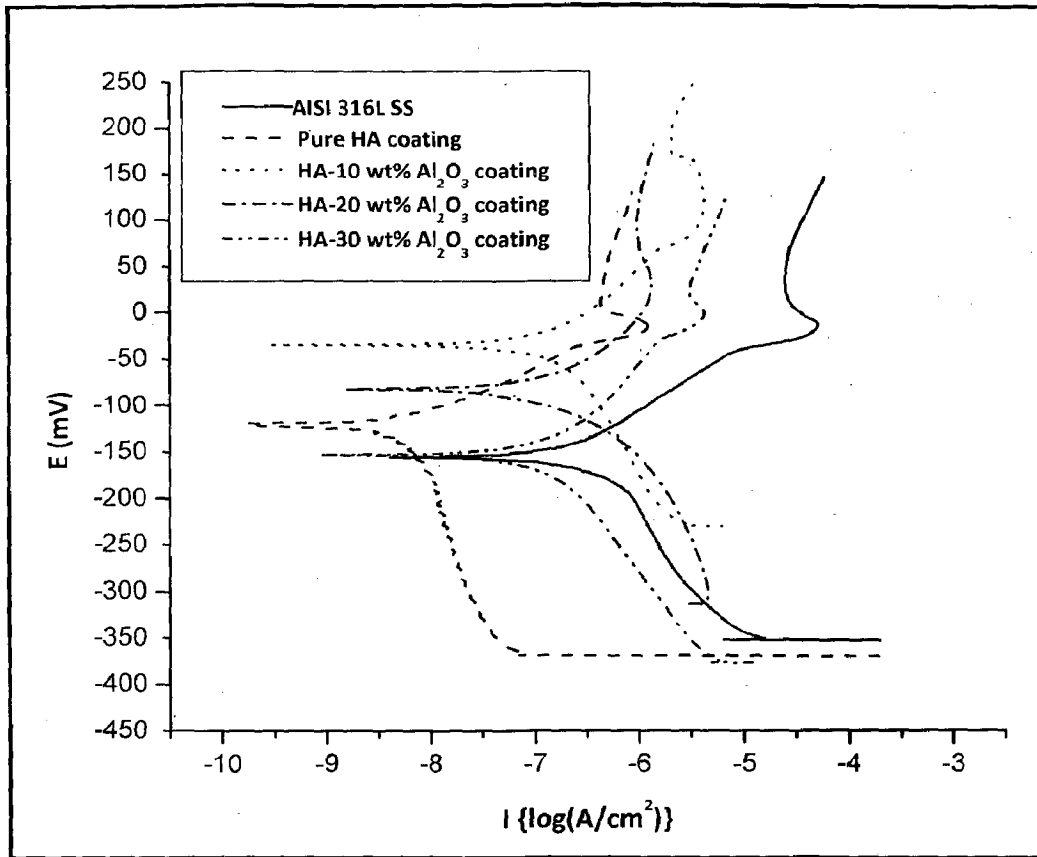


Fig. 6.5 Tafel plot for uncoated and coated AISI 316L SS

Table 6.6 Results of Tafel polarization test of uncoated and coated AISI 316L SS

Substrate/coating	E _{corr} (mV)	i _{corr} ($\mu\text{A}/\text{cm}^2$)	β_a (V/decade)	β_c (V/decade)	R _p ($\text{k}\Omega\text{-cm}^2$)	Pi
AISI 316L SS	-156	0.264	0.0804	0.1422	84.37	---
Pure HA coating	-120	0.0067	0.0493	0.3593	2805.2	97.46
HA-10 wt% Al ₂ O ₃ coating	-35	0.0347	0.1206	0.2023	944.53	86.84
HA-20 wt% Al ₂ O ₃ coating	-83	0.0309	0.0877	0.0805	588.36	88.27
HA-30 wt% Al ₂ O ₃ coating	-154	0.0244	0.1226	0.1656	1252.9	90.75

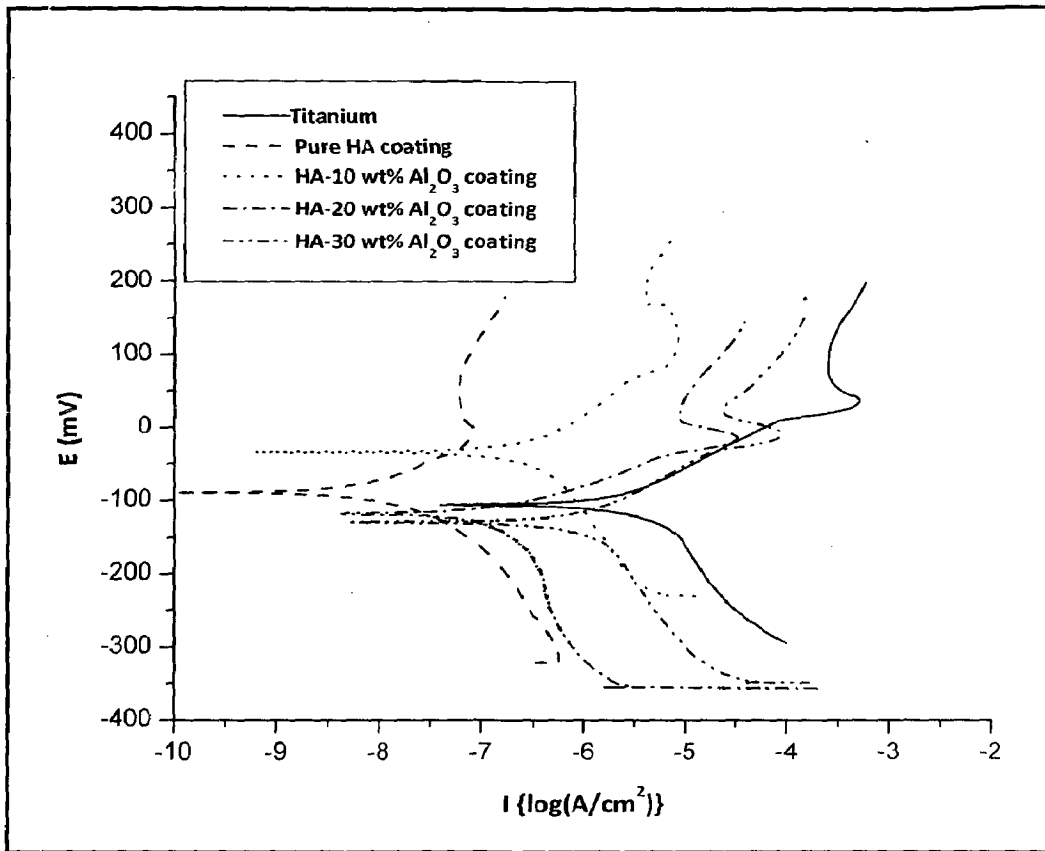


Fig. 6.6 Tafel plot for uncoated and coated titanium

Table 6.7 Results of Tafel polarization test of uncoated and coated titanium

Substrate/coating	E_{corr} (mV)	i_{corr} ($\mu\text{A}/\text{cm}^2$)	β_a (V/decade)	β_c (V/decade)	R_p ($\text{k}\Omega\text{-cm}^2$)	P_i
Titanium	-106	0.0724	0.0253	0.0872	117.6	---
Pure HA coating	-88	0.0112	0.2217	0.0637	1925.3	84.59
HA-10 wt% Al_2O_3 coating	-34	0.0292	0.2132	0.0914	927.8	59.61
HA-20 wt% Al_2O_3 coating	-120	0.0313	0.0480	0.3229	580.4	56.81
HA-30 wt% Al_2O_3 coating	-130	0.0344	0.0853	0.1933	747.3	52.50

Immersion Behavior of Coatings in Simulated Body Fluid

The coated titanium specimens were immersed in simulated body fluid (SBF) for a period of 5, 10, 15 and 20 days at controlled temperature of $37\pm 1^\circ\text{C}$. The specimen were removed from SBF after designated period of immersion, gently rinsed with double distilled water and dried at room temperature and weighed with accuracy of 0.1 mg. The plots for weight change versus immersion period for pure HA, HA-10 wt% Al_2O_3 , HA-20 wt% Al_2O_3 and HA-30 wt% Al_2O_3 are shown in Fig. 6.7 to Fig. 6.10 respectively. The calcium ion concentration of SBF after removal of immersed specimens was measured using ICP-MS. The Ca^{2+} ion concentration is plotted against time of immersion. The plots for Ca^{2+} ion concentration plots for pure HA, HA-10 wt% Al_2O_3 , HA-20 wt% Al_2O_3 and HA-30 wt% Al_2O_3 are shown in Fig. 6.7 to Fig. 6.10 respectively. The initial Ca^{2+} ion concentration in starting SBF was 655 ppm as measured using ICP-MS.

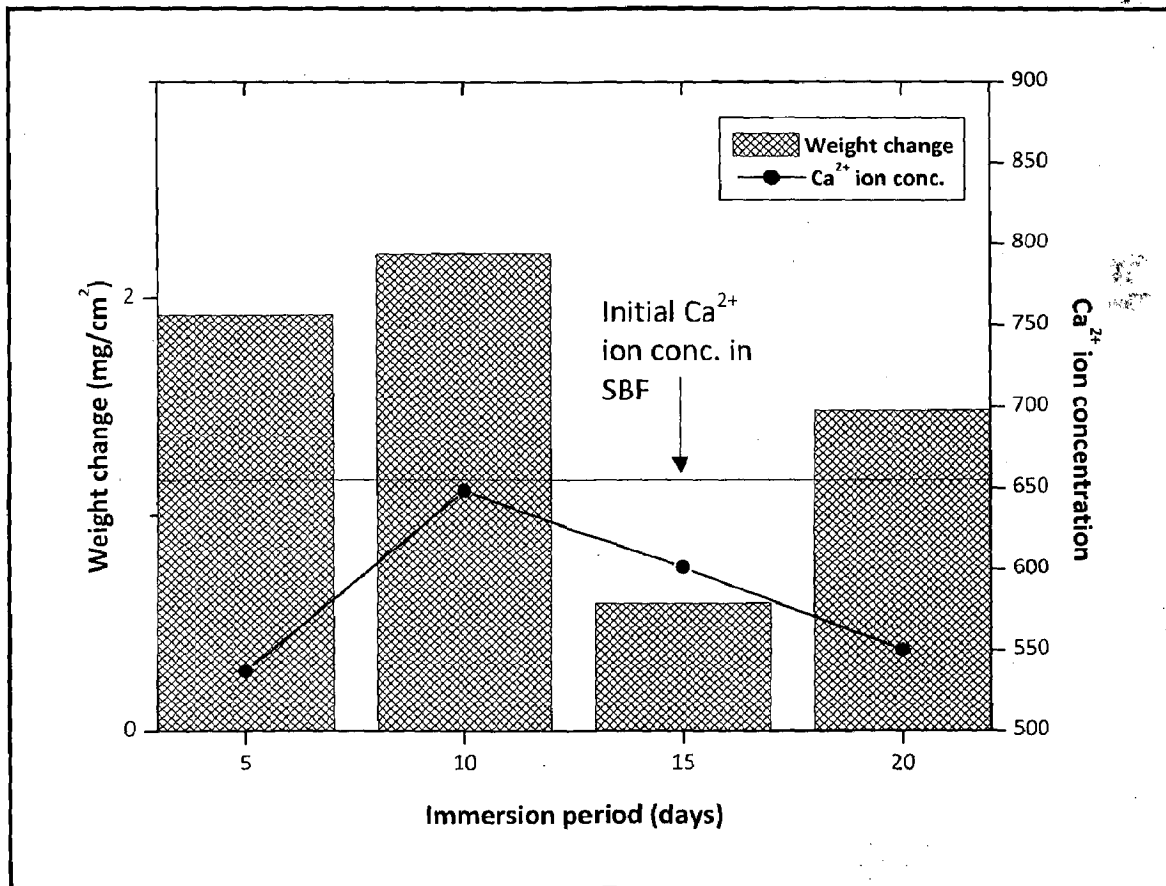


Fig. 6.7 Weight change (mg/cm^2) and Ca^{2+} ion concentration (ppm) versus immersion period for pure HA coatings

It can be seen from Fig. 6.7 that pure HA coatings gained weight after immersion in SBF for all time spans. The maximum weight gain of 2.2 mg/cm² had been recorded after immersion period of 10 days, whereas a minimum weight gain of 0.6 mg/cm² had been recorded after immersion period of 15 days. The calcium ion concentration in SBF after all immersion periods was found to be lesser than Ca²⁺ ion concentration in starting SBF (655 ppm). However, an increasing trend in Ca²⁺ ion concentration was observed for immersion period of 5 to 10 days, whereas it was found to decrease with further increase in immersion period.

The immersion behavior of HA-10 wt% Al₂O₃ coatings is shown in Fig. 6.8. It can be seen that the weight of specimen increased for immersion period of 5, 15 and 20 days, whereas the weight of specimen after immersion period of 10 days had been found to decrease as compared to original weight of specimen. The reduction in weight might be due to dissolution of amorphous phases of calcium and phosphate.

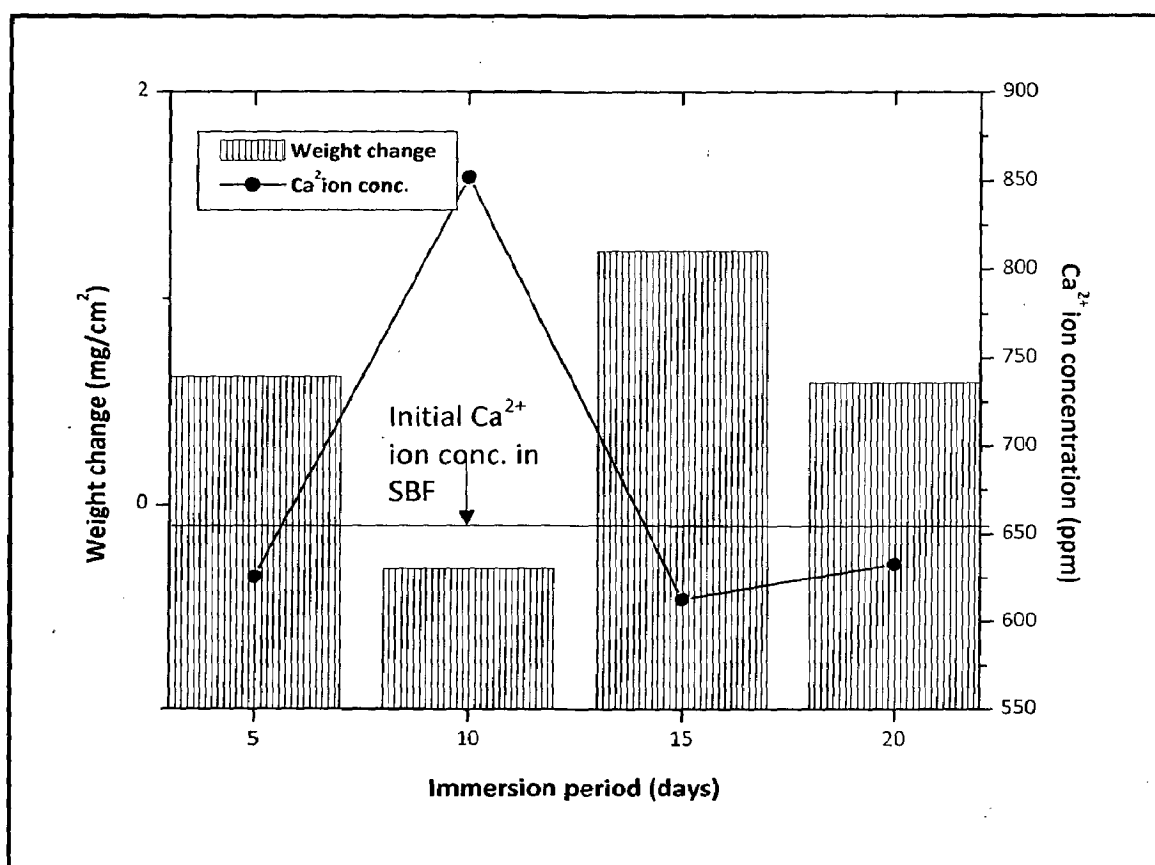


Fig. 6.8 Weight change (mg/cm²) and Ca²⁺ ion concentration (ppm) versus immersion period for HA-10 wt% Al₂O₃ coatings

The plot of Ca^{2+} ion concentration versus immersion period for HA-10 wt% Al_2O_3 coatings (Fig. 6.8) shows increase in Ca^{2+} ion concentration as compared to that of starting SBF for immersion period of 10 days, whereas it decreased for immersion period of 5, 15 and 20 days. The maximum Ca^{2+} ion concentration (851.8 ppm) for immersion period of 10 days correspond to 0.3 mg/cm^2 weight loss of coated specimen has been recorded. The weight loss due to dissolution of amorphous phases might have increased Ca^{2+} ion concentration in SBF. A relative decrease in Ca^{2+} concentration can be seen from the Fig. 6.8 for immersion period of 5, 15 and 20 days.

The HA-20 wt% Al_2O_3 coatings indicate decrease in weight for immersion period of 5 and 20 days, whereas increase in weight has been recorded for immersion period of 15 days as shown in Fig. 6.9.

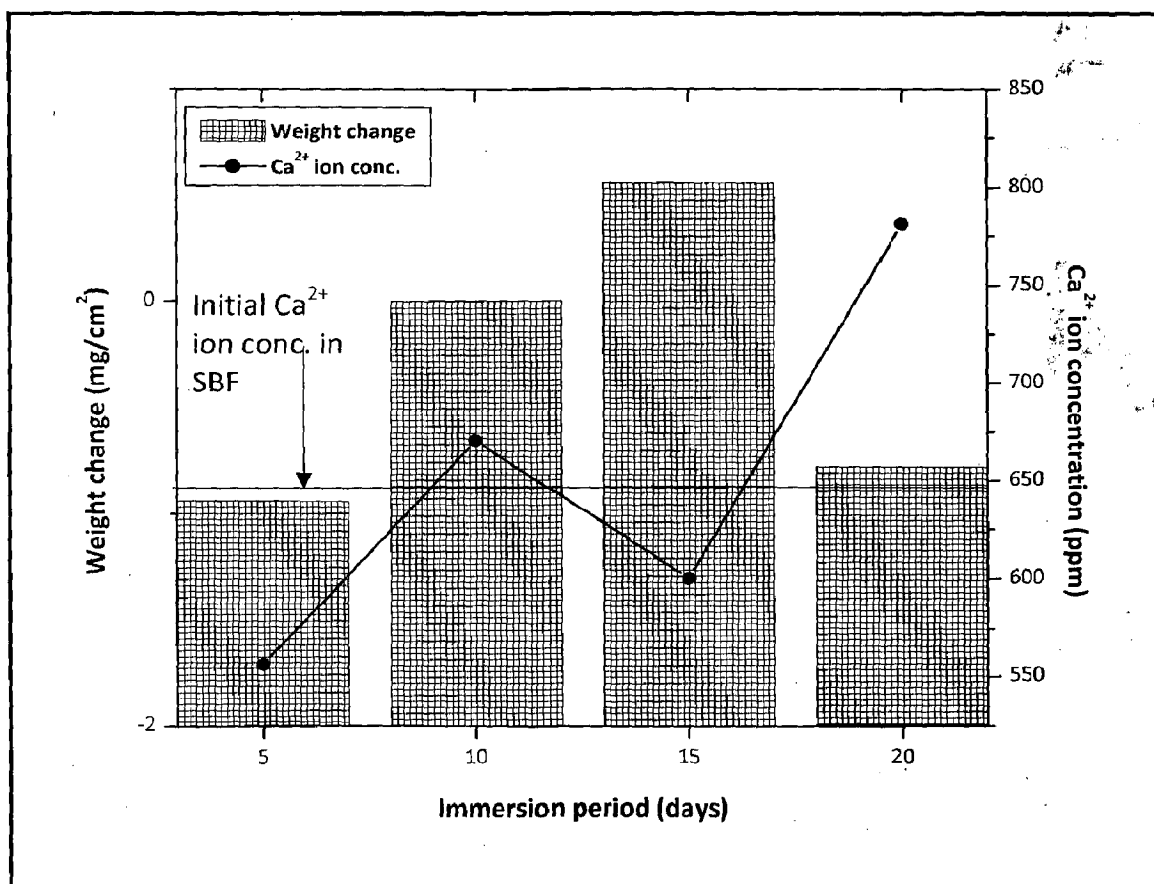


Fig. 6.9 Weight change (mg/cm^2) and Ca^{2+} ion concentration (ppm) versus immersion period for HA-20 wt% Al_2O_3 coatings

No weight change of specimens has been observed for immersion period of 10 days. The Ca^{2+} ion concentration in SBF was found to decrease for immersion period of 15 days as compared to that of starting SBF, whereas it increased for immersion period of 5, 10 and 20 days as compared to Ca^{2+} ion concentration in starting SBF.

The immersion behavior of HA-30 wt% Al_2O_3 coatings in SBF is shown in Fig. 6.10. It can be observed that weight is gained by the coatings for all immersion periods with maximum weight gain (2.27 mg/cm^2) for coatings immersed for 20 days and minimum weight gain (1.24 mg/cm^2) for coatings immersed for 10 days. The Ca^{2+} ion concentration in SBF was recorded lesser for immersion period of 5, 10 and 20 days as compared to Ca^{2+} ion concentration in starting SBF, whereas it was higher for immersion period of 15 days.

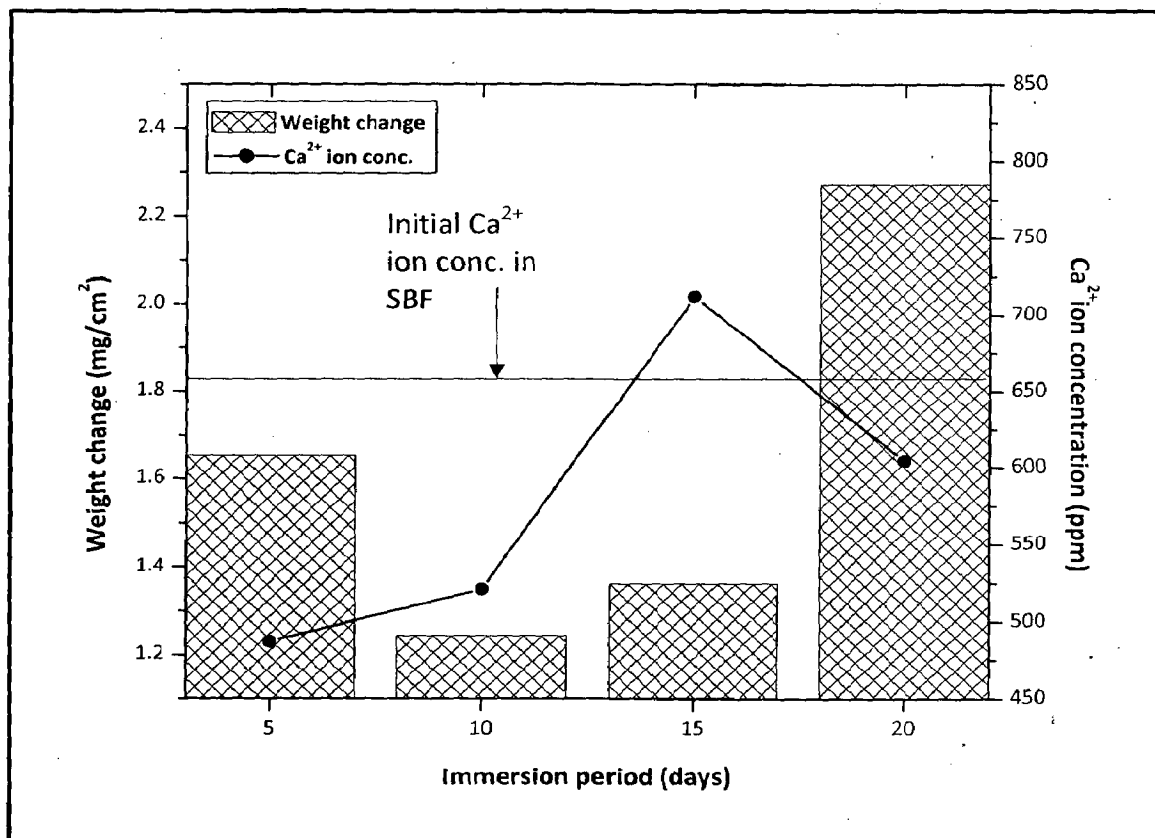


Fig. 6.10 Weight change (mg/cm^2) and Ca^{2+} ion concentration (ppm) versus immersion period for HA-30 wt% Al_2O_3 coatings

6.2.5.1 FE-SEM analysis of coatings after immersion in SBF

To analyze surface morphology of specimens after immersion in SBF some of the coated specimens after immersion test were subjected to field emission scanning electron microscopy. The surface morphology of HA, HA-10 wt% Al₂O₃, HA-20 wt% Al₂O₃ and HA-30 wt% Al₂O₃ coatings after immersion in SBF at 37±1°C for a period of 1, 5, 10, 15 and 20 days at different magnifications is shown in Fig. 6.11 to Fig. 6.31.

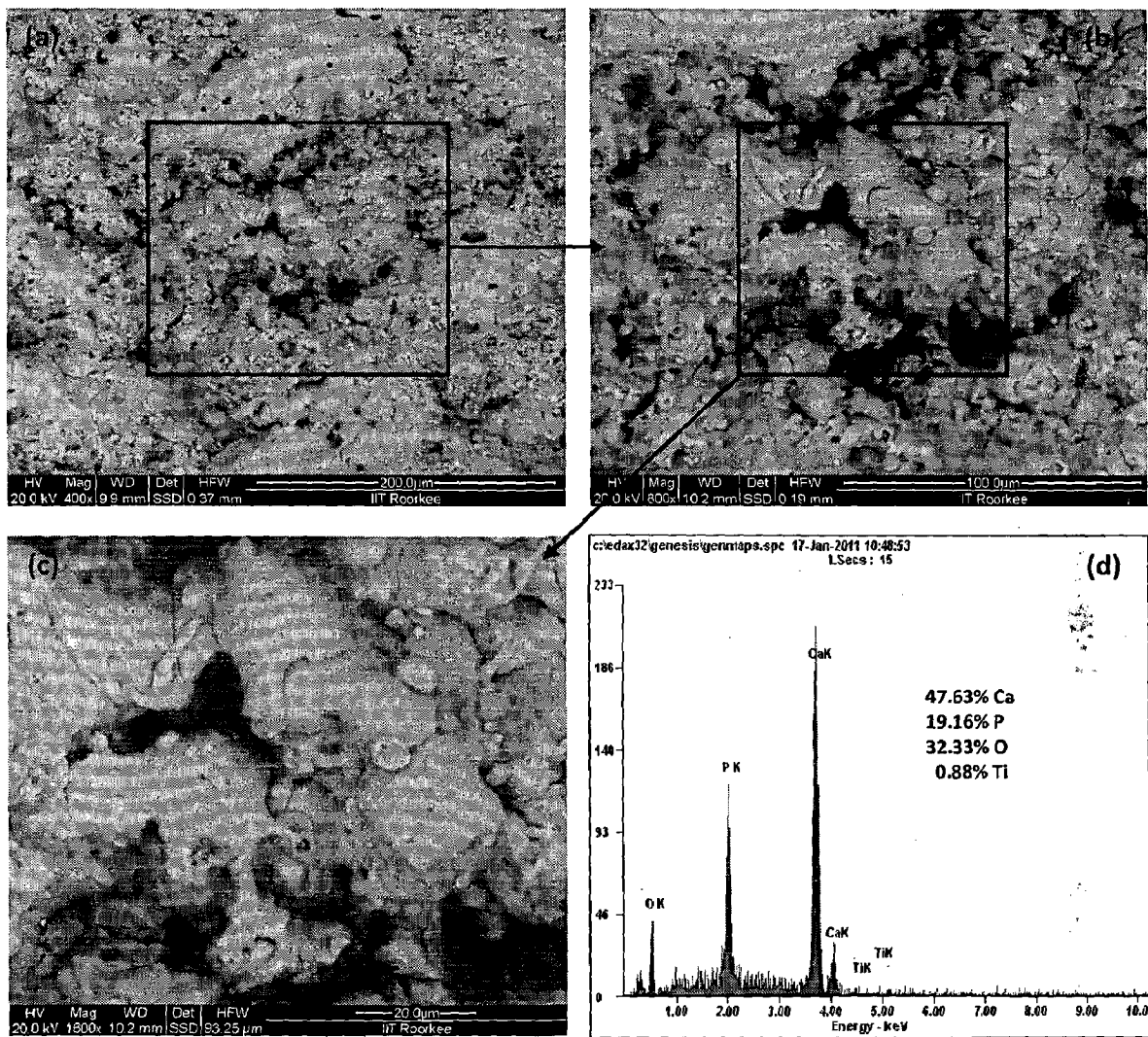


Fig. 6.11 FE-SEM micrographs and EDAX surface analysis of pure HA coating after immersion in SBF for 1 day: (a) at 400X; (b) at 800X; (c) at 1600X and (d) EDAX surface analysis of (c)

The surface morphology and EDAX surface analysis of pure HA and HA-30 wt% Al₂O₃ coatings after immersion in SBF for 1 day are shown in Fig. 6.11 and Fig. 6.12 respectively. Craters and pores can be seen in surface morphology of pure HA coating after immersion in SBF for 1 day at lower magnification (Fig. 6.11a). The depth of these craters and pores is not from end to end of coating as can be seen at higher magnification (Fig. 6.11b and c). Very fine pits can be seen on surface of fully molten splats at higher magnification (Fig. 6.11c). The coating surface show increased roughness.

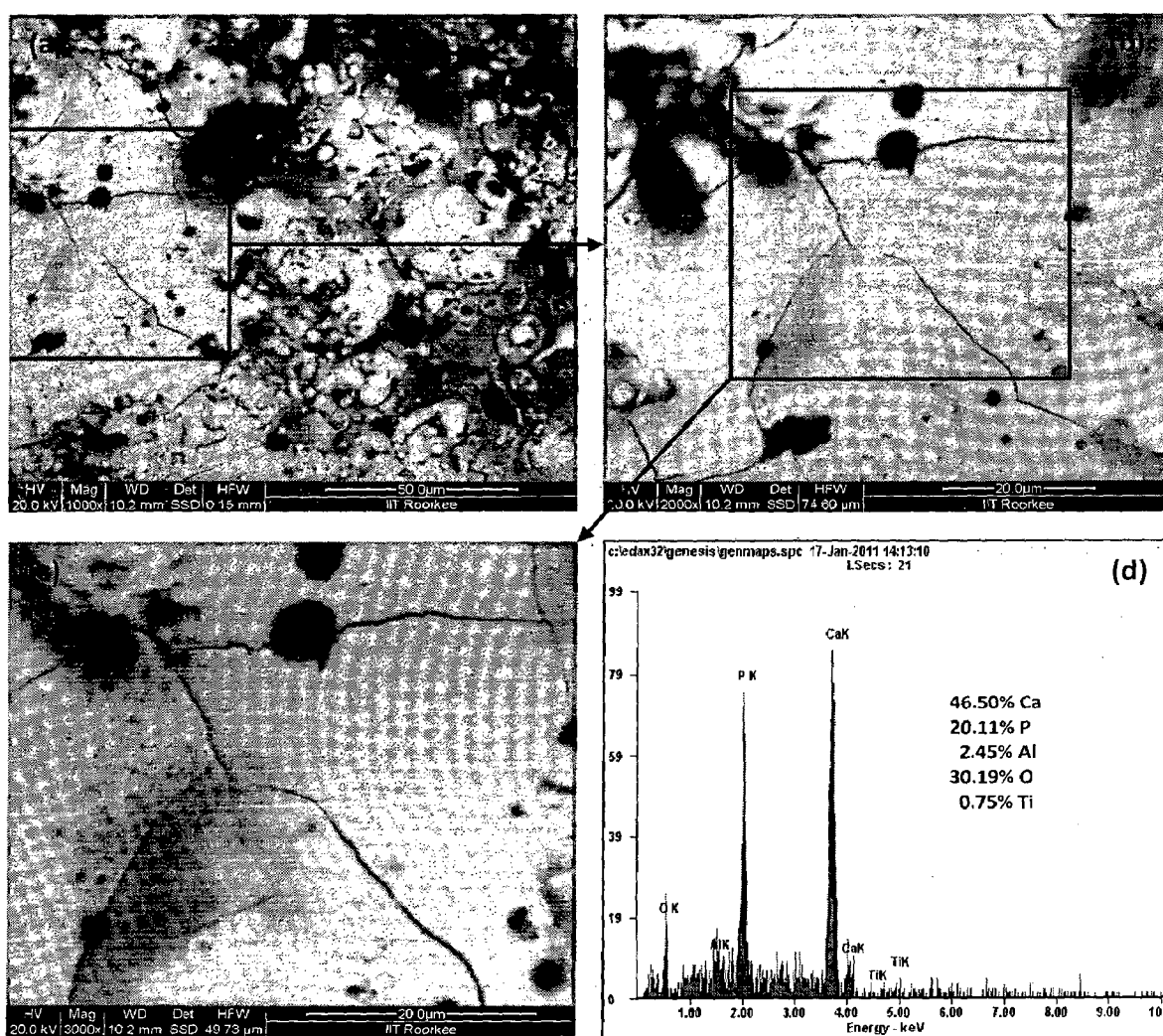


Fig. 6.12 FE-SEM micrographs and EDAX surface analysis of HA-30 wt% Al₂O₃ coating after immersion in SBF for 1 day: (a) at 1000X; (b) at 2000X; (c) at 3000X and (d) EDAX surface analysis of (c)

The EDAX surface analysis of pure HA coating after immersion period of 1 day is shown in Fig. 6.11d. It can be seen from EDAX surface analysis that coating mainly contains the elements of hydroxyapatite i.e. Ca, P and O with traces of elements from substrate. The formation of pores and craters after immersion in SBF for 1 day might be due to dissolution of amorphous phases. Surface morphology and EDAX surface analysis of HA-30 wt% Al₂O₃ coating after immersion in SBF for 1 day at 1000X, 2000X and 3000X magnification is shown in Fig. 6.12. Pores, craters and fine cracks can be seen in surface morphology of coating (Fig. 6.12a).

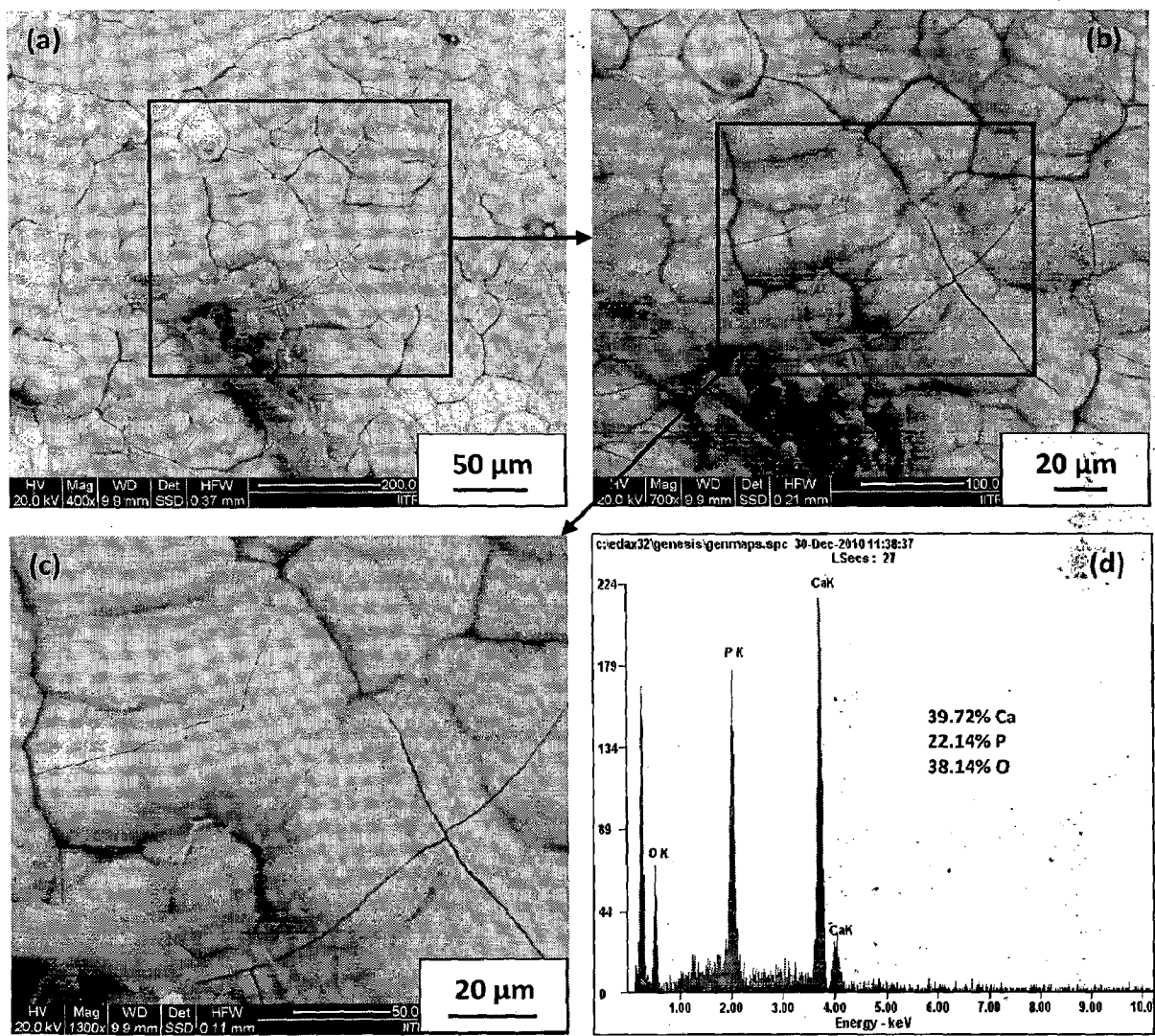


Fig. 6.13 FE-SEM micrographs and EDAX surface analysis of pure HA coating after immersion in SBF for 5 days: (a) at 400X; (b) at 700X; (c) at 1300X and (d) EDAX surface analysis of (c)

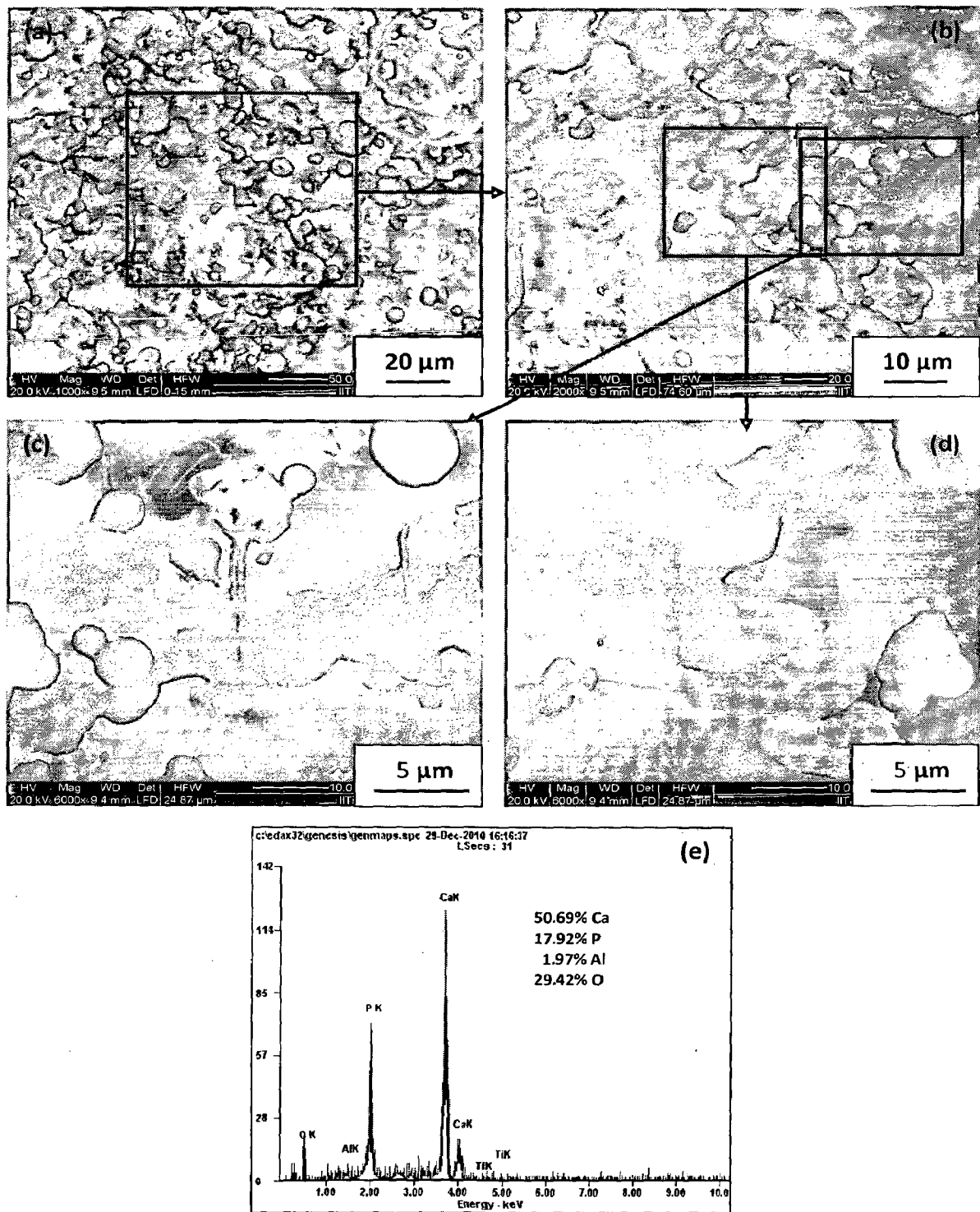


Fig. 6.14 FE-SEM micrographs and EDAX surface analysis of HA-10 wt% Al_2O_3 coating after immersion in SBF for 5 days: (a) at 1000X; (b) at 2000X; (c) at 6000X; (d) at 6000X from different location and (e) EDAX surface analysis of (c)

Surface morphology of coating at higher magnification suggest that pores and craters are only in the upper surface of coating however, surface of completely molten splats seems to be rougher due to development of fine pits (Fig. 6.12b and c). Rougher surface of molten splats might be due to dissolution of amorphous tiny particles. EDAX surface analysis of coating shows mainly constituent of coating elements along with traces (less than 1%) of substrate elements. Surface morphology and EDAX surface analysis of HA, HA-10 wt% Al₂O₃, HA-20 wt% Al₂O₃ and HA-30 wt% Al₂O₃ after immersion in SBF for 5 days at a controlled temperature of 37±1°C is shown in Fig. 6.13 to Fig. 6.16 respectively.

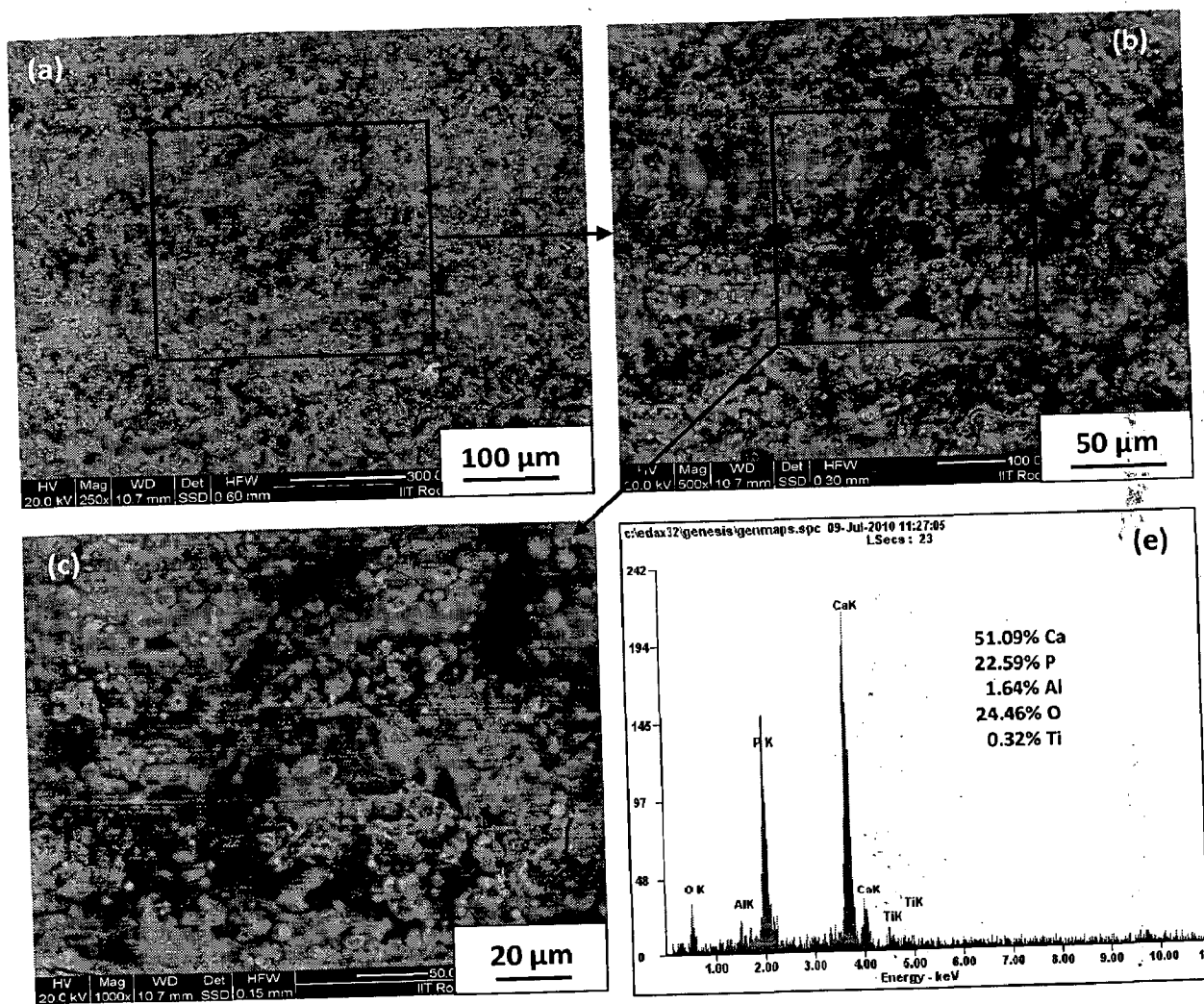


Fig. 6.15 FE-SEM micrographs and EDAX surface analysis of HA-20 wt% Al₂O₃ coating after immersion in SBF for 5 days: (a) at 250X; (b) at 500X; (c) at 1000X and (d) EDAX surface analysis of (c)

The surface morphology of pure HA coating after immersion in SBF for 5 days appears like tortoise shell with network of cracks as can be seen in Fig. 6.12a-c. The branching out of cracks is clearly visible on whole coating surface. Wide opened cracks are not visible on the coating surface. The EDAX surface analysis of coating (Fig. 6.13c) as shown in Fig. 6.13d does not reveal substrate element.

Surface morphology and EDAX surface analysis of HA-10% wt Al_2O_3 coating after immersion in SBF for 5 days is shown in Fig. 6.14. Some craters and pores can be seen in surface morphology of coating at 1000X and 2000X magnification (Fig. 6.14a and b) however, network of cracks is absent. Figure 6.14c and d show surface morphology of coating at higher magnification of 6000X. Some partially molten HA particles (about 5 μm or lesser in size) are visible on completely molten splats in Fig. 6.14c. Further, partially molten particles are also visible inside the crater as shown in Fig. 6.14d. Agglomerate of HA particles can be seen on completely molten splat at lower right corner in Fig. 6.14d. EDAX surface analysis of coating (Fig. 6.14c) as shown in Fig. 6.14e do not reveal substrate element.

Surface morphology and EDAX surface analysis of HA-20 wt% Al_2O_3 coating after immersion in SBF at a temperature of $37\pm 1^\circ\text{C}$ for a period of 5 days is shown Fig. 6.15. Partially molten/un-melted particles, pores, craters and some micro-cracks are visible in surface morphology of coating as shown in Fig. 6.15a-c however, network of cracks is absent. EDAX surface analysis of coating (Fig. 6.15c) is shown in Fig. 6.15d, which reveal elements mainly of coating. Traces of substrate elements can also be seen in EDAX surface analysis of coating.

Surface morphology and EDAX surface analysis of HA-30 wt% Al_2O_3 coating after immersion in SBF for a period of 5 days is shown Fig. 6.16. In general coating surface consists of pores, cracks, partially melted particles and craters as shown in Fig. 6.16a and b. Wide opened cracks along with network of thin cracks and craters are visible at higher magnification of 1000X and 2000X in surface of coating as can be seen in Fig. 6.16c and d. Partially molten particles, un-melted cores and corona can be seen in surface morphology of coating. EDAX surface analysis reveal elements mainly of coating with traces of element of substrate as can be seen in Fig. 6.16e.

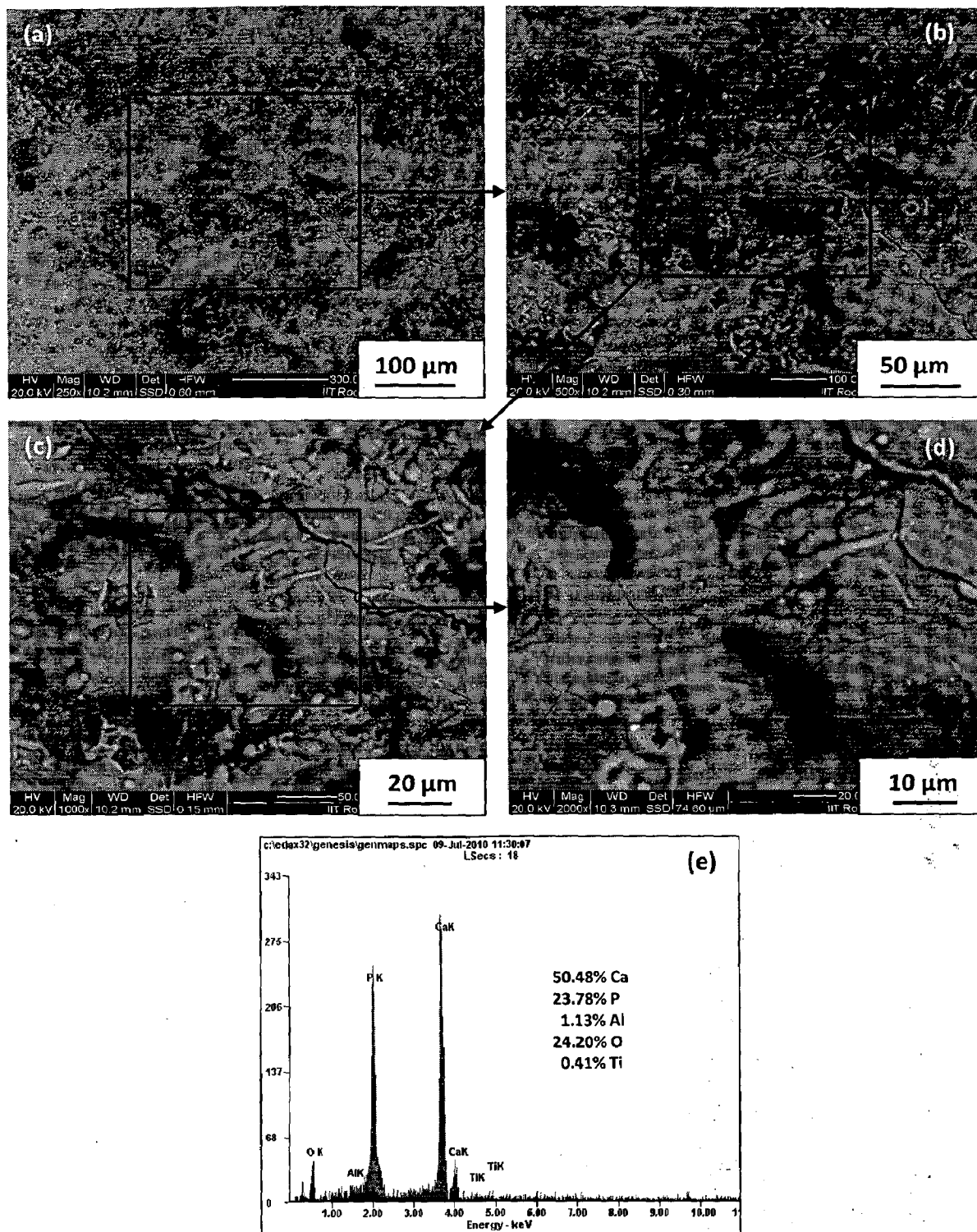


Fig. 6.16 FE-SEM micrographs and EDAX surface analysis of HA-30 wt% Al₂O₃ coating after immersion in SBF for 5 days: (a) at 250X; (b) at 500X; (c) at 1000X; (d) at 2000X and (e) EDAX surface analysis of (c)

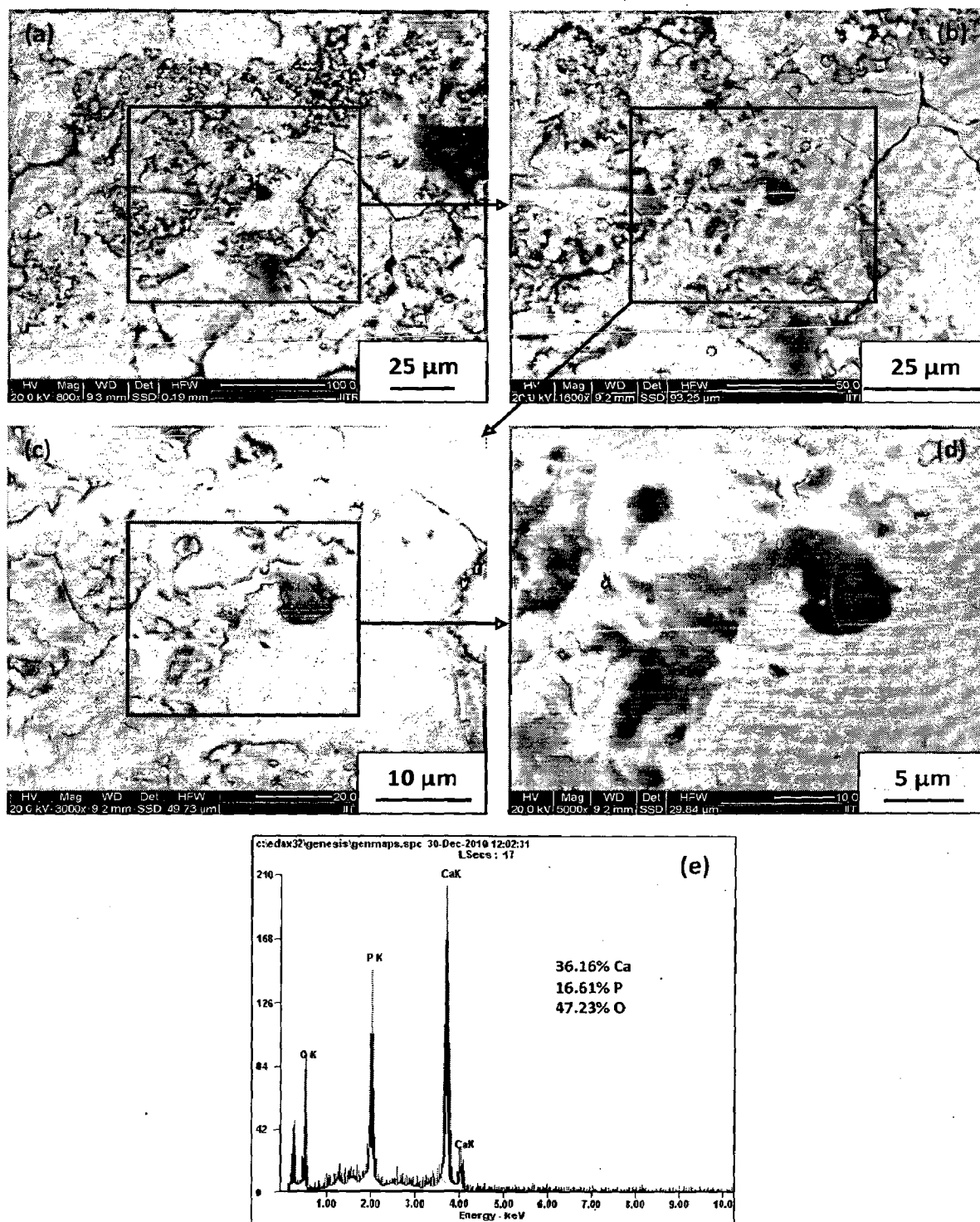


Fig. 6.17 FE-SEM micrographs and EDAX surface analysis of pure HA coating after immersion in SBF for 10 days: (a) at 800X; (b) at 1600X; (c) at 3000X; (d) at 5000X and (e) EDAX surface analysis of (d)

Surface morphology and EDAX surface analysis of pure HA, HA-10 wt%Al₂O₃, HA-20 wt%Al₂O₃ and HA-30 wt% Al₂O₃ coatings after immersion in SBF at a controlled temperature of 37±1°C for a period of 10 days is shown in Fig. 6.17 to Fig. 6.20 respectively. In top left region of Fig. 6.17a, surface morphology of coating is like tortoise shell. Some tiny particles can be seen inside the crater on top left corner of Fig. 6.17b. Wide opened cracks, pores, crater and rough surface can also be seen in morphology of coating after immersion in SBF for 10 days (Fig. 6.17b).

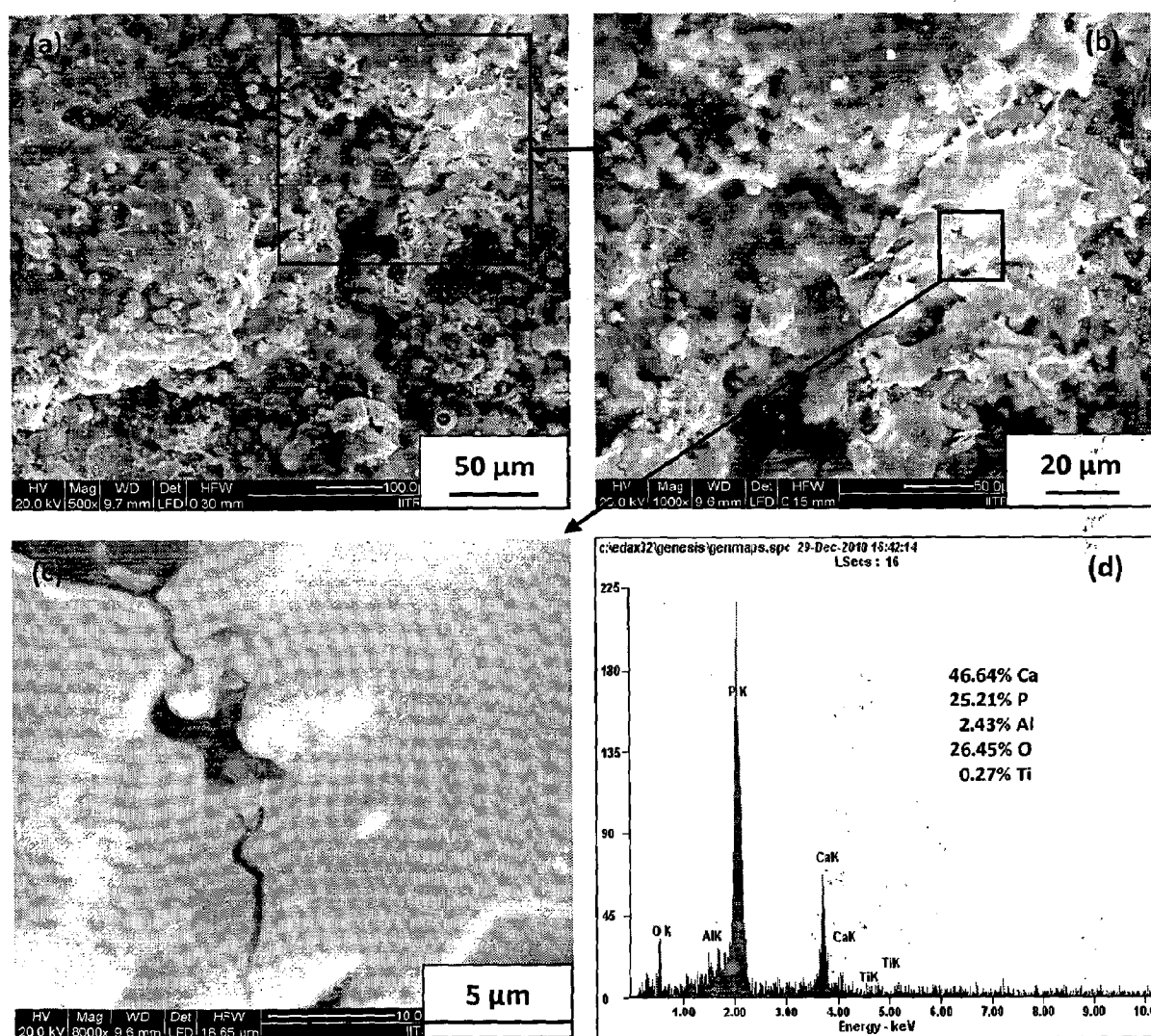


Fig. 6.18 FE-SEM micrographs and EDAX surface analysis of HA-10 wt% Al₂O₃ coating after immersion in SBF for 10 days: (a) at 500X; (b) at 1000X; (c) at 8000X and (d) EDAX surface analysis of (c)

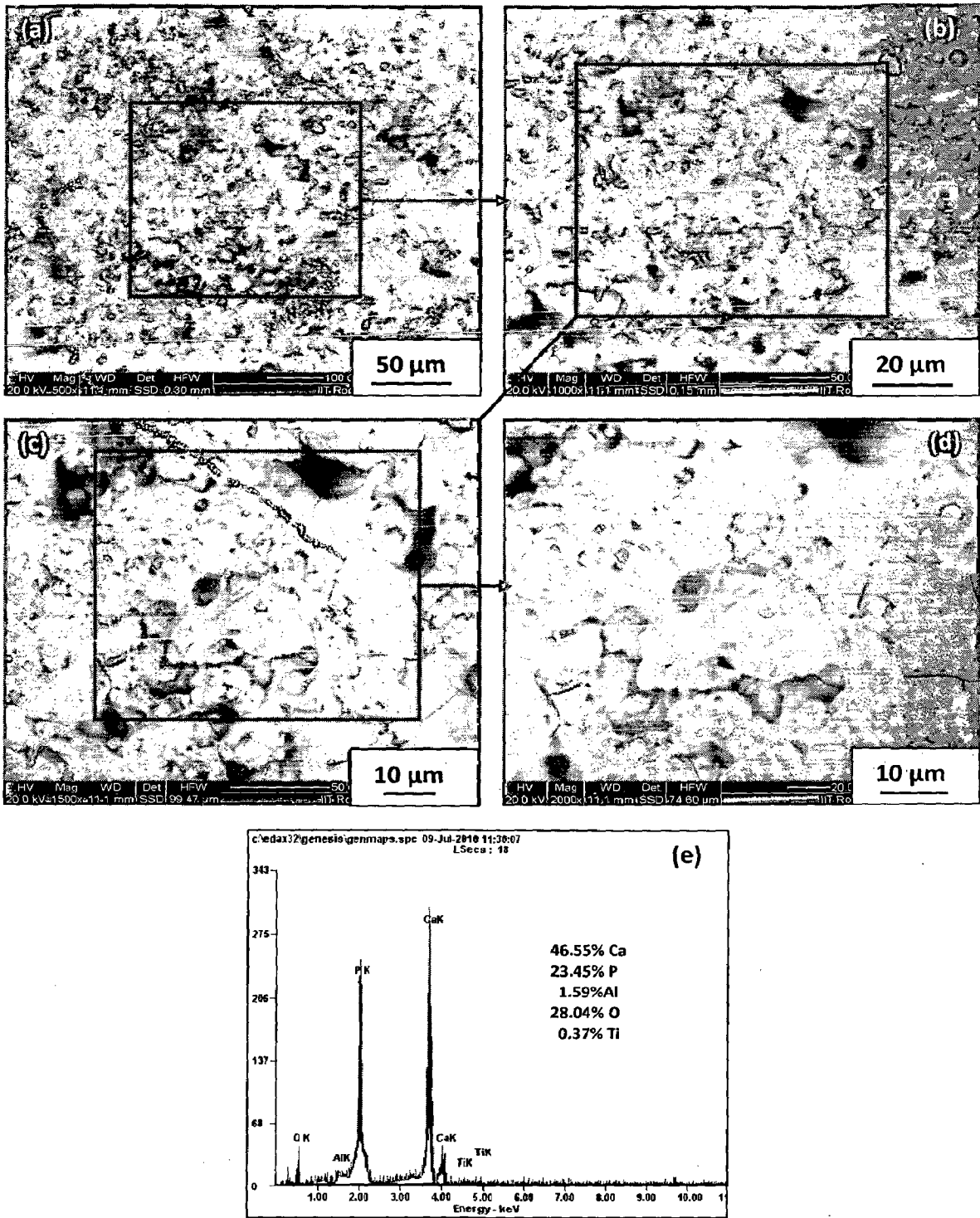


Fig. 6.19 FE-SEM micrographs and EDAX surface analysis of HA-20 wt% Al₂O₃ coating after immersion in SBF for 10 days: (a) at 500X; (b) at 1000X; (c) at 1500X; (d) at 2000X and (e) EDAX surface analysis of (c)

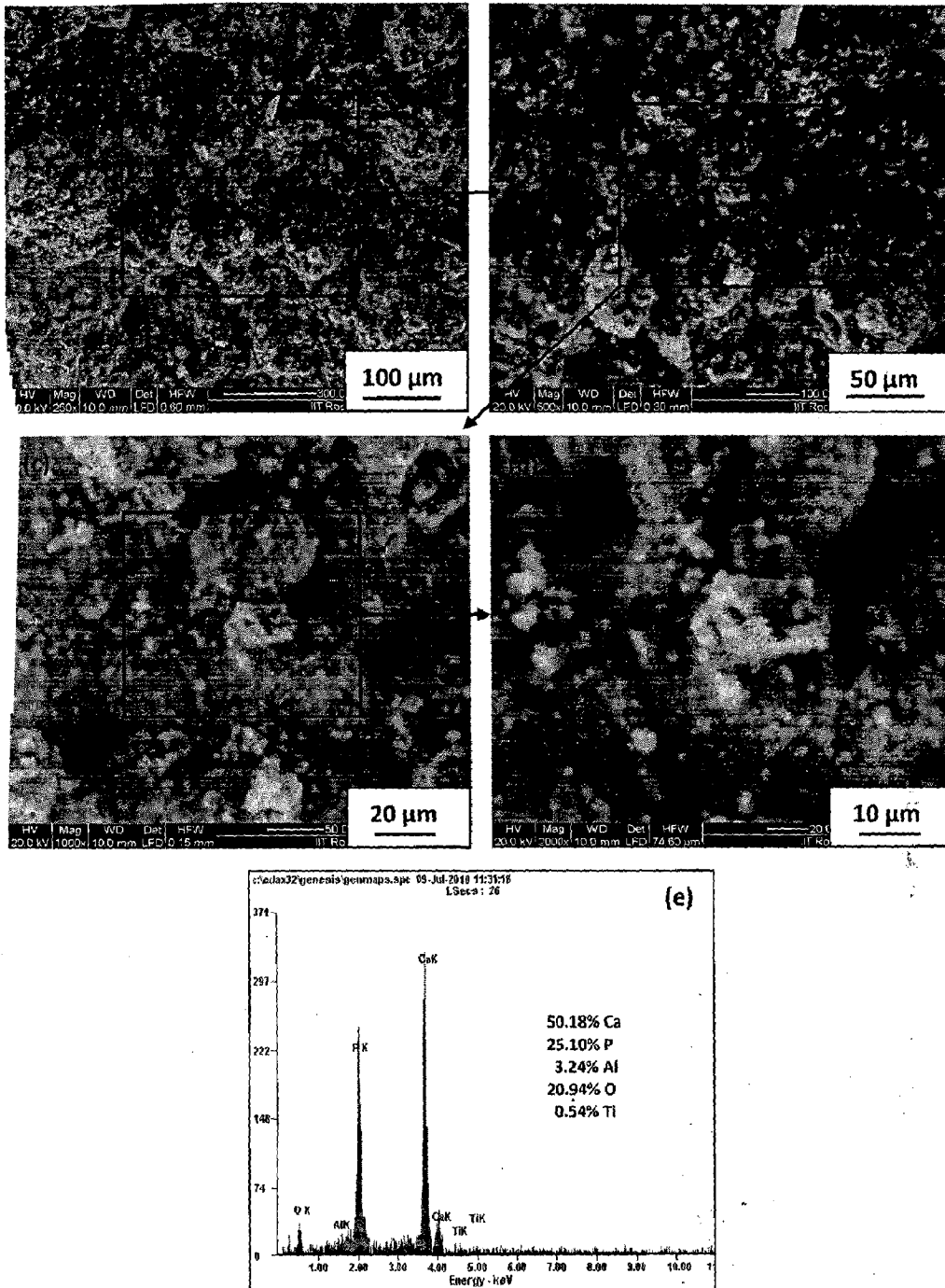


Fig. 6.20 FE-SEM micrographs and EDAX surface analysis of HA-30 wt% Al₂O₃ coating after immersion in SBF for 10 days: (a) at 250X; (b) at 500X; (c) at 1000X; (d) at 2000X and (e) EDAX surface analysis of (c)

Similar coating morphology can be seen at higher magnifications of 3000X and 5000X (Fig. 6.17c and d). EDAX surface analysis of coating (Fig. 6.17d) is shown in Fig. 6.17e, which reveal coating elements only. Figure 6.18 show the coating morphology and EDAX surface analysis of HA-10 wt% Al₂O₃ coating after immersion in SBF for 10 days at a temperature of 37±1°C. In general, coating surface contain un-melted HA particles and very fine pits on completely molten splats. A comparative light colored splat is visible in the upper right region of Fig. 6.18a (inside the box). To check the elemental composition of this splat, high magnification images were taken and analyzed using EDAX. A small portion of this splat is shown in Fig. 6.18c at 8000X magnification. The surface of this splat is comparatively smooth as compared to rest of coating surface. EDAX analysis of this region is shown in Fig. 6.18d, which reveal presence of elements of coating with traces of substrate element.

Surface morphology and EDAX surface analysis of HA-20 wt% Al₂O₃ and HA-30 wt% Al₂O₃ coatings after immersion in SBF for 10 days at controlled temperature of 37±1°C is shown in Fig. 6.19 and Fig. 6.20 respectively. Porosity, cracks, craters and rough splat surface are visible in the surface morphology of HA-20 wt% Al₂O₃ after immersion in SBF for 10 days as can be seen in Fig. 6.19a-d. Formation of rough splat surface of completely molten splats and development of craters might be due to dissolution of amorphous phases. Precipitation of tiny particles along cracks and splat boundaries can be seen at higher magnification of 2000X (Fig. 6.19d). EDAX surface analysis of SEM micrograph (Fig. 6.19d) is shown in Fig. 6.19e. EDAX surface analysis show mainly coating elements with traces of substrate element. Surface morphology and EDAX surface analysis of HA-30 wt% Al₂O₃ coating after immersion in SBF for 10 days at controlled temperature of 37±1°C is shown in Fig. 6.20. Porosity and very fine cracks are present in the surface morphology of coating however, craters and rough surface are not visible at magnification of 250X and 500X (Fig. 6.20a-b). Precipitation of tiny particles is visible on the surface of coating after immersion in SBF for 10 days as can be seen in Fig. 6.20c-d. From Fig. 6.20c, it can be seen that these tiny particles are eventually agglomerates of very fine particles. The size of agglomerates varies between 5 µm to 20 µm. EDAX surface analysis of coating (Fig. 6.20c) is shown in Fig. 6.20e. EDAX surface analysis show elements of coating with traces of substrate element.

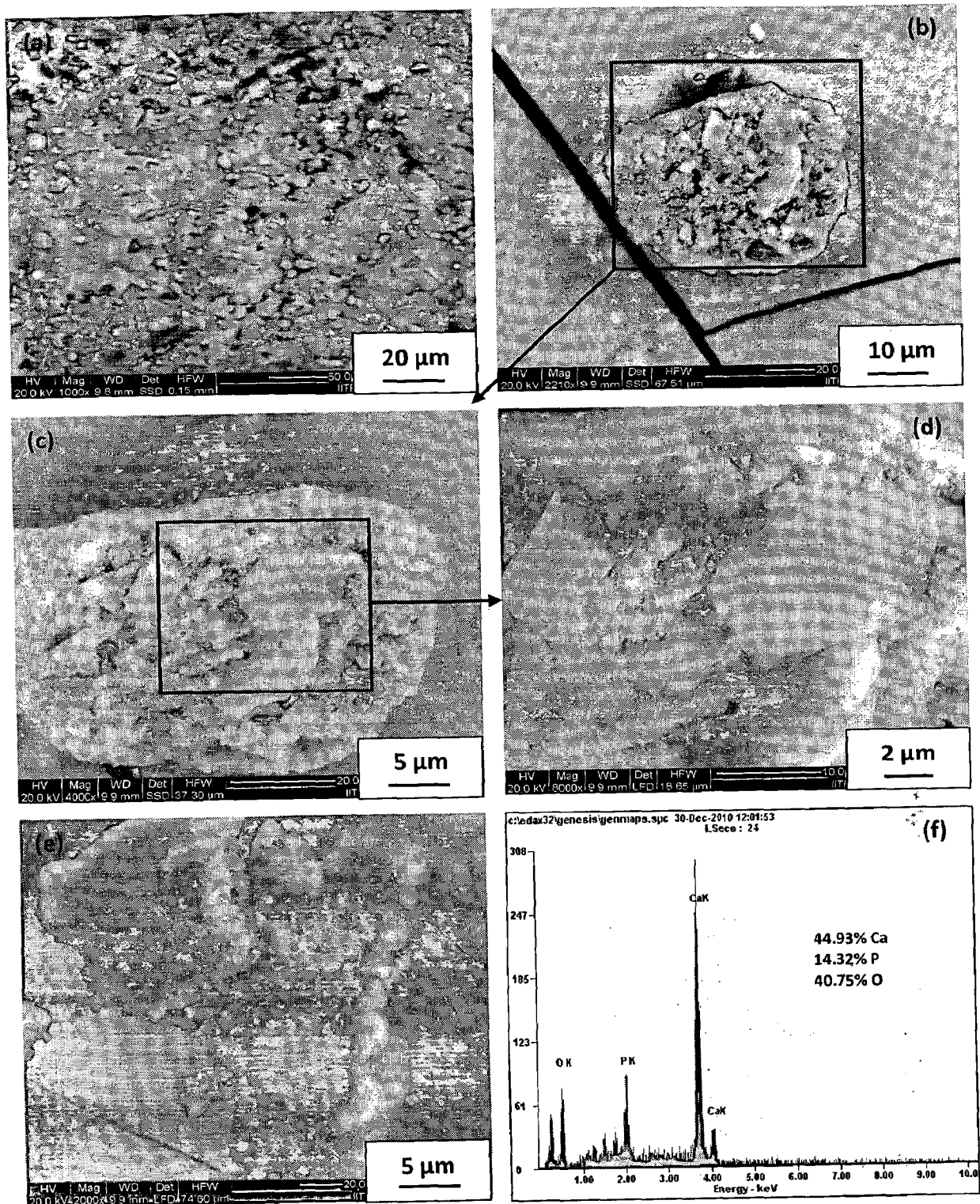


Fig. 6.21 FE-SEM micrographs and EDAX surface analysis of pure HA coating after immersion in SBF for 15 days: (a) at 1000X; (b) at 2210X; (c) at 4000X (d); at 8000X; (e) at 2000X from different location and (f) EDAX surface analysis of (d)

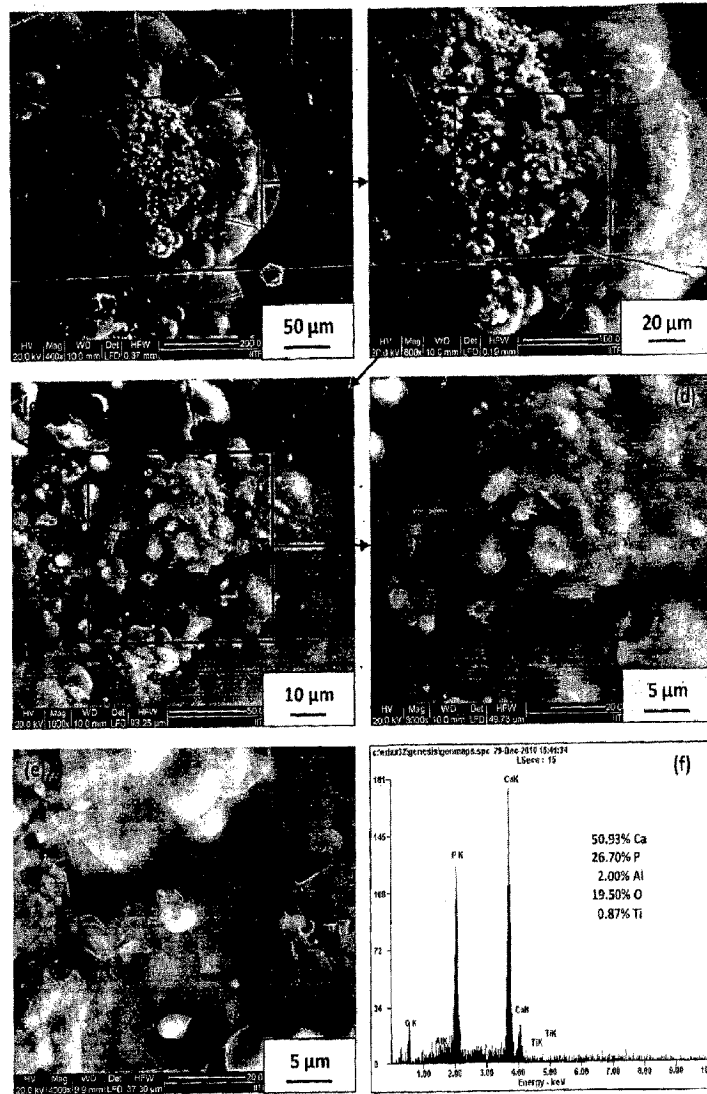


Fig. 6.22 FE-SEM micrographs and EDAX surface analysis of HA-10 wt% Al₂O₃ coating after immersion in SBF for 15 days: (a) at 400X; (b) at 800X; (c) at 1600X; (d) at 3000X; (e) at 4000X and (f) EDAX surface analysis of (e)

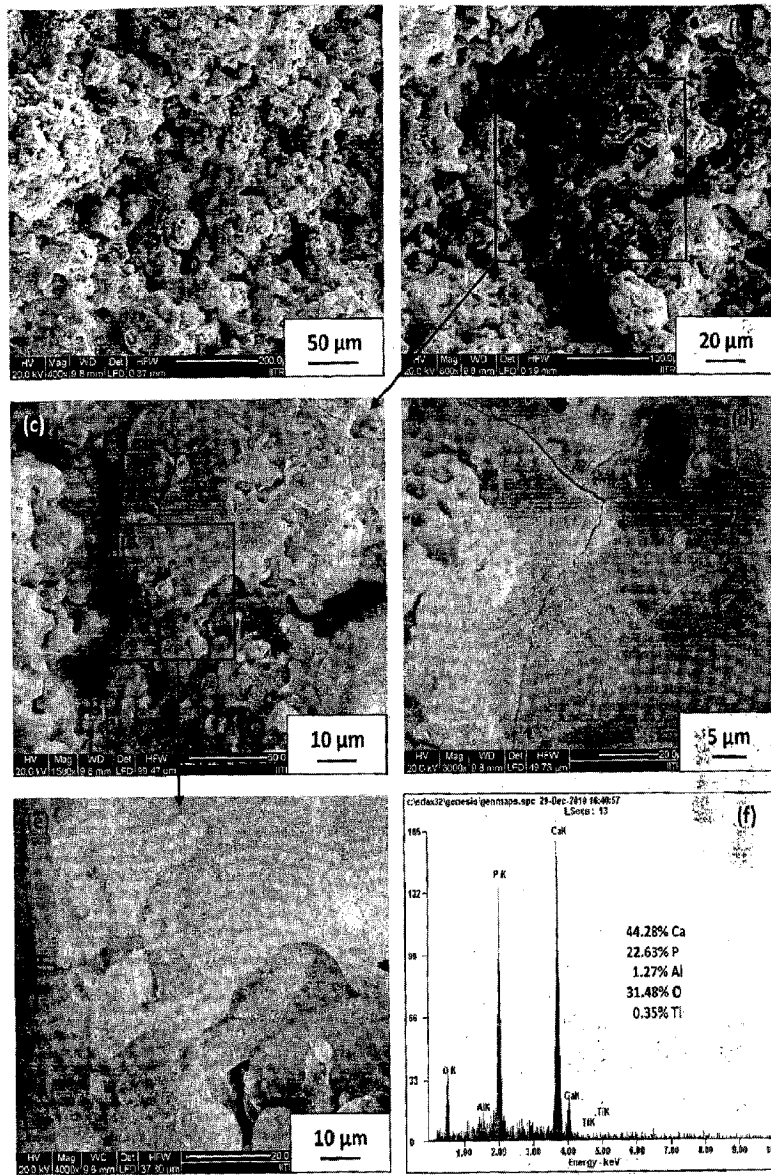


Fig. 6.23 FE-SEM micrographs and EDAX surface analysis of HA-20 wt% Al_2O_3 coating after immersion in SBF for 15 days: (a) at 400X; (b) at 800X; (c) at 1500X; (d) at 3000X; (e) at 4000X and (f) EDAX surface analysis of (e)

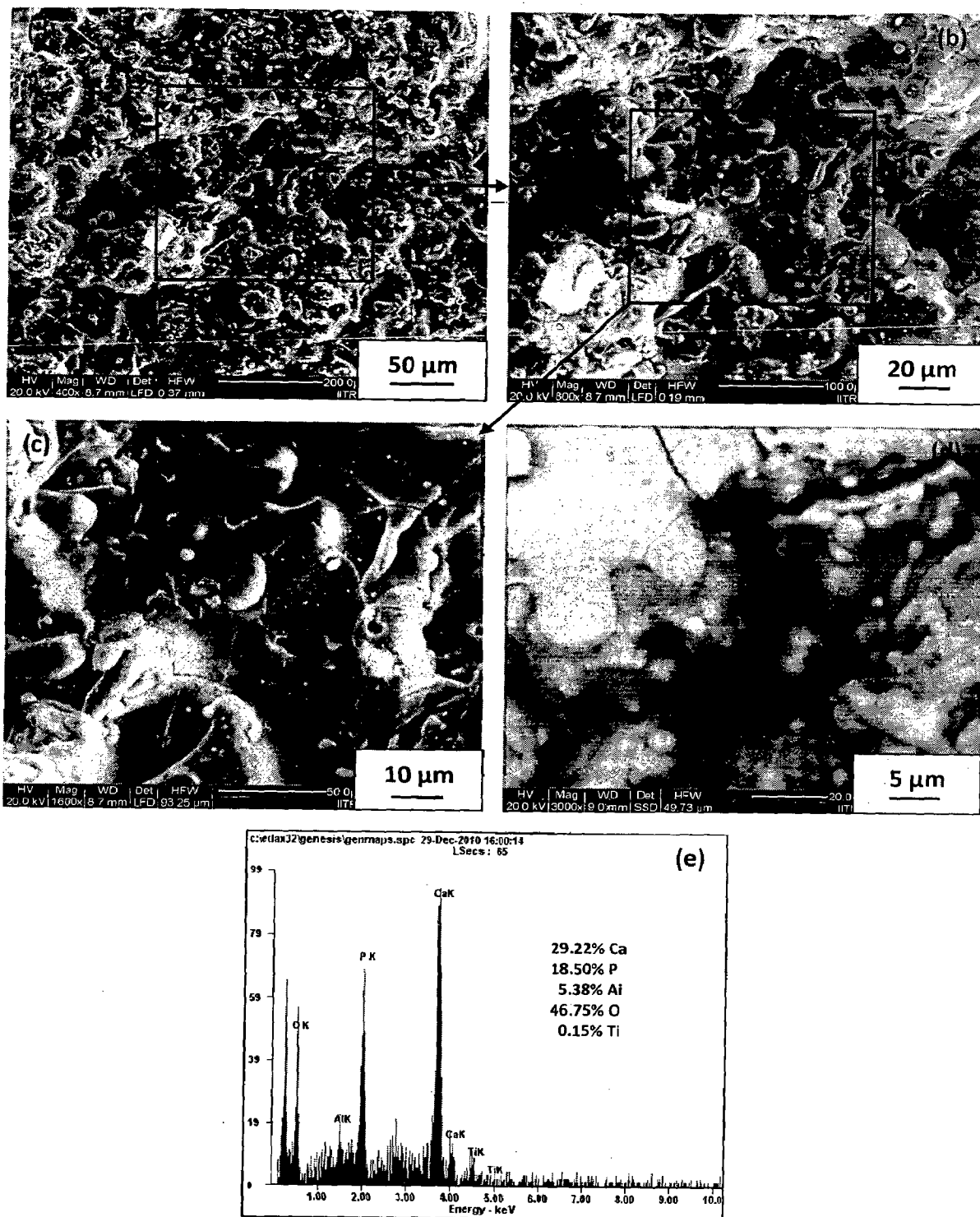


Fig. 6.24 FE-SEM micrographs and EDAX surface analysis of HA-30 wt% Al_2O_3 coating after immersion in SBF for 15 days: (a) at 400X; (b) at 800X; (c) at 1600X; (d) at 3000X from different location and (e) EDAX surface analysis of (d)

Surface morphology and EDAX surface analysis of HA, HA-10 wt% Al₂O₃, HA-20 wt% Al₂O₃ and HA-30 wt% Al₂O₃ after immersion in SBF for 15 days at controlled temperature of 37±1°C is shown in Fig. 6.21 to Fig. 6.24 respectively. Figure 6.21 shows the surface morphology and EDAX surface analysis of pure HA coating after immersion in SBF for 15 days. It can be seen from Fig. 6.21a that coating surface consists of craters, cracks, un-melted/partially molten particles and pores. At higher magnification, as shown in Fig. 6.21b, agglomerate can be seen near crack on relatively smooth molten splat. The morphology of this agglomerate was analyzed at higher magnification of 4000X and 8000X and shown in Fig. 6.21c and 6.21d respectively. It can be seen from Fig. 6.21d that agglomerate is made of very small particles having size about 5 µm. EDAX surface analysis of agglomerate (Fig. 6.21f) show constituent of HA such as Ca, P and O. The surface morphology of HA coating after immersion period of 15 days in SBF from different location at 2000X magnification is shown in Fig. 6.21e. Precipitation of fine particles can be seen on coating surface.

Surface morphology and EDAX surface analysis of HA-10 wt% Al₂O₃ coating after immersion in SBF for 15 days is shown in Fig. 6.22. The morphology of coating surface depicts tortoise shell morphology with network of thick cracks as can be seen in Fig. 6.22a. The central area of this micrograph (Fig. 6.22b) shows craters and pores along with precipitation of tiny particles on coating surface. This area of coating has been further magnified and shown in Fig. 6.22c. Very fine precipitates and cracks on comparatively smooth surface can be seen in Fig. 6.22c and Fig. 6.22d (higher magnification of 3000X). Figure 6.22e shows the morphology of coating at 4000X magnification, which reveals smooth coating surface. EDAX surface analysis of coating (Fig. 6.22e) is shown in Fig. 6.22f, which reveals constituents of coating elements with traces of substrate element.

Surface morphology and EDAX surface analysis of HA-20 wt% Al₂O₃ coating after immersion in SBF for 15 days is shown in Fig. 6.23. Craters, pores and some fine cracks are visible in surface morphology as can be seen in Fig. 6.23a and Fig. 6.23b at magnification of 400X and 800X respectively. Further, at higher magnification of 1500X as shown in Fig. 6.23c, pores, craters and some fine cracks are visible in surface morphology of coating. Figure 6.23e shows the surface morphology of coating at magnification of 4000X. Molten splats show rough surface, which might be due to dissolution of amorphous phases. However, tiny precipitates

can be seen around boundary of circular splats and inside the crater. Some very fine pits are also visible in lower left region of coating surface as shown in Fig. 6.23e. Fine pores, cracks and rough surface can be seen in surface morphology of coating from different location (Fig. 6.23d). EDAX surface analysis of coating (Fig. 6.23e) is shown in Fig. 6.23f, which show constituents of coating with traces of substrate element.

Surface morphology and EDAX surface analysis of HA-30 wt% Al_2O_3 coating after immersion in SBF for 15 days at magnification of 400X, 800X, 1600X and 3000X is shown in Fig. 6.24a-d respectively. Un-melted/partially melted particles, pores, craters and cracks can be seen in surface morphology of coating (Fig. 6.24a-c). At higher magnification of 3000X, wide opened cracks can be seen in surface morphology of coating (Fig. 6.24d). EDAX surface analysis of coating (Fig. 6.24d) shows constituents of coating elements with traces of substrate element (Fig. 6.24e).

Surface morphology and EDAX surface analysis of HA, HA-10 wt% Al_2O_3 , HA-20 wt% Al_2O_3 and HA-30 wt% Al_2O_3 coatings after immersion in SBF for 20 days at controlled temperature of $37\pm 1^\circ\text{C}$ is shown in Fig. 6.25 to Fig. 6.28 respectively. Partially molten/un-melted HA particles and some fine cracks are visible in surface morphology of HA coating after immersion period of 20 days in SBF at comparatively low magnification of 500X as can be seen in Fig. 6.25a. Small portion of Fig. 6.25a has been magnified to 2500X and shown in Fig. 6.25b. It can be seen from surface morphology that coating surface is completely covered with tiny precipitates. The coating surface from different location (Fig. 6.25c) shows similar morphology as that of Fig. 6.25b. Figure 6.25d shows the surface morphology of coating at magnification of 5000X. The coating surface is completely covered with tiny precipitates. EDAX analysis of coating (Fig. 6.25d) shows presence of only coating elements (Fig. 6.25e).

Surface morphology and EDAX surface analysis of HA-10 wt% Al_2O_3 coating after immersion in SBF for 20 days is shown in Fig. 6.26. Craters and pores are visible in surface morphology of coating as can be seen in Fig. 6.26a. A cluster of particles, comparatively lighter in color, is visible in Fig. 6.26a (highlighted in box). This area of the coating is analyzed at higher magnification of 4000X and 10000X as shown in Fig. 6.26b and c respectively. This agglomerate or cluster of un-melted particles might have been originated from coating feedstock as suggested by Gadow et al., (2010).

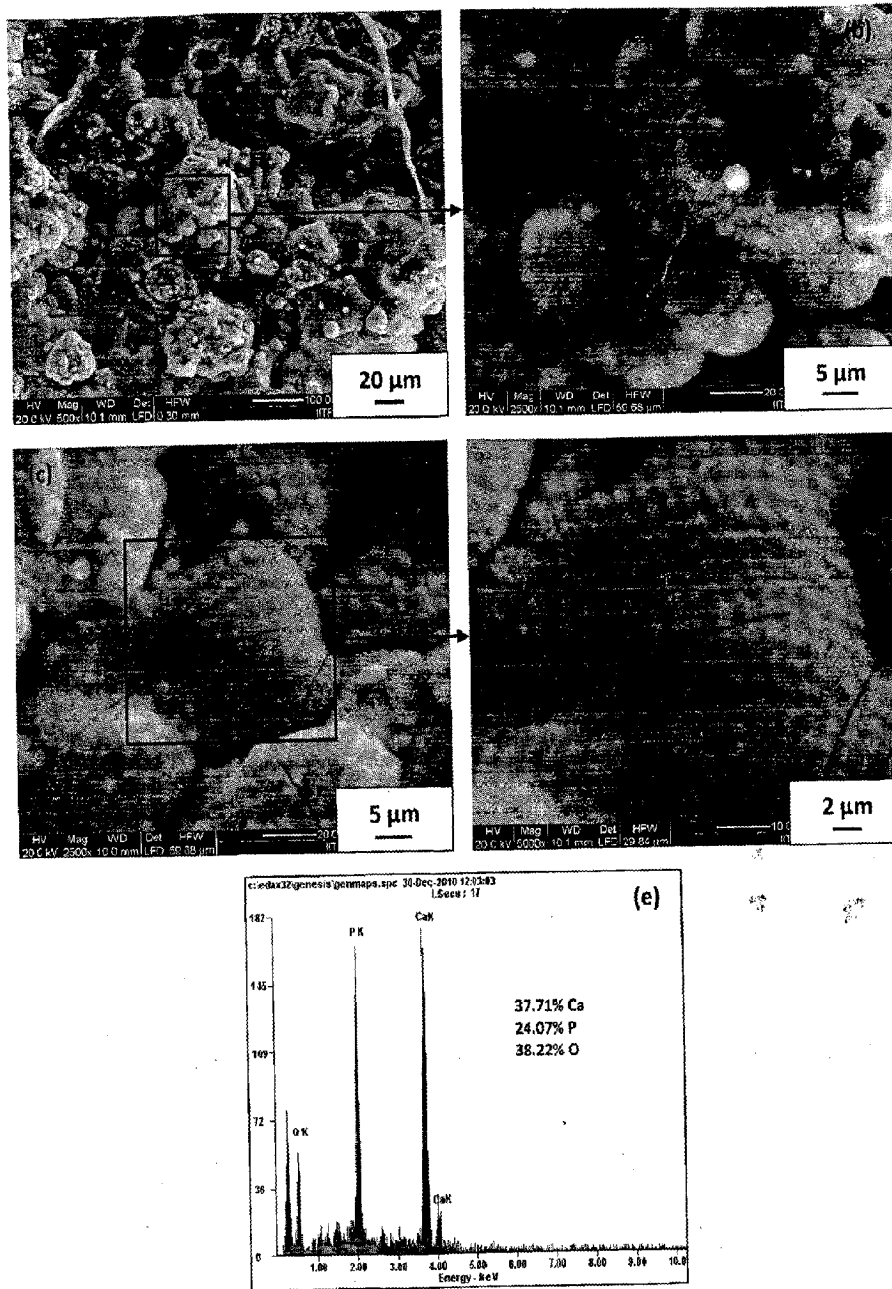


Fig. 6.25 FE-SEM micrographs and EDAX surface analysis of pure HA coating after immersion in SBF for 20 days: (a) at 500X; (b) at 2500X; (c) at 2500X from different location; (d) at 5000X and (e) EDAX surface analysis of (d)

It can be seen from these images that the particles do not have any specific shape and particle size that makes the cluster vary from 2 μm to 20 μm . EDAX analysis of coating (Fig. 6.26c) shows mainly elements from coating with traces of substrate element (Fig. 6.26d). Surface morphology and EDAX surface analysis of HA-20 wt% Al_2O_3 coating after immersion in SBF for 20 days is shown in Fig. 6.27. Craters, cracks and pits can be seen in surface morphology of coating (Fig. 6.27a). At higher magnification, small pits, cracks and rough surface along with tiny precipitates can be seen (Fig. 6.27b). EDAX surface analysis of coating (Fig. 6.27b) shows mainly coating elements with traces of substrate element (Fig. 6.27c).

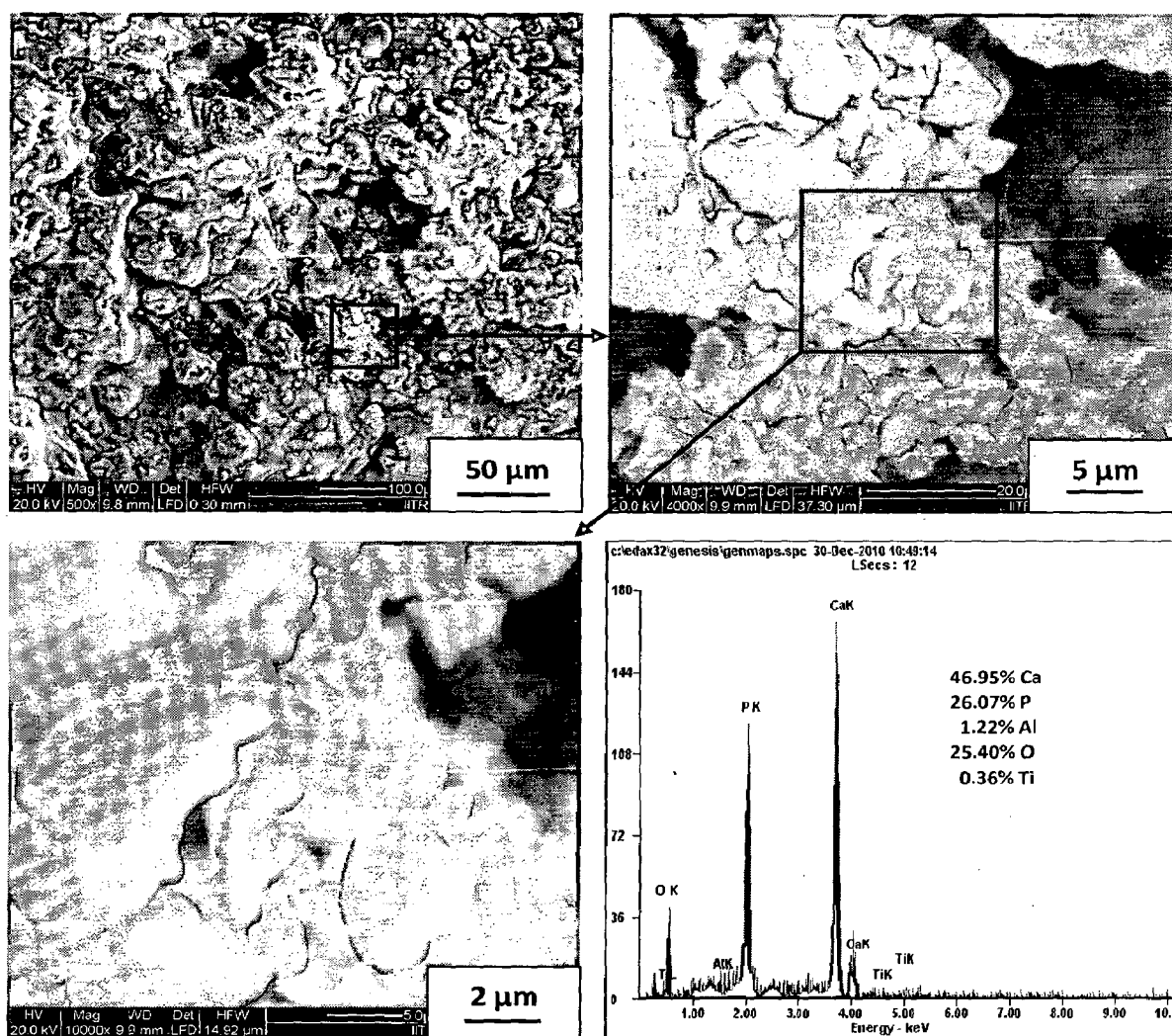
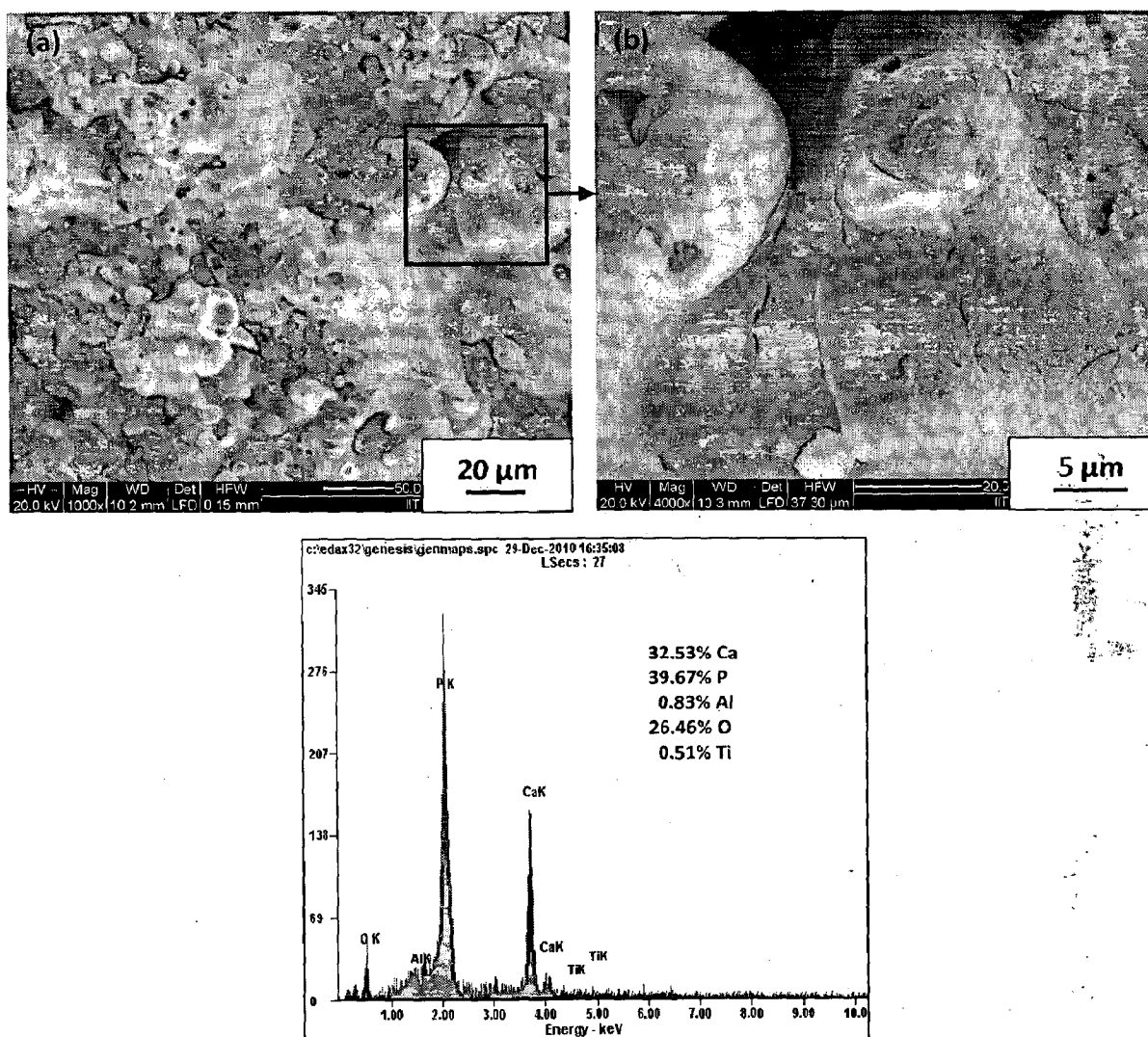


Fig. 6.26 FE-SEM micrographs and EDAX surface analysis of HA-10 wt% Al_2O_3 coating after immersion in SBF for 20 days: (a) at 500X; (b) at 4000X; (c) at 10000X and (d) EDAX surface analysis of (c)

Figure 6.28 shows the surface morphology and EDAX surface analysis of HA-30 wt% Al₂O₃ coating after immersion in SBF for 20 days. Craters, cracks and pores are visible in surface morphology of coating at magnification of 250X and 400X as shown in Fig. 6.28a and b respectively. At higher magnification of 6000X, smooth surface morphology can be seen (Fig. 6.28c). Tiny precipitates can be seen inside the craters (Fig. 6.28c). EDAX surface analysis of coating shows constituents of coating (Fig. 6.28c).



7 FE-SEM micrographs and EDAX surface analysis of HA-20 wt% Al₂O₃ coating after immersion in SBF for 20 days: (a) at 1000X; (b) at 4000X and (c) EDAX surface analysis of (b)

Some cross-sectioned specimens were immersed in SBF to analyze cross-sectional morphology after immersion in SBF for different time periods. The behavior of titanium in SBF regarding precipitation of apatite was also studied. The cross-sectional morphology of these specimens after immersion in SBF is shown in Fig. 6.29 to Fig. 6.31. The cross-sectional morphology of HA-30 wt% Al₂O₃ coating after immersion in SBF for 1 day at different magnifications is shown in Fig. 6.29. It can be seen from SEM image taken at magnification of 500X (Fig. 6.29a) that the coating cross-section is rough.

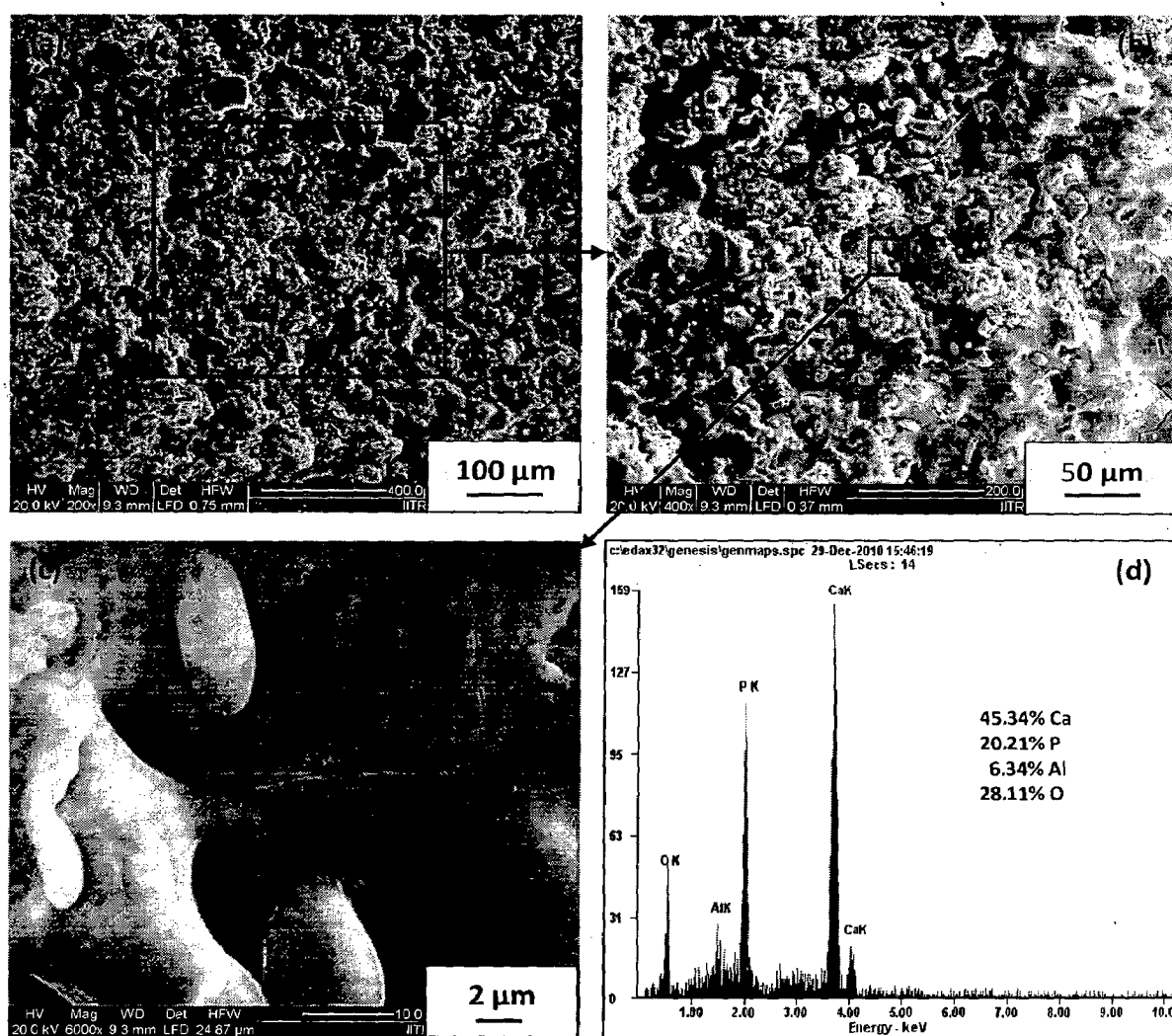


Fig. 6.28 FE-SEM micrographs and EDAX surface analysis of HA-30 wt% Al₂O₃ coating after immersion in SBF for 20 days: (a) at 200X; (b) at 400X; (c) at 6000X and (d) EDAX surface analysis of (c)

Figure 6.29b and c show the cross-sectional images taken at higher magnification of 2500X from different locations. It can be seen from these images that some craters have been formed in the cross-section of coating after immersion in SBF for 1 day. The formation of craters might be due to dissolution of amorphous phases. Higher roughness of coating cross sections suggests that the dissolution of amorphous phases took place in very first day of immersion in SBF. The cross-sectional morphology of HA-30 wt% Al₂O₃ coating after immersion in SBF for 5 days is shown in Fig. 6.30a, while Fig. 6.30b and c show the cross-sectional morphology of HA-30 wt% Al₂O₃ coating after immersion period of 10 days.

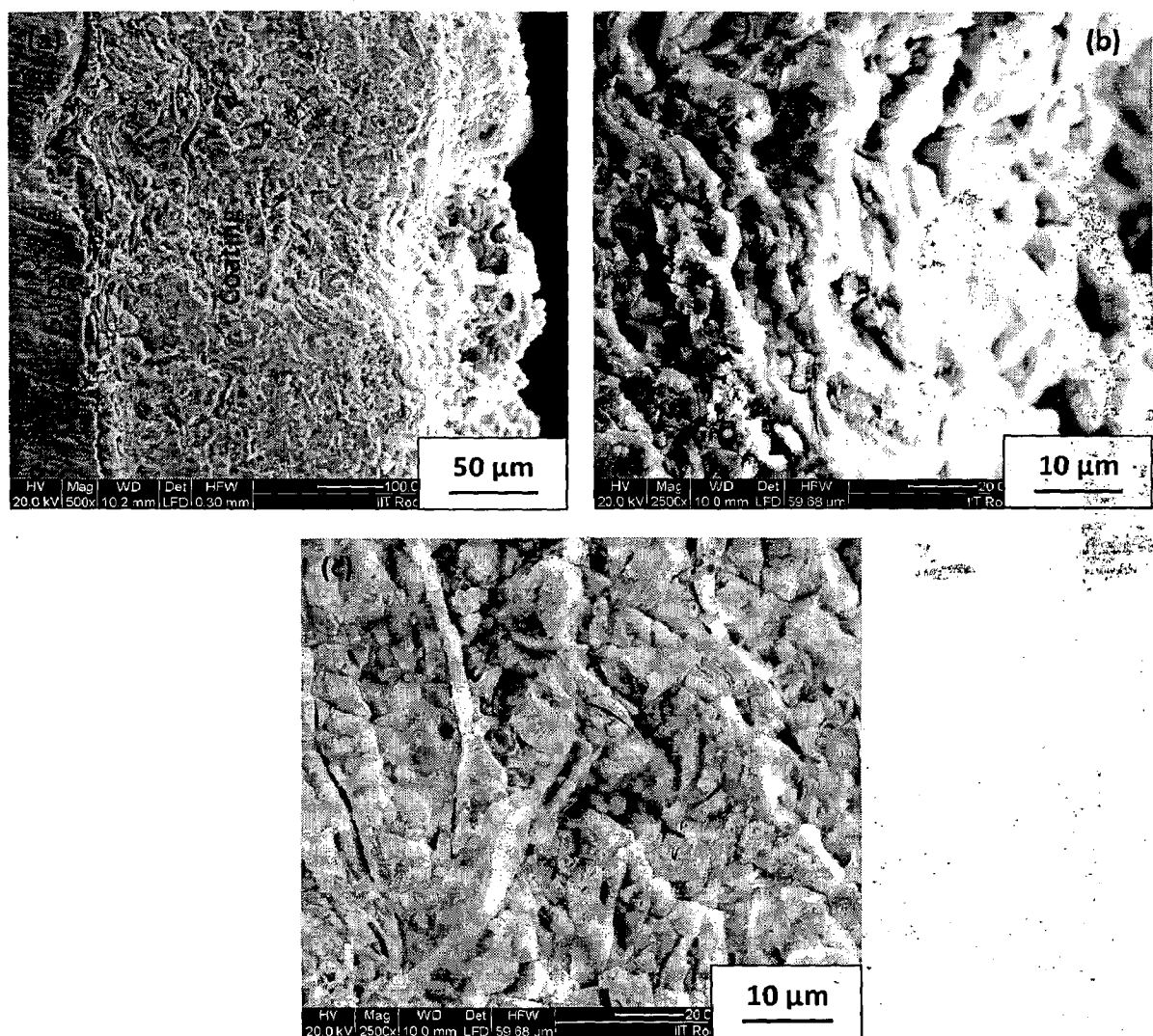


Fig. 6.29 FESEM showing cross-sectional morphology of HA-30 wt% Al₂O₃ coating after immersion in SBF for 1 day at different magnifications: (a) at 500X; (b) at 2500X and (c) at 2500X from different location

After immersion period of 5 days in SBF the cross-section show similar morphology as shown by coating after immersion period of 1 day (Fig. 6.29), which suggest that dissolution of amorphous phases continued for immersion period of 5 days in SBF. The SEM image shows that cross-section of coating is rough with presence of craters. The cross-sectional morphology of HA-30 wt% Al₂O₃ coating after immersion in SBF for 10 days at magnification of 400X and 800X is shown in Fig. 6.30 b and c respectively. It can be seen from Fig. 6.30b that the precipitation of tiny particles occurred at coating as well as substrate after immersion in SBF for 10 days. The magnified image of cross-section at 800X is shown in Fig. 6.30c, which reveal that the coating cross-section is completely covered with minute precipitates.

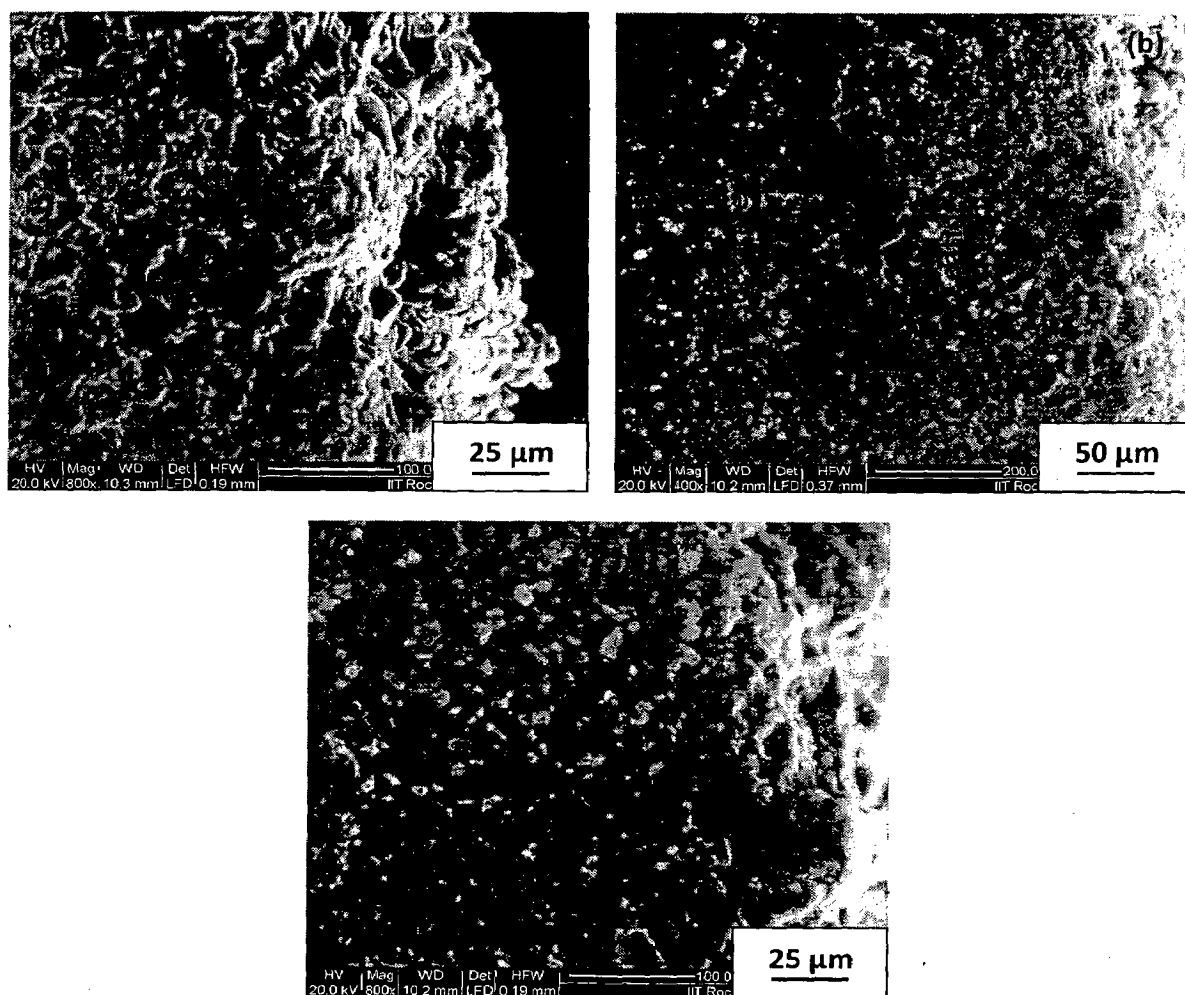


Fig. 6.30 FESEM showing cross-sectional morphology of HA-30 wt% Al₂O₃ coating after immersion in SBF: (a) for 5 days at 800X; (b) for 10 days at 400X and (c) for 10 days at 800X

The cross-sectional morphology of HA coating after immersion in SBF for 15 and 20 days is shown in Fig. 6.31a and b respectively. The SEM images of cross-section of HA coating after immersion in SBF for 15 days show that coating cross-section is completely covered with minute precipitates (Fig. 6.31a). The SEM image of cross-section and surface of HA coating after immersion in SBF for 20 days is shown in Fig. 6.31b. The coating surface shows rough morphology. By carefully examining the cross-section of HA coating after immersion period of 20 days in SBF it can be seen that tiny precipitates are present on the cross-section.

By examining the coating surface and cross-sections it can be concluded that the dissolution of amorphous phases started after immersion period of 1 day and dissolution took place up to immersion period of 5 days, thereafter the precipitation of tiny particles from SBF to coating as well as titanium (substrate) surface started and this phenomenon occurred throughout the immersion period of 20 days.

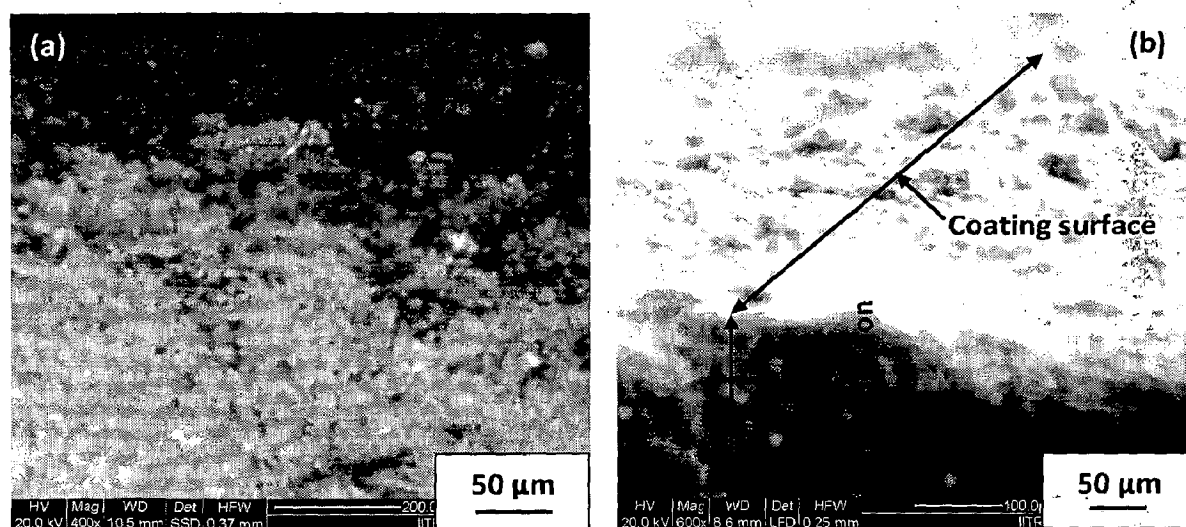


Fig. 6.31 FESEM showing cross-sectional morphology of pure HA coating after immersion in SBF: (a) for 15 days at 400X and (b) at for 20 days 600X.

6.2.5.2 X-ray diffraction analysis of coatings after immersion in SBF

The rinsed and dried specimens after immersion tests in SBF were subjected to X-ray diffraction analysis and XRD patterns of pure HA, HA-10 wt% Al₂O₃, HA-20 wt% Al₂O₃ and HA-30 wt% Al₂O₃ after immersion test for 5, 10, 15 and 20 days are shown in Fig.6.32 to Fig. 6.35

respectively. The as-sprayed coatings contain amorphous phases such as tri-calcium phosphate, tetra-calcium phosphate and CaO as can be seen from Fig. 6.32a, 6.33a, 6.34a and 6.35a. The respective position of these amorphous phases in XRD plots has already been stated in section 4.2.6 of Chapter 4.

The X-ray diffraction pattern of pure HA coating after immersion period of 5, 10, 15 and 20 days is shown in Fig. 6.32. It can be seen from XRD pattern that tetra-calcium phosphate (TTCP) is present in the coating, whereas all other amorphous phases are absent after immersion period of 5 days. The coatings after immersion test for 10 days or more in SBF do not contain any amorphous phases (Fig. 6.32c-e), which are generally present in original plasma sprayed hydroxyapatite coatings. The amorphous phases have a tendency to get dissolved in physiological solutions. Absence of amorphous phases in XRD pattern of coatings after immersion for 10 or more days may be due to dissolution of these phases in SBF.

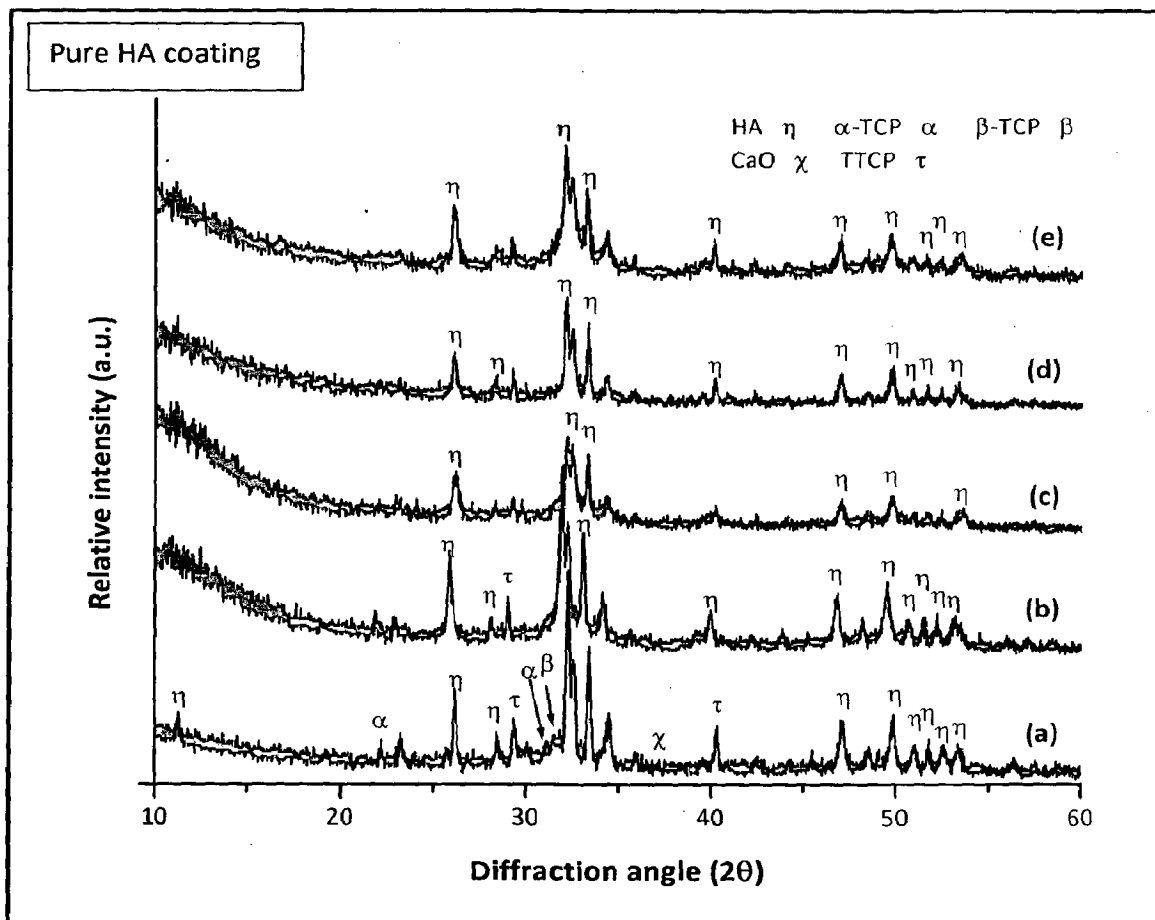


Fig 6.32 X-ray diffraction pattern of pure HA coating (a) as coated; after immersion test for: (b) 5 days; (c) 10 days; (d) 15 days and (e) 20 days

The XRD pattern of HA-10 wt% Al₂O₃ coating after different immersion periods is shown in Fig.6.33. The amorphous phases such as α -tri-calcium phosphate (α -TCP), β -tri-calcium phosphate (β -TCP), tetra-calcium phosphate (TTCP) and CaO can be seen in as-sprayed coatings (Fig. 6.33a). TCP and CaO phases are absent in the coatings after immersion period of 5 days, whereas TTCP shows its presence as can be seen from Fig. 6.33b. Aluminum oxide (Al₂O₃) can be seen near 57° (2 θ) in XRD pattern of coatings (Fig. 6.33a, c and e). After immersing the coatings for a period more than 5 days, XRD pattern do not show any peak corresponding to amorphous phases.

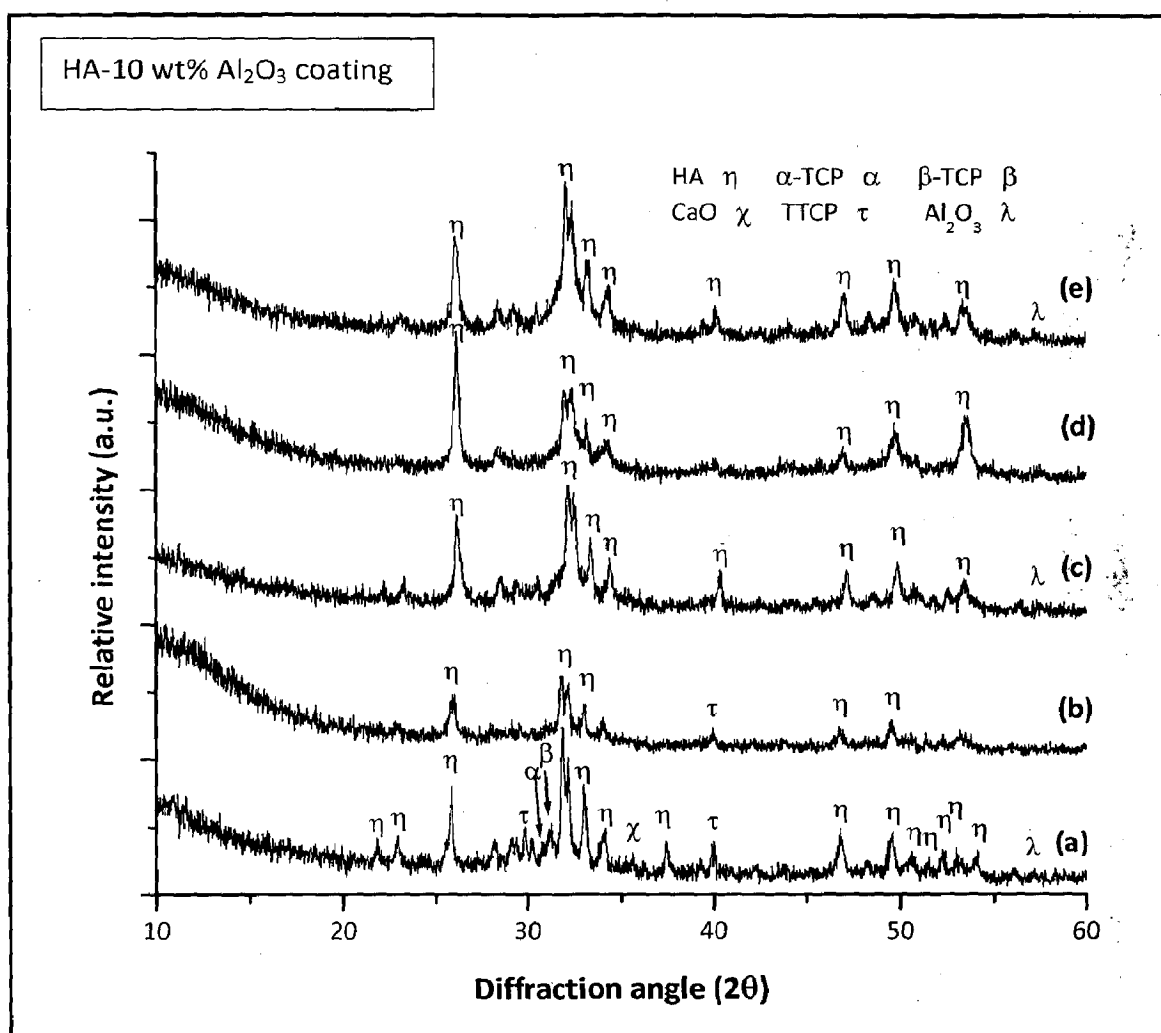


Fig 6.33 X-ray diffraction pattern of HA-10 wt% Al₂O₃ coating (a) as coated; after immersion test for: (b) 5 days; (c) 10 days; (d) 15 days and (e) 20 days

The XRD pattern of HA-20 wt% Al₂O₃ and HA-30 wt% Al₂O₃ after immersion in SBF for different periods is shown in Fig. 6.34 and 6.35 respectively. It can be seen from XRD pattern of HA-20 wt% Al₂O₃ coatings (Fig.6.34) that after immersion in SBF for 5 days TTCP is present, while other amorphous phases are absent. The XRD pattern of HA-30 wt% Al₂O₃ coating after immersion (Fig. 6.35) does not contain any amorphous phases after immersion period of 5 days or more. From XRD pattern Al₂O₃ peaks can be seen around 43° and 57° (2θ) in Fig. 6.34a, b, d, e and Fig. 6.35a-e respectively. By analyzing XRD patterns of all coatings after immersion for different period in SBF, it can be concluded that amorphous phases are absent in the XRD pattern of coatings after immersion period of 10 days.

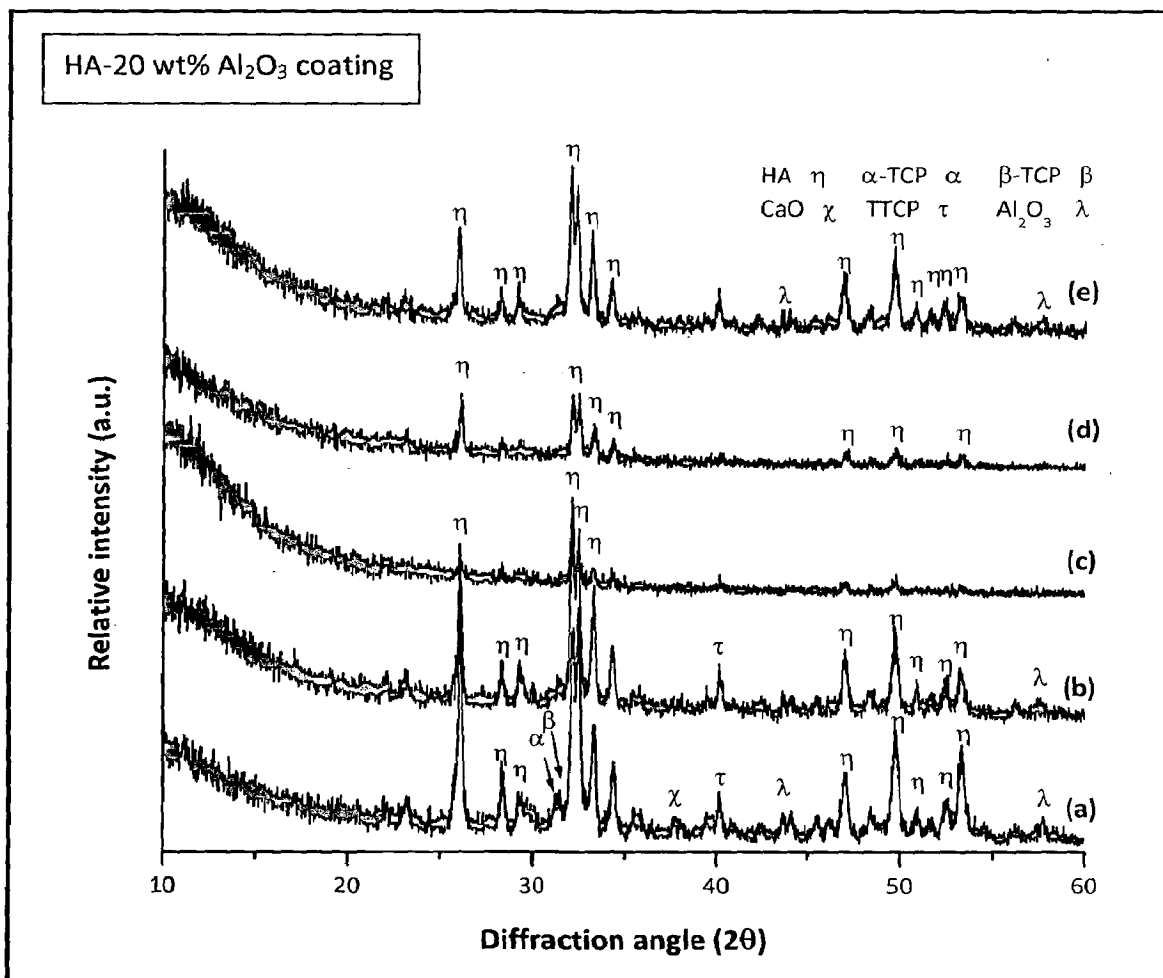


Fig 6.34 X-ray diffraction pattern of HA-20 wt% Al₂O₃ coating (a) as coated; after immersion test for: (b) 5 days; (c) 10 days; (d) 15 days and (e) 20 days

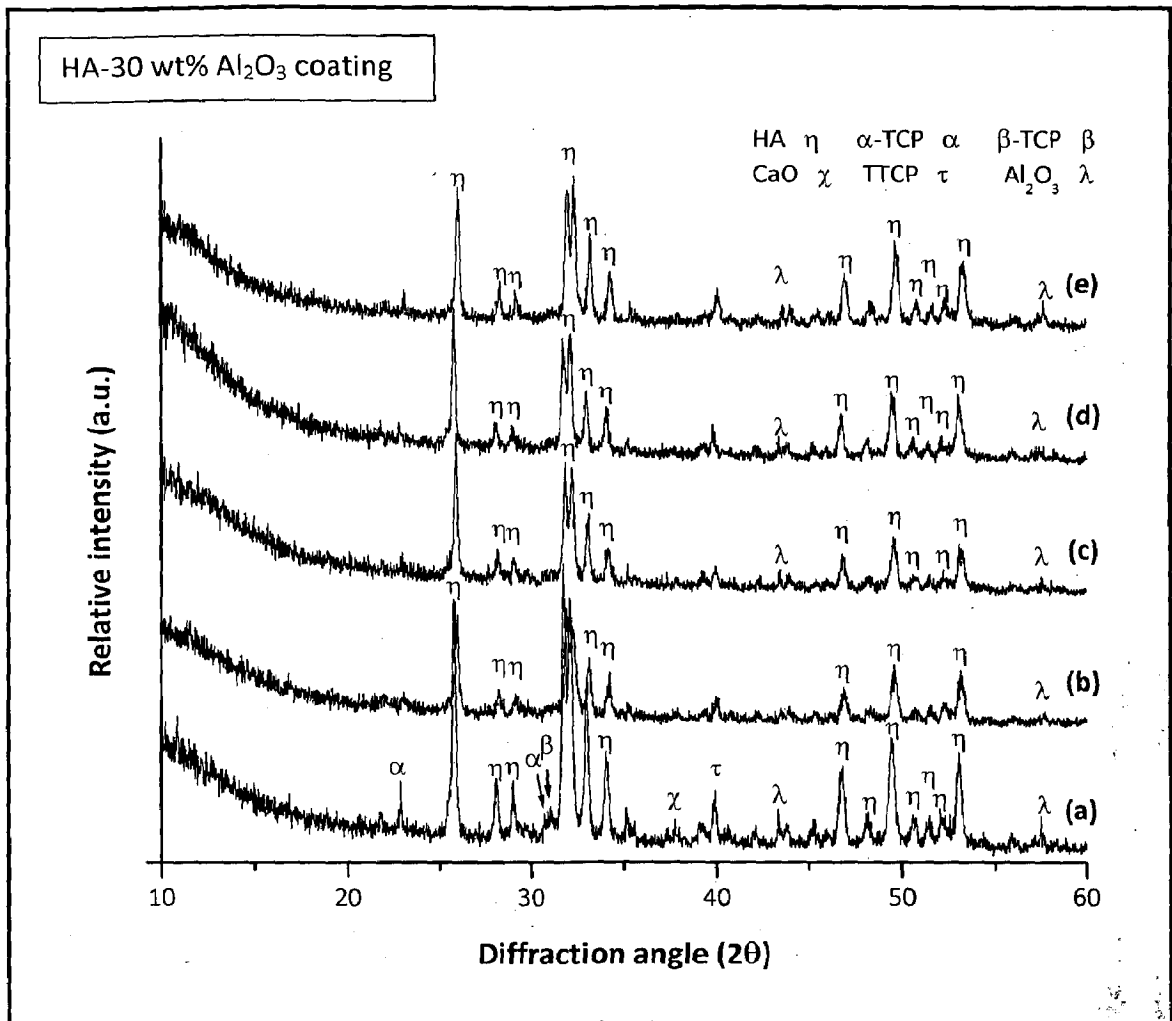


Fig 6.35 X-ray diffraction pattern of HA-30 wt% Al₂O₃ coating (a) as coated; after immersion test for: (b) 5 days; (c) 10 days; (d) 15 days and (e) 20 days

6.2.5.3 FTIR analysis of coatings after immersion in SBF

The FTIR plots for plasma sprayed pure HA, HA-10 wt% Al₂O₃, HA-20 wt% Al₂O₃ and HA-30 wt% Al₂O₃ coatings after immersion in SBF for designated time period are shown in Fig. 6.36 to Fig. 6.39 respectively. It can be seen from FTIR spectra of pure HA coatings after immersion in SBF (Fig. 6.36) that carbonate group (CO₃²⁻) is present 2386 cm⁻¹ in the spectrum of HA coating after immersion period of 5 and 10 days (Fig. 6.36a-b), whereas it can be seen at 2364 cm⁻¹ for the coating after immersion period of 15 and 20 days (Fig. 6.36c-d). The intensity of

peak corresponding to carbonate group is found to increase with increase in immersion period. The hydroxyl group (OH^-) is present at varying locations in FTIR spectrum of HA coatings after immersion in SBF for different time spans. It can be seen at 3764 cm^{-1} , 610 cm^{-1} ; 3655 cm^{-1} , 635 cm^{-1} ; 3677 cm^{-1} , 618 cm^{-1} and 3655 cm^{-1} , 613 cm^{-1} for HA coating after immersion period of 5, 10, 15 and 20 days respectively (Fig. 6.36a-d).

The PO_4^{3-} group can be seen at 569 cm^{-1} , 657 cm^{-1} , 975 cm^{-1} and 1090 cm^{-1} in FTIR spectrum of HA coating after immersion period of 5 days, whereas it can be seen at 560 cm^{-1} , 579 cm^{-1} , 972 cm^{-1} and 1040 cm^{-1} in FTIR spectrum of HA coatings after immersion period of 10 days. In FTIR spectrum of HA coating after immersion period of 15 days PO_4^{3-} can be observed at 576 cm^{-1} , 678 cm^{-1} , 953 cm^{-1} , 1008 cm^{-1} and 1106 cm^{-1} , whereas in FTIR spectrum of HA coating after immersion period of 20 days it can be observed at 569 cm^{-1} , 657 cm^{-1} , 970 cm^{-1} , 1050 cm^{-1} and 1095 cm^{-1} .

The FTIR spectra for HA-10 wt% Al_2O_3 coatings after immersion in SBF for different time periods are shown in Fig. 6.37. It can be seen from Fig. 6.37 that carbonate group is present at 2352 cm^{-1} , 2386 cm^{-1} , 2364 cm^{-1} and 2396 cm^{-1} in spectrum of HA-10 wt% Al_2O_3 coatings after immersion period of 5, 10, 15 and 20 days respectively. The most intense peak corresponding to CO_3^{2-} is present in FTIR spectrum of coating for immersion period of 15 days (Fig. 6.37c). The hydroxyl group (OH^-) can be seen at 3578 cm^{-1} , 613 cm^{-1} ; 3570 cm^{-1} , 603 cm^{-1} ; 3578 cm^{-1} , 603 cm^{-1} and 3556 cm^{-1} , 610 cm^{-1} in FTIR spectra of HA-10 wt% Al_2O_3 coating after immersion in SBF for 5, 10, 15 and 20 days respectively.

In FTIR spectrum of HA-10 wt% Al_2O_3 coating after immersion in SBF for a period of 5 days PO_4^{3-} can be seen at 560 cm^{-1} , 635 cm^{-1} , 947 cm^{-1} , 1018 cm^{-1} and 1095 cm^{-1} , whereas after immersion period of 10 days it can be seen at 560 cm^{-1} , 635 cm^{-1} , 1059 cm^{-1} and 1130 cm^{-1} . The phosphate group can be seen at 560 cm^{-1} , 635 cm^{-1} , 963 cm^{-1} , 1050 cm^{-1} and 1106 cm^{-1} in FTIR spectrum of coating after immersion period of 15 days, whereas it can be seen at 560 cm^{-1} , 635 cm^{-1} , 953 cm^{-1} , 1018 cm^{-1} and 1116 cm^{-1} in FTIR spectrum of coating immersed for a period of 20 days.

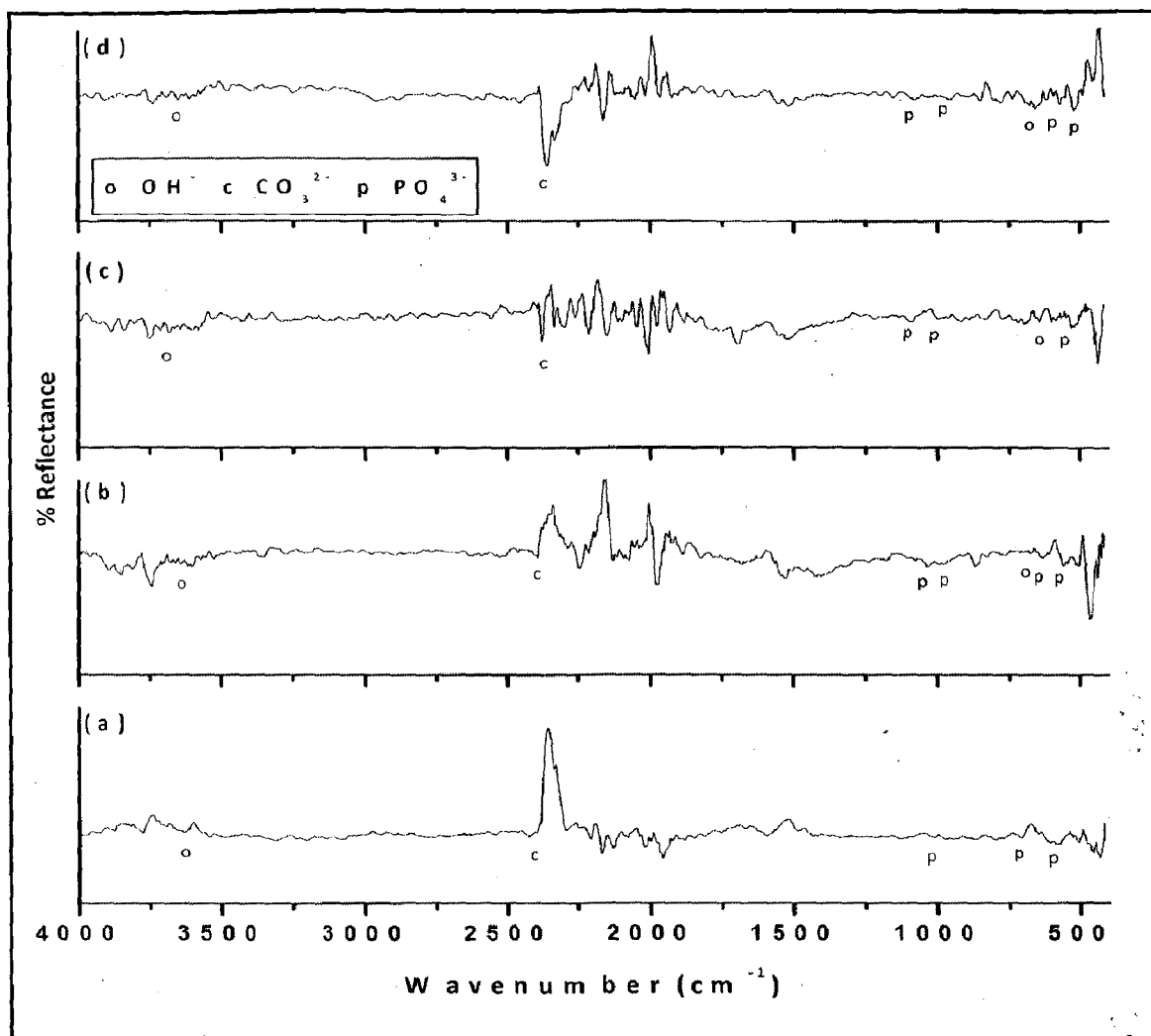


Fig. 6.36 FTIR spectra for plasma sprayed pure HA coating after immersion in SBF for: (a) 5 days; (b) 10 days; 15 days and (d) 20 days

The FTIR spectra for HA-20 wt% Al₂O₃ coating after immersion for different time spans are shown in Fig. 6.38. It can be seen from the spectra that carbonate group is present at 2364 cm⁻¹ and 2352 cm⁻¹ for coating after immersion period of 5 and 10 days respectively, whereas it is present at 2384 cm⁻¹ for coatings after immersion period of 15 and 20 days. The most intense peak of carbonate group (CO₃²⁻) can be seen at 2384 cm⁻¹ in spectrum of coating after immersion period of 15 days (Fig. 6.38c). Hydroxyl group can be observed at 3644 cm⁻¹, 635 cm⁻¹; 3611 cm⁻¹, 590 cm⁻¹; 3611 cm⁻¹, 613 cm⁻¹ and 3635 cm⁻¹, 613 cm⁻¹ for HA-20 wt% Al₂O₃ coating after immersion period of 5, 10, 15 and 20 days respectively.

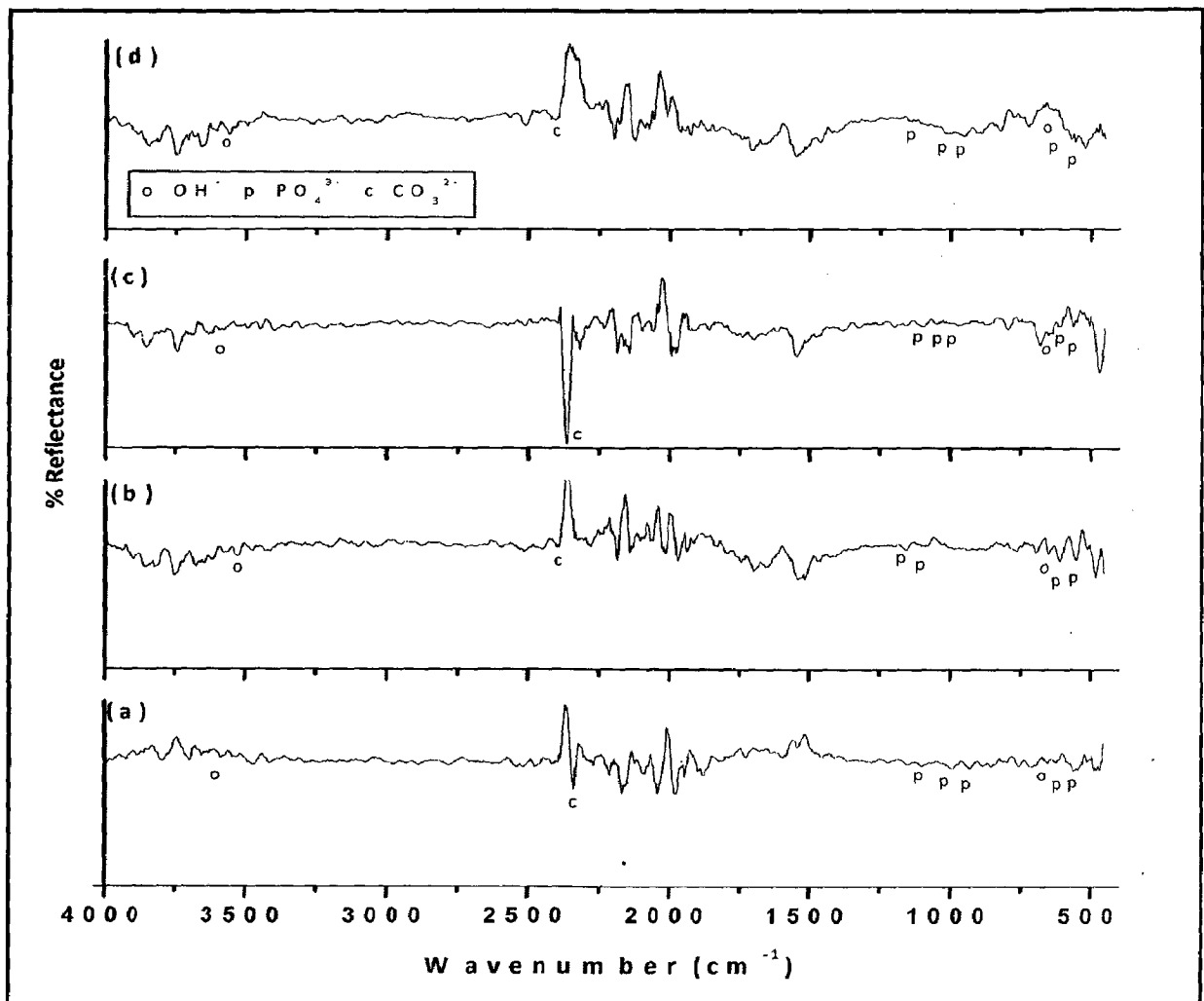


Fig. 6.37 FTIR spectra for plasma sprayed HA-10 wt% Al₂O₃ coating after immersion in SBF for: (a) 5 days; (b) 10 days; 15 days and (d) 20 days

In Fig. 6.38, the phosphate group can be seen at 547 cm⁻¹, 690 cm⁻¹, 953 cm⁻¹, 1018 cm⁻¹ and 1050 cm⁻¹ in FTIR spectrum of HA-20 wt% Al₂O₃ coating after immersion in SBF for 5 days, whereas it is present at 547 cm⁻¹, 657 cm⁻¹, 970 cm⁻¹, 1018 cm⁻¹ and 1073 cm⁻¹ in FTIR spectrum of coating after immersion period of 10 days. In FTIR spectrum of HA-20 wt% Al₂O₃ coating after immersion period of 15 days PO₄³⁻ can be seen at 560 cm⁻¹, 657 cm⁻¹, 930 cm⁻¹ and 1095 cm⁻¹, whereas it is present at 560 cm⁻¹, 635 cm⁻¹, 955 cm⁻¹ and 997 cm⁻¹ for coating immersed in SBF for 20 days.

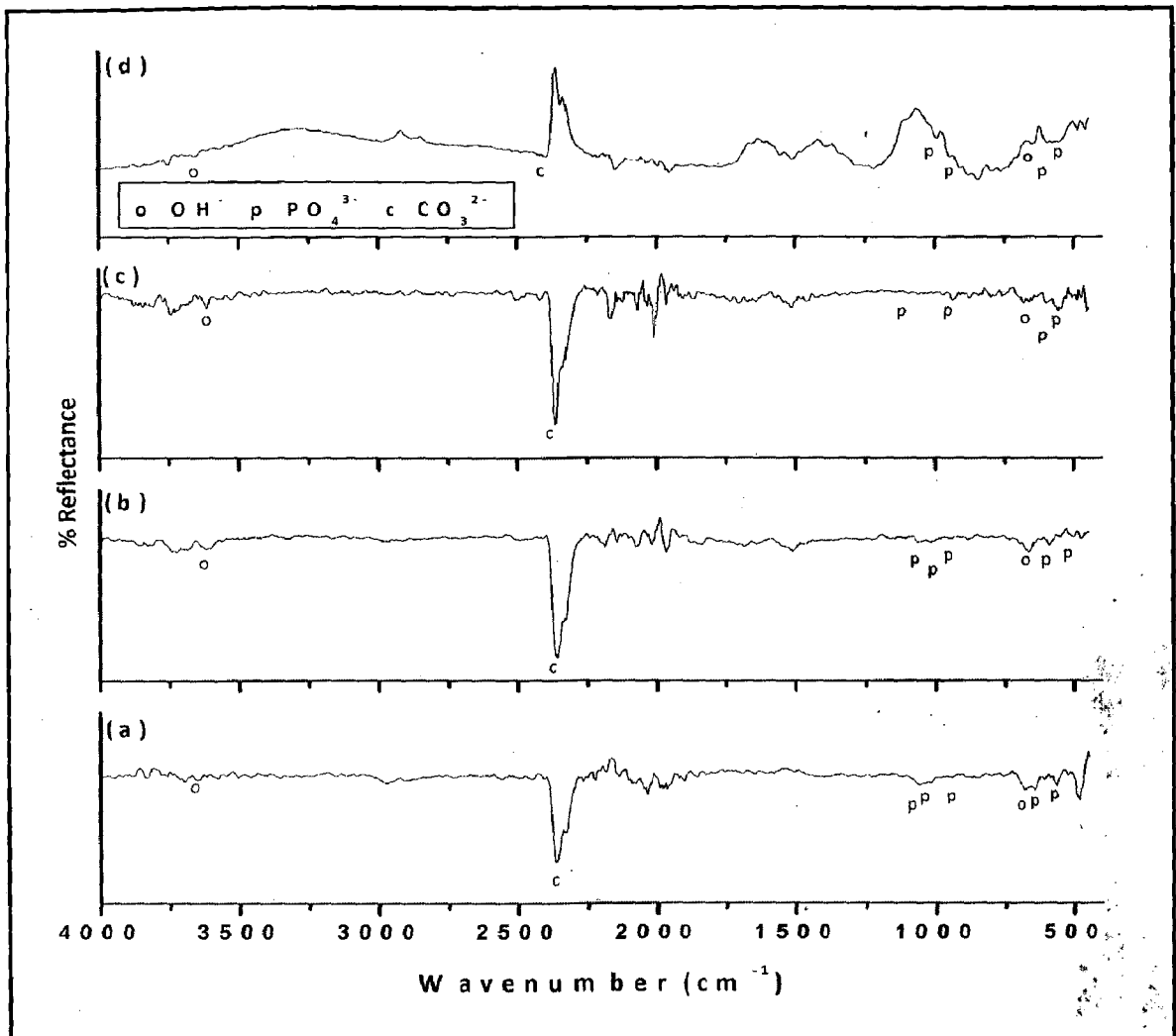


Fig. 6.38 FTIR spectra for plasma sprayed HA-20 wt% Al₂O₃ coating after immersion in SBF for: (a) 5 days; (b) 10 days; 15 days and (d) 20 days

The FTIR spectra of HA-30 wt% Al₂O₃ coatings after immersion in SBF for 5, 10, 15 and 20 days are shown in Fig. 6.39. It can be seen that carbonate group is present at 2364 cm⁻¹ in FTIR spectra of coatings after immersion period of 5, 10 and 20 days (Fig. 6.39a, b and d), whereas it can be seen at 2360 cm⁻¹ in FTIR spectrum of coating for immersion period of 15 days (Fig. 6.39c). Hydroxyl group show its presence at 3677cm⁻¹, 650 cm⁻¹; 3646 cm⁻¹, 603 cm⁻¹; 3633 cm⁻¹, 603 cm⁻¹ and 3644 cm⁻¹, 610 cm⁻¹ in FTIR spectra of HA-30 wt% Al₂O₃ coatings after immersion in SBF for 5, 10, 15 and 20 days respectively (Fig. 6.39a-d).

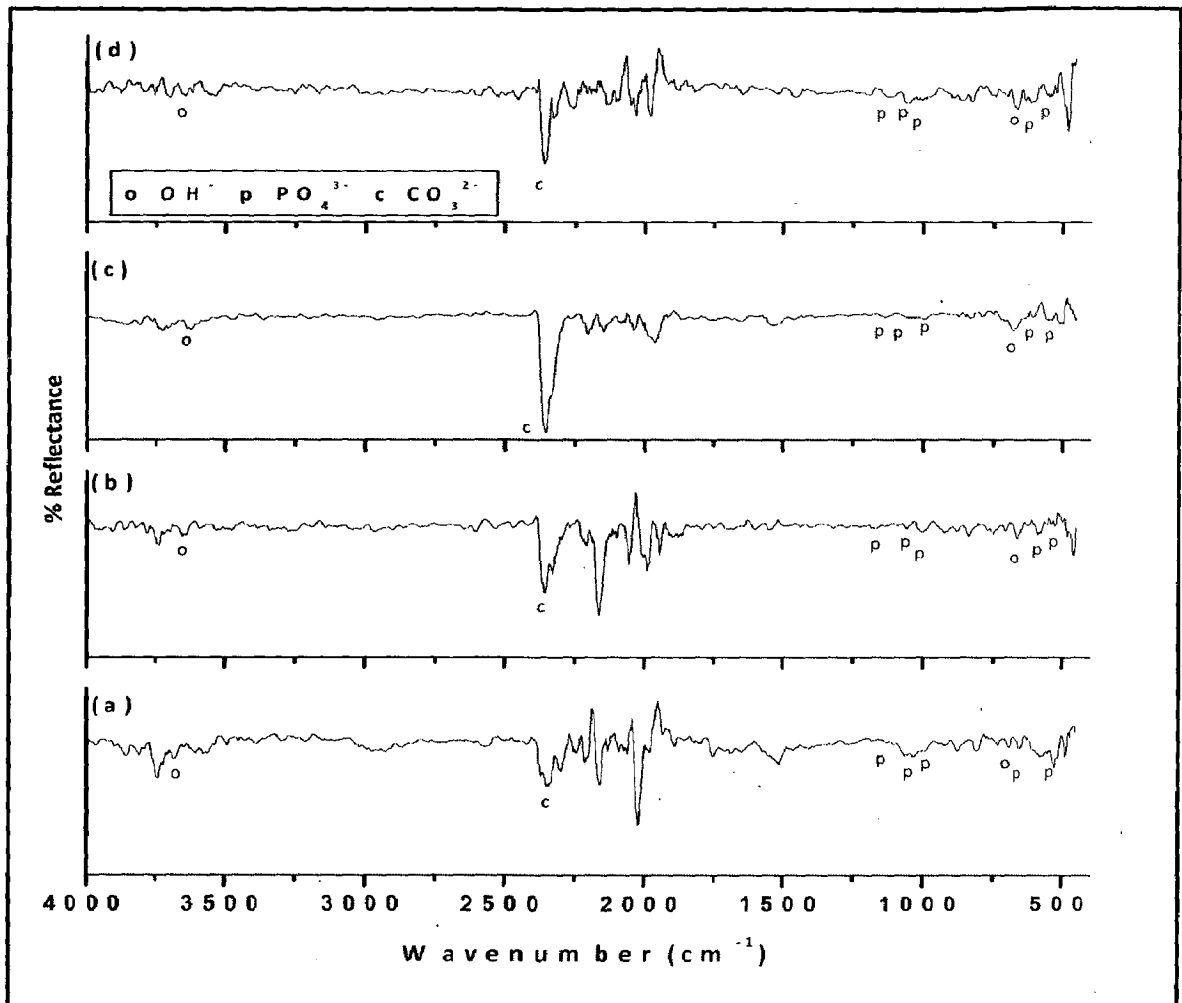


Fig. 6.39 FTIR spectra for plasma sprayed HA-30 wt% Al₂O₃ coating after immersion in SBF for: (a) 5 days; (b) 10 days; 15 days and (d) 20 days

Phosphate group (PO₄³⁻) in FTIR spectrum of HA-30 wt% Al₂O₃ coatings after immersion period of 5 days (Fig. 6.39a) can be seen at 530 cm⁻¹, 690 cm⁻¹, 970 cm⁻¹, 1051 cm⁻¹ and 1116 m⁻¹, whereas it can be seen at 550 cm⁻¹, 670 cm⁻¹, 980 cm⁻¹, 1051 cm⁻¹ and 1140 cm⁻¹ in FTIR spectrum of coating after immersion period of 10 days (Fig. 6.39b). In FTIR spectrum of HA-30 wt% Al₂O₃ coating after immersion in SBF for 15 days (Fig. 6.39c), PO₄³⁻ can be seen at 550 cm⁻¹, 980 cm⁻¹, 1060 cm⁻¹ and 1116 cm⁻¹, whereas it can be observed at 570 cm⁻¹, 657 cm⁻¹, 980 cm⁻¹, 1060 cm⁻¹, 1138 cm⁻¹ in coating immersed for 20 days (Fig. 6.39d).

6.3 DISCUSSION

The bare and coated specimens were evaluated for corrosion resistance by various electrochemical techniques in simulated body fluid environment maintained at pH 7.4 and 37°C to imitate actual body fluid conditions. After analyzing the results obtained from electrochemical tests on plasma spray coated and bare specimens, it was found that all the coatings are protective in nature and are able to reduce corrosion current density as compared to bare specimens. The corrosion current density of titanium is almost three times lower than that of AISI 316L SS, whereas corrosion current density of pure HA coating varies in a close range irrespective of substrate, which suggests that metallic substrate did not come in contact with electrolyte (SBF) during electrochemical testing. The results of corrosion studies obtained in present investigation for pure HA coatings are in close agreement with the findings of Fathi et al., (2003).

In present investigation corrosion current density for plasma sprayed pure HA coatings has been measured in the range varying from 6.7 to 11.2 nA/cm². Chen et al., (2004) studied corrosion resistance of plasma sprayed HA coatings in SBF using potentiodynamic polarization tests and reported a corrosion current density of 250±70 nA/cm². Lee et al., (2005) also reported corrosion current density of 146±40 nA/cm² for plasma sprayed HA coatings using potentiodynamic polarization experiments in SBF. The results obtained for plasma sprayed HA coatings in present study are in close agreement with findings of Chen et al., (2004) and Lee et al., (2005). Morks et al., (2008) deposited HA-15 wt% SiO₂-10 wt% Ti by plasma spraying onto SUS 304 SS by varying plasma gas flow rate during spraying and investigated their corrosion behavior in SBF. They reported corrosion current density of 9±3 µA for gas flow rate of 170 l/min.

Sousa and Barbosa, (1995) conducted a study on plasma sprayed HA coatings on 350 SS for corrosion behavior in Hank's balanced salt solution (HBSS) and reported that both thicker (200 µm) as well as thinner (50 µm) HA coatings offered better corrosion protection as compared to bare stainless steel and did not induce crevice attack at substrate-coating interface. Souto et al., (2003) investigated the corrosion behavior of plasma sprayed HA coatings on Ti-6Al-4V in Ringer's salt solution using electrochemical impedance spectroscopy

and reported that after exposure for 4 months to Ringer's solution, no evidence of coating detachment from metallic substrate was observed. They suggested that coated system can withstand longer exposure periods in Ringer's solution.

Three HA powders with different sizes and morphologies (needle, flake and spherical shaped) were electrophoretically deposited onto Ti-6Al-4V alloy and their corrosion resistance in Hank's physiological solution was compared by Kwok et al., (2009). They reported that coatings were more protective as compared to as-received alloy in terms of corrosion current density. Moreover coating deposited by spherical powder particles offered better corrosion resistance than coating deposited by other two powders (needle and flake shaped). The corrosion current densities (in present study) determined for plasma sprayed HA coatings in SBF using potentiodynamic polarization test was almost 100 times lower than quoted by Kwok et al., (2009) for electrophoretically deposited HA. This might be due to higher coating thickness of plasma sprayed coatings and absence of network of cracks and through pores due to which the electrolyte might not come to contact with metallic substrate.

Qiu et al., (2010) deposited HA-ZrO₂ composite coating on NiTi using electrochemical technique and studied its corrosion behavior in SBF using potentiodynamic polarization test and concluded that corrosion current density was least for HA-ZrO₂ composite coating followed by HA coating and NiTi alloy. In present study least corrosion current density is recorded for pure HA coatings however, all the coatings are protective and offered better corrosion resistance than uncoated substrates.

In present study presence of alumina in HA coating does not affected the biocompatibility of HA in SBF. Tercero et al., (2009) cultured the human fetal osteoblast cells on three types of coating (HA, HA-20% Al₂O₃ and HA-18.4% Al₂O₃-1.6% CNT) developed by plasma spraying process. They reported that addition of reinforcement had no negative effect on the biocompatibility of coating, moreover Al₂O₃ particles were reported to retain their bio-inertness without affecting the biocompatibility of HA.

Xie et al., (2009) deposited CaO-ZrO₂-SiO₂ coatings on Ti-6Al-4V substrate by plasma spraying process and studied their behavior in SBF for incubation period of 14 days. They reported formation of apatite on coating surface after immersion in SBF, which implies that the

coating possesses potential to chemically bond with bone tissue. Formation of apatite on the coating after immersion period of 15 and 20 days in SBF in present study matches with the findings of Xie et al., (2009).

In the present study the change of weight of coated specimen after immersion in SBF for different time periods is in close agreement with the calcium ion concentration in SBF after respective time period. Dissolution of amorphous phases leads to increase in Ca^{2+} ion concentration and can be clearly seen after immersion period of 10 days for HA-10 wt% Al_2O_3 coating (Fig. 6.8) and after immersion period of 5 days for HA-20 wt% Al_2O_3 (Fig. 6.9). Dissolution of impurity phases and as a consequence, an increase in Ca^{2+} ion concentration after soaking for 7 days has been reported by Gu et al., (2003).

The morphology of plasma sprayed coatings after immersion in SBF for 1 day (Fig. 6.11-6.12 and 6.29) show dissolution of some phases present in plasma sprayed HA coating leading to surface with increased roughness, formation of cracks, pores and craters. In general, after immersion in SBF for 5, 10, 15 and 20 days (Fig. 6.13-6.28 and Fig. 6.30-6.31), the dissolution of undesirable phases and formation of nano-crystalline phase due to precipitation of apatite phase was observed.

It can be inferred from XRD plots of coatings (Fig. 6.32-6.35) after immersion in SBF for different time periods that most of the amorphous phases including tri-calcium phosphate and CaO get dissolved within 5 days of immersion leaving some tetra-calcium phosphate, however after immersion period of 10 days, peaks corresponding to tetra-calcium phosphate are absent in XRD plots. The dissolution of amorphous phases and precipitation of apatite took place simultaneously, which can be visualized as the coexistence of rougher surface and precipitates of apatite on coatings. It can be seen from Fig. 6.13 and Fig 6.20 that an apatite layer has covered whole of the pure HA coating within 5 days of immersion in SBF and that of HA-30 wt% Al_2O_3 coating after immersion period of 10 days respectively.

The increase in intensity of hydroxyl and phosphate group in FTIR plots as can be seen in Fig. 6.36-6.39 indicates development of crystalline apatite layer on the surface of coating after immersion in SBF. The increase in intensity of carbonate group might be due to precipitation of carbonate ions on the surface of coating during immersion in SBF. Hesse et al., (2008)

conducted incubation experiments on plasma sprayed HA coatings for a period up to 8 weeks in simulated body fluid and reported the change in phase composition of coatings after incubation as CaO and amorphous calcium phosphates dissolved, whereas fine-grained HA crystallized on the surface of coatings. Once the dissolution of ceramic coating (coating containing HA and other amorphous phases) commences in SBF, super-saturation reaches rapidly as SBF already contains a high concentration of free calcium and phosphate ions. About 9% dissolution of amorphous calcium phosphate has been reported after immersion period of 21 days in SBF by Etok and Rogers, (2005). Ding et al., (2000) reported that during early stages of immersion, rapid dissolution of amorphous calcium phosphates and precipitation of apatite phase are dominating.

In present work tortoise shell like morphology on the surface of HA coatings have been seen after immersion in SBF for 5 days and on the surface of HA-10 wt% Al₂O₃ coating after soaking period of 15 days in SBF as shown in Fig. 6.13 and Fig. 6.22 respectively. The similar findings have been reported by Yu et al., (2003) for as-sprayed and spark plasma sintered HA coatings developed by plasma spraying after soaking period of 12 days in SBF and by Chen et al., (2010) for plasma sprayed silver-containing HA coating after soaking in SBF for 7 days.

Li et al., (2009) investigated the behavior of HA-ZrO₂ graded coatings in SBF for incubation period ranging from 3 to 30 days. They observed some single crystals and clustered ball-like particles on the surface of coating after incubation period of 3 days with rapid increase in calcium ion concentration in SBF for initial days of immersion, which has been attributed to dissolution of tri-calcium phosphate. They further reported that with increase in immersion time, the number of these ball-like particles increased until the surface was completely covered with newly formed layer of small granular structure. Similar structure was developed on surface of HA coating after 20 days of incubation period in SBF in present investigation as shown in Fig. 6.25. Li et al. (2009) reported decrease in calcium ion concentration and confirmation of the nucleation of apatite layer from the solution, which is in close agreement with the findings of present study.

Svetina et al., (2001) reported the deposition of calcium ions and formation of phosphate layer is crucial to initiate the growth of bone-like apatite on biocompatible implants.

Morks and Kobayashi (2008) reported that surface morphology of plasma sprayed ZrO_2-SiO_2 coating showed spreading of fine particles after immersion period of 20 days in SBF. EDAX analysis confirmed these particles as apatite. They concluded that growth of apatite on ceramic coating is a positive indication for growth of apatite layer with fine structure on the surface of ZrO_2-SiO_2 coatings.

Beherei et al., (2008) developed HA-calcium aluminate (CA: 5, 10, 15 and 20 wt%) biocomposite by pressing and annealing at 1250 and 1350°C and studied their behavior in SBF for a soaking period of 7 days. They reported formation of new layer on the whole of the surface of annealed (at 1250°C) composite containing 20 wt% CA. In present investigation the similar coating morphology is obtained after immersion period of 20 days in SBF on surface of pure HA coating as shown in Fig. 6.25. By comparing these results, it can be well said that calcium aluminate promoted the early apatite formation. Beherei et al., also suggested that composite containing 15 and 20 wt% CA has high ability to form apatite layer on their surface.

6.4 CONCLUSIONS

The electrochemical properties of coatings were studied in simulated body fluid by linear polarization, potentiodynamic polarization and Tafel polarization techniques. The precipitation/dissolution behavior of coatings in SBF was studied for an immersion period of 5, 10, 15 and 20 days. The detailed results have been discussed in current Chapter of this study. The conclusions drawn from results are presented hereunder:

1. The results obtained from linear polarization resistance test showed that the corrosion current densities of all the coatings on AISI316L and titanium were much lower than that of respective substrate. The corrosion current density offered by all the coatings was found to be in range of $0.006 \mu A/cm^2$ to $0.053 \mu A/cm^2$. The corrosion resistance of coatings and substrate observed the following sequence:

- i. AISI 316L substrate

Pure HA > HA-10 wt% Al_2O_3 > HA-20 wt% Al_2O_3 > HA-30 wt% Al_2O_3 > Substrate

ii. Titanium substrate

Pure HA > HA-20 wt% Al₂O₃ > HA-10 wt% Al₂O₃ > HA-30 wt% Al₂O₃ > Substrate

2. The potentiodynamic polarization resistance test showed similar results as shown by linear polarization test in reference to corrosion current densities. The corrosion current densities of all the coatings on AISI316L and titanium were found to be much lower than that of respective substrate. The least corrosion current density for both substrates was offered by pure HA coating, moreover the maximum variation in current densities offered by composite coatings was around 45 nA/cm². The corrosion current density of coatings and substrate observed the following sequence:

i. AISI 316L substrate

Pure HA > HA-30 wt% Al₂O₃ > HA-20 wt% Al₂O₃ > HA-10 wt% Al₂O₃ > Substrate

ii. Titanium substrate

Pure HA > HA-10 wt% Al₂O₃ > HA-20 wt% Al₂O₃ > HA-30 wt% Al₂O₃ > Substrate

3. The results obtained from Tafel polarization test showed that the corrosion current densities of all the coatings on AISI316L and titanium were much lower than that of respective substrate. The least corrosion current density for both substrates was offered by pure HA coating, moreover the maximum variation in current densities offered by composite coatings was about 30 nA/cm². The corrosion resistance of coatings and substrate observed the following sequence:

i. AISI 316L substrate

Pure HA > HA-30 wt% Al₂O₃ > HA-20 wt% Al₂O₃ > HA-100 wt% Al₂O₃ > Substrate

ii. Titanium substrate

Pure HA > HA-10 wt% Al₂O₃ > HA-20 wt% Al₂O₃ > HA-30 wt% Al₂O₃ > Substrate

4. The precipitation/dissolution behavior (weight gain/loss) of coatings after immersion in SBF for 5, 10, 15 and 20 days at controlled temperature of 37±1°C is summarized as under:

i. Pure HA coatings

10 days > 5 days > 20 days > 15 days: weight was gained by coatings for all period of immersion

II. HA-10 wt% Al₂O₃ coatings

15 days > 5 days > 20 days > 10 days: weight was lost by coating after immersion period of 10 days and gained by coatings for all other periods of immersion

III. HA-20 wt% Al₂O₃ coatings

15 days > 10 days (no wt. change) > 20 days > 5 days: weight was lost by coating after immersion period of 5 and 20 days and gained after immersion period of 15 days

IV. HA-30 wt% Al₂O₃ coatings

20 days > 5 days > 15 days > 10 days: weight was gained by coatings for all period of immersion

5. The concentration of Ca²⁺ ion concentration in SBF (decrease/increase) after immersion period of 5, 10, 15 and 20 days at controlled temperature of 37±1°C is summarized as under:

I. Pure HA coatings

5 days < 20 days < 15 days < 10 days: Ca²⁺ ion concentration decreased for all immersion periods as compared to Ca²⁺ ion concentration in starting SBF

II. HA-10 wt% Al₂O₃ coatings

15 days < 20 days < 5 days < 10 days: Ca²⁺ ion concentration increased for immersion period of 10 days and decreased for immersion period of 5, 15 and 20 days as compared to Ca²⁺ ion concentration in starting SBF

III. HA-20 wt% Al₂O₃ coatings

15 days < 10 days < 5 days < 20 days: Ca²⁺ ion concentration decreased for immersion period of 15 days and increased for immersion period of 5, 10 and 20 days as compared to Ca²⁺ ion concentration in starting SBF

IV. HA-30 wt% Al₂O₃ coatings

5 days < 10 days < 20 days < 20 days: Ca^{2+} ion concentration increased for immersion period of 15 days and decreased for immersion period of 5, 10 and 20 days as compared to Ca^{2+} ion concentration in starting SBF

6. All the amorphous phases get dissolved in SBF within first day of immersion, whereas precipitation/dissolution was observed on coating after immersion period of 5 days. the precipitation of new tiny particles on coatings as well as substrate was observed after immersion period of 10, 15 and 20 days in SBF.
7. Absence of peaks corresponding to amorphous phases in XRD plots suggests dissolution of amorphous phases and from FTIR plots, increase in intensity of hydroxyl, phosphate and carbonate group suggests precipitation of apatite.

POST COATING HEAT TREATMENT

This chapter deals with the results and discussion of plasma sprayed HA and HA composite coated specimens after post coating heat treatment. Post coating heat treatment was carried out to recrystallize the amorphous phases of calcium and phosphorous generated during plasma spraying of hydroxyapatite. The present work has been focused to compare the effect of post coating heat treatment temperature on properties of the coatings for holding time of 2h.

7.1 INTRODUCTION

In the present chapter the characterization of post coating heat treated specimens has been described. The coated specimens were heat treated at 500°C, 700°C and 900°C for 2h in air. It includes the results related to surface morphology and phase analysis of coated specimens after post coating heat treatment using field emission scanning electron microscopy/energy dispersive X-ray (FE-SEM/EDAX), X-ray diffraction (XRD) and FTIR techniques. The detailed experimental procedure is explained in Chapter 3 of present study.

7.2 RESULTS

7.2.1 Surface Morphology and EDAX Analysis of Post Coating Heat Treated Specimens

FE-SEM micrographs along with EDAX point analysis of some of post coating heat treated specimens at 500°C, 700°C and 900°C for 2h in air are shown in Fig. 7.1 to Fig. 7.12. As compared to as sprayed coatings, the surface morphology of post coating heat treated specimens show wide open cracks. The delamination of coating is not observed after post coating heat treatment. The opening of cracks might be due to recrystallization of amorphous phases of calcium phosphate to crystalline hydroxyapatite. The amorphous phases have loose packed structure, while crystalline phases have close packed structure. The reduction in volume due to recrystallization might have led to production of cracks in coating.

Surface morphology along with EDAX analysis of pure HA coated AISI 316L SS before and after post coating heat treatment is shown in Fig. 7.1. Wide cracks can be seen in the surface morphology of post coating heat treated specimens (Fig. 7.1b-d). The EDAX analysis at different points indicates mainly the presence of coating elements i.e. Ca, P and O with negligible amount of substrate elements. It can be revealed from Fig. 7.1b that after post coating heat treatment at 500°C no substrate element is detected in EDAX analysis. However, traces of substrate elements (less than 1%) can be seen in EDAX point analysis of coatings after heat treatment at 700°C and 900°C (Fig. 7.1c-d).

Surface morphology along with EDAX analysis of pure HA coated AISI 316L SS with bond coat of Al₂O₃-13 wt% TiO₂ before and after post coating heat treatment is shown in Fig. 7.2. EDAX point analysis presents a similar trend as that for post coating heat treated specimens without bond coat (Fig. 7.1) for elemental distribution. No substrate element has been detected by EDAX point analysis of post coating heat treated specimen at 500°C (Fig. 7.2b), however traces of substrate elements can be observed in EDAX point analysis of coating after post coating heat treatment at 700°C and 900°C (Fig. 7.2 c-d).

SEM micrographs and EDAX point analysis of HA coated titanium without bond coat and with bond coat before and after post coating heat treatment are shown in Fig. 7.3 and Fig. 7.4 respectively. No substrate element (titanium) has been observed in EDAX point analysis of post coating heat treated specimens at 500°C for 2h as can be seen in Fig. 7.3b and Fig. 7.4b. Traces of titanium can be observed at point 5, 6 and 8 in Fig. 7.3 and at point 5, 6, 7 and 8 in Fig. 7.4 respectively.

SEM micrographs and EDAX point analysis of HA-10 wt% Al₂O₃ coated AISI 316L SS without and with incorporation of bond coat are shown in Fig. 7.5 and Fig. 7.6 respectively. It can be observed from EDAX point analysis (Fig. 7.5) that as coated and post coating heat treated specimen at 500°C do not contain any substrate elements, however post coating heat treated specimens at 700°C and 900°C contain traces of substrate elements. Varying amount (wt%) of constituents of reinforcement (Al) can be seen at different points in EDAX point analysis of coatings. EDAX point analyses reveal the presence of 6.50 wt% and 6.73 wt% Al at point 1 and point 2 in Fig. 7.5a, 1.39 wt% and 3.67 wt% at point 3 and point 4 in Fig. 7.5b, 3.42 wt% and 3.81 wt% at point 5 and point 6 in Fig. 7.5c and 4.02 wt% and 1.35 wt% at point 7 and point 8 in Fig. 7.5d respectively. It can be seen from EDAX analysis that coating consists of elements mainly of hydroxyapatite i.e. Ca, P and O. It can be seen from EDAX point analysis (Fig. 7.6) that as coated and post coating heat treated specimen at 500°C for 2h mainly contain

coating elements, however post coating heat treated specimens at 700°C and 900°C for 2h contain traces of elements of bond coat (Al_2O_3 -13 wt% TiO_2). It can be revealed from EDAX analysis that varying amount of Al is present with minimum amount of 0.54 wt% at point 7 (Fig. 7.6d) and maximum amount of 10.02% at point 6 (Fig. 7.6c) respectively.

Figure 7.7 and 7.8 show the SEM micrographs and EDAX point analysis of HA-10 wt% Al_2O_3 coated titanium without and with incorporation of bond coat (Al_2O_3 -13 wt% TiO_2) respectively. It can be seen from Fig. 7.7 that as sprayed and post coating heat treated specimens without bond coat do not contain substrate elements except at point 6 (0.23 wt% Ti) in Fig. 7.7c. It can be seen from EDAX point analysis the minimum amount of Ca (42 wt%) is present at point 1 and 6, whereas maximum amount of Ca (52.91 wt%) can be seen at point 4 respectively. The amount of P vary with minimum amount of 8.25 wt% at point 3 and maximum amount of 25.88 wt% at point 4, whereas Al vary between 0.21 wt% at point 1 and 18.31 wt% at point 3 respectively. Figure 7.8 illustrate as sprayed and post coating heat treated HA-10 wt% Al_2O_3 coated titanium with incorporation of bond coat. EDAX analysis presents a similar trend as that for coating without incorporation of bond coat (Fig. 7.7), however a very high amount of Al (39.72 wt%) can be seen at point 7 in Fig. 7.8d. No substrate element is observed in coatings after post coating heat treatment at 500°C, 700°C and 900°C for 2h.

SEM micrographs and EDAX point analysis of HA-20 wt% Al_2O_3 coated AISI 316L SS and titanium with incorporation of bond coat are shown in Fig. 7.9 and Fig. 7.10 respectively. It can be observed from Fig. 7.9 that as sprayed and post coating heat treated (at 700°C and 900°C) specimens with incorporation of bond coat contain traces of substrate elements, whereas no substrate elements are observed in post coating heat treated specimens at 500°C for 2h. It can be seen from EDAX point analysis the minimum amount of Ca (34.68 wt%) is present at point 5, whereas maximum amount of Ca (68.99 wt%) can be seen at point 1 respectively. The amount of P vary with minimum amount of 6.28 wt% at point 1 and maximum amount of 22.79 wt% at point 3, whereas Al vary between 0.24 wt% at point 2 and 12.22 wt% at point 5 respectively. SEM micrographs and EDAX point analysis of HA-20 wt% Al_2O_3 coated titanium with incorporation of bond coat are shown in Fig. 7.10. It can be observed from EDAX analysis that traces of titanium (substrate) are present in as sprayed as well as post coating heat treated specimens at 700°C and 900°C for 2h, however substrate element is not present at point 6 in Fig. 7.10c for post coating heat treated specimen at 700°C for 2h. No substrate element can be seen at point 3 and 4 in post coating heat treated specimens at 500°C for 2h. EDAX analyses at different points show presence of coating elements i.e. Ca, P, Al and O.

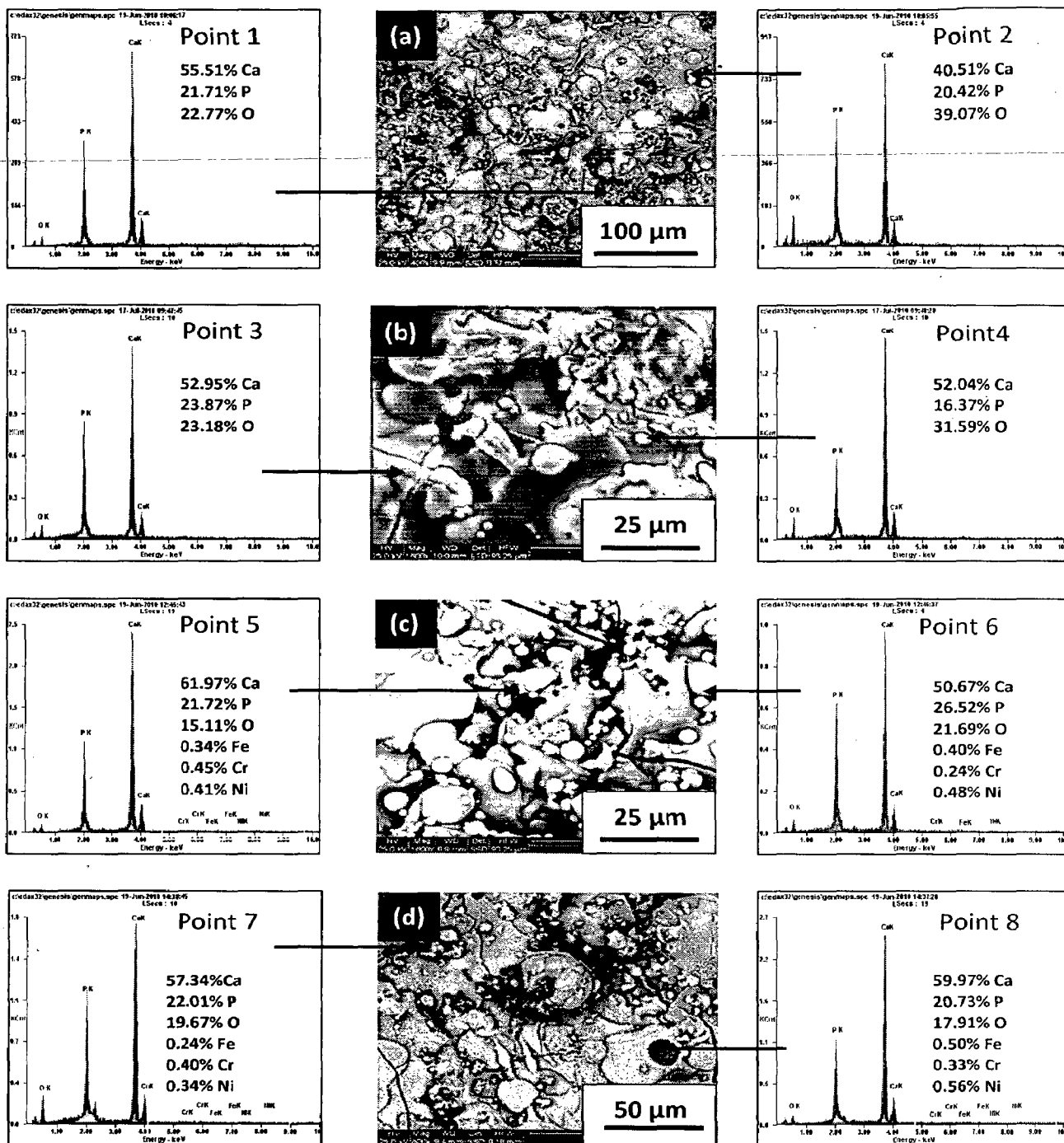


Fig. 7.1 Surface morphology and EDAX point analysis from different spots on pure HA coated AISI 316L SS: (a) as coated; (b) heat treated at 500° C for 2 h in air; (c) heat treated at 700° C for 2 h in air and (d) heat treated at 900° C for 2 h in air

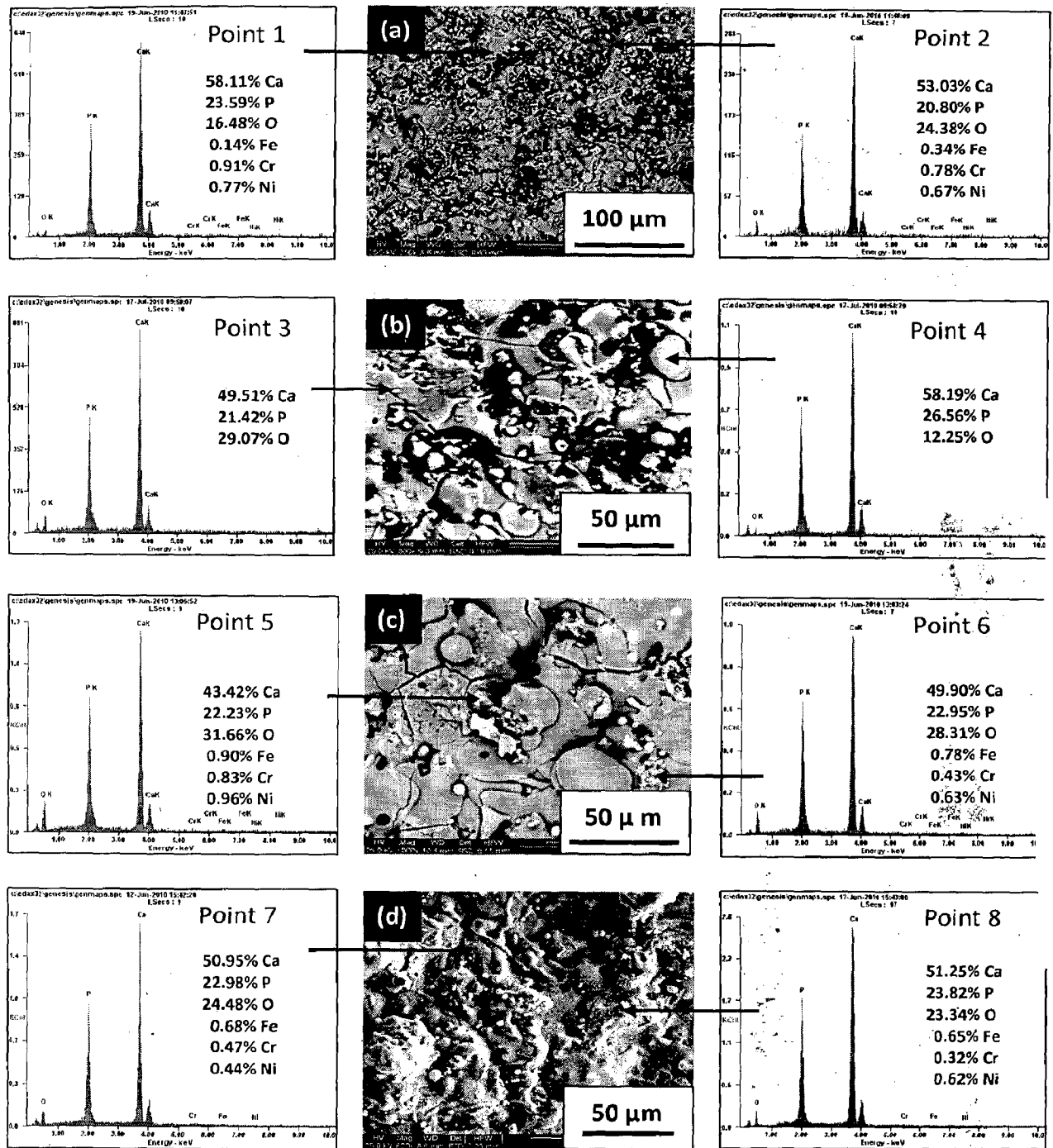


Fig. 7.2 Surface morphology and EDAX point analysis from different spots on pure HA coated AISI 316L SS with bond coat of $\text{Al}_2\text{O}_3 - 13 \text{ wt}\% \text{TiO}_2$: (a) as coated; (b) heat treated at 500°C for 2 h in air; (c) heat treated at 700°C for 2 h in air and (d) heat treated at 900°C for 2 h in air

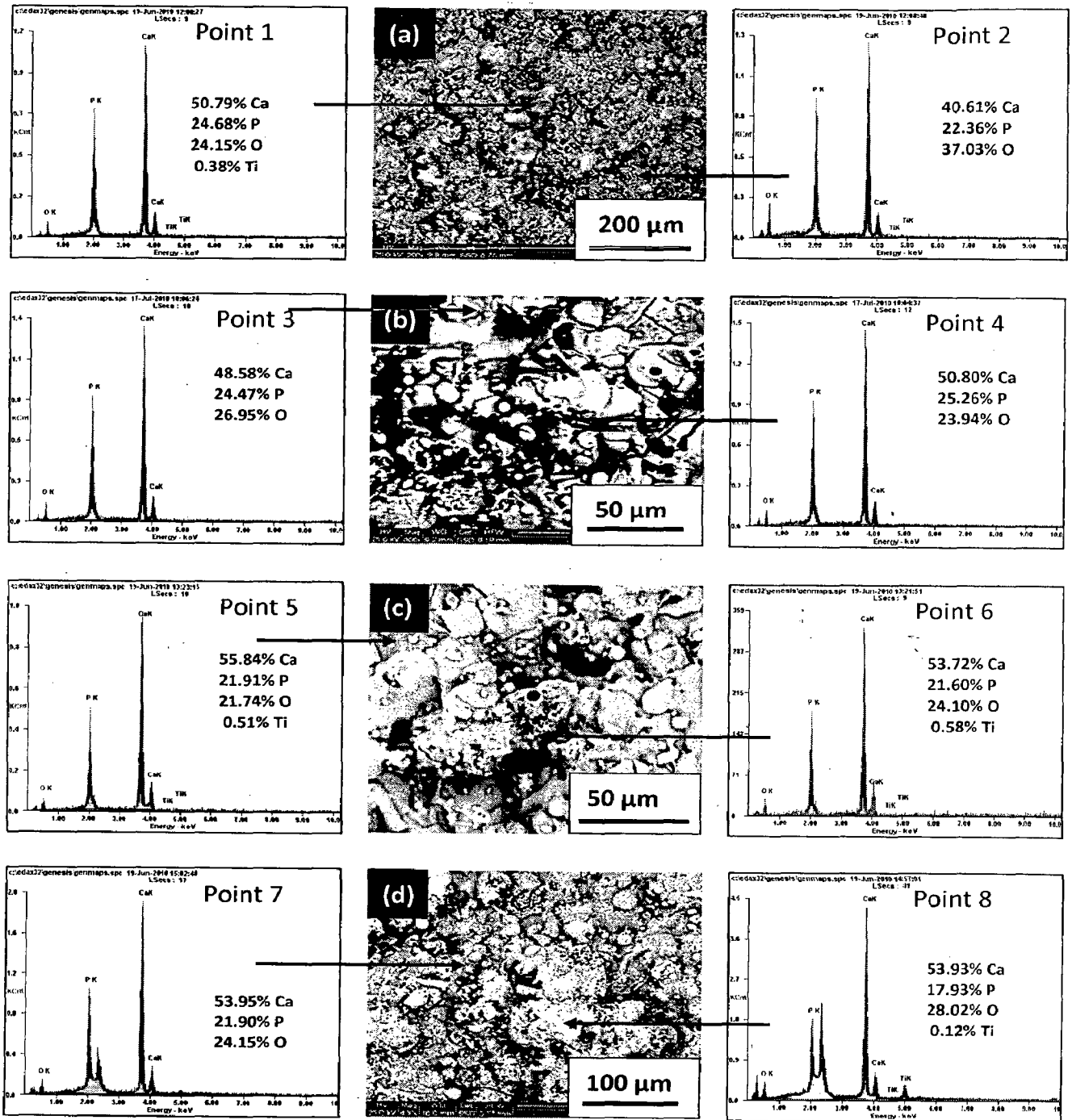


Fig. 7.3

Surface morphology and EDAX point analysis from different spots on pure HA coated titanium: (a) as coated; (b) heat treated at 500° C for 2 h in air; (c) heat treated at 700° C for 2 h in air and (d) heat treated at 900° C for 2 h in air

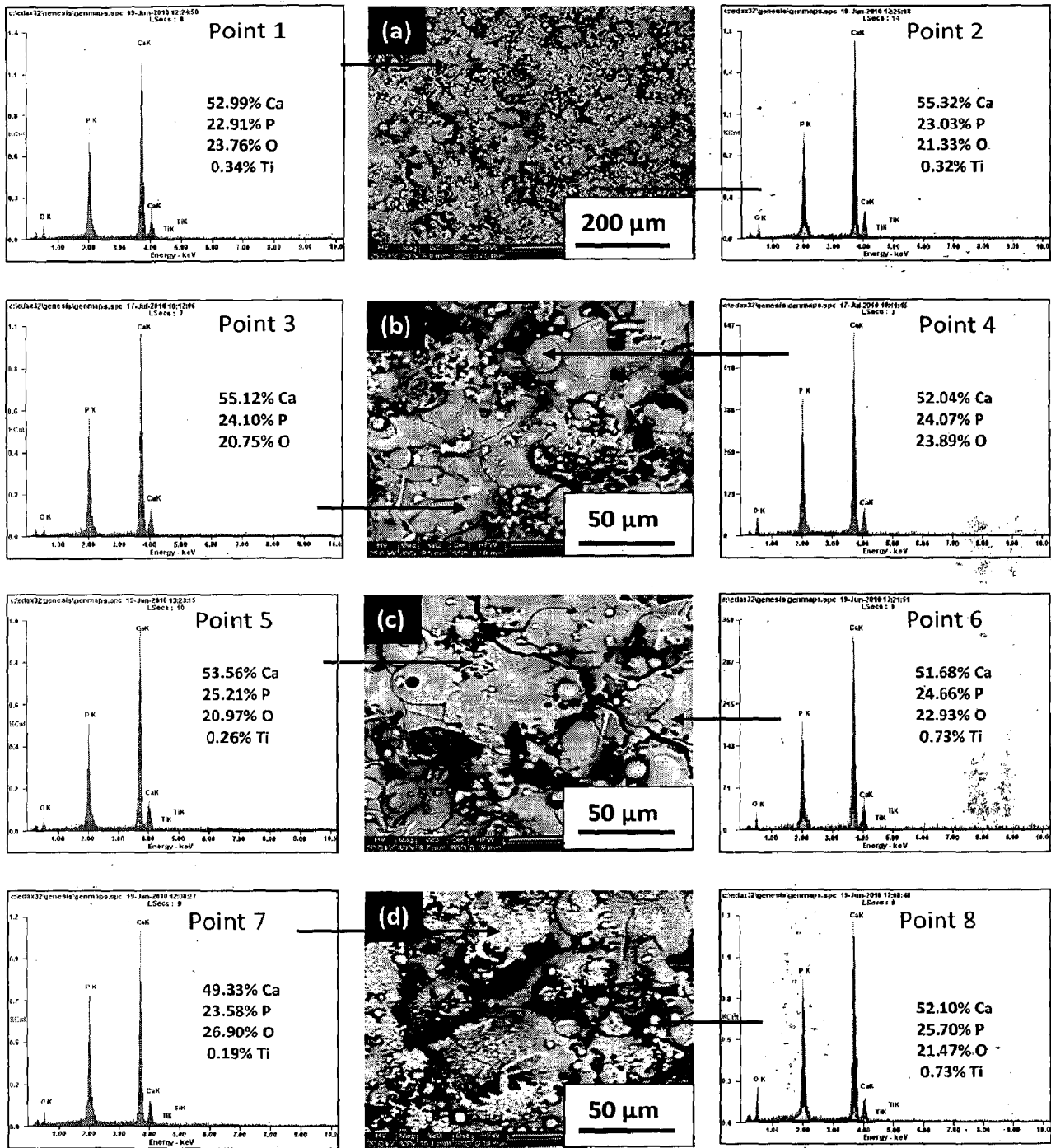


Fig. 7.4 Surface morphology and EDAX point analysis from different spots on pure HA coated titanium with bond coat of $\text{Al}_2\text{O}_3 - 13 \text{ wt}\% \text{ TiO}_2$: (a) as coated; (b) heat treated at 500°C for 2 h in air; (c) heat treated at 700°C for 2 h in air and (d) heat treated at 900°C for 2 h in air

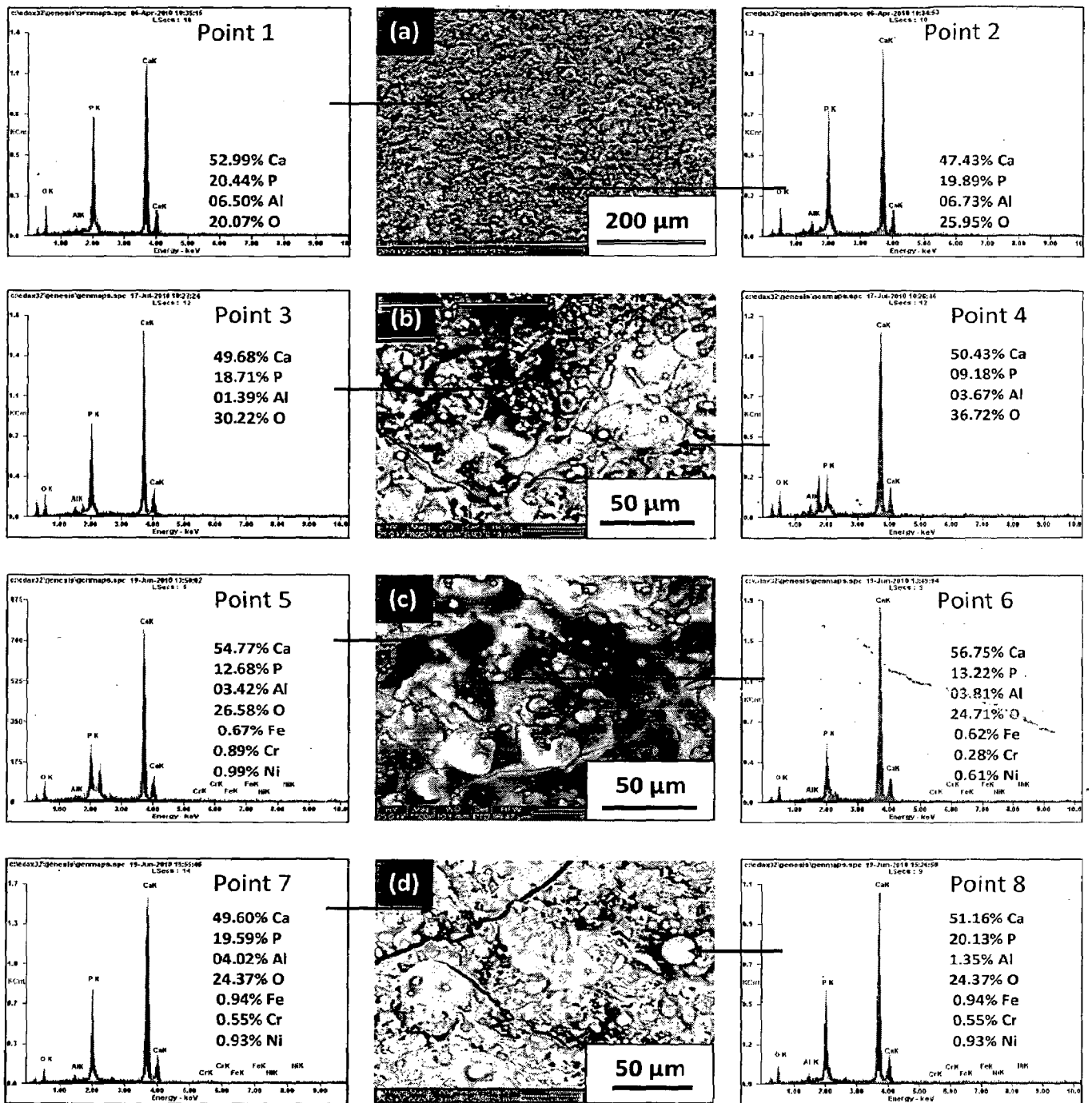


Fig. 7.5 Surface morphology and EDAX point analysis from different spots on HA-10 wt% Al_2O_3 coated AISI 316L SS: (a) as coated; (b) heat treated at 500° C for 2 h in air; (c) heat treated at 700° C for 2 h in air and (d) heat treated at 900° C for 2 h in air

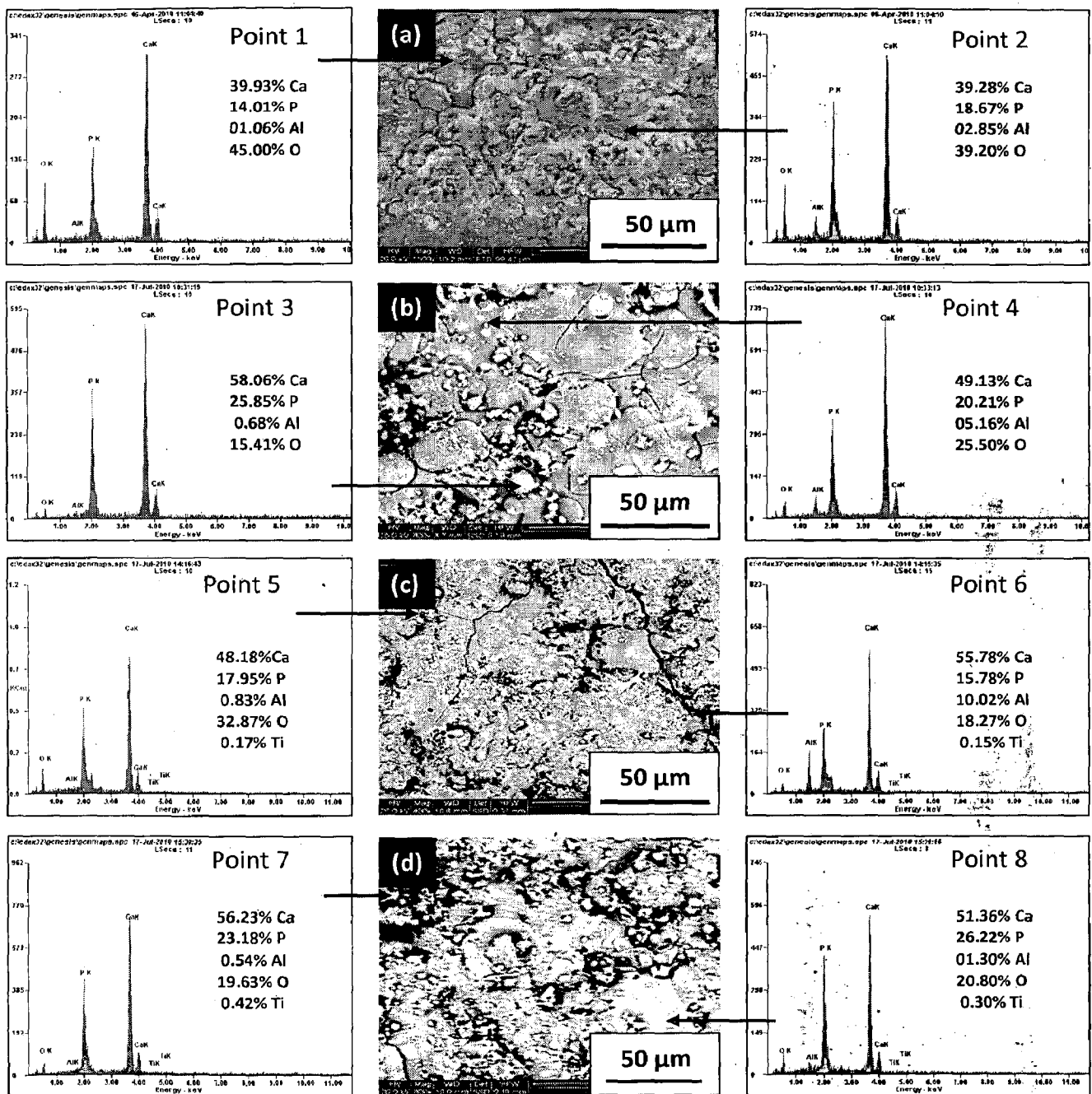


Fig. 7.6 Surface morphology and EDAX point analysis from different spots on HA – 10 wt% Al₂O₃ coated AISI 316L SS with bond coat of Al₂O₃ – 13 wt% TiO₂: (a) as coated; (b) heat treated at 500° C for 2 h in air; (c) heat treated at 700° C for 2 h in air and (d) heat treated at 900° C for 2 h in air

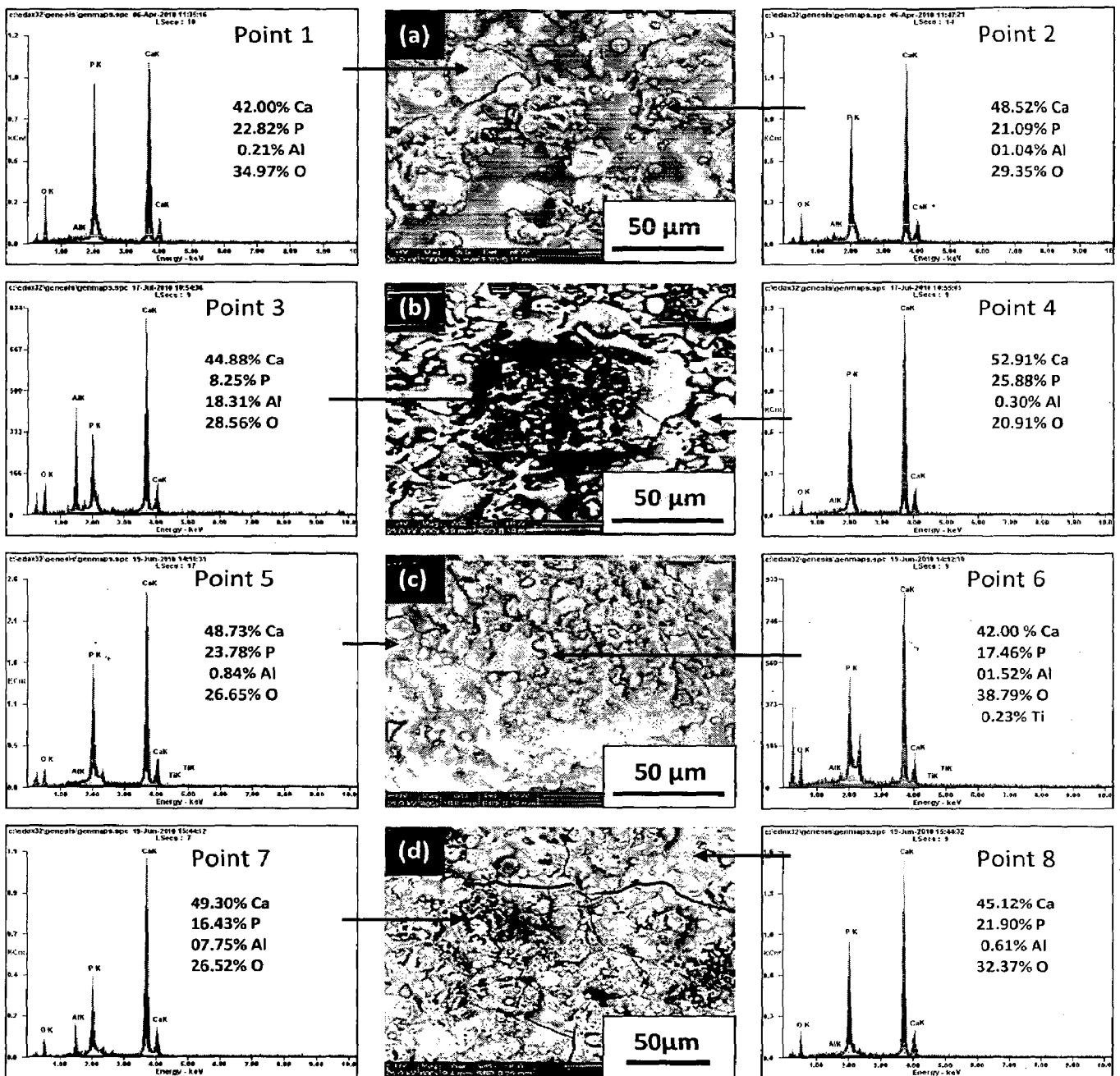


Fig. 7.7 Surface morphology and EDAX point analysis from different spots on HA – 10 wt% Al₂O₃ coated titanium: (a) as coated; (b) heat treated at 500° C for 2 h in air; (c) heat treated at 700° C for 2 h in air and (d) heat treated at 900° C for 2 h in air

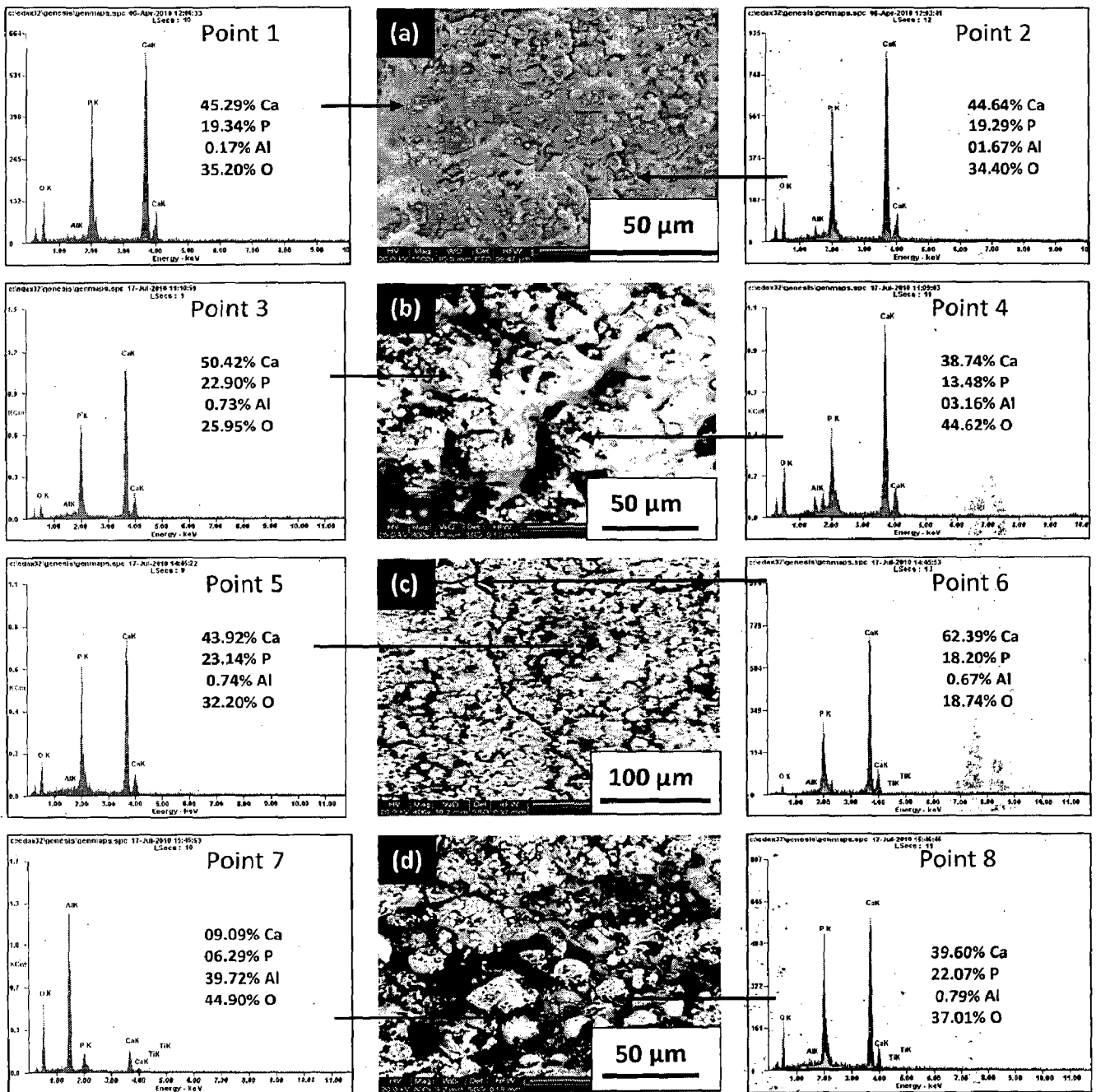


Fig. 7.8 Surface morphology and EDAX point analysis from different spots on HA – 10 wt% Al_2O_3 coated titanium with bond coat of Al_2O_3 – 13 wt% TiO_2 : (a) as coated; (b) heat treated at 500°C for 2 h in air; (c) heat treated at 700°C for 2 h in air and (d) heat treated at 900°C for 2 h in air

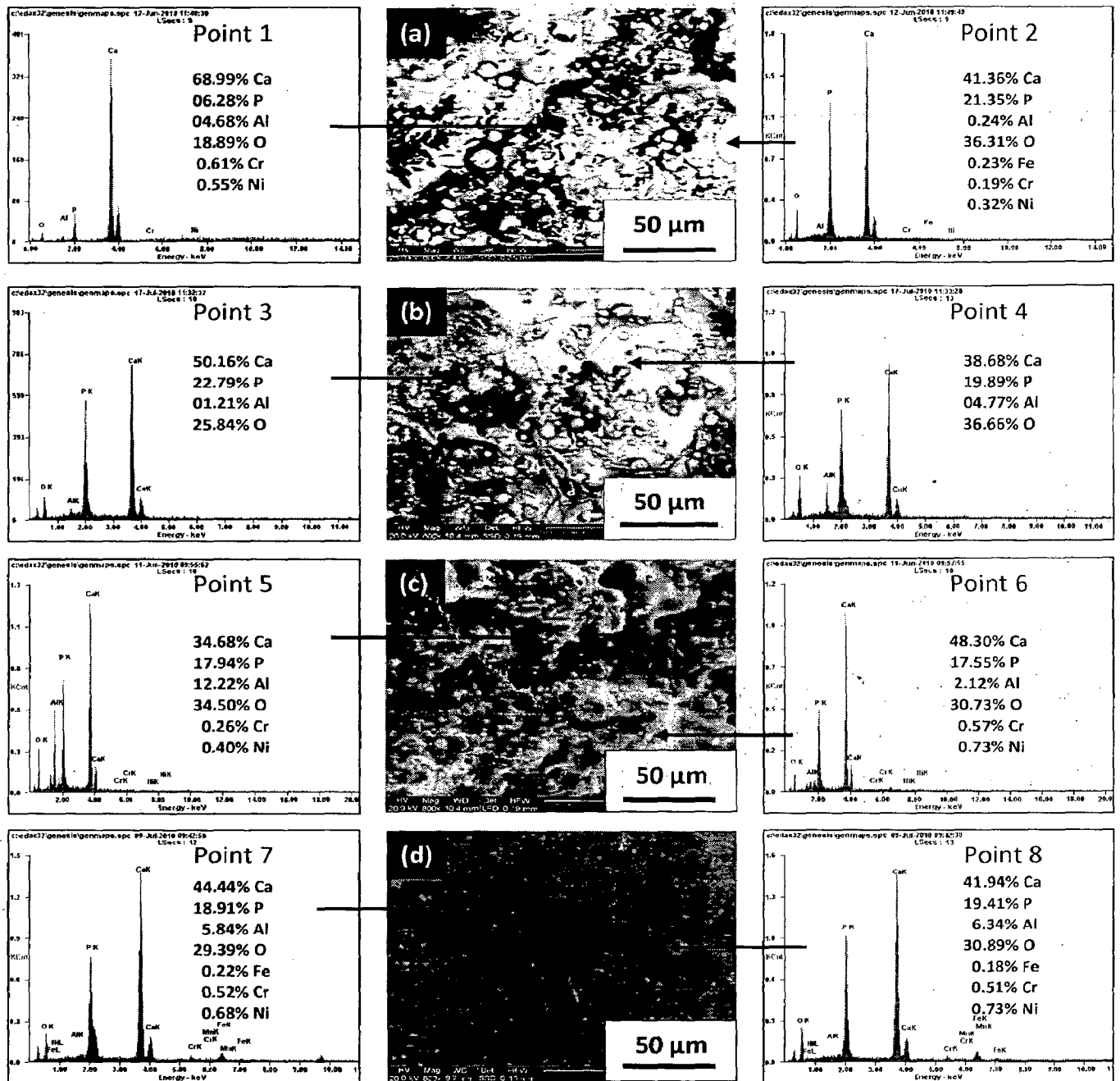


Fig. 7.9 Surface morphology and EDAX point analysis from different spots on HA – 20 wt% Al₂O₃ coated AISI 316L SS with bond coat of Al₂O₃ – 13 wt% TiO₂: (a) as coated; (b) heat treated at 500° C for 2 h in air; (c) heat treated at 700° C for 2 h in air and (d) heat treated at 900° C for 2 h in air

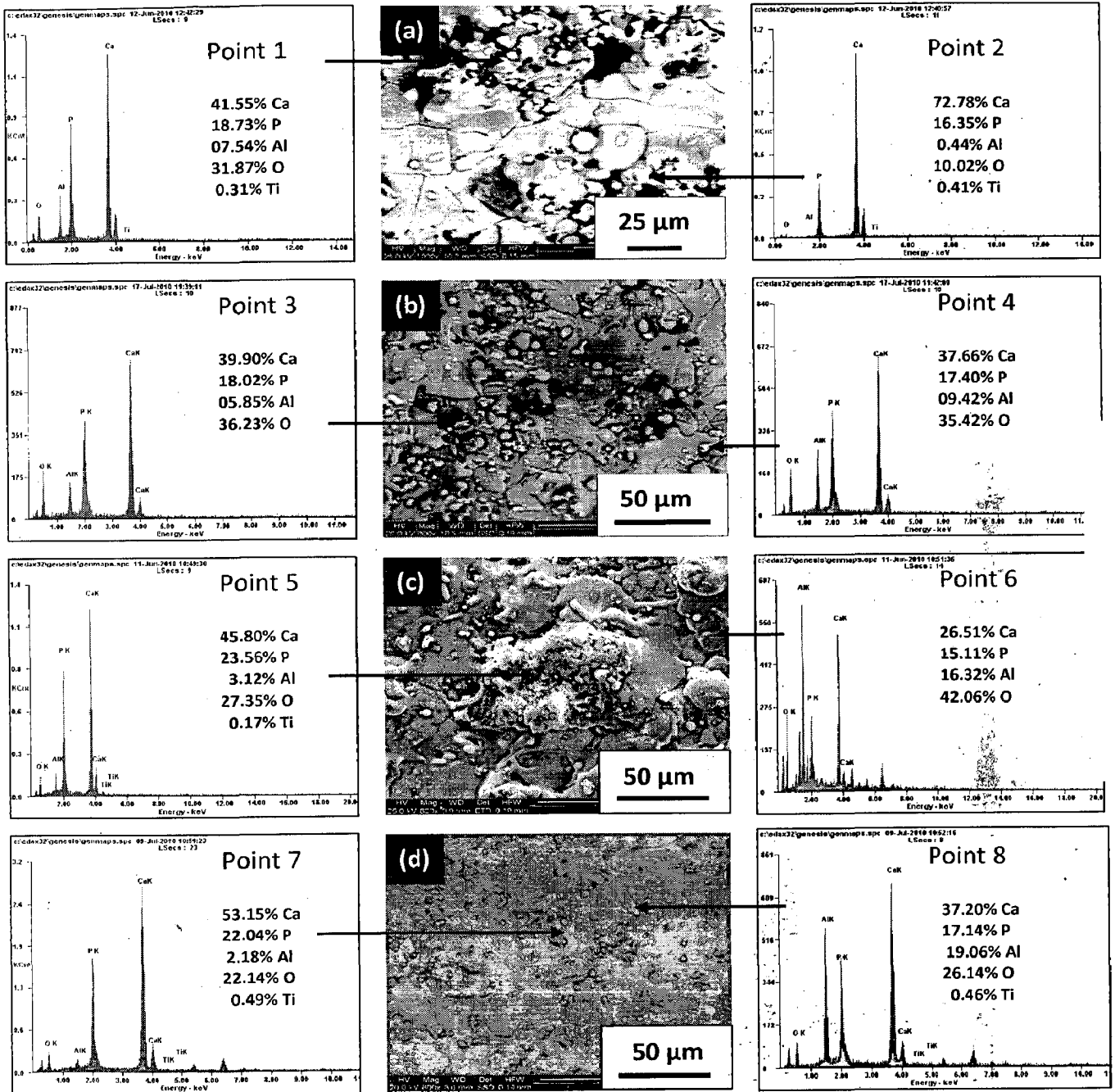


Fig. 7.10 Surface morphology and EDAX point analysis from different spots on HA – 20 wt% Al_2O_3 coated titanium with bond coat of Al_2O_3 – 13 wt% TiO_2 : (a) as coated; (b) heat treated at 500°C for 2 h in air; (c) heat treated at 700°C for 2 h in air and (d) heat treated at 900°C for 2 h in

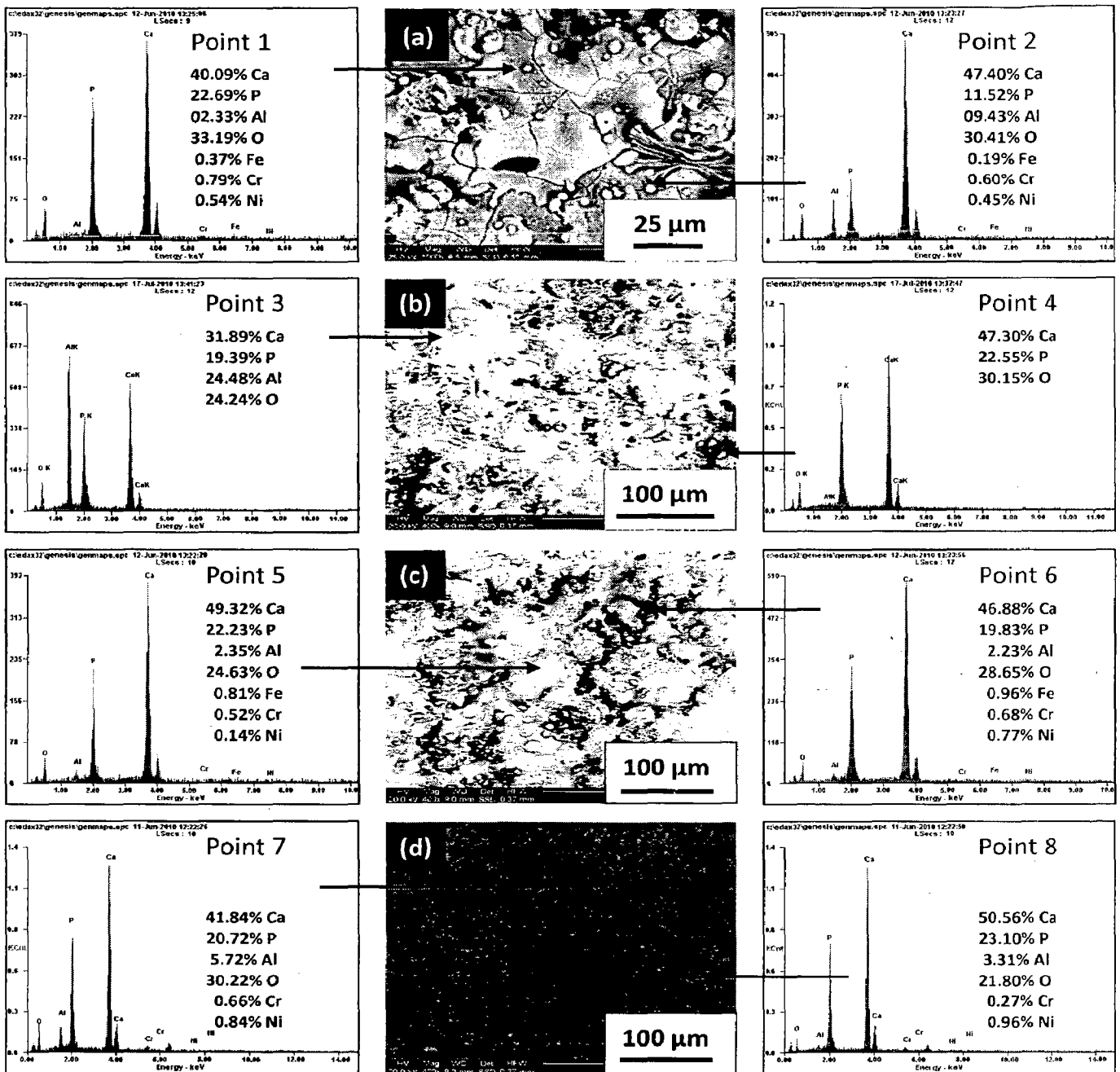


Fig. 7.11 Surface morphology and EDAX point analysis from different spots on HA – 30 wt% Al₂O₃ coated AISI 316L SS : (a) as coated; (b) heat treated at 500° C for 2 h in air; (c) heat treated at 700° C for 2 h in air and (d) heat treated at 900° C for 2 h in air

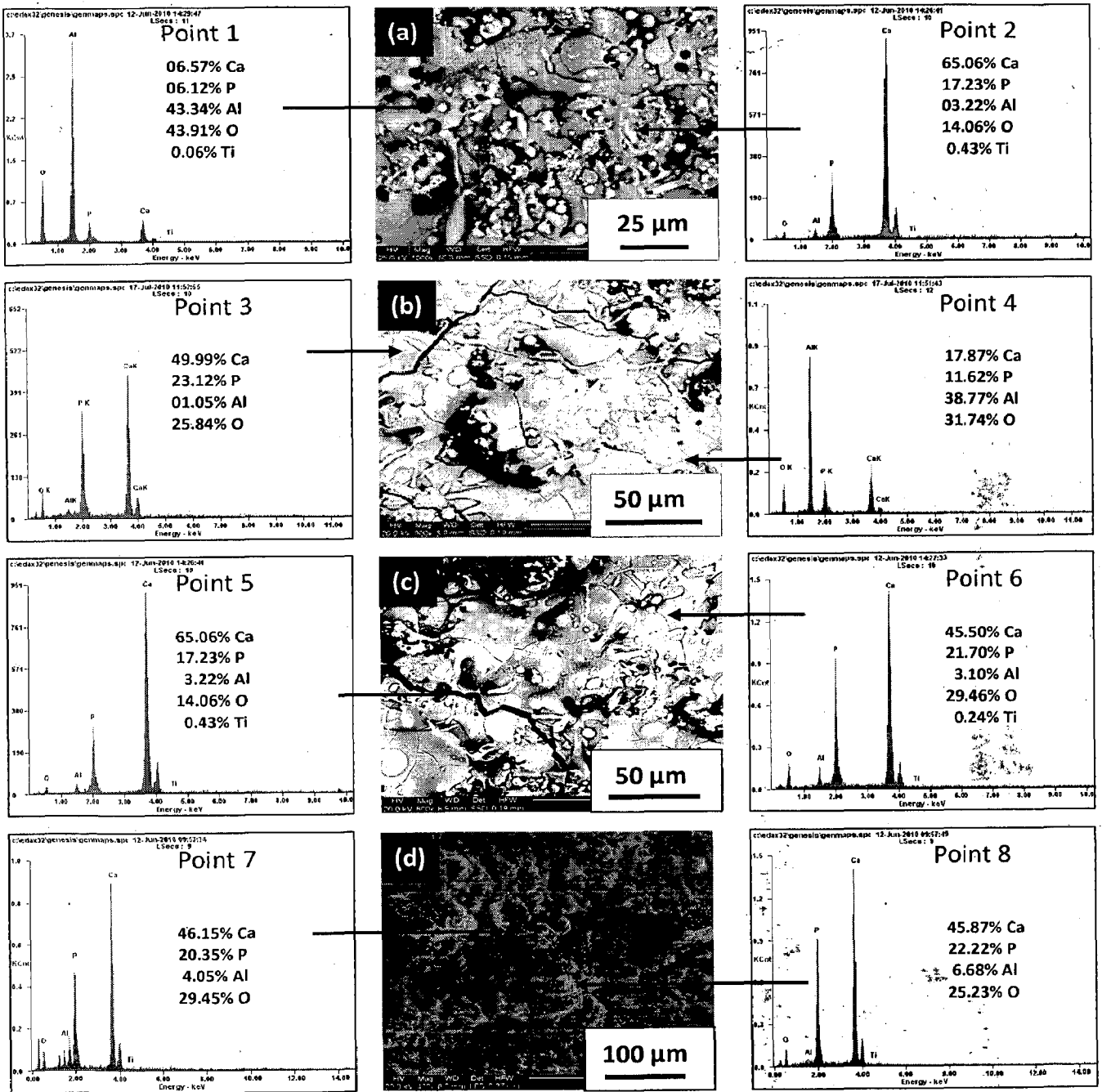


Fig. 7.12 Surface morphology and EDAX point analysis from different spots on HA – 30 wt% Al_2O_3 coated titanium (a) as coated; (b) heat treated at 500° C for 2 h in air; (c) heat treated at 700° C for 2 h in air and (d) heat treated at 900° C for 2 h in air

7.2.2 X-Ray Diffraction Analysis of Post Coating Heat Treated Specimens

XRD diffractograms for coated AISI 316L SS and titanium with and without bond coat after post coating heat treatment at different temperatures in air for 2h are shown in Fig. 7.13 to Fig. 7.24. It can be seen from XRD diffractograms that peaks of substrate elements as well as of bond coat elements are not present, which suggests that after post coating heat treatment considerable amount of diffusion/migration of elements from substrate or bond coat to top coat did not occur. XRD patterns of as-sprayed coatings are shown in Fig. 7.13a to 7.24a (lower most pattern in each Fig.). The presence of phases in as-sprayed coatings has been discussed in detail in Section 4.2.6 of Chapter 4 of present study.

After post coating heat treatment at 500°C, 700°C and 900°C for 2h in air, the amorphous phases such as α -tri-calcium phosphate (α -TCP), β -tri-calcium phosphate (β -TCP), tetra-calcium phosphate (TTCP) and calcium oxide (CaO) disappeared or got converted into crystalline hydroxyapatite. The sharp peaks with thin tails represent crystalline HA phase in Fig. 7.13 to Fig. 7.24. It can be observed from Fig. 7.13 to 7.24 that after post coating heat treatment, the intensity of HA peaks increase with increase in post coating heat treatment temperature from 500°C to 900°C. The crystallinity of as-sprayed and post coating heat treated specimens has been calculated in 20°-40° (2 θ) range by following equation suggested by LeGeros et al., (1994):

$$\text{Crystallinity (\%)} = \frac{\sum A_c}{\sum A_c + \sum A_a} \times 100\% \quad (7.1)$$

Where, $\sum A_c$ is the sum of the areas under all crystalline HA peaks and $\sum A_a$ is the sum of the area under amorphous peaks. The percentage crystallinity of as sprayed coatings and after post coating heat treatment at 500°C, 700°C and 900°C are presented in Table 7.1 to Table 7.12.

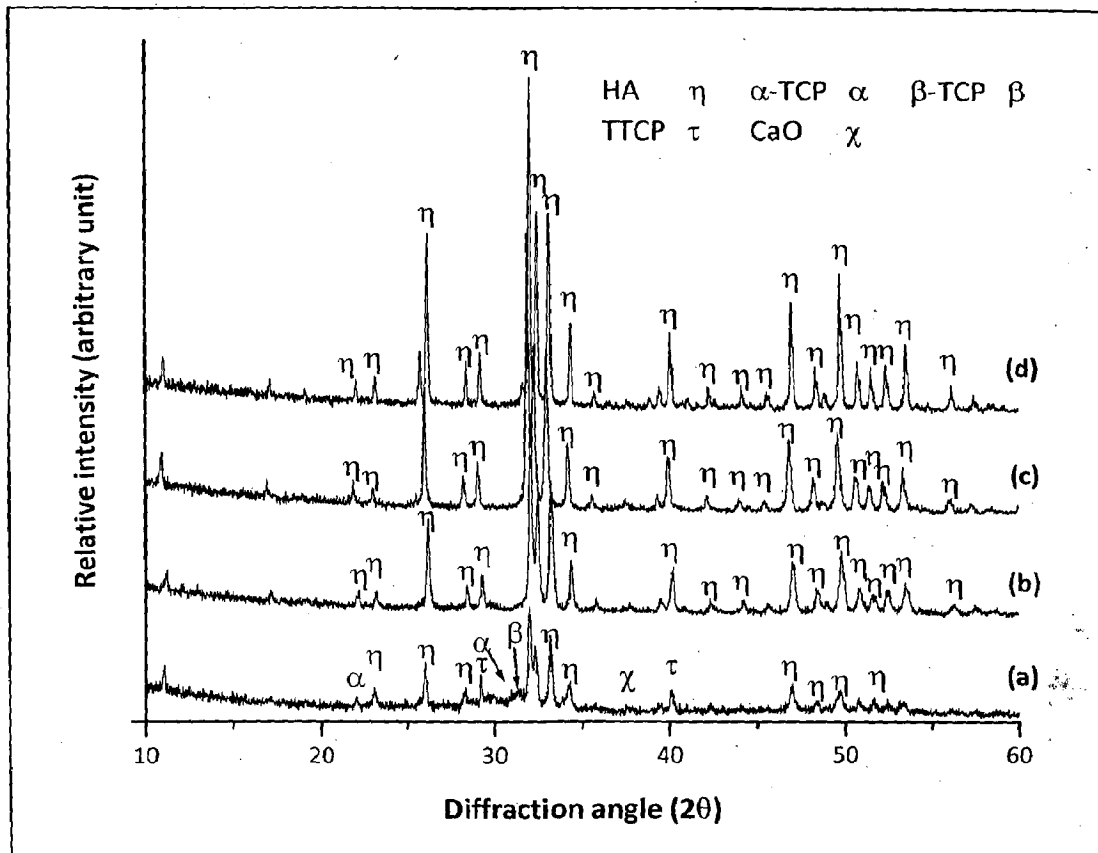


Fig. 7.13 X-ray diffraction pattern of pure HA coated AISI 316L SS: (a) as-coated; (b) post coating heat treated at 500° C for 2h in air; (c) post coating heat treated at 700° C for 2h in air and (d) post coating heat treated at 900° C for 2h in air

Table 7.1 Crystallinity of pure HA coatings on AISI 316L SS: as-sprayed and after post coating heat treatment

Pure HA coating on AISI 316L SS substrate	as-sprayed	Heat treated at 500°C	Heat treated at 700°C	Heat treated at 900°C
Crystallinity (%)	72.6%	84.1%	90.7%	93.2%

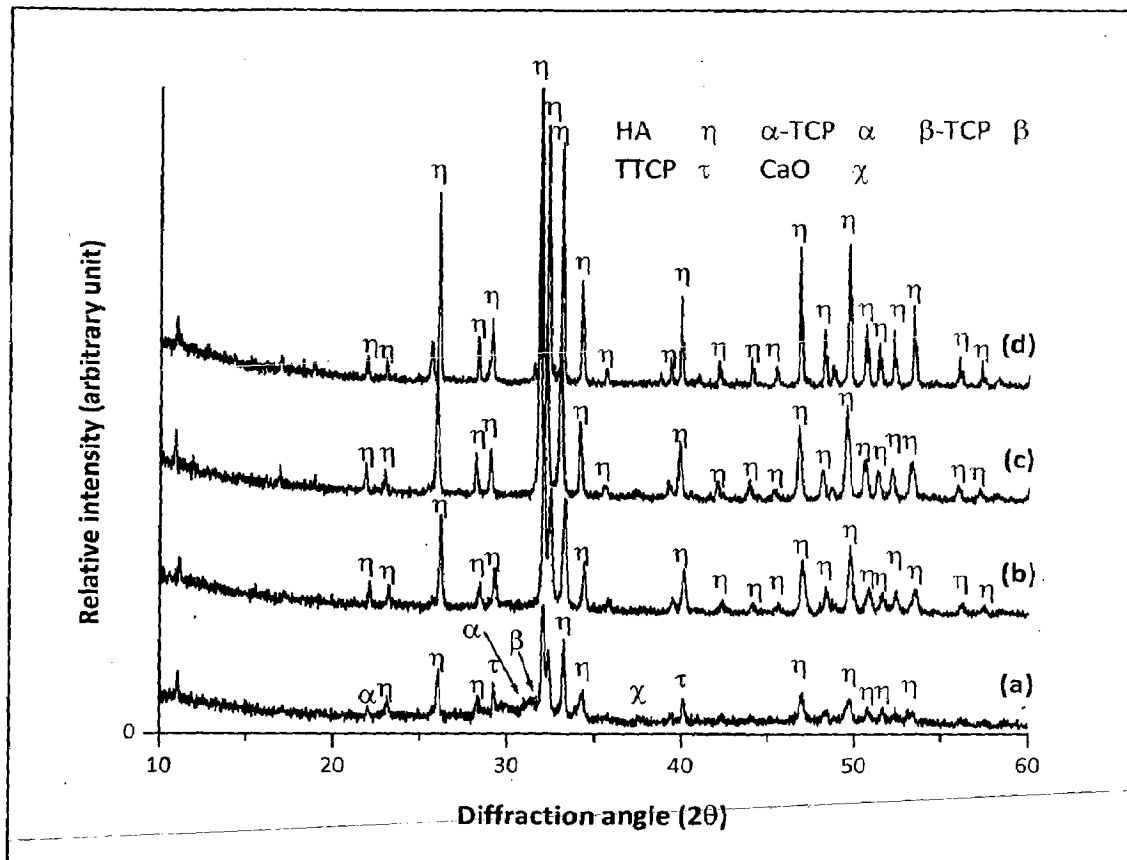


Fig. 7.14 X-ray diffraction pattern of pure HA coated AISI 316L SS with Al₂O₃-13 wt% TiO₂ bond coat: (a) as-coated; (b) post coating heat treated at 500° C for 2h in air; (c) post coating heat treated at 700° C for 2h in air and (d) post coating heat treated at 900° C for 2h in air

Table 7.2 Crystallinity of pure HA coatings on AISI 316L SS with Al₂O₃-13 wt% TiO₂ bond coat: as-sprayed and after post coating heat treatment

Pure HA coating on AISI 316L SS substrate with Al ₂ O ₃ -13 wt% TiO ₂ bond coat	as-sprayed	Heat treated at 500°C	Heat treated at 700°C	Heat treated at 900°C
Crystallinity (%)	74.2%	85.4%	92.6%	95.1%

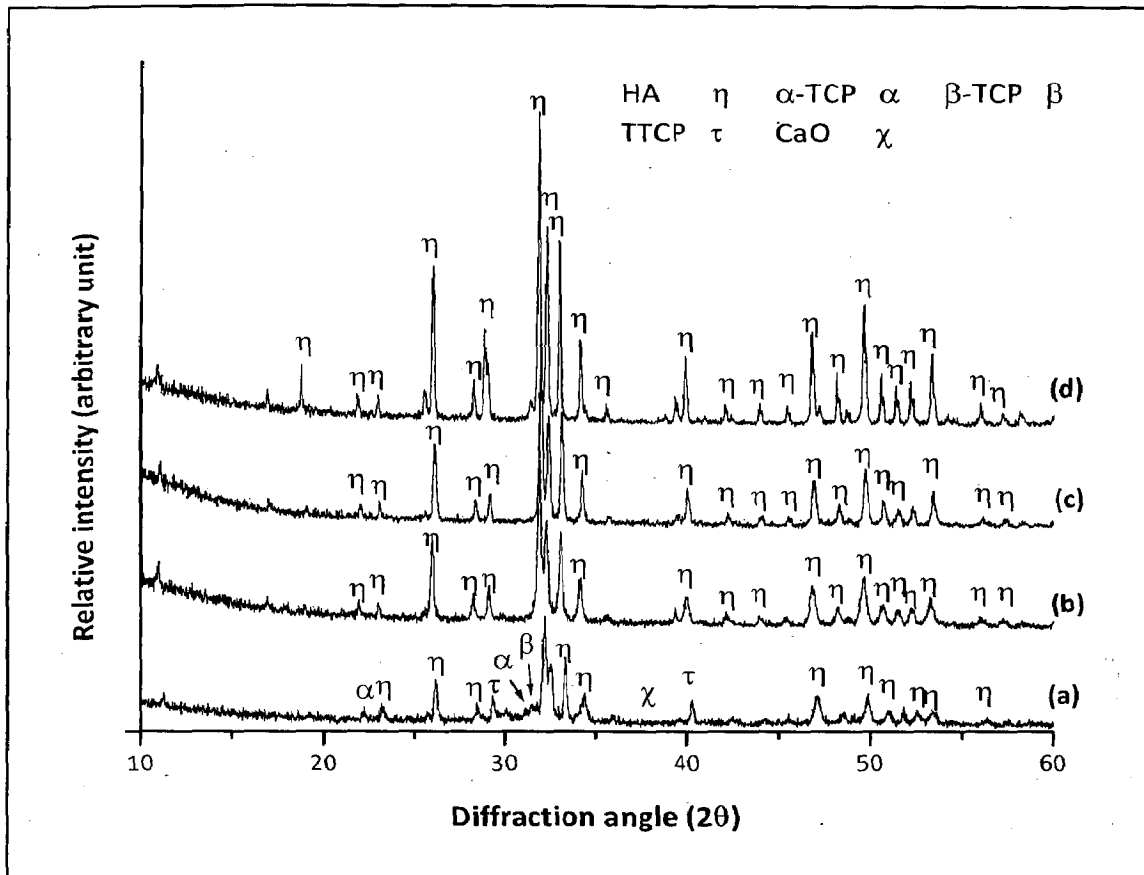


Fig. 7.15 X-ray diffraction pattern of pure HA coated titanium: (a) as-coated; (b) post coating heat treated at 500° C for 2h in air; (c) post coating heat treated at 700° C for 2h in air and (d) post coating heat treated at 900° C for 2h in air

Table 7. 3 Crystallinity of pure HA coatings on titanium: as-sprayed and after post coating heat treatment

Pure HA coating on titanium substrate	as-sprayed	Heat treated at 500°C	Heat treated at 700°C	Heat treated at 900°C
Crystallinity (%)	73.9%	84.2%	92.2%	93.5%

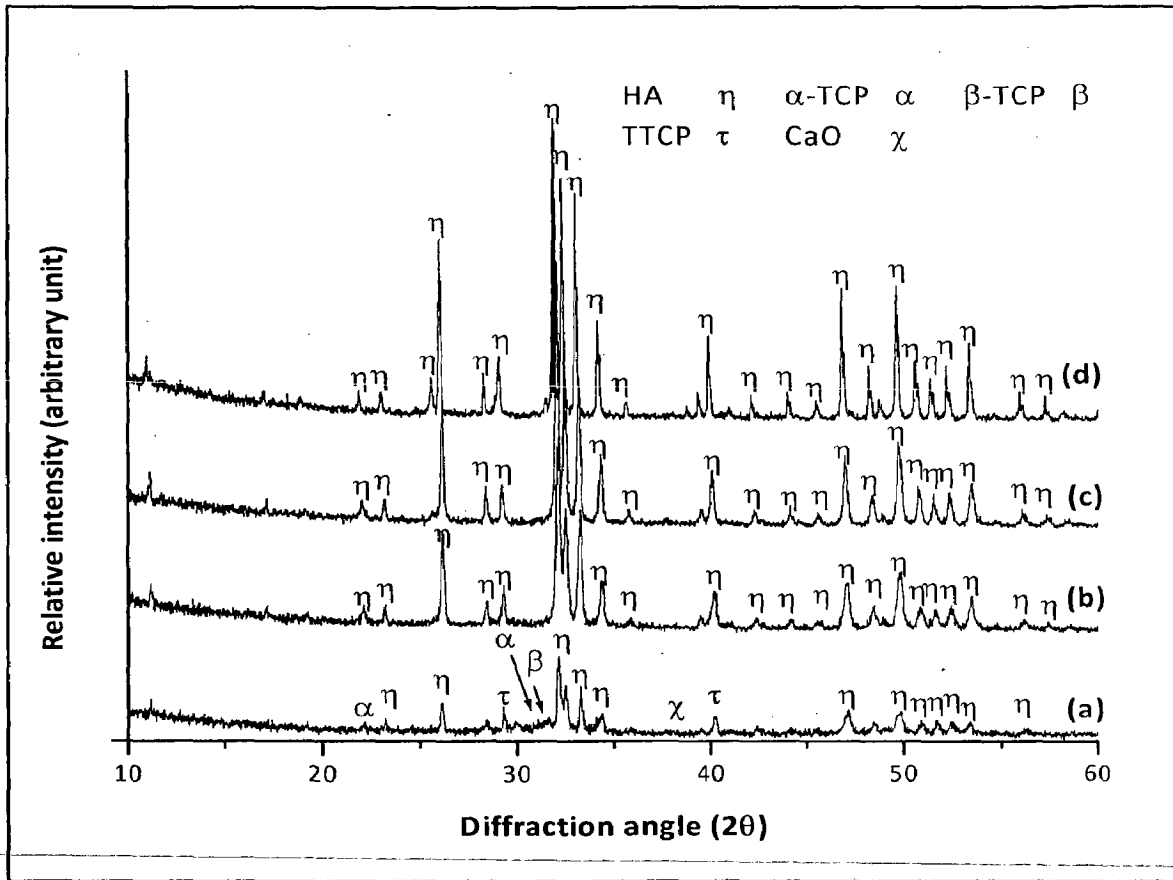


Fig. 7.16 X-ray diffraction pattern of pure HA coated titanium with Al_2O_3 -13 wt% TiO_2 bond coat: (a) as-coated; (b) post coating heat treated at 500°C for 2h in air; (c) post coating heat treated at 700°C for 2h in air and (d) post coating heat treated at 900°C for 2h in air

Table 7.4 Crystallinity of pure HA coatings on titanium with Al_2O_3 -13 wt% TiO_2 bond coat: as-sprayed and after post coating heat treatment

Pure HA coating on titanium substrate with Al_2O_3 -13 wt% TiO_2 bond coat	as-sprayed	Heat treated at 500°C	Heat treated at 700°C	Heat treated at 900°C
Crystallinity (%)	75%	84.1%	93.1%	94.3%

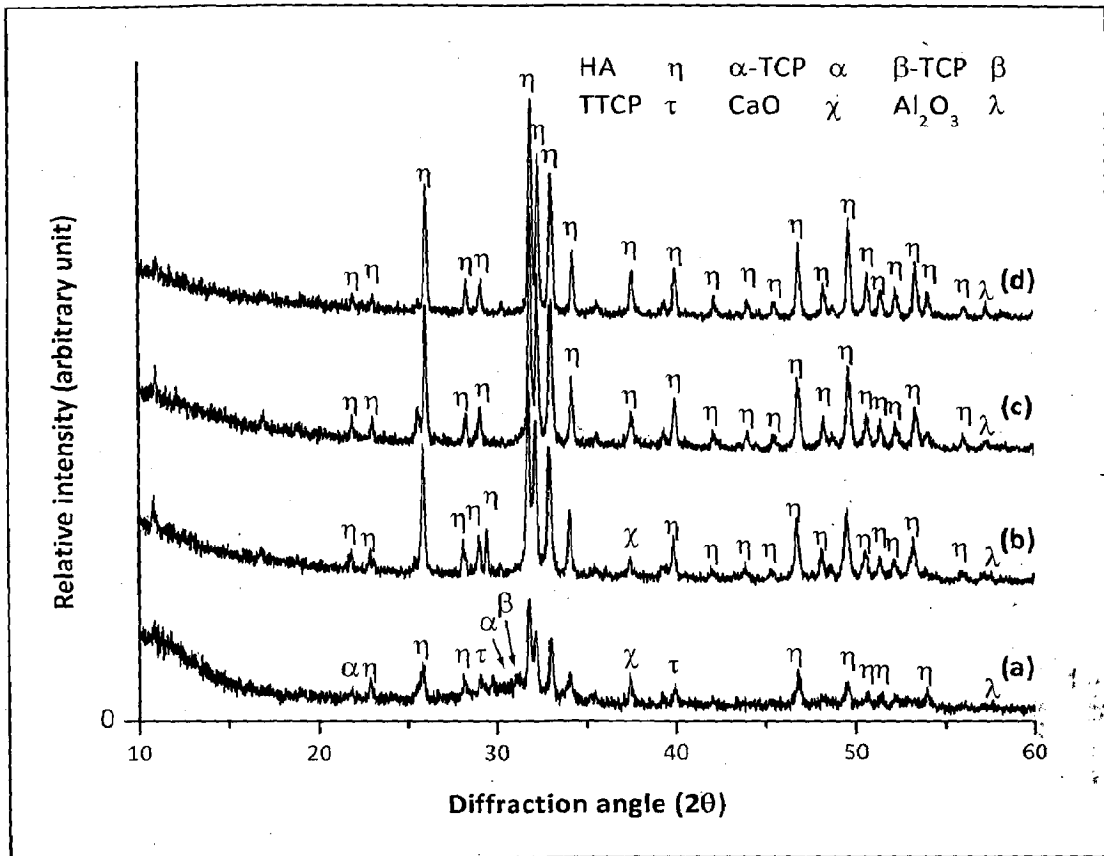


Fig. 7.17 X-ray diffraction pattern of HA-10 wt% Al₂O₃ coated AISI 316L SS: (a) as-coated; (b) post coating heat treated at 500° C for 2h in air; (c) post coating heat treated at 700° C for 2h in air and (d) post coating heat treated at 900° C for 2h in air

Table 7. 5 Crystallinity of HA-10 wt% Al₂O₃ coatings on AISI 316L SS: as sprayed and after post coating heat treatment

HA-10 wt% Al ₂ O ₃ coating on AISI 316L SS substrate	as-sprayed	Heat treated at 500°C	Heat treated at 700°C	Heat treated at 900°C
Crystallinity (%)	76.4%	85.4%	94.6%	96.2%

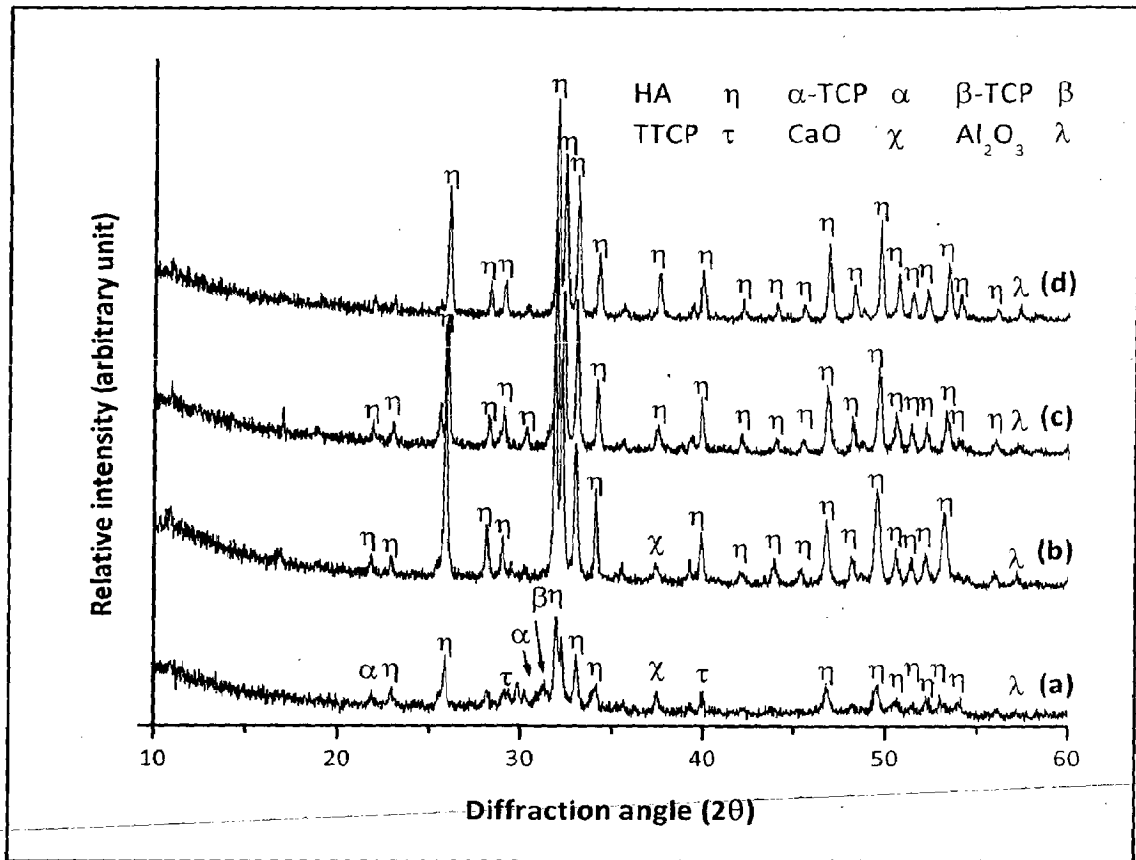


Fig. 7.18 X-ray diffraction pattern of HA-10 wt% Al_2O_3 coated AISI 316L SS with Al_2O_3 -13 wt% TiO_2 bond coat: (a) as-coated; (b) post coating heat treated at 500°C for 2h in air; (c) post coating heat treated at 700°C for 2h in air and (d) post coating heat treated at 900°C for 2h in air

Table 7. 6 Crystallinity of HA-10 wt% Al_2O_3 coatings on AISI 316L SS with Al_2O_3 -13 wt% TiO_2 bond coat: as-sprayed and after post coating heat treatment

HA-10 wt% Al_2O_3 coated AISI 316L SS with Al_2O_3 -13 wt% TiO_2 bond coat	as-sprayed	Heat treated at 500°C	Heat treated at 700°C	Heat treated at 900°C
Crystallinity (%)	76.6%	85.6%	94.9%	97.3%

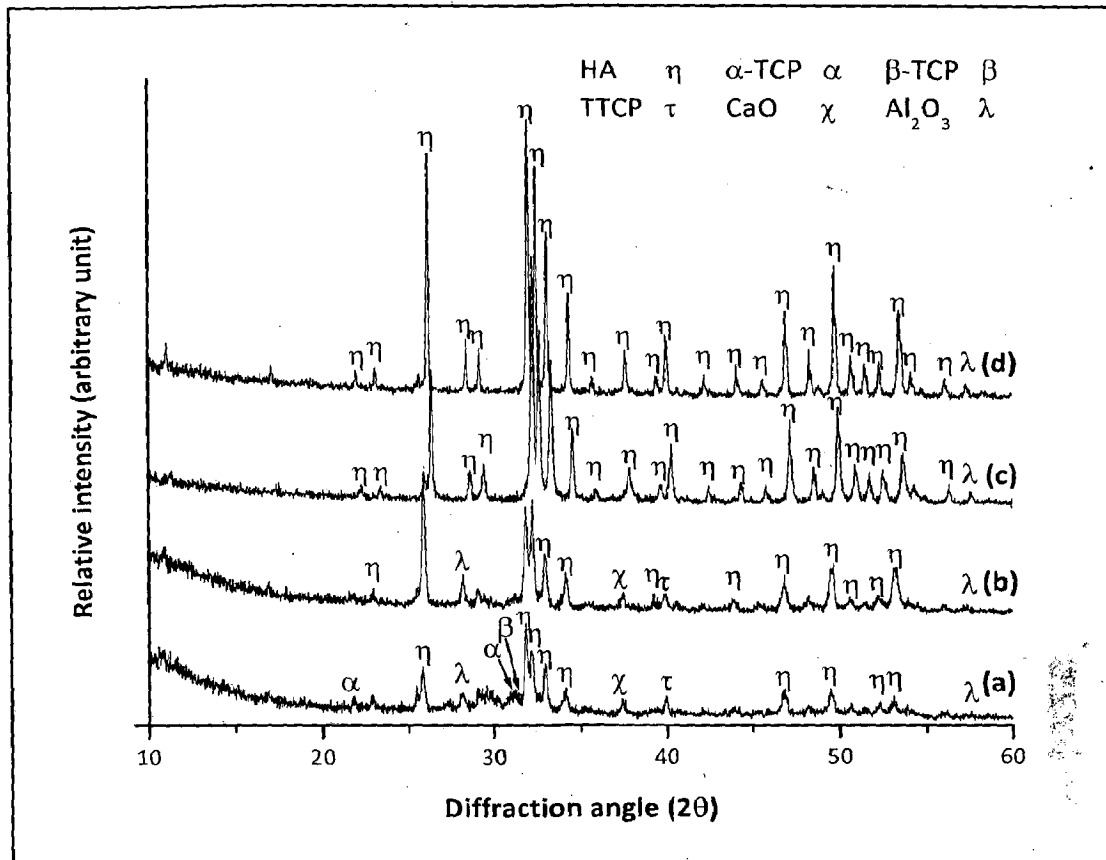


Fig. 7.19 X-ray diffraction pattern of HA-10 wt% Al_2O_3 coated titanium: (a) as-coated; (b) post coating heat treated at 500°C for 2h in air; (c) post coating heat treated at 700°C for 2h in air and (d) post coating heat treated at 900°C for 2h in air

Table 7.7 Crystallinity of HA-10 wt% Al_2O_3 coatings on titanium: as-sprayed and after post coating heat treatment

HA-10 wt% Al_2O_3 coated titanium	as-sprayed	Heat treated at 500°C	Heat treated at 700°C	Heat treated at 900°C
Crystallinity (%)	76.9%	85.3%	94.7%	97%

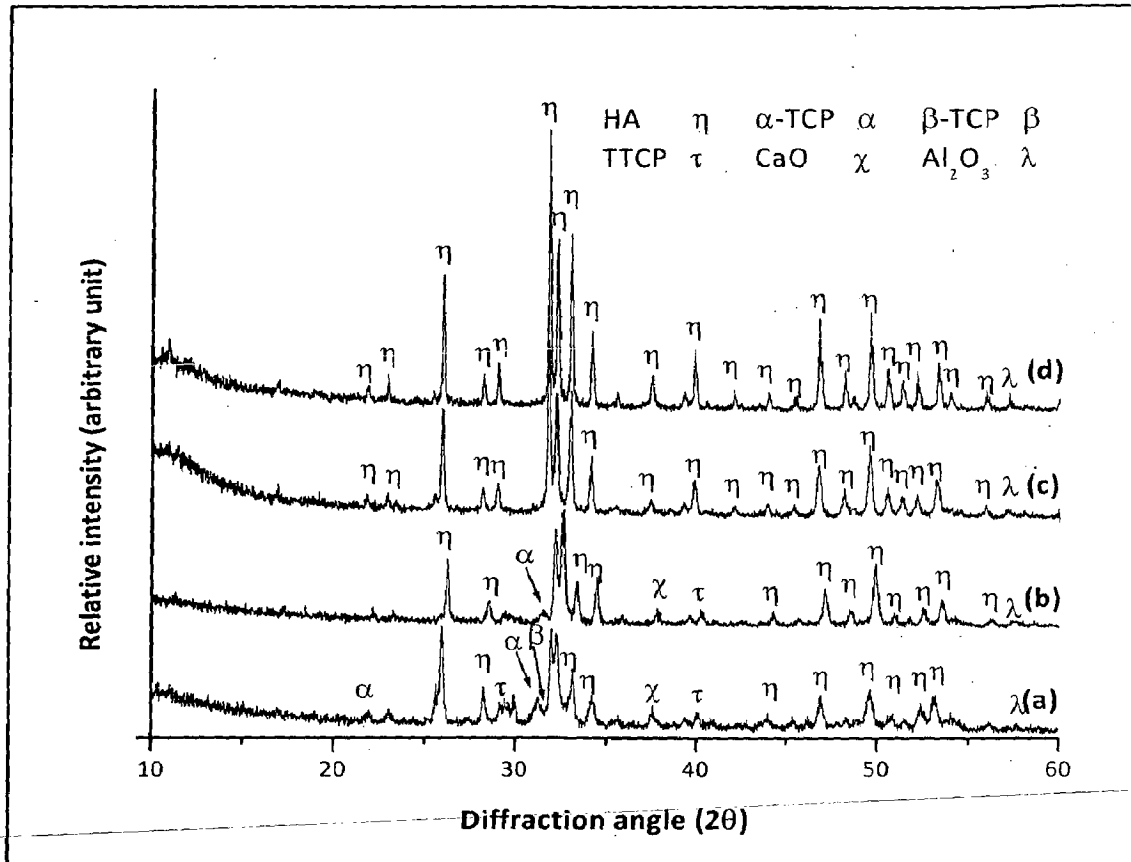


Fig. 7.20 X-ray diffraction pattern of HA-10 wt% Al₂O₃ coated titanium with Al₂O₃-13 wt% TiO₂ bond coat: (a) as-coated; (b) post coating heat treated at 500° C for 2h in air; (c) post coating heat treated at 700° C for 2h in air and (d) post coating heat treated at 900° C for 2h in air

Table 7.8 Crystallinity of HA-10 wt% Al₂O₃ coatings on titanium with Al₂O₃-13 wt% TiO₂ bond coat: as-sprayed and after post coating heat treatment

HA-10 wt% Al ₂ O ₃ titanium with Al ₂ O ₃ -13 wt% TiO ₂ bond coat	as-sprayed	Heat treated at 500°C	Heat treated at 700°C	Heat treated at 900°C
Crystallinity (%)	76.9%	86.1%	95.3%	97.6%

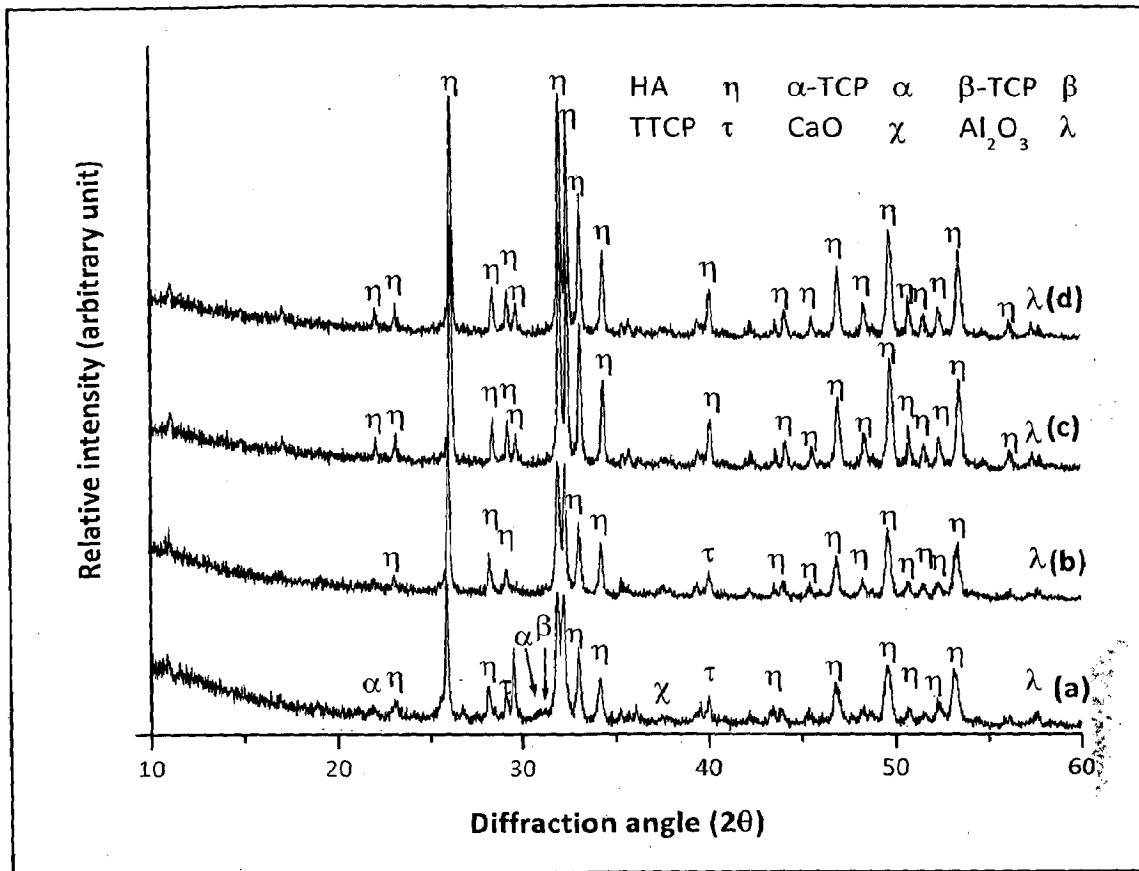


Fig. 7.21 X-ray diffraction pattern of HA-20 wt% Al₂O₃ coated AISI 316L SS with Al₂O₃-13 wt% TiO₂ bond coat: (a) as-coated; (b) post coating heat treated at 500°C for 2h in air; (c) post coating heat treated at 700° C for 2h in air and (d) post coating heat treated at 900° C for 2h in air

Table 7. 9 Crystallinity of HA-20 wt% Al₂O₃ coatings on AISI 316L SS with Al₂O₃-13 wt% TiO₂ bond coat: as-sprayed and after post coating heat treatment

HA-20 wt% Al ₂ O ₃ coated AISI 316L SS with Al ₂ O ₃ -13 wt% TiO ₂ bond coat	as-sprayed	Heat treated at 500°C	Heat treated at 700°C	Heat treated at 900°C
Crystallinity (%)	77%	86.5%	95.7%	97.9%

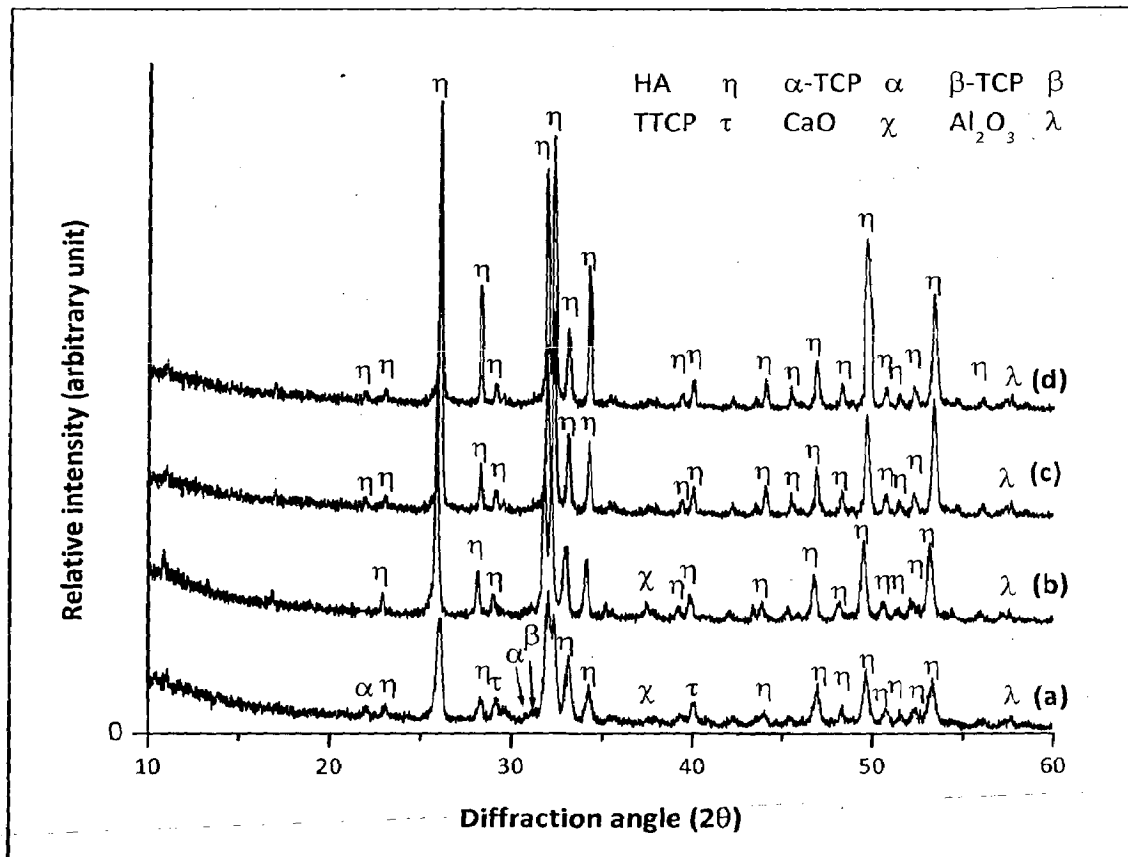


Fig. 7.22 X-ray diffraction pattern of HA-20 wt% Al_2O_3 coated titanium with Al_2O_3 -13 wt% TiO_2 bond coat: (a) as-coated; (b) post coating heat treated at 500° C for 2h in air; (c) post coating heat treated at 700° C for 2h in air and (d) post coating heat treated at 900° C for 2h in air

Table 7.10 Crystallinity of HA-20 wt% Al_2O_3 coatings on titanium with Al_2O_3 -13 wt% TiO_2 bond coat: as-sprayed and after post coating heat treatment

HA-20 wt% Al_2O_3 coated titanium with Al_2O_3 -13 wt% TiO_2 bond coat	as-sprayed	Heat treated at 500°C	Heat treated at 700°C	Heat treated at 900°C
Crystallinity (%)	77.1%	87%	95.9%	98.2%

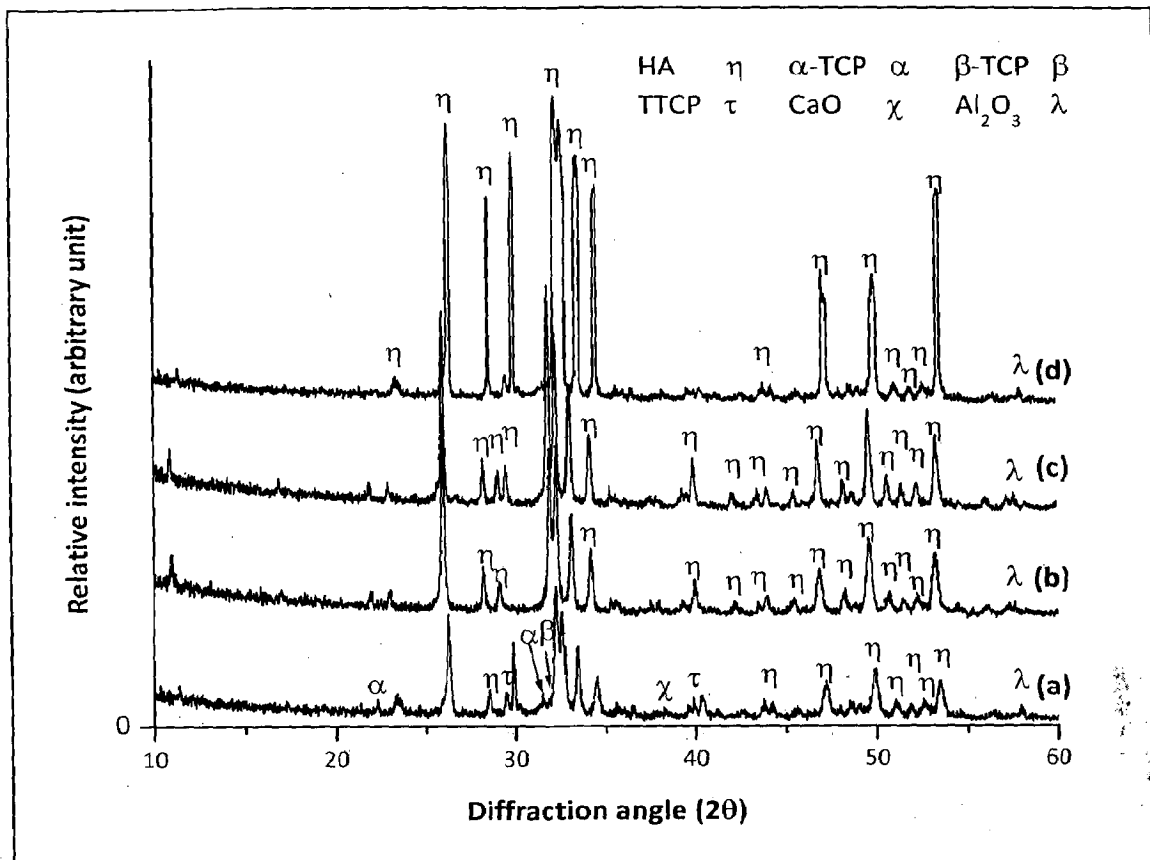


Fig. 7.23 X-ray diffraction pattern of HA-30 wt% Al_2O_3 coated AISI 316L SS (a) as-coated; (b) post coating heat treated at 500° C for 2h in air; (c) post coating heat treated at 700° C for 2h in air and (d) post coating heat treated at 900° C for 2h in air

Table 7. 11 Crystallinity of HA-30 wt% Al_2O_3 coatings on AISI 316L SS: as-sprayed and after post coating heat treatment

HA-30 wt% Al_2O_3 coated AISI 316L SS	as-sprayed	Heat treated at 500°C	Heat treated at 700°C	Heat treated at 900°C
Crystallinity (%)	78%	90.5%	96.9%	98%

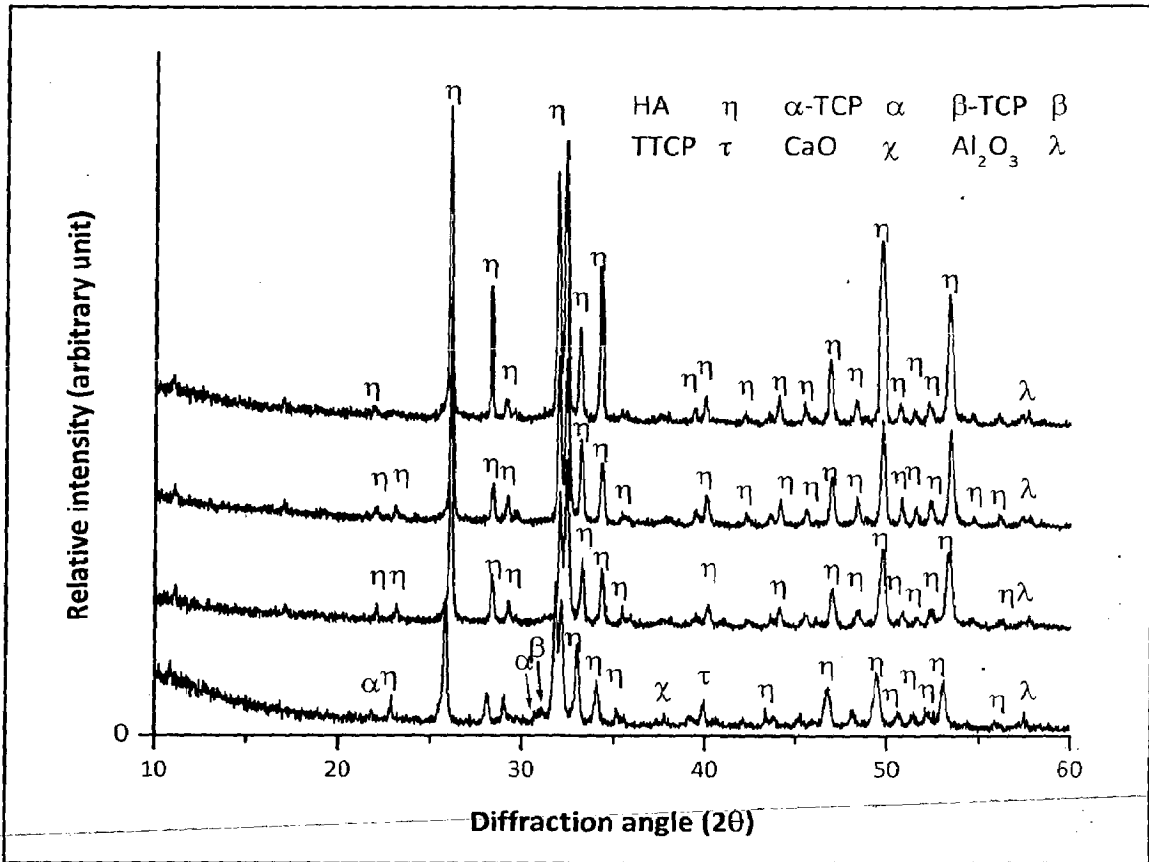


Fig. 7.24 X-ray diffraction pattern of HA-30 wt% Al₂O₃ coated titanium: (a) as coated; (b) post coating heat treated at 500° C for 2h in air; (c) post coating heat treated at 700° C for 2h in air and (d) post coating heat treated at 900° C for 2h in air

Table 7. 12 Crystallinity of HA-30 wt% Al₂O₃ coatings on AISI 316L SS: as-sprayed and after post coating heat treatment

HA-30 wt% Al ₂ O ₃ coated titanium	as-sprayed	Heat treated at 500°C	Heat treated at 700°C	Heat treated at 900°C
Crystallinity (%)	78.6%	90.1%	96.7%	98.2%

7.2.3 Surface Morphology of Post Coating Heat Treated Specimens

Highest crystallinity was obtained in plasma sprayed HA and HA-Al₂O₃ composite coatings after post coating heat treatment at 900°C for to 2h. Specimens after post coating heat treatment at 900°C for 2h in air were analyzed with scanning electron microscopy at higher magnification to find grain refinement and development of ultra-fine hydroxyapatite particles. FE-SEM micrographs showing surface morphology of post coating heat treated specimens are shown in Fig. 7.25 to Fig. 7.36. FE-SEM micrograph of hydroxyapatite coated AISI 316L SS after post coating heat treatment at 900°C for 2h in air is shown in Fig. 7.25.

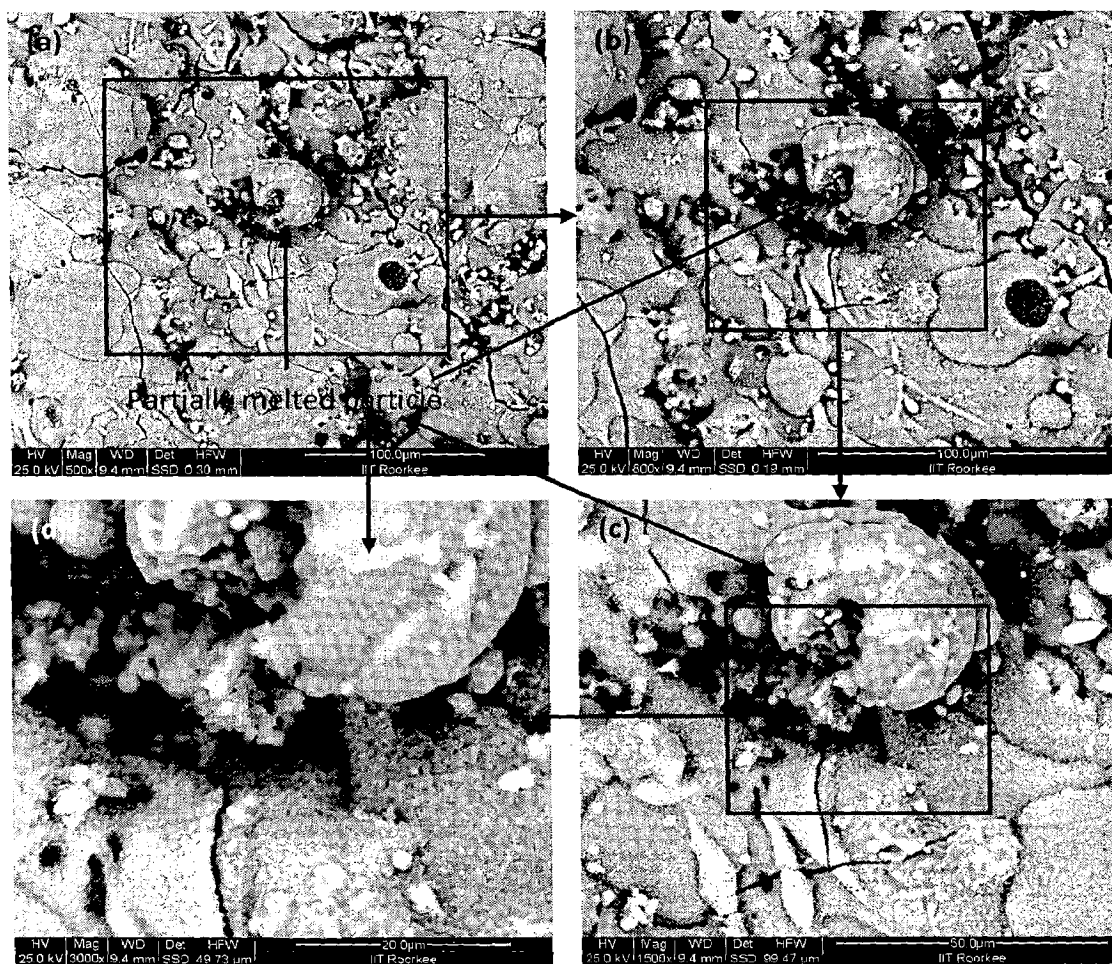


Fig. 7.25 FE-SEM micrograph showing surface morphology of pure HA coating on AISI 316L SS after post coating heat treatment at 900°C for 2h in air at different magnifications: (a) 500X; (b) 800X; (c) 1500X and (d) 3000X

It can be seen from micrograph shown in Fig. 7.25a taken at 500X that coating surface is covered with tiny particles. These tiny particles are not clearly visible near cracks at lower magnifications of 500X and 800X as shown in Fig. 7.25a and b, however at higher magnifications of 1500X and 3000X as shown in Fig. 7.25c and d, development of ultra-fine particles can be seen along the cracks. The size of these particles is slightly larger than that developed on completely molten HA splats. Further, it can be observed from Fig. 7.25c and d that surface of un-melted/partially molten particles does not contain ultra-fine particles.

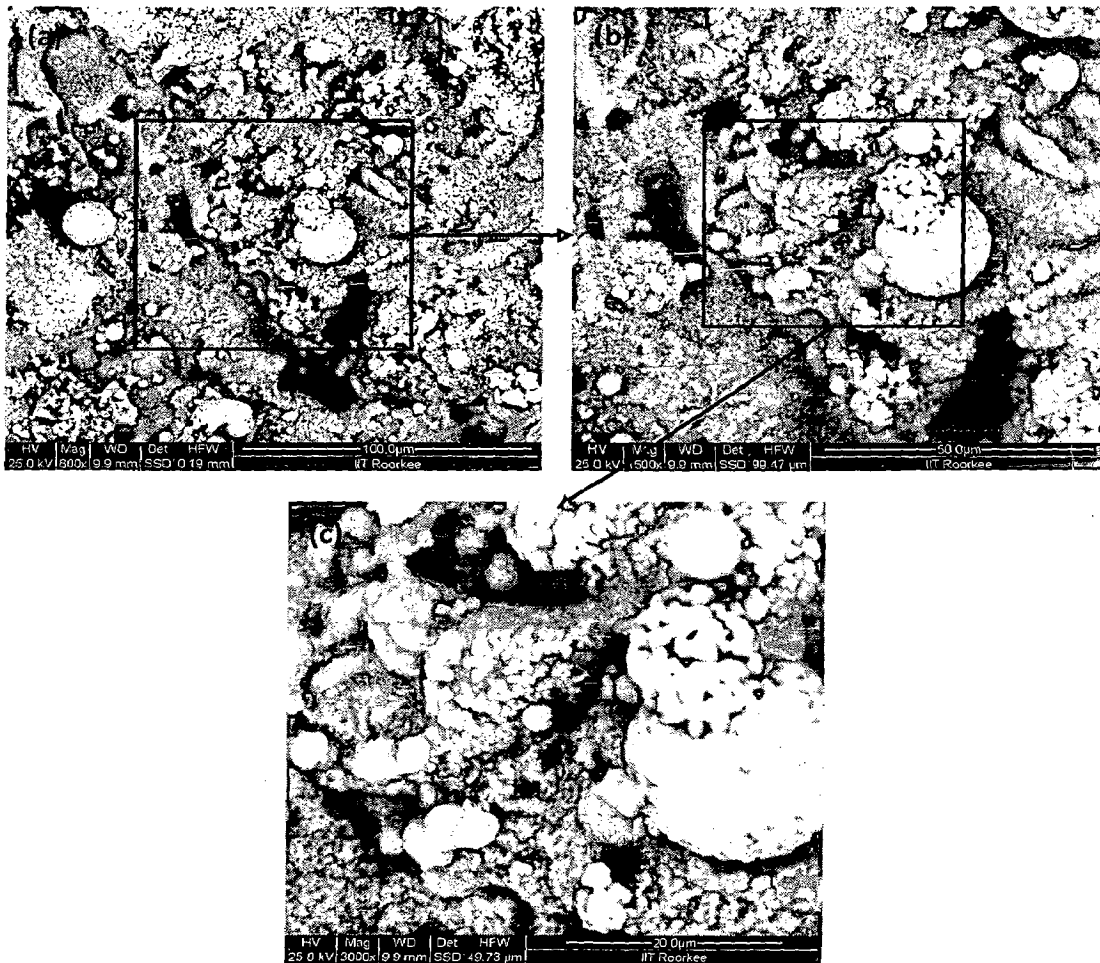


Fig. 7.26 FE-SEM micrograph showing surface morphology of pure HA coating on titanium after post coating heat treatment at 900°C for 2h in air at different magnifications: (a) 800X; (b) 1500X and(c) 3000X

FE-SEM micrograph of hydroxyapatite coated titanium after post coating heat treatment at 900°C for 2h in air is shown in Fig. 7.26. It can be seen from micrographs that the coating after post coating heat treatment is free from cracks. The surface of HA coated titanium after post coating heat treatment is totally covered with ultra-fine particles, whereas in case of AISI 316L SS substrate, partially molten particles were free from ultra-fine particles. Ultra-fine particles developed on HA coated titanium have almost same size as that of ultra-fine particles developed on HA coated AISI 316L SS. The size of these particles is between 200 nm to 300 nm.

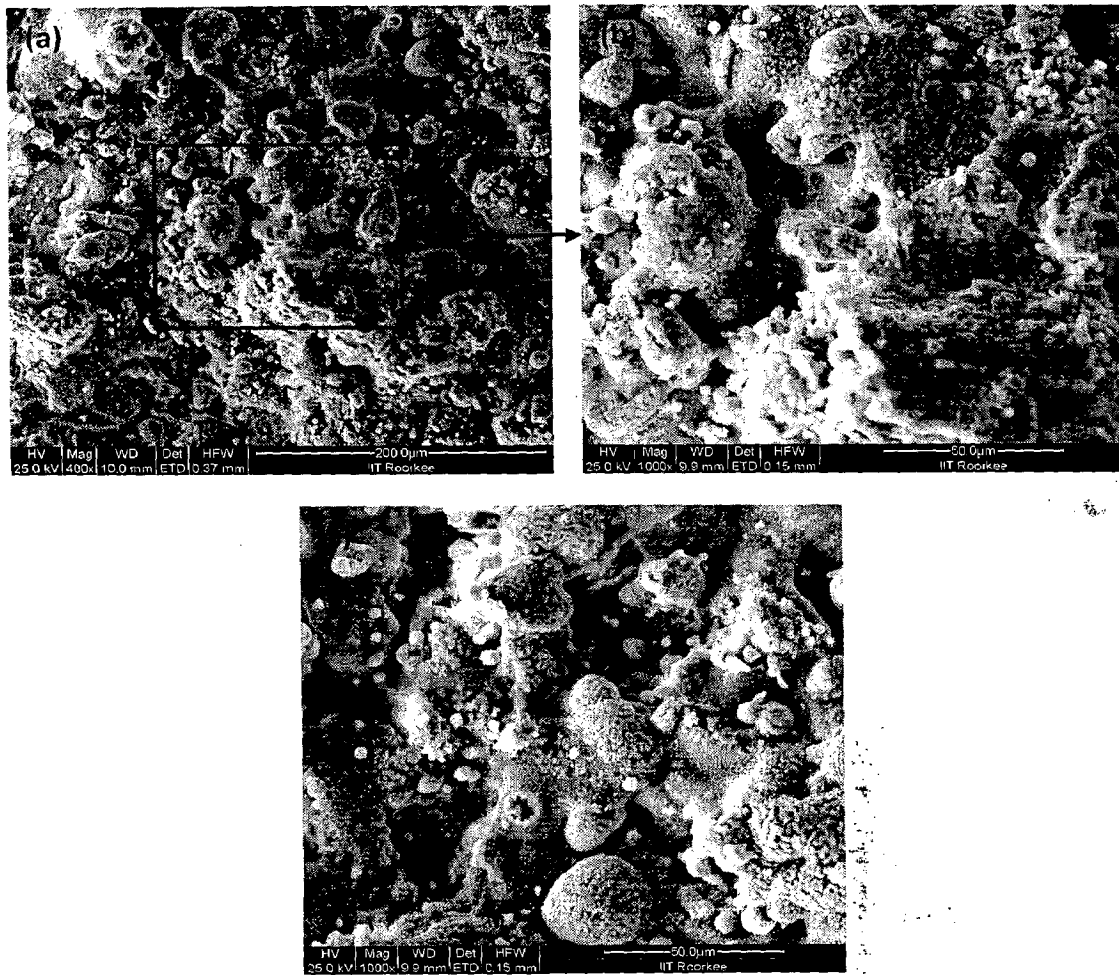


Fig. 7.27 FE-SEM micrograph showing surface morphology of pure HA coating on SS with bond coat of Al_2O_3 -13 wt% TiO_2 after post coating heat treatment at 900°C for 2h in air at different magnifications: (a) 400X; (b) 1000X and (c) 1000X from different location

Figure 7.27 shows the surface morphology of HA coated AISI 316L SS with bond coat of Al_2O_3 -13 wt% TiO_2 after post coating heat treatment at 900°C for 2h in air at 400X and 1000X. Micrographs shown in Fig. 7.27b and 7.27c are taken at same magnification of 1000X but from different locations. It can be observed from Fig. 7.27a (at lower magnification) as well as from Fig. 7.27b and c (at higher magnification) that almost whole of the surface is covered with newly developed ultra-fine particles.

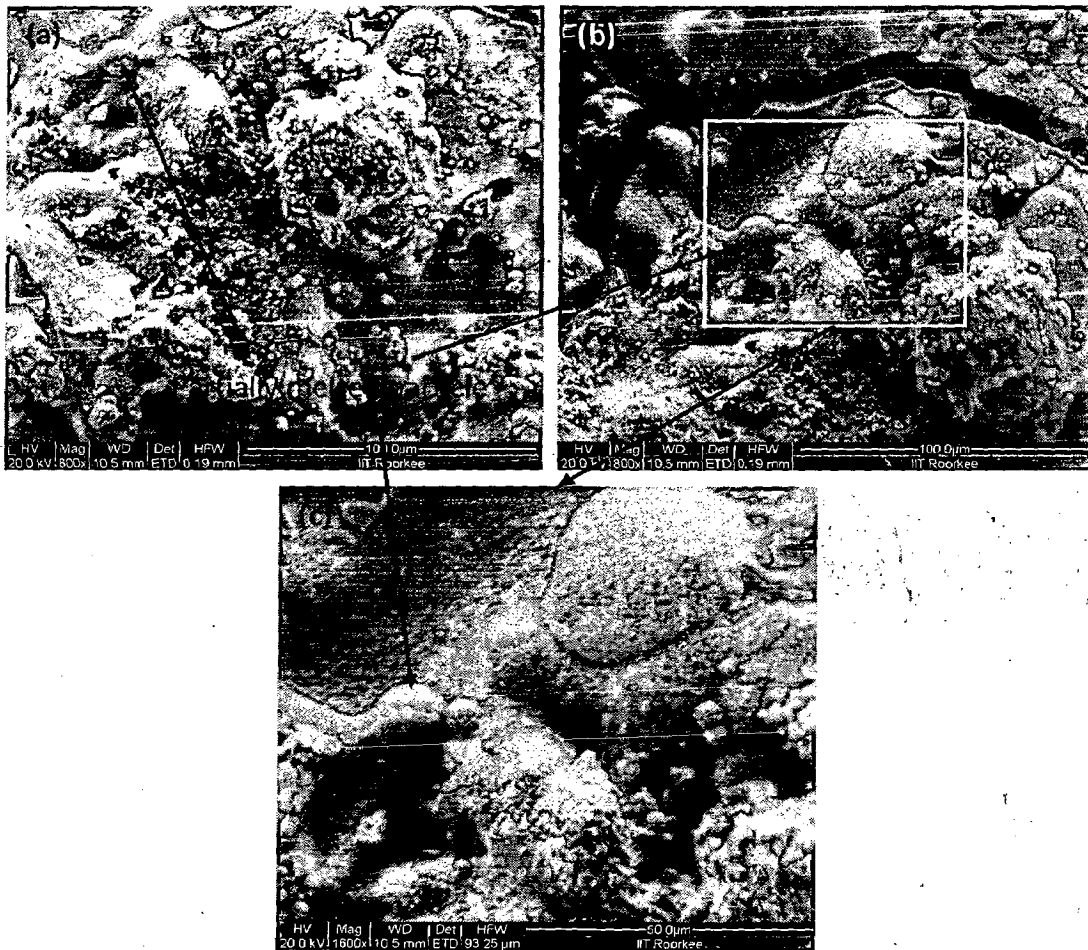


Fig. 7.28 FE-SEM micrograph showing surface morphology of pure HA coating on titanium with bond coat of Al_2O_3 -13 wt% TiO_2 after post coating heat treatment at 900°C for 2h in air at different magnifications: (a) 800X; (b) 800X from different location and (c) 1600X of (b)

Micrograph of hydroxyapatite coated titanium with bond coat of Al₂O₃-13 wt% TiO₂ after post coating heat treatment at 900°C for 2h in air is shown in Fig. 7.28. Figure 7.28a and 7.28b shows the micrograph at 800X magnification from slightly different sites. A wide opened crack with thickness around 10 μm can be seen within the coating as shown in Fig. 7.28b. The spherical un-melted/partially melted particles as shown in Fig. 7.28a-c do not contain ultra-fine particles on their surface, whereas completely molten splats are covered with newly developed ultra-fine particles.

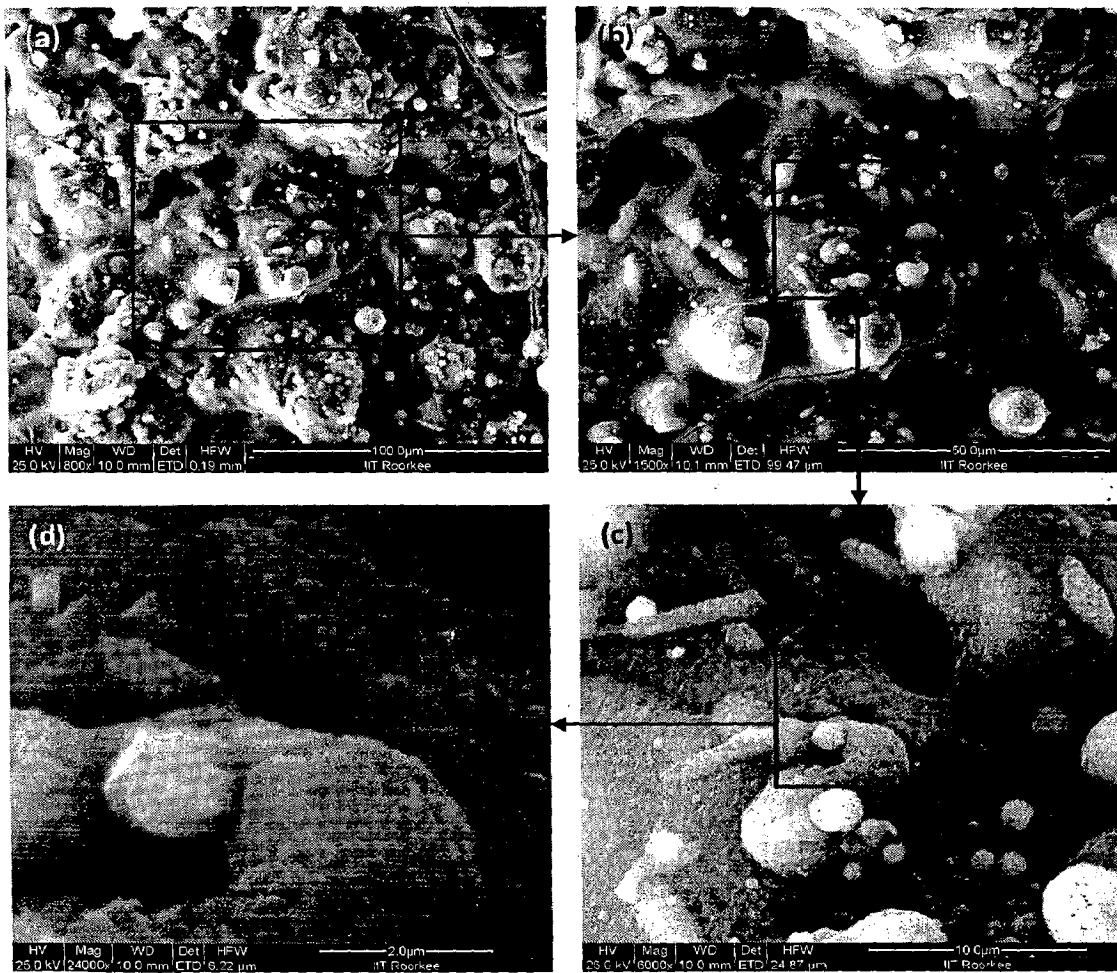


Fig. 7.29 FE-SEM micrograph showing surface morphology of HA-10 wt % Al₂O₃ coating on AISI 316L SS after post coating heat treatment at 900°C for 2h in air at different magnifications: (a) 800X; (b) 1500X; (c) 6000X and (d) 24000X

FE-SEM micrographs showing surface morphology of HA-10 wt% Al₂O₃ coating on AISI 316L SS after post coating heat treatment at 900°C for 2h in air at 800X, 1500X, 6000X and 24000X are presented in Fig. 7.29. At comparatively lower magnification of 800X and 1500X (Fig. 7.29a and b), development of ultra-fine particles is not clearly visible, however at higher magnifications as shown in Fig. 7.29c and d, very fine particles can be seen on coating surface. The size of these particles as measured from Fig. 7.29d is around 300 nm.

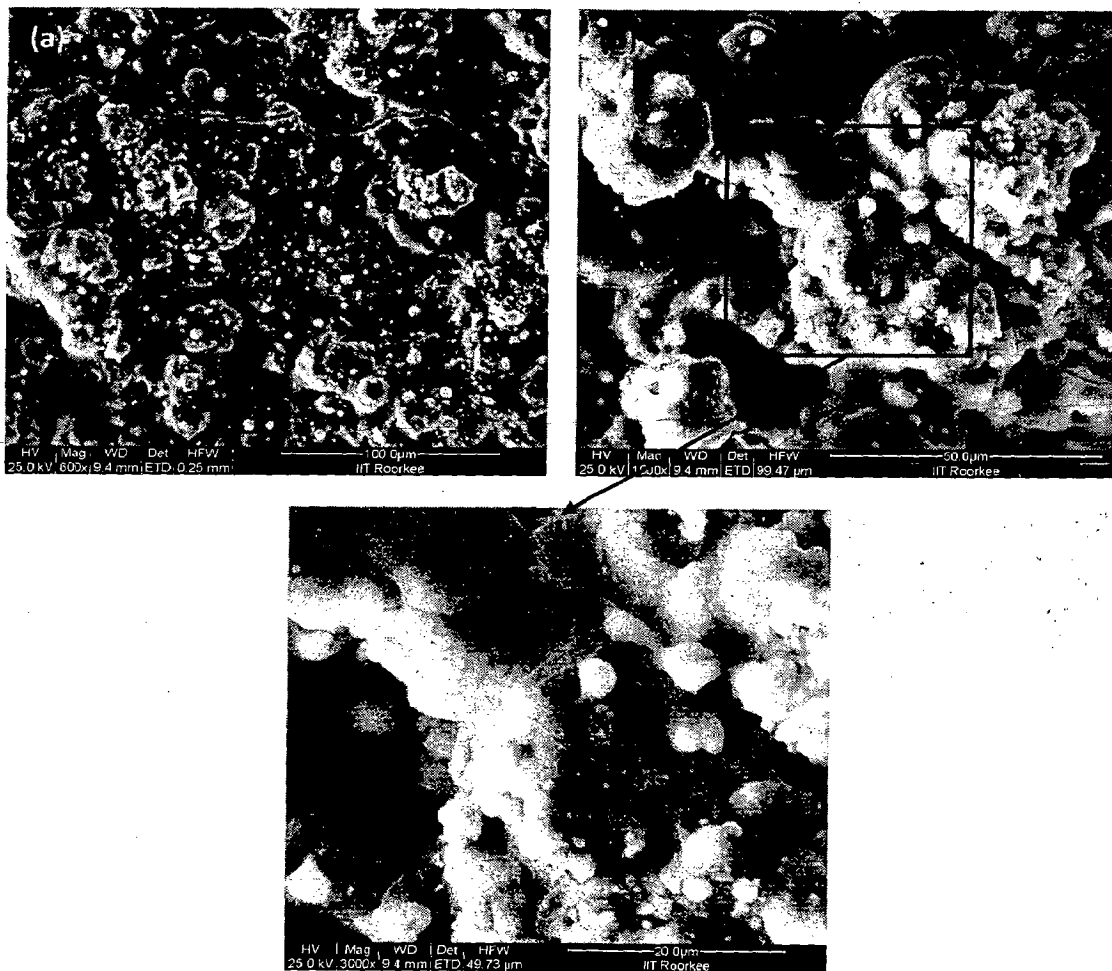


Fig. 7.30 FE-SEM micrograph showing surface morphology of HA-10 wt % Al₂O₃ coating on titanium after post coating heat treatment at 900°C for 2h in air at different magnifications: (a) 800X; (b) 1500X and (c) 3000X (crack filling by nano-scale HA particles is indicated by arrow)

FE-SEM micrographs showing surface morphology of HA-10 wt% Al₂O₃ coating on titanium after post coating heat treatment at 900°C for 2h in air at 800X, 1500X and 3000X are shown in Fig. 7.30. It can be seen from micrograph at 800X (Fig. 7.30a) that some fine cracks with wide crack are present on coating surface. Very fine particles can be seen on the coating surface as shown in Fig. 7.30c. Some agglomerates of ultra-fine particles can also be observed at lower right corner in Fig. 7.30c.

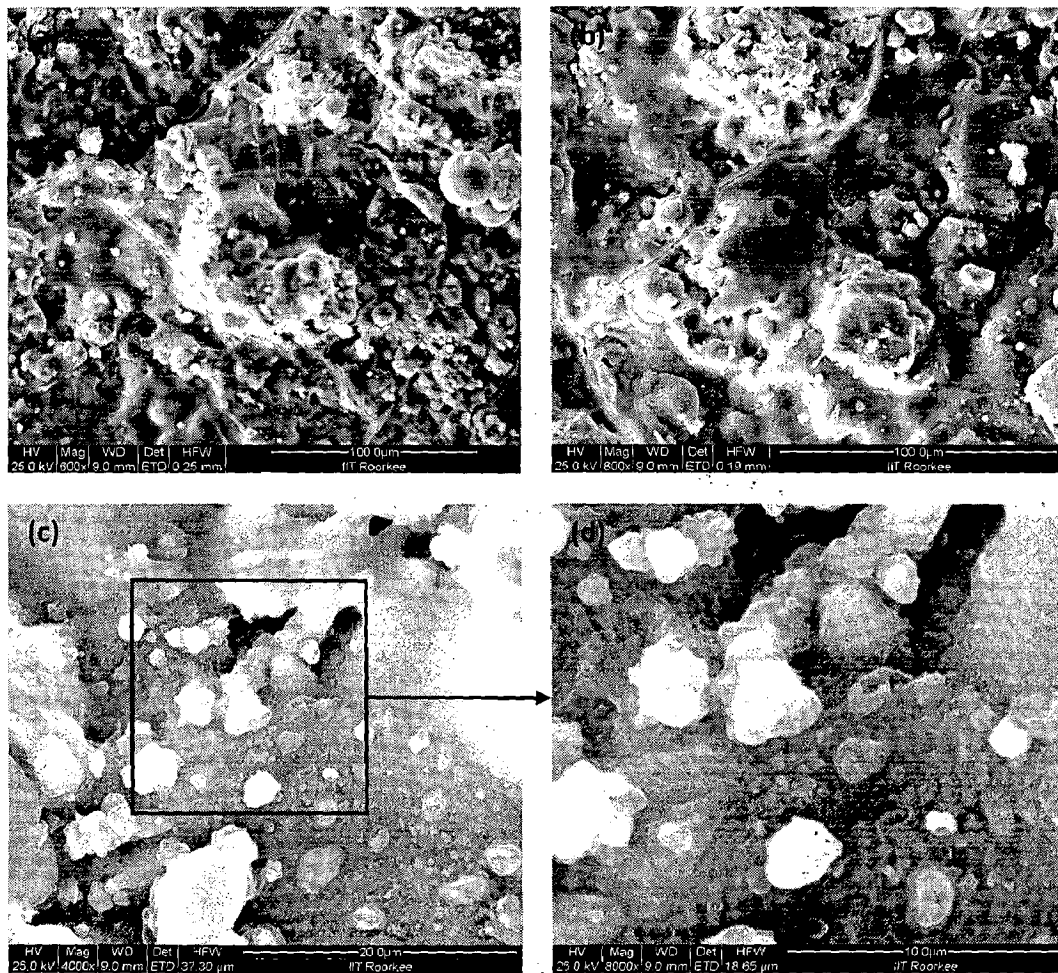


Fig. 7.31 FE-SEM micrograph showing surface morphology of HA-10 wt % Al₂O₃ coating on AISI 316L SS with bond coat of Al₂O₃-13 wt% TiO₂ after post coating heat treatment at 900°C for 2h in air at different magnifications: (a) 600X; (b) 800X; (c) 4000X and (d) 8000X

FE-SEM micrographs showing surface morphology of HA-10 wt% Al₂O₃ coating on AISI 316L SS with bond coat of Al₂O₃-13 wt% TiO₂ after post coating heat treatment at 900°C for 2h in air at 600X, 800X, 4000X and 8000X are presented in Fig. 7.31. At comparatively lower magnification of 600X and 800X (Fig. 7.31a and b), development of ultra-fine particles is not clearly visible, however at higher magnifications as shown in Fig. 7.31c and d, very fine particles and agglomerates of fine particles can be seen on coating surface.

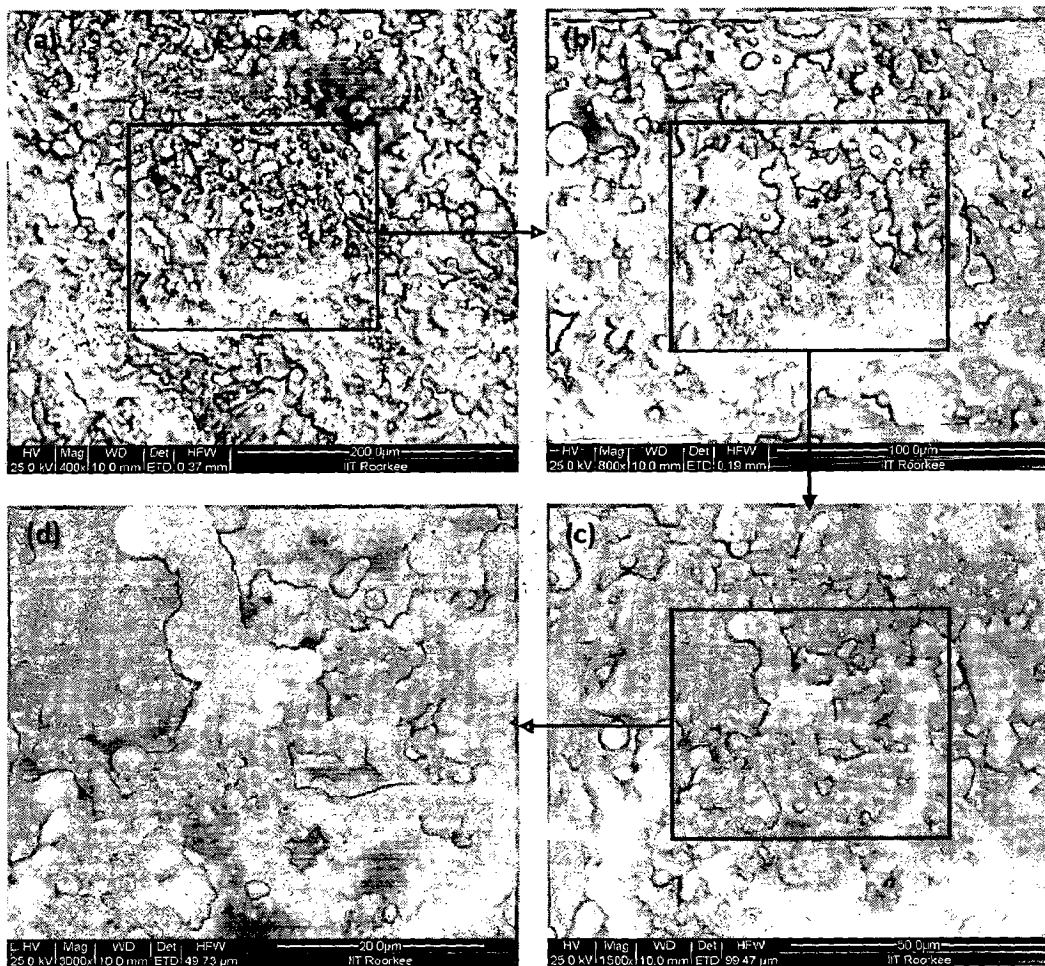


Fig. 7.32 FE-SEM micrograph showing surface morphology of HA-10 wt % Al₂O₃ coating on titanium with bond coat of Al₂O₃-13 wt% TiO₂ after post coating heat treatment at 900°C for 2h in air at different magnifications: (a) 400X; (b) 800X; (c)1500X and (d) 3000X

FE-SEM micrographs showing surface morphology of HA-10 wt% Al_2O_3 coating on titanium with bond coat of Al_2O_3 -13 wt% TiO_2 after post coating heat treatment at 900°C for 2h in air at 400X, 800X, 1500X and 3000X are presented in Fig. 7.32. Some un-melted/partially melted particles can be seen on coating surface. At comparatively lower magnification of 400X and 800X (Fig. 7.32a and b), ultra-fine particles are not clearly visible, however at higher magnifications as shown in Fig. 7.32c and d, very fine particles and agglomerates of fine particles can be seen on coating surface.

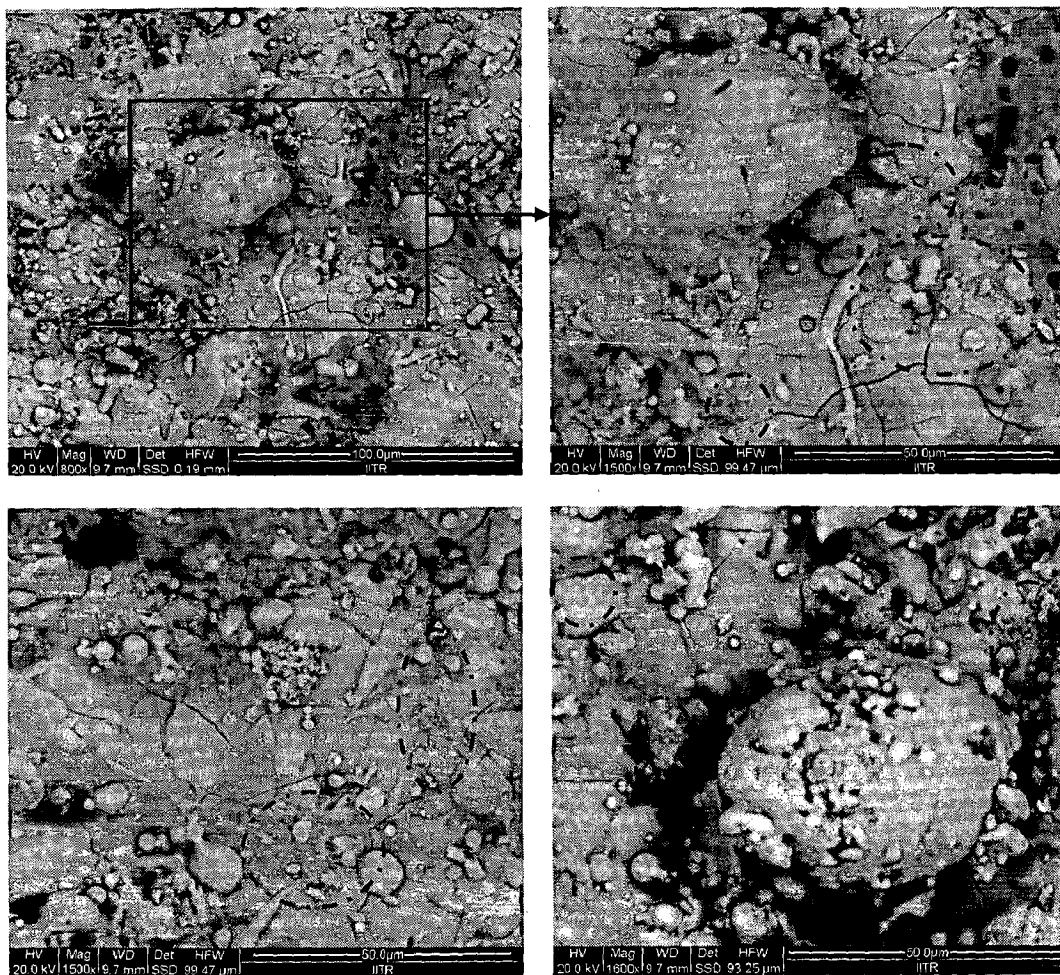


Fig. 7.33 FE-SEM micrograph showing surface morphology of HA-20 wt % Al_2O_3 coating on AISI 316L SS with bond coat of Al_2O_3 -13 wt% TiO_2 after post coating heat treatment at 900°C for 2h in air at different magnifications: (a) 800X; (b) 1500X; from different locations: (c) 1500X and (d) 1600X

Surface morphologies of HA-20 wt % Al_2O_3 coated AISI 316L SS with bond coat of Al_2O_3 -13 wt% TiO_2 after post coating heat treatment at 900°C for 2h in air are shown in Fig. 7.33. Some cracks along with un-melted/partially melted particles can be seen in Fig. 7.33a (at lower magnification). At higher magnification, ultra-fine particles can be seen in scattered manner on the coating surface as highlighted by dotted circles/ovals in Fig. 7.33b to d. A higher content of aluminum oxide in HA- Al_2O_3 composite coating might have restricted the grain refinement.

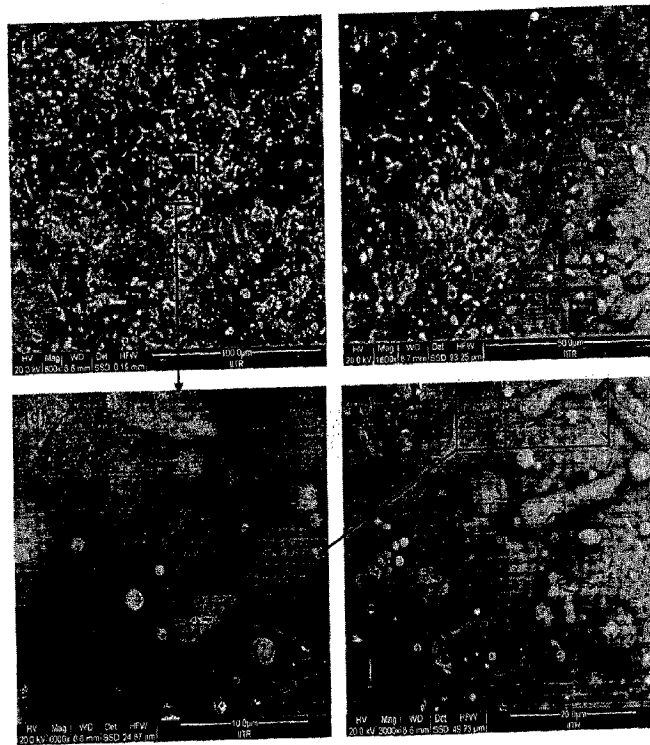


Fig. 7.34 FE-SEM micrograph showing surface morphology of HA-20 wt % Al_2O_3 coating on titanium with bond coat of Al_2O_3 -13 wt% TiO_2 after post coating heat treatment at 900°C for 2h in air at different magnifications: (a) 800X; (b) 1600X; (c) 3000X and (d) 6000X

FE-SEM micrographs showing surface morphology of HA-20 wt% Al₂O₃ coating on titanium with bond coat of Al₂O₃-13 wt% TiO₂ after post coating heat treatment at 900°C for 2h in air are presented in Fig. 7.34. Some cracks and un-melted/partially melted particles can be seen in coating. At higher magnification, nano-scale crystallites can be seen at scattered locations as highlighted by dotted circles/ovals in Fig. 7.34c and d.

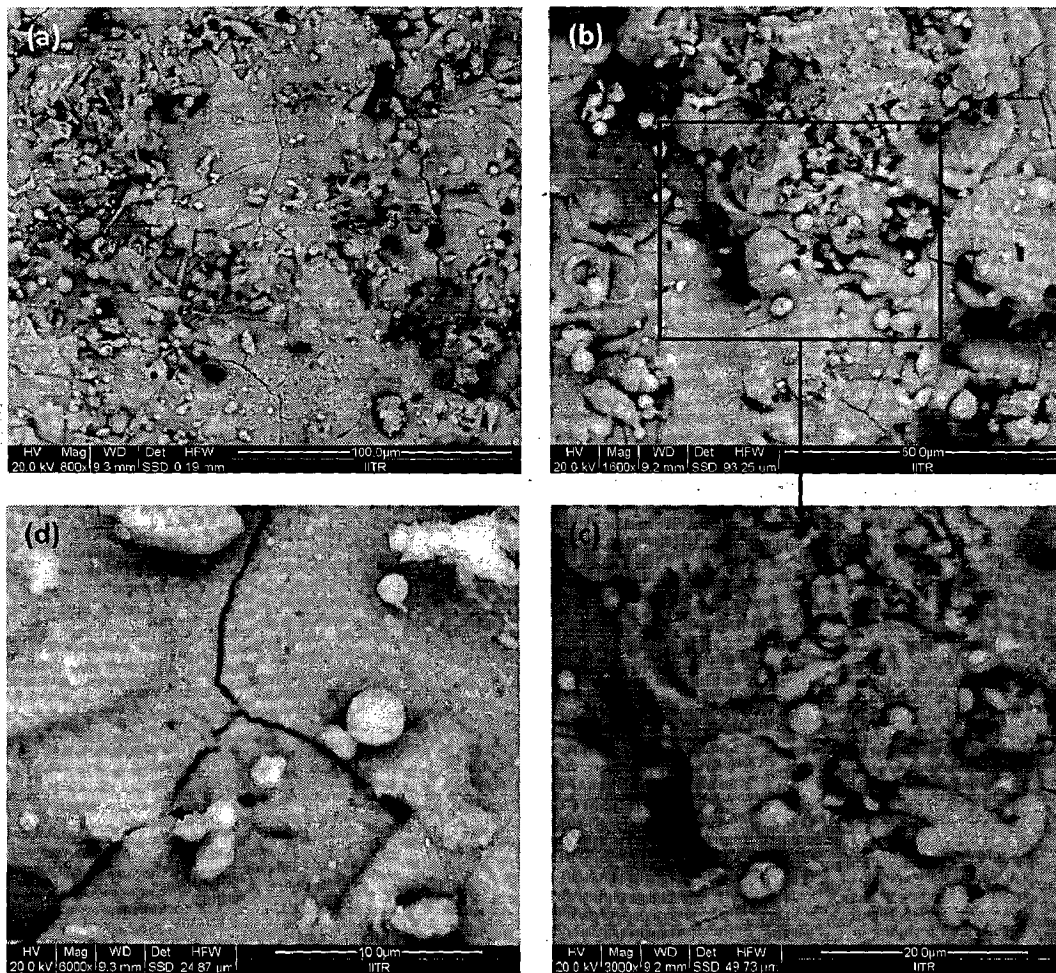


Fig. 7.35 FE-SEM micrograph showing surface morphology of HA-30 wt % Al₂O₃ coating on AISI 316L SS after post coating heat treatment at 900°C for 2h in air at different magnifications: (a) 800X; (b) 1600X; (c) 3000X and (d) 6000X (filling of crack by nano-scale HA particles is shown by arrow)

Surface morphologies of HA-30 wt% Al₂O₃ coated AISI 316L SS after post coating heat treatment at 900°C for 2h in air are shown in Fig. 7.35. Some cracks along with unmelted/partially melted particles can be seen in micrographs. Ultra-fine particles can be seen at scattered locations at lower magnification (Fig. 7.35b and c), however at higher magnification of 6000X, ultra-fine particles can be seen on coating surface (Fig. 7.35d). Nano-scale crystallites show the crack filling effect as indicated by arrow in Fig. 7.35d.

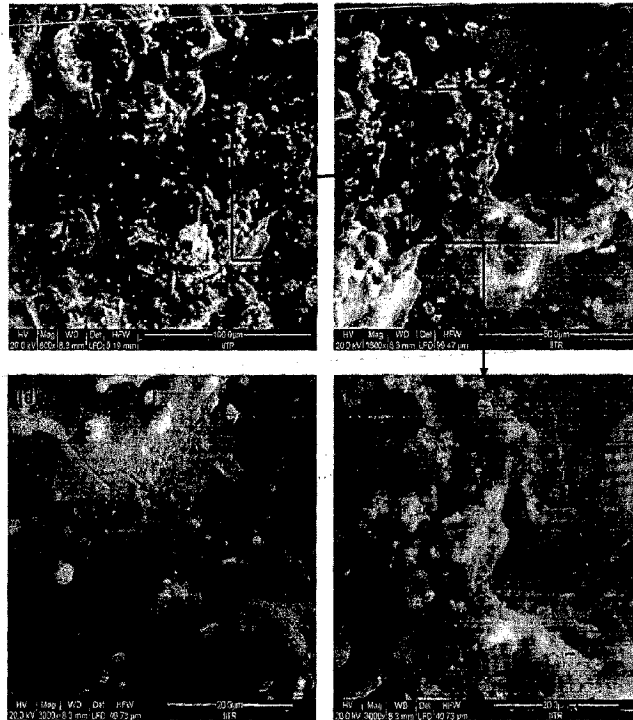


Fig. 7.36 FE-SEM micrograph showing surface morphology of HA-30 wt % Al₂O₃ coating on titanium after post coating heat treatment at 900°C for 2h in air at different magnifications: (a) 800X; (b) 1500X; (c) 3000X and (d) 3000X from different location

Surface morphologies of HA-30 wt% Al₂O₃ coated titanium after post coating heat treatment at 900°C for 2h in air are shown in Fig. 7.36. By careful examination of Fig. 7.36b and c, ultra-fine particles can be seen at scattered locations, however fair distribution of these particles can be seen in Fig. 7.36d. The healing of crack by nano-sized particles is indicated by arrow in Fig. 7.36d. The similar grain refinement as shown in Fig. 7.30 and Fig. 7.33-7.36 are reported by Yang and Lui, (2008).

7.2.4 FTIR analysis of Post Coating Heat Treated Specimens

FTIR spectra of as-sprayed and post coating heat treated pure HA, HA-10 wt% Al₂O₃, HA-20 wt% Al₂O₃ and HA-30 wt% Al₂O₃ coatings at 500°C, 700°C and 900°C for 2h in air are shown in Fig. 7.37-Fig. 7.40 respectively. FTIR spectrum of as-sprayed HA, HA-10 wt% Al₂O₃, HA-20 wt% Al₂O₃ and HA-30 wt% Al₂O₃ coatings are superimposed in Fig. 7.37 to Fig. 7.40 for comparing them with FTIR spectra of post coating heat treated specimens. Broad peaks at 650 cm⁻¹ and in range of 3300 cm⁻¹ to 3600 cm⁻¹ representing hydroxyl group can only be seen in plots for as-sprayed coatings. The detailed analysis of FTIR spectra of as-sprayed coatings has been already discussed in Section 4.2.4, Chapter 4 of present study.

FTIR spectrum for HA coatings after post coating at 500°C, 700°C and 900°C for 2h in air are shown in Fig. 7.37b to d respectively. Strong peaks corresponding to hydroxyl group can be seen around 3570 cm⁻¹ and 635 cm⁻¹ in FTIR spectrum of HA coating after post coating heat treatment (Fig. 7.37b-d). Peaks belonging to PO₄⁻³ (phosphate) group can be seen at 1095 cm⁻¹, 1051 cm⁻¹, 953 cm⁻¹, 603 cm⁻¹ and 569 cm⁻¹, whereas peak corresponding to carbonate group can be seen at 2364 cm⁻¹ in FTIR spectrum of HA coating after post coating heat treatment. The intensity of peaks corresponding to hydroxyl group has become prominent after post coating heat treatment (Fig. 7.37b-d) as compared to their intensity in FTIR spectrum of as-sprayed coating (Fig. 7.37a). Intensity of phosphate group increased after post coating treatment at 500°C for 2h in air (Fig. 7.37b); however it decreased slightly with increase in post coating heat treatment temperature to 700°C and 900°C as can be seen in Fig. 7.37c-d.

Figure 7.38 shows the FTIR spectra of as-sprayed and post coating heat treated HA-10 wt% Al₂O₃ coatings. Phosphate group can be seen around 1095 cm⁻¹, 1041 cm⁻¹, 957 cm⁻¹, 603 cm⁻¹ and 568 cm⁻¹ whereas carbonate is present around 2375 cm⁻¹ in FTIR spectrum of post coating heat treated specimen for 2h in air (Fig. 7.38b-d). Hydroxyl group shows its presence around 3570 cm⁻¹ and 635 cm⁻¹ in FTIR spectrum after post coating heat treatment at 500°C, 700°C and 900°C for 2h in air. Carbonate group can be seen around 2365 to 2400 cm⁻¹ in FTIR spectrum (Fig. 7.38b-d), moreover its intensity decreased with increase in post coating heat treatment temperature.

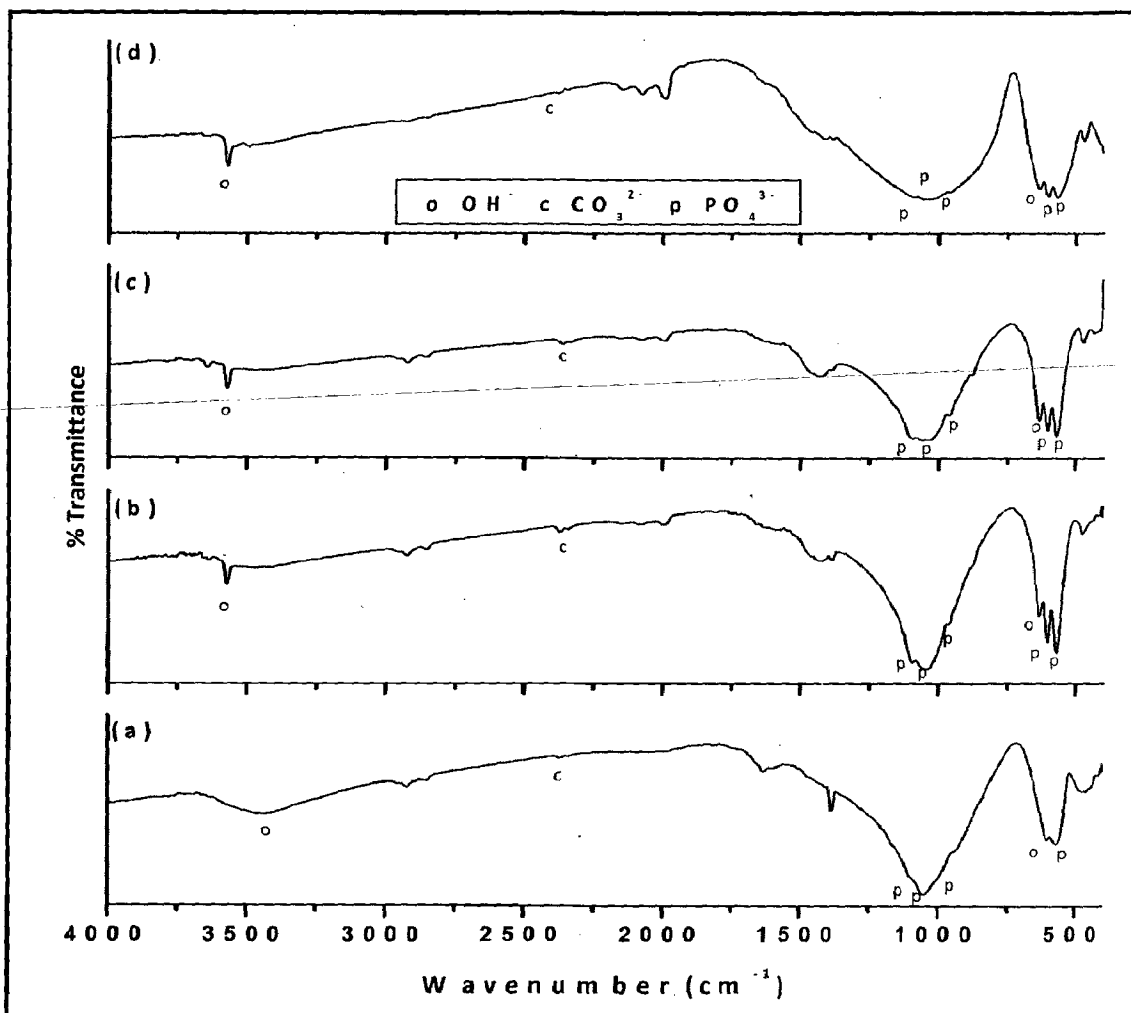


Fig. 7.37 FTIR spectra of pure HA coating: (a) as-sprayed coating; (b) post coating heat treated at 500°C; (c) post coating heat treated at 700°C and (d) post coating heat treated at 900°C

The intensity of peaks corresponding to hydroxyl (OH^-) substantially increased with increase in post coating heat treatment temperature, however intensity of peaks corresponding to phosphate group slightly decreased with increase in post coating heat treatment temperature.

FTIR spectrum for HA-20 wt% Al_2O_3 coatings after post coating heat treatment at 500°C for 2h in air is shown in Fig. 7.39b. Peaks belonging to PO_4^{3-} group can be seen at 1095 cm^{-1} , 1041 cm^{-1} , 957 cm^{-1} , 603 cm^{-1} and 568 cm^{-1} , whereas peak corresponding to carbonate group appears 2375 cm^{-1} in FTIR spectrum of HA coating after post coating heat treatment at 500°C .

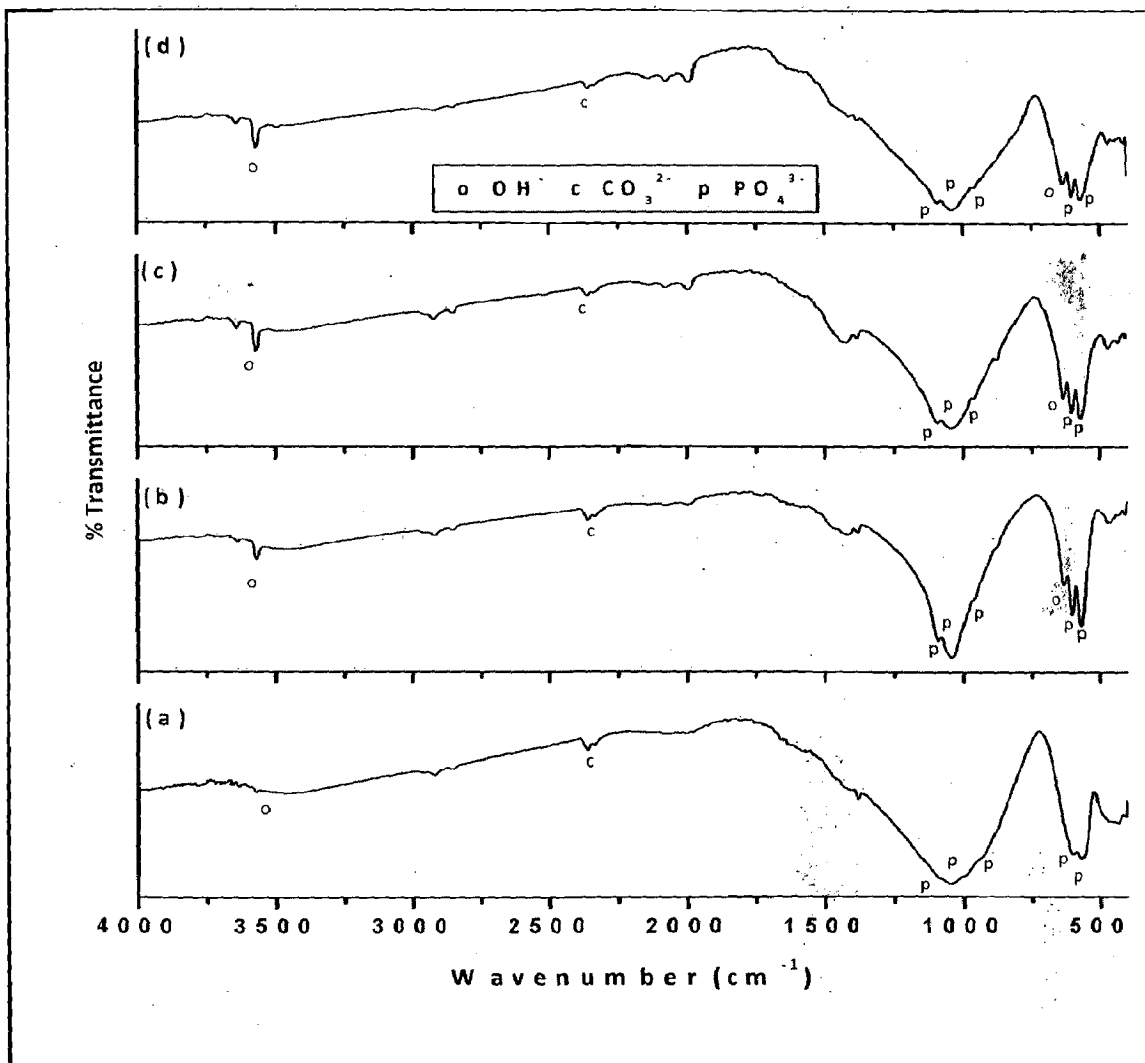


Fig. 7.38 FTIR spectra of HA-10 wt% Al_2O_3 coating: (a) as-sprayed coating; (b) post coating heat treated at 500°C ; (c) post coating heat treated at 700°C and (d) post coating heat treated at 900°C

After post coating heat treatment at 700°C (Fig. 7.39c), OH⁻ group can be seen at 3565 cm⁻¹ and 635 cm⁻¹, whereas carbonate group can be seen at 2374 cm⁻¹ in FTIR spectrum. PO₄³⁻ group can be seen at 1095 cm⁻¹, 1040 cm⁻¹, 953 cm⁻¹, 603 cm⁻¹ and 569 cm⁻¹ in FTIR spectrum of post coating heat treated specimens at 700°C for 2h in air. After post coating heat treatment at 900°C for 2h in air, hydroxyl group can be seen at 3568 cm⁻¹ and 635 cm⁻¹, whereas PO₄³⁻ group can be seen at 1095 cm⁻¹, 1040 cm⁻¹, 953 cm⁻¹, 603 cm⁻¹ and 569 cm⁻¹ in FTIR spectrum as shown in Fig. 7.39d. Carbonate group can be seen at 3568 cm⁻¹ in FTIR spectrum (Fig. 7.39d).

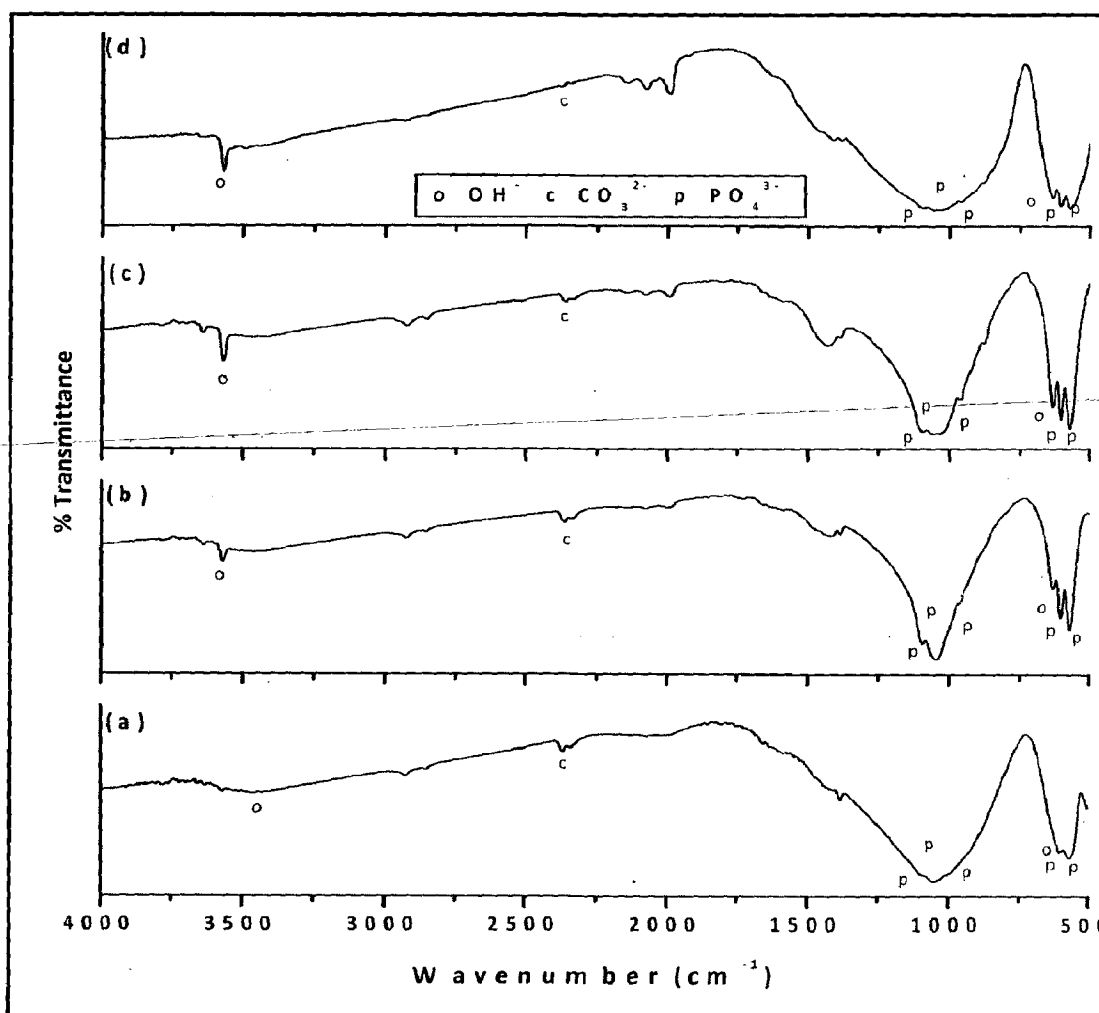


Fig. 7.39 FTIR spectra of HA-20 wt% Al₂O₃ coating: (a) as-sprayed coating; (b) post coating heat treated at 500°C; (c) post coating heat treated at 700°C and (d) post coating heat treated at 900°C

FTIR spectra for as-sprayed HA-30 wt% Al₂O₃ and post coating heat treated HA-30 wt% Al₂O₃ coatings at 500°C, 700°C and 900°C in air for 2h is shown in Fig. 7.40. Phosphate group is present at 1098 cm⁻¹, 1040 cm⁻¹, 957 cm⁻¹, 603 cm⁻¹ and 568 cm⁻¹ in post coating heat treated HA-30 wt% Al₂O₃ coatings at 500°C, 700°C and 900°C as can be seen in Fig. 7.40b-d. Hydroxyl group is present around 3568 cm⁻¹ and 635 cm⁻¹ in spectrum of post coating heat treated specimens at 500°C; 700°C; 900°C as can be seen in Fig. 7.40b-d respectively. Carbonate group shows its presence around 2375 cm⁻¹ in FTIR spectrum of post coating heat treated specimen at 500°C, 700°C and 900°C for 2h in air (Fig. 7.40b-d).

7.3 Discussion

The post coating heat treatment at 500°C, 700°C and 900°C in air for 2h did not affected the integrity of coating as shown in Fig. 7.1 to 7.12 and Fig. 7.25 to Fig. 7.36. No delamination of coating occurred after post coating heat treatment. However, some wide opened cracks appear with in the coating. These cracks are not through as suggested by absence of substrate elements in EDAX point analysis along the cracks in coating as shown at point 3 in Fig. 7.2b, point 6 in Fig. 7.6c and point 5 in Fig. 7.12c. The opening of cracks might be due to recrystallization of amorphous phases of calcium and phosphate to crystalline phase due to post coating heat treatment. Amorphous phases have loose packed structure, whereas crystalline phases have close packed structure. Production of cracks due to recrystallization of amorphous phases via post coating heat treatment has been reported by Ducheyne (1987). The migration/diffusion of substrate elements is found to reduce to almost negligible by incorporation of Al₂O₃-13 wt% TiO₂ bond coat between substrate and main coating (top coat) even after post coating heat treatment. The bond coat remained effective in reducing elemental migration/diffusion from substrate to coating after post coating heat treatment also.

The crystallinity of all coatings increased marginally with Al₂O₃ reinforcement and by incorporation of bond coat; however higher increase in crystallinity of coatings has been recorded by post coating heat treatment. Further, crystallinity of coatings is found to increase with increase in temperature of post coating heat treatment. The amorphous phases present in plasma sprayed coatings eliminated or get converted into crystalline phases. The high intensity peaks in XRD pattern as shown in Fig. 7.13 to Fig. 7.24 represent crystalline HA and it confirms the improvement in crystallinity as can be seen in Table 7.1-7.12 respectively. The restoration

of crystallinity of plasma sprayed HA coatings via post coating heat treatment between 600°C to 700°C has been reported by Lu et al., (2003A and 2003B). They also suggested that excessive high temperatures and in particular long holding times for post coating heat treatments are unfavorable for plasma sprayed HA coatings. Formation of HA phase and increase in crystallinity of plasma sprayed HA coatings by post coating heat treatment at 700°C for 1h has also been reported by Yu et al., (2003).

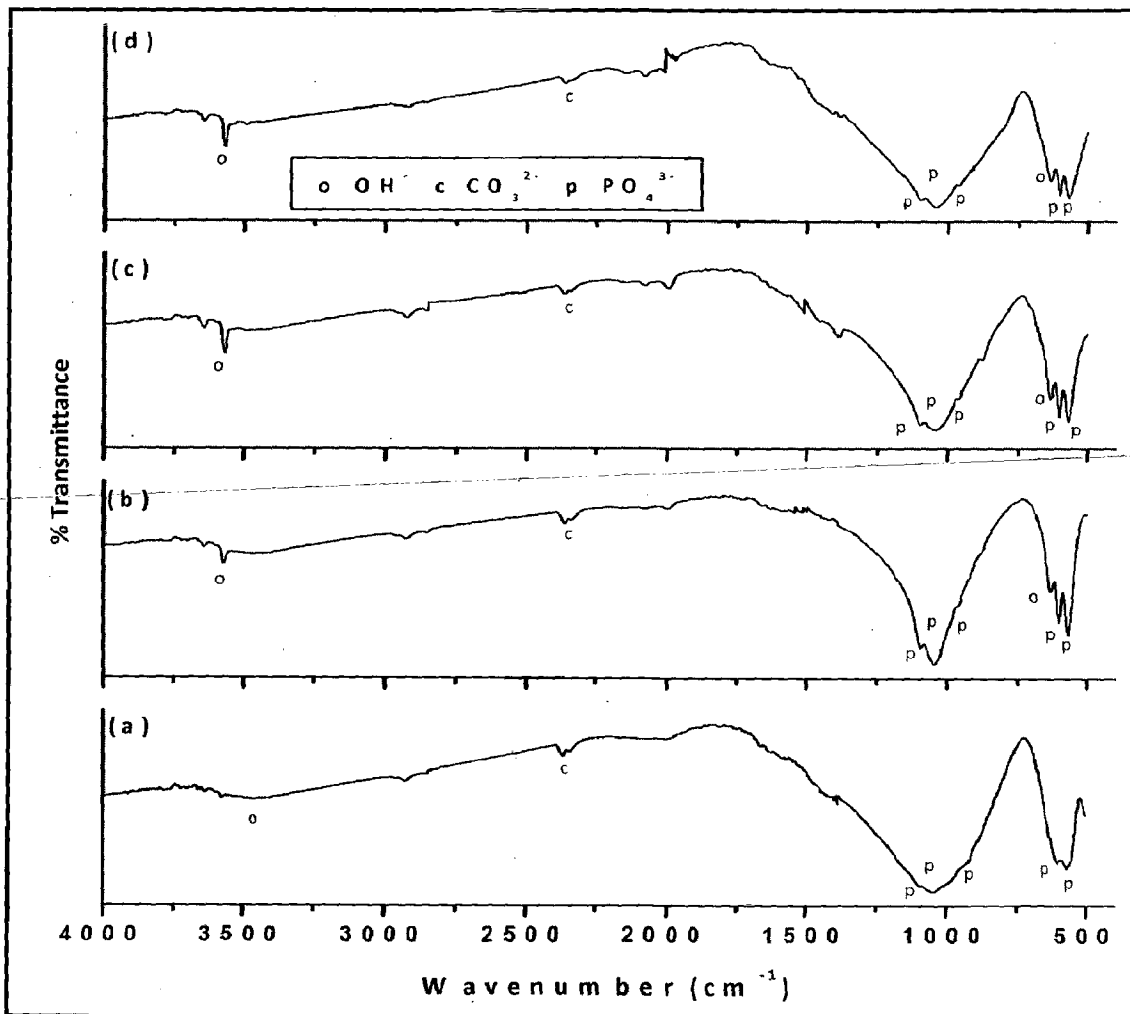


Fig. 7.40 FTIR spectra of HA-30 wt% Al₂O₃ coating: (a) as-sprayed coating; (b) post coating heat treated at 500°C; (c) post coating heat treated at 700°C and (d) post coating heat treated at 900°C

Yang, (2007) performed post coating heat treatment on plasma sprayed HA coatings at 400, 500, 600, 700, 800 and 900°C at heating rate of 10°C/min and for holding time of 3h in vacuum (1×10^{-5} torr) and reported increase in crystallinity of coatings with increase in post coating heat treatment temperature when compared with as-sprayed coatings. Improvement in phase content and crystallinity of plasma sprayed hydroxyapatite coatings by post coating heat treatment in vacuum has also been reported by Yang et al., (2009A). Increase in coating crystallinity by post coating heat treatment at 650°C has been reported to be a function of holding time by Lu et al., (2008). The maximum crystallinity of coating has been reported for holding time of 2h out of three different holding times (0.5, 1 and 2h). Inagaki and Kameyama (2007) reported that post coating heat treatment at 600°C for 2h converted tri-calcium phosphate and tetra-calcium phosphate into pure HA by radio-frequency thermal plasma sprayed HA coatings.

In a study carried out on post coating heat treatment of plasma sprayed hydroxyapatite coatings by Chen et al., (2004), the transformation of tri-calcium phosphate into pure hydroxyapatite has been reported by post coating heat treatment for 1h in air at a temperature of 650°C. They further stated that the amorphous calcium phosphate in as-sprayed coatings is thermodynamically metastable and an appropriate post coating thermal treatment could induce recrystallization.

Brossa, (1994) evaluated the effect of post coating heat treatment at a temperature of 950°C for 1, 12 and 24h in vacuum on high and low crystalline HA coatings developed by plasma spraying (by controlling spraying parameters) on Ti-6Al-4V substrate. The heating and cooling rate of 6°C/min was maintained for post coating heat treatment. He observed increase in crystallinity of low crystalline coatings with development of tetra-calcium phosphate in very small amount, while development of amorphous phases was observed in high crystalline coatings. He suggested that very high-temperature post coating heat treatments particularly for long holding time are not useful and recommended post coating heat treatments for low crystalline HA coatings only. In a study conducted by Khor et al., (1998), plasma sprayed coatings were developed using HA powder with different particle size range. They reported that the coatings developed by HA powder above 45 μm size could retain crystalline HA phase, however most of the crystalline phase was lost during plasma spraying for coating developed by smaller size HA particles. They further reported that, subsequent post spray heat treatment at

600, 700 and 800°C for 1h restored most of the crystalline phase in HA coatings, however suggested that the heat treatment at higher temperatures is not advisable as it lead to slight decrease in HA/CaO ratio at higher temperatures due to instability in calcium phosphate phases.

Kweh et al., (2000) investigated improvement in crystallinity of plasma sprayed HA coatings by post coating heat treatment in preheated furnace at 600, 800 and 900°C for 1h in air with cooling rate of 5°C/min and reported increase in crystallinity of HA coating at all heating temperatures as compared to original as-sprayed coatings. Zhang et al., (2003) carried out post coating treatments on plasma sprayed HA coatings with three different techniques: hydrothermal treatment, heating in vacuum and heating in air and reported almost same level of crystallinity for coatings treated in air at 650°C and in vacuum at 900°C for 1h, whereas hydrothermal treatment at 120°C for 6h resulted in the least coating crystallinity. However, improvement in crystallinity has been reported by them for post coating treatment carried out by all the three processes.

Wang et al., (1995) carried out post coating heat treatment on plasma sprayed HA coatings in a temperature range of 630-1000°C in vacuum and reported that in temperature range of 630-850°C, the concentration of impurity phases decreased and coating crystallinity increased. At least 95% crystallinity with fewer impurities in HA coating was obtained after annealing temperature of 850°C. They further reported that at annealing temperature in range of 850-1000°C, HA phases got seriously decomposed resulting in about 20% impurities in HA coating. The level of crystallinity obtained after post coating heat treatment at 900°C for 2h in air in present study matches with the findings of Wang et al., (1995) in regard to post coating heat treatment at 850°C in vacuum.

Cannillo et al., (2008) investigated post coating properties of plasma sprayed HA-TiO₂ graded coating (100% TiO₂ at substrate coating interface to 100% HA at top most coating layer) at 650, 750 and 850°C with heating rate of 10°C/min and holding for 1h at maximum temperature in air. The specimens were cooled inside the kiln naturally in a similar way as performed in present investigation. The crystallinity of coating is reported to increase with increase in post coating heat treatment temperature up to 850°C, whereas CaO contents remained almost same as that for as-sprayed coating.

In present investigation, after post coating heat treatment at 900° for 2h in air, development of ultra-fine particles have been observed as shown in Fig. 7.25 to Fig. 7.36. The nano-scale HA crystallites were found to have a tendency to cover the surface of plasma sprayed HA and HA-10 wt% Al₂O₃ coatings after post coating treatment, however this affect was found to reduced with higher alumina content (20 and 30 wt%) of HA composite coatings. Lu et al., (2003B) investigated the properties of plasma sprayed HA coatings on pure titanium substrate via post coating heat treatment in air for 2h at 500, 600, 700 and 800°C and reported the formation of new ultra-fine particles with nano-scale size on surface of post coating heat treated specimens at heating temperature of 700 and 800°C and suggested that these nano-particles promotes bone bonding. Development of ultra-fine particles by post coating treatment of plasma spray coatings has also been reported by Lv et al., (2009). Further, Lu et al., (2008) suggested that nanocrystallized surface has excellent cell compatibility, which is expected to promote bone formation during implantation surgery.

Lu et al., (2008) performed post coating heat treatment on plasma sprayed HA coatings at 650°C for 0.5, 1 and 2h and multi-step post coating heat treatment at 650°C for 1h followed by 650°C for 1.5 h and 650°C for 2h (specimens were cooled to room temperature after each heating step). Development of nano-sized on plasma sprayed HA coatings after multi-step post coating heat treating at 650°C for 0.5-2h has been reported by them, moreover aggregation of nano-sized particles occurred on coating surface after multi-step post coating heat treatment.

The filling (healing) of cracks by nano-sized particulates can be seen in Fig. 7.30c, Fig. 7.35d and Fig. 7.36d. Similar type of nano-scale crystallites in vicinity of micro-cracks are identified by Yang and Lui, (2008) via hydrothermal treatment of plasma sprayed HA coatings at 125°C for 6h. Microstructural homogeneity of plasma sprayed HA coatings through self-healing effect due to grain growth of crystalline HA by post coating treatments has been reported. However, they observed that nano-scale HA crystallites diminished when hydrotherma treatment time was increased to 12h.

7.4 CONCLUSIONS

Post coating heat treatment was carried out on plasma sprayed HA and HA-Al₂O₃ composite coatings to enhance their crystallinity and to refine their grain size. The post coating heat treatment was carried out in air at temperatures of 500°C, 700°C and 900°C for 2h and

detailed results are presented in current Chapter of this study. The conclusions drawn from above results are presented hereunder:

1. Delamination of coating did not occur via post coating heat treatment, whereas some wide opened cracks could be observed on the surface of coating. The opening of cracks might be due to reduction in coating volume after recrystallization.
2. No substrate elements were seen along the crack length in EDAX analysis of coatings after post coating heat treatment, which suggest that cracks were only confined to coating. This suggests that recrystallization of coatings by post coating heat treatment can be done.
3. Increment in crystallinity of coatings by addition of secondary phase and by incorporation of bond coat was found to be comparatively lower order than that achieved by post coating heat treatment. The crystallinity of as-sprayed coatings were in range of 72.6% to 78.6% whereas, after post coating heat treatment at 900°C crystallinity of 98.2% was achieved for HA-30 wt% Al₂O₃ coating.
4. The coating crystallinity was found to increase with increase in temperature of post coating heat treatment with least crystallinity of 84.1% for pure HA coating heat treated at 500°C and highest of 98.2% for HA-30 wt% Al₂O₃ coating heat treated at 900°C for 2h.
5. Development of nano-scale, ultra-fine HA crystallites (100 nm or less) and their agglomerated (in some cases) of different shape and size were observed on coating surface after post coating heat treatment at 900°C for 2h in air. The nano-scale HA particles have excellent compatible with living cells which is expected to promote bone formation.
6. The self healing of cracks by nano-scale and ultra-fine particulates was noticed in some cases after post coating heat treatment at 900°C for 2h in air.

COMPREHENSIVE DISCUSSION

The important results of present investigation are discussed in this chapter. This chapter describes the current investigation giving comparative performance of plasma sprayed pure HA and HA-Al₂O₃ composite coatings on metallic substrates. The performance of coatings for wear resistance against 400 grit SiC abrasive and between similar coatings and their bond strength by changing the amount of reinforcement has been discussed. The effect of bond coat in reducing migration of substrate elements to coating and in increasing the tensile bond strength has been described. The corrosion and dissolution/precipitation behavior of coated and bare substrates in simulated body fluid has been elucidated. The effect of post coating heat treatment on recrystallization of amorphous phases has also been discussed in present chapter.

8.1 MECHANICAL CHARACTERIZATION

The hardness of coatings has been found to increase with increase in aluminum oxide content of HA-Al₂O₃ composite coating (0-30 wt%), moreover maximum value of the hardness is found near substrate-coating interface for all coatings. The hardness values with respect to distance from interface for coatings without and with bond coat are shown in Fig. 8.1 and Fig. 8.2 respectively. The increase in coating hardness by reinforcement of secondary phase to HA have been reported by Zheng et al., (2001), Hyuschenko et al., (2002), Chou and Chang, (2002A & 2002B), Evis and Doremus (2005 & 2007), Lee et al., (2004) Balamurugan et al., (2007A) and Choubey et al., (2004). The hardness of substrate near interface was slightly higher than actual hardness of substrate material. The slight increase in hardness of substrate may be attributed to striking of high velocity powder particles as suggested by Singh, (2003) and Sidhu et al., (2004 and 2005). The bond coat showed the highest hardness value. The higher hardness of

coating near substrate-coating interface may be attributed to higher cooling rate of molten, semi-molten or un-melted particles at substrate, as metallic substrate acts as heat sink for incoming particles. The higher hardness of coating near interface has been reported by Morks et al., (2007).

The wear resistance of coatings was evaluated against 400 grit SiC abrasive and similar coatings; the mechanism of wear in first case was found to be abrasive whereas in later case it was adhesive wear. However there is no reported study on wear behavior of coatings when both the articulating surfaces are similar coatings. The wear resistance of coatings with respect to number of cycles is shown in Fig. 8.3. The results showed that abrasive wear resistance of coatings increased with increase in reinforcement (Al_2O_3) of composite coatings; whereas adhesive wear resistance between similar coatings showed completely different trend, where adhesive wear resistance decreased with increase in alumina content of composite coatings. In first case increase in hardness and strengthening of HA matrix by alumina addition might be the cause of higher wear resistance of the coatings while in later case might be due to the fact that alumina acted as a weak interface and might got pulled out from HA matrix when it comes in contact with alumina particles present in HA matrix of counter surface leading to formation of crater. By subsequent relative motion of two coating surfaces, higher material removal from the site of crater formation might be cause of lower wear resistance for similar coatings.

The tensile bond strength of coatings were found to increase with increase in alumina content of composite coatings but bond coat showed more significant contribution in improving tensile bond strength of coatings. The tensile bond strength of coatings with and without incorporation of bond coat is shown in Fig. 8.4. The increase in bonding strength by alumina reinforcement might be due to high strength and toughness provided by alumina to HA- Al_2O_3 matrix. The increase in tensile bond strength by incorporation of Al_2O_3 -13 wt% TiO_2 bond coat may be attributed to partial compensation of the thermal expansion mismatch of substrate and coating or rougher surface provided by bond coat. The matching of thermal

expansion coefficient of top coat and substrate through bond coat lowers the cooling rate of incoming molten splats. Slight increase in cooling time of molten splats lead to formation of dense coating made up of pancake type splats and fine equiaxed grains as discussed in detail in Section 2.1.2.8 and Section 2.5.3 of Chapter 2 (Kurzweg et al., 1998B and Pawlowski, 1995). Bond coat might have provided rough surface and increase in bonding strength may be due to mechanical interlocking of bond coat and top coat particles (Chou and Chang, 2002A and 2002B).

8.2 STUDIES IN SIMULATED BODY FLUID

To compare the corrosion behavior of coated and bare specimens, linear, potentiodynamic and Tafel polarization tests were conducted in simulated body fluid to mimic harsh body environment. The results obtained from electrochemical tests are summarized in Table 8.1. The results obtained from linear polarization test show that all the coatings were more protective than respective substrates with highest corrosion protection shown by HA coating with i_{corr} values of $0.00542 \mu\text{A}/\text{cm}^2$ and $0.00534 \mu\text{A}/\text{cm}^2$ on AISI 316L SS and Ti respectively; whereas i_{corr} values for uncoated AISI 316L SS and Ti were $0.245 \mu\text{A}/\text{cm}^2$ and $0.083 \mu\text{A}/\text{cm}^2$ respectively. The results obtained from potentiodynamic and Tafel polarization tests are similar to that obtained from linear polarization experiments with highest protection shown by HA coatings and least by uncoated specimens, moreover titanium was more protective as compared to AISI 316L SS. Further, the results obtained from all three polarization experiments show nearly same i_{corr} values for each specific coating, which suggest that substrates did not effected the corrosion protection of coatings and coatings did not allowed the electrolyte (simulated body fluid) to reach metallic substrate.

The in-vitro examination of coated and bare substrates in simulated body fluid show that dissolution of undesirable amorphous phases started on the very first day of immersion and took place up to 5 days of immersion. The coatings as well as titanium substrate was found

to covered with apatite phase after immersion period of 10, 15 and 20 days. The dissolution and precipitation in simulated body fluid takes places simultaneously, which further depends on concentration of Ca^{2+} ions in simulated body fluid. The results of in-vitro studies in form of weight change and Ca^{2+} ion concentration are shown in Fig. 8.5 and Fig. 8.6 respectively. All the coatings gained weight after immersion in simulated body fluid for different periods of immersion except three cases, in which weight loss has been recorded. The loss of weight was observed for pure HA coating after immersion period of 5 days, for HA-10 wt% Al_2O_3 coating for immersion period of 10 days and HA-20 wt% Al_2O_3 coatings for immersion period of 20 days.

8.3 POST COATING HEAT TREATMENT

Crystallinity of all the coatings increased by post coating heat treatment, moreover the increase in crystallinity was found to be a function of post coating heat treatment temperature i.e. crystallinity of coatings increased with increase in post coating heat treatment temperature. The crystallinity (%) of as-sprayed and heat treated coatings with post coating heat treatment temperature is summarized in Table 8.2. Highest crystallinity of 98.2% was obtained for HA-30 wt% Al_2O_3 coatings without bond coat and HA-20 wt% Al_2O_3 with bond coat after post coating heat treatment at 900°C for 2h in air. Moreover all the coatings showed the presence of ultra-fine nano-sized crystallite on their surfaces after post coating heat treatment at 900°C for 2h in air. However, intensity of these ultra-fine nano-sized crystallite decreased in some cases with increase in alumina content of HA composite coatings. These nano-sized crystals were hydroxyapatite as confirmed from XRD and FTIR analysis. The higher affinity for bone in-growth and bone bonding of these ultra-fine nano-sized particulates is reported in existing literature (Zyman et al., 1993B and Lu et al., 2003A & 2003 B).

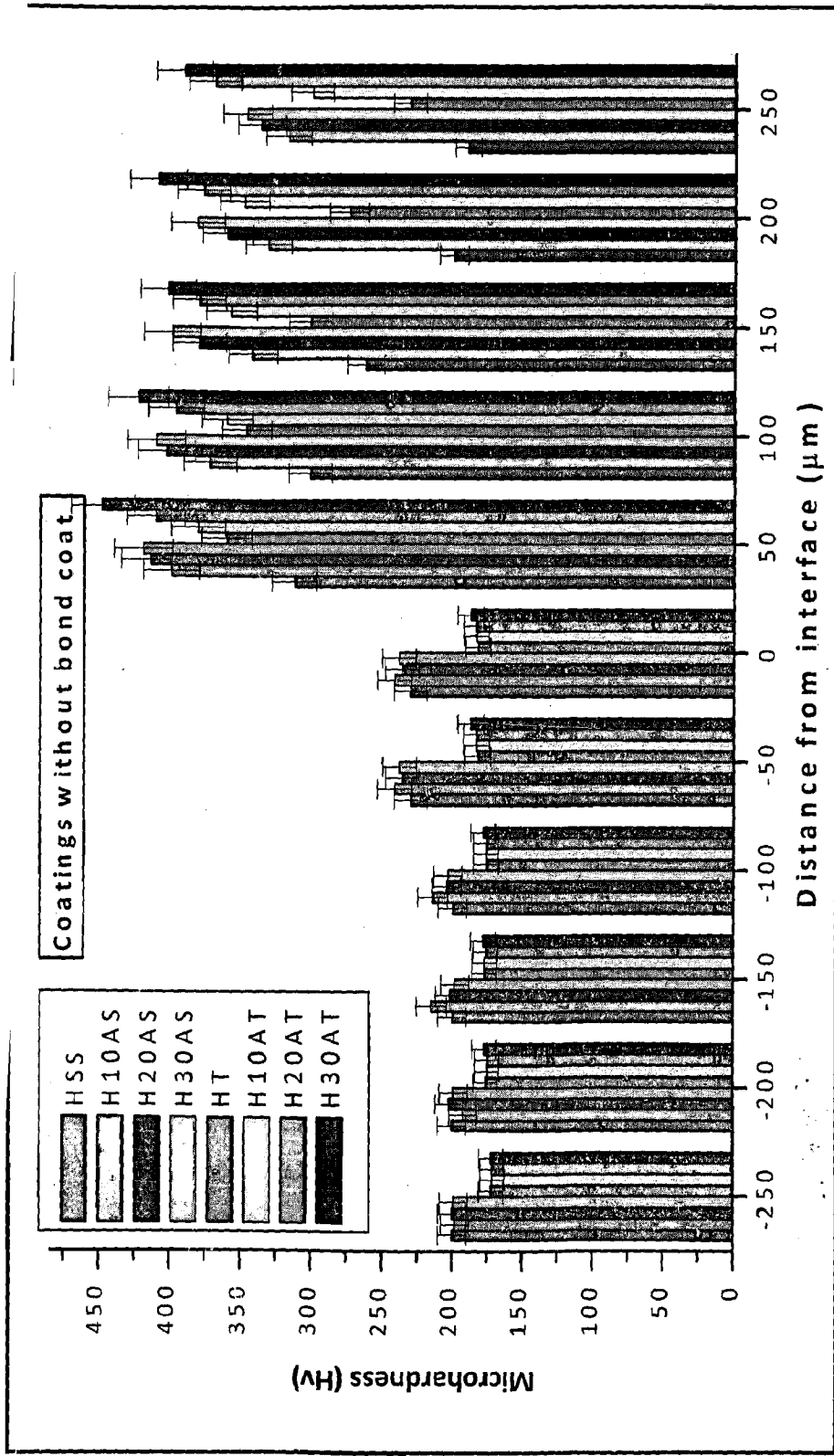


Fig. 8.1 Microhardness profile of different coatings on AISI 316 L stainless steel and titanium substrate without incorporation of bond coat: HSS: HA coated AISI 316L SS; H10AS: HA-10 wt% Al₂O₃ coated AISI 316L SS; H20AS: HA-20 wt% Al₂O₃ coated AISI 316L SS; H30AS: HA-30 wt% Al₂O₃ coated AISI 316L SS; HT: HA coated Ti; H10AT: HA-10 wt% Al₂O₃ coated Ti; H20AT: HA-20 wt% Al₂O₃ coated Ti; H30AT: HA-30 wt% Al₂O₃ coated Ti

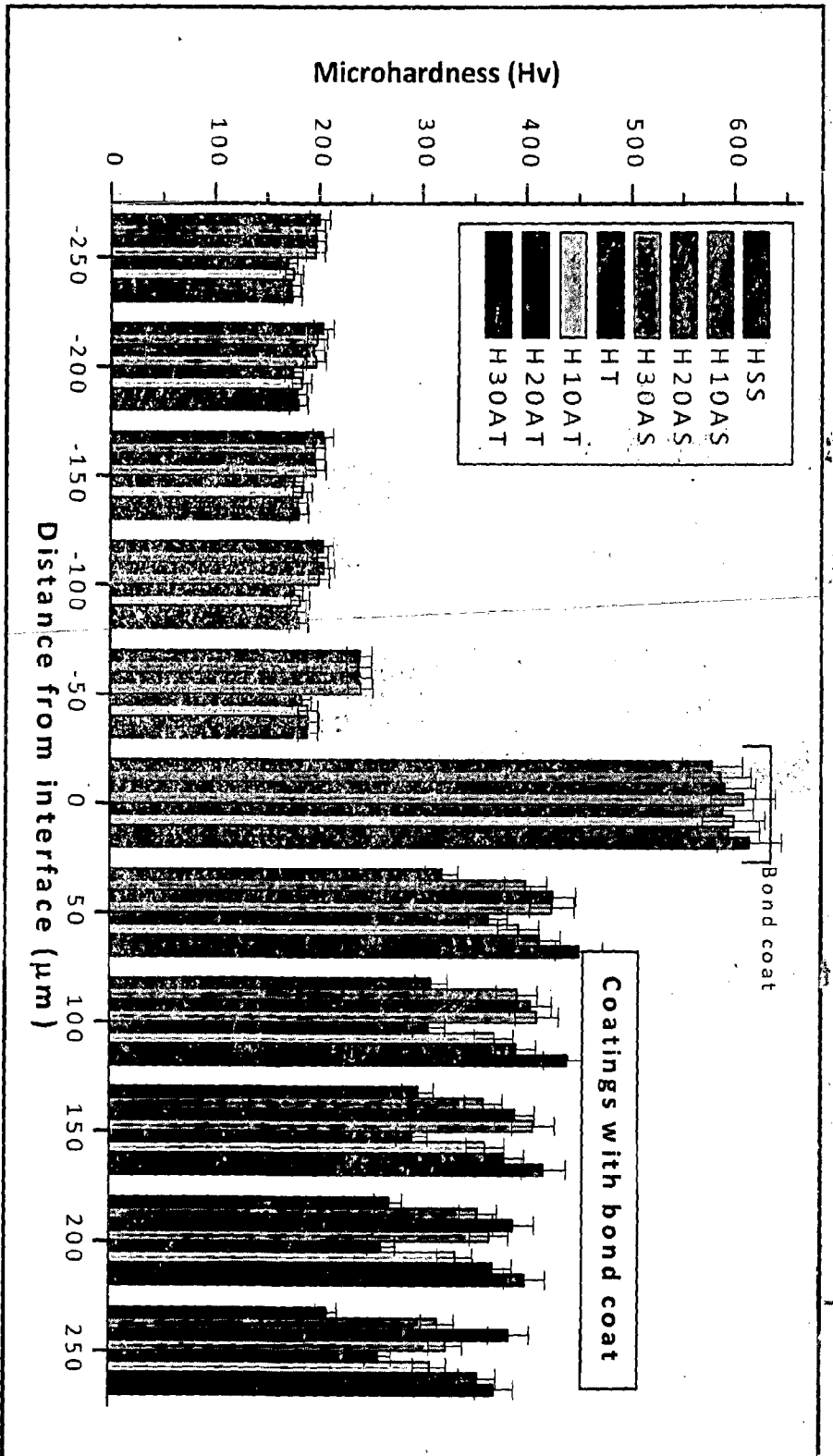


Fig. 8.2

Microhardness profile of different coatings on AISI 316 L stainless steel and titanium substrate with incorporation of bond coat: HSS: HA coated AISI 316L SS; H10AS: HA-10 wt% Al_2O_3 coated AISI 316L SS; H20AS: HA-20 wt% Al_2O_3 coated AISI 316L SS; H30AS: HA-30 wt% Al_2O_3 coated AISI 316L SS; HT: HA coated Ti; H10AT: HA-10 wt% Al_2O_3 coated Ti; H20AT: HA-20 wt% Al_2O_3 coated Ti; H30AT: HA-30 wt% Al_2O_3 coated Ti

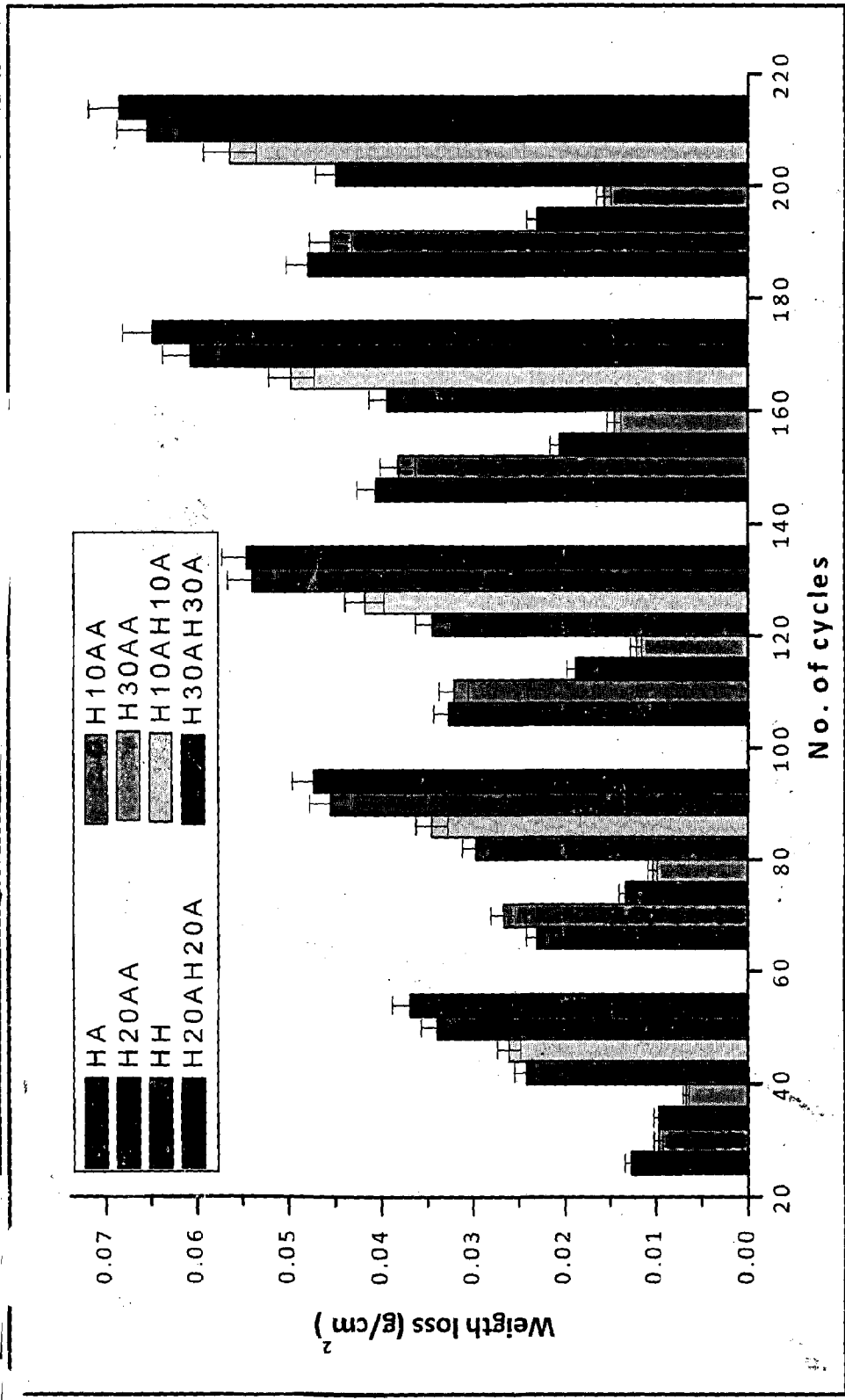


Fig. 8.3 Wear resistance of coatings: against 400 grit SiC abrasive: HA: HA coating; H10AA: HA-10 wt% Al₂O₃ coating; H20AA: HA-20 wt% Al₂O₃; H30AA: HA-30 wt% Al₂O₃; between similar coatings: HH: HA coating against HA coating; H10AH10A: HA-10 wt% Al₂O₃ against HA-10 wt% Al₂O₃; H20AH20A: HA-20 wt% Al₂O₃ against HA-20 wt% Al₂O₃; H30AH30A: HA-30 wt% Al₂O₃ against HA-30 wt% Al₂O₃

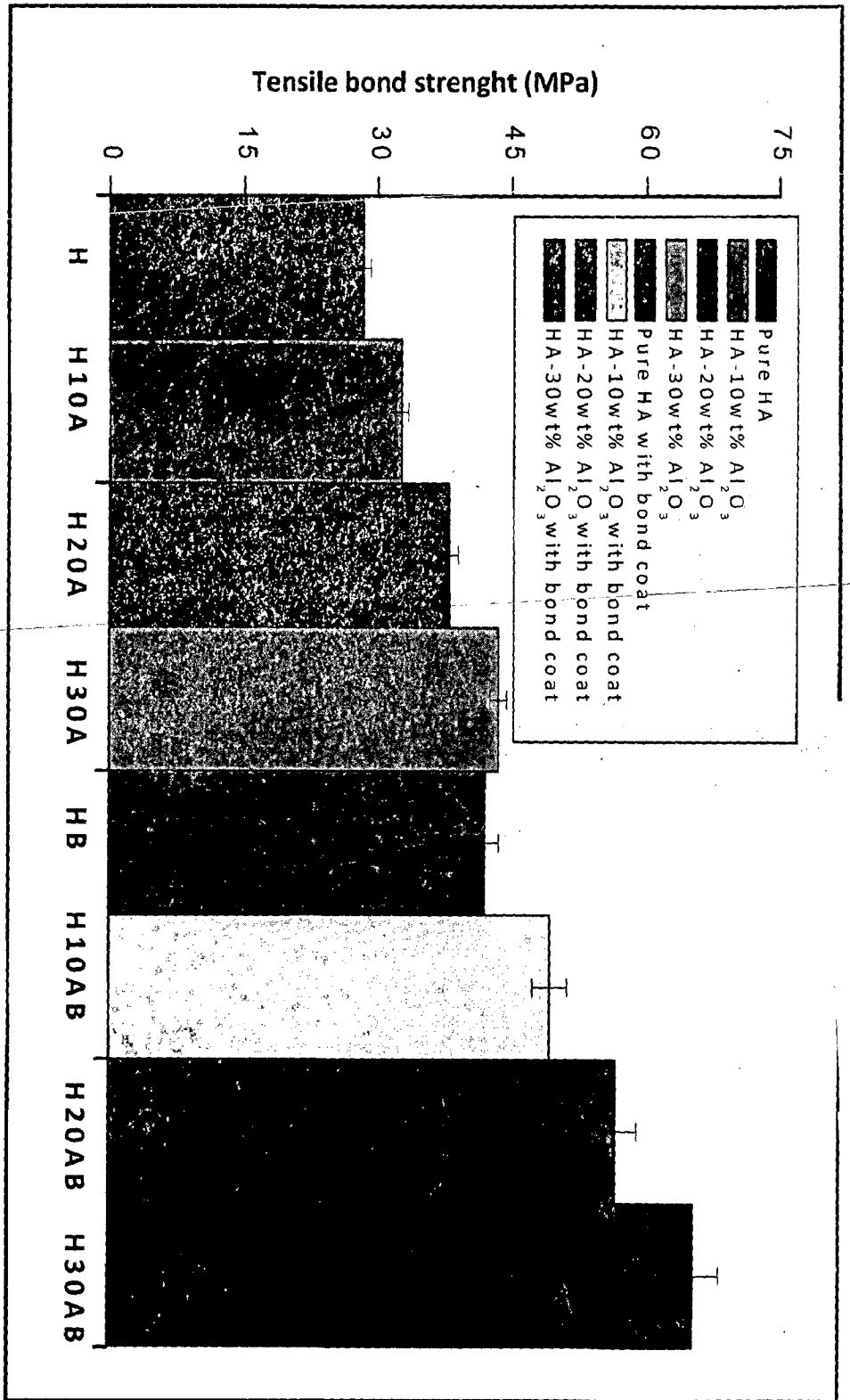


Fig. 8.4

Tensile bond strength of coatings

Table 8.1 Results of electrochemical tests in simulated body fluid of bare and coated specimens

Polarization test Substrate	Uncoated		Pure HA coating		HA-10 wt% Al ₂ O ₃ coating		HA-20 wt% Al ₂ O ₃ coating		HA-30 wt% Al ₂ O ₃ coating	
	<i>i</i> _{corr} (μA/cm ²)	R _p (kΩ-cm ²)	<i>i</i> _{corr} (μA/cm ²)	R _p (kΩ-cm ²)	<i>i</i> _{corr} (μA/cm ²)	R _p (kΩ-cm ²)	<i>i</i> _{corr} (μA/cm ²)	R _p (kΩ-cm ²)	<i>i</i> _{corr} (μA/cm ²)	R _p (kΩ-cm ²)
Linear polarization test										
AISI 316L SS	0.245	106	0.00542	4797	0.00735	3538	0.0234	1112	0.076	342
Titanium	0.083	314	0.00534	4864	0.00695	3740	0.00629	4129	0.0254	1024
Potentiodynamic polarization test										
AISI 316L SS	0.233	5.81	0.0085	249.55	0.0306	61.26	0.0285	80.16	0.0259	125.970
Titanium	0.0693	42.49	0.0091	228.34	0.0304	87.61	0.0373	43.93	0.0539	33.3
Tafel polarization test										
AISI 316L SS	0.264	84.37	0.0067	2805.2	0.0347	944.53	0.0309	588.36	0.0244	1252.9
Titanium	0.0724	117.6	0.0112	1925.3	0.0292	927.8	0.0313	580.4	0.0344	747.3

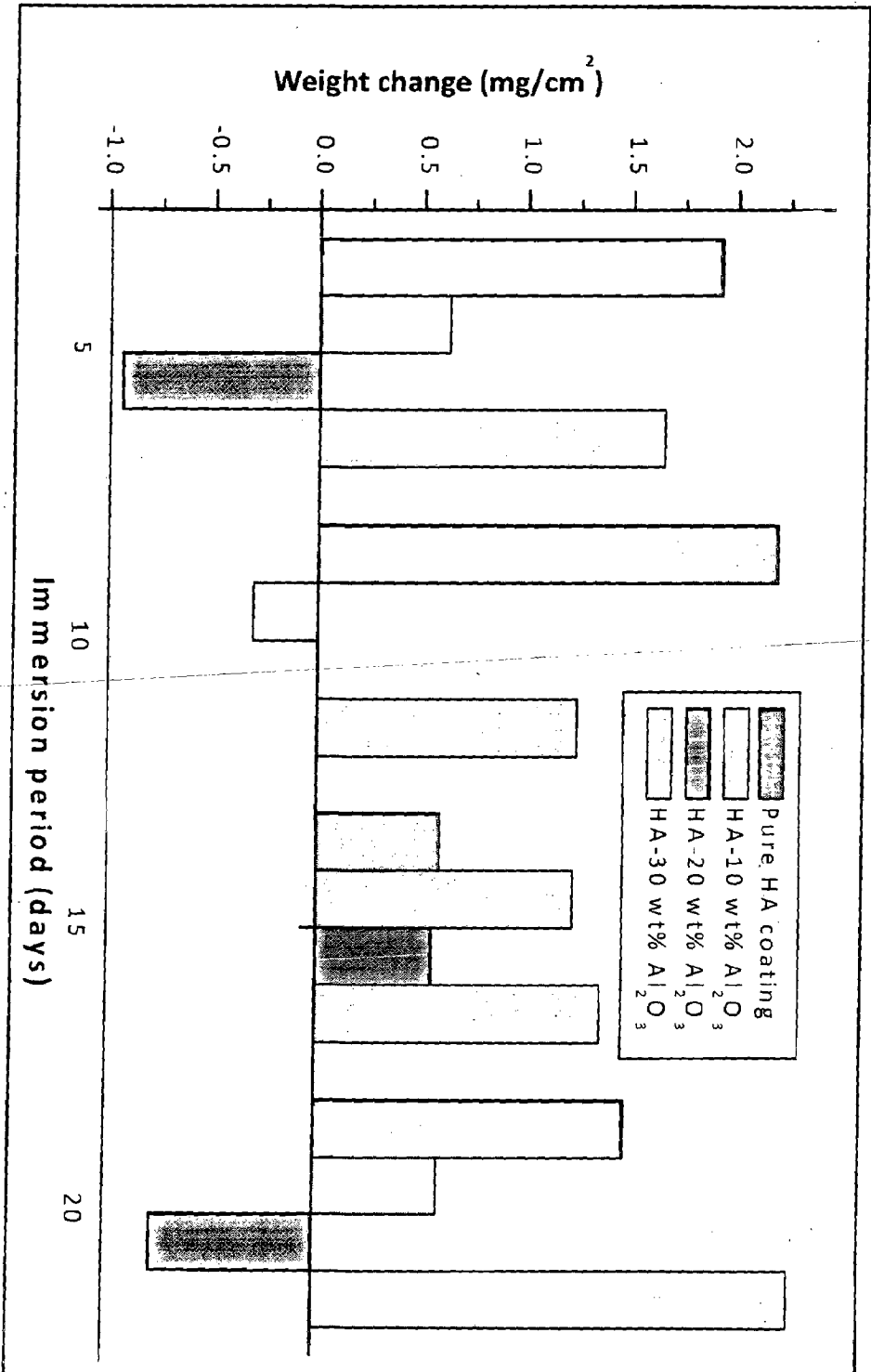


Fig. 8.5 In-vitro behavior of coatings in simulated body fluid

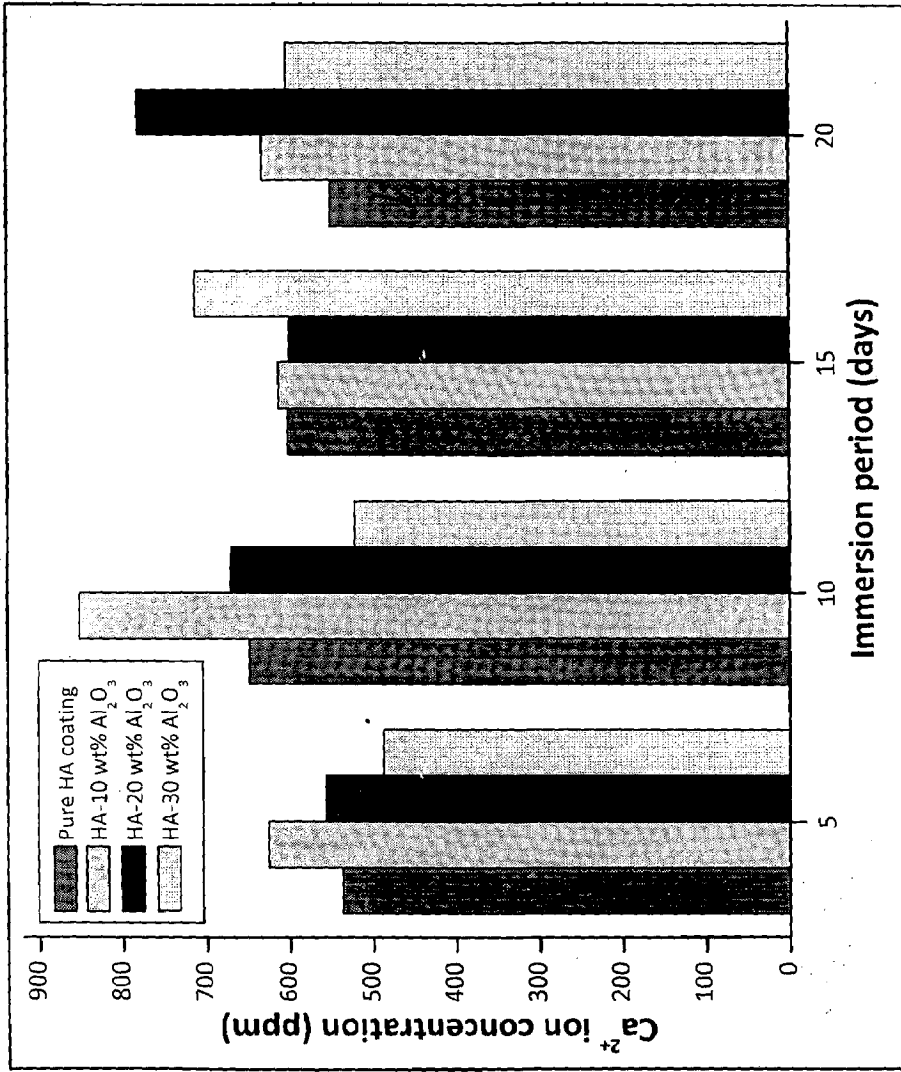


Fig. 8.6 Ca²⁺ ion concentration of simulated body fluid after immersion of coatings

Table 8.2 Crystallinity of as-sprayed and post coating heat treated specimens

Crystallinity (%)	AISI 316 L SS substrate			Titanium substrate				
	as-sprayed	Post coating heat treated in air for 2h			as-sprayed	Post coating heat treated in air for 2h		
		500°C	700°C	900°C		500°C	700°C	900°C
Pure HA Coatings	72.6	84.1	90.7	93.2	73.9	84.2	92.2	93.5
HA-10 wt% Al ₂ O ₃ coating	76.4	85.4	94.6	96.2	76.9	85.3	94.7	97
HA-30 wt% Al ₂ O ₃ coating	78	90.5	96.9	98	78.6	90.1	96.7	98.2
Pure HA Coatings with bond coat	74.2	85.4	92.6	95.1	74.2	84.1	93.1	94.3
HA-10 wt% Al ₂ O ₃ coating with bond coat	76.6	85.6	94.9	97.3	76.9	86.1	95.3	97.6
HA-20 wt% Al ₂ O ₃ coating with bond coat	77	86.5	95.7	97.9	77.1	87	95.9	98.2

CHAPTER 9

CONCLUSIONS

This chapter deals with the conclusions drawn from present investigation on coatings of HA, HA-10 wt% Al₂O₃, HA-20 wt% Al₂O₃ and HA-30 wt% Al₂O₃ with and without incorporation of bond coat of Al₂O₃-13 wt% TiO₂ deposited by shrouded plasma spray process on AISI 316L SS and commercially pure titanium. Various tests were conducted on coated specimens for evaluation of mechanical, electrochemical, dissolution/precipitation properties which include hardness, wear resistance, bond strength, corrosion studies in simulated body fluid (SBF) and in-vitro examination in SBF. The coated specimens were subjected to post coating heat treatment in air at 500°C, 700°C and 900°C for 2h. The significant conclusions drawn from results obtained for present investigation as summarized hereunder:

9.1 CHARACTERIZATION OF COATINGS

1. The surface morphology of coatings showed clear splat boundaries, un-melted powder particles and cores, micro-cracks and voids.
2. The cross-sectional morphology of coatings suggest that coatings were continuous, adherent to substrate as well as bond coat, have pores and micro-cracks, however typical crack network as characterized by plasma sprayed HA coatings is absent.
3. The porosity and surface roughness of coatings slightly increased with increase in alumina content of composite coating. Moreover, porosity measured on polished cross-sections was almost double than that measured on as-sprayed coating surfaces, which can be attributed to damage of surface caused during cutting, grinding and polishing for cross-section preparation.
4. Diffusion or migration of substrate elements to the coatings was found to substantially reduce by incorporation of bond coat layer between substrate and top coat.

5. The as-procured powder was 100% pure and crystalline, however plasma sprayed coatings contained a considerable amount of amorphous phases of calcium and phosphorous and CaO.
6. De-hydroxylation (removal of hydroxyl group) and carbonation (absorption of carbon dioxide) of hydroxyapatite took place during plasma spraying.
7. Water absorption capacity of feedstock increased with increase in alumina content in hydroxyapatite from 0 to 30 wt%.

9.2 MECHANICAL PROPERTIES OF COATINGS

8. Wear resistance of plasma sprayed coatings against abrasive (SiC) increased with increase in Al_2O_3 content of HA composite coating, whereas wear resistance between the similar coatings was found to decrease with increase in Al_2O_3 content of HA composite coating.
9. Coating fragments, surface ploughing and surface smoothing was observed in surface morphology of coatings obtained after abrasive wear, whereas plastic flow was recorded in surface morphology of coatings obtained after wear between the similar coatings.
10. Hardness of coatings as measured by nano-indentation was observed to increase with increase in Al_2O_3 content to HA with highest hardness near substrate coating interface. The hardness of bond coat was found to be higher than all the coatings.
11. The hardness of coatings as well as substrate was found to highest near substrate-coating interface for all substrate-coating combination.
12. The tensile bonding strength of coatings was found to increase with increase in alumina content of HA composite coating, whereas bond coat showed significant effect in increasing the tensile bonding strength of coatings.

9.3 CORROSION AND IN-VITRO STUDIES IN SIMULATED BODY FLUID

13. The results obtained from linear polarization resistance test showed that the corrosion current densities of all the coatings on AISI316L and titanium were much lower than that of respective substrate. The corrosion current density offered by all the coatings was found to be in range of $0.006 \mu\text{A}/\text{cm}^2$ to $0.053 \mu\text{A}/\text{cm}^2$. The corrosion resistance of coatings and substrate observed the following sequence:

I. AISI 316L substrate

Pure HA > HA-10 wt% Al_2O_3 > HA-20 wt% Al_2O_3 > HA-30 wt% Al_2O_3 > Substrate

II. Titanium substrate

Pure HA > HA-20 wt% Al_2O_3 > HA-10 wt% Al_2O_3 > HA-30 wt% Al_2O_3 > Substrate

14. The potentiodynamic polarization resistance test showed similar results as shown by linear polarization test in reference to corrosion current densities. The corrosion current densities of all the coatings on AISI316L and titanium were found to be much lower than that of respective substrate. The least corrosion current density for both substrates was offered by pure HA coating, moreover the maximum variation in current densities offered by composite coatings was around $45 \text{ nA}/\text{cm}^2$. The corrosion current density of coatings and substrate observed the following sequence:

III. AISI 316L substrate

Pure HA > HA-30 wt% Al_2O_3 > HA-20 wt% Al_2O_3 > HA-10 wt% Al_2O_3 > Substrate

IV. Titanium substrate

Pure HA > HA-10 wt% Al_2O_3 > HA-20 wt% Al_2O_3 > HA-30 wt% Al_2O_3 > Substrate

15. The results obtained from Tafel polarization test showed that the corrosion current densities of all the coatings on AISI316L and titanium were much lower than that of respective substrate. The least corrosion current density for both substrates was offered by pure HA coating, moreover the maximum variation in current densities offered by composite coatings was about $30 \text{ nA}/\text{cm}^2$. The corrosion resistance of coatings and substrate observed the following sequence:

v. AISI 316L substrate

Pure HA > HA-30 wt% Al₂O₃ > HA-20 wt% Al₂O₃ > HA-10 wt% Al₂O₃ > Substrate

vi. Titanium substrate

Pure HA > HA-10 wt% Al₂O₃ > HA-20 wt% Al₂O₃ > HA-30 wt% Al₂O₃ > Substrate

16. The precipitation/dissolution behavior (weight gain/loss) of coatings after immersion in SBF for 5, 10, 15 and 20 days at controlled temperature of 37±1°C is summarized as under:

vii. Pure HA coatings

10 days > 5 days > 20 days > 15 days: weight was gained by coatings for all period of immersion

viii. HA-10 wt% Al₂O₃ coatings

15 days > 5 days > 20 days > 10 days: weight was lost by coating after immersion period of 10 days and gained by coatings for all other periods of immersion

ix. HA-20 wt% Al₂O₃ coatings

15 days > 10 days (no wt. change) > 20 days > 5 days: weight was lost by coating after immersion period of 5 and 20 days and gained after immersion period of 15 days

x. HA-30 wt% Al₂O₃ coatings

20 days > 5 days > 15 days > 10 days: weight was gained by coatings for all period of immersion

17. The concentration of Ca²⁺ ion concentration in SBF (decrease/increase) after immersion period of 5, 10, 15 and 20 days at controlled temperature of 37±1°C is summarized as under:

xi. Pure HA coatings

5 days < 20 days < 15 days < 10 days: Ca²⁺ ion concentration decreased for all immersion periods as compared to Ca²⁺ ion concentration in starting SBF

xii. HA-10 wt% Al₂O₃ coatings

15 days < 20 days < 5 days < 10 days: Ca^{2+} ion concentration increased for immersion period of 10 days and decreased for immersion period of 5, 15 and 20 days as compared to Ca^{2+} ion concentration in starting SBF

XIII. HA-20 wt% Al_2O_3 coatings

15 days < 10 days < 5 days < 20 days: Ca^{2+} ion concentration decreased for immersion period of 15 days and increased for immersion period of 5, 10 and 20 days as compared to Ca^{2+} ion concentration in starting SBF

XIV. HA-30 wt% Al_2O_3 coatings

5 days < 10 days < 20 days < 20 days: Ca^{2+} ion concentration increased for immersion period of 15 days and decreased for immersion period of 5, 10 and 20 days as compared to Ca^{2+} ion concentration in starting SBF

18. All the amorphous phases get dissolved in SBF within first day of immersion, whereas precipitation/dissolution was observed on coating after immersion period of 5 days. the precipitation of new tiny particles on coatings as well as substrate was observed after immersion period of 10, 15 and 20 days in SBF.

19. Absence of peaks corresponding to amorphous phases in XRD plots suggests dissolution of amorphous phases and increase in intensity of hydroxyl, phosphate and carbonate group in FTIR suggests precipitation of apatite.

9.4 RECRYSTALLIZATION AND GRAIN REFINEMENT OF COATINGS

20. Delamination of coating did not occur via post coating heat treatment, whereas some wide opened cracks could be observed on the surface of coating.

21. No substrate elements were seen along the crack length in EDAX analysis of coatings after post coating heat treatment, which suggest that cracks were only confined to coating.

22. Increment in crystallinity of coatings by addition of secondary phase and by incorporation of bond coat was found to be comparatively lower order than that achieved by post coating heat treatment.
23. The coating crystallinity was found to increase with increase in temperature of post coating heat treatment.
24. Development of nano-scale, ultra-fine HA crystallites and their agglomerated (in some cases) of different shape and size were observed on coating surface after post coating heat treatment at 900°C for 2h in air.
25. The self healing of cracks by nano-scale and ultra-fine particulates was noticed in some cases after post coating heat treatment at 900°C for 2h in air.

SCOPE FOR FUTURE WORK

In light of results obtained from present investigation, some suggestions for further studies on bioceramic coatings are affirmed below:

1. Effect on mechanical and electrochemical properties may be compared by adding different reinforcements to hydroxyapatite coatings. Effect of different thermal spray processes on the properties of hydroxyapatite coatings may be compared.
2. Studies may be performed to evaluate wear and corrosion behavior of coatings in physiological environment simultaneously. As wear and corrosion coexist in body environment.
3. Hot stage microscopy and XRD analysis may be utilized during post coating heat treatment to evaluate the exact temperature and holding time for recrystallization of phases and grain refinement in plasma sprayed hydroxyapatite composite coatings.
4. Different post coating treatment to recrystallize the amorphous phases present in plasma sprayed hydroxyapatite coatings may be studied and compared. Mechanical and electrochemical properties of coatings after post coating heat treatment may be studied.

REFERENCES

1. **Albayrak, O., El-Atwani, O. and Altintas, S., (2008), "Hydroxyapatite Coating on Titanium Substrate by Electrophoretic Deposition Method: Effects of Titanium Dioxide Inner Layer on Adhesion Strength and Hydroxyapatite Decomposition", Surf. Coat. Technol., Vol. 202, pp. 2482-2487.**
2. **Aoki, H., (1991), "Science and Medical Application of Hydroxyapatite", Japanese Association of Apatite Science, pp. 179-192, Tokyo, Japan.**
3. **Balamurugan, A., Balossier, G., Kannan, S. and Rajeswari, S., (2006), "Elaboration of Sol-gel Derived Apatite Film on Surgical Grade Stainless Steel for Biomedical Applications, Mater. Lett., Vol. 60, pp. 2288-2293.**
4. **Balamurugan, A., Balossier, G., Kannan, S., Michel, J. and Rajeswari, S., (2007B), "In Vitro Biological, Chemical and Electrochemical Evaluation of Titania Reinforced Hydroxyapatite Sol-gel Coatings on Surgical Grade 316L SS", Mater. Sci. Eng., Vol. C27, pp. 162-171.**
5. **Balamurugan, A., Balossier, G., Kannan, S., Michel, J., Faure, J. and Rajeswari, S., (2007A), "Electrochemical and Structural Characterization of Zirconia Reinforced Hydroxyapatite Bioceramic Sol-gel Coatings on Surgical Grade 316L SS for Biomedical Applications", Ceram. Int., Vol. 33, pp. 605-614.**
6. **Balamurugan, A., Balossier, G., Kannan, S., Michel, J., Rebelo, A.H.S. and Ferreira, J.M.F., (2007), "Development and In Vitro Characterization of Sol-Gel Derived CaO-P₂O₅-SiO₂-ZnO Bioglass", Acta Biomater., Vol. 3, pp. 255-262.**
7. **Balani, K., Anderson, R., Laha, T., Andara, M., Tercero, J., Crumpler, E. and Agarwal, A., (2007B), "Plasma-sprayed Carbon Nanotube Reinforced Hydroxyapatite Coatings and their Interaction with Human Osteoblasts In Vitro", Biomaterials, Vol. 28, pp. 618-624.**
8. **Balani, K., Chen, Y., Harimkar, S. P., Dahotre, N. B. and Agarwal A., (2007A), "Tribological Behavior of Plasma-sprayed Carbon Nanotube-reinforced Hydroxyapatite Coating in Physiological Solution", Acta Biomater., Vol. 3, pp. 944-951.**
9. **Bauer, T. W., Stulber, B. N., Ming, J. and Geesink, R. G. T., (1993), "Uncemented Acetabular Composites: Histologic Analysis of Retrieved Hydroxyapatite-coated and Porous Implants", J. Arthroplasty, Vol. 8, pp. 167-177.**
10. **Bearinger, J. P., Castner, D. G., Golledge, S. L., Rezania, A., Hubchak, S., and Healy, K. E., (1997), "P (AAm-co-EG) Interpenetrating Polymer Networks Grafted to Oxide Surfaces:**

Surface Characterization, Protein Adsorption, and Cell Detachment Studies"; *Langmuir*, Vol. 13, pp. 5175-5183.

11. **Beherei, H.H., El-Bassyouni, G.T., Mohamed, K.R., (2008), "Modulation, Characterization and Bioactivity of New Biocomposites Based on Apatite", *Ceram. Inter.*, Vol. 34, pp. 2091-2097.**
12. **Bell, B. F. Jr., (2004), "Functionally Graded, Multilayered Diamond Like Carbon-Hydroxyapatite Nanocomposite Coatings for Orthopedic Implants", M.Sc. Thesis, School of Materials Science and Engineering, Georgia Institute of Technology, Georgia, USA.**
13. **Bhushan, B. and Gupta, B. K., (1991), "Handbook of Tribology: Material Coatings and Surface Treatments", McGraw Hill, New York, USA.**
14. **Birtwistle, S. J., Wilson, K. and Porter, M. L., (1996), "Long-term Survival Analysis of Total Hip Replacement", *Annals of the Royal College of Surgeons of England*, Vol. 78, pp. 180-183.**
15. **Black, J., (1999), "Biological Performance of Materials: Fundamentals of Biocompatibility", Marcel Dekker Inc., Basel, Switzerland.**
16. **Blunn, G. W., Walker, P. S., Joshi, A. and Hardinge, K., (1991), "The Dominance of Cyclic Sliding in Producing Wear in Total Knee Replacements, *Clin. Orthop*, Vol. 273, pp. 253-260.**
17. **Bohner, M. and Lemaître, J., (2009), "Can Bioactivity be Tested In Vitro with SBF Solution?", *Biomaterials*, Vol. 30, pp. 2175-2179.**
18. **Bolelli, G., Cannillo, V., Gadow, R., Killinger, A., Lusvardi, L. and Rauch, J., (2009), "Microstructural and In Vitro Characterization of High-Velocity Suspension Flame Sprayed (HVSFS) Bioactive Glass Coatings", *J. Eur. Ceram. Soc.*, Vol. 29, pp. 2249-2257.**
19. **Bolelli, G., Cannillo, V., Lusvardi, L. and Manfredine, T., (2006), "Wear Behavior of Thermally Sprayed Ceramic Oxide Coatings", *Wear*, Vol. 261, pp. 1298-1315.**
20. **Bonfield, W., (1987), "New Trends in Implant Materials", In *Biomaterials in Clinical Applications*, Proc. of 6th European Conference on Biomaterials, Eds. Pizzoferrato, A., Elsevier Science Publishers, pp. 13-21.**
21. **Boskey, A. L. and Posner, A. S., (1973), "Conversion of Amorphous Calcium Phosphate to Microcrystalline Hydroxyapatite. A pH Dependent, Solution Mediated, Solid-Solid Conversion", *J. Phys. Chem.*, Vol. 77, pp. 2313-2317.**

22. **Boyer, P., Hutten, D., Loriaut, P., Lestrat, V., Jeanrot, C. and Massin, P., (2010), "Is Alumina-on-Alumina Ceramic Bearings Total Hip Replacement the Right Choice in Patients Younger Than 50 Years of Age? A 7 to 15 Year Follow-up Study", Orthop. Traumatol.: Surg. Res., Vol. 96, pp. 616-622.**
23. **Brossa, F., (1994), "Post-deposition Treatment Effects on Hydroxyapatite Vacuum Plasma Spray Coatings", J. Mater. Sci.- Mater. Med., Vol. 5, pp. 855-857.**
24. **Browne, M and Gregson, P. J., (1995), "Metal Ion Release from Wear Particles Produced by Ti-6Al-4V and Co-Cr alloy Surfaces Articulating Against Bone", Mater. Lett., Vol. 24, pp. 1-6.**
25. **Buma, P., Van Loon, P. J. M., Versleyen, H., Weinams, H., Slooff, T. J. J. H., de Groot, K. and Huiskes, R., (1997), "Histological and Biomechanical Analysis of Bone and Interface Reactions Around Hydroxyapatite-coated Intramedullary Implants of Different Stiffness: A pilot Study on the Goat", Biomaterials, Vol. 18, pp. 1251-1260.**
26. **Bunshah, R. F., (2001), "Thermal Spraying and Detonation Gun Processes", Ch. 12 In Handbook of Hard Coatings, Deposition Technologies, Properties and Applications, William Andrew Publishing, LLC, New York, USA.**
27. **Cannillo, V., Lusvarghi, L. and Sola, A., (2008), "Production and Characterization of Plasma-sprayed TiO₂-Hydroxyapatite Functionally Graded Coatings", J. Euro. Ceram. Soc., Vol. 28, pp. 2161-2169.**
28. **Cannillo, V., Lusvarghi, L., Sola, A. and Barletta, M., (2009), "Post-Deposition Laser Treatment of Plasma Sprayed Titania-Hydroxyapatite Functionally Graded Coatings", J. Eur. Ceram. Soc., Vol. 29, pp. 3147-3158.**
29. **Carlsson, L. V., MacDonald, W., Jacobsson, C. M. and Albrektsson, T., (2004), "Osseointegration Principles in Orthopedics: Basic Research and Clinical Applications", In Biomaterials in Orthopedics, Eds. Yaszemski, M. J., Trantolo, D. J., Lewandrowski, K., Hasirci, V., Altobelli, D. E. and Wise D. L., Marcel Dekker, New York, pp. 223-239.**
30. **Çelik, E., Avci, E. and Yilmaz, F., (1997), "Evaluation of Interface Reactions in Thermal Barrier Ceramic Coatings", Surf. Coat. Technol., Vol. 97. pp. 361-365.**
31. **Champion, E., Gautier, S. and Bernache-Assollant, D., (1996), "Characterization of Hot Pressed Al₂O₃-Platelet Reinforced Hydroxyapatite Composites", J. Mater. Sci. Mater. Med., Vol. 7, pp. 125-130.**
32. **Chander, S. and Fuerstenau, D. W., (1979), "Interfacial Properties and Equilibria in Apatite-Aqueous Solution System", J. Colloid Interface Sci., Vol. 70, (3), pp. 506-516.**

33. **Cheang, P., Khor, K. A., Teoh, L. L. and Tam, S. C., (1996), "Pulsed Laser Treatment of Plasma Sprayed HA Coatings", *Biomaterials*, Vol. 17, pp. 1901-1904.**
34. **Chen, C. C., Huang, T. H., Kao, C. T. and Ding, S. J., (2004), "Electrochemical Study of the In Vitro Degradation of Plasma-Sprayed Hydroxyapatite/Bioactive Glass Composite Coatings after Heat Treatment", *Electrochim. Acta*, Vol. 50, pp. 1023-1029.**
35. **Chen, J., Cao, Y., Feng, J. and Zhang, X., (1993), "Crystallization of Amorphous Phase in HA Coating During Heat Treatment, Proc. of 1st Far Eastern Symposium on Biomedical Materials, Beijing, PRC, pp. 17.**
36. **Chen, J., Tong, W., Cao, Y., Feng, J. and Zhang, X., (1997), "Effect of Atmosphere on Phase Transformation in Plasma-Sprayed Hydroxyapatite Coatings During Heat Treatment", *J. Biomed. Mater. Res.*, Vol. 34, pp. 15-20.**
37. **Chen, Y., Zhang, T. H., Gan, C. H. and Yu, G., (2007), "Wear Studies of Hydroxyapatite Composite Coating Reinforced by Carbon Nanotubes", *Carbon*, Vol. 45, pp. 998-1004.**
38. **Chen, Y., Zheng, X., Xie, Y., Ji, H., Ding, C., Li, H. and Dai, K., (2010), "Silver Release from Silver-containing Hydroxyapatite Coatings", *Surf. Coat. Technol.*, Vol. 205, pp. 192-1896.**
39. **Chou, B-Y. and Chang, E., (2001), "Interface Investigation of Plasma-sprayed Hydroxyapatite Coating on Titanium Alloy with ZrO₂ Intermediate Layer as Bond Coat", *Scr. Mater.*, Vol. 45, pp. 487-493.**
40. **Chou, B-Y. and Chang, E., (2002A), "Plasma-sprayed Hydroxyapatite Coating on Titanium Alloy with ZrO₂ Second Phase and ZrO₂ Intermediate Layer", *Surf. Coat. Technol.*, Vol. 153 (1), pp. 84-92.**
41. **Chou, B-Y. and Chang, E., (2002B), "Plasma-Sprayed Zirconia Bond Coat as an Intermediate Layer for Hydroxyapatite Coating on Titanium Alloy Substrate", *J Mater. Sci. Mater. Med.*, Vol. 13, pp. 589-595.**
42. **Choubey, A., Balasubramaniam, R. and Basu, B., (2004), "Effect of Replacement of V by Nb and Fe on the Electrochemical and Corrosion Behavior of Ti-6Al-4V in Simulated Physiological Environment", *J. Alloys Compd.*, Vol. 381, pp. 288-294.**
43. **Chow, L. C., (1991), "Development of Self-setting Calcium Phosphate Cements", *J. Ceram. Soc. Jpn. (Int. Ed.)*, Vol. 99, pp. 927-935**
44. **Chow, L. C., (2000), "Calcium Phosphate Cements: Chemistry, Properties and Applications", In *Proc. Materials Research Society*, Vol. 599. pp. 27-37.**

45. **Cleries, L., Martinez, E. and Fernandez, Pradas, J. M., (2000), "Mechanical Properties of Calcium Phosphate Coatings Deposited by Laser Ablation", *Biomaterials*, Vol. 21, pp. 967-971.**
46. **Coathup, M. J., Blackburn, J., Goodship, A. E., Cunningham, J. L., Smith, T. and Blunn, G. W., (2005), "Role of Hydroxyapatite Coatings in Resisting Wear Particle Migration and Osteolysis around Acetabular Components", *Biomaterials*, Vol. 26, pp. 4161-4169.**
47. **Collier, J. P., Mayor, M. B., McNamara, J. L., Suprenant, V. A. and Jensen, R. E., (1991), "Analysis of Failure of 122 Polyethylene Inserts from Uncemented Tibial Knee Components", *Clin. Orthop.*, Vol. 273, pp. 232-242.**
48. **Collier, J. P., Suprenant, V. A., Mayor, M. B., Wrona, M., Jensen, R. E. and Suprenant, H. P., (1993), "Loss of Hydroxyapatite Coating on Retrieved Total Hip Components", *J. Arthroplasty*, Vol. 8, pp. 389-392.**
49. **Cooley, D. R., Van Dellen, A. F., Burgess, J. O. and Windeler, S., (1992), "The Advantages of Coated Titanium Implants Prepared by Radiofrequency Sputtering from Hydroxyapatite", *Prosthetic Dent.*, Vol. 67, pp. 93-100.**
50. **Cordingley, R., Kohan, L., Ben-Nissan, B and Pezzotti, G., (2003), "Alumina as an Orthopedic Biomaterial – Characteristics, Properties, Performance and Applications", *J. Aust. Ceram. Soc.*, Vol. 39 (1), pp. 20-28.**
51. **Currey, J., Unsworth, A. and Hall, D. A., (1981), "Properties of Bone, Cartilage and Synovial Fluid", In *An Introduction to the Bio-mechanics of Joints and Joint Replacement*, Eds. Dowson, D. and Wright, V., Mechanical Engineering Publications Ltd., pp. 103-119.**
52. **D'Antonio, J.A., Capello, W.N., Bierbaum, B., Manley, M. and Naughton, M., (2006), "Ceramic-on-Ceramic Bearings for Total Hip Arthroplasty: 5-9 Year Follow-Up", *Sem. Arthroplasty*, Vol. 17, pp. 146-152.**
53. **De Groot, K., (1984), "Calcium Phosphate Ceramics: Their Current Status", In *Contemporary Biomaterials-Material and Host Response, Clinical Applications, New Technology and Legal Aspects*, Eds., Boretos, J. W. and Eden, M., Noyes Publications, New Jersey, pp. 477-492.**
54. **De With, G. and Corbijn, A. J., (1989), "Metal Fiber Reinforced Hydroxyapatite Ceramics", *J. Mater. Sci.*, Vol. 24, pp. 3411-3415**

55. **Deram, V., Minichiello, R., Vannier, R-N., Le Maguer, A., Pawlowski, L. and Murano, D.,** (2003), "Microstructural Characterization of Plasma Sprayed Hydroxyapatite Coatings", *Surf. Coat. Technol.*, Vol. 166, pp. 153-159.
56. **Dey, A., Mokhopadhyay, A.K., Gangatharan, S., Sinha, M.K., Badu, D.,** (2009A), "Characterization of Microplasma Sprayed Hydroxyapatite Coating", *J. Therm. Spray Technol.*, Vol. 18 (4), pp 578-592.
57. **Dey, A., Mokhopadhyay, A.K., Gangatharan, S., Sinha, M.K., Badu, D.,** (2009 B), "Development of Hydroxyapatite Coating by Microplasma Spraying", *Mater. Manuf. Processes*, Vol. 24, pp. 1321-1330.
58. **Ding, S.J., Ju, C.P. and Lin, J.H.C.,** (2000), "Morphology and Immersion Behavior of Plasma-sprayed Hydroxyapatite/Bioactive Glass Coatings", *J. Mater. Sci. Mater. Med.*, Vol. 11, pp. 183-190.
59. **Ding, S-J., Huang, T-H. and Kao, C-T.,** (2003), "Immersion Behavior of Plasma-Sprayed Modified Hydroxyapatite Coatings After Heat Treatment", *Surf. Coat. Technol.*, Vol. 165, pp. 248-257.
60. **DiPalam, J.A.,** (2004), "Current Treatment Options for Chronic Constipation" *Reviews in Gastroenterological Disorders*, Vol. 4, pp. S34-S42.
61. **Dong, Z. L., Khor, K. A., Quek, C. H., White, T. J. and Cheang, P.,**(2003), "TEM and STEM analysis on Heat- Treated and In Vitro Plasma-Sprayed Hydroxyapatite/Ti-6Al-4V Composite Coatings", *Biomaterials*, Vol. 24, pp. 97-105.
62. **Ducheyne, P. and Qiu, Q.,** (1999), "Bioactive Ceramics: The Effect of Surface Reactivity on Bone Formation and Bone Cell Function", *Biomaterials*, Vol. 20, pp. 2287-2303.
63. **Ducheyne, P.,** (1987), "Bioceramics: Materials Characteristic Versus In Vivo Behavior", *J. Biomed. Mater. Res.*, Vol. 21, pp. 219-236.
64. **Ducheyne, P., Beight, J., Cuckler, B., Evans, B. and Radin, S.,** (1990), "Effect of Calcium Phosphate Coating Characteristics on Early Post-operative Bone Tissue Ingrowth", *Biomaterials*, Vol. 11, pp. 531-540.
65. **Dyshlovenko, S., Pateyron, B., Pawlowski, L. and Murano, D.,** (2004), "Numerical Simulation of Hydroxyapatite Powder Behavior in Plasma Jet", *Surf. Coat. Technol.*, Vol. 179, pp. 110-117.
66. **Eduardo, G-C., Eduardo, G-R., Antonio, M-M. and Eduardo, M.,** (2008), "Alumina-on-Alumina in THA: A Multicenter Prospective Study", *Clin. Orthop. Relat. Res.*, Vol. 466, pp. 309-316.

67. **Emery, D.F.G., Clarke, H.J. and Grover, M. L., (1997), "Stanmore Total Hip Replacement in Younger Patients - Review of a Group of Patients Under 50 Years of Age at Operation", J. Bone Joint Surg. (Br), Vol. 79B, pp. 240-246.**
68. **Engh, G. A., Dwyer, K. A. and Hanes, C. K., (1992), "Polyethylene Wear of Metal Backed Tibial Components in Total and Unicompartmental Knee Prostheses", J. Bone Joint Surg. (Br), Vol. 74(1), pp. 9-17.**
69. **Escobedo, J.C., Ortiz, J. C., Almanza, J. M. and Cortés, D. A., (2006), "Hydroxyapatite Coating on a Cobalt Base Alloy by Investment Casting", Scr. Mater., Vol. 54, pp. 1611-1615.**
70. **Etok, S.E. and Rogers, K.D., (2005), "Dissolution Behavior of Plasma Sprayed Apatite Coatings", J. Mater. Sci., Vol. 40, pp. 5627-5633.**
71. **Evis, Z. and Doremus, R. H., (2005), "Coatings of Hydroxyapatite – Nanosize Alpha Alumina Composite on Ti-6Al-4V", Mater. Lett., Vol. 59 (29-30); pp. 3824-3827.**
72. **Evis, Z. and Doremus, R. H., (2007), "Hot Pressed Hydroxylapatite/Monoclinic Zirconia Composites with Improved Mechanical Properties", J. Mater. Sci. Vol. 42. pp. 2426-2431.**
73. **Fang, Y., Agrawal, D. K. and Roy, D. M., (1994), "Thermal Stability of Hydroxyapatite", In Hydroxyapatite and Related Material, Eds. Brown, P. W. and Constantz, B., CRC Press, London.**
74. **Fantassi, S., Vardelle, M., Fauchais, P. and Moreau, C, (1992), "Investigation of the Splat Formation versus Different Particulate Temperature and Velocities Prior to Impact", In Proc. Thermal Spray: International Advances in Coatings Technology, Eds., Berndt. C. C., 13th International Thermal Spray, Orlando, Florida, 28th May – 5th June.**
75. **Fathi, M.H., Salehi, M., Saatchi, A., Mortazavi, V. and Moosavi, S.B., (2003), "In Vitro Behavior of Bioceramic, Metallic and Bioceramic-metallic Coated Stainless Steel Dental Implant", Dent. Mater., Vol. 19, pp. 188-198.**
76. **Fauchais, P., (2004), "Understanding Plasma Spraying", J. Phys. D: Appl. Phys., Vol. 37, pp. R86-R108**
77. **Fazan, F. and Marguis, P. M., (2000), "Dissolution Behavior of Plasma-sprayed Hydroxyapatite Coatings", J. Mater. Sci. Mater. Med., Vol. 11, pp. 787-792.**
78. **Fernández, J., Gaona, M. and Guilemany, J. M., (2007), "Effect of Heat Treatment on HVOF Hydroxyapatite Coatings", J Therm. Spray Technol., Vol. 16, pp. 220-228.**

79. **Filiaggi, M.J., Coombs, N.A. and Pillar, R.M., (1991), "Characterization of Interface in the Plasma-sprayed HA coating/Ti-6Al-4V Implant System", J. Biomed. Mater. Res., Vol. 25, pp. 1211-1229.**
80. **Flannery, M., McGloughlin, T., Jones, E. and Birkinshaw, C., (2008), "Analysis of Wear and Friction of Total Knee Replacements Part I. Wear Assessment on a Three Station Wear Simulator", Wear, Vol. 265, pp. 999-1008.**
81. **Fu, L., Khor, K.A. and Lim, P. J., (2001), "The Evaluation of Powder Processing on Microstructure and Mechanical Properties of Hydroxyapatite (HA)/Yttria Stabilized Zirconia (YSZ) Composite Coatings", Surf. Coat. Technol., Vol. 140, pp. 263-268.**
82. **Fu, L., Khor, K.A. and Lim, P. J., (2002), "Effects of Yttria-stabilized Zirconia on Plasma-sprayed Hydroxyapatite/Yttria-stabilized Zirconia Composite Coating", J. Am. Ceram. Soc., Vol. 85, pp. 800-806.**
83. **Fu, Y. Q., Batchelor, A. W. and Loh, N. L., (1998), "Revealing the Hidden World of Fretting Wear Processes of Surface Coatings by X-ray Mapping", Surf. Coat. Technol., Vol. 107, pp. 133-141.**
84. **Gadow, R., Killinger, A. and Stiegler, N., (2010), "Hydroxyapatite Coatings for Biomedical Applications Deposited by Different Thermal Spray Techniques, Surf. Coat. Technol., Vol. 205, pp. 1157-1164.**
85. **Gauthier, O., Bouler, J. and Aguado, E., (1998), "Macroporous Biphasic Calcium Phosphate Ceramics: Influence of Macropore Diameter and Macroporosity Percentage on Bone Ingrowth., Biomaterials, Vol. 19, pp. 133-139.**
86. **Gautier, S., Champion, E. and Bernache-Assollant, D., (1997), "Processing, Microstructure and Toughness of Al₂O₃ Platelet-reinforced Hydroxyapatite", J. Euro. Ceram. Soc., Vol. 17, pp. 1361-1369.**
87. **Gledhill, H. C., Turner, I. G. and Doyle, C., (1999), "Direct Morphological Comparison of Vacuum Plasma Sprayed and Detonation Gun Sprayed Hydroxyapatite Coatings for Orthopedic Applications", Biomaterials, Vol. 20, pp. 315-322.**
88. **Gledhill, H. C., Turner, I. G. and Doyle, C., (2001A), "In Vitro Fatigue Behavior of Vacuum Plasma and Detonation Gun Sprayed Hydroxyapatite Coatings", Biomaterials, Vol. 22, pp. 1233-1240.**
89. **Gledhill, H. C., Turner, I. G. and Doyle, C., (2001B), "In Vitro dissolution Behavior of Two Morphologically Different Thermally Sprayed Hydroxyapatite Coatings", Biomaterials, Vol. 22, pp. 695-700.**

90. **Golant**, V. E., Zhilinsky, A. R., Sakharov, I. E. and Brown, S. C., (1980), "Fundamental of Plasma Physics", Wiley, New York.
91. **Goller**, G., (2004), "The Effect of Bond Coat on Mechanical Properties of Plasma Sprayed Bioglass-titanium Coatings", *Ceram. Int.*, Vol. 30, pp. 351-355.
92. **Gopi**, D., Collins, A. P. V. and Kavitha, L., (2008), "Evaluation of Hydroxyapatite Coatings on Borate Passivated 316 L SS in Ringer's Solution", *Mater. Sci. Eng. C*, Vol. 29 (3), pp. 955-958.
93. **Gordon** England, England, <http://www.gordonengland.co.uk>.
94. **Gottlander**, M. and Albrektsson, T., (1991), "Histomorphometric Studies of Hydroxyapatite Coated and Uncoated CP Titanium Threaded Implants in Bone", *Inter. J. Oral Maxillofac Implants*, Vol. 6, pp. 399-404.
95. **Gottlander**, M., (1994), "On Hard Tissue Reactions to Hydroxyapatite-coated Titanium Implants", Ph.D. Thesis, Biomaterials Group, University of Gothenburg, Gothenburg.
96. **Gottlander**, M., Albrektsson, T. and Carlsson, L. V., (1992), "Histomorphometric Studies of Hydroxyapatite Coated and Uncoated CP Titanium Threaded Implants in Bone", *Inter. J. Oral Maxillofac Implants*, Vol. 7, pp. 485-490.
97. **Grandjean-Laquerriere**, A., Laquerriere, P., Jallot, E., Nedelec J. M., Guenounou, M., Laurent-Maquuin, D. and Philips, T. M., (2006), "Influence of Zinc Concentration of Sol-gel Derived Zone Substituted Hydroxyapatite on Cytokine Production by Human Monocytes in Vitro", *Biomaterials*, Vol. 27, pp. 3195-3200.
98. **Griss**, P. and Heimke, G., (1981), "Five Years Experience with Ceramic-Metal Composite Hip Endo-prostheses", *Arch. Orthop. Traumat. Surg.*, Vol. 98, pp. 157-165.
99. **Gross**, K. A. and Babovic, M., (2002), "Influence of Abrasion on the Surface Characteristics of Thermally Sprayed Hydroxyapatite Coatings", *Biomaterials*, pp. 4731-4737.
100. **Gross**; K. A., Chai, C. S., Kannangara, G. S. K. and Ben-Nissan, B., (1998), "Thin Hydroxyapatite Coatings via Sol-gel Synthesis", *J. Mater. Sci. Mater. Med.*, Vol. 9, pp. 839-843.
101. **Gu**, Y. W., Khor, K. A. and Cheang, P., (2003), "In Vitro Studies of Plasma-sprayed Hydroxyapatite/Ti-6Al-4V Composite Coatings in Simulated Body Fluid (SBF)", *Biomaterials*, Vol. 24, pp. 1603-1611.

102. **Guo, H., Khor, K. A., Boey, Y. C. and Miao, X., (2003), "Laminated and Functionally Graded Hydroxyapatite/Yttria Stabilized Tetragonal Zirconia Composites Fabricated by Spark Plasma Sintering", *Biomaterials*, Vol. 24, pp. 667-675**
103. **Hamdi, M. and Ide-Ektessabi, A., (2007), "Dissolution Behavior of Simultaneous Vapor Deposited Calcium Phosphate Coatings In Vitro", *Mater. Sci. Eng. C*, Vol. 27, pp. 670-674.**
104. **Harris, W. H., (1995), "The problem in Osteolysis", *Clin. Orthop.*, Vol. 311, pp. 46-53.**
105. **Heimann, R. B., (1999), "Design of Novel Plasma Sprayed Hydroxyapatite-bond Coat Bioceramic Systems", *J. Therm. Spray Technol.*, Vol. 8 (4), pp. 597-604.**
106. **Heimann, R. B., (2006), "Thermal Spraying of Biomaterials", *Surf. Coat. Technol.*, Vol. 201, pp. 2012-2019.**
107. **Heimann, R.B. and Vu, T.A., (1997), "Low-pressure Plasma-sprayed (LPPS) Bioceramic Coatings with Improved Adhesion Strength and resorption Resistance", *J. Therm. Spray Technol.*, Vol. 6, pp. 145-149.**
108. **Heimann, R.B., Vu, T.A. and Wayman, M.L., (1997), "Bioceramic Coatings: State-of-the Art and Recent Development Trends", *Eur. J. Mineral*, Vol. 9, pp. 597-615.**
109. **Hemmerle, J., Qncag, A. and Erturk, S., (1997), "Ultrastructural Features of Bone Response to a Plasma-sprayed Hydroxyapatite Coating in Sheep", *J. Biomed. Mater. Res.* Vol. 36, pp. 418-425.**
110. **Hench, L. L. and Ethridge, E. C., (1982), "Biomaterials: An interfacial Approach", Academic Press, New York, USA.**
111. **Hench, L. L. and Polak, J. M., (2002), "Third-generation Biomedical Materials", *Science*, Vol. 295, pp. 1014-1017.**
112. **Hench, L. L. and Wilson, J., (1993), "An Introduction to Bioceramic", In *Advanced Series in Ceramics*, World Scientific, Singapore, Vol. 1, pp. 1-23.**
113. **Hench, L. L., (1991), "Bioceramics: From Concept to Clinic", *J. Am. Ceram. Soc.*, Vol. 74, pp. 1487-1510.**
114. **Hench, L. L., (1998), "Bioactive Materials: The Potential for Tissue Regeneration", *J. Biomed. Mat. Res.*, Vol. 41 (4), pp. 511-518.**
115. **Hesse, C., Hengst, M., Kleeberg, R. and Götze, J., (2008), "Influence of Experimental Parameters on Spatial Phase Distribution in as-sprayed and Incubated Hydroxyapatite Coatings", *J. Mater Sci. Mater. Med.*, Vol. 19, pp. 3235-3241.**

116. **Hirakawa, K., Jacobs, J. J., Urban, R. and Saito, T., (2004), "Mechanism of Failure Total Knee Replacements – Lessons Learned from Retrieval Studies", Clin. Ortho., Vol. 420, pp. 10-17.**
117. **Hood, R. W., Wright, T. W. and Burstein, A. H., (1983), "Retrieval Analysis of Total Knee Prostheses A Method and its Application to 48 Total Condylar Prostheses", J. Biomech Mater. Res., Vol. 17, pp. 829-842.**
118. **Hoppner, D. W. and Chandrasekaran, V., (1994), "Fretting in Orthopedic Implants: A Review", Wear, Vol. 173, pp. 189-197.**
119. **<http://www.azom.com/details.asp> Article ID: 542.**
120. **<http://www.azom.com/details.asp> Hydroxyapatite Coatings, Article ID: 1405.**
121. **Hughes, J. M. and Rakovan, J.,(2002), "The Crystal Structure of Apatite, $\text{Ca}_5(\text{PO}_4)_3(\text{F}, \text{OH}, \text{Cl})$ ", In Phosphates: Geochemical, Geobiological, and Materials Importance, Reviews in Mineralogy and Geochemistry, Eds., Kohn, M. J., Rakovan, J. and Hughes, M., ISBN 093996060X, Vol. 48.**
122. **Hulbert, S. F., Bokros, J.C., Hench, L. L., Wilson J. and Heimke, G., (1987), "Ceramics in Clinical Applications: Past, Present and Future", In High Technology Ceramics, Eds. Vineenzini, P., Elsevier, Amsterdam, Netherlands, pp. 189-213.**
123. **Hyschenko, A. P., Okovity, V. A. and Shevtsov, A. I., (2002), " Investigation of Composite Hydroxyapatite Powder for Plasma Spraying Bioceramic Coatings", Mater. Manuf. Processes, Vol. 17 (2), pp. 177-185.**
124. **"Implants for Surgery- Hydroxyapatite. Part – I: Ceramic Hydroxyapatite", (2000), BS ISO 13778-1: 2000, International Organization for Standards.**
125. **Inagaki, M. and Kameyama, T., (2007), "Phase Transformation of Plasma-sprayed Hydroxyapatite Coating with Preferred Crystalline Orientation", Biomaterials, Vol. 28, pp. 2923-2931.**
126. **Inagaki, M., Yokogawa, Y. and Kameyama, T., (2003), "Bond Strength Improvement of Hydroxyapatite/Titanium Composite Coating by Partial Nitriding During RF-Thermal Plasma Spraying", Surf. Coat. Technol., Vol. 173, pp. 1-8.**
127. **Inagaki, M., Yokogawa, Y. and Kameyama, T., (2006), "Effects of Plasma Gas Composition on Bond strength of Hydroxyapatite/Titanium Composite Coatings Prepared by RF-Plasma Spraying", J. Eur. Ceram. Soc., Vol. 26, pp. 495-499.**
28. **Ji, H., Pinton, C. B. and Marquis, P. M., (1992), "Microstructural Characterization of Hydroxyapatite Coatings on Titanium", J. Mater. Sci. Mater. Med., Vol. 3, pp. 283-287.**

129. **Johnson, S.**, (2005), "Pulsed laser Deposition of Hydroxyapatite Thin Films", M.Sc. Thesis, School of Materials Science and Engineering, Georgia Institute of Technology, Georgia, USA.
130. **Juang, H. Y. and Hon, M. H.**, (1994), "Fabrication and Mechanical Properties of Hydroxyapatite-Alumina Composites", *Mater. Sci. Eng. C*, Vol. 2, pp. 77-81
131. **Kalin, M.**, (2003), "Wear of Hydroxyapatite Sliding Against Glass-infiltrated Alumina", *J. Mater. Res.*, Vol. 18 (1), pp. 27-36.
132. **Kalin, M., Jahanmir, S. and Ives, L. K.**, (2002), "Effect of Counterface Roughness on Abrasive Wear of Hydroxyapatite", *Wear*, Vol. 252, pp. 679-685.
133. **Kannan, S., Balamurugan, A. and Rajeswari, S.**, (2003), "Hydroxyapatite Coatings on Sulfuric Acid Treated Type 316L SS and Its Electrochemical Behavior in Ringer's Solution", *Mater. Lett.*, Vol. 57, pp. 2382-2389.
134. **Karanjai, M., Manoj Kumar, B. V., Sundaresan, R., Basu, B., Rama Mohan, T. R. and Kashyap, B. P.**, (2008), "Fretting Wear Study on Ti-Ca-P Biocomposite in Dry and Simulated Body Fluid", *Mater. Sci. Eng. A*, Vol. 475, pp. 299-307.
135. **Kaya, C.**, (2008), "Electrophoretic Deposition of Carbon Nanotubes-Reinforced Hydroxyapatite Bioactive Layers on Ti-6Al-4V Alloys for Biomedical Applications", *Ceram. Int.*, Vol. 34, pp. 1843-1847.
136. **Kennedy, F. E., Currier, J. H., Plumet, S., Duda, J. L., Gestwick, D. P., Collier, J. P., Currier, B. H. and Dubourg, M. C.**, (2000), "Contact Fatigue Failure of Ultra-High Molecular Weight Polyethylene Bearing Components of Knee Prostheses", *ASME J. Tribol.* Vol. 122, pp. 332-339.
137. **Kennedy, F. E., Van Citters, D. W., Wongseedakaew, K. and Mongkolwongrojn**, (2007), "Lubrication and Wear of Artificial Knee Joint Materials in a Rolling/Sliding Tribotester", *Trans. ASME*, Vol. 129, pp. 326-335.
138. **Kettner, R.**, (1996), "The Unique Interface Reaction of H-A-C", In Proc. A Two Day Symposium on Hydroxyapatite Ceramics, A Decade of Experience in Hip Arthroplasty, Eds. Furlong, R., Royal College of Surgeons of England, London, 2nd-3rd November, Furlong Research Foundation, pp. 41-55.
139. **Khan, M. A., Williams, R. L. and Williams, D. F.**, (1996), "In-vitro Corrosion and Wear of Titanium Alloys in the Biological Environment", *Biomaterials*, Vol. 17, pp. 2117-2126.

140. **Khor, K. A., Li, H. and Cheang, P., (2004), "Significance of Melt-Fraction in HVOF Sprayed Hydroxyapatite Particles, Splats and Coatings", *Biomaterials*, Vol. 25, pp. 1177-1186.**
141. **Khor, K. A., Yip, C. S. and Cheang, P., (1997), "Post-Spray Hot Isostatic Pressing of Plasma Sprayed Ti-6Al-4V/Hydroxyapatite Composite Coatings", *J. Mater. Process. Technol.*, Vol. 71, pp. 280-287.**
142. **Khor, K.A., Cheang, P. and Wang, Y., (1998), "Plasma Spraying of Combustion Flame Spheroidized Hydroxyapatite (HA) Powders", *J. Therm. Spray Technol.*, Vol. 260, pp. 254-260.**
143. **Khor, K.A., Fu, L., Lim, V.J.P. and Cheang, P., (2000), "The Effect of ZrO₂ on the Phase Compositions of Plasma Sprayed HA/YSZ composite Coatings", *Mater. Sci. Eng. A.*, Vol. 276, pp. 160-166.**
144. **Kim, H., Koh, Y., Li, L., Lee, S. and Kim, H., (2004), "Hydroxyapatite Coating on Titanium Substrate with Titania Buffer Layer Processed by Sol-gel Method", *Biomaterials*, Vol. 25, pp. 2533-2538.**
145. **Kim, K. J., Sato, K., Kotabe, S., Katoh, Y. and Itoh, T., (1993), "Biochemical and Histochemical Analysis of Bone Marrow Cells Activated by HA Particles", *Bioceramics*, pp. 365-369.**
146. **Klein, C. P. A. T., (1990), "Study of Solubility of Different Calcium Phosphates and Other Ceramic Particles In Vitro", *Biomaterials*, Vol. 11, pp. 509-512.**
147. **Klein, C. P. A. T., Wolke, J. G. C. and de Groot, K., (1993), "Stability of Calcium Phosphate Ceramics and Plasma Spray Coating", In *An Introduction to Bioceramic*, Eds. Hench, L. L. and Wilson, J., World Scientific, London, pp. 192-221.**
148. **Kokubo, T. and Takadama, H., (2006), "How Useful is SBF in Predicting In Vivo Bone Bioactivity?", *Biomaterials*, Vol. 27, pp. 2907-2915.**
149. **Kokubo, T., (1991), "Bioactive Glass Ceramics: Properties and Applications", *Biomaterials*, Vol. 12, pp. 155-163.**
150. **Kokubo, T., Kushitani, S., Sakka, S., Kitsugi, T. and Yamamaro, T., (1990), "Solutions Able to Produce In Vivo Surface Structure Changes in Bioactive Glass Ceramic", *J. Biomed. Mater. Res.*, Vol. 24, pp. 721-734.**
151. **Kunz-Schughart, L. A., Doetsch, J., Mueller-Klieser, W. and Groebe, K., (2000), "Proliferative Activity and Tumorigenic Conversion: Impact on Cellular Metabolism in 3-D Culture", *American Journal of Physiology*, Vol. 278, pp. C765-C780.**

152. Kurashina, K., Kurita, H., Wu, Q., Ohtsuka, A. and Kobayashi, H., (2002), "Ectopic Osteogenesis with Biphaic Ceramics of Hydroxyapatite and Tricalcium Phosphate in Rabbits", *Biomaterials*, Vol. 23, pp. 407-412.
153. Kurzweg, H., Heimann, R. B. and Troczynski, T., (1998B), "Adhesion of Thermally sprayed Hydroxyapatite-bond-coat Systems Measured by a Novel Peel Test", *J. Mater. Sci. Mater. Med.*, Vol. 9, pp. 9-16.
154. Kurzweg, H., Heimann, R. B., Troczynski, T. and Wayman, M. L., (1998A), "Development of Plasma-Sprayed Bioceramic Coatings with Bond Coats Based on Titania and Zirconia", *Biomaterials*, Vol. 19, pp. 1507-1511.
155. Kweh, S. W. K., Khor, K. A. and Cheang, P., (2000), "Plasma-sprayed Hydroxyapatite (HA) Coatings with Flame-spheroidized Feedstock: Microstructure and Mechanical Properties", *Biomaterials*, Vol. 21, pp. 1223-1234.
156. Kweh, S. W. K., Khor, K. A. and Cheang, P., (2002), "High Temperature In-Situ XRD of Plasma Sprayed HA Coatings", *Biomaterials*, Vol. 23, pp. 381-387.
157. Kwok, C.T., Wong, P.K., Cheng, F.T. and Man, H.C., (2009), "Characterization and Corrosion Behavior of Hydroxyapatite Coatings on Ti6Al4V fabricated by Electrophoretic Deposition", *Appl. Surf. Sci.*, Vol. 255, pp. 6736-6744.
158. Lahiri, D., Benaduce, A.N., Rouzaud, F., Solomon, J., Keshri, A.K., Kos, L. and Agarwal, A., (2010), "Wear Behavior and In vitro Cytotoxicity of Wear Debris Generated from Hydroxyapatite-carbon Nanotubes Composite Coating", *J. Biomed. Mater. Res. A.*, Vol. 96, pp. 1-12.
159. Lambardi, A. L., Mallory, T. H., Vaughn, B. K. and Drouillard, P., (1989), "Aseptic Loosening in Total Hip Arthroplasty Secondary to Osteolysis Induced by Wear Debris from Titanium Alloy Modular Heads", *J. Bone Joint Surg. (Am.)*, Vol. B 71, pp. 1337-1342.
160. Lamy, D., Pierre, A.C. and Heimann, R.B., (1996), "Hydroxyapatite Coatings with a Bond Coat of Biomedical Implants by Plasma Projection", *J. Mater. Res.*, Vol. 11, pp. 680-686.
161. Landy, M. M. and Walker, P. S., (1988), "Wear of Ultra High Molecular Weight Polyethylene Components of 90 Retrieved Knee Prostheses", *J. Arthroplasty (Suppl.)*, Vol. 3, pp. S73-S85.
162. Lazic, S., Zee, S., Miljevic, N. and Milonjic, S., (2001), "The Effect of Temperature on the Properties of Hydroxyapatite Precipitated from Calcium Hydroxide and Phosphoric Acid", *Thermochim. Acta*, Vol. 374, pp. 13-22.

163. **Le Geros, J. P. and Le Geros, R. Z., (1991), "Characterization of Calcium Phosphate Coatings on Implants", Transactions of the Annual Meeting of the Society for Biomaterials in Conjunction with the International Biomaterials Symposium 14. pp. 192.**
164. **Le Geros, R. Z. and Le Geros J. P., (1984), "Phosphate Minerals in Human Tissues, In Phosphate Minerals, Eds. Nriagu, J. O. and Moore, P. B., Springer-Verlag, pp. 351-385.**
165. **Le Geros, R. Z. and Le Geros, J. P., (1993), "Dense Hydroxyapatite", In An Introduction to Bioceramics, Eds., Hench, L. L. and Wilson, J., World Scientific, London, pp. 139-180.**
166. **Le Geros, R. Z., (1988), "Significance of Porosity and Physical Chemistry of Calcium Phosphate Ceramics, Biodegradation-Bioresorption", In Bioceramics: Material Characteristics Versus In Vivo Behavior, Eds., Ducheyne, P. and Lemons, J. E., Ann. N. Y. Acad. Sci., Vol. 523, pp. 268-271.**
167. **Le Geros, R. Z., (1991), "Calcium Phosphate in Oral Biology and Medicine", In Monographs in Oral Science, Eds. Myers, H., Basel: Karger, Vol. 15, pp. 1-201.**
168. **Le Geros, R. Z., (1994), "Hydroxyapatite and Related Materials", Eds. Brown, P. W. and Constantz, B., CRC, Boca Raton, Florida, USA, pp. 3-28.**
169. **Le Geros, J.P., LeGeros, R.Z., Burgess, A., Edwards, B. and Zitelli, J., (1994), "X-ray Diffraction Method for the Quantitative Characterization of Calcium Phosphate Coatings", In Characterization and Performance of Calcium Phosphate Coatings for Implant, Eds. Horowitz, E. and Parr, J.E., ASTM STP 1196, ASTM, Philadelphia, PA, pp. 33-42.**
170. **Lee, J. M., Lee, J. I. and Lim, Y. J., (2010), "In Vitro Investigation of Anodization and CaP Deposited Titanium Surface Using MG63 Osteoblast-Like Cells", App. Surf. Sci., Vol. 256, pp. 3086-3092.**
171. **Lee, T. M., Yang, C. Y., Chang, E. and Tsai, R. S., (2004), "Comparison of Plasma-Sprayed Hydroxyapatite Coatings and Zirconia-Reinforced Hydroxyapatite Composite Coatings: In Vivo Study", J. Biomed. Mater. Res. A, Vol. 71A, pp. 652-660**
172. **Lee, Y-P., Wang, C-K., Huang, T-H., Chen, C-C., Kao, C-T. and Ding, S-J., (2005), "In Vitro Characterization of Postheat-Treated Plasma-Sprayed Hydroxyapatite Coatings", Surf. Coat. Technol., Vol. 197, pp. 367-374.**
173. **Leung, K., Heberlein, J. and Pfender, E., (1995), "Particle Trajectory Control with the Use of Different Carrier Gases", In Proc. of 8th National Thermal Spray Conference on**

- "Thermal Spray Science and Technology", Eds. Berndt, C. C. and Sampath, S., Houston, Texas, 11-15, September.
174. **Levingstone, T. J.**, (2008), "Optimisation of Plasma Sprayed Hydroxyapatite Coatings", Ph. D. Thesis, School of Mechanical and Manufacturing Engineering, Dublin City University, Ireland.
175. **Li, H., Khor, K. A. and Cheang, P.**, (2002A), "Titanium Dioxide Reinforced Hydroxyapatite Coatings Deposited by High Velocity Oxy-fuel (HVOF) Spray", *Biomaterials*, Vol. 23, pp. 85-91.
176. **Li, H., Khor, K. A. and Cheang, P.**, (2002B), "Properties of Heat-Treated Calcium Phosphate Coatings Deposited by High-Velocity Oxy-Fuel (HVOF) Spray", *Biomaterials*, Vol. 23, pp. 2105-2112.
177. **Li, H., Khor, K. A. and Cheang, P.**, (2002C), "Young's Modulus and Fracture Toughness Determination of High Velocity Oxy-Fuel-Sprayed Bioceramic Coatings", *Surf. Coat. Technol.*, Vol. 155, pp. 21-32.
178. **Li, H., Khor, K. A. and Cheang, P.**, (2003), "Impact Formation and Microstructure Characterization of Thermal Sprayed Hydroxyapatite/Titania Composite Coatings", *Biomaterials*, Vol. 24, pp. 949-957.
179. **Li, H., Li, Z-X., Li, H., Wu, Y-Z. and Wei, Q.**, (2009), "Characterization of Plasma Sprayed Hydroxyapatite/ZrO₂ Graded Coating", *Mater. Des.*, Vol. 30, pp. 3920-3924.
180. **Li, J., Fartash, B. and Hermansson, L.**, (1995), "Hydroxyapatite – Alumina Composites and Bone Bonding", *Biomaterials*, Vol. 16 (5), pp. 417-422.
181. **Liao, C., Lin, F., Chen, K. and Sun, J.**, (1999), "Thermal Decomposition and Reconstitution of Hydroxyapatite in Air Atmosphere", *Biomaterials*, Vol. 20, pp. 1807-1813.
182. **Lim, V. J. P., Khor, K. A., Fu, L. and Cheang, P.**, (1999), "Hydroxyapatite-Zirconia Composite Coatings via the Plasma Spraying Process", *J. Mater. Proces. Technol.*, Vol. 89-90, pp. 491-496.
183. **Lima, R. S. and Marple, B. R.**, (2006), "From ASP to HVOF Spraying of Conventional and Nanostructured Titania Feedstock Powders: A Study on the Enhancement of the Mechanical Properties", *Surf. Coat. Technol.*, Vol. 200, pp. 3428-3437.
184. **Lin, J-H., Lou, C-W., Chang, C-H., Chen, Y-S., Lin, G-T. and Lee, C-H.**, (2007), "In Vitro Study of Bone-Like Apatite Coatings on Metallic Fiber Braids", *J. Mater. Proces. Technol.*, Vol. 192-193, pp. 97-100.

185. **Liven, L.**, (2007), "Study of Hydroxyapatite Osteoinductivity with an Osteogenic Differentiation Assay using Mesenchymal Stem Cell" M. Phil. Thesis, Hong Kong University of Science and Technology, Hong Kong, China.
186. **Long, M.** and **Rack, H. J.**, (1998), "Titanium Alloys in Total Joint Replacement – A Materials Science Perspective", *Biomaterials*, Vol. 19, pp. 1621-1639.
187. **López, D. A.**, **Rosero-Navarro, N. C.**, **Ballarre, J.**, **Durán, A.**, **Aparicio, M.** and **Cerá, S.**, (2008), "Multilayer Silica-Methacrylate Hybrid Coatings Prepared by Sol-gel on Stainless Steel 316L: Electrochemical Evaluation", *Surf. Coat. Technol.*, Vol. 202, pp. 2194-2201.
188. **Lu, Y-P.**, **Chen, Y-M.**, **Li, S-T.** and **Wang, J-H.**, (2008), "Surface Nanocrystallization of Hydroxyapatite Coating", *Acta Biomater.*, Vol. 4, pp. 1865-1872.
189. **Lu, Y-P.**, **Li, M-S.**, **Li, S-T.**, **Wang, Z-G.** and **Zhu, R-F.**, (2004), "Plasma-Sprayed Hydroxyapatite + Titania Composite Bond Coat for Hydroxyapatite Coating on titanium Substrate", *Biomaterials*, Vol. 25, pp. 4393-4403.
190. **Lu, Y-P.**, **Li, S-T.**, **Zhu, R-F.**, **Li, M-S.** and **Lei, T-Q.**, (2003B), "Formation of Ultrafine Particles in Heat Treated Plasma-Sprayed Hydroxyapatite Coatings", *Surf. Coat. Technol.*, Vol. 165, pp. 65-70.
191. **Lu, Y-P.**, **Song, Y-Z.**, **Zhu, R-F.**, **Li, M-S.** and **Lei, T-Q.**, (2003A), "Factors Influencing Phase Composition and Structure of Plasma Sprayed Hydroxyapatite Coatings during Heat Treatment", *Appl. Surf. Sci.*, Vol. 206, pp. 345-354.
192. **Lu, Y-P.**, **Xiao, G-Y.**, **Li, S-T.**, **Sun, R-X.** and **Li, M-S.**, (2006), "Microstructural Inhomogeneity in Plasma-Sprayed Hydroxyapatite Coatings and Effect of Post-Heat Treatment", *Appl. Surf. Sci.*, Vol. 252, pp. 2412-2421.
193. **Luo, Z. S.**, **Cui, F. Z.**, **Fenf, Q. L.**, **Li, H. D.**, **Zhu, X. D.** and **Spector, M.**, (2000), "In Vitro and In Vivo Evaluation of Degradability of Hydroxyapatite Coatings Synthesized by Ion Beam-Assisted Deposition", *Surf. Coat. Technol.*, Vol. 131, pp. 192-195.
194. **Lv, Y-P.**, **Chen, Y-M.**, **Chen, L-B.**, **Li, S-T.** and **Zhu, R-F.**, (2009), "Effects of Post-heat Treatment on Phase Composition, Surface Morphology and Bond Strength of Hydroxyapatite Coatings", *J. Func. Mater.*, Vol. 40, pp. 1713-1715.
195. **MaGee, M. A.**, **Howie, D. W.**, **Neale, S. D.**, **Haynes, D. R.** and **Pearcy, M. J.**, (1997), "The Role of Polyethylene Wear in Joint Replacement Failure", *Proc. Instn. Mech. Engrs., Part H, J. Eng. Med.*, Vol. 211(H1), pp. 65-72.

196. **Mahabole, M.P., Aiyer, R.C., Ramakrishna, C.V., Sreedhar, B. and Hhairnar, R.S., (2005),** "Synthesis, Characterization and Gas Sensing Property of Hydroxyapatite Ceramic", *Bull. Mater. Sci.*, Vol. 28, pp. 534-545.
197. **Mann, S., (2001),** "Biomaterialization-principles and Concepts in Bioinorganic Materials Chemistry, Oxford University Press, Oxford.
198. **Materials Characterization, (1992),** ASM Handbook, The Materials Information Society, American Society of Metals, Vol. 10, Ohio, USA.
199. **Mondragón-Cortez, P. and Varagas-Gutiérrez, G., (2004),** "Electrophoretic Deposition of Hydroxyapatite Submicron Particles at High Voltage", *Mater. Lett.*, Vol. 58, pp. 1336-1339.
200. **Montazeri, M., Dehghanian, C., Shokouhfar, M. and Baradarn, A., (2011),** "Investigation of the Voltage and Time Effects on the Formation of Hydroxyapatite-containing Titania Prepared by Plasma Electrolytic Oxidation on Ti-6Al-4V Alloys and Its Corrosion Behavior", *Appl. Surf. Sci.*, Vol. 257, pp. 7268-7275.
201. **Morales, J.G., Burgues, J.T., Boix, T., Fraile, J. and Clemente, R.R. (2001),** "Precipitation of Stoichiometric Hydroxyapatite by a Continuous Method", *Crys. Res. Technol.*, Vol. 36, pp. 15-26.
202. **Morks, M. F. and Kobayashi, A., (2006),** "Influence of Gas Flow Rate on the Microstructure and Mechanical Properties of Hydroxyapatite Coatings Fabricated by Gas Tunnel Type Plasma Spraying", *Surf. Coat. Technol.*, Vol. 201, pp. 2560-2566.
203. **Morks, M. F. and Kobayashi, A., (2007B),** "Influence of Spray Parameters on the Microstructure and Mechanical Properties of Gas-Tunnel Plasma Sprayed Hydroxyapatite Coatings", *Mater. Sci. Eng. B.*, Vol. 139, pp. 209-215.
204. **Morks, M. F. and Kobayashi, A., (2008),** "Development of ZrO₂/SiO₂ Bioinert Ceramic Coatings for Biomedical Application", *J. Mech. Behav. Biomed. Mater.*, Vol. 12, pp. 165-171
205. **Morks, M. F. and Akimoto, K., (2008),** "The Role of Nozzle Diameter on the Microstructure and Abrasion Wear Resistance of Plasma Sprayed Al₂O₃/TiO₂ Composite Coatings", *J Manuf. Processes*, Vol. 10, pp. 1-5.
206. **Morks, M. F., (2008),** "Fabrication and Characterization of Plasma Sprayed HA/SiO₂ Coatings for Biomedical Application", *J. Mech. Behav. Biomed. Mater.*, Vol. 1, pp. 105-111.

207. **Morks, M. F., Fahim, N. F. and Kobayashi, A., (2008), "Structure, Mechanical Performance and Electrochemical Characterization of Plasma Sprayed SiO₂/Ti-Reinforced Hydroxyapatite Biomedical Coatings", Appl. Surf. Sci., Vol. 255, pp. 3426-3433.**
208. **Morks, M. F., Kobayashi, A. and Fahim, N. F., (2007), "Abrasive Wear Behavior of Sprayed Hydroxyapatite Coatings by Gas Tunnel Type Plasma Spraying", Wear, Vol. 262, pp. 204-209.**
209. **Morks, M.F. and Kobayashi, A., (2007A), "Effect of Gun Current on the Microstructure and Crystallinity of Plasma sprayed Hydroxyapatite Coatings", Appl. Surf. Sci., Vol. 253, pp. 7136-7142.**
210. **Moses, M. A., Brem, H. and Langer, R., (2003), "Advancing the Field of Drug Delivery: Taking Aim at Cancer", Cell, Vol. 4, pp. 337-341.**
211. **Mudali, U.K., Sridhar, T.M. and Raj, B., (2003), "Corrosion of Bio Implants", Sadhana, Vol. 28, pp. 601-637.**
212. **Muthukumar, V., Selladurai, V., Nandhakumar, S. and Senthilkumar, M., (2010), "Experimental Investigation on Corrosion and Hardness of Ion Implanted AISI 316L Stainless Steel", Mater. Des., Vol. 31, pp. 2813-2817.**
213. **Nagano, M., Nakamura, T., Kokubo, T., Tanahashi, M. and Ogawa, M., (1996), "Differences of Bone Bonding Ability and Degradation Behavior In Vivo Between Amorphous Calcium Phosphate and Highly Crystalline Hydroxyapatite Coating", Biomaterials, Vol. 17 (9), pp. 1771-1777.**
214. **Nanomi, T. and Satoh, N., (1995), "Preparation of Elongated Diopside/hydroxyapatite Composite and Their Cell Culture Test", J. Ceram. Soc. Japan, Vol. 103, pp. 804-809.**
215. **National Materials Advisory Board, (1996), "Coatings for High Temperature Structural Materials: Trends and Opportunities", National Academy Press, Washington D. C., <http://www.nap.edu/openbook/0309053811/html>, pp. 1-85.**
216. **Netter, F. H., Hammoud, G., Kozinn, H. C., Wilson, P. D., Jr. and Pillicci, P. M., (1989), "The Ciba Collection of Medical Illustrations", In Musculoskeletal System, Part. II, Eds., Summit, N. J., Ciba Geigy Corporation, Vol. 8, pp. 235-246.**
217. **Neville-Smith, M., Trujillo, L. and Ammundson, R., (2000), "Special Feature: Consistency in Postoperative Education Programs Following Total Hip Replacement. Topics in Geriatric Rehabilitation, Vol. 15, pp. 68-76.**

218. **Nicholson, J. W.**, (2002), "The Chemistry of Medical and Dental Materials", Royal Society of Chemistry, Cambridge, UK.
219. **Nie, X.**, **Leyland, A.** and **Mattews, A.**, (2000), "Deposition of Layered Bioceramic Hydroxyapatite/TiO₂ Coatings on Titanium Alloys Using a Hybrid Technique of Micro-Arc Oxidation and Electrophoresis", *Surf. Coat. Technol.*, Vol. 125, pp. 407-414.
220. **Noma, T.**, **Shoji, N.**, **Wada, S.** and **Suzuki, T.**, (1993), "Preparation of Spherical Al₂O₃ Particle Dispersed Hydroxyapatite Ceramics", *J. Ceram. Soc. Japan, (Int. Ed.)*, Vol. 101, pp. 923-927
221. **Oktar, F. N.**, (1999), "Characterization of Processed Tooth Hydroxyapatite and Bioglass for Potential Application in Dentistry", PhD Thesis, Bosphorous University, Biomedical Engineering Institute.
222. **Oktar, F.N.**, **Yetmez, M.**, **Agathopoulos, S.**, **Lopez Goerne, T.M.**, **Goller, G.**, **Ipeker, I.** and **Ferreira, J.M.F.**, (2006), "Bond-coating in Plasma-sprayed Calcium-phosphate Coatings", *J. Mater. Sci. Mater. Med.*, Vol. 17, pp. 1161-1171.
223. **Oosterbos, C. J. M.**, **Rahmy, A. I. A.**, **Tonino, A. J.** and **Witpered, W.**, (2004), "High Survival Rate of Hydroxyapatite-coated Hip Prostheses 100 Consecutive Hips Followed for 10 Years", *Acta Orthop. Scand.*, Vol. 75. pp. 127-133.
224. **Oyane, A.**, **Kim, H-M.**, **Furuya, T.**, **Kokubo, T.**, **Miyazaki, T.** and **Nakamura, T.**, (2003), "Preparation and Assessment of Revised Simulated Body Fluids", *J. Biomed. Mater. Res. A*, Vol. 65, pp. 188-195.
225. **Paital, S.R.** and **Dahotre, N.B.**, (2009), "Calcium Phosphate Coatings for Bio-implant Applications: Materials, Performance Factors and Methodologies", *Mater. Sci. Eng. R*, Vol. 66, pp. 1-70.
226. **Park, E.** and **Condrate, R.A.**, (1999), "Graded Coating of Hydroxyapatite and Titanium by Atmospheric Plasma Spraying", *Mater. Lett.*, Vol. 40, pp. 228-234.
227. **Park, E.**, **Condrate Sr., R. A.**, **Lee, D.**, **Kociba, K.** and **Gallagher, P. K.**, (2002), "Characterization of Hydroxyapatite: Before and After Plasma Spraying", *J. Mater. Sci. Mater. Med.*, Vol. 13, pp. 211-218.
228. **Park, J. B.**, and **Lakes, R. S.**, (2007), "Biomaterials an Introduction", 3rd Ed., Springer, New York, USA, ISBN:978-0-387-37879-4
229. **Pawlowski, L.**, (1995), "The Science and Engineering of Thermal Spray Coatings", Wiley, New York.

230. **Plenk, H.**, (1982), "Biocompatibility of Ceramics in Joint Prostheses", In *Biocompatibility of Orthopedic Implants*, C. R. C. Press, Vol. 1, pp. 269-295, Boca Raton, Florida, USA.
231. **Porter, A. E., Hobbs, L. W., Rosen, V. B. and Spector, M.**, (2002), "The Ultrastructure of Plasma-sprayed Hydroxyapatite-bone Interface Predisposing to Bone Bonding", *Biomaterials*, Vol. 23 (2), pp. 725-733.
232. **Porter, A. E., Patel, N., Skepper, J. N., Best, S. M. and Bonfield, W.**, (2003), "Comparison of In Vivo Dissolution Processes in Hydroxyapatite and Silicon-substituted Hydroxyapatite Bioceramic", *Biomaterials*, Vol. 24, pp. 4609-4620.
233. **Qiu, D., Wang, A. and Yin, Y.**, (2010), "Characterization and Corrosion Behavior of Hydroxyapatite/zirconia Composite Coating on NiTi Fabricated by Electrochemical Deposition", *Appl. Surf. Sci.*, Vol. 257, pp. 1774-1778.
234. **Que, W., Khor, K.A., Xu, J.L. and Yu, L.G.**, (2008), "Hydroxyapatite/titania Nanocomposites Derived by Combining High-energy Ball Milling with Spark Plasma Sintering Process", *J. Eur. Ceram. Soc.*, Vol. 28, pp. 3083-3090.
235. **Raemdonck, W. V., Ducheyne, P. and DeMeester, P.**, (1984), "Calcium Phosphate Ceramics", In *Metal and Ceramic Biomaterials II-Strength and Surface*, Eds., Ducheyne, P. and Hastings, G. W., CRC Press, Boca Raton, FL, pp. 143-166.
236. **Rakngarm, A and Mutoh, Y.**, (2009), "Characterization and Fatigue Damage of Plasma Sprayed Hap Top Coat with Ti and Hap/Ti Bond Coat Layers on Commercially Pure Titanium Substrate", *J. Mech. Behav. Biomed. Mater.*, Vol. 2, pp. 444-453.
237. **Ray, C.**, (2004), "Dissolution Properties of Calcium Phosphates", 2nd Annual Biomaterials Workshop, Cranfield University, UK.
238. **Raynaud, S., Champion, E. and Bernache-Assollant, D.**, (2002), "Calcium Phosphate Apatites with Variable Ca/P Atomic Ratio, Calcination and Sintering", *Biomaterials*, Vol. **23, pp. 1073.**
239. **Rives, J., Rabbe, L. M. and Comrade, P.**, (1995), "Fretting Wear Corrosion of Surgical Implant Alloys: Effect of Ion Implantation and Ion Nitriding on Fretting Behavior of Metals/PMMA Contacts", In *Surface Modification Technologies VIII*, Eds. Sudarshan, M. and Jeandin, M., The Institute of Materials, pp. 43-52.
240. **Rootare, H. M., Powers, J. M. and Craig, R. G.**, (1978), "Sintered Hydroxyapatite Ceramic for Wear Studies", *J. Dent. Res.* Vol. 57, pp. 777-783.

241. **Rosnagel**, S. M., Cuomo, J. J. Westwood, W. D., (1990), "Handbook of Plasma Processing Technology: Fundamentals, Etching, Deposition and Surface Interaction", Noyes Publication, Park Ridge, N.J.
242. **Rouahi**, M., Champion, E., Hardouin, P. and Anselme, K., (2006), "Quantitative Kinetic Analysis of Gene Expression during Human Osteoblastic Adhesion on Orthopaedic Materails", *Biomaterials*, Vol. 27, pp. 2829-2844.
243. **Ryu**, S., Youn, H. J., Hong, K. S., Kim, S. J., Lee, D. H. and Chang, B. S., (2002), "Correlation Between MgO Doping and Sintering Characteristics in Hydroxyapatite/ β -Tricalcium Phosphate Composite", *Key Eng. Mater.*, Vol.21-24, pp. 218-220.
244. **Saikko**, V., Ahlroos, T. and Calonijs, O., (2001), "A Three-axis Knee Wear Simulator with Ball-on-flat Contact", *Wear*, Vol. 249, pp. 310-315.
245. **Sarao**, T.S., Singh, H., Singh, H., Saheet, H.S. and Chibber, R., (2009), "Surface Modification Techniques for Metallic Implants used in Biomedical Applications", In Proc., *Joining of Advanced and Specialty Materials, Materials Science Technology*, held on Oct. 25-29, 2009 at Pittsburgh, Pennsylvania, USA.
246. **Scheller**, G. and Jani, L., (2003), "The Cementless Total Hip Arthroplasty", In *Pelvic Ring and Hip*, Eds. DuParc, J., Elsevier, Paris, Vol. 6.
247. **Schneider**, S. J. Jr., (1991), "Ceramics and Glasses", ASM international, Vol. 4, Ohio, USA.
248. **Sedlak**, J. M. and Beebe, R. A., (1974), "Temperature Programmed Dehydration of Amorphous Calcium Phosphate", *J. Colloid. Interface Sci.*, Vol. 47, pp. 483.
249. **Setton**, L. A., Elliott, D. M. and Mow, V. C., (1998), "Altered Mechanics of Cartilage with Osteoarthritis: Human Osteoarthritis and An Experimental Model of Joint Degeneration", *Osteoarthr. Cartilage*, Vol. 7, pp. 2-14.
250. **Shi**, J., (2004), "From Dental Enamel to Synthetic Hydroxyapatite-based Biomaterials", Ph.D. Thesis, Department of Earth Sciences, University of Hamburg, Hamburg, Germany.
251. **Shin**, H., Jo, S. and Mikos, A. G., (2003), "Biomimetic Materials for Tissue Engineering"; *Biomaterials*, Vol24, pp. 4353-4364.
252. **Sidhu**, B. S., Singh, H., Puri, D. and Prakash, S., (2007), "Wear and Oxidation Behavior of Shrouded Plasma Sprayed Fly Ash Coatings", *Tribol. Int.*, Vol. 40, pp. 800-808.

253. Sidhu, B.S., Puri, D. and Prakash, S., (2004), "Characterization of Plasma Sprayed and Laser Remelted NiCrAlY Bond Coats and Ni₃Al Coatings on Boiler Tube Steel", Mater. Sci. Eng. A, Vol. 166, pp. 89-100.
254. Sidhu, T.S., Prakash, S. and Agarwal, R.D., (2005), "Cyclic Oxidation Behavior of Ni and Fe Based Superalloys in Air and Na₂SO₄-25% NaCl Molten Salt Environment at 800°C", Scripta Materialia, vol. 55, pp. 179-182.
255. Simmons, C. A., Valiquette, N. and Pilliar, R. M., (1999), "Osseointegration of Sintered Porous-surfaced and Plasma Spray-coated Implants: An Animal Model Study of Early Post Implantation Healing Response and Mechanical Stability", J. Biomed. Mater. Res., Vol. 47 (2), pp. 127-138.
256. Singh, B., (2003), "Studies on the Role of Coatings in Improving Resistance to Hot Corrosion and Degradation", Ph.D. Thesis, Metallurgical and Materials Engineering Department, Indian Institute of Technology Roorkee, Roorkee, India.
257. Singh, H., Puri, D., Prakash, S. and Maiti, R., (2007), "Characterization of Oxide Scales to Evaluate High Temperature Oxidation Behavior of Ni-20Cr Coated Superalloys", Mater. Sci. Eng. A, Vol. 464, pp. 110-116.
258. Slosarczyk, A., Stobierska, E., Paszkiewicz, Z. and Gawlicki, M., (1996), "Calcium Phosphate Materials Prepared from Precipitates with Various Calcium: Phosphorus Molar Ratio", J Am. Ceram. Soc., Vol. 79. pp. 2539.
259. Soballe, K., (1996), "The Role of H-A-C in In-growth Prosthesis", In Proc. of Two Day Symposium on Hydroxyapatite Ceramics, A Decade of Experience in Hip Arthroplasty, Eds. Furlong, R., Furlong Research Foundation, Royal College of Surgeons of England, London, 2nd-3rd November, pp. 57-67.
260. Sousa, S. R. and Barbosa, M. A., (1995), "The Effect of Hydroxyapatite Thickness on Metal Ion Release from Stainless Steel Substrate", J. Mater. Sci. Mater. Med., vol. 6, pp. 818-823.
261. Sousa, S. R. and Barbosa, M. A., (1996), "Effect of Hydroxyapatite Thickness on Metal Ion Release from Ti6Al4V Substrates", Biomaterials, Vol. 17, pp. 397-404.
262. Souto, R.M., Laz, M.M. and Reis, R.L., (2003), "Degradation Characteristics of Hydroxyapatite Coatings on Orthopaedic TiAlV in Simulated Physiological Media Investigated by Electrochemical Impedance Spectroscopy", Biomaterials, Vol. 24, pp. 4213-4221.

263. **Spector, M.**, (1990), "Prostheses: Materials, Design and Strategies for Fixation in Orthopedic Knowledge Update 3", American Academy of Orthopedic Surgeons, pp. 115-129.
264. **Spector, M.**, Shortkroff, S., Sledge, C. B. and Thornhill, T.S., (1991), "Advances in Our Understanding in Implant-bone Interface: Factors Affecting Formation and Degradation", In Instructional Course Lecture XI, Eds. Tullos, H.S., American Academy of Orthopedic Surgeons, Park Ridge, IL, pp. 101-113
265. **Sridhar, T. M.**, Mudali, U.K. and Subbaiyan, M., (2003), "Sintering Atmosphere and Temperature Effect on Hydroxyapatite Coated Type 316L Stainless Steel", Corros. Sci., Vol. 45, pp. 2337-2359.
266. "Standard Specification for Comparison of Ceramic Hydroxyapatite for Surgical Implants", (2003), ASTM F1185-03, ASTM International.
267. **Suchanek, W.** and Yoshimura, M., (1998), "Processing and Properties of Hydroxyapatite-based Biomaterials for Use as Hard Tissue Replacement Implants", J. Mater. Res. Vol. 13 (1), pp. 94-117.
268. **Sulzer Metco**, <http://www.sulzermetco.com>.
269. **Sun, L.**, Berndt, C. C., Khor, K.A., Gross, K. A. and Cheang, H. N., (2002), "Surface Characterization and Dissolution Behavior of Plasma-sprayed Hydroxyapatite Coating", J. Biomed. Mater. Res., Vol. 62, pp. 228-236.
270. **Sun, L.**, Berndt, C.C. and Grey, C.P., (2003), "Phase, Structural and Microstructural Investigations of Plasma Spray Hydroxyapatite Coatings", Mater. Sci. Eng. A, Vol. 36, pp. 70-84.
271. **Sun, L.**, Berndt, C.C., Gross, K.A. and Kucuk, A., (2001), "Material Fundamentals and Clinical Performance of Plasma-sprayed Hydroxyapatite Coatings: A Review", J. Biomed. Mater. Res., Vol. 58(5), pp. 570-592.
272. **Sun, R.**, Li, M., Lu, Y., Wang, A., (2006), "Immersion Behavior of Hydroxyapatite (HA) Powders Before and After Sintering", Mater. Charact., Vol. 56, pp 250-254.
273. **Svetina, M.**, Ciacchi, L.C., Sbaizero, O., Meriani, S. and De Vita, A., (2001), "Deposition of Calcium Ions on Rutile (110): A First-Principles Investigation", Acta Mater., Vol. 49, pp. 2169-2177.
274. **Take, S.**, Kasahara, M., Itou, Y., Kawaguti, M., Oshima, M. and Itoi, Y., (2010), "Evaluation of Credibility of Plasma Spray Biocompatible HAp Coatings by

- Electrochemical Impedance Technique”, ECS Transactions, Eds. Hansen, D., Alfantazi, A. and Missert, N., Vol. 33, pp. 49-55.
275. **Tampieri, A., Celotti, G., Sprio, S. and Mingazzini, C., (2000),** “Characterization of Synthatic Hydroxyapatite and Attempt to Improve Their Thermal Stability”, Mater. Chem. Phys., Vol. 64, pp. 54-61.
276. **Tercero, J. E., Namin, S., Lahiri, D., Balani, K., Tsoukyas, N. and Agarwal, A., (2009),** “Effect of Carbon Nanotube and Aluminum Oxide Addition on Plasma-sprayed Hydroxyapatite Coating’s Mechanical Properties and Biocompatibility”, Mater. Sci. Eng., C, Vol. 29, pp. 2195-2202.
277. **Tetsworth, K. and Paley, D., (1994),** “Accuracy of Correction of Complex Lower-extremity Deformities by the Ilizarov Method”, Clin. Orthop. Relat. Res., Vol. 301, pp. 102-110.
278. **The Engineering ToolBox,** http://www.engineeringtoolbox.com/linear-expansion-coefficients-d_95.html.
279. **Thomas, K. A., (1994)** “Hydroxyapatite Coatings”, Orthopedics, Vol. 17, pp. 267-278.
280. **Thomas, K. A., Kay, J. F., Cook, S. D. and Jarcho, M., (1987),** “The Effect of Surface Macrotecture and Hydroxyapatite Coating on the Mechanical Strength and Histologic Profiles of Titanium Implant Material”, J. Biomed. Mater. Res., Vol. 21, pp. 1395-1414.
281. **Todd, R. C., Lightowl, C. D. and Harris, J., (1972),** “Total Hip Replacement in Osteioarthrosis using Charnley Prosthesis”, Br. Med. J., Vol. 2, pp. 752.
282. **Tomaszek, R., Pawlowwski, L., Gengembre, L., Laureyys, J. and le Maguer, A., (2007),** “Microstructure of Suspension Plasma Sprayed Multilayer Coatings of hydroxyapatite and Titanium Dioxide”, Surf. Coat. Technol., Vol. 201, pp. 7432-7440.
283. **Tong, W., Chen, J. and Zhang, X., (1995),** “Amorphorization and Recrystallization during Plasma Spraying of Hydroxyapatite”, Biomaterials, Vol. 16, pp. 829-832.
284. **Tong, W., Yang, Z., Zhang, X., Yang, A., Feng, J., Cao, Y and Chen, J., (1998),** “Studies on Diffusion in X-ray Diffraction Patterns of Plasma Sprayed Hydroxyapatite Coatings”, J. Biomed. Mater. Res. Vol. 40, pp. 407-413.
285. **Trommer, R. M., Santos, L. A. and Bergmann, C.P., (2007),** “Alternative Techniques for Hydroxyapatite Coatings”, Surf. Coat. Technol., Vol. 201, pp. 9587-9593.
286. **Tucker, C., (1982),** “Hand Book of Deposition Technologies for Films and Coatings”, Eds. Bunshah, R.F., Noyes Publications, Park Ridge, NJ, USA, ISBN: 0-8155-1337-2 pp. 617-665.

287. **United Performance Metals, O'Neal High-Performance Metals Group**, www.upmet.com/316-physical.shtml.
288. **Ústel, F.**, (1995), "Plasma Spray Coating Technology", M. Sc. Thesis, Istanbul Technical University, Maslak, Istanbul, Turkey.
289. **Vallet-Regi, M. and Gonzalez-Calbet, J. M.**, (2004), "Calcium Phosphate as Substitution of Bone Tissues", *Prog. Solid State Chem.*, Vol. 32 (1-20), pp. 1-31.
290. **Van Citters, D. W., Kennedy, F. E., Currier, J. H., Collier, J. P. and Nichols, T. D.**, (2004), "A Multi-Station Rolling/Sliding Tribotester for Knee Bearing Materials", *ASME J. Tribol.*, Vol. 126, pp. 380-385.
291. **Wakai, F., Kodama, Y., Sakagawa, S. and Nonami, T.**, (1990), "Superplasticity of Hot Isostatically Pressed hydroxyapatite", *J. Am. Ceram. Soc.*, Vol. 73, pp. 457-460.
292. **Walker, P.S., Schneeweis, P., Murphy, S. and Nelson, P.**, (1987), "Strains and Micromotions of Press-fit Femoral Stem Prostheses", *J. Biomech.*, Vol. 20, pp. 693-702.
293. **Wang, A., Essner, A., Stark, C. and Dumbleton, J. H.**, (1999), "A Biaxial Line-contact Wear Machine for the Evaluation of Implant Bearing Materials for Total Knee Joint Replacement, *Wear*, Vol. 225-229, pp. 707-707
294. **Wang, B.C., Chang, E., Lee, T.M. and Yang, C.Y.**, (1995), "Changes in Phases and Crystallinity of Plasma-sprayed Hydroxyapatite Coatings under Heat Treatment: A Quantitative Study", *J. Biomed. Mater. Res. A*, Vol. 29, pp. 1483-1492.
295. **Wang, B.S. H.**, (2004), "Hydroxyapatite Degradation and Biocompatibility", B.Phil. Thesis, Graduate School of Ohio State University, Ohio State University, USA.
296. **Wang, Q., Shirong, G. and Dekun, Z.**, (2005), "Nano-mechanical Properties and Tribological Behaviors of Nanosized HA/partially-stabilized Zirconia composites", *Wear*, Vol. 259, pp. 952-957.
297. **Wang, X., Li, Y., Lin, J., Hodgson, P. D. and Wen, C.**, (2008), "Effect of Heat Treatment on the Bond Strength of Apatite Layer on Ti Substrate", *Dent. Mater.*, Vol. 24, pp. 1549-1555.
298. **Wang, Y., Khor, K. A. and Cheang, P.**, (1998), "Thermal Spraying of Functionally Graded Calcium phosphate Coatings for Biomedical Implants", *J. Therm. Spray Technol.*, Vol. 7(1), pp. 50-57.
299. **Wang, Y., Zhang, S., Zeng, X., Cheng, K., Qian, M. and Weng, W.**, (2007), "In Vitro Behavior of Fluoridated Hydroxyapatite Coatings in Organic-containing Simulated Body Fluid", *Mater. Sci. Eng.*, Vol. C27, pp. 244-250.

300. **Weast, R.C.**, (1985-1986), "The CRC Handbook of Chemistry and Physics", 85th ed., Eds. Lide, D.R., CRC Press, Boca Raton, Florida, USA, ISBN: 9781420090840
301. **Weimlaender, M.**, Kennedy, E. B., Lekovic, V., Beumer, J., Moy, P. K. and Lewis, S., (1992), "Histomorphometry of Bone Apposition Around Three Types of Endosseous Dental Implants", *Inter. J. Oral Maxillofac Implants*, Vol. 7, pp. 491-496.
302. **Weng, J.**, Liu, Q, Wolke, J. G. C., Zhang, X. and de Groot, K., (1997), "Formation and Characteristics of the Apatite Layer on Plasma-sprayed Hydroxyapatite Coatings in Simulated Body Fluid", *Biomaterials*, Vol. 18, pp. 1027-1035.
303. **Weng, J.**, Liu, X., Li, X. and Zhang, X., (1995), "Intrinsic Factors of Apatite Influencing its Amorphization during Plasma-Sprayed Coating" *Biomaterials*, Vol. 16, pp. 39-44.
304. **Weng, J.**, Liu, X., Zhang, X. and de Groot, K., (1996), "Integrity and Thermal Decomposition of Apatite in Coatings Influenced by Underlying Titanium during Plasma-spraying and Post-heat-treatment", *J. Biomed. Mater. Res.*, Vol. 30, pp. 5-11.
305. **Weng, J.**, Liu, X., Zhang, X. and Ji, X., (1994), "Thermal Decomposition of Hydroxyapatite Structure Induced by Titanium and its Dioxide", *J. Mater. Sci. Lett.*, Vol. 13, pp. 159-161.
306. **Wolke, J. G. C.**, Klein, C. P. A. T. and de Groot, K., (1991), "Bioceramics for Maxillofacial Applications", In *Bioceramic and The Human Body*, Eds. Ravaglioli, A. and Krajewski, A., Elsevier, Amsterdam, pp. 166-180.
307. **Wroblewski, B. M.**, (1997), "Wear of High Density Polyethylene Socket in Total Hip Arthroplasty and Its Role in Endosteal Cavitation", *Proc. Instn. Mech. Engrs., Part H, J. Engineering in Medicine*, Vol. 211(H1), pp. 109-118.
308. **Wu, Z-J.**, He, L-P. and Chen, Z-Z., (2006), "Fabrication and Characterization of Hydroxyapatite/Al₂O₃ Biocomposite Coating on Titanium", *Trans. Nonferrous Met. Soc., China*, Vol. 16, pp. 259-266.
309. **Xie, Y.**, Zheng, X., Ding, C., Zhai, W., Chang, J. and Ji, H., (2009), "Preparation and Characterization of CaO-ZrO₂-SiO₂ Coating for Potential Application in Biomedicine", *J. Therm. Spray Technol.*, Vol. 18, pp. 678-685.
310. **Xu, Y.**, Wang, D., Yang, L. and Tang, H., (2001), "Hydrothermal Conversion of Coral into Hydroxyapatite", *Mater. Charact.*, Vol. 47 (2), pp. 83-87.
311. **Xue, W.**, Tao, S., Liu, X., Zheng, X. and Ding, C., (2004), "In Vivo Evaluation of Plasma Sprayed Hydroxyapatite Coatings Having Different Crystallinity", *Biomaterials*, Vol. 25, pp. 415-421.

312. **Yamada, K.,** Imamura, K., Itoh, H., Iwata, H. and Maruno, S., (2001), "Bone Bonding Behavior of the Hydroxyapatite Containing Glass-titanium Composite Prepared by Cullet Method", *Biomaterials*, Vol. 22, pp. 2207-2214.
313. **Yang, C-W. and Lui, T-S.,** (2008), "Microstructural Self-healing Effect of Hydrothermal Crystallization on Bonding Strength and Failure Mechanism of Hydroxyapatite Coatings", *J. Euro. Ceram. Soc.*, Vol. 28, pp. 2151-2159.
314. **Yang, C-W., Lee, T-M., Lui, T-S. and Chang, E.,** (2006), "Effect of Post Vacuum Heating on the Microstructural Feature and Bonding Strength of Plasma-Sprayed Hydroxyapatite Coatings", *Mater. Sci. Eng. C.*, Vol. 26, pp. 1395-1400.
315. **Yang, C-W., Lui, T-S. and Chen, L-H.,** (2009B), "Hydrothermal Crystallization Effect on the Improvement of Erosion Resistance and Reliability of Plasma-sprayed Hydroxyapatite Coatings", *Thin Solid Films*, Vol. 517, pp. 5380-5385.
316. **Yang, Y.C. and Chang, E.,** (2003), "The Bonding of Plasma-sprayed Hydroxyapatite coatings to Titanium: Effect of Processing, Porosity and residual Stress", *Thin Solid Films*, Vol. 444, pp. 260-275.
317. **Yang, Y-C.,** (2007), "Influence of Residual Stress on Bonding Strength of the Plasma-sprayed Hydroxyapatite Coating after the Vacuum Heat Treatment", *Surf. Coat. Technol.*, Vol. 201, pp. 7187-7193.
318. **Yang, Y-C., Yang, C-W., Chen, L-R., Wu M-C., Lui, T-S., Kuo, A. and Lee, T-M.,** (2009A), "Effect of Vacuum Post-heat Treatment of Plasma-sprayed Hydroxyapatite Coatings on Their In Vitro and In Vivo Biological Responses", *J. Med. Bio. Eng.*, Vol. 29, pp. 296-302.
319. **Yankee, S. J. and Pletka, B. J.,** (1991), "An Investigation of Plasma Sprayed Hydroxyapatite Splat", In *Proc. Thermal Spray Coatings: Properties, Processes and Applications*, 4th National Thermal Spray Conference, Eds. Bernecki, T. F., Pittsburgh, 4th – 10th May.
320. **Yankee, S. J. and Pletka, B. J.,** (1992), "Microstructural Analysis of Impacted Hydroxyapatite Droplets", In *Proc. Thermal Spray: International Advances in Coatings Technology*, Eds., Berndt, C. C., 13th International Thermal Spray, Orlando, Florida, 28th May – 5th June.
321. **Yilmaz, Ş.,** (2009), "An Evaluation of Plasma-sprayed Coatings Based on Al₂O₃ and Al₂O₃-13 wt% TiO₂ with Bond Coat on Pure Titanium Substrate", *Ceram. Inter.*, Vol. 35, pp. 3017-2022.

322. **Yip, C. S., Khor, K. A., Loh, N. L. and Cheang, P., (1997), "Thermal Spraying of Ti-6Al-4V/Hydroxyapatite Composite Coatings: Powder Processing and Post-Spray Treatment", J. Mater. Process. Technol., Vol. 65, pp. 73-79.**
323. **Yoo, Y.H., Le, D.P., Kim, J.G., Kim, S.K. and Vinh, P.V., (2008), "Corrosion Behavior of TiN, TiAlN, TiAlSiN Thin Films Deposited on Tool Steel in the 3.5 wt% NaCl Solution", Thin Solid Films, Vol. 516, pp. 3544-3548.**
324. **Yoshida, M., (1993), "Effect of Hot Corrosion on the Mechanical Performances of Superalloys and Coating Systems", Corros. Sci., Vol. 35 (5-8), pp. 1115-1124.**
325. **Yu, L-G., Khor, K.A., Li, H. and Cheang, P., (2003), "Effect of Spark Plasma Sintering on the Microstructure and In Vitro Behavior of Plasma Sprayed HA Coatings", Biomaterials, Vol. 24, pp. 2695-2705.**
326. **Zangh, C., (2000), "Mechanical Integrity of Plasma-sprayed Hydroxyapatite Coatings on Ti-6Al-4V Implants", Ph.D., Thesis, Department of Mechanical Engineering, Hong Kong University of Science and Technology, Hong Kong, China.**
327. **Zhang, M., Liu, C., Zhang, X., Pan, S. and Xu, Y., (2010), "Al₂O₃/diopside Ceramic composites and Their Behavior in Simulated Body Fluid", Ceram. Inter., Vol. 36, pp. 2505-2509.**
328. **Zhang, Q., Chen, J., Feng, J., Cao, Y, Deng, C. and Zhang, X., (2003), "Dissolution and Mineralization Behaviors of HA Coatings", Biomaterials, Vol. 24, pp. 4741-4748.**
329. **Zhao, G-L., Wen, G-W. and Wu, K., (2009), "Influence of Processing Parameters at Heat Treatment on Phase Composition and Microstructure of Plasma Sprayed Hydroxyapatite Coatings", Trans. Nonferrous Met. Soc. China, Vol. 19, pp. s463-s469.**
330. **Zheng, X. B., Shi, J. M. and Liu, X. Y., (2001), "Developments of Plasma-sprayed Biomedical Coatings", J. Ceram. Process Res., Vol. 2 (4), pp. 174-179.**
331. **Zheng, X., Huang, M. and Ding, C., (2000), "Bonding Strength of Plasma-sprayed Hydroxyapatite/Ti Composite Coatings", Biomaterials, Vol. 21, pp. 841-849.**
332. **Zyman, Z., Gao, Y., Chen, J. and Zhang, X. ., (1993B), "Crystal Growth in the Surface Layers of HA Coating During Their Dissolution in Water", in Proc. The 1st Far-Eastern Symposium on Biomedical Materials, Beijing, China, pp. 119**
333. **Zyman, Z., Weng, J., Liu, X., Zhang, X. and Ma, Z., (1993A), "Amorphous Phase and Morphological Structure of Hydroxyapatite Plasma Coatings", Biomaterials, Vol. 14 (3), pp. 225-228.**

Appendix I

Exova (UK) Ltd
Formerly Bodycote Testing Ltd
Lochend Industrial Estate
Newbridge
Midlothian
EH28 8PL

T: 0131 333 4360
F: 0131 333 5135
E:
W: www.exova.com



CERTIFICATE OF ANALYSIS

PRODUCT : Analysis of Hydroxylapatite Powder
CLIENT : Plasma Biotol Limited, Whitecross Road Industrial Est, Tideswell, North Derbyshire
SK17 8PY
BATCH No. : Batch P301 S (Sample 3) 1190
CERT. No. : L030655
ISSUE No. : 1
LAB REF No. : 054858
ORDER No. : 3203

Page 1 of 1

Item	Test	Specification	Method	Results
1	Heavy Metals	0.003%	USP	passes test

ANALYSED BY : M Nash

DATE OF ANALYSIS: 12 Aug 2009

Certificate Comments

APPROVED BY :

DATE APPROVED : 12 Aug 2009

L. McFaul
Operations Manager
For and on behalf of
Exova (UK) Ltd

Appendix II



HEALTH AND SAFETY

STATUS CURRENT	DEPARTMENT ALL	
SUBJECT	CALCIUM HYDROXYLAPATITE	
Chemical Formula	$\text{Ca}_{10}(\text{PO}_4)_6(\text{OH})_2$	
Trivial Name	Synthetic Bone Mineral	
Trade Name	Captal	
Physical Form	Powder, Granules	
Flammability	Non Inflammable	
Toxicity	Non Toxic	
Chemical Reactivity	Acids	Dissolves Below pH 5.5
	Alkalis	Insoluble
	Organic Solvents	Non Reactive
Emergency Phone Number	+44 (0)1298 872348	
Manufacturer	Plasma Biotals Ltd Unit 1 Whitecross Road Industrial Estate Tideswell SK17 8PY UK	
EEC Food Codex	E341	
CAS Registry Number	12167-74-7	
EINECS Registry Number	2353306	
General Handling Precautions Powder		
Avoid breathing dust. Masks suitable for sub-micron particle removal should be worn. Airborne dust may cause eye irritation. Goggles should be worn.		
Prolonged handling of the powder tends to remove natural oils from the skin and lead to dryness. Wear Rubber gloves.		

Appendix III



Laboratory Report

Health Improvement Group
Health and Safety Laboratory
Harpur Hill Buxton SK17 9JN
An agency of the Health and Safety Executive

Worksheet No: 08-0747B Job Code: JC9900042 Receipt Date: 03/08/2009

Sample Origin: Plasma Diotal Limited, Whitecross Rd Ind Estate, Tideswell, Derbyshire, SK17 8PY
Customer Name and address: Mr Paul Stoverson
Plasma Diotal Limited, Whitecross Rd Ind Estate,
Tideswell, Derbyshire, SK17 8PY
Date tests complete: 06/08/2009 Report Issue No. 2

This report has been re-issued to correct the sample results due to a calculation error being found.

The results below are for the analysis of the HA powder sample provided.

The sample was ultrasonically digested in nitric acid prior to analysis by Inductively Coupled Plasma - Mass Spectrometry (ICP-MS)

Concentration of element (ppm) - (mg/kg)

HSL Sample No.	Sample Ref No.	As	Cd	Hg	Pb
05542/09	HA Powder - P301S Sample 3 XRD Ident 7479	< 1.0	< 1.0	< 1.0	< 1.0

Reported by:

D Musgrave (Higher Scientist)

Signature:

Date: 05/11/2009

Checked by:

J Fordur (Scientist)

Signature:

Date: 05/11/2009

Opinions and interpretations expressed herein are outside the scope of UKAS accreditation

Sample retention time from report date
(* Choose one)

1 mth / 3 mths / 6 mths / 12 mths / according to
legal proceedings storage policy / not applicable

EM1b Issued March 2007

Page 1 of 1

Appendix IV

Material	Coefficient of thermal expansion 10^{-6} m/m°C	Reference
AISI 316L SS	16.5	United Performance Metals
Pure Ti	8.6	The Engineering ToolBox
Al ₂ O ₃	8.4	Schutze et al., (2006)
TiO ₂	8.6	Jagpat et al., (2004)
Hydroxyapatite	10.6	Miyazaki et al., (2009)
Human Teeth (perpendicular to growth)	15.5	Miyazaki et al., (2009)
Human Teeth (parallel to growth)	18.9	Miyazaki et al., (2009)